
LECTURES ON
SUPERCONDUCTIVITY IN
NETWORKS AND
MESOSCOPIC SYSTEMS

In memory of Robert D. Parmentier

19980923 012

REPORT DOCUMENTATION PAGE

Form Approved OMB No. 0704-0188

Public reporting burden for this collection of information is estimated to average 1 hour per response, including the time for reviewing instructions, searching existing data sources, gathering and maintaining the data needed, and completing and reviewing the collection of information. Send comments regarding this burden estimate or any other aspect of this collection of information, including suggestions for reducing this burden to Washington Headquarters Services, Directorate for Information Operations and Reports, 1215 Jefferson Davis Highway, Suite 1204, Arlington, VA 22202-4302, and to the Office of Management and Budget, Paperwork Reduction Project (0704-0188), Washington, DC 20503.

1. AGENCY USE ONLY (Leave blank)		2. REPORT DATE 28 July 1998	3. REPORT TYPE AND DATES COVERED Conference Proceedings	
4. TITLE AND SUBTITLE Lectures On Superconductivity in Networks and Mesoscopic Systems			5. FUNDING NUMBERS F6170897W0185	
6. AUTHOR(S) Conference Committee				
7. PERFORMING ORGANIZATION NAME(S) AND ADDRESS(ES) Univerita di Roma Via della Ricerca Scientifica 1 Rome I-00133 Italy			8. PERFORMING ORGANIZATION REPORT NUMBER N/A	
9. SPONSORING/MONITORING AGENCY NAME(S) AND ADDRESS(ES) EOARD PSC 802 BOX 14 FPO 09499-0200			10. SPONSORING/MONITORING AGENCY REPORT NUMBER CSP 97-1059	
11. SUPPLEMENTARY NOTES				
12a. DISTRIBUTION/AVAILABILITY STATEMENT Approved for public release; distribution is unlimited.			12b. DISTRIBUTION CODE A	
13. ABSTRACT (Maximum 200 words) The Final Proceedings for Superconductivity in Networks and Mesoscopic Systems, 7 September 1997 - 21 September 1997.				
14. SUBJECT TERMS Superconductivity, Superconductivity, Josephson junctions, Josephson junctions, Mesoscopic systems, Mesoscopic systems			15. NUMBER OF PAGES 423	
			16. PRICE CODE N/A	
17. SECURITY CLASSIFICATION OF REPORT UNCLASSIFIED	18. SECURITY CLASSIFICATION OF THIS PAGE UNCLASSIFIED	19. SECURITY CLASSIFICATION OF ABSTRACT UNCLASSIFIED	20. LIMITATION OF ABSTRACT UL	

NSN 7540-01-280-5500

Standard Form 298 (Rev. 2-89)
Prescribed by ANSI Std. Z39-18
298-102

DTIC QUALITY INSPECTED 1

LECTURES ON SUPERCONDUCTIVITY IN NETWORKS AND MESOSCOPIC SYSTEMS

Pontignano, Italy September 1997

EDITORS

Carlo Giovannella

Università di Roma "Tor Vergata," Italy

Colin J. Lambert

University of Lancaster, United Kingdom

AIP

American Institute of Physics

**AIP CONFERENCE
PROCEEDINGS 427**

Woodbury, New York

Editors:

Carlo Giovannella
Dipartimento di Fisica
Università di Roma "Tor Vergata"
Via della Ricerca Scientifica 1
I-00173 Roma
ITALY
Email: supnet@roma2.infn.it

Colin J. Lambert
School of Physics and Chemistry
Lancaster University
Lancaster LA1 4YB
UNITED KINGDOM
Email: c.lambert@lancaster.ac.uk

Authorization to photocopy items for internal or personal use, beyond the free copying permitted under the 1978 U.S. Copyright Law (see statement below), is granted by the American Institute of Physics for users registered with the Copyright Clearance Center (CCC) Transactional Reporting Service, provided that the base fee of \$15.00 per copy is paid directly to CCC, 222 Rosewood Drive, Danvers, MA 01923. For those organizations that have been granted a photocopy license by CCC, a separate system of payment has been arranged. The fee code for users of the Transactional Reporting Service is: 1-56396-750-2/98 /\$15.00.

© 1998 American Institute of Physics

Individual readers of this volume and nonprofit libraries, acting for them, are permitted to make fair use of the material in it, such as copying an article for use in teaching or research. Permission is granted to quote from this volume in scientific work with the customary acknowledgment of the source. To reprint a figure, table, or other excerpt requires the consent of one of the original authors and notification to AIP. Republication or systematic or multiple reproduction of any material in this volume is permitted only under license from AIP. Address inquiries to Office of Rights and Permissions, 500 Sunnyside Boulevard, Woodbury, NY 11797-2999; phone: 516-576-2268; fax: 516-576-2499; e-mail: rights@aip.org.

L.C. Catalog Card No. 98-70645
ISBN 1-56396-750-2
ISSN 0094-243X
DOE CONF-9709193

Printed in the United States of America

CONTENTS

Preface	vii
---------------	-----

I. ARRAYS IN CLASSICAL REGIME: VORTEX DYNAMICS AND APPLICATION

Nonlinear Dynamics of the Josephson Junction.	3
P. L. Christiansen and N. F. Pedersen	
Long Josephson Junctions and Stacks.	31
A. Ustinov	
General Introduction to Classical Arrays Formalism and Physics.	56
G. Costabile and G. Filatrella	
Dynamics of Josephson Junction Arrays—Models and Numerical Simulations	70
J. C. Ciria and C. Giovannella	
Dynamics of Josephson Junction Arrays—Microscopic Investigations and Applications.	104
Th. Doderer	
RSFQ Logic Devices: Non-Linear Properties and Experimental Investigation	126
J. Mygind	
High- T_c Josephson Junction Arrays and Their Application	144
M. Darula	

II. ARRAYS IN CLASSICAL REGIME: CRITICAL PROPERTIES

Confinement and Quantization Effects in Mesoscopic Superconducting Structures	171
V. V. Moshchalkov, V. Bruyndoncx, E. Rosseel, L. Van Look, M. Baert, M. J. Van Bael, T. Puig, C. Strunk, and Y. Bruynseraede	
Vortex Unbinding in 2D Classical JJ Arrays.	200
P. Minnhagen	
Critical Properties of Classical Josephson Junction Arrays.	217
J. V. José	

III. ARRAYS IN QUANTUM REGIME: VORTEX PROPERTIES AND APPLICATIONS

Particle-Like Aspects of Vortices in Josephson Arrays	237
H. S. J. van der Zant	
Single Electron Tunneling Devices.	256
P. Hadley	

IV. ARRAYS IN QUANTUM REGIME: CRITICAL PROPERTIES

Quantum Phase Transitions in Josephson Junction Arrays.....	273
R. Fazio and G. Schön	
Phase Transitions in Arrays of Ultrasmall Two-Dimensional Josephson Junction Arrays.....	295
J. V. José	
Two-Dimensional Arrays of Low Capacitance Tunnel Junctions: General Properties, Phase Transitions and Hall Effect	313
P. Delsing, C. D. Chen, D. B. Haviland, T. Bergsten, and T. Claeson	

V. TRANSPORT AND PROXIMITY EFFECT IN MESOSCOPIC STRUCTURES

Methods of Quasiclassical Green's Functions in the Theory of Transport Phenomena in Superconducting Mesoscopic Structures	343
A. F. Volkov and V. V. Pavlovskii	
Boundary Conditions in the Theory of Superconductivity.....	359
R. Raimondi	
Phase Coherent Transport in Hybrid Superconducting Nanostructures	377
C. J. Lambert	
Experiments on Proximity Effect.....	396
P. Charlat, H. Courtois, and B. Pannetier	
Author Index.....	417
Subject Index	419

Preface

The last 10 years research on macroscopic quantum phenomena in superconductivity has made a number of significant advances and continues to forge-ahead at a breathtaking pace. On the one hand, improvements in lithographic techniques and deposition technologies have made it possible to decrease the spatial dimensions structures to sub-micron scales, thereby enabling the observation of charging and proximity effects in single junctions and the realization of complex dynamical systems formed from 3D superlattices. On the other hand, the development of powerful desk-top computers has made it possible to simulate the physical properties of very complex classical systems (by including the effect of the full inductance matrix), as well, those of quantum systems (by means of quantum-Monte Carlo and multiple-scattering techniques). In parallel with these developments, the discovery of high T_c superconductivity opened the doors to the possible use of superconducting devices at the nitrogen temperature and acted as a stimulus for further technological developments.

This book is aimed at filling a gap in the current literature on macroscopic quantum phenomena in superconducting arrays and mesoscopic systems. In the recent past, specialist workshops devoted to possible technological applications of Josephson junction arrays (JJA) have been organized in Europe and USA, but the proceedings from these have been of a specialized nature. Moreover all existing texts written to introduce people to properties of superconducting hybrid structures are out-of-date and miss the latest developments in the field. The EU-financed Euroschool on Superconductivity in networks and mesoscopic systems held in Pontignano in September 1997, provides a timely opportunity to fill this lacuna. Thank to the efforts of all the lecturers involved in the Euroschool and to the support of the EOARD (European Office of Aerospace Research and Development) and the GNSM (Gruppo Nazionale di Struttura della Materia) it has been possible to compile this volume of top-level tutorial-style contributions, which encompasses the physics of classical long Josephson junctions, classical and quantum JJAs and phase-coherent quasi-particle transport in hybrid superconducting-normal (S-N) structures. Our efforts have been directed towards ensuring a coherent and harmonic development of the material contained in the School. The enthusiastic response of students attending the Euroschool convinced us of the need to publish the volume in the present form. We believe that the book will be an asset to PhD students in Solid State Physics, to scientists wishing to know more about macroscopic quantum phenomena in superconducting arrays and mesoscopic systems and to researchers already involved in the subject who wish to have a reference book on their desk.

The volume is divided in five sections. The first is devoted to vortex dynamics in classical systems because the displacement of vortices is the phenomena on which is based the development of many cryodevices. This section is opened by a tutorial lecture on the dynamical properties of a single Josephson junction given by P.L. Christiansen and N.F. Pedersen. The basic nonlinear equation of motion is introduced and then applied (sine-Gordon equation) to the case of long and annular Josephson junctions. The condition for the formation of solitonic excitations are discussed, together with the stability conditions and the development of chaotic trajectories. This dynamical description is extended by A. Ustinov to the case of the stacked junctions describing the fluxon-fluxon interaction and the Cerenkov radiation of fluxons. A simple introduction to JJ arrays is given by G. Costabile and G. Filatrella who discuss implications of discretizing the sine-Gordon equation. A detailed and rigorous description of how to model the JJAs is given in the contribution by J.C. Ciria and C. Giovannella. Starting from the JJA Lagrangian, a general equation of motion, that includes the contribution of the full inductance-matrix, is derived and then extended to the more complex case of granular superconductors. A description of vortex dynamics in over damped JJAs follows together with the numerical procedures employed in the simulations. An experimental verification of vortex dynamics in JJA is described in the contribution by T. Doderer that uses LTSEM (Low Temperature Scanning Electron Microscopy) to study average vortex dynamics, JJ locking induced by an

external microwave field and, finally, JJ microwave emission. An overview of possible applications of the JJA is given in the two concluding papers of section I: the first by J. Mygind, describes the present state-of-the-art in the development of low-Tc RSFQ (Rapid Single Flux Quantum) cryoelectronics while the second focuses on possible applications of high-Tc JJ arrays as voltage standards, microwave radiation sources and mixers.

The second section of this volume deals with critical properties of the JJ arrays and related systems. It opens with a contribution, by V.V. Moschchalkov et al., on static magnetic properties of wire-arrays, ranging from a single plaquette to extended arrays. An accurate description of the boundary conditions that determine the $T_c(H)$ phase boundary is given. A detailed description of the critical unbinding of vortices as a function of temperature is given by P. Minnhagen. The mapping between the XY model and the 2D coulomb gas is described and the characteristics of the BKT (Berezinskii-Kosterlitz-Thouless) transition reviewed. An up-to-date overview of the present understanding of the critical properties of the JJA, as obtained by computer simulations, is given by J.V. Jose. He discusses, first, the values of the critical exponents of unfrustrated and fully frustrated XY model as obtained by Monte Carlo simulations and compares critically the RSJ (Resistive Shunted Junction) and the TDGL (Time Dependent Ginzburg Landau) dynamics by applying both to the description of experimental results on magnetic flux noise.

The contribution of H.S.J van der Zant introduces the reader to quantum aspects of the vortex dynamics in JJA, when the charging term, E_c , is no longer negligible. After a description the vortex motion in underdamped JJA, where vortices can be described as classical massive particles, the author introduces the concept of Bloch wave function and discusses the macroscopic quantum tunneling of vortices and phenomena such as Bloch oscillations. When the charging energy dominates, single electron tunneling becomes the only relevant transport mechanism in JJ. Based on such phenomena a new family of devices, starting with the SET transistor, can be envisaged and many new experiments realized. The reader is introduced to this fascinating subject by P. Hadley.

As for the classical counterpart, a very interesting subject is represented by the investigation of the critical properties of the quantum JJA. A first overview on the subject is given by R. Fazio and G. Schön. Following an introduction to the basic formalism (coarse-grain approach and duality transformation) the authors discuss the phase diagram and transport properties of the quantum JJA. A complementary theoretical and numerical view of the subject can be found in the contribution by J.V. Jose. The paper focuses on semi-classical analytic studies (WKB-RG) and quantum Monte Carlo simulations giving a detailed comparison with experimental results. Finally the last contribution of the fourth section by P. Delsing et al. is devoted to experiments on low capacitance JJA, including phase transitions and the Hall effect.

The fifth and last section of the book is dedicated to a recent development in weak superconductivity, namely the proximity effect and the transport properties in hybrid normal-superconducting nanostructures. This section is opened by a review of quasi classical Green's function methods by A.F. Volkov and V.V. Pavlovskii. The potentiality of the method is shown by applying it to the conductance of different S/N structures, to the subgap conductance of the SIN tunnel junctions and to the long-range phase coherence in SNS structures. This overview is complemented by a contribution from R. Raimondi, who discusses the boundary conditions used by the theory. An alternative approach to transport in hybrid superconducting nanostructures is described by C.J. Lambert, who gives an introduction to the multiple scattering approach to transport and describes several paradigms of Andreev scattering, including phase-coherent transport, reentrant and long range proximity effects, Andreev reflection and Andreev interferometers. This section is concluded by a tutorial introduction to experiments by P. Charlat, H. Courtois and B. Pannetier, which outlines recent experiments on proximity effects in metallic mesoscopic structures.

The topics covered by this book are all vibrant areas of current research, though with different levels of maturity. Many questions are still without answers and many problems have not been solved.

Progress in physics depends on people and this book and the related euroschool would have not been realizable without the encouragement, advice and optimism of one man, Robert Dana Parmentier, who we dearly missed one year ago at the end of 1996. Bob was a rare man who was always looking for a constructive solution to problems and for ways to encourage people to achieve the best from themselves. It often happened that an e-mail arrived from Bob pointing out a novel paper or a particular opportunity for research. Bob has been a huge loss not only for his coworkers and Salerno University but for the physics community as a whole. We hope that this book will form a small tribute to his memory.

C. Giovannella
C. Lambert

Acknowledgments

The publication of the present book has been possible only thanks to the financial support of the EOARD (European Office of Aerospace Research and Development) and of the GNSM (Gruppo Nazionale Struttura della Materia) that are warmly acknowledged. We wish to thank Lt. Col. Donald L. McGillen and Prof. Umberto M. Grassano for the interest in our efforts and, as well, Prof. P.L. Christiansen, N. Pedersen, and P. Delsing as members of the Scientific Committee of the Euroscool. Finally we wish to thank the EU for the financial support to the Euroscool under the TMR contract ERBFMMACT960088.

**I. ARRAYS IN CLASSICAL REGIME:
VORTEX DYNAMICS AND APPLICATION**

NONLINEAR DYNAMICS OF THE JOSEPHSON JUNCTION

P.L. Christiansen

Department of Mathematical Modelling, The Technical University of Denmark, DK-2800 Lyngby, Denmark

N.F. Pedersen

Department of Physics, The Technical University of Denmark, DK-2800 Lyngby, Denmark

Abstract.

The basic equations for the Josephson junction are derived in a simple way. We discuss the properties of such junctions under various circumstances - including the effects of damping and capacitance - according to the shunted junction model. Also the effects of an external rf bias current are discussed; this leads to a definition of the various characterizing frequencies and to the appearance of many new phenomena. rf-applications such as SIS-mixers and parametric amplifiers will be mentioned. The introduction of spatial dimensions leads to problems concerning cavity excitations, solitons, and their stability. Finally, conditions for the appearance of chaos in Josephson junctions will be discussed.

Introduction

The following description concentrates on the properties of superconducting Josephson junctions, in particular the unique nonlinear properties that have so much promise for useful applications. Although we largely think in terms of the "old" superconductors, simply because the corresponding thin film Josephson junctions are well characterized, we expect most of the following to hold also for the new high T_c ceramic superconductors; modifications may occur, of course, because of changed parameters.

The basic physics of superconductivity ("old" and new) has been discussed in [1,?] and will not be dealt with in any detail here. However, Section 1 gives a brief

account of the properties of the (autonomous) Josephson junction. Section 2 deals with the Josephson junction in external circuits, in particular a cavity. Section 3 discusses the properties of a long Josephson junction, i.e. a Josephson transmission line with solitons. The section summarizes soliton dynamics by perturbation theory, soliton experiments for the overlap geometry and the annular geometry, sampling measurements of solitons, stability of solitons, and applications of the Josephson transmission line. Section 4 introduces very briefly the topic of external pumping with time-varying signals, i.e. rf properties. Finally, Section 5 discusses the chaos that appears in the special case of very large pumping signals. The paper is summarized in Section 6.

1. The Autonomous Josephson Junction

The most widely investigated Josephson junction system is the current-driven Josephson junction, a description of which may be found, for example in one of the good recent books on the subject [3,4].

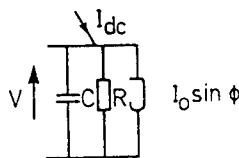


Figure 1. Equivalent diagram for a small Josephson junction.

The Josephson junction consists of two superconducting electrodes separated by a tunnelling barrier. The equations with an external driving current I_{DC} may be written [3,4]

$$CdV/dt + V/R + I_0 \sin \phi = I_{DC} \quad (1)$$

$$d\phi/dt = 2eV/\hbar. \quad (2)$$

Eq. (2) is the famous Josephson frequency to voltage relation and Eq. (1) is Kirchhoff's law applied to the Josephson junction equivalent circuit shown in Fig. 1. The equation for a Josephson junction also describes other important physical systems, such as the synchronous motor, the phase-locked loop, pinned charge density waves, and the damped driven pendulum. In a Josephson junction the tunnelling currents are due to two different kinds of charge carriers, Cooper pairs and normal electrons. The unique nonlinear properties are due to the Cooper pair current, which may be expressed as $I_0 \sin \phi$. Here ϕ is the pair phase difference across the junction, and I_0 is the maximum pair current. In addition, a shunt resistance R carries a normal electron current (V/R), and a capacitance C carries a

capacitive current $C(dV/dt)$. (\hbar is Planck's constant and e is the electron charge). With time normalized to the reciprocal plasma frequency $\omega_0^{-1} = (\hbar C/2eI_0)^{1/2}$ and current normalized to the critical current I_0 , these equations may be combined into a single dimensionless equation, [3,4]

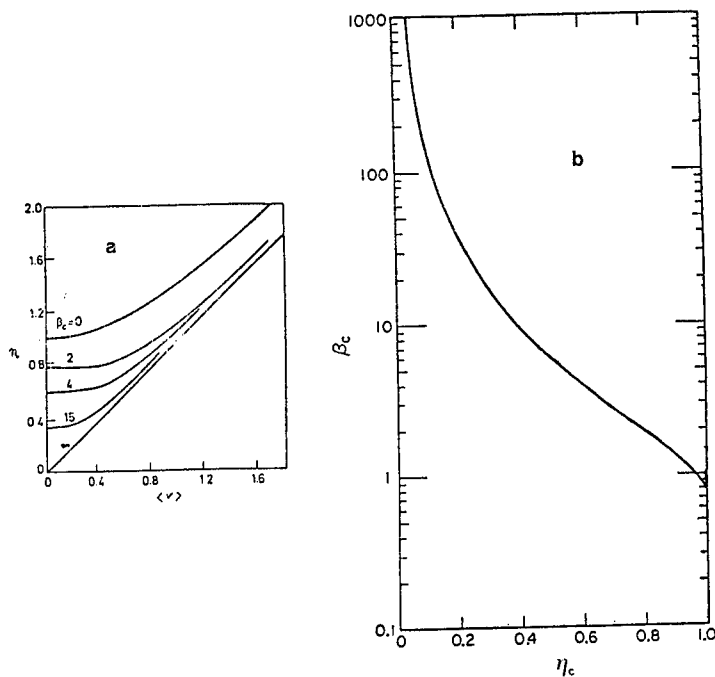


Figure 2. (a) I-V curves for the shunted junction model. (b) The McCumber curve.

$$\Phi_{tt} + \alpha \Phi_t + \sin \Phi = \eta \quad (3)$$

$$v = \Phi_t. \quad (4)$$

The plasma frequency, ω_0 , is a natural oscillation frequency for the Josephson junction, corresponding to the pendulum frequency in a pendulum. The damping parameter α is given by $(1/\sqrt{\beta_c})$ where β_c - the McCumber parameter - is given by $\beta_c = 2eR^2 I_0 C / \hbar$, η is the normalized (to I_0) dc bias current, and v is the voltage normalized to $\hbar \omega_0 / 2e$.

The dynamical behaviour of Eq. (3,4) may be described in the following way. For η (current) below one, a time-independent solution $\Phi = \arcsin \eta$ and voltage

$v = 0$ is possible.

For very large values of η the average voltage $\langle v \rangle$ is determined by the resistance (the average value of the supercurrent is less than one), i.e. $\eta \approx \alpha \langle \Phi_t \rangle$. If we choose another normalizing frequency, the so-called characteristic frequency $\omega_C = 2eRI_0/\hbar$, and normalize the time to $1/\omega_C$ and the voltage to RI_0 , we may obtain a convenient plot of a series of I-V curves with β_C as a parameter [3,4]. These are shown in Fig. 2a. We notice that for high damping, $\beta_C = 0$, the curve is single valued. For $\beta_C = 0$ hysteresis occurs, i.e. for $\eta_c < \eta < 1$ a zero-voltage solution coexists with a solution at a finite voltage. The threshold bias value η_c is a function of the damping parameter, which is shown in Fig. 2b. The details of the dynamical behaviour of the so-called shunted junction model may be found in [3,4]; it is the most important and widely used Josephson junction model. It should be mentioned that no general analytical solution to it exists; however, the qualitative behaviour, approximation formulas, and numerical calculations are described in great detail in the literature.

2. The Josephson Junction with External Circuits

For the purpose of the present paper we will write Eqs. (3,4) as a set of two coupled first-order equations.

$$\dot{\Phi} = v \quad (5)$$

$$\dot{v} = \eta - \alpha v - \sin \Phi - i_s \quad (6)$$

where we have introduced i_s for the interaction with the external circuit (see Fig. 3). Eqs. (5,6) is a set of coupled first order differential equations that with $i_s = 0$ describes the bare junction. For a Josephson junction interaction with external circuits ($i_s > 0$) additional equations describing those circuits are necessary. An example is a Josephson junction coupled to a cavity. Its equivalent diagram is shown in Fig. 3a; with time normalized to the inverse plasma frequency $\omega_0^{-1} = (\hbar C/2eI_0)^{1/2}$ it is described by Eqs. (5,6) for the basic Josephson junction together with

$$\dot{i}_s = (v - (\omega_0/\sqrt{\beta_c})r'i_s)\beta_L \quad (7)$$

for the series resonance circuit. Here, r' is the resistance normalized to the junction shunt resistance R and $\beta_L = 2eLI_0/\hbar$.

We choose instead to normalize to the characteristic frequency $\omega_C = (2eRI_0/\hbar)$. Further, for all practical purposes we have $r' \ll R$ and may thus disregard the current through R . Accordingly, we will use r' instead of R in the definition of ω_C and β_C [5].

Eqs. (5-7) then we get the nice structure of two equations for the Josephson junction, Eqs. (8-9), and one for the external circuit, Eq. (10), with coupling between them, Eqs. (9-10), through i_s

$$\dot{\Phi} = v \quad (8)$$

$$\dot{v} = (\eta - rv - \sin\Phi - i_s)/\beta_C \quad (9)$$

$$\dot{i}_s = (v - i_s)/\beta_L. \quad (10)$$

The qualitative behaviour of a junction coupled to a cavity is the following. A Josephson junction with a dc voltage V_0 oscillates at a frequency which is given by $\omega = 2eV_0/\hbar$. When that frequency is in the vicinity of the cavity resonance frequency, a nonlinear interaction with frequency locking may occur. For strong locking the oscillation frequency is determined by the cavity frequency. When the frequency is only slightly detuned from resonance, the system may oscillate at the cavity frequency for some time and then shift to the "Josephson frequency" for some time - before going back to the cavity frequency, and so on. The motion becomes intermittent [4,5]. The I-V-curve of such a system is shown qualitatively in Fig. 3b. The detailed dynamical behaviour of the system, Eq. (8 - 10), is described in [5].

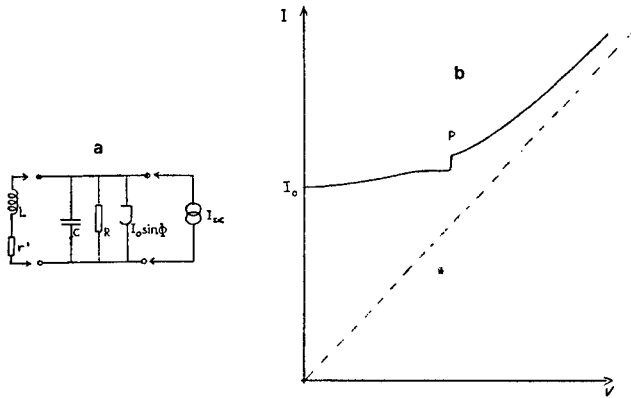


Figure 3. Josephson junction coupled to a cavity. (a) Equivalent diagram. (b) The I-V curve with a cavity-induced step near P.

3. Long Josephson Junctions: Spatial Dependence

Already in the previous section, the cavity mode involves a spatial variation of the phase, although it is not explicitly visible in the lumped element equivalent circuit diagram.

As another extension of the simple Josephson junction let us consider what happens when a spatial variation of the pair phase is allowed. We may get a new type of excitation called a **soliton**. Indeed, the long Josephson junction, or the Josephson transmission line (JTL), is one of the physical systems where soliton propagation is accessible for direct experimental measurements [6,7]. For the purpose of this presentation it suffices to note that the physical manifestation of the soliton is a fluxon, i.e. a quantum of magnetic flux $\Phi_0 = h/2e = 2.064 \times 10^{-15}$ Vs. Moving fluxons in the Josephson transmission lines manifest themselves as the so-called zero field steps (ZFS) in the dc current-voltage characteristic of the Josephson junction - somewhat similar in appearance to the cavity step discussed in the previous section. Fig. 4a shows the equivalent diagram for a JTL and Fig. 4b shows the geometry of a long junction of the so-called overlap type. The physical origin of the inductance L' shown in Fig. 4a is Cooper pair currents within the so-called London penetration layer of thickness λ_L (Fig. 4b). A possible resistance, R' , due to a flow of normal electrons in the same layer is also shown. Taking all these circuit elements into account, the wave equation for the JTL may be written as an extension of Eqs. (3-4)

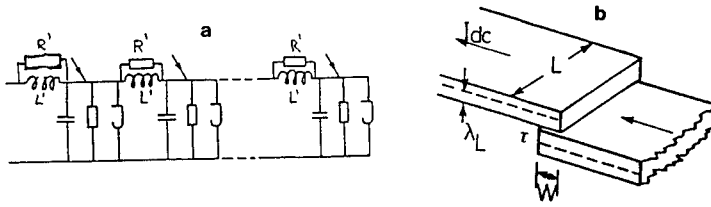


Figure 4. (a) Equivalent diagram for a Josephson transmission line. (b) Schematic drawing of junction geometry.

$$-\Phi_{xx} + \Phi_{tt} + \sin\Phi = \eta - \alpha\Phi_t + \beta\Phi_{xt} \quad (11)$$

with (normalized) voltage $v = \Phi_t$ (as in Eq. (4)) and (normalized) current $i = -\Phi_x$. Eq. (11) is the perturbed sine-Gordon equation [8]. The additional normalizations used are as follows: Length is measured in units of the so-called Josephson penetration depth $\lambda_J = \sqrt{(\hbar/2de\mu_0 J)}$. The damping parameter β is given by $\beta = L'\omega_0/R'$, J is the current density, and d is the magnetic thickness of the junction, $d = 2\lambda_L + \tau$. The junction length, L , is assumed large, and the width, W , is assumed small compared with Josephson penetration depth. Finally, velocities become normalized to the velocity of light in the barrier, c , given by $\bar{c} = c\sqrt{\tau/d}$, where c is the velocity of light in vacuum. The expression for \bar{c} reflects the fact that electric fields exist only across the tunnelling barrier of thickness, τ , whereas magnetic fields exist both in the barrier and the penetration layers (see Fig. 4b). For typical experimental junctions ("old" superconductors) \bar{c} is a few per cent of c .

3a. Perturbation Calculation for the Infinite Line Soliton Dynamics

The methods and ideas in this section are largely based on the work of McLaughlin and Scott [6]. With right-hand side equal to zero, Eq. (11) is the sine-Gordon equation. The loss and bias terms on the right-hand side are considered as a perturbation to the sine-Gordon equation. The unperturbed sine-Gordon equation has the well-known analytical single-soliton solution [6].

$$\Phi = 4 \tan^{-1} \exp \theta \quad (12)$$

where $\theta = (x - ut)\gamma(u)$ and $\gamma(u) = 1/\sqrt{1 - u^2}$ is the Lorentz factor. The solution gives rise to a 2π phase shift over a length of a few λ_J , and its derivative Φ_x represents a voltage pulse. Note that the form of the solution — a travelling wave in the parameter $\theta = \gamma(u)(x - ut)$ — is a consequence of the Lorentz invariance of the sine-Gordon equation. The sine-Gordon soliton behaves very much like a relativistic particle with energy, H , and momentum, P , given by

$$H = 8\gamma(u), P = 8u\gamma(u). \quad (13)$$

With the normalizations used here the rest mass of the soliton is 8. In Eq. (12) the velocity u is a free parameter. As shown in [6] the perturbation terms are included by assuming a solution of the same form as that in Eq. (12), but with u to be determined by a power balance equation. Requiring either the hamiltonian or the momentum to be independent of time on finds the velocity (momentum) to be determined by [6,7,9]

$$\pi\eta/4 = u\gamma(u)(\alpha + \beta/(3(1 - u^2))). \quad (14)$$

As is clear from Eq. (14) the velocity is determined by a balance between the losses represented by α and β and the energy input represented by the bias term η . In the case $\beta = 0$ the velocity may be found explicitly as

$$u = 1/\sqrt{1 + (4\alpha/\pi\eta)^2}. \quad (15)$$

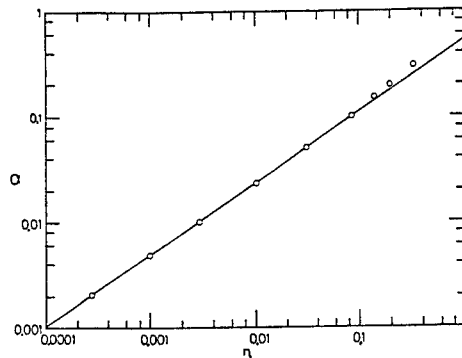


Figure 5. Soliton-antisoliton annihilation curve on the infinite line. Full curve: Eq. (21). Circles: Numerical simulation.

Because Eqs. (14-15) are derived by a perturbational approach, they are not expected to be valid if the perturbing terms are large, i.e. if the bias term approaches one, and/or the system is heavily damped. Various corrections have been considered in [10].

Another solution to the sine-Gordon equation that may be perturbed under the influence of bias and losses is the soliton-antisoliton solution that may be written [6,7,11]

$$\Phi = 4 \tan^{-1}(\sinh T/u \cosh X) \quad (16)$$

where $T = u\gamma(u)t$ and $X = \gamma(u)x$. Assuming only shunt-losses (for $\beta > 0$ a calculation was done in [12]) it is possible in a similar way as for the single soliton case to perform a power balance calculation by requiring the time rate of change of the energy, H , to be zero, i.e. calculating the integral [7,11]

$$dH/dt = \int (\eta \Phi_t - \alpha \Phi_t^2 - \beta (\Phi_{xt})^2) dx \quad (17)$$

with Φ inserted from Eq. (16). For this case a qualitatively new phenomenon occurs. For high incident energies the soliton and antisoliton will pass through each other with a phase shift δ (spatial advance) given by [6]

$$\delta = -2\sqrt{1-u^2} \ln u. \quad (18)$$

For bias below a certain threshold, ηTH , to be calculated below, the soliton and antisoliton will annihilate each other, create a breather, and eventually die out as small amplitude damped plasma oscillations. In evaluating Eq. (17) one finds after rather lengthy calculations [11] that the collision gives rise to an energy loss, ΔH , for $\beta = 0$ given by

$$\Delta H = 4\pi^2 \alpha. \quad (19)$$

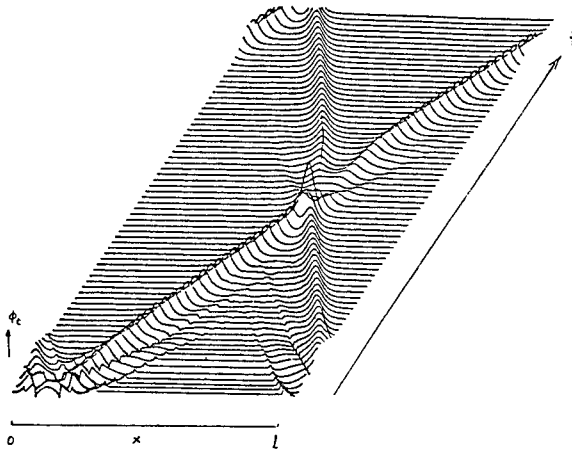


Figure 6. Collision between a soliton and an antisoliton. $\alpha = 0.2$, $\eta = 0.22$, $l = 40$. The wiggles for small time are transients that have not yet been damped out. [A. Davidson and N. F. Pedersen, unpublished].

Part of this energy is dissipated on propagating but decaying oscillations of the line. The annihilation threshold [11] may be found by requiring that the total energy of the soliton and antisoliton before the collision, $H = 16\gamma(u)$, is equal to the energy loss plus the rest of a stationary soliton and antisoliton, i.e.

$$16\gamma(u) \approx 4\pi^2\alpha + 16\gamma(0). \quad (20)$$

Eq. (20) together with Eq. (15) leads to [11]

$$\eta_{TH} \approx (2\alpha)^{3/2}. \quad (21)$$

Figure 5 shows Eq. (21) together with a numerical simulation. The agreement is excellent except for α larger than approximately 0.2. Fig. 6 shows a numerical calculation of a soliton-antisoliton collision where both the above phenomena - the energy loss and the phase shift - are easily observed. The case $\eta = 0$ is treated in Ref. [13].

3b. Soliton Experiments: dc I-V-curves

The overlap JTL

In the overlap junction (Fig. 4b) the bias current is uniformly distributed over the junction length, and $\eta = I_0/JWL$ may be assumed in Eq. (11). Due to the moving fluxon, the mechanism of which is described below, a phase shift of 2π takes place in a time interval ℓ/u , where ℓ is the (normalized) length of the junction. This in turn gives rise to a (normalized) dc voltage, v , given by

$$v = (2\pi/\ell)u. \quad (22)$$

The overlap junction has boundary conditions requiring that no currents flow out at the ends, i.e.

$$\Phi_x(0, t) = \Phi_x(\ell, t) = 0. \quad (23)$$

This boundary condition is mathematically equivalent to a soliton-antisoliton collision, which was treated in the previous section.

In the I-V-curve the moving soliton gives rise to the so-called zero field steps (ZFS). The mechanism for the first ZFS, $n = 1$, is that a fluxon moves along the junction and is reflected at the boundary as an antifluxon. Since the reflection at $x = \ell$ is equivalent to a collision with a virtual antifluxon at $x = \ell$, the problem may be treated in the framework of Eq. (18) for the phase shift and Eq. (20) for the energy loss. If the junction length, ℓ , is very large, the details at the boundaries play only a minor role, and the voltage of the first step is given by Eq. (22). Thus,

for example Pedersen and Welner [9] were able to completely neglect the effects of collision in a comparison between experimental soliton ZFS on a very long overlap junction ($\ell = 45$) and perturbation theory. Fig. 7 shows an example of one of their experimental curves. If the junction length is smaller (for example of the order 5-10), the energy loss and the phase shift will give rise to corrections [11].

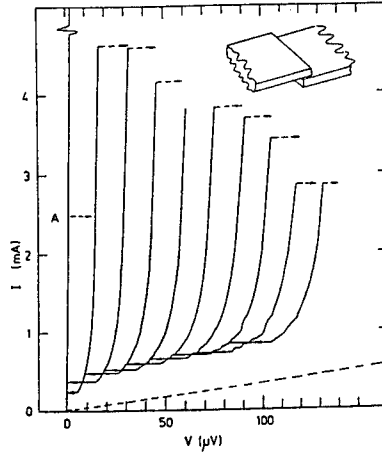


Figure 7. Experimental zero field steps a long overlap junction. (From [9]).

The annular JTL

This circular geometry, which looks mostly like an overlap junction that is folded back into itself, has the simple periodic boundary conditions

$$\Phi_x(0, t) = \Phi_x(\ell, t) + 2p\pi \quad (24)$$

used by many authors [14,15]. Here p gives the number of full phase rotations along the line. For topological reasons p is a conserved number; for example in experiments it may only be changed by taking the junction through the transition temperature, thus changing the superconducting wave function completely.

The simplest case to consider is $p = 1$, i.e. a single fluxon on the circular line. This case is shown in Fig. 8 [16]. In that case there is no supercurrent, since as soon as a uniform bias current is applied, the fluxon starts moving with a velocity u determined by Eq. (15), and a voltage (Eq. (22)) develops.

Hence for the annular junction with one trapped fluxon on supercurrent exists and the dc voltage is a direct measurement of the velocity of the single soliton [17]. The I-V-curve is shown qualitatively in Fig. 9. In addition to the single soliton further solitons may be created only by introducing soliton-antisoliton pairs (for topological reasons), in which case the effects of collisions must be taken into account. Disregarding the collisions for simplicity, the voltage of these different configurations are given by multiplying the voltage in Eq. (22) by the total number, n , of fluxons and antifluxons, i.e. voltage steps are to be expected at voltage $v_1, v_3 = 3v_1, v_5 = 5v_1$, ect. (shown as the dashed curves in Fig. 9). For the higher order branches, v_3, v_5, \dots , the qualitative effect of the collisions is to lower the average voltage somewhat compared with nv_1 . Also a lower bias threshold, η_{TH} , where a fluxon and an antifluxon annihilate each other (cf. Eq. (21)) is to be expected. Fig. 9. shows qualitatively the higher order steps based on these arguments (full curves). Ref. [15] shows for $p = 2$ a numerically simulated I-V-curve, which contains all the essential features of Fig. 9.

Experimental measurements of solitons on the annular junction have been reported [16,17]. In the experiment the p -value could be changed only by taking the junction through the transition temperature. $p = 1$ appeared qualitatively as discussed above. $p = 0$ (zero fluxons trapped) showed the full supercurrent and fluxon-antifluxon steps at voltages $v_2 \approx 2v_1, v_4 \approx 4v_1, \dots$, etc..

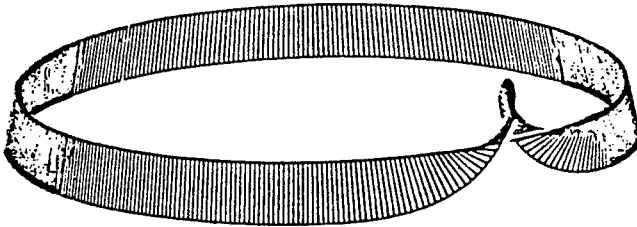


Figure 8. Computer-generated equivalent pendulum array with a 2π -kink. $\alpha = 0.02$, $\beta = 0.01$, $\eta = 0.4$, $\ell = 8$. (From [16]).

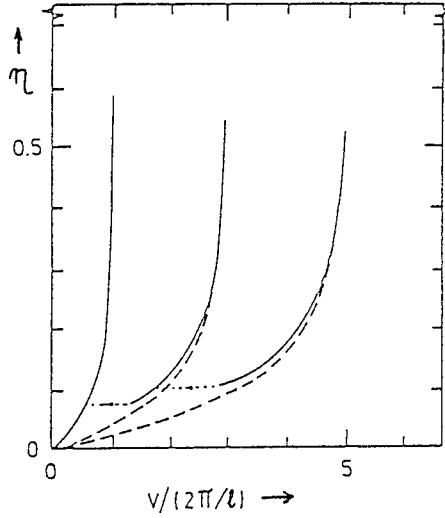


Figure 9. Qualitative I-V-curve of the annular JTL with one trapped soliton. Details of the curves are discussed in the text.

The long annular junction experiment demonstrates in a very clean way the existence of a topological sine-Gordon soliton with a phase change of 2π . The experiment and its interpretation are elegantly connected with fundamental theory of superconductivity, which requires the phase to change only in multiples of 2π along a superconducting ring [1] - [4].

3c. Stability of Solitons

In this section we discuss the stability of the solitons under the influence of small and large perturbations [18,19]. In the previous sections we have seen that the current singularities in the I-V characteristic, the so-called zero-field steps (ZFS), can be ascribed to solitons travelling forth and back on the JTL. Thus n solitons will be present on the n 'th ZFS.

Another excitation of the JTL is the spatially uniform solution $\Phi_0 = \Phi_0(t)$, which for $\alpha = \beta = \eta = 0$ in Eqs. (11,23) is given [20]

$$\Phi_0(t) = 2am[t/k; k] \quad (25)$$

where am is the Jacobian elliptic function of modulus k . for non-zero small values of α , β , and η we may assume that (25) still solves Eq. (11) in the power-balance approximation. As a result

$$\left. \begin{aligned} \eta &= 4\alpha E(k)/(\pi k) \\ \langle \Phi_t \rangle &= \pi/(kK(k)) \end{aligned} \right\} \quad (26)$$

where $K(k)$ and $E(k)$ are complete elliptic integrals of first and second kind respectively. The spatially uniform excitation gives rise to the so-called McCumber branch (MCB) of the I-V characteristic for the JTL.

Fig. 10 shows an experimental measurement of the I-V characteristic for a Josephson junction of length $\ell = 3.2$ and an α -loss term with $\alpha = 0.02$, while the β -loss term is not well defined.

It is seen that if the JTL operators on the McCumber branch and the bias current I is lowered switching to the zero field steps (ZFS 1 and ZFS 2) occurs at certain critical values of the bias current. The switching is indicated by dotted lines. Thus at these critical values the spatial excitation is no longer stable and solitons are found instead.

A similar result was found by direct numerical solution of the perturbed sine-Gordon equation (11). Fig. 11 illustrates the results for $\alpha = 0.05$, $\beta = 0.02$, and $\ell = 2$. The inset shows in detail the region where ZFS1 forms the

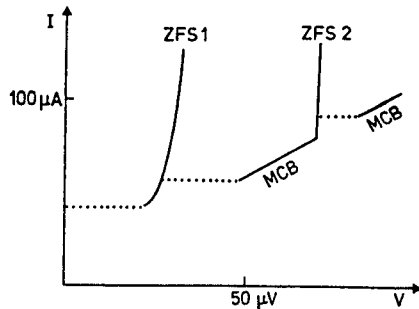


Figure 10. Detail of the I-V characteristic of an experimental sample. Dotted lines indicate switching from higher-voltage to lower-voltage states. (From [18]).

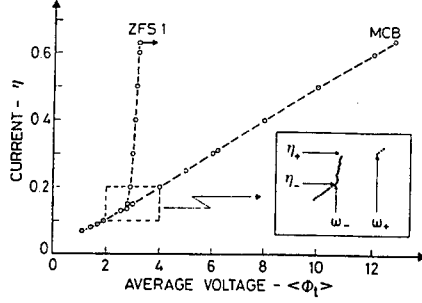


Figure 11. I-V characteristic calculation from Eqs. (11,23) using $\alpha = 0.05$, $\beta = 0.02$, and $\ell = 2$, showing the McCumber background curve (MCB) and the first zero field step (ZFS1). Inset shows detail where ZFS1 joins the MCB. (From [18]).

MCB-curve. In order to demonstrate the instability numerically the imposition of an inhomogeneous initial condition is required. Accordingly, for a given η , a "pure" McCumber solution was launched and allowed to stabilize for 100 normalized time units, after which a small perturbation was added. In the instability region, i.e. for $\eta_- \leq \eta \leq \eta_+$ or $\omega_- \leq \omega \leq \omega_+$ (see Fig. 11), the perturbation grows, causing the system to switch to ZFS1. Outside of the instability region the perturbation decays, and the system relaxes back to the McCumber curve.

In order to perform the stability analysis we express the solution of Eq. (11) in the vicinity of the McCumber solution as

$$\Phi(x, t) = \Phi_0(t) + \bar{\Phi}(x, t) \quad (27)$$

where $\Phi_0(t)$ is given by (26), and $\bar{\Phi}$ is a small perturbation of the form

$$\bar{\Phi}(x, t) = y(t) \exp(ibx) \quad (28)$$

with b constant. Inserting Eqs. (28 and 27) into Eqs. (11,23) we obtain an ordinary differential equation for $y(t)$:

$$\ddot{y} + (\alpha + \beta b^2) \dot{y} + \{b^2 + \cos[\Phi_0(t)]\} y = 0 \quad (29)$$

where $b = n\pi/\ell$, $n = 0, 1, 2, \dots$. Eq. (29) is a damped Hill's equation [21], which may have unstable solutions in certain regions of parameter space. In such regions small initial disturbances will lead to a large response in the solution, giving rise to the onset of a solution with spatial structure, in contrast to the McCumber solution. The equation is investigated in Refs. [18,22]. In the limit of small k it can be shown that the stability boundaries of ω , ω_+ , and ω_- are solutions to

$$b^2 = \left(\frac{\omega}{2}\right)^2 + \frac{1}{2\omega^2}\left(1 - \frac{1}{8\omega^4}\right) \pm \frac{1}{2}\left[\left(1 - \frac{1}{8\omega^4}\right)^2 - \omega^2(\alpha + \beta b^2)\right]^{1/2} - \frac{1}{8\omega^2}\left(1 - \frac{1}{8\omega^4}\right)^2 \quad (30)$$

provided the argument of the square root is positive. If the argument is negative, no instability region exists for the given parameter values. Using Eq. (26) the voltage-stability boundaries ω_+ and ω_- can be translated into the corresponding current value, η_+ and η_- . Inserting the parameter values $\alpha = 0.05, \beta = 0.02, b = \pi/2$ into Eq. (30) we thus obtain $\eta_+ = 0.1711$ and $\eta_- = 0.1404$. From the direct numerical solution of Eqs. (11,23) described above we find the corresponding values $\eta_+ = 0.1712 \pm 0.0005$ and $\eta_- = 0.1401 \pm 0.0001$, which are in satisfactory agreement taking the approximations made in order to obtain Eq. (30) into account.

In the case of an external magnetic field the boundary conditions Eq. (23) for the overlap JTL are replaced by

$$\Phi_x(0, t) = \Phi_x(\ell, t) - H, \quad (31)$$

where H is the normalized external magnetic field. In Ref. [18] the stability analysis is generalized to the case $H \neq 0$, and the full curves for ω_+ and ω_- as functions of H , shown in Fig. 12, are obtained. The curves are seen to be

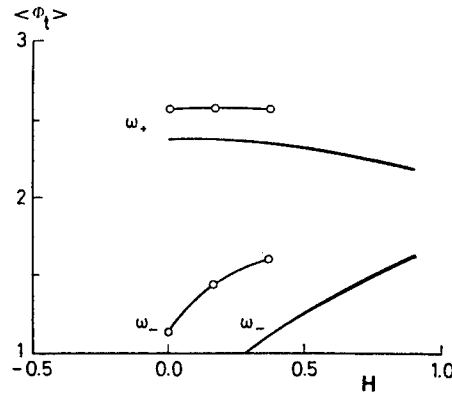


Figure 12. Stability boundaries for ZFS1 in average voltage $\langle \Phi_t \rangle$ as a function of magnetic field H measured experimentally (circles) and calculated from generalized stability theory [18]. Fixed parameter values: $\alpha = 0.026$ and $\ell = 3.16.0 \leq \beta \leq 0.07$ giving rise to the shaded regions between solid curves. (From [18]).

in reasonable agreement with the experimental results indicated by circles in the figure. Thus classical stability theory provides an approximate prediction of the switching between the two nonlinear dynamic states in the JTL.

For high values of the bias current, η , the soliton state becomes unstable again and the JTL switches to the running state. Thus the ZFS's have a finite height and

a jump back to the McCumber branch occurs. In Ref. [19] this switching mechanism is studied both in the annular geometry Eq. (24) with $p = 1$ and the overlap geometry Eq. (23). In the former case there are no collisions with boundaries, which makes the dynamics more smooth. This is important when the perturbation η in Eq. (11) becomes large.

As a result of the large perturbation term the shape of the solitons is changed away from the sine-Gordon soliton shape given by Eq. (12). The modification becomes more pronounced as the bias current is increased. In Fig. 13 we show the numerical computation of the x-derivative of the soliton

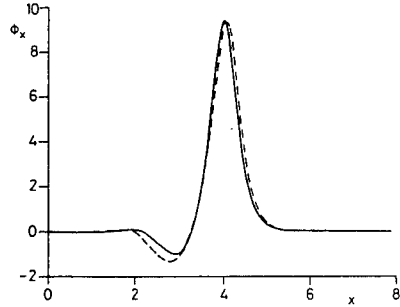


Figure 13. Φ_x at two different bias levels $\eta = 0.75$ (solid curve) and $\eta = 0.8$ (dashed curve). (From [19]).

shape of the solution to Eqs. (11,24) with $p = 1$. Parameter values are $\alpha = 0.05$, $\beta = 0.02$, $\ell = 8$, and $\eta = 0.75$ (full curve) and $\eta = 0.8$ (dashed curve). The main difference from sine-Gordon soliton shape is the presence of an overshoot at the travelling edge of the soliton. This overshoot is present when the surface impedance term $\beta\Phi_{xxt}$ is not negligible. In the following we shall show that it is the presence of this term in Eq. (11) that limits the maximum bias current η that sustains the soliton motion in the annular JTL with periodic boundary conditions Eq. (24). As η is increased the overshoot develops more and more and ultimately at a critical value, η_{sw} , the JTL switches to the McCumber branch (MCB in Fig. 11). In Fig. 14a-g a detailed time sequence of the switching is shown. The parameter are in this case: $\alpha = 0.18$, $\beta = 0.1$, $\ell = 32$, and $0.89 \leq \eta \leq 0.90$. All the plots are referred to reference frame moving with soliton. The switching can be described in the following way: first the overshoot at the trailing edge of the soliton starts to grow in size and decreases its speed (Fig. 14a-b); when the overshoot is large enough it breaks into a soliton-antisoliton pair (Fig. 14b, in this plot a soliton is represented by a positive pulse); the new soliton starts to move forward bunching with the original soliton, while the antisoliton starts to move backwards driven

by current bias (Fig. 14c); the process of nucleation of soliton-antisoliton pairs continues to add new solitons and

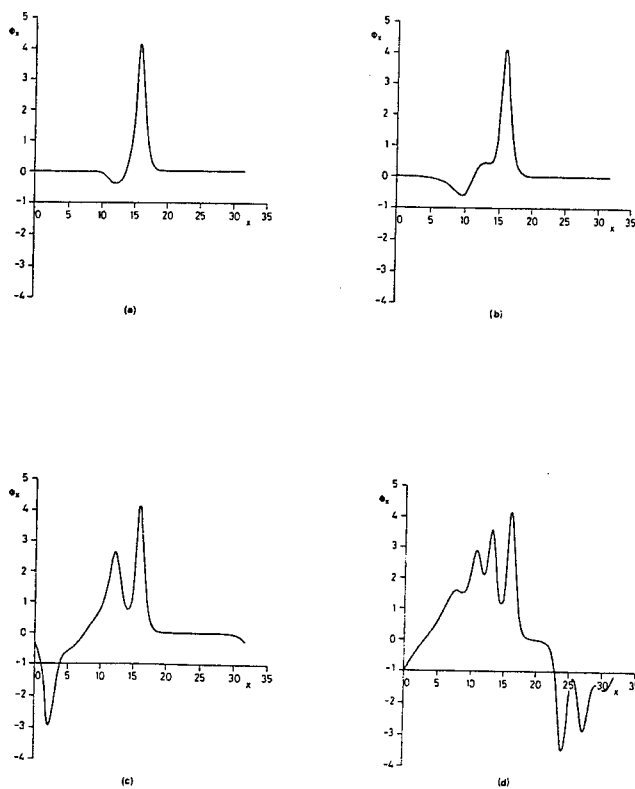


Figure 14. Time sequence of the switching in the annular JTL. Parameters given in text. (a) $t = 25$; (b) $t = 50$; (c) $t = 55$; (d) $t = 60$. (From [19]).

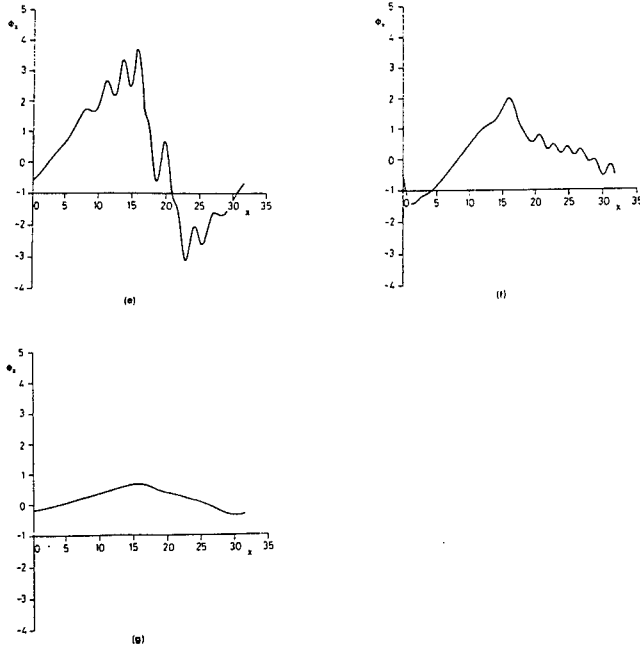


Figure 14. Time sequence of the switching in the annular JTL. Parameters given in text. (e) $t = 65$; (f) $t = 70$; (g) $t = 75$. (From [19])

antisolitons pairs continues to add new solitons and antisolitons (Fig. 14d); when the group of solitons meets the group of antisolitons which has travelled all the way around the JTL a multiple collision occurs (Figs. 14 e and f). As a result a net energy loss occurs in each soliton and antisoliton to such an extent that are unable to survive the next collision, breather-like structures are formed, and these waves do not gain energy from the bias current and relax down to a flat configuration with $\Phi_x = 2\pi/\ell$, $\Phi_t \gg 1$ (Fig. 14g). Finally, a uniform phase twist increasing quickly in time is obtained. This state corresponds to the McCumber branch for the annular JTL.

In Ref. [23] a travelling wave assumption is inserted into Eq. (11). The resulting ordinary differential equation contains the parameters α, β, η , and u , where u is the velocity of the travelling wave. The travelling pulse corresponds to a trajectory connecting two fixed points on phase space. For each value of the driving bias η this trajectory exists for a given value of the velocity $u = u(\eta)$ up to a certain value of the bias, $\eta_{critical}$. For $\eta = \eta_{cr}$ a global bifurcation is found numerically. Since η_{cr} has the same value as the η_{sw} in the direct computational solution of the partial

differential equation (6,19) the global bifurcation is associated with the switching phenomenon. Also the spectral analysis introduced in Ref. [24] may be interesting to use in a study of the development of the switching despite the fact that a large bias perturbation is applied in Eq. (11).

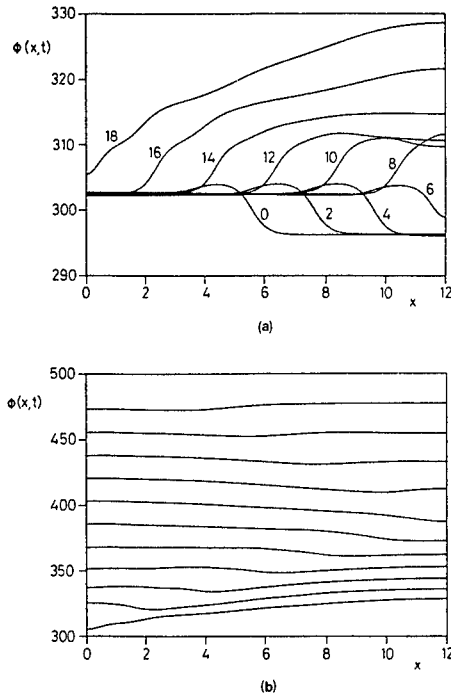


Figure 15. Time sequence of switching in overlap JTL. Parameters given in text. (a) $0 \leq t \leq 18$. (b) $18 \leq t \leq 38$. (From [19])

The switching in the overlap geometry Eq. (11,23) is now considered. In Fig. 15 this transient is shown in detail for an overlap JTL with $\alpha = 0.05$, $\beta = 0.02$, $\ell = 12$ and $\eta = 0.74$. The phase, $\Phi(x, t)$, is displayed at successive times t during the switching starting at the arbitrarily chosen reference time $t = 0$. at $\eta = 0.73$ the soliton oscillation is stable. Increasing η to the value of 0.74 the soliton becomes unstable and after a couple of oscillations forth and back on the JTL the soliton hits the right-hand boundary at $x = \ell = 12$ at $t \sim 6$ and during the reflection at this boundary it becomes unstable. Immediately after the reflection the phase has increased by 4π but it is now unstable and continues to increase after the time $t \sim 14$ leading to the formation of additional solitons which travel from the right-hand boundary towards the left boundary. At time $t \sim 18$ these solitons are reflected from the left-hand boundary and annihilate the oncoming ones. Eventually the phase develops into the spatially uniform rotation as can be seen from Fig. 15b.

From Fig. 15 it is evident that the soliton is destabilized at one of the boundaries during the reflection and thereby triggers the formation of successive solitons which unwind during the next reflection at the opposite boundary. Thus switching on the overlap JTL occurs at a lower value of the bias than on the annular JTL where the overshoot of the soliton causes the switching as we have seen.

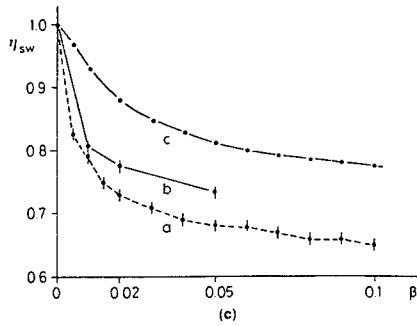


Figure 16. η_{sw} as a function of β for $\alpha = 0.05$ and $\ell = 12$. (a) overlap geometry. (b) annular geometry. (c) boundary model. (From [19])

In Fig. 16 we show the switching value of the bias, η_{sw} , as a function of β for (a) the overlap geometry and (b) the annular geometry. For $\beta \rightarrow 0$ all curves tend to $\eta_{sw} = 1$. For increasing values of β , η_{sw} decreases more for the overlap JTL (a) than for the annular JTL (b).

The interesting decrease of stability for increasing surface resistance loss term is predicted by the boundary model introduced in [19]. In this model the dynamics of a single pendulum at the JTL boundary at $x = \ell$ under the soliton-antisoliton collision corresponding to the soliton reflection at this boundary is investigated. In the perturbed sine-Gordon equation (11) the terms $\Phi_{tt} + \alpha\Phi_t + \sin\Phi$ at $x = \ell$ are then being driven in time by the terms $\eta + \Phi_{xx} + \beta\Phi_{xxt}$ with the soliton-antisoliton collision given by

$$\Phi(x, t) = \sin^{-1} \eta + 4 \tan^{-1} \left[\frac{1}{u} \sinh(u\gamma^* t) \operatorname{sech}(\gamma^* x) \right] \quad (32)$$

inserted. Here γ^* is the corrected Lorentz factor

$$\gamma^* = (1 - \eta^2)^{1/4} \gamma(u), \quad (33)$$

u is the soliton velocity, and $x = \ell$. The boundary model predicts switching at the η_{sw} -values shown as a function of β in curve c in Fig. 16. Apart from an almost constant shift for $\beta > 0$ the boundary model is seen to be capable of predicting qualitatively the switching values for the overlap JTL. Of course the introduction

of the soliton-antisoliton collision expression Eq. (32) leads to too high stability in the model.

3d. Applications of Solitons on the JTL

Solitons on the JTL may very well have technical applications. We will briefly discuss three possible applications that have emerged; these are (i) microwave oscillators and amplifiers, (ii) digital information processing, and (iii) analog amplifiers.

(i) Microwave Oscillators and Amplifiers

Several designs of microwave oscillators based on the properties of fluxons in overlap or annular JTL's exist [6,25,26]. A particularly promising scheme is the flux flow oscillator [27] with a demonstrated performance of as much as 10^{-6} Watts available on the substrate at frequencies tunable between 100 and 400 GHz. This is far superior to other results and is fully sufficient for a pump source in an integrated Josephson junction millimeter wave receiver.

(ii) Digital Information Processing

The basic idea behind digital applications is the use of the soliton as the basic bit of information. Already in the early seventies, the so-called flux shuttle was proposed by Fulton et al. [28]. In the flux shuttle, fluxons are situated in potential wells created by perturbing the geometry of the JTL at desired positions. The fluxons may be moved around and manipulated by applying currents and magnetic fields. Results described in [29] and elsewhere demonstrate that this is possible.

(iii) Analog Amplifiers

The Josephson junction has been demonstrated to have superior properties in almost all areas of electronics. It is therefore remarkable that the fundamental element - a Josephson transistor - does not directly exist. However, Likharev et al. [30] suggested that an overlap JTL with current injection in many points in parallel is an almost complete analog of a semiconductor transistor, where the role of electric charge carriers is being played by Φ_0 -fluxons. In that scheme the control current is being applied to a film on top of the upper electrode but isolated from it. Somewhat similar concepts have been investigated experimentally [31] - [33]. Current gain of order 2-5, very fast responder and low power dissipation have been found.

4. **rf-Properties of Josephson Junctions**

A very important topic within Josephson junctions are the rf-applications as the millimeter wave sources [34] and as SIS mixers and detectors [35]. For the last-mentioned devices the situation is the same as in the next section dealing with chaos. The main difference is that the pump power levels are below the threshold for chaos, though often not very far below for best performance. In the next sec-

tion on chaos we will consider the situation when the pump strength is above the threshold.

5. Chaos in Josephson Junctions

Another non-linear signature appearing quite often in Josephson junctions is chaos together with its accompanying bifurcations. In fact, quite often the Josephson junction is used as a model system for chaos in numerical simulations. A particular feature of chaos in Josephson junctions is that both the effect of thermal noise and the effect of deterministic noise (chaos) are very important for experiments. The interplay between those two sources of noise is at best very complicated, and at worst makes it impossible to interpret experiments. This has led to new theoretical and numerical work on 500 the non-linear interaction between thermal and deterministic noise.

5a. Deterministic Chaos in the Josephson Junction

The most widely investigated Josephson junction system is the rf-driven Josephson junction for which the equation may be obtained by adding a term $i_{RF}\sin\omega t$ to Eq. (2a), i.e. in normalized units

$$\phi_{tt} + \alpha\phi_t + \sin\phi = \eta_0 + \eta_1\sin\omega t. \quad (34)$$

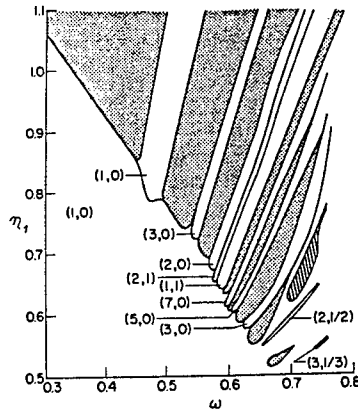


Figure 17. Characterization of solutions in the $\Omega - \eta_1$ plane $\beta_c = 25, \eta = 0$. crosshatched region: chaos. Hatched region: complicated periodic. Indexing (p,q) corresponds to the p th subharmonic on the q th rf induced step. (From [37]).

Since analytical solutions do not exist one has to do numerical simulations in the four-dimensional parameter space of α , η_0 , and ω [36] - [41]. A Particularly thorough investigation of the parameter space was done in [41]. Typically, the system has been investigated numerically in the $\eta_1 - \omega$ plane for a fixed damping parameter α , a plot which more or less has become a standard for such systems [36] - [39]. Fig. 17 shows such a plot with its complicated mapping of different dynamical behaviour.

Note that for $\omega > \omega_0$, i.e. $\Omega > 1$, the threshold rises dramatically because the capacitor shorts out the applied rf-current. For $\omega < 1/RC$, i.e. $\Omega < 1/\sqrt{\beta_c}$, the system is able to adiabatically follow the rf-current, and chaos occurs only if $\eta_1 > 1$. For $\omega \approx \omega_0$, the threshold for chaos is lowest.

Another method of a somewhat computational nature is to use electronic analogous simulating the Josephson equation. Such systems have the advantage of being very fast, and Poincaré sections and bifurcation diagrams may be readily displayed [38,42]. The disadvantage is the limited precision and resolution, and the drift of analog electric circuits.

5b. Thermally Affected Chaos in the Josephson Junction

In [43] a Josephson junction system with parameters such that two solutions existed, was investigated. The authors found that the basin boundaries between the two solutions were fractal, and thus the solutions could come infinitely close to each other in the phase plane. Under such circumstances a small amount of thermal noise may take the system back and forth between the solutions. The authors found that this mechanism gave rise to approximately 1/f noise for some parameter regions.

In another extensive numerical simulation including a thermal noise term in Eq. (2), Kautz [44] was able to obtain the very high noise temperatures ($\approx 10^6$) that have been observed experimentally, for example in [45]. For a situation with overlapping rf-induced steps the origin of the very high noise temperatures [44] was hopping between phaselocked and metastable chaotic states induced by thermal fluctuations. This may even lead to the surprising result that the low-frequency noise power increases as the temperature is reduced.

In the absence of thermal noise numerical calculations of chaotic regions in the I-V curve typically contain a wealth of complicated-structure displaying bifurcations, chaos, periodic solutions, etc. This may be seen in Fig. 18, which shows a numerical calculation of an rf-induced step with loss of phase lock [46]. In experiments, such interesting and complicated structure is typically washed out because of thermal noise, and only a smooth curve - which does not in a simple and convincing way demonstrate chaos - is obtained. Thermal smoothing due to a temperature of less

than 100 mK is sufficient to

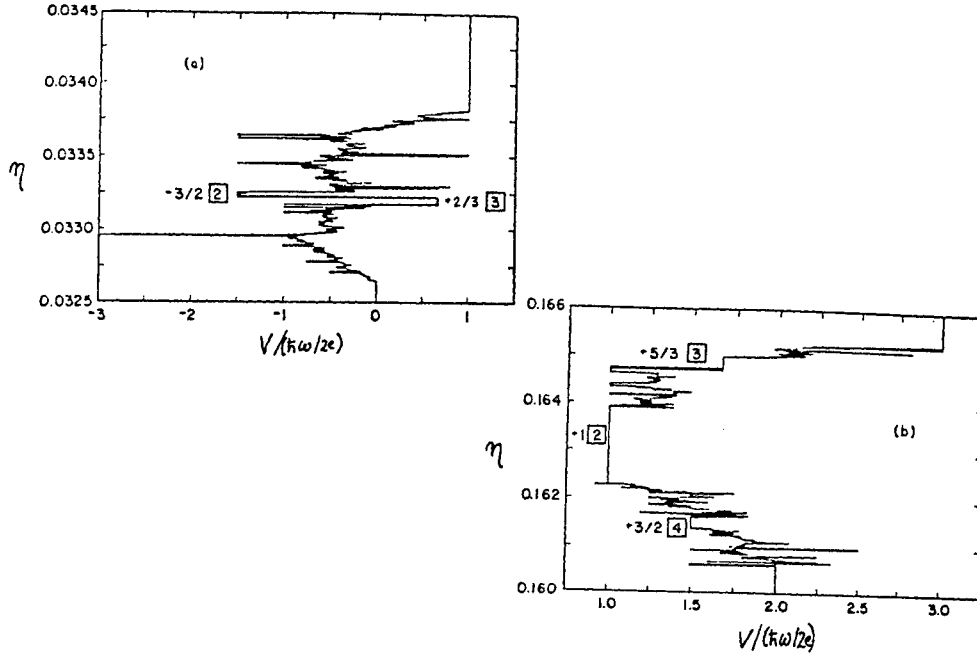


Figure 18. Typical results of a numerical calculation for zero temperature $\Omega = 0.16$, $\beta_c = 4$, $\eta_1 = 1.05$. (a) the zeroth rf-induced step and (b) the second step. The numbers inside the squares denote the periodicity on the substep. (From [46])

remove most of the traces of complicated dynamically behaviour. By comparing experiments with a calculation that includes thermal noise, however, the existence of chaos may be demonstrated indirectly ([46]).

5c. Experiments on Real Josephson Junction

Common to all the experimental results is that they are not nearly as spectacular as the numerical simulations. The main reason is that thermal noise, which is most often not taken into account in simulations, has a major effect on the outcome of the experiments. This is because the energy levels in the thermal oscillations may very well be of the same order of magnitude as the intrinsic energy levels in the Josephson junction, and complicated non-linear interactions occur. Thermal effects may produce not only quantitative changes but also qualitative and quite dramatic changes as we shall see below.

5d. dc Observation of Chaos

Before the term chaos was connected to Josephson junctions, researchers sometimes noted very irregular and erratic I-V curves in samples subject to strong applied rf signals. In many cases such junctions were discarded because of assumed defects during fabrication.

It is now known that such irregular I-V curves may be a signature of chaos. Examples of such irregular behaviour, in particular the loss of phaselock on an rf-induced step, may be found in [46] - [48].

By comparing such experimentally obtained, irregular I-V curves with numerically obtained ones, one has in principle the simplest experiment on chaos [46]. An example of such a dc experiment is illustrated in Fig. 19, which shows an experimentally obtained I-V curve with loss of phaselock on the rf induced step. Also shown in the figure is the spectrum of halfharmonic generation as measured with a sensitive microwave spectrometer. Note that these experimental curves, which contain two period-doubling bifurcations and a chaotic region on a rf-induced step, can be considered as a standard example of the period-doubling route to chaos. These experimental results are very similar to the numerical results shown in Fig. 1 of Ref. [40] and to analog results [42].

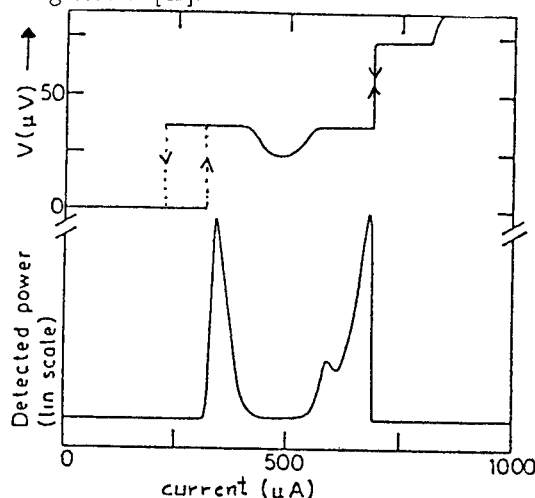


Figure 19. Experimental microwave irradiated I-V curve and corresponding half-harmonic generation. $f = 17.6 GHz$, $T = 3.54 K$. (From [48]).

5e. Chaos and Parametric Amplification

For Josephson junction parametric amplifiers low-noise temperatures were found in some cases, often, however, experiments showed considerable excess noise [49]. For experimentalist the observed noise rise has been a major puzzle. A large number of theoretical and numerical papers [50] have dealt with the problem. The conclusion is that the very large noise temperatures cannot be explained by traditional noise

sources such as Johnson noise, shot noise, or quantum noise. Hubermann et al. [36] first suggested that chaos was the origin of the excess noise. This suggestion was further substantiated in Ref. [37].

More recently, a slightly different type of Josephson junction Parametric amplifier was investigated [51] by another group, which drew the conclusion that noise in this amplifier cannot arise from deterministic chaos alone: The observed noise rise required the presence of thermal noise. They suggested that the noise rise was due to thermally induced hopping between a bias point that would be stable in the absence of thermal noise and an unstable point. The observation demonstrates the importance of thermal noise in modelling chaos in Josephson junction systems. As much as 106 K of noise temperature may be obtained.

5f. Other Josephson Junction Systems

One of the first experiments to demonstrate chaos in Josephson junctions was done on a system different from the standard system in Eq. (16). Miracky et al. [5,52] used a junction shunted with a resistor having a substantial self-inductance (see Fig. 3a,b), i.e. a junction coupled to a cavity as described in section 3. By varying the bias current they found experimentally very large increases in the low-frequency voltage noise, with noise temperatures as high as 101 K or more. The excess noise arose from switching between subharmonic Josephson relaxation modes. More moderate noise increases (101 K) could be characterized as noise affected chaotic. The experiment was done in a 1 GHz bandwidth where low-noise amplifiers and frequency-independent coupling is available.

Simulations on this system indicated that for certain bias points the addition of thermal noise gave rise to an approximately $1/f$ noise spectrum by creating hopping between subharmonic modes.

6. Conclusion

This paper has discussed mainly the non-linear properties of Josephson junctions that have so much promise for both applications and continued research on fundamental problems. The problems we have dealt with have all been defined on the basis of the old superconductors. The future work involving the new high T_c superconductors will most likely have to deal not only with the same type of problems with changed parameters, but also with completely new non-linear phenomena, for example due to anisotropy. It may be safely predicted that a lot of interesting non-linear physics lies ahead.

Acknowledgements

The financial support from the European Research office of the United States Army through Contract No. DAJA-45-8S-C-0042 and from the European Economic Community through Contract St-2-0267-J-C(A) is acknowledged.

REFERENCES

1. J.R. Clem, in: Superconducting Electronics, eds H. Weinstock and M Nisenoff, Springer (1989).
2. Y. Bryunserade, *ibid*.
3. A. Barone and G. Paterno, Physics and Applications of the Josephson Effect, New York: Wiley-Interscience, (1982).
4. K.K. Likharev, Dynamics of Josephson Junctions and Circuits, Gordon and Breach, New York (1986).
5. R.F. Miracki, H.M. Devoret, and J. Clarke, Phys. Rev. A31, 2509 (1985).
6. D.W. McLaughlin and A.C. Scott, Phys. Rev. A18, 1652 (1978).
7. N.F. Pedersen in "Solitons in Action" MPCMS, Eds. A.A. Maraduddin and V.H. Agranovich, North Holland, 1986, p. 469.
8. P.S. Lomdahl, O.H. Soerensen, and P.L. Christiansen, Phys. Rev. B25, 5737 (1982).
9. N.F. Pedersen and D. Welner, Phys. Rev. B29 2551 (1984).
10. M. Buttiker and H. Thomas, Phys. Rev. A37, 235 (1988). M. Buttiker and R. Landauer, Nonlinear Phenomena at Phase Transitions and Instabilities, (Plenum Publishing Corp.), 1982, p. 111.
11. N.F. Pedersen, M.R. Samuelsen, and D. Welner, Phys. Rev. B30, 4057 (1984).
12. A. Matsuda, Phys. Rev. B34, 3127 (1986).
13. P.L. Christiansen and O.H. Olsen, Wave Motion, 185 (1980).
14. P.M. Marcus and Y. Imry, Sol. Stat. Comm. 33, 345 (1980). S.E. Burkov and A.E. Lifsic, Wave Motion 5, 197 (1983). F. If, P.L. Christiansen, R.D. Parmentier, O. Skovgaard, and M.P. Soerensen Phys. Rev. B32, 1512 (1985).
15. A. Davidson and N.F. Pedersen, Appl. Phys. Lett. 44, 465 (1984).
16. A. Davidson, B. Dueholm, and N.F. Pedersen, J. Appl. Phys. 60, 1447 (1986).
17. A. Davidson, B. Dueholm, B. Kryger, and N.F. Pedersen, Phys. Rev. Lett. 55, 2059 (1985).
18. S. Pagano, M.P. Soerensen, R.D. Parmentier, P.L. Christiansen, O. Skovgaard, J. Mygind, N.F. Pedersen, and M.R. Samuelsen, Phys. Rev. B33, 174 (1986).
19. S. Pagano, M.P. Soerensen, P.L. Christiansen, and R.D. Parmentier, Phys. Rev. B38, 4677 (1988).
20. R.D. Parmentier in "Solitons in Action", eds. K. Lonngren and A.C. Scott, New York: Academic Press, 1978, p.173.
21. A.H. Nayfeh and D.T. Mook, Nonlinear Oscillations, New York: Wiley-Interscience, 1979, Chap. 5.
22. G. Costabile, S. Pagano, and R.D. Parmentier, Phys. Rev. B36, 5525 (1987).
23. M.G. Forest, S. Pagano, R.D. Parmentier, P.L. Christiansen, and M.P. Soerensen, Wave Motion 12, 213 (1990).
24. E.A. Overman II, D.W. McLaughlin, and A.R. Bishop, Physica D19, 1 (1986). A.R. Bishop, M.G. Forest, D.W. McLaughlin, and E.A. Overman II, Physica D23, 293 (1986).
25. S. Sakai, H. Akoh, and H. Hayakawa, Jap. Journ. of App. Phys. 23, L610 (1984).
26. B. Dueholm, O.A. Levring, J. Mygind, N.F. Pedersen, O.H. Soerensen and M. Cirillo, Phys. Rev. Lett. 46, 1299 (1981).

27. T. Nagatsuma, K. Enpuku, K. Yoshida, and F. Irie, J. App. Phys. 56, 3284 (1984).
T. Nagatsuma, K. Enpuku, K. Sueoka, K. QYoshida, and F. Irie, J. App. Phys. 58, 441 (1985).
28. T.A. Fulton, R.C. Dynes, and P.W. Anderson, Proc. IEEE 61, 28, (1973).
29. H. Akoh, S. Sakai, and H. Hayakawa, IEEE Trans. MAG-21, 737 (1985).
30. K.K. Likharev, V.K. Semenov, O.V. Snigirev, and B.M. Todorov, IEEE, Trans. Magn. MAG-15, 420 (1979).
31. T.V. Rajeevakumar, App. Phys. Lett. 39, 439 (1981).
32. B.J. Zeghbroeck, IEEE Trans. Magn. MAG-21, 916 (1985).
33. D. P. McGinnis, J. E. Nordman, and J. B. Beyer, IEEE Trans. Magn. MAG-23, 699 (1987).
34. J. Lukens, Proceedings of NATO ASI superconducting electronics, II Ciocco, Italy, 1988.
35. T. Klapwijk. *ibid*.
36. B.A. Huberman, J.P. Crutchfield, and N.H. Packard, Appl. Phys. Lett. 37, 750 (1980).
37. N.F. Pedersen and A. Davidson, Appl. Phys. Lett. 39, 830 (1981).
38. D.D'Humieres, M.R. Beasley, B.A. Huberman, and Libchaber, Phys. Rev. A26, 3483 (1982).
39. R.L. Kautz, J. Appl. Phys. 52, 3528 (1981).
M. Octavio, Phys. Rev. B29, 1231 (1984).
Kazuo Sakai and Yoshihiro Yamaguchi, Phys. Rev. B30, 1219 (1984).
40. R.L. Kautz, J. Appl. Phys. 52, 6241 (1981).
41. R.L. Kautz and R. Monaco, J. Appl. Phys. 57, 875 (1985).
42. M. Cirillo and N.F. Pedersen, Phys. Lett. 90A, 150 (1982).
W.J. Yeh and Y.H. Kao, Appl. Phys. Lett. 42, 299 (1983).
H. Seifert, Phys. Lett. 98A, 213 (1983).
Da-Ren He, W.J. Yeh, and Y.H. Kao, Phys. Rev. B31, 1359 (1985).
V.K. Kornev, K. Yu. Platov, and K.K. Likharev. IEEE Trans. Magn. MAG-21, 586 (1985).
43. M. Iansiti, Quing H, R.M. Westervelt, and M. Tinkham, Phys. Rev. Lett. 55, 746 (1985).
44. R.L. Kautz, J. Appl. Phys. 58, 424 (1985).
45. M. Octavio and C. Resdi Nasser, Phys. Rev. B30, 1586 (1984).
46. D.C. Cronmeyer, C.C. Chi, A. Davidson, and N.F. Pedersen, Phys. Rev. B31, 2667 (1985).
47. K. Okuyama, H.J. Hartfuss, and K.H. Grundlach, J. Low Temp. Phys. 44, 283 (1981).
48. N.F. Pedersen, O.H. Soerensen, B. Dueholm, and J. Mygind, J. Low Temp. Phys. 38, 1 (1980).
49. R.Y. Chiao, M.J. Feldman, D.W. Peterson, B.A. Tucker, and M.T. Levinsen, *Fu@*, uxe trends in superconductive electronics AIP Confernece Proceedings 44, 259 (1978).
50. For references on this see, e.g. N.F. Pedersen in SQUID 80, edited by H.D. Hahlbohm and H. Lubbig (de Gruyter, Berlin, 1980), p.739.
51. R.F. Miracky and I. Clarke, Appl. Phys. Lett. 43, 508 (1983).
52. R.F. Miracky, J. Clarke, and R.H. Koch, Phys. Rev. Lett. 50, 856 (1983).

Long Josephson Junctions and Stacks

A. V. Ustinov

*Physikalisches Institut III, Universität Erlangen-Nürnberg
D-91054, Erlangen, Germany*

Abstract. Magnetic fluxons in long Josephson junctions in many cases behave as solitons. Soliton dynamics can be experimentally studied in Josephson junctions with a great degree of precision, impossible for many other physical systems with solitons. This fact brought together the interest of mathematicians, physicists, and engineers which resulted in many theoretical and experimental studies of long Josephson junctions during the past three decades. This review describes fluxon properties and experiments with long junctions, as well as recent studies of stacked junctions (Josephson superlattices). High-frequency applications of fluxon oscillators are also discussed.

I INTRODUCTION

As a field of research, physics of solitons in long Josephson junctions appears in various contexts within nonlinear physics, superconductivity, and high-frequency device applications. A soliton in a long Josephson junction is often called a “fluxon” since it accounts for a magnetic flux quantum $\Phi_0 = h/2e = 2.07 \times 10^{-15}$ Wb moving between two superconducting electrodes of the junction.

Mathematical aspects of the solitons in Josephson junctions are introduced by Christiansen [1] in the preceding review of this book. Here, I will focus mainly on the experimental side, discussing physical effects associated with the soliton motion in long Josephson junctions and stacked arrays of such junctions. For an interested reader, several earlier reviews of the field of fluxons in long junctions should be also recommended [2–4]. Progress in studies of stacked junctions has been reviewed more recently [5,6].

This paper is structured as follows. First, fluxons in conventional quasi-one-dimensional Josephson junctions are discussed. The mutual coupling between fluxons, their interaction with environment and other excitations in the junction are explained using an annular Josephson junction as an example. The most recently developed field of fluxon dynamics in stacked junctions is introduced starting from the simplest case of two coupled junctions. Recently discovered beautiful phenomenon is the fluxons’s Cherenkov radiation in these systems. I briefly discuss stacks of many junctions (Josephson superlattices) which are at the front of present

research and their complex properties are not yet well understood. Finally, applications of long Josephson junctions as oscillators for the integrated receivers in the sum-millimeter wave band are addressed.

II LONG JOSEPHSON JUNCTIONS

A fluxon in a long Josephson junction carries a magnetic flux equal to one flux quantum Φ_0 . Its appearance can be understood from Fig. 1. This figure sketches the cross view of the junction in the plane perpendicular to the external magnetic field H . Josephson tunnel barrier is a thin ($1 - 2$ nm thick) layer of insulator (I) between two superconducting electrodes (S), which are formed usually as thin films evaporated on a dielectric substrate. Due to the Meissner effect, the external field is screened by circulating supercurrents and it penetrates inside a bulk superconductor to the distance known as the London penetration depth, λ_L . Typically, λ_L is of the order of 100 nm. In the region of the Josephson barrier the screening effect is weakened, thus the magnetic field penetration distance is larger. This distance is called the Josephson penetration depth, λ_J . Its value depends on the strength of the Josephson coupling (determined by the thickness of the tunnel barrier) and typically is of the order of $10 \mu\text{m}$. The screening currents form a "tangle" penetrating to the distance of about λ_J into the Josephson junction.

We will be interested in the case when the junction is "long", so that the Josephson barrier extends over the distance considerably larger than λ_J in the substrate plane. With increasing the magnetic field, the screening current tangle at the junction edge becomes unstable and forms a closed loop which enters the interior of the junction. This circulating supercurrent is often called Josephson vortex. Due to the flux quantization inside a superconductor the magnetic flux generated by the supercurrent loop is equal to Φ_0 . This is why the Josephson vortex is often named as fluxon. One can easily estimate the critical value of the external magnetic field H_{c1} which is required for the fluxon to penetrate inside the junction. Since the area surrounded by the circulating currents of the fluxon is about $(2\lambda_L + t) \times \lambda_J$ (where t is the oxide thickness, $t \ll \lambda_L$), we can guess $H_{c1} \sim \Phi_0 / (2\lambda_L \lambda_J)$. Ex-

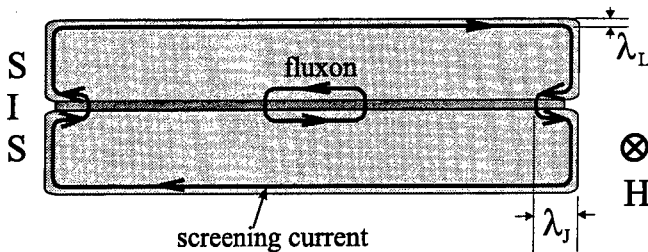


FIGURE 1. Schematic cross section of a long Josephson junction with a magnetic field applied perpendicular to the plane of the picture. Dimensions are not to scale.

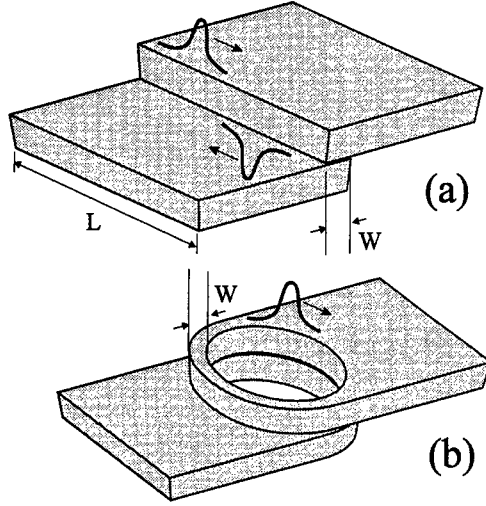


FIGURE 2. Practical geometries of long quasi-one-dimensional Josephson junctions: (a) commonly used overlap junction; (b) annular junction. Dimensions are not to scale.

act calculation of the fluxon penetration field in infinitely long junction gives $H_{c1} = \Phi_0 / [\pi(2\lambda_L + t)\lambda_J]$ [7].

So far we did not consider the influence of the junction's extension in the y -direction, perpendicular to the plane of Fig. 1. The junction can be viewed as quasi-one-dimensional if it is either infinitely large in the y -direction or very narrow, with the width $W \ll \lambda_J$. Of course, only the second option has physical sense. The examples of the two most common quasi-one-dimensional junction geometries, the straight overlap junction and annular junction (Josephson ring), are shown in Fig. 2. In both cases, the junction width W is made smaller than λ_J and the junction length L larger than λ_J (for the annular junction L is equal to the circumference of the ring).

A Perturbed Sine-Gordon Model

Mathematically, the fluxon corresponds to a 2π kink of the quantum-mechanical phase difference φ between the two superconducting electrodes of the junction. The perturbed sine-Gordon equation which describes the quasi-one-dimensional dynamics of the system [2,8], in normalized form, is

$$\varphi_{xx} - \varphi_{tt} - \sin \varphi = \alpha \varphi_t - \beta \varphi_{xxt} - \gamma. \quad (1)$$

Here, the subscripts denote the derivatives in x and t . Time t is measured in units of ω_0^{-1} , where ω_0 is the Josephson plasma frequency, the spatial coordinate x is measured in units of λ_J , α is a dissipative term due to quasi-particle tunneling, β

is a dissipative term due to surface impedance of the superconductors, and γ is a normalized bias current density. The derivation of Eq. (1) is based on the Maxwell and Josephson equations and can be found, e.g., in Refs. [2,7,8]. The characteristic velocity for electromagnetic waves propagating in the junction is called the Swihart velocity, $\bar{c} = \lambda_J \omega_0$. In fact, the velocity \bar{c} plays a role of the velocity of light in the junction and, typically, is two orders of magnitude smaller than the velocity of light in vacuum. To account for the behavior of a real junction, Eq. (1) must be solved together with the appropriate boundary conditions which depend on the junction geometry and take into account the magnetic field applied in the plane of the junction [2-4,8]. We will discuss the boundary conditions below in Sec. II C 1.

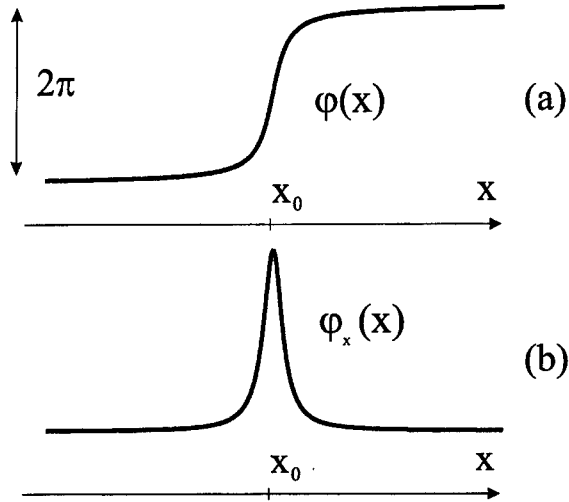


FIGURE 3. A fluxon in a long Josephson junction accounts for a 2π -kink in the phase difference $\phi(x)$ (a) with the self-generated magnetic field proportional to $\phi_x(x)$ (b).

Equation (1) for both open and periodic boundary conditions has been discussed in detail by Christiansen in the preceding review [1]. Let us summarize the most essential facts which we will need here. An important solution to Eq. (1) with zero r.h.s. is the *soliton*

$$\phi = 4 \tan^{-1} e^{\frac{x-x_0-ut}{\sqrt{1-u^2}}} . \quad (2)$$

This solution is sketched in Fig. 3(a). It describes a 2π -kink moving with a velocity u and located at $x = x_0$ for $t = 0$. The velocity u is measured in units of \bar{c} . A unique property of real Josephson junctions is that the parameters α , β , and γ are small. Thus, the solution of the perturbed Eq. (1) can be well approximated by (2). According to the perturbation theory of McLaughlin and Scott [8], the soliton velocity is determined by a balance between the losses, governed by α and β , and

the energy input due to the bias γ . According to the perturbational approach, u is approximately given by the expression

$$u = \frac{1}{\sqrt{1 + \left(\frac{4\alpha}{\pi\gamma}\right)^2}} \quad (3)$$

and thus may assume values $0 < u < 1$. In this formula, in order to obtain an explicit expression for u , we assume $\beta = 0$; see also Eqs. (14) and (15) in Ref. [1]. For low values of the bias current $u \propto \gamma$, while for large values of γ/α the normalized velocity u asymptotically approaches unity, *i.e.*, a fluxon behaves like a *relativistic particle* with respect to the limiting velocity \bar{c} . As $u \rightarrow 1$, the magnitude of the local magnetic field φ_x in the center of the fluxon increases and its width decreases, according to the well-known relativistic effect of the Lorentz contraction.

B How to observe fluxons?

Now, let us discuss how to detect fluxons in experiments with long Josephson junctions. In general, a fluxon passing by a given point $x = x_0$ inside the junction induces the time-dependent voltage proportional to $\varphi_t(x_0)$. To have fluxon moving one just has to apply a dc bias current through the junction which is easy to do in experiment. The bias current acts with a Lorentz force on the fluxon and provides the energy input which is sufficient to compensate the dissipative losses. After the fluxon has passed the point x_0 , the phase difference $\varphi(x_0)$ increases by 2π . It is easy to see that in the annular junction shown in Fig. 2(b) the fluxon will return to the same point after one turn around the junction. Thus, the fluxon will continue revolving as long as the bias current flows through the junction. Since every fluxon's turn around the junction increases the phase by 2π , fluxon motion will be accompanied by a dc voltage $V = \langle d\Phi/d\tau \rangle = \Phi_0 u \bar{c}/L$ (Φ is the flux and τ is time). Below we discuss various ways by which the voltage generated by moving fluxons can be observed in experiments.

1 Steps on $I - V$ characteristics

In experiments with long Josephson junctions, the most common signatures of fluxon motion are the so-called *zero-filed steps* (ZFSs) at voltages $V_n = n\Phi_0 \bar{c}/L$ which appear in the current-voltage characteristics ($I - V$ curve) of the junction. These steps were first observed by Fulton and Dynes in 1973 [9] who suggested that the step index n is equal to the number of fluxons oscillating in the junction. The $I - V$ curve reflects the dependence of the average fluxon velocity $u \propto V$ on the driving force $\gamma \propto I$. In a long overlap junction, such as that shown in Fig. 2(a), a fluxon arriving at the junction boundary undergoes reflection into an anti-fluxon which is driven then back into the junction by the bias current. A discussion of

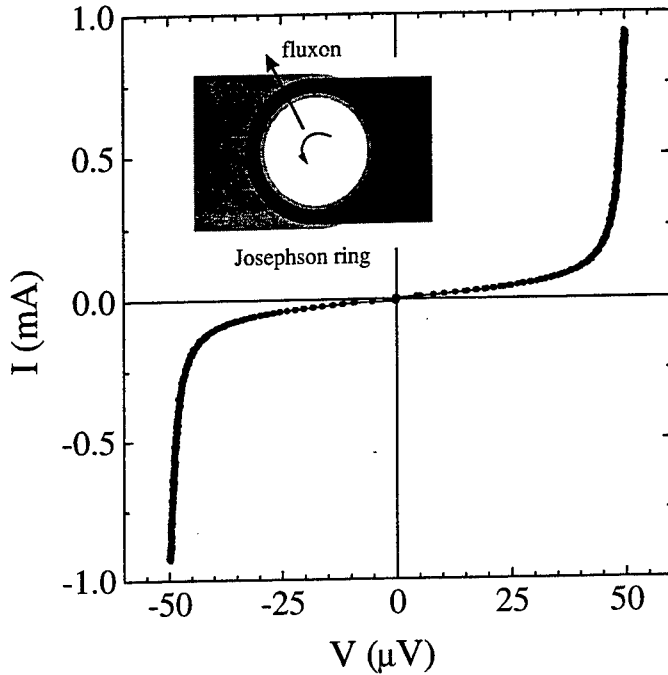


FIGURE 4. Experimentally measured current-voltage characteristics ($I - V$ curve) of a single fluxon in an annular Josephson junction. Junction diameter $D \approx 130 \mu\text{m}$, temperature 5.7 K.

The influence of boundaries can be avoided in the special case of a ring-shaped (annular) junction geometry. An annular junction serves as an excellent model for investigation of soliton dynamics, it can be studied here under periodic boundary conditions. Due to the magnetic flux quantization in a superconducting ring, the number of fluxons initially trapped in the annular junction is conserved. An example of experimentally measured $I - V$ curve of a single fluxon trapped in an annular Josephson junction is given in Fig. 4. A circular motion of the fluxon under the influence of a current passing through the junction induces a dc voltage proportional to its average velocity. When increasing the bias current, the fluxon velocity increases and approaches the Swihart velocity which corresponds to the dc voltage $V_1 = \Phi_0 \bar{c} / (\pi D) \approx 50 \mu\text{V}$, with D being the junction diameter. In Fig. 4 one can see that the critical current of the annular junction with the trapped fluxon is very small, it means that we need to apply a very small force to start the fluxon motion in this almost pinning-free system. Below we will see that in annular junction one can also induce a well-defined potential well for fluxons and control it in the experiment. While the fabrication of annular junctions is rather easy, trapping of fluxons in them remains a difficult art. Using various trapping techniques, both single-fluxon [10] and multi-fluxon [11,12] dynamics have been investigated in annular junctions.

Let us return to conventional junctions with open boundaries such as that shown in Fig. 2(a). Subjected to a sufficiently large external magnetic field H , a long Josephson junction operates in the so-called flux-flow regime. In this mode fluxons are created at one boundary of the junction, move through the junction under the influence of the bias current, and annihilate at the other boundary. The spacing between the moving fluxons is inversely proportional to H . At large bias current, the fluxon motion with the velocity close to the Swihart velocity \bar{c} is manifested experimentally by the *flux-flow step* (FFS) in the $I - V$ characteristics [13]. The step appears at the dc voltage $V_{\text{FF}} = (2\lambda_L + t)\bar{c}H$. The flux-flow regime is the very important for high-frequency applications of long Josephson junctions as discussed below in Sec. IV.

2 Observation of fluxon voltage pulses

Direct measurements of the shape of the fluxons is possible by detecting the voltage pulses which fluxons generate during their motion. The technique of doing this is rather difficult since it requires detection of small voltages (below 1 mV) with very high time resolution (of the order of 1 ps). Such experiments have been done using Josephson junction sampling circuits [14,15] and as well as traditional electronics [16]. Using direct measurements of fluxon pulses it was possible to observe fluxon propagation, contraction, reflection and fluxon-antifluxon collisions.

3 Radiation detection

Fluxons are moved by the bias current flowing through the junction and their motion leads to an electromagnetic radiation. The radiation is mainly emitted during fluxon collisions with the junction boundary which can be coupled by some sort of antenna to a receiver. The frequency f of the radiation emitted by a moving fluxon chain is given by the Josephson relation $f = V/\Phi_0$, where V is a dc voltage induced by the fluxon motion. Fig. 5 shows an example of the radiation spectrum measured from a long Josephson junction coupled by means of the so called finline antenna to a room temperature receiver. One can see that the radiation linewidth is very small ($\Delta f/f \sim 10^{-5}$ in Fig. 5, but even much smaller linewidth have been measured in other experiments). This makes long Josephson junctions attractive for oscillator applications.

For a shuttle-like fluxon motion, such as ZFS regime, fluxons and antifluxons undergo reflections from the junction boundaries and their radiation frequency $f_{\text{ZFS}} = v/(2L)$ is determined by the junction length L and the fluxon velocity $v = u\bar{c}$. In general, for both ZFS and FFS regimes, the radiation linewidth Δf is related to thermal fluctuations of the fluxon velocity v . Joergensen et al. [17] showed that, in spite of a different nature of the phase slippage in short (small) and long junctions, the linewidth of the resonant single-fluxon radiation in a long junction (at ZFS) is given by the formula similar to that of small junctions. In contrast

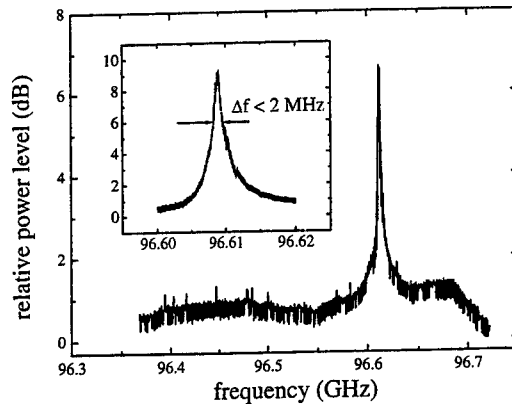


FIGURE 5. Direct radiation spectrum measurements from Nb/Al-AlO_x/Nb long Josephson junction at $T = 4.2$ K coupled with a finline antenna to a W-band room temperature receiver; estimated integral power at the receiver input is of the order of several pW.

to ZFS, the contribution of thermal fluctuation into the radiation linewidth of the flux-flow regime is not yet well understood, this problem is discussed below in the review of oscillator applications.

4 Imaging of fluxons

In the past decade spatially-resolved imaging of fluxons has proved to be a powerful experimental approach for studying fluxon dynamics in large Josephson junctions. The major method which has been used by now for such imaging is the low temperature scanning electron microscopy (LTSEM). A high energy electron beam carrying negligible current is used for local heating the junction area of about few microns around its focus, as sketched in Fig. 6. This hot spot acts as a small thermal perturbation and can be used as an active [11] or a passive probe [18,20]. In the first case a beam of high power is used as a tool to modify the state of the junction – for example, to introduce fluxons into the system. In the second case, where an e-beam of low power does not destroy the dynamic state of the junction; a small beam-induced perturbation of the junction voltage or its critical current is measured as a function of the beam coordinate in the junction plane. The obtained 2D response maps the dynamical state of the junction. The largest voltage perturbation typically occur in the region of fluxon collisions with other fluxons or junction boundaries. Using LTSEM, the Lorentz contraction of solitons [19], various multi-fluxon modes in long junctions [20–23], and complex dynamics in two-dimensional junctions [24] have been investigated. A review of the results obtained by LTSEM technique is given by Doderer [25].

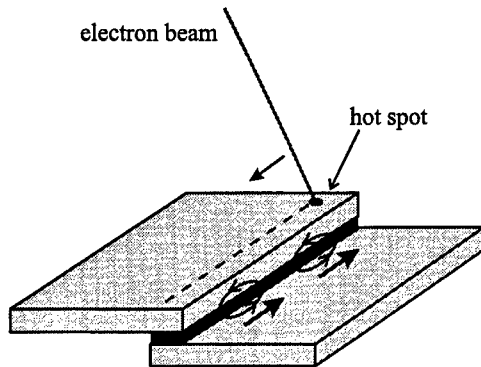


FIGURE 6. Electron beam scanning of a long Josephson junction in a dynamic state with moving fluxons.

C Fluxon interactions

Fluxons moving in a long junction cannot avoid interaction with the environment of the junction and with other fluxons. Here we will discuss some of such interactions.

1 Fiske steps and displaced linear slope

The simplest type of the interaction with environment is the interaction with the boundaries. It has to take into account the externally applied magnetic field and injected currents. The common way to write the boundary conditions for Eq. (1) is

$$\varphi_x(0, t) + \beta\varphi_{xxt}(0, t) = \eta + \kappa; \quad \varphi_x(\ell, t) + \beta\varphi_{xxt}(\ell, t) = \eta - \kappa, \quad (4)$$

where $\ell = L/\lambda_J$, η is a normalized measure of the y - component of the external magnetic field, κ is the normalized external current injected at the junction boundary. For an ideal quasi-one-dimensional Josephson junction the fluxons are well described by the perturbed sine-Gordon model (1) with the boundary conditions (4) [2-4,8].

According to the boundary conditions (4), a small magnetic field $\eta > 0$ adds energy to fluxons reflecting at $x = \ell$ and subtracts energy from fluxons reflecting at $x = 0$. Sufficiently large η kills fluxon reflections at $x = 0$ and leads to the appearance of the so-called Fiske steps at half the voltages of ZFSs. Fiske steps occur at voltages $V_m = m\Phi_0\bar{c}/(2L)$, where m is an integer. Using the fluxon model, Fiske steps were attributed to fluxon absorption at $x = 0$ accompanied by emission of a packet of small-amplitude oscillations [26]. This wave packet propagates towards the opposite boundary $x = \ell$ of the junction and triggers a new fluxon which starts moving towards $x = 0$, and so on [4].

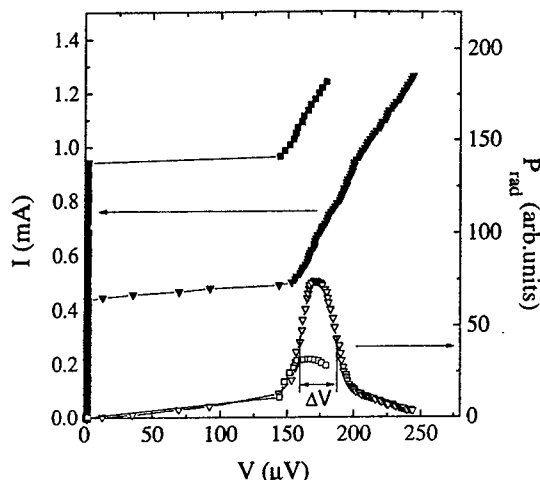


FIGURE 7. Displaced linear slope on the $I - V$ characteristics of a long junction measured at two values of magnetic field (solid symbols). The detected radiation power in the 3 GHz band around the local oscillator frequency $f_{LO} = 89.2$ GHz is shown by open symbols.

The above described mechanism, however, yields stable Fiske steps only in the very narrow parameter range at low η . At high fields $\eta \gg 1$ long junctions show Fiske steps [27] which are very similar to that in short junctions; they correspond to resonances between the Josephson frequency and the cavity modes of the junction [28]. In the intermediate field range $\eta \sim 1$ the junction dynamics is very complicated and manifested by the so-called displaced linear slope (DLS) on $I - V$ characteristics [29]. DLS does not have a pronounced resonant shape and, in a limited range, its voltage can be smoothly tuned by the magnetic field. Recent radiation measurements and numerical simulations showed that DLS is characterized by intrinsically chaotic fluxon dynamics [30]. Typical radiation measurements of DLS regime are shown in Fig. 7. The half-power radiation linewidth estimated from the voltage width ΔV of the emission peak is as large as 13 GHz! Indeed, numerical simulations of the junction dynamics at low fluxon density indicate a chaotic state in the junction [30].

2 Potential well inside the junction

Another type of fluxon interaction with environment takes place in an *annular* junction placed in the external magnetic field H parallel to the plane of the junction. Grønbech-Jensen et al. [31] proposed a model suggesting that the field adds an additional term $h \sin \frac{2\pi\varphi}{\ell}$ in the r.h.s of Eq. (1). The dimensionless field amplitude h is proportional to the external magnetic field H . [31,32]. This additional term

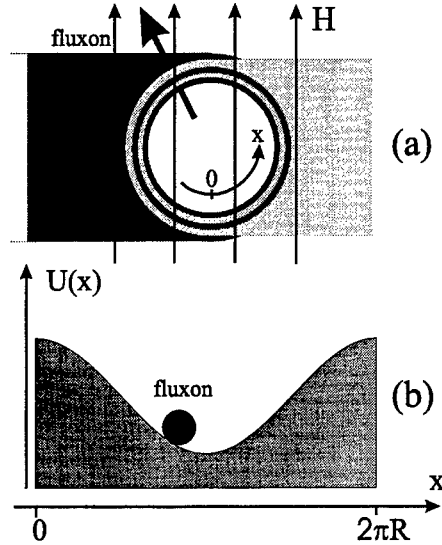


FIGURE 8. (a) Schematic top view of an annular junction placed in the external magnetic field H . The fluxon trapped in the junction feels the field-induced potential well (b).

leads to an effective field-induced potential for fluxons in the junction. As it is schematically sketched in Fig. 8, a fluxon trapped in a Josephson ring interacts with the radial field component and therefore experience a \cos -like potential with the amplitude proportional to H . The minimum of the potential is located in the region of the ring where the magnetic moment of a fluxon is directed along the field. When the bias current is applied through the junction, the potential tilts and its average slope increases with current.

The fluxon coordinate is described by the equation which equivalent to that for the coordinate of a particle placed in the washboard potential [33]. This equation describes a driven pendulum in a lossy medium, as well as the superconducting phase difference on small underdamped Josephson junction with no spatial extension. Both static [34] and dynamic [35,36] properties of fluxons in annular junctions with the field-induced potential have been recently studied experimentally.

3 Interaction with plasma waves

Besides the nonlinear soliton solution discussed above, Eq. (1) has also well-known small-amplitude solutions of the type $\varphi = \varphi_0 e^{i(kx - \omega t)}$ called plasma waves. These quasi-linear waves have the dispersion relation $\omega^2 = 1 + k^2$. Fluxon interaction with plasma waves leads to experimental signatures called fine structure resonances on ZFSs [37–39]. Plasma waves are generated when fluxons move through some inhomogeneous regions in the junction such as tunnel barrier inhomogeneities

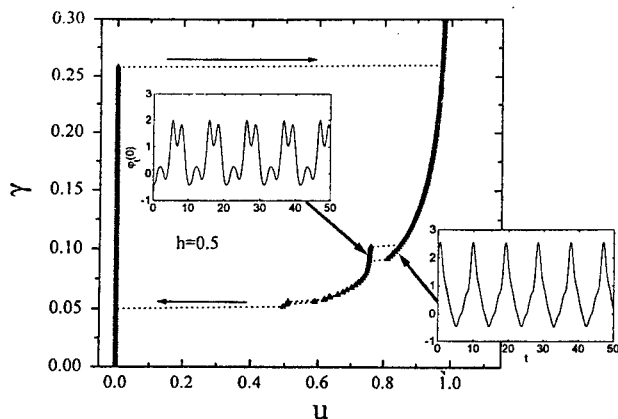


FIGURE 9. Numerically simulated current-voltage characteristics of a single fluxon in annular junction with parameters $\ell = 7.8$, $\alpha = 0.05$ and $h = 0.5$. The resonant step associated with the fluxon interaction with plasma waves is seen at $u \approx 0.75$. The insets show voltage oscillations at $x = 0$ for two different points of the $\gamma(u)$ curve.

[40] or imperfect junction boundaries [41].

Let us return to the example of the field-induced potential discussed above in Sec. II C 2. This system offers an elegant and well controlled way to generate plasma waves in the junction [36]. If a moving soliton, as a particle, is accelerated or decelerated in the potential, it emits radiation. Therefore, the soliton rotation in the junction under the action of the bias current leads to an emission of plasma waves. The interference between the soliton and plasma waves which it radiates leads to a resonance at a certain soliton velocity. The resonance indicates locking of the fluxon rotation frequency to the frequency of plasma waves. This effect is illustrated in Fig. 9 showing numerical simulations which well agree with experiment and with simple kinematic model [36].

4 Bunching of fluxons

Very interesting phenomenon in multi-fluxon dynamics is the so-called bunching effect between moving fluxons of the same polarity. Static fluxons of equal polarity repel each other. It turns out that at high velocity they can form a bound (bunched) state which, within a certain length scale, is characterized by mutual attraction. This bunching effect is usually explained by the influence of the β -term in Eq. (1) as it was first discovered in computer simulations [42]. A fluxons moving with velocity close to the Swihart velocity develops a trailing “tail” which is oscillating. The oscillating tail acts as a trap for other fluxons and leads to a formation of multifluxon bound states.

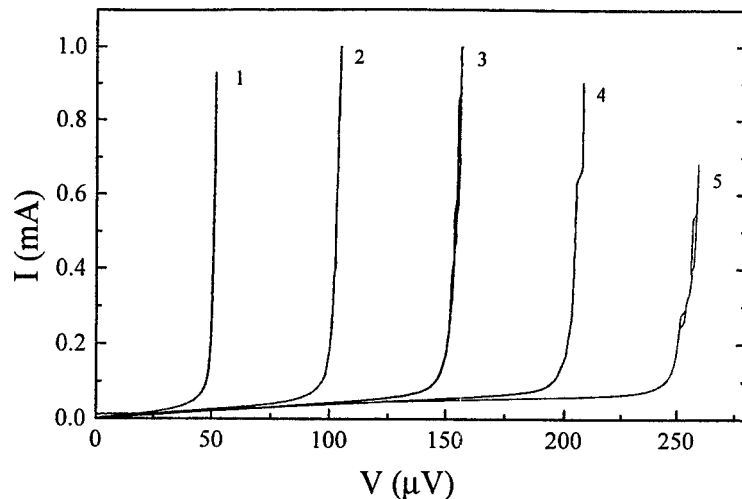


FIGURE 10. Measured current-voltage characteristics of an annular Josephson junction for different number n of trapped fluxons (n is indicated on the plot for every curve). Junction diameter $D \approx 130 \mu\text{m}$, temperature 4.2 K, zero magnetic field.

First experimental indication for fluxon bunching [43] has been found by measuring the radiation emitted from a linear junction. Later experiments [11] and detailed numerical study [12] of annular junctions have indicated that the bunching effect breaks the symmetry and “helps” the chain of fluxons to overcome dissipative losses. The average velocity of fluxons at a given bias current becomes higher than that of a single isolated fluxon. As an example, recent author’s measurements of the annular Josephson junction with different number n of trapped fluxons are shown in Fig. 10. The top parts of the curves for $n = 1, 2$ are very smooth, while that for larger n clearly indicate a complicated fine structure. This structure can be explained by states with various configurations of fluxons moving at the velocity close to \bar{c} . The bunching effect breaks the equidistant fluxon chain into different bunched states such as, e.g. for the step $n = 5$, states “1 + 2 + 2”, “3 + 2”, “4 + 1”, etc.

III STACKED JUNCTIONS

Fluxons in coupled long junctions have recently become a subject of intensive theoretical and experimental investigations. The discovery of the intrinsic Josephson effect in some high-temperature superconductors such as $\text{Ba}_2\text{Sr}_2\text{CaCu}_2\text{O}_{8+y}$ (BSCCO) convincingly showed that these materials are essentially natural superlattices of Josephson junctions formed on the atomic scale [44–48]. The spatial period of such a superlattice is only 1.5 nm, so the Josephson junctions are extremely densely packed. The superconducting electrodes are formed by the copper

oxide bilayers as thin as 0.3 nm and are separated by the non-superconducting BiO layers.

Superlattices with many Josephson layers can naturally be expected to show very complex dynamics. Therefore, it is important at first to understand in detail the dynamics of stacked junctions with very few layers.

A Two coupled junctions

For the first time fluxon dynamics in two inductively coupled long Josephson junctions was considered theoretically by Mineev et al. [49]. The perturbation approach for small coupling has been further explored by Kivshar and Malomed [50] and Grønbech-Jensen et al. [51]. A very important step towards quantitative comparison with real experiments was made by Sakai et al. [52] who derived a model for arbitrary strong coupling between the junctions. According to that model, two stacked junctions are described by a system of coupled perturbed sine-Gordon equations:

$$\begin{aligned} \frac{1}{1-S^2} \varphi_{xx}^A - \varphi_{tt}^A &= \sin \varphi^A + \alpha \varphi_{tt}^A + \gamma^A + \frac{S}{1-S^2} \varphi_{xx}^B; \\ \frac{1}{1-S^2} \varphi_{xx}^B - \varphi_{tt}^B &= \sin \varphi^B + \alpha \varphi_{tt}^B + \gamma^B + \frac{S}{1-S^2} \varphi_{xx}^A. \end{aligned} \quad (5)$$

Here $\varphi^A(x, t)$ and $\varphi^B(x, t)$ are the superconducting phase differences across the stacked junctions A and B, respectively, and γ^A and γ^B are the bias currents. The coupling coefficient $S = - \left[\left(\frac{t}{\lambda_L} + \coth \frac{d}{\lambda_L} + \coth \frac{d_e}{\lambda_L} \right) \sinh \frac{d}{\lambda_L} \right]^{-1}$ can be calculated from experimental parameters such as the tunnel barrier thickness t , the middle electrode thickness d , the thickness of the top and bottom electrodes d_e . Obviously, the coupling parameter S vanishes for $d \gg \lambda_L$. It is associated with screening currents in superconducting electrodes which are shared by fluxons belonging to different layers. A typical experimental value for S lies in the interval from -0.2 to -0.9 .

Eqs. (5) lead to two different modes, one with in-phase and another with out-of-phase oscillations in the two junctions. These modes have been predicted in the linear approximation many years ago by Ngai [53], but only recently observed experimentally [54]. The wave propagation velocities for these modes are noted as $\bar{c}_- = \bar{c}/\sqrt{1-S}$ (out-of-phase) and $\bar{c}_+ = \bar{c}/\sqrt{1+S}$ (in-phase) [55].

When applying a magnetic field H parallel to the Josephson barrier, one finds the Fiske steps in the $I-V$ curve of stacks. By measuring the voltage spacings between neighboring Fiske steps $\Delta V_- = \bar{c}_- \Phi_0/(2L)$ and $\Delta V_+ = \bar{c}_+ \Phi_0/(2L)$ the characteristic velocities \bar{c}_- and \bar{c}_+ can be measured experimentally for double-junction stacks with different thickness d of the common superconducting layer [55]. With decreasing d , the coupling is increasing, thereby increasing the difference between \bar{c}_- and \bar{c}_+ . A detailed analysis of experimental data is found to be in good quantitative agreement with theory [55].

Possible configurations of fluxon chains in a two-stack junction are shown in Fig. 11. In statics, the only stable state at high magnetic field is that in Fig. 11(a).

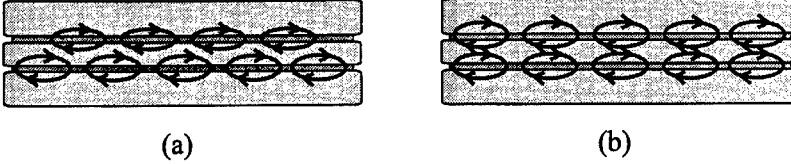


FIGURE 11. Sketches of a cross-section of two stacked long Josephson junctions. Fluxons may occupy both junctions in either out-of-phase configuration (a) corresponding to repulsion, or in-phase configuration (b) corresponding to mutual attraction between fluxons in different layers.

Its formation was studied by Song et al. [56]. In the dynamic state, in general, both configurations (a) and (b) may exist [57]. The transition from the state of Fig. 11(a) in the state of Fig. 11(b) is accompanied by a change in the spectrum of radiation generated by fluxon motion, as observed by Shitov et al. [58]. Numerical study of the states shown in Fig. 11 versus fluxon velocity can be found in Refs. [59,60]. Due to the difference of parameters (damping, bias current) between two junctions the locked state of moving fluxon chains may exist in a limited velocity range and can be destroyed via delocking transition [61] accompanied by flux-flow drag [62].

Fluxon configurations in two-stacked junction can be noted $[N|M]$ meaning N fluxons located in one LJJ and M fluxons in the other LJJ ($N, M < 0$ describe anti-fluxons). Using numerical simulations [52], it has been demonstrated that two solitary fluxons form the stable bound state $[1|1]$ with identical phases in two junctions $\varphi^A(x, t) = \varphi^B(x, t)$. This state has been analytically shown to be stable in the velocity range $\bar{c}_-/\bar{c} < u < \bar{c}_+/\bar{c}$ [63]. The coherent fluxon-antifluxon state ($[1|-1]$) which is stable up to the limiting velocity \bar{c}_- has been reported in experiments by Carapella et al. [64]. The asymmetric $[1|0]$ fluxon mode in two-fold stack leads to Cherenkov radiation which is discussed below in Sec. III C.

B Multi-layer stacked junctions

Josephson superlattices consisting of many stacked tunnel junctions were discussed in the literature long before they first became available for experiments [65–67,52]. Such a multi-junction stack of the overlap geometry is sketched in Fig. 12. It consists of N alternating superconducting and isolating layers. In a magnetic field H applied parallel to the layers, fluxons penetrate into different Josephson junctions and, under the influence of the bias current I_b , may move coherently due to the interaction of their screening currents flowing in the inner superconducting layers.

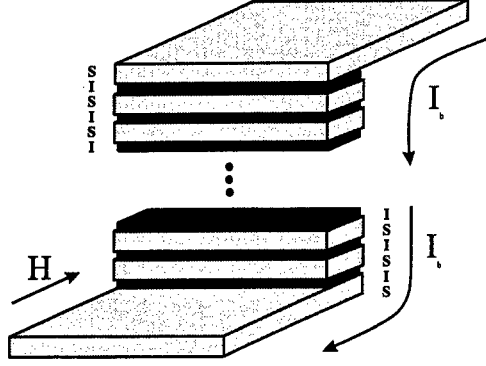


FIGURE 12. Stack of long Josephson junctions of the overlap geometry. In a typical experiment the magnetic field H is applied in the plane the tunnel barriers and the bias current I flows across them.

1 Model

The equations for such a stacked junction system may be obtained as a generalization of the single junction sine-Gordon equation [52]. Josephson junction stacks consisting of N junctions ($i = 1, \dots, N$) contain $N + 1$ superconducting layers. The system of equations which describe the Josephson phase dynamics in the stack can be written in the following form [52]:

$$\frac{\Phi_0}{2\pi\mu_0} \frac{\partial^2}{\partial x^2} \begin{pmatrix} \varphi_1 \\ \vdots \\ \varphi_i \\ \vdots \\ \varphi_N \end{pmatrix} = \begin{bmatrix} d_1'' & s^1 & 0 & 0 & 0 & 0 & 0 \\ s^1 & d_2'' & s^2 & 0 & 0 & 0 & 0 \\ 0 & \ddots & \ddots & \ddots & 0 & 0 & 0 \\ 0 & 0 & s^{i-1} & d_i'' & s^i & 0 & 0 \\ 0 & 0 & 0 & \ddots & \ddots & \ddots & 0 \\ 0 & 0 & 0 & 0 & s^{N-2} & d_{N-1}'' & s^{N-1} \\ 0 & 0 & 0 & 0 & 0 & s^{N-1} & d_N'' \end{bmatrix} \begin{pmatrix} J_1^Z \\ \vdots \\ J_i^Z \\ \vdots \\ J_N^Z \end{pmatrix} \quad (6)$$

where φ_i is the superconducting phase difference on i -th junction, x is the coordinate (not normalized). The coupling is determined by the parameters

$$d' = t_i + \lambda^{i-1} \coth \frac{d^{i-1}}{\lambda^{i-1}} + \lambda^i \coth \frac{d^i}{\lambda^i} \quad \text{and} \quad s^i = \frac{-\lambda^i}{\sinh(d^i/\lambda^i)}, \quad (7)$$

where t_i is the tunnel barrier thickness, d_i and λ_i are the thicknesses of the superconducting layer i and its London penetration depth, respectively. The sum of current components across the junction is

$$J_Z^i = \frac{\Phi_0}{2\pi} C^i \varphi_{tt}^i + \frac{\Phi_0}{2\pi} \frac{1}{R^i} \varphi_t^i + j_c^i \sin(\varphi^i) - j^i. \quad (8)$$

Here C , R , j_c and j are the junction capacitance, resistance, critical current and bias current densities, respectively.

Resonant modes for superlattices have been first calculated by Kleiner [68]. Similar to Fiske modes of conventional single-barrier junctions, Kleiner obtained general expressions for eigenfrequencies corresponding to standing wave patterns in the directions normal to the layers and along the layers. For N -junction stacks there exist N different modes [68,55]. Kleiner modes are characterized by phase shifts between Josephson oscillations in different layers. In fact, the above mentioned \bar{c}_- and \bar{c}_+ Fiske modes of two-fold stacks are nothing else but the lowest and the highest Kleiner modes: For a two-junction stack there are only two modes possible, the symmetric mode and the antisymmetric mode.

2 Low- T_C technology

Superconducting thin film technology of our days allows to grow high-quality multilayers with many Josephson tunnel barriers. Artificially prepared low- T_c stacked junctions serve as model systems for layered high- T_c superconductors [69]. The best multi-junction low- T_c stacks are made using Nb/Al-AlO_x/Nb junctions [70,71]. Recent achievements in this technology allowed fabrication of high quality stacks [72] with up to 28 layers [73] having parameter spread between layers of less than 5%. Other multi-layer junction technologies based on NbN [74] and NbCN [75] until now did not achieve parameter spread and junction quality comparable with Nb-based technology.

3 Experiments and simulations

Experiments with (Nb/Al-AlO_x) _{N} /Nb stacks with $N = 7$ and $N = 9$ [72,76] demonstrated collective motion of fluxons in $N - 2$ layers of the stack under the influence of the bias current. For the intermediate magnetic field range, pronounced resonant modes with large voltage spacing were found and interpreted as Kleiner resonances discussed above. Due to rather complex dynamics it is difficult to treat experimental data without detailed numerical modeling of these systems. Using the parameters of experimentally studied Nb/Al-AlO_x/Nb stacks, such simulations were presented by Thyssen et al. [77]. Fig. 13 shows numerically simulated $I - V$ curves for a 7-junction stack which indicates voltage-locked flux flow among the inner 5 junctions. The numbers of fluxons in the top and bottom junction were found to be larger than those in the inner junctions because of the thicker top and bottom Nb-electrodes. Numerical data showed good overall agreement with the experiment. The obtained voltage spacing between resonances is found to be very close to the experiment. This suggests that the dominating Kleiner mode is the lowest mode and every junction oscillates out of phase with its neighbor.

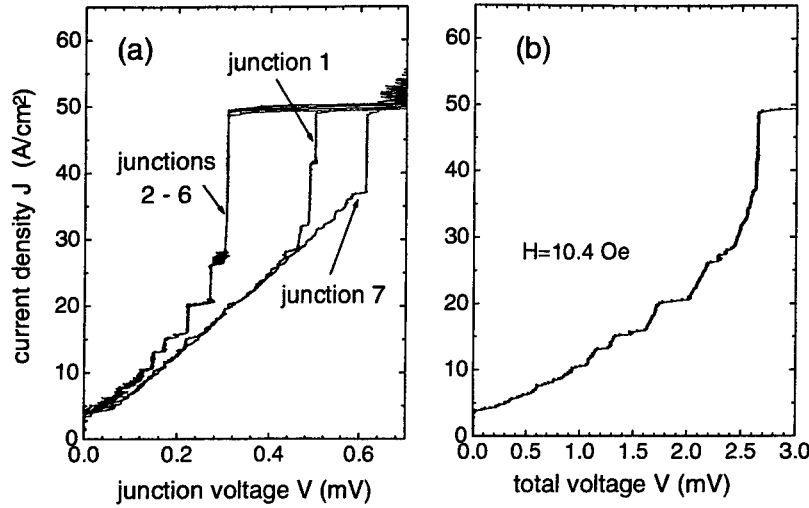


FIGURE 13. Simulated $I - V$ characteristics for the 7-fold stack [77]:(a) individual junction voltages; (b) total voltage on the stack.

4 Intrinsic high- T_C stacks

Single crystals of BSCCO and as well as some other exotic superconducting materials [78] show many properties of natural multi-layer Josephson junctions. Among these properties are the multi-hysteretic switching of individual tunnel junctions to gap voltages [44–46], the magnetic field dependence of the c -axis critical current [47] and flux-flow voltage [48,79], and Josephson radiation emission detected in several frequency bands [79]. Though some important intuitive knowledge can be inferred from comparing experimental data with numerical simulations using Eqs. (6) [68], the intrinsic junction stacks remain much more difficult to compare with theoretical models that artificially made Nb-based stacks.

C Cherenkov radiation of fluxons

The idea of possible Cherenkov radiation by a fluxon moving in a Josephson junction has been discussed in several theoretical papers [50,80,81]. Very recently, first experimental evidences for Cherenkov radiation have been obtained. These experiments, performed on two very different systems are briefly discussed below. The mechanism of the phenomenon is very general: Cherenkov radiation can be generated if the fluxon velocity $v = u\bar{c}$ becomes equal to the phase velocity ω/k of linear electromagnetic waves. This condition can be satisfied if the fluxon velocity v exceeds the lowest phase velocity of linear waves in the junction. Naturally, this can not be the case in conventional long junctions described by Eq. (1).

Very clear evidence for Cherenkov radiation by moving fluxon has been found by Goldobin et al. [82] in a system of two stacked annular Josephson junctions. Numerical simulations of the so called $[1|0]$ configuration (1 fluxon moving in junction A and no fluxon in junction B) shown in Fig. 14(a)-(d) demonstrate that the fluxon in junction A moves together with its image in junction B. As soon as the fluxon velocity v exceeds \bar{c}_- , an oscillating wake corresponding to Cherenkov radiation arises behind the moving fluxon and its image, as shown in Fig. 14(b)-(d). With increasing the fluxon velocity, the wavelength of the radiation increases while the amplitude and length of the wake quickly grow. When an integer number of Cherenkov radiation wavelengths fit into the circumference of the junction, resonances occur. Resonances result from interaction of the Cherenkov wave with the fluxon. The experimentally measured single-fluxon step with Cherenkov resonances is shown in Fig. 14(e). Resonances CS_2 and CS_3 are observed at $v > \bar{c}_-$ where \bar{c}_- corresponds to the junction voltage of about $29 \mu\text{V}$. Numerical simulations of the $I - V$ curve using experimental parameters showed excellent agreement with measurements [82].

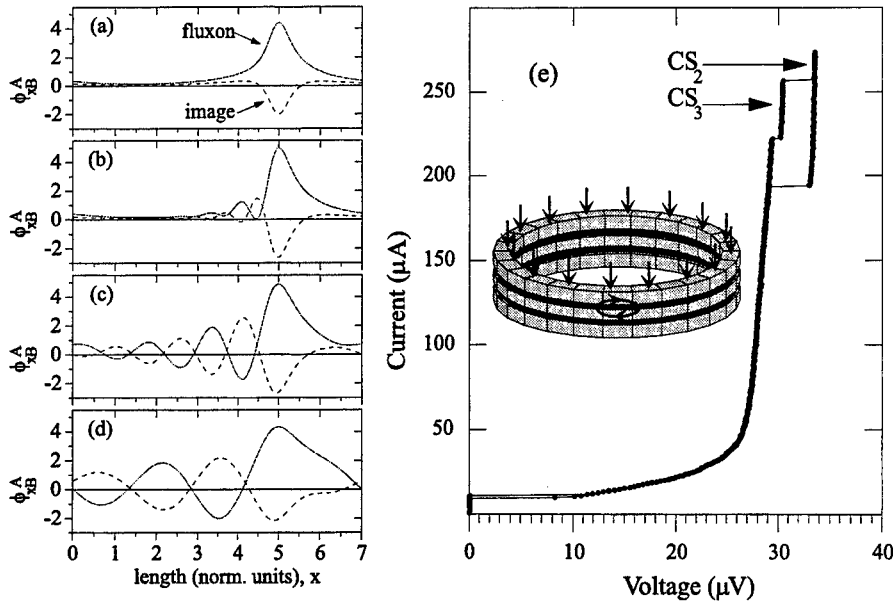


FIGURE 14. (Simulated profiles of $\varphi_x^{A,B}(x)$ in $[1|0]$ state of two stacked annular junctions [82]: (a) fluxon at velocity $v < \bar{c}_-$, and (b), (c), and (d) with steadily increasing of v above \bar{c}_- . (e) Experimental $I - V$ characteristic of such stack in $[1|0]$ state [82]. Cherenkov resonances are marked $CS_{2,3}$. The inset shows schematically the sample geometry.

Recently, Hechtfisher et al. [83] observed very unusual broadband non-Josephson radiation emission from BSCCO samples. At the higher magnetic fields, an addi-

tional microwave emission is found at voltages much higher than the voltage of the Josephson signal. The intensity of this signal is increasing towards the top of the flux-flow branch and is by almost one order of magnitude higher than that of the Josephson signal. Based on the magnetic field dependence of the radiation power and numerical simulations Hechtfischer et al. [83] suggested that the emission is due to the Cherenkov radiation by Josephson vortices moving in the multilayered stack. For a stack with N junctions, there are N different linear mode velocities. For strong coupling, the lowest mode velocity is about $\bar{c}/\sqrt{2}$ [79]. As soon as the fluxon velocity v rise above $\bar{c}/\sqrt{2}$ Cherenkov emission should appear. A numerical illustration of this effect in a system of 7 stacked Josephson junctions is shown in Fig. 15 [83]. To eliminate the influence of the boundaries, periodic boundary conditions were used. Fig. 15 shows a single vortex steadily moving in the middle junction with a velocity of $0.816 \bar{c}$, which is above the lowest two linear mode velocities. The waves trailing the vortex are caused by Cherenkov radiation: these waves are only observed when the lowest mode velocity of $0.721 \bar{c}$ is exceeded! For real intrinsic stacks with large number of layers simultaneous Cherenkov emission is expected at many close frequencies, therefore mixing between them does explain the broad band emission found in the experiment [83].

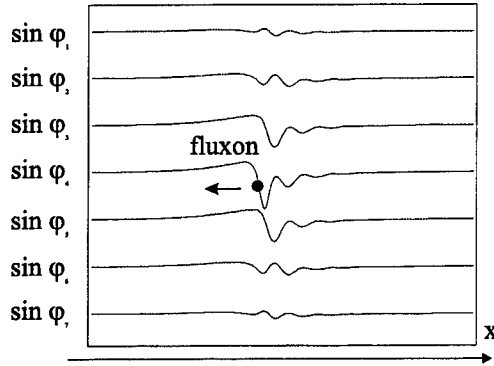


FIGURE 15. Spatial distribution of the supercurrents in a strongly coupled stack of seven Josephson junctions with periodic boundary conditions. A single vortex indicated by a circle is moving in the middle junction at a velocity of $0.816 \bar{c}$ which is higher than the lowest two mode velocities, 0.721 and $0.765 \bar{c}$. Cherenkov radiation in the form of a trailing wave and waves induced in the neighboring junctions can clearly be seen [83].

IV APPLICATIONS

Millimeter-wave oscillators using Josephson junctions go up to sub-THz frequencies and are promising devices for various sub-millimeter band applications. A significant stimulus for the development of Josephson millimeter-wave oscillators

is undoubtedly the fact that another Josephson element, the SIS mixer, is already firmly established as the best choice for a low-noise front-end detector in the range from ~ 100 GHz to ~ 1 THz. The intrinsic noise temperature of SIS mixers is limited only by fundamental quantum-uncertainty effects. Consequently, the idea of a fully integrated superconducting receiver assumes considerable importance, especially for space-borne communications and radio-astronomical systems in which high sensitivity and low weight, volume and power consumption are crucial. Long Josephson junctions operated in the flux-flow mode have shown rapid success as local oscillators in integrated sub-millimeter wave superconducting receivers [84,85]. Koshelets et al. [86,87] have already demonstrated an integrated 500 GHz quasi-optical receiver which combines a flux-flow oscillator and an SIS mixer on a single chip. The receiver showed the tuning range of more than 100 GHz and the double-side-band noise temperature as low as 140 K at 500 GHz. This is only a few times the fundamental quantum value $2\pi\hbar f/k_B$ (\hbar is Planck's constant, k_B is Boltzmann's constant).

Flux-flow oscillators based on long Nb/Al-AlO_x/Nb Josephson junctions have been successfully tested up to 850 GHz. This is already above the gap frequency of Nb! The power levels of up to $5\ \mu\text{W}$ at 440 GHz sufficient to pump an SIS-mixer, have been convincingly demonstrated. For spectral radio astronomy applications, besides the low noise temperature, also a high frequency resolution of the receiver is very important. This resolution is determined mainly by the *linewidth* of the local oscillator, and its longtime frequency stability which should be better than 10^{-6} of the center frequency.

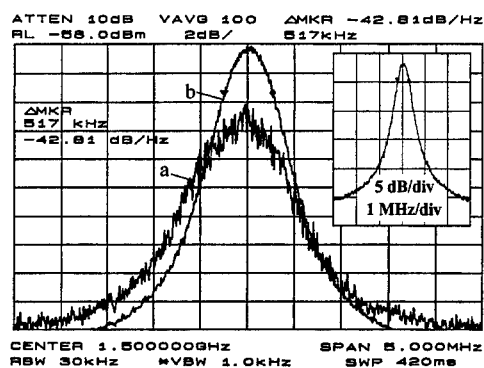


FIGURE 16. IF power spectra recorded at 4.2 K when the signal from the flux-flow oscillator ($f = 435$ GHz) is mixed with 45-th harmonic of the synthesizer signal ($f = 9.7$ GHz) for the case of (a) an autonomous flux-flow oscillator (b) the frequency locked by the microwave counter. The inset shows the IF power spectrum (b) recorded with a 5 dB/div scale.

Although the output power level of flux-flow oscillators is quite satisfactory for the integrated receiver applications, the radiation linewidth of the flux-flow oscillator remains one of the basic unsolved problems. Experimental measurements of the

linewidth of flux-flow oscillators have demonstrated reasonably low values. One of the best results obtained by Koshelets and co-workers [88] is presented in Fig. 16. The flux-flow oscillator spectra measured at the intermediate frequency (IF) of 1.5 GHz. In this type of measurements, the linewidth Δf (full width at half power level) as low as 200 kHz has been measured at 450 GHz at the temperature of 2 K. It should be noted that the narrowest linewidth has been measured on very steep resonant steps Fiske steps which have extremely low dynamic resistance. But even at the resonant steps the flux-flow oscillator linewidth appears to be by almost one order of magnitude larger than that predicted by the theory for Josephson oscillations in a lumped tunnel junction. The theoretical model for the flux-flow oscillator linewidth [89] predicts its extreme broadening at high fluxon velocities while the existing experimental data [88] show some radiation linewidth broadening but without clear velocity dependence.

For receiver applications, there is a need to get a more detailed understanding of the performance of the flux-flow oscillators under various operating conditions (losses, magnetic field, etc.), thus, more detailed study of the multi-fluxon regime should be done. Problems to investigate are the conditions of subharmonic locking by the external signal, the parameter range of stable operation, and the radiation linewidth problem mentioned above. In general, phase-locking of several oscillators offers larger output power and a narrower linewidth. Using stacked junctions is a very promising way to realize mutually phase-locked operation of flux-flow oscillators [58].

REFERENCES

1. P. L. Christiansen, preceding review in this book.
2. R. D. Parmentier, in: *Solitons in Action*, K. Lonngren, A. C. Scott, eds. (Academic Press, New York, 1978), p. 173.
3. N. F. Pedersen, in: *Solitons*, S. E. Trullinger, V. E. Zakharov, V. L. Pokrovsky, eds. (Elsevier, Amsterdam, 1986), p. 469.
4. R. D. Parmentier, in: *The New Superconducting Electronics*, H. Weinstock, R. W. Ralston, eds. (Kluwer, Dordrecht, 1993), p. 221.
5. N. F. Pedersen and A. V. Ustinov, *Supercond. Sci. Technol.* **8**, 389 (1995).
6. A. V. Ustinov, "Solitons in Josephson junctions", to appear in *Physica D* (1997).
7. K.K. Likharev, *Dynamics of Josephson Junctions and Circuits*, Gordon and Breach, New York (1986).
8. D. W. McLaughlin and A. C. Scott, *Phys. Rev. A* **18**, 1652 (1978).
9. T. A. Fulton and R. C. Dynes, *Sol. St. Commun.* **12**, 57 (1973).
10. A. Davidson, B. Dueholm, B. Kryger, and N. F. Pedersen, *Phys. Rev. Lett.* **55**, 2059 (1985).
11. A. V. Ustinov, T. Doderer, R. P. Huebener, N. F. Pedersen, B. Mayer, and V. A. Oboznov, *Phys. Rev. Lett.* **69**, 1815 (1992).
12. I. V. Vernik, N. Lazarides, M. P. Sørensen, A. V. Ustinov, N. F. Pedersen, and V. A. Oboznov, *J. Appl. Phys.* **79**, 7854 (1996).

13. T. Nagatsuma, K. Enpuku, F. Irie, and K. Yoshida, *J. Appl. Phys.* **54**, 3302 (1983); **56**, 3284 (1984); **58**, 441 (1985); **63**, 1130 (1988).
14. H. Akoh, S. Sakai, and S. Takada, *Phys. Rev. B* **35**, 5357 (1987).
15. A. Fujimaki, K. Nakajima, and Y. Sawada, *Phys. Rev. Lett.* **59**, 2895 (1987).
16. J. Nitta and A. Matsuda, *Phys. Rev. B* **35**, 4764 (1987).
17. E. Joergensen, V. P. Koshelets, R. Monaco, J. Mygind, M. R. Samuelsen, and M. Salerno, *Phys. Rev. Lett.* **49**, 1093 (1982).
18. B. Mayer, T. Doderer, R. P. Huebener and A. V. Ustinov, *Phys. Rev. B* **44**, 12463 (1991).
19. A. Laub, T. Doderer, S. G. Lachenmann, R. P. Huebener, and V. A. Oboznov, *Phys. Rev. Lett.* **75**, 1372 (1995).
20. S. G. Lachenmann, T. Doderer, R. P. Huebener, D. Quenter, J. Niemeyer, and R. Pöpel, *Phys. Rev. B* **48**, 3295 (1993).
21. S. G. Lachenmann, G. Filatrella, A. V. Ustinov, T. Doderer, N. Kirchmann, D. Quenter, R. P. Huebener, J. Niemeyer, and R. Pöpel, *J. Appl. Phys.* **77**, 2598 (1995).
22. D. Quenter, A. V. Ustinov, S. G. Lachenmann, T. Doderer, R. P. Huebener, F. Müller, J. Niemeyer, R. Pöpel, and T. Weimann, *Phys. Rev. B* **51**, 6542 (1995).
23. S. Keil, T. Doderer, I. V. Vernik, A. Laub, H. Pressler, R. P. Huebener, N. Thyssen, A. V. Ustinov, and H. Kohlstedt, *Phys. Rev. B* **54**, 14948 (1996).
24. S. G. Lachenmann, G. Filatrella, T. Doderer, J. C. Fernandez, and R. P. Huebener, *Phys. Rev. B* **48**, 16623 (1993).
25. T. Doderer, *Int. J. Mod. Phys. B* **11**, 1979 (1997); on using LTSEM for arrays of small Josephson junctions see also the paper by T. Doderer in this book.
26. S. N. Erne, A. Ferrigno, and R. D. Parmentier, *Phys. Rev. B* **27**, 5440 (1983).
27. M. Cirillo, T. Doderer, S. G. Lachenmann, F. Santucci, and N. Grønbech-Jensen, *Phys. Rev. B* **56**, 11889 (1997).
28. I. O. Kulik, *Sov. Phys. JETP* **24**, 1307 (1967).
29. S. Pace and U. Gambardella, *J. Low Temp. Phys.* **62**, 197 (1986); M. Cirillo, U. Gambardella, and S. Pace, *Phys. Scripta* **38**, 600 (1988).
30. A. V. Ustinov, P. Henne, and H. Kohlstedt, *Phys. Rev. Lett.* **77**, 3617 (1996).
31. N. Grønbech-Jensen, P. S. Lomdahl, and M. R. Samuelsen, *Phys. Lett. A* **154**, 14 (1991).
32. N. Martucciello and R. Monaco, *Phys. Rev. B* **53**, 3471 (1996).
33. N. Grønbech-Jensen, P. S. Lomdahl, and M. R. Samuelsen, *Phys. Rev. B* **43**, 12799 (1991).
34. I. V. Vernik, S. Keil, N. Thyssen, T. Doderer, A. V. Ustinov, H. Kohlstedt, and R. P. Huebener, *J. Appl. Phys.* **81**, 1335 (1997).
35. A. V. Ustinov, B. A. Malomed, and N. Thyssen, *Phys. Lett. A* **233**, 239 (1997).
36. A. V. Ustinov, *Pis'ma Zh. Eksp. Teor. Fiz.* **64**, 178 (1996) [*Sov. Phys. JETP Lett.* **64**, 191 (1996)].
37. M.R. Scheuermann, T.V. Rajeevakumar, J.J. Chang, and J.T. Chen, *Physica* **107B**, 543 (1981).
38. J. J. Chang, J. T. Chen, M. R. Scheuermann, D. J. Scalapino, *Phys. Rev. B* **31**, 1658 (1985).
39. R. Monaco, P. Barbara, J. Mygind, *Phys. Rev. B* **47**, 12292 (1993).

40. A. V. Ustinov, in: *Nonlinear Superconductive Electronics and Josephson Devices*, eds. G. Costabile et al., Plenum Press, New York, 1991, pp.315.
41. P. Barbara, R. Monaco, and A. V. Ustinov, *J. Appl. Phys.* **79**, 327 (1996).
42. W. J. Johnson, *Ph. D. Thesis*, University of Wisconsin (1968), unpublished; A. Davidson, N. F. Pedersen, and S. Pagano, *Appl. Phys. Lett.* **48**, 1306 (1986).
43. B. Dueholm, O. A. Levring, J. Mygind, N. F. Pedersen, O. H. Sørensen and M. Cirillo, *Phys. Rev. Lett.* **46**, 1299 (1981).
44. R. Kleiner, F. Steinmeyer, G. Kunkel and P. Müller, *Phys. Rev. Lett.* **68**, 2394 (1992).
45. R. Kleiner, P. Müller, H. Kohlstedt, N. F. Pedersen, and S. Sakai, *Phys. Rev. B* **50**, 3942 (1994).
46. A. Yurgens, D. Winkler, N. Zavaritsky, and T. Claeson, *Phys. Rev. B* **53**, R8887 (1996).
47. Yu. I. Latyshev, J. E. Nevelskaya, and P. Monceau, *Phys. Rev. Lett.* **77**, 932 (1996).
48. J. U. Lee, J. E. Nordman, and G. Hohenwarter, *Appl. Phys. Lett.* **67**, 1471 (1995).
49. M. B. Mineev, G. S. Mkrtchjan, and V. V. Schmidt, *J. Low Temp. Phys.* **45**, 497 (1981).
50. Yu. S. Kivshar and B. A. Malomed, *Phys. Rev. B* **37**, 9325 (1988).
51. N. Grønbech-Jensen, M. R. Samuelsen, P. S. Lomdahl, and J. A. Blackburn, *Phys. Rev. B* **42** 3976 (1990); N. Grønbech-Jensen, O. H. Olsen, and M. R. Samuelsen, *Phys. Lett. A* **179A**, 27 (1993).
52. S. Sakai, P. Bodin, and N. F. Pedersen, *J. Appl. Phys.* **73** (1993) 2411.
53. K. L. Ngai, *Phys. Rev.* **182** 555 (1969).
54. A. V. Ustinov, H. Kohlstedt, M. Cirillo, N. F. Pedersen, G. Hallmanns, and C. Heiden, *Phys. Rev. B* **48** (1993) 10614.
55. S. Sakai, A. V. Ustinov, H. Kohlstedt, A. Petraglia, and N. F. Pedersen, *Phys. Rev. B* **50**, 12905 (1994).
56. S. N. Song, P. R. Auvil, M. Ulmer, and J. B. Ketterson, *Phys. Rev. B* **53**, R6018 (1996).
57. A. V. Ustinov and H. Kohlstedt, *Phys. Rev. B* **54**, 6111 (1996).
58. S. V. Shitov, A. V. Ustinov, N. Iosad, and H. Kohlstedt, *J. Appl. Phys.* **80**, 7134 (1996).
59. A. Petraglia, A. V. Ustinov, N. F. Pedersen, and S. Sakai, *J. Appl. Phys.* **77**, 1171 (1995).
60. A. Wallraff, E. Goldobin, and A. V. Ustinov, *J. Appl. Phys.* **80**, 6523 (1996).
61. E. Goldobin, A. Wallraff, B. A. Malomed, and A. V. Ustinov, *Phys. Lett. A* **224**, 191 (1997).
62. R. D. Parmentier, P. Barbara, G. Costabile, A. D'Anna, B. A. Malomed, and C. Soriano, *Phys. Rev. B* **55**, 15165 (1997).
63. N. Grønbech-Jensen, D. Cai, and M. R. Samuelsen, *Phys. Rev. B* **48**, 16160 (1993).
64. G. Carapella, G. Costabile, A. Petraglia, N. F. Pedersen, and J. Mygind, *Appl. Phys. Lett.* **69**, 1300 (1996).
65. P. R. Auvil and J. B. Ketterson, *J. Appl. Phys.* **61**, 1957 (1987).
66. A. F. Volkov, *Pis'ma Zh. Exsp. Teor. Fiz.* **45**, 299 (1987) [*JETP Lett.* **45**, 376 (1987)]; A. F. Volkov, *Pis'ma Zh. Exsp. Teor. Fiz.* **50**, 127 (1989) [*JETP Lett.* **50**, 139 (1989)].

67. B. A. Malomed, I. B. Khalfin, and B. Ya. Shapiro, *Sol. St. Commun.* **87**, 223 (1993).
68. R. Kleiner, *Phys. Rev. B* **50**, 6919 (1994).
69. R. Kleiner, P. Müller, H. Kohlstedt, N. F. Pedersen, and S. Sakai, *Phys. Rev. B* **73**, 3942 (1994).
70. R. Monaco and A. Oliva, *Appl. Phys. Lett.* **64**, 3042 (1994).
71. H. Kohlstedt, F. König, P. Henne, N. Thyssen, and P. Caputo, *J. Appl. Phys.* **80**, 5512 (1996).
72. N. Thyssen, A. V. Ustinov, and H. Kohlstedt, *J. Low Temp. Phys.* **106**, 201 (1997).
73. N. Thyssen, unpublished (1997).
74. Z. H. Barber and M. G. Blamire, *IEEE Trans. Appl. Supercond.* **7**, 3609 (1997).
75. T. Kikuchi, S. Kiryu, S. Kohjiro, Q. Wang, A. Shoji, S. Sato, and S. Nagao, *IEEE Trans. Appl. Supercond.* **7**, 2426 (1997).
76. N. Thyssen, H. Kohlstedt, and A. V. Ustinov, *IEEE Trans. Appl. Supercond.* **7**, 2901 (1997).
77. N. Thyssen, H. Kohlstedt, S. Sakai, and A. V. Ustinov. Josephson Flux Flow in Multi-Junction Stacks: Experiment and Simulation. To be published in: *Proc. of the Third European Conference on Applied Superconductivity*, Eindhoven, June 1997.
78. P. Müller, in: *Festkörperprobleme / Advances in Solid State Physics*, vol. 34, ed. by Helbig (Vieweg, Braunschweig), p.1 (1995).
79. G. Hechtfischer, R. Kleiner, K. Schlenga, W. Walkenhorst, P. Müller, and H. L. Johnson, *Phys. Rev. B* **55**, 14638 (1997).
80. R. G. Mints and I. B. Snapiro, *Phys. Rev. B* **52**, 9691 (1995).
81. V. V. Kurin and A. V. Yulin, *Phys. Rev. B* **55**, 11659 (1997).
82. E. Goldobin, A. Wallraff, N. Thyssen, and A. V. Ustinov, Cherenkov Radiation in coupled long Josephson junctions. To appear in *Phys. Rev. B* (1997).
83. G. Hechtfischer, R. Kleiner, A. V. Ustinov, and P. Mueller, *Phys. Rev. Lett.* **79**, 1365 (1997).
84. V. P. Koshelets, A. V. Shchukin, S. V. Shitov, and L. V. Filippenko, *IEEE Trans. Appl. Supercond.* **3**, 2524 (1993).
85. V. P. Koshelets, S. V. Shitov, A. M. Baryshev, I. L. Lapitskaya, L. V. Filippenko, H. van de Stadt, J. Mees, H. Schaeffer, T. de Graauw, *IEEE Trans. Appl. Supercond.* **5**, 3057 (1995).
86. V. P. Koshelets, S. V. Shitov, L. V. Filippenko, A. M. Baryshev, H. Golstein, T. de Graauw, W. Luinge, H. Schaeffer, and H. van de Stadt, *Appl. Phys. Lett.* **68**, 1273 (1996).
87. V. P. Koshelets, S. V. Shitov, L. V. Filippenko, A. M. Baryshev, W. Luinge, H. Golstein, H. van de Stadt, J.-R. Gao, T. de Graauw, *IEEE Trans. Appl. Supercond.* **7**, 3589 (1997).
88. V. P. Koshelets, S. V. Shitov, A. V. Shukin, L. V. Filippenko, J. Mygind, and A. V. Ustinov, *Phys. Rev. B* **56**, 5572 (1997).
89. A. A. Golubov, B. A. Malomed, and A. V. Ustinov, *Phys. Rev. B* **54**, 3047 (1996).

General introduction to classical arrays formalism and physics

G. Costabile and G. Filatrella

*Dipartimento di Fisica and Unità INFN
University of Salerno
I-84081 Baronissi - Italy*

INTRODUCTION

The investigation of discrete structures consisting of a network of lumped Josephson junctions has followed the study of the continuous case of extended junctions. In fact, the technology to build reproducible and accurately defined structures consisting of many junctions has become available only after extended investigations of the electrically long structures. Also the theoretical investigations of the properties and the modelling of discrete structures has followed the development of the model for the continuous case. In this Chapter we will introduce the modelling of Josephson junction arrays following somehow the historical developments, *i.e.*, showing that a parallel array is but a discretized version of the continuous long Josephson junctions governed by the well known sine-Gordon equation (plus perturbative terms).

The modelling of 2-D arrays will be introduced as an extension of the equations of the 1-D case. The model equations can be derived with a different degree of accuracy, and the conditions under which the different models can be utilized is of particular importance for a comparison between the theoretical predictions and the experimental results. In fact most of the analytical predictions have been worked out in the context of the simplest Hamiltonian describing the system, the so called *XY* model. Actually most of the interest in 2D arrays of Josephson junctions has arisen because of the possibility to apply to such systems the known results for the *XY* model. It is therefore of great importance to understand under which conditions the *XY* equations are an acceptable model for 2-D arrays.

Another point that must be borne in mind are the conditions to neglect the so called charge effects. The problem arises when one considers junctions of very small capacitance, for which the passage of a single electron produces an appreciable voltage. In more accurate terms, when the energy of the capacitors E_C charged with a single electron is comparable to the Josephson energy E_J , the models introduced here are not complete. In the crudest approximation, the condition $E_J \gg E_C$ can be expressed in terms of the junctions parameters as $\hbar I_0/2e \gg e^2/2C$ (I_c being

the critical current of the junction and C the capacitance), and therefore one can decide *a priori* if the model described in the following is adequate for a specific array. Since the new terms are due to the granular nature of the charge, the arrays for which the charge effects can be neglected are often referred to as *classical* arrays.

ONE-DIMENSIONAL ARRAYS

One-dimensional superconductive arrays (1-D arrays) are periodic structures made of a row of Josephson tunnel junctions (or microbridges) biased in parallel and connected by superconductive links. Here, we shall not consider the case of series biased arrays, that, though very important for some applications (*e.g.*, voltage standard) exhibit a dynamic behaviour that is very different from the behaviour of the parallel arrays. The main reason for the difference is that the junctions in series arrays are not closed in superconducting loops and therefore the quantization rule does not apply. The derivation of the equations for these arrays is straightforward from Kirchhoff laws and will not be shown here.

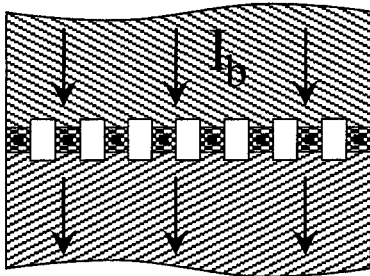


FIGURE 1. Sketch of an experimental geometry...

Among the several geometries that can be adopted to fabricate a 1-D array, the most simple is shown in Fig. 1, where the bias current is supplied through the two superconducting electrodes to the Josephson tunnel junctions that are fabricated (mostly using a *window* technique) in the region where the "fingers" of the electrodes overlap. A schematic diagram of the array is shown in Fig. 2, with the equivalent circuit based on the assumption that the junctions (*SIS* type) are well described by the *RSJ* model, that the current distribution is uniform, and that the "holes" between the junctions can be modeled by inductances connecting the *RSJ* elements; the resistance in parallel to the inductance accounts for high frequency losses in the superconductive films when some excitations propagate along the array.

Much of the basic dynamics of 1-D arrays can be understood looking at their *continuum* counterpart, *i.e.*, to the long *overlap* junction shown in Fig. , having

in mind, however, that the discreteness introduces some typical phenomena (like the localization of magnetic flux quanta) that cannot take place in continuous, homogeneous structures.

For a long *overlap* junction, the partial differential equation that describes the dynamics of the system [1], the Perturbed Sine Gordon Equation (*PSGE*), in normalized form, is:

$$\varphi_{xx} - \varphi_{tt} - \sin(\varphi) = \alpha\varphi_t + \beta\varphi_{xt} - \gamma, \quad (1)$$

with the boundary conditions

$$\varphi_x(0, t) + \beta\varphi_{xt}(0, t) = \varphi_x(L, t) + \beta\varphi_{xt}(L, t) = \eta. \quad (2)$$

In Eq. 1, φ is the quantum phase difference between the two superconducting electrodes of the junction, φ_t is the normalized voltage, α is a dissipative term due to quasiparticle tunneling, β is a dissipative term arising from the surface resistance (at high frequency) of the superconductors, γ is the bias current (normalized to the critical current I_0), and x and t are normalized space and time, respectively. In Eq. 2, η is a normalized magnetic field applied in the plane of the junction, perpendicular to its long dimension and L is the normalized junction length. The normalization is such that the length scale is given by the Josephson penetration length

$$\lambda_J = \sqrt{\frac{\hbar}{2e\mu_0 J_0 d}} \quad (3)$$

and the time scale by the inverse of the plasma frequency

$$\omega_J = \sqrt{\frac{2eJ_0}{\hbar C}} \quad (4)$$

where J_0 is the critical current density, d is the magnetic thickness, *i.e.* the sum of the London penetration depth in the electrodes plus the barrier thickness, and C is the distributed capacitance.

The long Josephson junction can sustain a large variety of dynamical states [2]: small and large amplitude localized oscillations, localized oscillations, and solitons, the most interesting in this context. A soliton here is an excitation that carries a magnetic flux quantum $\Phi_0 = h/2e$ in different dynamical configurations. The most important configurations, that can be clearly identified from current structures in the $I - V$ characteristics of the junctions, are:

1. the zero-field steps, states that arise with no external magnetic field. They consist of one or more fluxons oscillating back and forth in the junction with constant period; at each end, a fluxon is reflected as an antfluxon. In a more detailed analysis one finds [3] that the fluxon is reflected only if the energy lost by radiation at the reflection (due to the dissipation parameter α) is small enough;

2. the Fiske steps, consisting of fluxons, forced into the junction by an external magnetic field, propagating in one direction. When a fluxon reaches the junction end, it is not reflected, but a wave comes back and triggers a novel fluxon in;
3. the flux-flow steps, originated in such a high magnetic field that a chain of fluxons is established in the junction. The chain moves in the junction with constant (average) velocity and constant (on the average) number of fluxons.

A quite standard approach for the numerical integration of Eqs. 1-2 involves spatial discretization [4]. The approximation of the first derivative with the central difference and the approximation of the second derivative with a three-point difference, assuming an array of N points having a lattice spacing of a , yields the following set of equations:

- at point 1:

$$\frac{dV_1}{dt} = \frac{2}{a^2} (\varphi_2 - \varphi_1) + \frac{2\beta}{a^2} (V_2 - V_1) - \sin \varphi_1 - \alpha V_1 + \gamma - \frac{2\eta}{a}; \quad (5)$$

- at point n , $2 \leq n \leq N - 1$:

$$\frac{dV_n}{dt} = \frac{1}{a^2} (\varphi_{n-1} - 2\varphi_n + \varphi_{n+1}) + \frac{\beta}{a^2} (V_{n-1} - 2V_n + V_{n+1}) - \sin \varphi_n - \alpha V_n + \gamma; \quad (6)$$

- at point N :

$$\frac{dV_N}{dt} = \frac{2}{a^2} (\varphi_{N-1} - \varphi_N) + \frac{2\beta}{a^2} (V_{N-1} - V_N) - \sin \varphi_N - \alpha V_N + \gamma - \frac{2\eta}{a}; \quad (7)$$

- at all points:

$$\frac{d\varphi_n}{dt} = V_n. \quad (8)$$

Therefore the discretization of the *PSGE* produces a set of $2N$ first-order ordinary differential equations that are recognized to be the Kirchhoff circuit-law equations for the 1-D array that one would write down for the schematic model of Fig. 2. In other words, the discretization process applied to the distributed parameter model of the continuous *overlap* junction turns into a lumped element approximation that is, on the other hand, the most appropriate model for the 1-D array.

The question that arises is to what extent the solitonic solutions of the *PSGE* are preserved in the set of Eqs.5-7, or, physically, to what extent we can expect that the various dynamical states (zero-field steps, Fiske steps, flux-flow steps) considered

above may take place in the 1-D array, and to which extent they are modified. To answer this question, numerical simulations [5] were performed, showing that a crucial role is played by the parameter a . In fact, as long as $a \ll 1$ the discreteness effects are negligible, but as $a \rightarrow 1$ the effects become appreciable.

In both cases, as the shape of the fluxon is modulated by the discreteness of the array, small amplitude oscillations are generated, which can interact significantly with the fluxon itself. Therefore it is relevant to investigate, numerically and analytically, this mechanism. The idea of linearizing the equation for the small oscillations radiated by a modulated fluxon, and looking for stationary solutions of the linearized equations was first introduced by Peyrard and Kruskal [7], and later on developed by Ustinov *et al.* [8]. The starting point for the analysis [8] is the dispersion relation for the discrete system, that is qualitatively different from the dispersion relation in the continuous system. In fact, while the dispersion relation for Eq. 1 (neglecting losses and bias, and assuming an infinite line) is

$$\omega^2 = 1 + k^2 \quad (9)$$

where ω is the angular frequency and k is the wave number, the dispersion relation for Eq. 8 is

$$\omega^2 = 1 + \frac{4}{a^2} \sin^2 \frac{ka}{2}, \quad (10)$$

which reduces to Eq. 9 in the limit $a \rightarrow 0$. From Eq. 10 one can calculate the phase velocity for small amplitude oscillations and find the conditions for resonant interaction with a fluxon [8]. The interaction is manifested in the I - V characteristic of the array by the splitting of the zero-field step in sub-steps regularly spaced.

TWO-DIMENSIONAL ARRAYS

To describe the fundamental features of a two-dimensional (2-D) array, it is not as convenient as in the 1-D case to start from considering its *continuum* counterpart, as the progress in the knowledge of the dynamical states in two-dimensional Josephson junctions is far behind that of long Josephson junctions. Hence, after a summary of basic definitions, we shall start from the most elementary cell to identify the physical quantities that are relevant to model the 2-D array and the meaning of the approximations that can be introduced.

Basic definitions

We shall assume that a 2-D array is made by a planar structure consisting of *SIS* Josephson tunnel junctions connected by superconducting films as shown in Fig. 4. The lattice of Fig. 4 is made by elementary cells that are squares having one junction at each side. One may consider, alternatively, other geometries that can fill the

plane with a periodic structure (*e.g.* triangles), but the complexity of the problem will be the same. One can also consider arrays made of *SNS* Josephson junctions, or resistively shunted Josephson junctions. Such arrays, indeed, are fabricated and investigated whenever a nonhysteretic behaviour is required, and can be modeled with simpler models neglecting the junction capacitance. However, for the sake of generality we shall consider the array of Fig. 4 with the assumption that the junctions are described by *RSJ* model, as for the 1-D array, and we show in Fig. 5 the circuit model of a single cell.

In Fig. 6 it is shown a schematic view of an $N \times M$ array with the nomenclature commonly used in the literature. In the figure, $\varphi_{i,j}^h$ is the phase difference across the junction to the right of node i,j , while $\varphi_{i,j}^v$ is the phase difference across the junction on top of node i,j .

The elementary cell

To elucidate the problem of modelling a 2-D array, we shall consider the simplest structure coupling two Josephson junctions in a superconducting loop, *i.e.* the Josephson interferometer sketched in Fig. 7. Since there is a single superconducting loop, the fluxoid quantization [9] requires that

$$\varphi_2 - \varphi_1 = \frac{2\pi}{\Phi_0} \oint \mathbf{A} \cdot d\mathbf{l} + 2n\pi = 2\pi \frac{\Phi}{\Phi_0} + 2n\pi. \quad (11)$$

where $\varphi_{1,2}$ are the gauge invariant phases across the two junctions and Φ is the *total* magnetic flux threading the loop. The same condition can be re-written in terms of the circuit model from the Kirchhoff's law:

$$\frac{\hbar}{2e} (\dot{\varphi}_2 - \dot{\varphi}_1) + L \frac{dI_s}{dt} = 0 \quad (12)$$

that can be integrated producing

$$\varphi_2 - \varphi_1 = 2\pi \frac{\Phi}{\Phi_0} + \text{const.} \quad (13)$$

In Eq. 12 I_s is the screening current circulating in the loop. This interpretation clearly shows that the most general model for the 2-D array should take into account either *any* magnetic flux threading each cell, or, equivalently, the sum of the screening currents generated in each cell by the magnetic flux, in addition to the bias current. (In the literature, the screening current is often named "mesh" current).

Considering again the simple interferometer configuration, using current balance we may write the following equations of motion for the phase difference in the two junctions:

$$I_s = -I_b + I_0 \sin \varphi_1 + \frac{1}{R} \frac{\hbar}{2e} \dot{\varphi}_1 + C \frac{\hbar}{2e} \ddot{\varphi}_1 \quad (14)$$

$$-I_s = -I_b + I_0 \sin \varphi_2 + \frac{1}{R} \frac{\hbar}{2e} \dot{\varphi}_2 + C \frac{\hbar}{2e} \ddot{\varphi}_2 \quad (15)$$

that must be solved with the supplementary condition of Eq. 13 in order to find the three quantities φ_1 , φ_2 and I_s . The magnetic flux linked to the interferometer can be splitted in two parts, one generated by an external independent field (*e.g.*, generated by an external coil), one generated by the screening current I_s :

$$\Phi = \Phi^{ext} + LI_s. \quad (16)$$

Hence, Eq. 13 may be put in the form

$$\varphi_2 - \varphi_1 = 2\pi f + \frac{2\pi L}{\Phi_0} I_s \quad (17)$$

introducing the parameter f , said the *frustration* parameter, defined as

$$f = \frac{\Phi^{ext}}{\Phi_0} \quad (18)$$

Substituting Eq. 17 in Eqs. 14-15 we obtain two normalized independent nonlinear equations, in the form

$$\ddot{\varphi}_1 + \dot{\varphi}_1 + \sin \varphi_1 = \gamma - \frac{1}{\beta_L} (\varphi_2 - \varphi_1) + \frac{2\pi}{\beta_L} f \quad (19)$$

$$\ddot{\varphi}_2 + \dot{\varphi}_2 + \sin \varphi_2 = \gamma - \frac{1}{\beta_L} (\varphi_2 - \varphi_1) - \frac{2\pi}{\beta_L} f \quad (20)$$

where

$$\alpha = \frac{1}{R} \sqrt{\frac{\Phi_0}{2\pi C I_0}} \quad (21)$$

is the dissipation parameter,

$$\beta_L = \frac{2\pi L I_0}{\Phi_0} \quad (22)$$

is the so-called SQUID parameter or coupling parameter, γ is the bias current normalized to the critical current I_0 , the time is normalized to the inverse of the Josephson frequency

$$\omega_J = \sqrt{\frac{2e I_0}{\hbar C}} \quad (23)$$

If we neglect the screening current, we obtain a drastic simplification. In fact, Eqs.19-25 take the form

$$\ddot{\varphi}_1 + \dot{\varphi}_1 + \sin \varphi_1 = \gamma \quad (24)$$

$$\ddot{\varphi}_2 + \dot{\varphi}_2 + \sin \varphi_2 = \gamma \quad (25)$$

and the fluxoid quantization becomes

$$\varphi_2 - \varphi_1 = 2\pi f. \quad (26)$$

Taking the sum of Eqs. 24-25 and inserting Eq. 26, one obtains the equation for φ_1 :

$$\gamma = \ddot{\varphi}_1 + \dot{\varphi}_1 + \frac{1}{2} [\sin \varphi_1 + \sin (\varphi_1 - 2\pi f)] \quad (27)$$

i.e., a single equation, that in the special case $f = 1/2$ is further simplified into a linear equation. In other words, the suppression of the screening current eliminates one degree of freedom: the system is now "rigid" as the difference between the Josephson phases of the junctions is constant, only determined by the external magnetic field.

The screening currents

The discussion in the previous section shows clearly that the approximation of the magnetic flux Φ affecting a superconducting loop containing Josephson junctions with the flux Φ^{ext} generated by an external coil can change qualitatively the model, and, of course, the expected behaviour of the system. To proceed further in the analysis of the problem, we may think of the total flux threading an array cell as consisting, in the most general case, of three contribution:

$$\Phi = \Phi^{ext} + \Phi^s + \Phi^{circ}. \quad (28)$$

The first two contribution, Φ^{ext} and $\Phi^s = LI_s$, are those that have been discussed in the simple case of the single interferometer. The third contribution, Φ^{circ} , arises in the case of a multiple cell device, *i.e.*, a 1-D or a 2-D device. It comes from the field lines threading a cell generated by currents circulating in other cells of the array. In other words, Φ^s is due to the self-inductance of the cell and Φ^{circ} is due to the mutual inductance between the cells. Therefore, we can list the models in increasing order of complexity:

1. neglecting all but the flux generated by an external, independent source Φ^{ext} we put rigid constraints between the junction phases given by the external field (*XY* or *spin glass* model);
2. adding the self-field flux $\Phi^s = LI_s$ we add internal degrees of freedom to the system and a more complex model (the *Nakajima-Sawada approximation*) [10];

3. adding the mutual inductance effects as well,

- (a) we can take into account only the interactions between cells that have a branch in common (*nearest neighbours approximation*);
- (b) we can take into account the interaction of any cell on any other of the array (*full matrix description*) [12].

Unfortunately, it is not always a simple matter to understand to what degree a given array can be approximated with one of the simplest models, because this depends not only on the intrinsic parameters of the array, but also on the operating range. To clarify this point, we shall consider the calculation of the maximum screening current I_s^m (defined as $I_s^m = \max |I_s/I_0|$, i.e. the maximum value of the screening current normalized to the critical current of a single junction) of a 10×10 array using the Nakajima-Sawada approximation [11].

In Fig. 8 it is evident that in some regions of the parameter space the screening currents could be neglected and the XY model could provide a satisfactory description of the arrays, while in others the screening currents can be several times larger than the junction critical currents.

The XY model

The two extrema in the complexity scale of the array modelling are the full matrix approach and the XY model. The latter is very appealing, not only for the sake of simplicity, but also because it relates the arrays to other physical systems and brings in some very useful tools of analysis [13]. There is a very wide literature on this topic; here we will give only a simple description of the approach, referring the reader to the bibliography cited in Ref. [13].

Let us consider a Josephson junction lattice as in Fig. 6 and indicate by ϕ_k the gauge invariant phase of the superconducting electrode that is at node (i, j) and by ϕ_l the gauge invariant phase of the superconducting electrode of node $(i + 1, j)$ so that

$$\varphi_{ij}^h = \phi_l - \phi_k - \frac{2e}{\hbar c} \int_k^l \mathbf{A} \cdot d\mathbf{l}. \quad (29)$$

Therefore, the Josephson current and the voltage across the considered junction are given by

$$i_{ij}^h = I_0 \sin \left(\phi_l - \phi_k - \frac{2e}{\hbar c} \int_k^l \mathbf{A} \cdot d\mathbf{l} \right) \quad (30)$$

and

$$V_{ij}^h = \frac{\hbar}{2e} \frac{d}{dt} \left(\phi_l - \phi_k - \frac{2e}{\hbar c} \int_k^l \mathbf{A} \cdot d\mathbf{l} \right). \quad (31)$$

The energy stored in the junction can be calculated from the last two equations [14] as

$$E_{ij}^h = -\frac{\hbar I_0}{2e} \cos \left(\phi_l - \phi_k - \frac{2e}{\hbar c} \int_k^l \mathbf{A} \cdot d\mathbf{l} \right), \quad (32)$$

where the coefficient $E_J \equiv \hbar I_0/2e$ is known as the "Josephson coupling energy". If there is no external magnetic field, the last term in Eq. 32 is zero, and the Hamiltonian for the whole array, summing the interactions of each electrode with its nearest neighbours, can be written as

$$H = - \sum_{kl} E_J \cos(\phi_l - \phi_k). \quad (33)$$

If the electrode wavefunction phase ϕ is reinterpreted as the angle that a unit vector \mathbf{s} makes with a fixed axis, then the last equation can be put in the form

$$H = - \sum_{kl} E_J \mathbf{s}_k \cdot \mathbf{s}_l, \quad (34)$$

i.e., the same Hamiltonian that is written for a two-dimensional lattice of spins. From this observation, one can translate into the array description a number of results already worked out for the so-called spin glass system. The most important is the spontaneous insurgence of vortices at finite temperature and the possibility of a Kosterlitz-Thouless (KT) transition. In the spin system, at zero temperature in the ground state all the spins are parallel; in the array, this corresponds to no difference between the electrode phases whatsoever, and hence no current in any junction. But at finite temperature vortex-antivortex pairs are spontaneously generated. In the spin glass, they consist of the spins pointing radially around a symmetry center, directed outward (vortex) or inward (antivortex). In the array, this would correspond to a current circulating around the symmetry center, with a density decreasing as $1/r$, clockwise or counterclockwise. The current is originated by the difference between the phases being other than zero, and its density decreases as $1/r$ because the larger is the radius of the circumference considered, the smaller is the phase difference between nearest neighbours. At low temperature, the pairs are bound. But there is a critical temperature, said the Kosterlitz-Thouless transition temperature T_{KT} , at which the pairs start to unbind. Without giving any detail, we shall only mention that theory predicts a different behavior of the $I-V$ characteristic obtained biasing the array: below T_{KT} a power law is expected, $V \propto I^{\alpha(T)}$, while exceeding T_{KT} the free vortex motion produces ohmic dissipation and, therefore, a linear dependence is expected. If an external magnetic field is applied to the array, the full Hamiltonian must be considered:

$$H = - \sum_{kl} E_J \cos \left(\phi_l - \phi_k - \frac{2e}{\hbar c} \int_k^l \mathbf{A} \cdot d\mathbf{l} \right) \quad (35)$$

and the states are quite more complex, as the magnetic field breaks the symmetry of the system and favours the generation of vortices of one polarity.

CONCLUSIONS

The choice of the appropriate model for discrete arrays cannot be done easily, the model to be used not only depends on the numbers of details that one wants to reproduce, but also by the value of the parameters of the array. In fact a model that can prove to be appropriated in a certain region of the parameters can be inadequate to describe the array in another region of the parameters. While the model choice for numerical simulations might be just a problem of computational cost, the analytical investigations of the arrays has been developed essentially with the simplest XY model. It has therefore happened that the problem has been quite often reversed: to try to fabricate an array whose behavior is described accurately enough by the simplest model.

ACKNOWLEDGMENTS

This lecture was scheduled as the opening lecture to be given by the late Prof. R. D. Parmentier. The authors have followed his approach to the description of arrays [15], as a tribute to his memory.

REFERENCES

- ¹ N. F. Pedersen, in *Solitons*, S. E. Trullinger, V. E. Zakharov, V. L. Pokrovsky, eds. (Elsevier, Amsterdam, 1986) 469.
- ² R. D. Parmentier, in *The New Superconducting Electronics*, H. Weinstock, R. W. Ralston, eds. (Kluwer, Dordrecht, 1993) 221.
- ³ D. W. McLaughlin, A. C. Scott, Phys. Rev. A **18** (1978) 1652.
- ⁴ P. J. Davis, I. Polonsky, in *Handbook of Mathematical Functions*, 9th printing, M. Abramowitz, I. A. Stegun, eds. (Dover, New York, 1965), chap. 25.
- ⁵ J. F. Currie, S. E. Trullinger, A. R. Bishop, and J. A. Krumhansl, Phys. Rev. B **15** (1977) 5567.
- ⁷ M. Peyrard and M. D. Kruskal, Physica D **14** (1984) 88.
- ⁸ A. V. Ustinov, M. Cirillo, and B. A. Malomed, Phys. Rev. B **47** (1993) 8537.
- ⁹ A. Barone and G. Paternò, *Physics and Applications of the Josephson Effect* (Wiley, New York, 1982).
- ¹⁰ K. Nakajima and Y. Sawada, J. Appl. Phys. **52** (1981) 5732.
- ¹¹ A. Petraglia, G. Filatrella, and G. Rotoli, Phys. Rev. B **53** (1996) 2732.
- ¹² J.R. Phillips, H.S.J. Van der Zant, J. White, and T.P. Orlando, Phys. Rev. B **47** (1993) 5219.
- ¹³ D. Dominguez and J.V. Jose', Int. J. Mod. Phys. B **8** (1994) 3749.
- ¹⁴ K. K. Likharev, *Dynamics of Josephson Junctions and Circuits* (Gordon and Breach, New York, 1986).
- ¹⁵ R.D. Parmentier, Acta Physica Slovaca **44** (1994) 303.

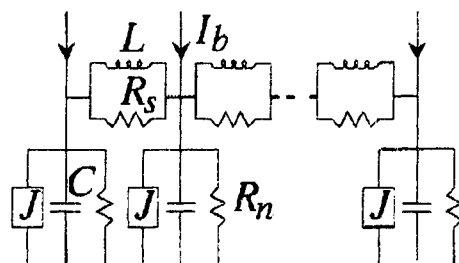


FIGURE 2. Schematic model of the 1-D array

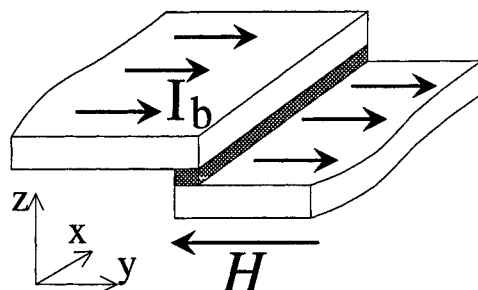


FIGURE 3. Sketch of the geometry of a long *overlap* Josephson junction

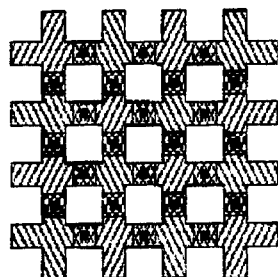


FIGURE 4. A 2-D array of square cells, having one junction at each side.

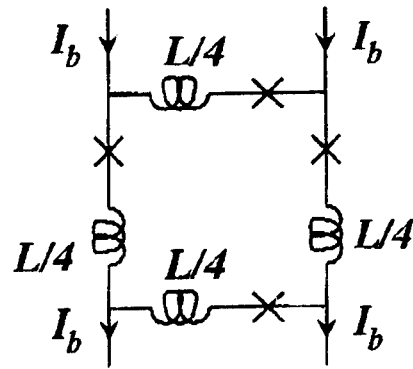


FIGURE 5. Circuit model for a single cell of the array of Fig. 4. The inductance of the superconductive loop, L , is evenly shared among the four sides. I_b is the bias current.

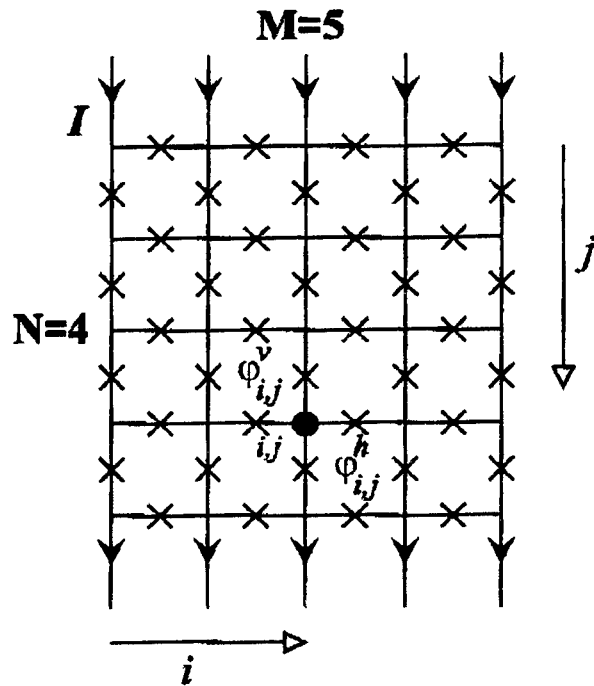


FIGURE 6. A schematic representation of the 2-D array. To simplify the figure, the loop inductances were suppressed from the drawing.

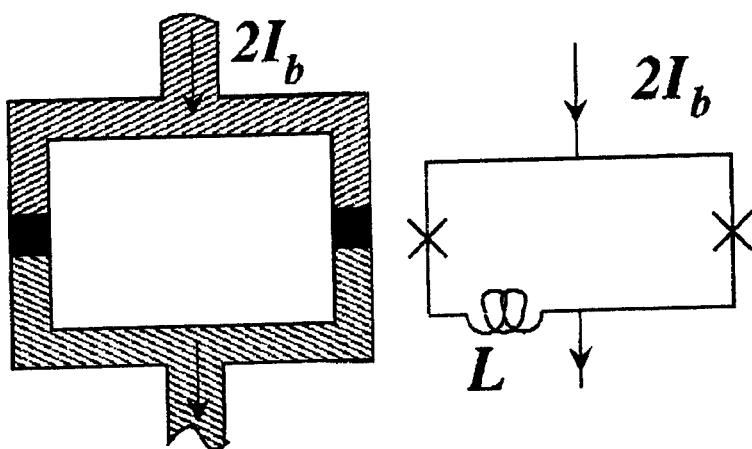


FIGURE 7. The Josephson interferometer and its circuit model.

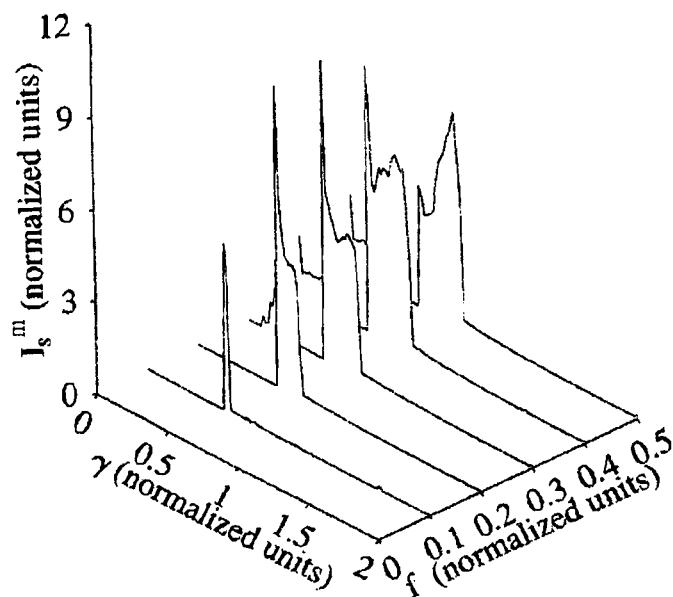


FIGURE 8. Maximum screening current as a function of γ and f for an array 10×10 with $\beta_L = 1$ and $\alpha = 1$.

Dynamics in classical Josephson Junction Arrays: models and numerical simulations

José C. Ciria † and C. Giovannella ‡‡

† *Departamento de Física Teórica, Universidad de Zaragoza C/ Pedro Cerbuna 12. 50010 Zaragoza, España.*

‡ *Dipartimento di Fisica, Sezione INFN and Sezione INFM dell'Università di Roma Tor Vergata, Via della Ricerca Scientifica 1, 00133 Roma, Italy.*

Abstract.

These lecture notes are divided in three main sections. In the first one we give a detailed derivation of the equation of motion of an array of resistively and capacitively shunted Josephson Junctions (JJA). The derivation starts from a Lagrangian written for the gauge invariant phase, ϕ_{ij} , and its conjugate variable, ϕ_{ij} , and it is done in the full inductance-matrix approximation. The ohmic dissipation due to the shunting resistances is taken in account through the introduction in the Euler-Lagrangian equation of a convenient Rayleigh's function. The JJA formalism, then, is extended to the much more complex case of a granular superconductor. In order to make clear the relationship between the JJA formalism and those developed in the framework of other discrete models, like the discrete sine-Gordon and the Frenkel-Kontorova ones, a paragraph is devoted to their comparative analysis. The relationship between phase and 'particle' dynamics is also briefly discussed. In the second section we provide the 'beginners' with some basic ideas on how to perform numerical simulations based on the JJA formalism. Finally, in the third section we give a flavour of the physical problems that one can solve by 'running' numerical codes like the ones we have developed. The dynamical properties of single massless and massive vortices and those of a JJA subjected to an external ac driving force are briefly discussed.

INTRODUCTION

Arrays of Josephson Junctions (JJAs), see fig. 1, constitute one of the most intriguing examples of coupled non-linear oscillators [1], [2], due to the richness of their physics (macroscopic quantum phenomena, phase transitions, locking and chaos, etc.) which finds counterparts in many physical and biological systems [3]. and to the possibility of using JJAs in the production of useful cryoelectronic devices

CP427, *Superconductivity in Networks and Mesoscopic Systems*

edited by Giovannella/Lambert

© 1998 The American Institute of Physics 1-56396-750-2/98/\$15.00

with unique properties and an extreme low power consumption (see the lectures notes by T. Doderer, J. Mygind and M. Darula).

All the interesting applications of JJAs in cryoelectronics rely on the formation and on the displacement of special quasi-solitonic excitations in the gauge invariant phase: the so called vortices/antivortices.

As shown in the previous lecture notes by G. Filatrella and G. Costabile, a vortex is an 'object' that obeys the fluxoid quantization rule: the sum of the gauge invariant phase circulation along any path enclosing the vortex plus the magnetic flux through the surface defined by this path has to be always $2n\pi$ where n is an integer number, see fig. 3 of the by A. Ustinov's lecture notes.

Vortex-antivortex couples develop in JJAs whenever a perturbation breaks the symmetry of the flowing current on a local scale and acts for long enough to transfer into the system the needed formation energy. As an example, in biased samples, vortices form because of current spikes, of geometrical defects, of an inhomogeneous spatial distribution of the bias current, of a perturbation caused by an incoming photon, and so on [4].

Why are vortices/antivortices so relevant for cryoelectronics devices?

In overdamped JJAs vortices can be likened to massless particles; their displacement can be used to transfer elemental bits of information.

In underdamped JJ systems, on the other hand, the vortices acquire a mass (i.e. a kinetic contribution to their energy) and can be reflected at the border of the sample. One can use the periodic reflections of the vortices to fabricate oscillators able to emit and detect electromagnetic radiation in the hyperfrequency domain. Unfortunately, the e.m. power emitted by a single oscillator (vortex/antivortex) is quite low (of the order of a microWatt) as, also, its output impedance (a few Ohms) [5]. In JJAs, however, under certain experimental conditions, several vortices may couple each others giving origin to a coherent motion (a dynamical locked state) that, in principle, should lead to an electromagnetic emission whose power is proportional to N^2 , where N is the number of the oscillators involved in the process (see the lecture notes by T. Doderer and M. Darula for further details).

The main aim of this lecture notes is to give a rigorous derivation of the equation of motion that regulates the dynamics of the vortices in the JJAs.

THE DISCRETE 'JJ ARRAY FORMALISM'

The discrete JJA Lagrangian

The Lagrangian of a Josephson junction array subjected to the action of an external forcing term (a bias current applied along the y-direction) and to a local random force (the thermal noise) is given by:

$$L = E_J \left\{ \sum_{ij} (\cos \phi_{ij} - 1) + \frac{\beta_c}{2} \sum_{ij} \dot{\phi}_{ij}^2 + \sum_{i;kl} i_{ext;i} [(DG)^{-1} D]_{i;kl} \phi_{kl} - \sum_{ij} \tilde{i}_{ij} \phi_{ij} \right\}$$

$$\begin{aligned}
& -\frac{1}{2} \sum_{p,q} (R\phi + 2\pi f)_p \Lambda_{p,q}^{-1} (R\phi + 2\pi f)_q \\
& - \sum_{p,i} (R\phi + 2\pi f)_p \left(\Lambda^{-1} \Delta - (RR^T)^{-1} RM \right)_{p,i} i_{ext;i} \}. \quad (1)
\end{aligned}$$

Here, $\phi_{ij} = \theta_i - \theta_j - a_{ij}$ is the gauge invariant phase difference along the junction ij . θ_i is the phase of the pseudo-wavefunction describing the state of grain i , $|\Psi_i| \exp(i\theta_i)$, where $|\Psi_i|^2 = n_s$ (n_s is the density of the superconducting pairs and $|\Psi_i|$ is constant for all the grains: $|\Psi_i| = |\Psi|$). a_{ij} is related to the vector potential \vec{A} through $a_{ij} = \frac{2\pi}{\Phi_0} \int_i^j \vec{A} \cdot d\vec{x}$. i, j stand for nearest-neighbour points and p runs over the plaquettes of the array. Λ and Δ will be defined further on in this section.

The physical meaning of operators P_r , D and G is simple to understand. As is well-known, any vector field can be expressed as the sum of a solenoidal field plus an irrotational one (with vanishing divergence and curl, respectively). We call the operator that, applied to any field, select its solenoidal (irrotational) component P_r (P_d). These operators can be expressed as $P_d = G(DG)^{-1}D$ (where G and D are discrete versions of the operators gradient and divergence), $P_r = R^T(RR^T)^{-1}R$ (with R the discrete rotational operator). Of course, $RG = 0$, $P_r P_d = 0$, $P_r P_r = P_r$, $P_d P_d = P_d$, $P_r + P_d = 1$. We have chosen the London gauge ($\vec{\nabla} \cdot \vec{A} = 0$), so that $(DG)^{-1}D\phi = \theta$, $(P_d\phi)_{ij} = \theta_i - \theta_j$ and $(P_r\phi)_{ij} = -a_{ij}$.

The ϕ_{ij} are connected to the normalized junction voltage drop $v = (2e/h)V$ measurable at the junction through the Josephson relation: $\dot{\phi}_{ij} = 2\pi v$.

$E_J = (\Phi_0 I_c / 2\pi)$ is the junction coupling energy and Φ_0 is the elemental quantum of flux. ($\Phi_0 = h/2e = 2.068 \cdot 10^{-15} \text{Vs}$). $\Lambda_{ij;kl}$ is the full inductance matrix, normalized to $\Phi_0 / (2\pi I_c)$. $\beta_c = \frac{2e I_c R^2 C}{\hbar}$ is the McCumber parameter where R and C are respectively a characteristic shunt resistance and capacitance (see further on for their definition). \tilde{i} is a thermal-induced noise current. The currents are normalized to the critical current of the junction, I_c . $\tau = \frac{2e R_e I_c}{\hbar} t$ is the normalized time.

Equation (1) has been written using the conjugate pair of variables ϕ and $\dot{\phi}$ to stress that the gauge invariant phases are the relevant dynamical variables (the equivalence between phase and vortex dynamics is discussed further on either in these lecture notes and in the lectures notes by H. van der Zant).

Let us now examine one by one the terms of the Lagrangian. The first one accounts for the energy stored in the Josephson junctions. The second term represents the energy stored in the electric field; it depends both on the capacitance of each single island with respect to the ground, C_i , and on the capacitance between the nearest-neighbour islands, C_{ij} , i.e. the capacitance of the junctions. Since C_{ij} is always much larger than C_i [6], in the rest of this lecture notes the contribution due to the self-capacitance will be neglected.

The third and fourth terms are related to the work done on the system by the external current generator (either dc or ac) and by a white-noise current (that takes into account the thermal noise generated by the resistors). Usually this latter is chosen so that $\langle i_{ij}(\tau) \rangle = 0$ and $\langle i_{ij}(\tau + \tau_0) i_{kl}(\tau) \rangle = \frac{2k_B T}{R_{ij}} \delta(\tau_0) \delta_{ij;kl}$.

The last terms of equation (1) represent the main difference between the XY formalism, where λ_{\perp} is always taken equal to ∞ [7] and the 'JJ array formalism' where λ_{\perp} can assume finite values [8], [9], [10]. They are related to the energy stored in the magnetic field due to the mutual inductance of branches of the array. The normalized inductance matrix (Λ) connects the induced magnetic flux through the plaquettes to the mesh currents defined on each cell (the relation between link and mesh current is given further on in this section, see also figure 1):

$$\Phi_{ind;p} = \sum_{p,q} \Lambda_{p,q} i_q. \quad (2)$$

The vector potential includes the contributions from both the external and the internal magnetic fields:

$$a_{ij} = \frac{2\pi}{\Phi_0} \int_i^j (\vec{A}_{ij;ext} + \vec{A}_{ij,int}) d\vec{r}. \quad (3)$$

The flux of the external magnetic field through plaquette p is

$$(Ra_{ext})_p = 2\pi f_p = \frac{2\pi}{\Phi_0} \int_p \vec{B}_{ext} d\vec{S}, \quad (4)$$

where \vec{S} is normal to the surface of the plaquette, S , and $\vec{B}_{ext} = \nabla \times \vec{A}_{ext}$.

The $a_{ij,int}$ are due to the currents circulating in the array (i_{ij}) [10]:

$$a_{ij,int} = \sum_{kl} \frac{1}{4\pi\lambda_{\perp}} f f_{ij,kl} i_{kl}, \quad (5)$$

where λ_{\perp} is the normalized effective penetration depth of the array [8]:

$$\lambda_{\perp} = \frac{1}{2\pi} \frac{\Phi_0}{\mu_0 I_c l_a} \quad (6)$$

with l_a the lattice spacing of the array. $f f_{ij,kl}$ is a form factor matrix related to the geometry of the array. In most cases all the non-diagonal elements of the $f f$ matrix can be assumed to depend only on the relative distance between the links of the array, $r = r_{ij} - r_{kl}$ and not on the shape of the Josephson junction. The self-term, on the other hand, diverges when $r \rightarrow 0$ and this forces us to consider the particular geometry of the junction in order to introduce the appropriate geometrical cut-off. For further details see next section.

The link currents are related to mesh currents through $\mathbf{i}_{link} = R^T \mathbf{i}_{mesh} + M \mathbf{i}_{ext}$. $M_{ij,k} = 1$ if k is a site belonging to the first row, and ij is a vertical link aligned with it; otherwise, $M_{ij,k} = 0$. The Biot-Savart equation (5) can be expressed as

$$\Phi_{ind} = \Lambda \mathbf{i}_{mesh} + \Delta \mathbf{i}_{ext} \Rightarrow \mathbf{i}_{mesh} = \Lambda^{-1} (\Phi_{ind} - \Delta \mathbf{i}_{ext}). \quad (7)$$

where the matrix Δ is defined as:

$$\Delta = \frac{1}{4\pi\lambda_{\perp}} R f f M; \quad (8)$$

and Λ can be easily related to $f f$:

$$\Lambda = \frac{1}{4\pi\lambda_{\perp}} R f f R^T. \quad (9)$$

We stress that by means of eq. (5) the current contribution to the local vector potential, $a_{ij;int}$, can be worked out exactly for each link and is no any longer introduced as a mean-field quantity [11]. The difference may be quite important, especially for finite 2D systems with relatively small dimensions, such as the ones commonly used in the experiments.

Since in this lecture notes we deal with arrays for which charging effects and the fluctuations of the amplitude of the superconducting order parameter are negligible, we have dropped Lagrangian terms like $-\hbar n_s P_d \theta_i$ and $-(n_s - \tilde{n}) q P_d V_i$ that are related to the displacement of charges (n_s is the density of the superfluid, \tilde{n} is the back-ground charge density and V_i is the scalar potential); by applying Lagrangian equations to these terms, the Josephson voltage relationship can be obtained [12].

The equation of motion

The Euler-Lagrange equations for our system are

$$\frac{d}{dt} \left(\frac{\partial L}{\partial \dot{\phi}_{ij}} \right) - \frac{\partial L}{\partial \phi_{ij}} + \frac{\partial \mathcal{F}}{\partial \dot{\phi}_{ij}} = 0, \quad (10)$$

where \mathcal{F} is Rayleigh's function giving the ohmic dissipation

$$\mathcal{F} = \frac{1}{2} \sum_{ij;kl} \dot{\phi}_{ij}(s) \alpha_{ij;kl} \dot{\phi}_{kl}(s). \quad (11)$$

α is an operator defined as

$$\alpha = G(DG)^{-1} r^{-1} (DG)^{-1} D + R^{-1}, \quad (12)$$

where r and R are diagonal operators whose elements are, respectively, R_i (the resistance of the superconducting island i with respect to the ground), and R_{ij} (the resistance between the i^{th} and the j^{th} islands, i.e. the junction resistance due to the tunneling of the quasi-particles for SIS junctions and the normal state resistance for the SNS junctions). In general one neglects the self-resistance (Resistive Shunted Model, RSJ) and, as well, the coupling between the tunneling quasiparticles and the environment; one has to note, however, that island resistance with respect to the ground is the basic dissipative term in the TDGL model [13] (see the lecture notes by J. José), while the coupling to the environment may lead to a redefinition

of E_J for junctions with a normal resistance of the order of 100Ω (the environment impedance) [14]. Moreover almost always one assumes a constant R_{ij} , neglecting the dependence of R_{ij} on ϕ ; basically, this is equivalent shunting the junction with an external resistance R_e smaller than the junction resistance. To take account of the dependence of $R_{ij}(\phi) = 1/G(\phi)$ on ϕ one can use the following expression [15]: $G(V) = G_{sg} + (1 - G_{sg})[1 - \tanh\alpha(1 - V/V_g)]/2$, where G_{sg} is the ratio of subgap conductance to normal-state conductance, K is a constant, and $v_g = 4I_c R_n / \pi$ is the gap voltage.

Another common approximation is to neglect the spatial distributions of the R_{ij} that may result from the limits of the fabrication process.

Thus neglecting R_i and taking R_{ij} as a constant, from equation 42 one obtains a set of equations whose matrix form, in normalized units, is

$$\beta_c \ddot{\phi} + \dot{\phi} + \mathbf{i}_c \sin \phi + \tilde{\mathbf{i}} - [G(DG)^{-1}] \mathbf{i}_{\text{ext}} - P_r M \mathbf{i}_{\text{ext}} + R^T \Lambda^{-1} (R\dot{\phi} + 2\pi \mathbf{f}) + R^T \Lambda^{-1} \Delta \mathbf{i}_{\text{ext}} = 0 \quad (13)$$

By considering the irrotational and solenoidal components of eq. (13) one obtains the two sets of the Kirchoff and the Biot-Savart equations. In fact, by taking the divergence of eq. (13) one has

$$D(\beta_c \ddot{\phi} + \dot{\phi} + \mathbf{i}_{c;\phi} \sin \phi + \tilde{\mathbf{i}}) \equiv D \mathbf{i}_{\text{link}} = \mathbf{i}_{\text{ext}}, \quad (14)$$

where \mathbf{i}_{link} are the currents flowing along the links. This vector equation reads, for each node i ,

$$\sum_j \beta_c \frac{d^2 \phi_{ij}}{d\tau^2} + \sum_j \frac{d\phi_{ij}}{d\tau} + \sum_j i_{c;ij} \sin(\phi_{ij}) + \sum_j \tilde{i}_{ij} - i_{i;\text{ext}} = 0, \quad (15)$$

On the other hand, by realizing that $G(DG)^{-1} \mathbf{i}_{\text{ext}} = G(DG)^{-1} D \mathbf{i}_{\text{link}} \equiv P_d \mathbf{i}_{\text{link}}$ and using $\mathbf{i}_{\text{link}} = R^T \mathbf{i}_{\text{mesh}} + M \mathbf{i}_{\text{ext}}$, $P_r + P_d = 1$ and $P_d R^T = 0$ we can group the first six terms in eq. (13) to give

$$\mathbf{i}_{\text{link}} - G(DG)^{-1} \mathbf{i}_{\text{ext}} - P_r M \mathbf{i}_{\text{ext}} = R^T \mathbf{i}_{\text{mesh}}. \quad (16)$$

Applying $(RR^T)^{-1} R$ to (13), one obtains the Biot-Savart equation (7).

It is worthwhile stressing that, since the nodes of the array are represented by point grains, fluxoid quantization is automatically fulfilled:

$$\sum_{ij \in p} \phi_{ij} + 2\pi f + \Phi_{\text{ind}} = 2n_p \pi. \quad (17)$$

$\sum_{ij \in \alpha}$ stands for the counterclock-wise sum along the links of the α -plaquette and ϕ_{ij} are restricted to vary in the interval $(-\pi, \pi]$. $\Phi = 2\pi f + \Phi_{\text{ind}}$ is the total flux through the cell.

It should be noted that the dynamics of the mesh currents and that of the phases of the superconducting nodes can be separated by operating the following

substitution for the gauge invariant phase [16] $\phi = D^T \theta + R_L^T i_{mesh}$ (a fact that implies the existence of two dynamics having different time-scales, as clearly pointed out in ref. [9]); if just the self-inductance of the cells are considered than R_L can be factorized as LR , where L is the self-inductance. As a consequence a reduction of the number of the coupled differential equations is obtained.

The JJA formalism and the granular superconductors

The 'JJ array formalism' and its lagrangian allows us also to describe the case of weakly coupled granular superconductors for which the phases are not uniform inside each grain. To do this one should consider the intragranular currents and phase shifts. A way of implementing this is to describe each superconducting site as a plaquette, see figure 1; a supercurrent, linear with the phase, flows within it. Thus, we must generalize the gauge-invariant phases, currents and fluxes, to add new variables corresponding to the superconducting-grain links and cells:

$$\phi \rightarrow \hat{\phi} \equiv \{\phi_J, \phi_S\}, \quad \Phi \rightarrow \hat{\Phi} \equiv \{\Phi_J, \Phi_S\}, \quad i_{link} \rightarrow \hat{i}_{link} \equiv \{i_{link;J}, i_{link;S}\} \quad i_{mesh} \rightarrow \hat{i}_{mesh} \equiv \{i_{mesh;J}, i_{mesh;S}\}.$$

The intragranular currents are proportional to the gradient of the phase along the border of the grain: $i_{ij;S} = \varsigma \phi_{ij;S}$ where $\varsigma = n_s e \hbar / m$ and n_s is, as usual, the density of the superconducting pairs. The discrete operators used up to now must also be generalized. Now, the curl along a plaquette contains contributions both from Josephson and superconducting branches, see fig. 1

$$\begin{pmatrix} \Phi_J \\ \Phi_S \end{pmatrix} = -\hat{R} \begin{pmatrix} \phi_J \\ \phi_S \end{pmatrix}. \quad \hat{R} \equiv \begin{pmatrix} R & R_{JS} \\ 0 & R_{SS} \end{pmatrix} \quad (18)$$

Inside the grain, the magnetic flux is 0 ($R_{SS}\phi_S = 0$), thus ϕ_S is an irrotational field ($\phi_S = G_{SS}V$). On the other hand, $\hat{i}_{link} = (\hat{R})^T \hat{i}_{mesh} + \hat{M} i_{ext}$ (\hat{M} is the immediate generalization of matrix M defined above). The divergence and gradient operators are also generalized $D \rightarrow \hat{D}$, $G \rightarrow \hat{G}$, and expressions $\hat{D} = (\hat{G})^T$, $\hat{R}\hat{G} = 0$ are still valid. The Biot-Savart equation now reads

$$\Phi_{ind;J} = \hat{\Lambda} \hat{i}_{mesh} + \hat{\Delta} i_{ext}. \quad \hat{\Lambda} \equiv (\Lambda \quad \Lambda_{JS}), \quad (19)$$

where contributions coming both from Josephson-like and superconducting currents are considered. As previously stated, link-currents are related to mesh currents through

$$\begin{pmatrix} i_{link;J} \\ i_{link;S} \end{pmatrix} = \begin{pmatrix} R^T & 0 \\ R_{JS}^T & R_{SS}^T \end{pmatrix} \begin{pmatrix} i_{mesh;J} \\ i_{mesh;S} \end{pmatrix} + \hat{M} i_{ext} \quad (20)$$

Zero magnetic flux inside grains implies $R_{SS}\phi_{link;S} = 0$. This, together with eq. (20) gives $R_{SS}R_{JS}^T i_{mesh;J} = -R_{SS}R_{SS}^T i_{mesh;S}$; here \hat{M} has been defined in such a

way that the curl of $\hat{M}\mathbf{i}_{\text{ext}}$ is null in the superconducting plaquettes (see fig 1). We can now re-express the Biot-Savart relation as

$$\Phi_{\text{ind};J} = \tilde{\Lambda}\mathbf{i}_{\text{mesh};J} + \hat{\Delta}\mathbf{i}_{\text{ext}} \cdot \tilde{\Lambda} \equiv \Lambda - \Lambda_{JS}(R_{SS}R_{SS}^T)^{-1}R_{SS}R_{JS}^T. \quad (21)$$

The generalized lagrangian is now

$$\begin{aligned} L(\hat{\phi}, \dot{\hat{\phi}}) = E_J \{ & \cos \phi_J - 1 + \frac{\beta_c}{2} \dot{\hat{\phi}}_J^T \dot{\hat{\phi}}_J + (\mathbf{i}_{\text{ext}})^T [(\hat{D}\hat{G})^{-1} \hat{D}] \hat{\phi} - \tilde{\mathbf{i}}^T \phi_J - \frac{\varsigma}{2} \phi_S^T \phi_S \\ & - \frac{1}{2} (\hat{R}\hat{\phi} + 2\pi\mathbf{f} + \hat{\Delta}\mathbf{i}_{\text{ext}})^T \tilde{\Lambda}^{-1} (\hat{R}\hat{\phi} + 2\pi\mathbf{f} + \hat{\Delta}\mathbf{i}_{\text{ext}}) \\ & + \hat{\phi} \hat{R}^T (\hat{R}\hat{R}^T)^{-1} \hat{R} \hat{M} \mathbf{i}_{\text{ext}} \}. \quad (22) \end{aligned}$$

Equation (42) applied to (22) gives a set of Euler-Lagrange equations. On applying \hat{D} to this equations, Kirchoff expressions are obtained. The Biot-Savart law is then obtained by applying $(\hat{R}\hat{R}^T)^{-1}\hat{R}$. As $\phi_S = G_{SS}V$, $\Phi_S = 0$ is trivially obtained.

This procedure increases considerably the number of independent variables of the problem, and becomes highly CPU-time consuming.

To conclude this subsection, we wish to point out that the forcing term, $i_{i;\text{ext}}$, may include both a dc component and an ac term, $i_{ac} \sin(\omega t)$. The presence of the latter opens a vast field of research related to the competition between the frequency of the external forcing terms and the characteristic frequencies of the JJAs. This latter is a subject that will be discussed briefly in the third section of these lecture notes. An interesting, although not complete, review on this specific topic can be found in ref. [9].

Comparison with other discrete models

From the previous lecture notes one has learned how to described the physics of a long junction by means of the sine-Gordon equation. Here we discuss in more details its discretization and its relation with the 'JJA formalism'. We have seen that the phase-invariant gauge is a continuous function that varies along the junction $\phi(x)$, and obeys the equation [17]

$$\beta_c \ddot{\phi} - c \frac{\partial^2 \phi}{\partial x^2} + \sin(\phi) = -\alpha \dot{\phi} + d \frac{\partial^2 \dot{\phi}}{\partial x^2} - \gamma. \quad (23)$$

We remind that here β_c is the Mc Cumber parameter, $\alpha \dot{\phi}$ is the usual resistive term due to the tunnelling of normal electrons across the junction; the $d \frac{\partial^2 \dot{\phi}}{\partial x^2}$ term accounts for the dissipation due to the flow of normal electrons parallel to the junction [18]; $\gamma = i/i_c$ is the usual bias term. If one neglects the third-derivative term and discretizes this model [19], [20] one obtains

$$\beta_c \ddot{\phi}_n + \alpha \dot{\phi}_n + i_n \sin(\phi_n) = i_{\text{ext};n} + \frac{1}{w^2} \nabla^2 \phi_n \quad (24)$$

where $\nabla^2 \phi_n = (\phi_{n+1} + \phi_{n-1} - 2\phi_n)$ is the discrete Laplacian, and $w = D/\lambda_j$ is the discreteness parameter (D is the distance between points i and j , and λ_j is the junction penetration depth). The continuous model is obtained by making $w \rightarrow 0$.

An analogous model is obtained when considering 1D Josephson junction arrays, as shown in fig. 1. In fact, conservation of the current at node i yields

$$\beta_c \ddot{\phi}_i + \dot{\phi}_i + \sin(\phi_i) = i_{ext} + i_i - i_{i-1} \quad (25)$$

Here, ϕ_i are the vertical gauge-invariant phases, and i_i is the mesh current for cell i , as defined above. Along the superconducting horizontal links the current density is given by $J_S = [(n_s e \hbar)/m][(\nabla\theta - (2\pi/\Phi_0)A)]$ (n_s is the superfluid density). Making the approximation that J_S is uniform, the (normalized) superconducting current is $i_S = \sigma J_S / I_c$ (σ is the cross-section of the current). Integrating the term $\nabla\theta$ along the border of plaquette i , one obtains $\oint(\nabla\theta)dx = 2n\pi$, which implies

$$2i_i = \frac{\sigma}{I_c D} \frac{n_s e \hbar}{m} (2n_i \pi + \phi_{i+1} - \phi_i - \Phi_i), \quad (26)$$

thus

$$i_i - i_{i-1} = \frac{\sigma}{I_c D} \frac{n_s e \hbar}{2m} (\phi_{i+1} + \phi_{i-1} - 2\phi_i) + \Phi_{i-1} - \Phi_i + 2\pi(n_i - n_{i-1}) \quad (27)$$

If the array inductance is neglected and the external field is uniform, ($\Phi_i = 2\pi f$) we obtain an equation which is formally equivalent to (24), with $w^2 = (I_c D / \sigma) 2m / (n_s e \hbar)$, plus an extra term taking into account the vortices existing in the array. Note that here the expression of w is strictly related to the characteristics of the supercurrent flowing in the horizontal branches, while that given in eq. (24) derives from the discretization of the Josephson current, a procedure needed to perform numerical simulations.

To include screening effects [21], one can proceed as follows. The mesh currents are linked to the flux across the plaquettes by $\Phi = \Lambda \mathbf{i}_{mesh} + \Delta \mathbf{i}_{ext}$. If the external current is homogeneous $\Delta_{p,j} i_{ext,j} = \xi_i i_{ext}$, where $\xi_i = \sum_j \Delta_{p,j}$. Now, on neglecting the non-diagonal terms of Λ , the magnetic flux is given by $\Phi_i = \Lambda_{0,0} i_i + \xi_i i_{ext} + 2\pi f$ and thus the current i_i is given by

$$(1 + \alpha \Lambda_{0,0}) i_i = \alpha (2n_i \pi + \phi_{i+1} - \phi_i) - \alpha \xi_i i_{ext} - \alpha 2\pi f, \quad (28)$$

where $\alpha = \frac{\sigma}{I_c D} \frac{n_s e \hbar}{2m}$. The limit $\lambda \rightarrow \infty$ implies $\Lambda_{0,0} \rightarrow 0$, and equation (27) is obtained. Instead when λ_\perp is small enough so that $\Lambda_{0,0} \geq 1$, the whole equation (28) must be considered, and thus the current conservation at the i th node reads

$$\beta_c \ddot{\phi}_i + \dot{\phi}_i + \sin(\phi_i) = i_{ext} \left(1 - \frac{\alpha}{1 + \alpha \Lambda_{0,0}} (\xi_i - \xi_{i-1}) \right) + \frac{2\pi \alpha}{1 + \alpha \Lambda_{0,0}} (n_i - n_{i-1}) + \frac{\alpha}{1 + \alpha \Lambda_{0,0}} \nabla^2 \phi_i + \epsilon \quad (29)$$

where ϵ contains the contribution to the currents i_i, i_{i-1} coming from the fluxes across the rest of the plaquettes. Neglecting the non-diagonal components of Λ , again an equation formally equivalent to (24) is obtained, with $w = \sqrt{\Lambda_{0,0}}$ (provided that $\alpha\Lambda_{0,0} \gg 1$); note that in this particular system $\lambda_j \propto \sqrt{\Lambda_{0,0}}$.

In all the sine-Gordon-like equations considered above, w can be interpreted as a generic coupling strength between the vertical phases. The limit $w \rightarrow 0$ implies that $\phi_i \rightarrow \phi_{i+1}$; large values of a allow large horizontal variations of the phases.

In fact, the discrete sine-Gordon form is an approximate version of the equation of motion derived from the 'JJ array formalism', for when the phases vary slowly along the x-direction [22]. In fact, if one writes down the equations of motion (imposing Kirchhoff's law) for any pair of opposite nodes in the array ($\theta_{i,up}, \theta_{i,down}$), and subtracts them, one gets the following equation:

$$\begin{aligned} [1 - (\frac{C_x}{2C_y} \nabla^2)] \beta_c \frac{d^2}{dt^2} (\phi)_{n;y} + [1 - (\frac{R_y}{2R_x} \nabla^2)] \frac{2}{R_y} \frac{d}{dt} (\phi)_{n;y} + i_c \sin(\phi_{n;y}) \\ - \frac{i_x}{2i_y} \sum_{i=\pm 1} \cos[\psi(n) - \psi(n+i)] \sin[\phi(n) - \phi(n+i)]/2 = i_{ext}. \end{aligned} \quad (30)$$

Here, $\psi(i) = \theta_{i,up} + \theta_{i,down}$, and the ϕ 's are, as usual, the gauge-invariant phases along vertical links. Equation (30) becomes sine-Gordon like if: a) all the combined space and time derivative of order three or higher are negligible; b) the variation of θ along the x axis is sufficiently slow so that the cosine factor can be taken as 1, and the sine factor can be linearized,

$$\beta_c \frac{d^2}{dt^2} (\phi)_{n;y} + \alpha \frac{d}{dt} (\phi)_{n;y} + i_{n;y} \sin(\phi_{n;y}) - i_{ext} - \frac{i_x}{2i_y} \nabla^2 (\phi)_{n;y} = 0. \quad (31)$$

The ∇^2 operator emerges in a natural way because of the coupling along the x direction and because of the imposition of Kirchhoff's conservation law at the nodes.

By comparing eqs. (24) and (31) one immediately sees that in the latter the role of the discreteness factor is played by the coupling anisotropy of the array, $i_x/2i_y$. Indeed, for $i_x \gg i_y$, in order to keep the currents within reasonable limits, the horizontal phases must be small; their time derivatives ($\dot{\phi}_x, \ddot{\phi}_x$) become thus negligible, and conditions a) and b) are fulfilled.

Thus the discrete sine-Gordon model, which describes systems of non-linear oscillators linearly coupled along the x -direction, is equivalent to the 'array formalism' in the limit of a highly anisotropic JJ ladders.

It may be also interesting to point out that if, in eq. (30), one does not neglect all the combined space and time derivative, a term formally identical to the $\partial^2 \phi / \partial x^2$ present in eq. (23) is obtained. Their physical meaning, however, does not coincide.

Let us now consider the Frenkel-Kontorova (FK) model. For a recent review on this model see ref. [23]. The FK model is used to describe systems composed of a set of particles, interacting through a linear force, placed on a periodic potential. see fig. 1, where, as an example, the 1D case is shown. The Hamiltonian is

$$H = \sum_{i,j} \{V(u_i) + U(\Delta u_{ij})\} = \sum_{i,j} \left\{ \frac{K}{(2\pi)^2} [1 - \cos(2\pi u_i)] + \frac{1}{2} (\Delta u_{ij})^2 \right\} \quad (32)$$

where u is the position of the i th particle and the sum on j is over first-nearest neighbours; K gives the amplitude of the periodic potential. The FK model applies to systems of particles whose number is not constrained to be equal to the number of the potential minima, it can be either larger or smaller. In order to apply the FK model to the case of the JJ ladder we have to identify the positions of the particles with the gauge invariant phases of the JJs lying along the y direction, $\phi_{i;y}$. As a consequence the number of the minima of periodic potential is fixed and equal to the number of the $\phi_{i;y}$ minus one. If one adds also a dissipative and a kinetic term, the FK model can be straightforwardly mapped onto the discrete sine-Gordon one.

'Particle' vs phase dynamics

In the previous subsections we have shown that a complete description of the JJA dynamics can be given in terms of the gauge invariant phases. To conclude this section and, as well, that part of the review devoted to the 'JJ array formalism', we would like to discuss the relationship that exists between the vortex and phase descriptions of JJA dynamics.

In a very general manner, a vortex can be treated as a particle [24], [25] that, under the action of a certain potential, $V(x)$, is forced to move in a viscous medium. Periodically it has to overcome energy barriers related to the links encountered along its trajectory.

When we consider the dynamics of a single vortex the potential $V(x)$ can be identified with its Gibbs energy, $U(x)$. This latter can be decomposed into six terms [27], [28]: the core energy $U_c = \pi^2/2$, defined as half the energy needed to create a vortex-antivortex pair; the energy of a vortex in the absence of magnetic fields and external currents, $U_0(x)$; the energies due to the interactions with the external field and with the bias current, $U_f(x)$ and $U_i(x)$; the term related to the periodicity of the array, $U_{pot}(x)$, and $U_{mag}(x)$ the term due to the screening currents. Strictly speaking, U depends also on the vertical coordinate, y . Here, in order to simplify the discussion, we assume that the vortex moves along the central row of the array ($y=0$). The analytic expressions of $U_i(x)$, $U_f(x)$, $U_{pot}(x)$ and $U_{mag}(x)$ in terms of $\hbar I_c/(2e)$, with x normalized to a , are given by

$$U_i(x) = -2\pi i \left(x + \frac{L}{2} \right), \quad (33)$$

$$U_f(x) = -\frac{\pi^2 L^2}{2} f \left(1 - 4 \left(\frac{x}{L} \right)^2 \right), \quad (34)$$

$$U_{pot}(x) = -\frac{1}{2} E_B \cos(2\pi x). \quad (35)$$

$$U_{mag}(x) = \frac{1}{2} \mathbf{i}_{link}^T \frac{1}{4\pi\lambda_{\perp}} f f \mathbf{i}_{link} = \frac{1}{2} \mathbf{a}^T 4\pi\lambda_{\perp} f f^{-1} \mathbf{a}. \quad (36)$$

where L is the array dimension in the direction perpendicular to the flow of the bias current; the coordinates are normalized to the cell dimension a ; and E_B is the energy barrier the vortex must overcome to move from one cell to the next one. We fixed the origin of the coordinates, $x = 0$, at the central column of the array.

As far as $U_0(x)$ its expression for finite samples and $\lambda_{\perp} = \infty$ is

$$U_0(x) = \pi \ln \left(\frac{2L}{\pi} \cos \left(\frac{\pi x}{L} \right) \right). \quad (37)$$

The modification of $U_0(x)$ for finite value of λ_{\perp} [28] is discussed in details in a recent review [29].

Given the above expression the equation of motion for the vortex can be written in the following way:

$$M_v l_a \ddot{x} = -\frac{E_J}{l_a} \frac{dU}{dx} - \eta l_a \dot{x} \Rightarrow M_v l_a \ddot{x} + \eta l_a \dot{x} + \frac{E_J}{l_a} \left(\pi E_B \sin(2\pi x) - 2\pi i + 4\pi^2 f x + \frac{dU_0}{dx} + \frac{dU_{magn}}{dx} \right) = 0 \quad (38)$$

Where η is the coefficient of viscosity. The equation of motion of the particle (vortex), thus, resembles very much that of the phase of a single JJ subjected to a washboard potential.

It is natural to associate the kinetic term $1/2 C \sum_{ij} V_{ij}^2$ with $1/2 M_v \dot{x}^2$. In zero magnetic field and in the no-screening approximation the profile of the phase around a vortex is given by [30], $\phi = \arctan[(y_i - y_0)/(x_i - x_0)]$. In the quasistatic limit one obtains [12] $V_{ij} = (\Phi_0/2\pi)(\dot{x}/l_a)(\phi_i - \phi_j)$ and by summing over the phases one arrives at, in agreement with ref. [25] to the following mass expression:

$$M_v = \frac{\Phi_0^2 C}{2l_a^2} \quad (39)$$

On the other hand, the power dissipated by the moving vortex is equal to the sum of the power dissipated in all the links of the array, $\eta u^2 = \sum_{ij} V_{ij}^2 / R_{ij}$. η can be expressed in terms of the effective shunt resistance r_e (i.e. the equivalent resistance of the whole circuit between two sites i and j) [26]

$$\eta = \frac{\Phi_0^2}{2l_a^2 r_e} \quad (40)$$

Now, if in eq. (38) one makes the substitution $2\pi x \rightarrow \phi$ one obtains, in the limit of very large samples ($L \rightarrow \infty$), the following expression:

$$\frac{\Phi_0^2 C}{2\pi^2} \ddot{\phi} + \frac{\Phi_0^2}{2\pi^2} \frac{1}{2r_e} \dot{\phi} + E_J (E_B \sin \phi - 2i_{ext}) = 0. \quad (41)$$

that shows the equivalence between phase and 'particle' dynamics in the limit of large samples and $f \rightarrow 0$. Indeed, only in these limits are U_{magn} and U_0 independent of x in the bulk of the array (i.e. at a distance from the border larger than the vortex size), and the "arctan" expression is applicable. From eq. (41) it emerges that the depinning current of the array is $i_d = E_B/2$. We can define vortex-like quantities analogous to junction-like ones β_c and $\omega_p = \sqrt{\beta_c}/(RC)$ (the plasma frequency) by $\beta_{cv} = E_B\beta_c$ and $\omega_{pv} = \sqrt{E_B}\omega_p$.

Finally one has to note that eq. (39) implies no dependence of M on screening and, also, a linear dependence of M on C while eq. (40) implies a constant η if, like in the Bardeen-Stephens model, r_e is taken constant. However, strong deviation from the behavior predicted by eq. (39) and (40) have been 'observed' [31], [32], [28], [33] in both overdamped and underdamped junctions. A detailed discussion on this topic can be found either in the lecture notes by H. van der Zant (only for the underdamped JJAs) and in ref. [29].

NUMERICAL SIMULATIONS

The models described in the previous section are not analytically solvable. As a consequence, one has to perform numerical simulations in order to extract useful information on quantities measurable in the experiments. In this section we give a short introduction to the numerical simulations of the JJA dynamics. We will provide the readers with some elementary advices and tricks on how to make the simulations easier and faster. Due to their number and complexity, such algorithms deserve a more extended description. We suggest the reader to take these lecture notes just as a starting point: if he likes the flavour of it, a wide world opens in front of him, willing to be explored.

Solving differential equations

To study the JJA dynamics one has to solve a set of non-linear differential equations. Basically, one knows

a) the value of a certain group of variables ϕ_i at a given time t

and

b) the functional expression of their time derivative $\dot{\phi}_i \equiv f(t, \phi)$.

Which are the values of the ϕ 's at $t + \Delta t$? A simple answer to this question can be given by the following equation

$$\phi(t + \Delta t) = \phi(t) + \Delta t f(t, \phi), \quad (42)$$

known as the *Euler method*.

The Euler method, in fact, can be applied also to the case of second order differential equations: if we know $\phi(t)$, $\dot{\phi}(t)$ and the function $\ddot{\phi}(t) = f(\phi(t), \dot{\phi}(t))$ an immediate generalization of (42) leads to

$$\begin{aligned}\dot{\phi}(t + \Delta t) &= \dot{\phi}(t) + \Delta t f(\dot{\phi}(t), \phi(t)) \\ \phi(t + \Delta t) &= \phi(t) + \Delta t \dot{\phi}(t).\end{aligned}\quad (43)$$

The Euler's method is based on a Taylor expansion in Δt of $\phi(t + \Delta t)$ cut at the first term; the associated error, thus, is of the order $O(\Delta t^2)$.

When the procedure is iterated the error propagates and one has to find a convenient way to control it. Of course, it is always possible to reduce $\Delta t \rightarrow 0$, but the price to pay is an increase of the computing time. It is, thus, essential to find a compromise between precision and CPU time consumption.

In equation (42) one considers only the derivative of ϕ at the leftmost point of the interval $(t, t + \Delta t)$. A more accurate calculation of $\phi(t + \Delta t)$ can be obtained by considering also the derivatives at intermediate points of the time interval Δt . In fact we can guess the value of $\phi(t + \Delta t/2)$ and then calculate the derivative at this point:

$$\begin{aligned}k_1 &= \frac{\Delta t}{2} f(t, \phi(t)) \\ \phi(t + \Delta t) &= \phi(t) + \Delta t f(t + \Delta t/2, \phi + k_1),\end{aligned}\quad (44)$$

This is known as the *second order Runge-Kutta* formula. What we have done is, basically, to construct an expression (44) that reproduces a Taylor expansion up to the term of order $O(\Delta t^3)$:

$$\begin{aligned}f\left(t + \frac{\Delta t}{2}, \phi + \frac{\Delta t}{2} \frac{d\phi}{dt}\right) &= f(t, \phi) + \frac{\Delta t}{2} \left(\frac{\partial f}{\partial t} + \frac{d\phi}{dt} \frac{\partial f}{\partial \phi} \right) + O(\Delta t^2) = \\ f(t, \phi) + \frac{\Delta t}{2} \frac{df}{dt} &= \frac{d\phi}{dt} + \frac{\Delta t}{2} \frac{d^2\phi}{dt^2} + O(\Delta t^2).\end{aligned}\quad (45)$$

This result would encourage to iterate the procedure: in principle, one can choose extra terms that, added to (44), reproduce a Taylor series expansion with any desired precision. However, it turns out (and this is the key-point) that one does not need to use derivatives of ϕ of second and higher order. It is enough to work with the function $f(t, \phi)$ and choose a series of adequate points (t_n, ϕ_n) . Provided that the $f(t_n, \phi_n)$ values are multiplied by adequate coefficients, it is possible to build up expressions with a precision of the order of $O(\Delta t^4)$, $O(\Delta t^5)$, $O(\Delta t^6)$... By far, the most popular of these approximations is the *fourth-order Runge-Kutta* formula [34]

$$\begin{aligned}k_1 &= \frac{1}{2} \Delta t f(t, \phi(t)) \\ k_2 &= \frac{1}{2} \Delta t f(t + \Delta t/2, \phi(t) + k_1) \\ k_3 &= \frac{1}{2} \Delta t f(t + \Delta t/2, \phi(t) + k_2) \\ k_4 &= \Delta t f(t + \Delta t, \phi(t) + k_3) \\ \phi(t + \Delta t) &= \phi(t) + \frac{k_1}{6} + \frac{k_2}{3} + \frac{k_3}{3} + \frac{k_4}{6},\end{aligned}\quad (46)$$

characterized by an error of the order $O(\Delta t^5)$ (as one can verify by developing the series expansion for all these terms, adding them up, and comparing the sum with the Taylor expansion of ϕ).

Obviously one may ask: *is it worthwhile to get into such a mess ?*. f must be evaluated 4 times over the interval $(t, \Delta t)$ and to evaluate f one has to multiply a given vector for a matrix whose size increases as N^2 , where N is the size of the array. In which case is this method preferable with respect to the Euler's one? We should use it provided that it allows us to operate over an interval $4\Delta t$ in one step and, to obtain at least the same accuracy we would achieve by using the Euler's method on four Δt -steps.

A crucial point is the choice of Δt . Its optimal value depends on the form of the function f . For a linear f , any value of Δt is reasonable, no matter how large it is because we can cover large time intervals in just one step; on the other hand, a jagged f with sharp peaks and valleys requires very small steps. To improve the method, one can add a "controller" to the program and adjust the value of Δt to satisfy the requirements of the moment. Such an algorithm is known as *adaptive stepsize Runge-Kutta* method. We will describe a very simple way to perform such an adaptive control. Let us suppose one uses the *fourth-order Runge-Kutta* formula. The results obtained with steps Δt and $\Delta t/2$ must be compared, let us call them ϕ_a and ϕ_b ; the related errors are $\Delta t^5 A$ and $2(\Delta t/2)^5 A$ ($A \approx 1/(15!) d^5\phi/dt^5$, as is obtained by the Taylor expansion). The difference $\phi_a - \phi_b = \epsilon$ can be taken an indication of the error. If we want determine ϕ with a precision higher than ϵ_0 , we must modify Δt in such a way that

$$\Delta t \rightarrow \tilde{\Delta t} = \Delta t \left(\frac{\epsilon_0}{\epsilon} \right)^{0.2}. \quad (47)$$

Matrix multiplication

The dynamical behaviour of JJA's is governed by the matricial equation

$$\dot{\phi} = M\mathbf{d}(\phi). \quad (48)$$

In the previous section we have illustrated some methods useful to solve this equation. Whichever of the methods discussed above one intend to use, it will always involve several matrix multiplications.

If the self-inductance of the array is neglected, there are $n_x n_y - 1$ degrees of freedom (DOF). This is because an array $n_x n_y$ has a $U(1)$ symmetry, i.e. its properties are invariant under a global shift of all the phases. As a consequence we are allowed to fix one of the phases; this reduces the number of DOF by one unity. The DOF of the systems increases if one consider also the self-inductance of the array; in fact one has to consider $(n_x - 1)(n_y - 1)$ additional DOF that are related to the magnetic fluxes that thread the plaquettes of the array. In both cases, however, the range of M is of the order or $n_x n_y$ so that to solve the equation

(48) one has to perform $(n_x n_y)^2$ operations. It would be certainly advisable to have an efficient method to perform matrix multiplication!

In the case of periodic boundary conditions (pbc), the equation (48) represents just the discrete convolution of vectors r and ϕ (r being the first row of M). In fact

$$(\phi * r)(m) = \sum_{n=0}^{N-1} \phi_n r_{m-n} = (M\phi)_n, \quad (49)$$

Due to the convolution theorem

$$(\phi * r) = \tilde{\phi} \tilde{r}, \quad (50)$$

(where $\tilde{\phi}$ and \tilde{r} are the Fourier transforms of ϕ and r) to calculate $M\phi$ one needs to:

1. Calculate $\phi \rightarrow \tilde{\phi}$: K operations
2. Multiply $\tilde{\phi} \tilde{r}$: N operations
3. Calculate $\tilde{\phi} \rightarrow \phi$: K operations

If $K < N^2$ (i.e. if one can find a fast method to calculate the Fourier transforms), because of the convolution theorem, a reduction of the CPU time would be achieved.

And what about free boundary conditions (fbc)? In this case, $M\phi$ is not any longer a convolution. With some make up, however, a system with fbc may be mapped on another one with pbc. In fact, one can apply the following transformation

$$\begin{aligned} \phi_{i,j} \text{ } i:0 \rightarrow n_x-1; j:0 \rightarrow n_y-1 &\rightarrow \hat{\phi}_{i,j} \text{ } i:0 \rightarrow 3n_x/2-1; j:0 \rightarrow 3n_y/2-1 \\ \hat{\phi}_{i,j} &= \begin{cases} \phi_{i,j} & (i < n_x, j < n_y) \\ 0 & \text{elsewhere} \end{cases} \end{aligned} \quad (51)$$

and substitute M by \hat{M} , (where \hat{M} is a $3n_x/2 \times 3n_y/2$ matrix obtained from M that represents a periodic system), see figure (2).

Such a technique is known as *zero padding*. Up to now, with this transformation we have not gained any CPU time, on the contrary we have lost some of it because \hat{M} is larger than M . Anyway, as we will see in the next subsection, the possibility to deal with discrete convolution will make us obtain profit from this investment.

Fast Fourier Transform

The problem is, now, to calculate the Fourier transform, \mathbf{D} , of the vector $d(\phi)$:

$$\mathbf{D} = F \mathbf{d}, \quad F_{k,l} = \exp\{2\pi i \, kl/N\} \quad (52)$$

Here F is a $N \times N$ matrix. As a consequence the calculation of equation (52) involves $N \times N$ operations. If there were not any mathematical shortcut to calculate a Fourier transform we would have nothing to gain in following this method with respect to the standard procedure used to solve equation (48).

Fortunately, Daniel and Lanczos showed that a discrete Fourier transform involving N components is equivalent to two transforms that involve $N/2$ components each: it is enough to separate the even and the odd components of the vector:

$$D_k = \sum_{l=0}^{N-1} \exp\{2\pi i k 2l/N\} d_{2l} + \sum_{l=0}^{N-1} \exp\{2\pi i k(2l+1)/N\} d_{2l+1} \\ \equiv D_k^e + \exp\{2\pi i k/N\} D_k^o. \quad (53)$$

where k ranges from 0 up to N ; D_k^e, D_k^o are periodic with period $N/2$ ($D_k^e = D_{k+N/2}^e$). One can iterate this process and obtain, at the different steps, transforms with a periodicity $N/4, N/8$, and so on.

Let us suppose that N is even and a power of 2. After $\log_2 N$ steps, we obtain a set of 1-periodic transforms D :

1 st stage k is N/2-periodic	2 nd stage k is N/4-periodic	3 rd stage k is N/8-periodic
$D_k^e = D_k^{ee} + F_k^4 D_k^{eo}$	$D_k^{ee} = D_k^{eee} + F_k^8 D_k^{eeo}$ $D_k^{eo} = D_k^{eoe} + F_k^8 D_k^{eoo}$	$D_k^{eee} = \dots$ $D_k^{eeo} = \dots$ $D_k^{eoe} = \dots$ $D_k^{eoo} = \dots$
$D_k^o = D_k^{oe} + F_k^4 D_k^{oo}$	$D_k^{oe} = D_k^{oee} + F_k^8 D_k^{oeo}$ $D_k^{oo} = D_k^{ooe} + F_k^8 D_k^{ooo}$	$D_k^{oee} = \dots$ $D_k^{oeo} = \dots$ $D_k^{ooe} = \dots$ $D_k^{ooo} = \dots$

where $F_k^m = \exp \frac{imk\pi}{N}$. At the d th step one has to calculate 2^d coefficients $D_k^{eoe\dots}$ for each value of k . The computation of each D implies an addition and a multiplication. Due to the k symmetry ($D_k^{eoe\dots} = D_{k+N/(2^d)}^{eoe\dots}$), it is not necessary to compute all the D factors for each value of k ; it is enough to consider only those values of k contained in the range $0 \rightarrow N/(2^d) - 1$. The total number of operations needed at each step is, thus, proportional to N . Since one needs to perform $\log_2(N)$ steps, the total number of operation needed to complete the FFT procedure is $N \log_2(N)$.

The calculation of the FFT begins from the last step by evaluating $D_k^{eoeoe\dots} = \exp(2\pi i km) d_m$. The key point of the FFT algorithm lies in the following observation: $D_k^{eoeoe\dots}$ is symmetric and periodic in k with period 1, i.e. $D_k^{eoeoe\dots}$ takes the same value for whichever value of k . This implies that each last-step

$D_k^{eoeoe...} \equiv D^{eoeoe...}$ give us one of the components of $\{d\}$. The question that it lasts to answer now is the following: which is the map $\{d\} \rightarrow \{D\}$? Or, in other words, which d_m should be put in correspondance to each $D_k^{eoeoe...}$?

By using the binary code to identify the $\{d\}$ components the answer is immediate: $d(0) = d(00..0)$, $d(4) = d(0..0100)$ and so on. In working out D^e we have considered only the even components of d , i.e. those components for which the least significant bit is zero. To calculate D^{ee} one has to consider only those d components for which the second bit is equal to 0, and so on. In general, to calculate D^{eoeo} we have to select the numbers for which the last four digits of the d components are: ...1010. This gives us the key rule: the D components calculated with the last step are equal to the d ones over which has been operated a bit-reversal. As an example, let's consider the case $N = 8$:

$$\begin{pmatrix} D^{eee} \\ D^{eeo} \\ D^{eoe} \\ D^{eoo} \\ D^{oeo} \\ D^{oeo} \\ D^{ooo} \\ D^{ooo} \end{pmatrix} = \begin{pmatrix} d_{000} \\ d_{100} \\ d_{010} \\ d_{110} \\ d_{001} \\ d_{101} \\ d_{011} \\ d_{111} \end{pmatrix}, \quad (54)$$

The d quantities have been organized in such a way that: $d_{000} \leftrightarrow d_{000}$, $d_{001} \leftrightarrow d_{100}$, $d_{010} \leftrightarrow d_{010}$, $d_{011} \leftrightarrow d_{110}$, $d_{101} \leftrightarrow d_{101}$ and $d_{111} \leftrightarrow d_{111}$.

Up to now we have assumed that N is a power of 2. If not, we can choose between two different procedures: the simplest one consists in adding a set of 0 to our vector with the aim to build up a new one whose length is a power of 2. An alternative is to develop an algorithm, analogue to that we have just discussed, with the aim to reduce progressively the size of the sub-vectors down to a factor which divides N . However this is a quite dangerous procedure: if such factor is too large, the efficiency of our new algorithm will be very poor (in the limit of a N that is a prime number, one has to perform again N^2 operations!!).

There exist other algorithms that are based on the subdivision of the initial vector into subvectors of length 4 (*based-4 FFT's*), 8 (*based-8 FFT's*), etc. by making profit of the special symmetries of these numbers. For example, the coefficients of the Fourier transform of a vector with 4 components are simply 1, i, -1, -i and the transformation of such vectors is immediate. These algorithms are slightly faster than the based-1 FFT described above.

To conclude with this topic it is worth noting that the computation time can be reduced by realizing that the vectors we are working on are real. In fact, it is possible to pack the numbers into an $N/2$ complex vector (the even components become the real parts of the new vector while the odd ones become its imaginary parts). The transform of this $N/2$ vector can be trivially related to that of the original N -real vector:

$$d = \begin{pmatrix} d_0 \\ d_1 \\ \vdots \\ d_{N-1} \end{pmatrix} \rightarrow \tilde{d} \begin{pmatrix} \tilde{d}_0 \\ \vdots \\ \tilde{d}_l \\ \vdots \\ \tilde{d}_{N/2-1} \end{pmatrix} \equiv \begin{pmatrix} d_0 + i d_1 \\ \vdots \\ d_{2l} + i d_{2l+1} \\ \vdots \\ d_{N-2} + i d_{N-1} \end{pmatrix} \quad (55)$$

It is easy to calculate the $D_k (k = 0 \dots N-1)$ terms once that their respective transforms $\tilde{D}_k (k = 0 \dots N/2-1)$ are known, in fact:

$$D_k = \frac{\tilde{D}_k + \tilde{D}_{N/2-k}^*}{2} + e^{i2\pi k/N} \frac{\tilde{D}_k - \tilde{D}_{N/2-k}^*}{2i} \quad (k = 0 \rightarrow N/2-1)$$

$$D_k = D_{N-k}^* \quad (k = N/2 \rightarrow N-1) \quad (56)$$

The Inductance Matrix

Another delicate point of the simulations of the JJA properties is the calculation of the full inductance matrix. Such a matrix can be calculated starting from the Biot-Savart law: at a point \vec{r} , the magnetic field due to a current density J is given by

$$\vec{B}(\vec{r}) = \frac{\mu_0}{4\pi} \int \frac{\vec{J}(\vec{r}') \times \vec{r}}{|\vec{r} - \vec{r}'|^3} d\vec{r}'. \quad (57)$$

If we choose the gauge $\nabla \cdot A = 0$, the expression for the vector potential becomes

$$\vec{A}(\vec{r}) = \frac{\mu_0}{4\pi} \int \frac{\vec{J}(\vec{r}')}{|\vec{r} - \vec{r}'|} d^3\vec{r}', \quad (58)$$

where J is the current density.

Let us consider a uniform current flowing in the link ij ($I_{ij} = J_{ij}/\sigma_{ij}$, with σ_{ij} the cross section of the conductor). The integral of the vector potential along the path connecting the points k and l is related to the current I_{ij} in the following way:

$$A_{kl} = \int_k^l \vec{A} d\vec{l} = \frac{\mu_0}{4\pi} \int_k^l \int \frac{1}{\sigma_{ij} |\vec{r} - \vec{r}'|} d^3\vec{r}' d\vec{l} I_{ij} = \frac{\mu_0}{4\pi} f f_{kl,ij} I_{ij}. \quad (59)$$

The matrix ff can be calculated from eq. (59), either numerically or analytically. There exist several methods to solve equation 59 and their degree of complexity depends on the specific geometry of the systems [35]. As far as the case dealt with in these lecture notes, some general indications can be given at a glance considering the form of the equation (59):

- Since \vec{A} is parallel to \vec{J} , only mutual inductances between parallel links have to be considered.

- ff and thus the mutual inductances have to falls as $1/r$ with the distance r

When two links are far enough (i.e. when their cross section are small compared with their distance) their mutual inductances are independent of their specific shape. This latter, on the other hand, becomes important and must be taken into account when one calculates the self-inductance (and, as well, the mutual inductances between close thick conductors).

The general form of the mutual inductance between two parallel filaments of respective lengths l and m is (see figure 3)

$$ff = \frac{\mu_0}{4\pi} \left(\alpha \sinh^{-1} \left(\frac{\alpha}{d} \right) - \beta \sinh^{-1} \left(\frac{\beta}{d} \right) - \gamma \sinh^{-1} \left(\frac{\gamma}{d} \right) + \delta \sinh^{-1} \left(\frac{\delta}{d} \right) - \sqrt{\alpha^2 + d^2} + \sqrt{\beta^2 + d^2} + \sqrt{\gamma^2 + d^2} - \sqrt{\delta^2 + d^2} \right). \\ \alpha = l + m + \delta, \beta = l + \delta, \gamma = m + \delta. \quad (60)$$

We remember that, in MKSA units, $\mu_0/(4\pi) = 10^{-7} \text{ Henry/m}$. δ may have negative values (e.g., in figure (3)b, $\delta = -l$).

If the axes of both filaments are aligned (figure (3)c), equation (60) reduces to

$$ff = \frac{\mu_0}{4\pi} ((l + m + \delta) \ln(l + m + \delta) - (l + \delta) \ln(l + \delta) - (m + \delta) \ln(m + \delta) + \delta \ln(\delta)) \quad (61)$$

that becomes even simpler if their extremes are in contact (figure (3)d):

$$ff = \frac{\mu_0}{4\pi} \left(l \ln \left(\frac{l+m}{l} \right) + m \ln \left(\frac{l+m}{m} \right) \right) \quad (62)$$

To conclude, we give the expressions that one has to use to calculate the self-inductance of either a round conductor of radius ρ and length l

$$ff_{self} = \frac{\mu_0}{4\pi} 2l \left(\ln \left(\frac{2l}{\rho} \right) - \frac{3}{4} \right), \quad (63)$$

and a wire with rectangular cross section of sides b and c :

$$ff_{self} = \frac{\mu_0}{4\pi} 2l \left(\ln \left(\frac{2l}{b+c} \right) + \frac{1}{2} \right). \quad (64)$$

From the above expressions the matrix Λ relating the fluxes and the mesh currents ($\Phi = \Lambda i$) can be easily obtained since $\Lambda = \frac{1}{4\pi\lambda_L} R f f^T$. It may be interesting for the reader that we point out some general characteristics of the matrix Λ : [9]:

- The diagonal terms are all positive; all the off-diagonal terms are negative.
- The sum of all the Λ -components of a row is zero (because of the continuity of the flux lines).
- The value of the Λ -components decrease with r as r^{-3}

SOME NOTES ON THE COMPUTER SIMULATIONS APPLIED TO THE STUDY OF THE VORTEX DYNAMICS IN JJAs

These lecture notes cannot be extended enough to review all the interesting results that have been obtained by numerical simulations in the recent past. Here we give only an up-to-date list of some intriguing topics that are still objects of the current research and that may stimulate the readers to get involved into the JJA subject. Detailed reviews can be found in the references [29] and [9].

Dynamics of massless vortices: overdamped JJAs

Massless vortices are the excitations characteristic of the overdamped JJAs for which, we remind it, the capacitance $C \simeq 0$. The dynamical properties of massless vortices in ladders and 2-D JJAs have been almost completely revised in the recent past. In particular, by temporarily breaking a vertical link, it has been possible to study the dynamics of a single vortex [36] and, as a consequence:

- to determine the dynamical value of the energy barrier that a vortex must overcome in order to pass from one cell to the next, E_B . It has been shown that either for the ladders and for 2D arrays [28], [32], the dynamical E_B takes quite different values from the static ones [30], [37] (we recall that these latter define the strength of the pinning potential and the value of the depinning current). E_B , either static [8] [38] or dynamic [28], [32], is substantially affected by the decrease of λ_\perp and also by finite-size effects.
- to determine the vortex velocity under various operative conditions [28], [32], and to show that also this physical quantity is strongly affected by the value of λ_\perp , by that of the coupling anisotropy J_x/J_y [29] [39] and, in some conditions, by the vertical size of the array.
- to show that the viscosity coefficient cannot be assumed constant [28] [29] [31] [32], but that it depends on λ_\perp , the size of the array and the bias current: i.e. on the size of the vortex, the core of which is normal. This means that the Bardeen-Stephens model [40], by itself, does not give a satisfactory description of the dissipative mechanisms associated with the motion of the vortex.

In addition it has been possible:

- to image, by means of the LTSEM (Low Temperature Electron Scanning Microscope) [41], a new dynamical state, the so-called alternate-vortex motion, AVM [42]. The computer simulations have confirmed the hypothesis formulated by the experimentalists [43] and contributed to understand the conditions under which such dynamical state develops [28] [29] [44]. It turns out that,

provided that the bias current is high enough, the existence of an initial vortex (generated because of any symmetry-breaking mechanism, including the self-inductance of the array) is a sufficient condition for the development of the AVM (for further details see the lecture notes by T. Doderer and ref. ([29])).

At present the research on the vortex dynamics in overdamped JJAs is concentrated mainly on the anisotropic systems for which $J_x \neq J_y$ [39], while the vortex-vortex and the multi-vortex interaction remains as an almost unexplored subject.

If one wishes to compare the dynamical properties of the anisotropic JJAs (often called also inductive coupled arrays) with those of continuous systems, like long and stacked Josephson junctions, one has to move to the study of vortex dynamics in the underdamped JJAs.

Dynamics of massive vortices: underdamped JJAs

In underdamped JJAs the capacitance is not negligible, $\beta_c \neq 0$, and the vortex acquires a mass.

Many detailed information on the physical properties of the underdamped JJAs can be found in other lecture notes included in this book and in the references cited therein. In these lecture notes, again, we can only summarize the most relevant results achieved in the recent past.

Information on the average vortex dynamics can be obtained by measuring the I-V characteristics, which in underdamped arrays become hysteretic providing evidence of a finite value of the vortex mass [6].

By numerical simulations one can investigate the details of the vortex motion and, as shown in figure 4 [29], prove the existence of many different dynamical regimes [45]. In a different way, instead of using the $v - \beta_c$ plane, one can calculate the average voltage drop at the edge of the array and plot the results in the I-V plane, as shown in many other lecture notes, to compare simulations and measured I-V characteristics.

To give to the reader an idea about the present 'state of the art' of the research on the vortex dynamics in underdamped JJAs we resume here the most relevant results obtained in the recent past:

- The depinning current decreases as $\sqrt{\beta_{v,c}}$ [46].
- The vortex velocity, v , decreases with $\beta_{v,c}$ and, as for the massless vortices, depends on i_{dc} and λ_{\perp} . Up to now there are no detailed studies on its dependence of the size of the array. A detailed study of the energy barrier for the cell-to-cell vortex motion is also missing.
- For low values of $\beta_{v,c}$ there exists an 'annihilation' regime: a vortex generated everywhere in the array annihilate at the borders [45] [29] [39]. When the

current of bias is high enough vortices are continuously generated at one border and annihilate at the opposite one so that a non-zero voltage is measured: this regime, in analogy with the case of the long Josephson junction, is called the flux-flow regime. It is worth to mention that a certain number of studies has been dedicated to investigate the flux flow resistance [31] .

- When $\beta_{v,c}$ is high enough a vortex/antivortex is reflected at the border in an antivortex/vortex [45] [29] [39]: iterated reflections produce a Zero-field step similar, although not identical, to what observed in long Josephson junction [45].
- A Bardeen-Stephens-like ohmic dissipation [40] does not explain the experimental observations. An additional dissipation mechanism has been identified in the excitation of spin waves in the wake of the moving vortices [6]. This mechanism has been proved correct by numerical simulations [37] [46] and by the appearance of resonances in the I-V characteristics recorded in both the linear [47] and the non-linear (Fiske steps) regimes [48].
- The discreteness of the system induces a bending of the acoustic branch at the border of the Brillouin zone (as observed for the array modes of a 1D system in the linear regime) and the appearance of an optical branch when the array is composed by alternate junctions having two different critical currents [49].
- In particular conditions, i.e. if the vortices have an energy just higher than what they need to overcome the depinning barriers (being these latter as low as possible like in triangular arrays) and are allowed to move in an unbiased sample, then it is possible to observe experimentally a ballistic vortex motion [50]. From the point of view of the simulations, however, the situation is not very clear and does not seem to agree with experiments. The realization of some more simulations and experiments would be advisable.
- Beyond a certain value of $\beta_{v,c}$ the vortex dynamics becomes unstable and one observes the so-called row-switch [51] [15]. It consists in the switch to the normal state of one or more entire rows of Josephson junctions. The row-switched phenomena have been imaged and confirmed by LTSEM [42].

The investigation of the underdamped JJAs, however, is far away to be completed and, in fact, many groups are still working on the subject.

Non-autonomous dynamics: phase locking in underdamped JJAs

When a JJA is driven by an external current that has an ac component, $i_{ac} \sin(\omega t)$, it becomes isomorphic to a system composed by a set of non-linear coupled oscillators driven by an external torque, see equation (14). This is another

very interesting field of investigation that spans from collective synchronization to chaos and turbulence. Once more we cannot go here in all the details; in the following we give only a short introduction to the subject and, then, summarize some relevant results.

The key point is the competition between the frequency of the driving force and the natural frequencies of the arrays. The solution of the conflict depends strongly on the boundary conditions of the problem (the amplitude of the driving force, its frequency, the coupling strength of the junctions, etc.). In a very general manner, like for a single junction [52], one may observe:

- a locked dynamics, i.e. the driving force and the array synchronize:
- a quasiperiodic dynamics: i.e. the ratio of the two characteristic frequencies is an irrational number;
- a chaotic dynamics.

In the first case the motion of the oscillators is periodic. For a single junction one can write: $\phi(t_0 + qT) = \phi(t_0) + 2\pi p \rightarrow \langle \dot{\phi} \rangle = \frac{2\pi p}{q} \nu$, where $T = \frac{1}{\nu}$ is the period of the driving force and p and q are integer numbers. Making use of the Josephson equation $V = \frac{\hbar}{2e} \dot{\phi}$, one obtains the relationship between ν and the average voltage values, $\langle V \rangle$, that, in the I-V characteristic, manifest themselves as set of plateaux: the so called Shapiro steps:

$$\langle V \rangle = \frac{p}{q} \frac{\hbar}{2e} \nu. \quad (65)$$

Periodic solution are observed also in the case of the JJAs [53]. Experiments and numerical simulations can be fitted by an expression similar to that of a single junction:

$$\langle V \rangle = \frac{p}{q} \frac{N_J \hbar \nu}{2e} \quad (66)$$

Note that now the height of the Shapiro steps are multiplied by a factor N_J , the number of junctions along the direction of the bias current. Because of this they are usually call Giant Shapiro Steps (GSS). When the ratio $\frac{p}{q}$ is equal to an integer n all the junctions along the direction of the incoming current oscillate coherently, as they were a single oscillator, and their contributions to the total average voltage add up.

When the ratio $\frac{p}{q}$ is not equal to a integer number one can observe also the so called Fractional Giant Shapiro Steps (FGSS). This has been first observed for JJAs placed in a magnetic field when the normalized flux density across the plaquettes of the array was ($f = \Phi/\Phi_0 = p/q$). It is worth to note that in a single Josephson junction Fractional Shapiro Steps are observed only if the junction is underdamped [54] while in more complex systems, like the JJAs, FGSS are observed also when the

arrays are composed by overdamped JJs. A simple explanation to the appearance of the FGSS in the JJAs has been first given by Benz et al. [55] (BRTL description) and confirmed by the numerical simulations reported in ref. [56]: when an external field of intensity $f = \frac{p}{q}$ is applied to the array, the dynamical ground state of the array consists of q vortices arranged in a sub-array of $q \times q$ -cells. The application of a bias current is able to induce a coherent motion of the whole sub-array. It is the synchronization between the motion of the sub-arrays and the frequency of external ac-current that causes the observation of the GFSS's: in fact, the vortex configuration reproduces itself periodically with a period $T = \frac{2}{\nu}$.

The BRTL description, however, is only a part of the story; in fact we know now that:

- there are several vortex configurations compatible with one locking state. As an example, for $f = 1/2$ the ground state coincides with that given by the usual checker-board configuration, but other vortex configurations, characterized by the presence of one or more domain-walls, are also allowed [57] [58]. These extra configurations are stable against field perturbations and temperature fluctuations. Moreover, when the array inductance increases (λ_{\perp} decreases), the vortex-vortex interaction becomes attractive [9], and configurations with more and more domain-walls become stable.
- a complete set of FGSSs are observed also in very small arrays (included the smallest one: a single plaquette) [59]. This is an observation that cannot be explained by the simple BRTL description. And this is not all, in fact by tuning the geometrical disorder of the array a spectacular result has been achieved: the observation of a Devil's staircase structure with the expected fractal dimension, $D = 0.87$ [60]. The appearance of a Devil's staircase constitutes a strong evidence for the occurrence of a competition between the frequency of the driving force and those characteristic of the array. The physical reason for that can be found in the breaking of the translational symmetry of the array that may be caused by the presence of any form of defect or disorder, by an inhomogeneity of the bias current, or, more simply, by the screening currents due to the self-inductance of the array. Many computer simulations support this idea [9]. The ground state configuration of the vortices associated to each FGSS and the relative extension of the plateau depend strongly on the geometry of the sample and on the particular cause of the symmetry breaking.

As an example, a non-inductive array exhibits subharmonic steps if it has defects, or if edge fields are generated 'ad hoc'. A microscopical insight shows a structure defined by tilted rows of vortices and antivortices (in half-integer steps, vortex/antivortex rows are alternate; for $n/3$ steps, for each vortex row there are two antivortex ones).

The inclusion of the array inductance also leads to the creation of subharmonic steps. The detailed form of the vortex patterns depends very much on the interaction voltage between vortices (which, in turn, is a function of the value

of λ_{\perp} , the way of modelling the induced fields, etc.). For a long penetration depth, the vortex-vortex interaction is repulsive, while for short values of λ_{\perp} it is attractive, and vortices tend to group together [9].

In small systems the choice of a particular geometry favours the selection of specific FGSSs, those for which the vortex distribution is commensurate to the size and to the geometry of the array [57], in agreement with the BRTL interpretation.

To conclude this subsection we wish to point out for the JJAs not too much is known on the route to chaos and that very few studies have been devoted, up to now, to the turbulent regime.

Acknowledgments: the authors wish to thank T. Doderer, J.V. José, R. Newrock, N. Pedersen, A. Ustinov, H.J.S. van der Zant which kindly read the first version of the manuscript and gave a certain number of constructive suggestions.

REFERENCES

1. Giovannella C and M. Tinkham (ed.) 1995 *Macroscopic Quantum Phenomena and Coherence in Superconducting Networks* (Singapore: World Scientific) and; Cerdeira H.A., Shenoy S.R. (ed.) 1996 *Physica B* **222** 253-406
2. as general reference books on the physics of the Josephson junctions see:
Likharev K.K. 1986 *Dynamics in Josephson Junctions and Circuits* (Gordon and Breach, New York),
Barone A. and Paterno G. 1982 *Physics and Application of the Josephson Effect* (New York: Wiley)
Tinkham M. 1996 *Introduction to superconductivity* (New York: McGraw-Hill)
3. Strogatz S.H., Stewart I. 1993 *Sc. Amer. N.* **12** 68
4. Ciria J.C., Pacetti P., Paoluzi L., Giovannella C. 1996 *Nucl. Instr. and Meth. in Phys. Res. A* **370** 128 and references therein
5. Mygind J., Pedersen N.F. in Giovannella C and Tinkham M. (ed.) 1995 *Macroscopic Quantum Phenomena and Coherence in Superconducting Networks* (Singapore: World Scientific) p. 339, and references therein
6. van der Zant H.S.J., Fritschy F.C., Orlando T.P., Mooij J.E. 1993 *Phys. Rev. B* **47** 295
7. Mon K K, Teitel S. 1989 *Phys Rev. Lett.* **62** 673;
Chung J.S., Lee K.H., Stroud D. 1989 *Phys. Rev. B* **40** 6570;
Shenoy S R 1985 *J. Phys. C: Solid State Phys.* **18** 5163
8. Phillips J.R., van der Zant H.S.J., White J., Orlando T.P. 1993 *Phys. Rev. B* **47** 5219
9. Domínguez D., José J.V., 1994 *Int. J. Mod. Phys. B* **8** 3749 and references therein
10. Nuvoli A., Giannelli A., Ciria J.C., Giovannella C 1994 *Nuovo Cimento* **16** 2045
11. Nakajima K., Sawada Y 1981 *J. Appl. Phys.* **52** 5732;
Majhofer A., Wolf T., Dieterich W. 1991 *Phys. Rev. B* **44** 9634
12. Orlando T.P., Mooij J.E., van der Zant H.S.J. 1991 *Phys. Rev. B* **43** 10218
13. see for example Beck H. and Ariosa A. 1991 *Sol. St. Comm* **80** 657 and references therein
14. Joyez P., Le transistor a une paire de Cooper: un systeme quantique macroscopique, Ph. Dr. Thesis, Université Paris 6, 1996
15. Phillips J.R., van der Zant H.S.J., Orlando T.P. 1994 *Phys. Rev. B* **50** 9380
16. Lucheroni C. 1997 *Phys. Rev. B* **55** 6559
17. McLaughlin D.W., Scott A.C. 1978 *Phys. Rev. A* **18** 1652
18. Davidson A., Dueholm B., Kryger B., Pedersen N.F. 1985 *Phys. Rev. Lett* **55** 2059
19. Peyrard M., Kruskal M.D. 1984 *Physica D* **14** 88
20. Pedersen N.F., Ustinov A.V. 1995 *Supercond. Sci. Technol.* 1995 **8** 389 and reference therein
21. Bock R.D., Phillips J.R., van der Zant H.S.J., Orlando T.P. 1994 *Phys. Rev. B* **49** 10009
22. Ryu S., Yu W., Stroud D., unpublished
23. Floria L.M., Mazo J.J. 1996 *Adv. Phys.* **45** 505
24. Larkin A.I., Ovchinnikov Yu. N., Schmid A. 1988 *Physica B* **152** 266

25. Eckern U., Schmid A. 1989 Phys. Rev. B **39** 6441
26. Rzchowski M., Benz S., Tinkham M., Lobb C.J. 1990 Phys. Rev. B **42** 2041
27. van der Zant H.J.S., Rijken H.A., Mooij J.E., 1983 J. Low Temp. Phys. **27** 150
28. Ciria J.C., Giovannella C., 1997 J. Phys.: Cond. Mat. **9** 2571
29. Ciria J.C., Giovannella C., 1998 J. Phys.: Cond. Mat. **10**, to be published
30. Lobb C.J., Abraham D.W. and Tinkham M., 1983 Phys. Rev. B **27** 150
31. Hagenaars, Tiesinga P.H.E., van Himbergen J.E., José J.V. Phys. Rev. B 1994 **50** 1143
32. Ciria J.C., Giovannella C., 1996 J. Phys.: Cond. Mat. **8** 7463
33. Trias E., Orlando T.P., van der Zant H.S.J., Phys Rev. B 1996 **54** 6568
34. Gear, C.W. *Numerical Initial Value Problems in Ordinary Differential Equations* (Englewood Cliffs, NJ: Prentice-Hall).
35. See, eg. Grover F. W., *Inductance Calculations* (D. van Nostrand Company, NY).
36. Ciria J.C., Giovannella C., Pacetti P., Paoluzi L. in Giovannella C and M. Tinkham (ed.) 1995 *Macroscopic Quantum Phenomena and Coherence in Superconducting Networks* (Singapore: World Scientific), p. 378
37. Bobbert P.A., 1992 Phys. Rev. B **45** 7540
38. Mazo J.J., Ciria J.C. 1997 Phys. Rev. B **68** 16068
39. Ciria J.C., Giovannella C. (to be published)
40. Bardeen J., Stephens M.J 1965 Phys. Rev. **140A** 1197
41. Huebener R.P., in Hawkes P.W. (ed.) 1988 *Advances in Electronics and Electron Physics* (New York: Academic) p. 1
Doderer T., 1997 Int. J. Mod. Phys. B **11** 1979
42. Lachenmann S.G., Doderer T., Hoffmann D., Huebener R.P. 1994 Phys. Rev. B **50** 3158
43. Hagenaars T.J., van Himbergen J E, Tiesinga P.H.E., José J.V. Lachenmann S.G. in Giovannella C and M. Tinkham (ed.) 1995 *Macroscopic Quantum Phenomena and Coherence in Superconducting Networks* (Singapore: World Scientific), p. 329
44. Lachenmann S.G., Doderer T., Huebener R.P., Hagenaars T.J., van Himbergen J.E., Tiesinga P.H.E., José J.V., preprint
45. Hagenaars T.J., van Himbergen J.E., José J.V., Tiesinga P.H.E. 1996 Phys. Rev. B **53** 2719
46. Geigenmüller U., Lobb C.J., Whan C.B. 1993 Phys. Rev. B **47** 348
47. van der Zant H.S.J., Orlando T.P., Watanabe S., Strogatz S.H. 1995 Phys. Rev. Lett. **74** 174
48. Ustinov A.V., Cirillo M., Malomeed B.A., 1993 Phys. Rev. B **47** 8357
49. van der Zant H.S.J., Berman D., Orlando T.P., Delin K.A. 1994 Phys. Rev. B **49** 12945
50. van der Zant H.S.J., Fritschy F.C., Orlando T.P., Mooij J.E. 1992 Europhys. Lett. **18** 343
51. van der Zant H.S.J., Muller C.J., Geerlings L.J., Harmans P.M., Mooij J.E. 1988 **38** 5154
52. see, e.g. D. D'Humiers, M.R. Beasley, B.A. Huberman and A. Libchaber, Phys. Rev. A **26**, 3483 (1982); M. Octavio, Phys. Rev. B **29**, 1231 (1984).
53. T.D. Clark, Phys. Rev. B **8**, 137 (1973); Ch. Leeman, Ph. Lerch and P. Martinoli.

- Physica **126B**, 475 (1984).
54. R.L. Kautz and R. Monaco, J. Appl. Phys. **57**, 875 (1985).
 55. S.P. Benz, M. Rzchowski, M. Tinkham and C.J. Lobb, Phys. Rev. Lett. **64**, 693 (1990); H.C. Lee, D.B. Mast, R.S. Newrock, L. Bortner, K. Brown, F.P. Esposito, D.C. Harris and J.C. Garland, Physica B **165-166**, 1571 (1990).
 56. J.U. Free, S.P. Benz, M.S. Rzchowski, M. Tinkham, C.J. Lobb and M. Octavio, Phys. Rev. B **41** 7267 (1990); S.P. Benz, J.U. Free, M.S. Rzchowski, M. Tinkham, C.J. Lobb and M. Octavio, Physica B **165-166** 1647 (1990).
 57. J.C. Ciria and C. Giovannella, in "Macroscopic Quantum Phenomena and Coherence in Superconducting Networks", C. Giovannella and M. Tinkham ed., (World Scientific, Singapore, 1985) , 302;
 58. Ciria J.C., Giovannella C. 1996 J. Phys.: Cond. Matt. **8** 3057
 59. W. Yu, E.B. Harris, S.E. Hebboul, J.C. Garland and D. Stroud, Phys. Rev. B **45**, 12624 (1992); J. Kim and H.J. Lee, Phys. Rev. B **47**, 582 (1993).
 60. Giovannella C., Ritort F., Giannelli A. 1995 Europhys. Lett. **29** 419;

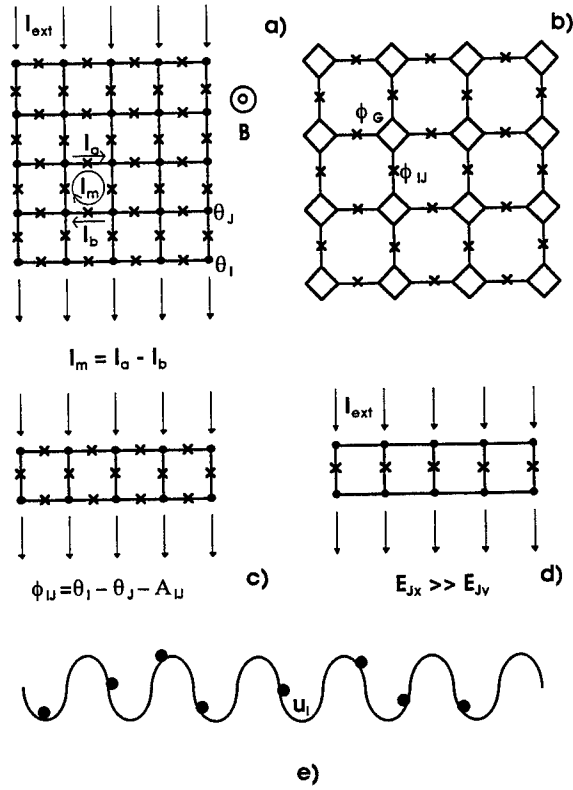


FIGURE 1. Examples of JJ arrays: (a) a 2D square network, (b) 2D triangular network, (b) 2D granular superconductors: the grains are now extended and the phase, changes along the grain. The ϕ s are the gauge invariant phases variations along the junction (J) and along the grain (G): $\phi_J = \theta_i - \theta_j - A_{ij}$. A_{ij} is the contribution due to the vector potential and it is defined in text; (c) a JJ ladder (one JJ is placed on each branch of the array and each grain is characterized by a single phase, θ_j). (d) an extremely anisotropic ladder (inductively coupled 1D JJ chain); (e) a schematic representation of a dynamical system described by the Frenkel-Kontorova equation.

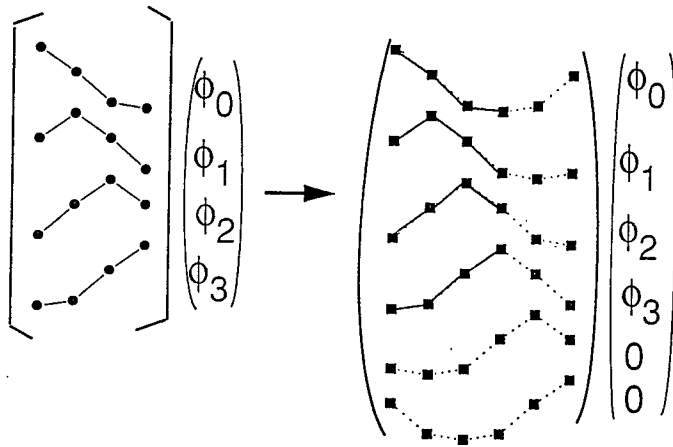


FIGURE 2. Transformation of the M matrix in the \hat{M} by the zero padding technique.

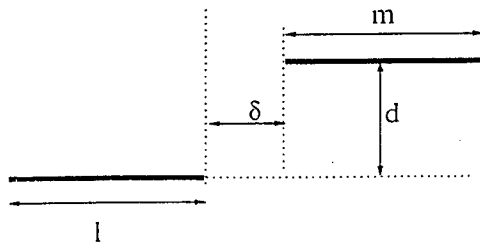


FIGURE 3. Relative positions of two parallel links on an array. Definition of the quantities l , m , δ and d used in the text.

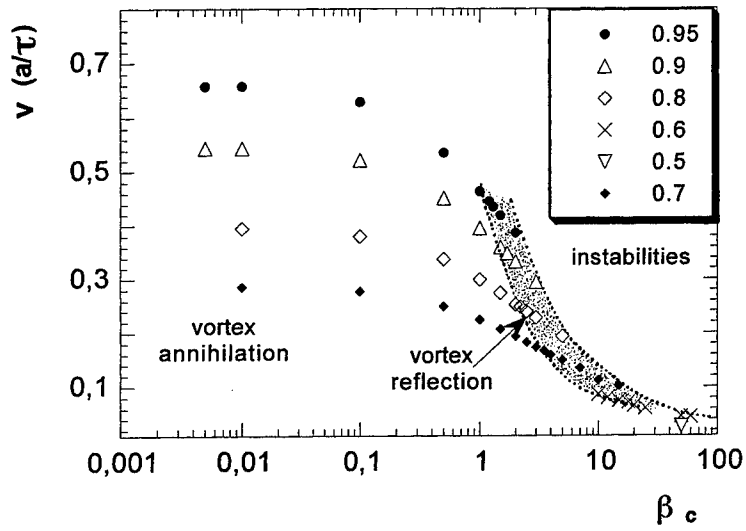


FIGURE 4. Steady state velocity vs β_c in the case of massive vortex in a 2×32 ladder for different values of i_{de} the legend. The lines indicate the borders between different dynamical regions where one observes vortex annihilation, vortex reflection and dynamical instabilities.

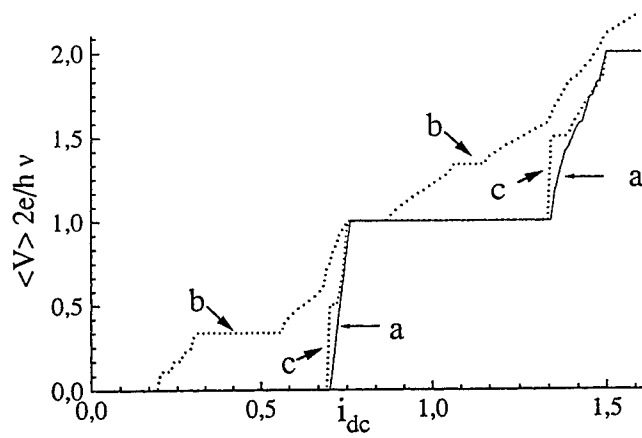


FIGURE 5. Example of Integer and Fractional Giant Shapiro Steps in a 6×6 -cell array: a) $f=0$, no self-inductance; b) $f=1/3$, no self-inductance; c) $f=0$, the self-inductance of the array is considered.

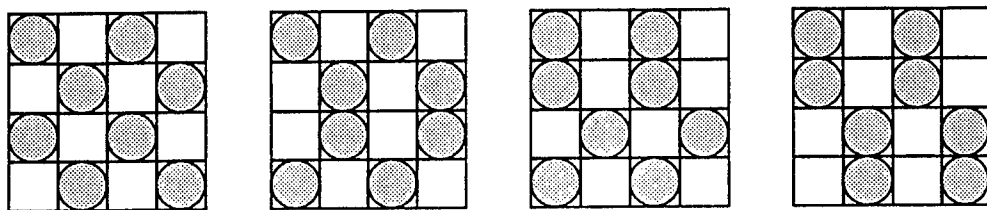


FIGURE 6. Allowed vortex configurations observed for a 4 time 4 array on the $1/2$ Shapiro Step when $f = 1/2$; from left to right the energy increases.

Dynamics of Josephson junction arrays – Microscopic investigations and applications

Thomas Doderer

*Physikalisches Institut, Lehrstuhl Experimentalphysik II, Universität Tübingen,
Auf der Morgenstelle 14, D-72076 Tübingen, Germany*

Abstract. We discuss the dynamics of two-dimensional arrays of Josephson junctions in the overdamped regime. Our discussion is restricted to “classical” arrays, where the Josephson coupling energy is much larger than the charging energy. Such arrays represent a highly controllable system to study the dynamics of vortices. Furthermore, they are promising for applications like, e.g., a coherent microwave source. The experiments have been performed with arrays of Nb/AIO_x/Nb-tunnel junctions allowing a high degree of junction uniformity across the array. The typical array size is 10×10 junctions. We show spatially resolved measurement results obtained by low-temperature scanning electron microscopy, and demonstrate the merit of these investigations for the clarification of complex regimes of vortex dynamics as well as for the optimization of coherent microwave sources. In the case of external microwave irradiation with increasing power, a continuous transition from a non-locked to a completely locked oscillation state is presented. In addition, we report on the quantitative measurement of the emitted microwave power from the arrays.

INTRODUCTION

Arrays of Josephson junctions have been extensively studied for various reasons both experimentally and theoretically (see, e.g., [1]). The experimental investigations deal with various problems, such as vortex dynamics under the influence of dc or ac currents, or the application of arrays as coherent microwave radiation sources. Due to the complexity of the nonlinear coupled differential equations used for approximation, the theoretical studies have focused on numerical calculations during the recent years. Two-dimensional arrays are appealing for basic research of superconductivity because they represent an artificial two-dimensional system, and they can be considered, to some extent, as a discrete version of a superconducting thin film having well-defined properties. On the other hand, they represent a set of nonlinear (Josephson) oscillators which are coupled to each other by means of the superconducting wires. Thus, for achieving maximum microwave emission, one is interested in a circuit that favors the in-phase oscillation state.

CP427, *Superconductivity in Networks and Mesoscopic Systems*

edited by Giovannella/Lambert

© 1998 The American Institute of Physics 1-56396-750-2/98/\$15.00

In this article we shall first discuss the fabrication of Josephson junction arrays based on the Nb-technology. Since we are mainly interested in producing highly reliable and large arrays (typically 10×10 junctions and larger) having small margins, we have restricted our studies to Nb/ AlO_x /Nb-junctions. In the subsequent section the dynamics of overdamped arrays is explained in terms of the motion of individual vortices in the case of a small dc bias current. In the last two sections microwave experiments are presented. Here we shall see that there is a close correspondence between microwave injection and microwave emission.

SAMPLE FABRICATION

The arrays consist of rectangular or square networks of superconducting wires with Josephson junctions placed between the line crossings. A sketch of a network is shown in Fig. 1. Most of the arrays consist of square elementary cells with four junctions each. We have used different array circuits for the experiments: samples from the National Institute of Standards and Technology (NIST) in Boulder (CO) and others from the Physikalisch-Technische Bundesanstalt (PTB) in Braunschweig, Germany. The basic design of both series of arrays is similar to each other. One difference is the size a of the unit cell: the NIST arrays have $a \approx 17 \mu\text{m}$, whereas the PTB arrays have $a \approx 41 \mu\text{m}$. The NIST samples and their fabrication are described in [2]. In the following we give a brief description of the fabrication process of the PTB samples.

Figure 2 shows a sketch of a single junction together with an external shunt resistor (about 1Ω for each junction). We have used a sample fabrication process that defines the junction area by anodization and includes external shunt resistors. This process has been developed at PTB for the manufacture of rapid single flux quantum circuits [3]. Seven photomasks are needed to prepare the circuits. Thermally oxidized silicon wafers are used as substrates. All Nb layers are deposited

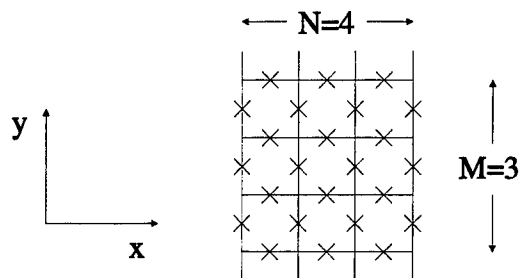


FIGURE 1. Sketch of typical array geometry with N columns of M junctions. Each junction is symbolized by a cross. The notation of the x and y direction is shown. The dc bias current flows in the direction of the y axis. The array voltage drop along the whole array is measured in the same direction.

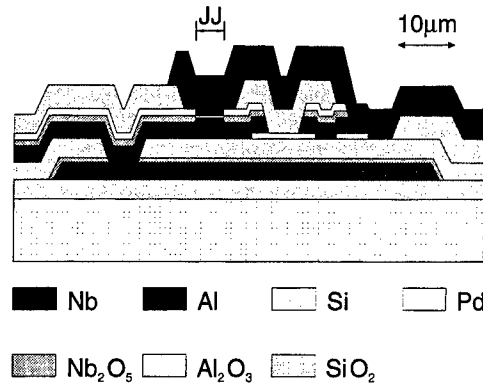


FIGURE 2. Cross-sectional view of a complete shunted Josephson junction (vertical axis not to scale).

by dc magnetron sputtering and patterned by CF_4/O_2 reactive ion etching (RIE). Insulating SiO_2 layers are rf-sputtered, holes for connecting metal layers through the insulating layers are etched by CHF_3/O_2 RIE. The Pd layer is deposited by magnetron sputtering and patterned in an Ar plasma to form the resistors. To improve electrical insulation the groundplane and the base electrode are anodized up to voltages of 25 V and 45 V, respectively. By depositing the shunted Josephson junctions on top of a superconducting groundplane we can put the groundplane as close as 200 nm to the junctions, shielding magnetic fields very effectively, thus significantly decreasing the self-inductance of a unit cell and the mutual inductances of the array.

The areas of the junctions are between $9 \mu\text{m}^2$ and $25 \mu\text{m}^2$, and the critical current density is about $1 \text{ kA}/\text{cm}^2$ at 4.2 K. The McCumber parameter is $\beta_C \lesssim 1$. The inductance of a single loop has been measured yielding the SQUID parameter $\beta_L = 2\pi L i_c / \Phi_0 \approx 1.5$ at 4.2 K for a loop on top of a superconducting groundplane; L is the loop inductance, i_c the critical current of a junction, and Φ_0 the flux quantum. For the spread of the critical currents of the junctions, values of 3% have been obtained for one standard deviation from the mean value. To improve the bias current uniformity in the array, 1Ω feeding resistors have been used, connecting each current injection line at both sides of the array to a Nb busbar (not shown in Fig. 1).

For on-chip detection of the emitted microwave power the array is coupled to a detector Josephson junction via a microstripline. A coupling capacitance allows separate dc biasing of the detector and the array. The layout of our microwave circuit is schematically shown in Fig. 3. The detector junction, acting as a load, is matched to the microstripline by choosing its shunt resistor such that the impedances of both are expected to be equal.

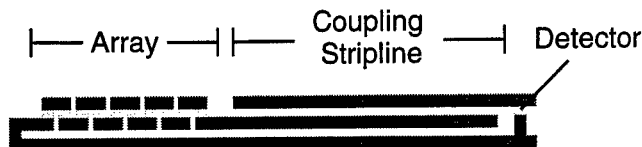


FIGURE 3. Cross-sectional view of an array with a microwave coupling circuit and a detector junction (not to scale).

DYNAMICS OF VORTICES

Very similar to the current-induced breakdown of superconductivity in superconducting wires and thin films, the resistive state of a two-dimensional array of Josephson junctions can be described by the propagation of current vortices perpendicular to the bias current I of the array. The array's critical current I_c is thus determined by the critical Lorentz force that equals the pinning force of the vortices. Without externally applied magnetic field, there are current-induced vortices penetrating the array from the boundaries if $I > I_c$, and I_c is given by the edge pinning potential. This conception is powerful in particular if the magnetic radius of a vortex, namely the magnetic penetration depth $\lambda_\perp = \hbar/(2e\mu_0 i_c)$ of the array, is smaller than a . \hbar denotes Planck's constant divided by 2π , e the elementary charge, and μ_0 the permeability of free space. For the arrays used for the present investigations, $\lambda_\perp < a$. This situation somehow resembles that of a type-I superconductor in the sense that there is the possibility to observe more than one flux quantum in a single unit cell. On the other hand, if $\lambda_\perp > a$ we are dealing with a situation similar to a type-II superconductor.

Now we are interested in experimental observations which yield further information about the array's dynamics that can be described in terms of the dynamics of vortices. The simplest experiment is just the recording of the dc current-voltage ($I - V$) characteristic. Figure 4 shows an example. Obviously, there is a rich structure in this curve which becomes very obvious if one looks at the derivative $(dV/dI)(I)$. Such kind of characteristic has been observed for all of our arrays, and Fig. 4 shows a typical example. One can roughly divide this curve into three main parts: (I) is the subcritical region, (II) is the region showing rich structure, and (III) is a region having constant differential resistance.

In the following, we shall link up the three regions with particular modes of the vortex dynamics. A more extensive discussion together with the presentation of the results of numerical simulations is given in [4]. Dealing with region (I), there is no dynamics. However, by means of a local perturbation of the system close to a pinning center, one can depin individual vortices from this site and, subsequently, they will propagate through the array, if there is some bias current present for driving them. During propagation there is a voltage drop at the array that can be measured. With this method it becomes possible to identify the pinning centers. Such a local perturbation can be made available by a focused electron beam

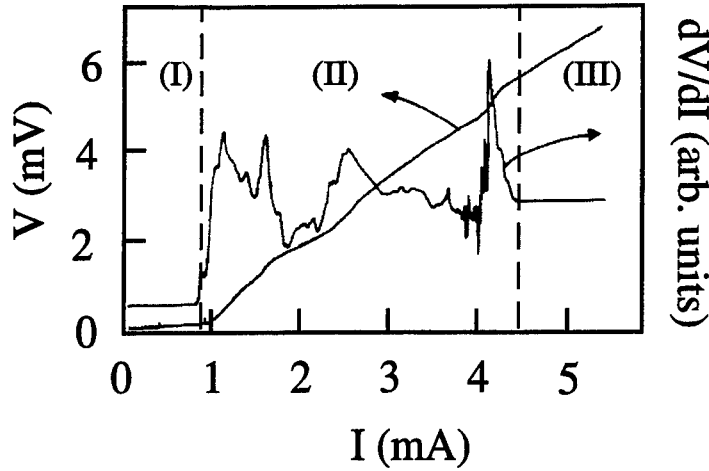


FIGURE 4. $I - V$ characteristic of a 10×10 array together with the differential resistance $(dV/dI)(I)$ measured at a temperature $T \approx 4.5$ K.

which locally heats the sample. With the help of a scanning electron microscope equipped with a low-temperature sample stage, we have been able to perform such experiments. The technique is called low-temperature scanning electron microscopy (LTSEM) [5-7].

The LTSEM images of the array dynamics shown in this paper always represent so-called voltage images, which are generated as follows. We apply a constant bias current to the array and scan the electron beam across the sample surface. With the beam parameters use for most of our studies (25 kV, approximately 100 pA) the temperature increase at the beam focus amounts to about 0.4 K. The sample is thermally well coupled to a liquid helium bath and kept at a temperature of about 4.5 K. It is well shielded from dc and ac magnetic fields by means of μ -metal shielding at both room and liquid-helium temperature. The electron-beam-induced voltage change $\Delta V(x_0, y_0)$ is recorded as a function of the coordinates (x_0, y_0) of the beam focus. In order to increase the sensitivity, the beam is chopped at a certain frequency (about 20 kHz) and the voltage response signal ΔV is phase-sensitively detected by a lock-in amplifier. The spatial extension of the heated area close to (x_0, y_0) , namely the thermal healing length η , determines the spatial resolution of this imaging technique. η is of the order of a few μm . For the interpretation of these voltage images one has to recognize that the measured response signal represents a time average on the time scale of the Josephson dynamics because the time constant of the former is in the range of ms, whereas the time constant of the

latter is in the range of ps to ns.

Let us now briefly discuss what kind of voltage image is expected in the subcritical region. For $I < I_c$ vortices are pinned at those edges of the array which are parallel to the bias current (parallel to the y axis in Fig. 1). If the electron beam increases the temperature at a position close to an edge junction, the critical current of this edge junction is decreased, and thus the energy barrier for vortex entrance is lowered. Note that the energy barrier for a vortex to enter the array or to move from one unit cell to the neighboring one is proportional to the Josephson coupling energy $E_J = \hbar i_c / (2e)$ of the junction at the border-line of the array or of the two neighboring unit cells [8]. From this, a positive voltage signal $\Delta V(x_0, y_0)$ is expected if the beam's focus (x_0, y_0) is close to the edges of the array parallel to the bias current flow. Figure 5 shows such an example. This voltage image totally agrees with our expectation and thus confirms the conception of vortex edge pinning.

Notice the negative voltage response signals at the position of the feeding resistors. Since the response signal is measured across these resistors in addition to the voltage drop across the array, any temperature dependence of these resistors results in a response signal. From the sign of these signals it follows that the resistor show a negative differential temperature dependence. However, it is not clear whether really the resistors behave like this or if this is more due to some interface effects occurring between the resistive and the superconducting thin films.

Next, we shall discuss the vortex behavior in region (II) (see Fig. 4). Figure 6(a) shows the LTSEM image for a bias current in the low-current regime of this region. The voltage image is taken for a bias current of $I = 1.5I_c$ with I_c denoting the

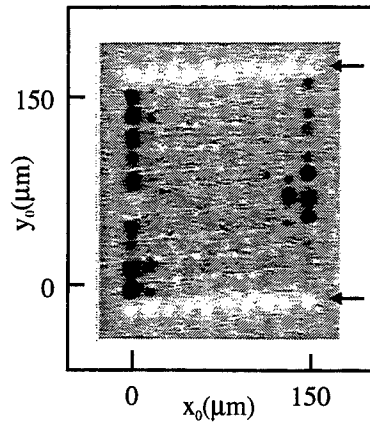


FIGURE 5. Gray value representation of the voltage image $\Delta V(x_0, y_0)$ of a 10×10 array at $T \approx 5$ K. The array is biased at $I \approx 0.9I_c$. The dc bias current flows vertically through the array. The array boundaries lie between 0 and 150 μm in both directions. A positive (negative) e-beam induced voltage signal ΔV is indicated by the dark (bright) areas, whereas zero signal is shown by the areas surrounding the array. The rows of feeding resistors are marked by the arrows.

array's critical current. In Fig. 6(c) a line scan for row No. 3 is presented.

In order to understand this image in more detail it is important to discuss the generation of the e-beam-induced voltage response signal in dependence of the vortex dynamics at (x_0, y_0) . In this article we can only give a brief introduction to this problem; for more details, see [9]. Qualitatively, the basic principle of the LTSEM imaging of vortex dynamics in arrays of junctions is simple. It turns out that the most prominent response signals are generated for (x_0, y_0) close to the array's edges which are parallel to the bias current [9]. For a qualitative discussion it is very helpful to consider so-called image vortices, which are virtual vortices of opposite vorticity outside the array, and located as a mirror image of a real vortex inside the array with the array's edge as the mirror axis. Since vortices of opposite vorticity attract each other, every array vortex is attracted towards the

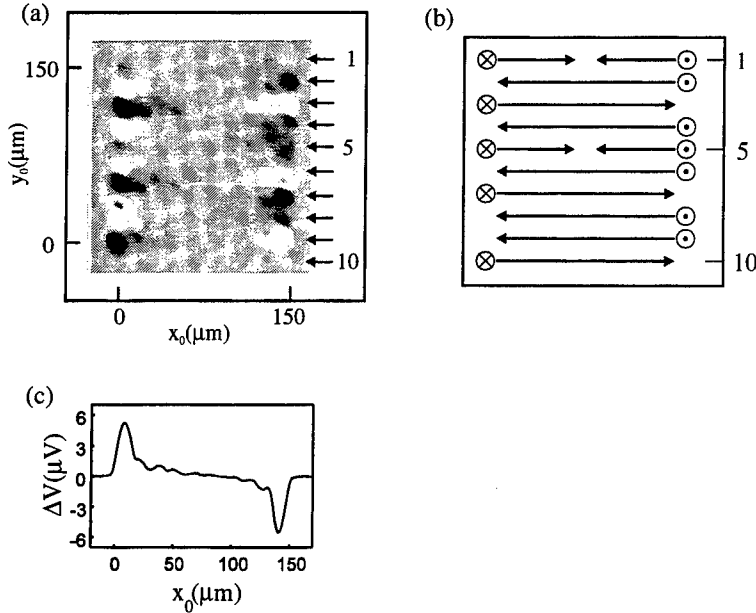


FIGURE 6. (a) Gray value representation of the voltage image $\Delta V(x_0, y_0)$ for a 10×10 array at $T \approx 5$ K. The array is current biased at $I = 1.5I_c$ and a voltage of 0.9 mV. The dc bias current flows vertically through the array. The array boundaries lie between 0 and 150 μm in both directions. A positive (negative) e-beam induced voltage signal ΔV is indicated by the dark (bright) areas, whereas zero signal is shown by the areas surrounding the array. The individual rows of junctions are indicated by the small arrows numbered 1–10 from top to bottom. (b) Schematic display of the vortex motion found by inspection of (a). \odot and \otimes denote the vorticities of the vortices. The rows of junctions are numbered as in (a). (c) Line scan for row No. 3.

array's edges. Due to the e-beam-induced decrement of E_J the vortex-antivortex attraction is decreased. Now let us consider a vortex that enters the array. The beam-induced decrement of the intervortex force accelerates the real vortex during its propagation at the beginning. From this, we expect a beam-induced voltage increase at every junction where vortices enter the array. For a vortex that is close to the point of exit, we expect just the opposite because the electron beam causes a decrement of the intervortex force and, hence, the attraction towards the image vortex is decreased. From this the velocity of the real vortex passing (x_0, y_0) is lower compared to the situation when the beam is switched off. Therefore, we expect a beam-induced voltage decrease at every junction where vortices leave the array.

Figure 6(b) shows the vortex dynamics which can be inferred from Fig. 6(a). It is worth to recall that the LTSEM images taken with the technique of the lock-in amplifier yield only results in the time average and, thus only steady vortex modes are visible. In principle, three cases are possible for the motion of current-induced vortices driven by the Lorentz force across the array in zero applied magnetic field: (1) nucleation of a vortex and an antivortex at the two opposite edges, respectively, both moving towards the center where they annihilate; (2) nucleation of a single vortex at one sample edge, moving subsequently to the opposite edge; (3) the inverse process of case (2) for an antivortex. All three possibilities are observed in the array as can be seen in Fig. 6.

Figure 7 represents an impressive result obtained with a larger array. Here, it becomes very obvious that the propagation of the vortices is correlated in the different rows (perpendicular to the bias current). The dynamics is characterized by a large spatial domain located around the center of the array, where vortices and antivortices move across the array in opposite directions in adjacent rows (alternating crossing vortex motion, ACVM). In [10] we have shown more details about the nucleation of the ACVM domain together with the transition from ACVM to other modes when the bias current is increased. The ACVM can be qualitatively explained for energetic reasons, namely the repulsion of vortices of the same vorticity [9]. It is worth to add, that such kind of vortex motion is unknown for continuous systems like thin film microbridges of superconductors. The ACVM mode was also found in numerical simulations of the array dynamics performed with realistic parameters [4,11].

Up to now, we restricted our discussion to bias currents just above I_c and found the ACVM mode as the only steady mode. When the bias current is increased further but is still in region (II), the LTSEM voltage images look less regular [4], and it is by no means straight forward to infer details about the vortex dynamics any more. Extensive numerical simulations have been performed also for this region and found a highly complex vortex motion, representing a transition from pure ACVM to coherent behavior [4].

Summarizing the dynamics of region (II) (see Fig. 4), for low bias currents (just above the array's critical current) the vortices propagate in a specific mode, the ACVM mode, where vortices and antivortices tend to move in opposite direction in adjacent rows. For higher transport currents in this region, a transition to a more

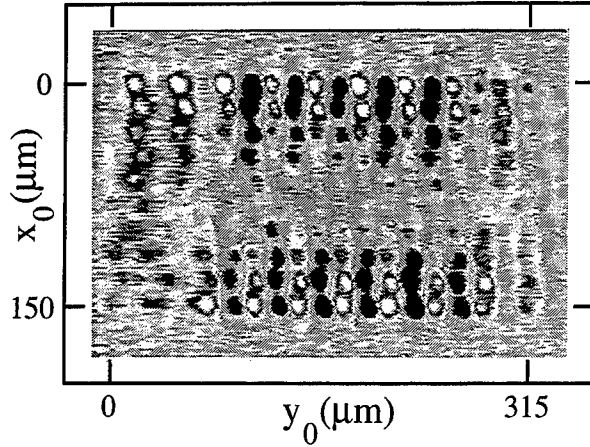


FIGURE 7. Voltage image for the 20×10 array with superconducting groundplane at $T \approx 5$ K. The array is current biased at 1.25 mA and a corresponding voltage of 3.0 mV. The array critical current $I_c \approx 750 \mu\text{A}$. Notice that in this image the dc bias current flows horizontally through the array (the image is turned by 90° with respect to the other images in this article). The array boundaries lie between 0 and 150 μm in x direction and between 0 and 315 μm in y direction. A positive (negative) e-beam-induced signal $\Delta V(x_0, y_0)$ is indicated by the white (black) areas, whereas $\Delta V(x_0, y_0) \approx 0$ is shown by the gray value of the areas surrounding the array.

complicated vortex dynamics can be observed. Since the $I - V$ curve shows rich structure in region (II), we attribute part of this structure to the vortex dynamics, as has already been done for the vortex dynamics in the current-induced resistive state of continuous superconducting thin films [12]. In addition, at least the broad resonance around 2.6 mA in Fig. 4 can be explained by a $L_s C$ -resonance with L_s being the inductance of the external shunt resistor and C being the capacitance of a single junction [13]. This resonance stabilizes the coherent oscillations of the junctions.

Finally, in the third region (see Fig. 4) the LTSEM images are simple [an example is shown in Fig. 9(a)]. The voltage response of every junction is practically the same [10], and the numerical simulations indicate a wave-like dynamics, where fronts of vortices move inwards from the boundaries [4]. In the middle the vortex fronts annihilate.

MICROWAVE INJECTION

The most prominent application of two-dimensional arrays of Josephson junctions is using them as a microwave radiation source [2]. For a thorough review on microwave sources based on Josephson junctions, see [14]. Before we shall dis-

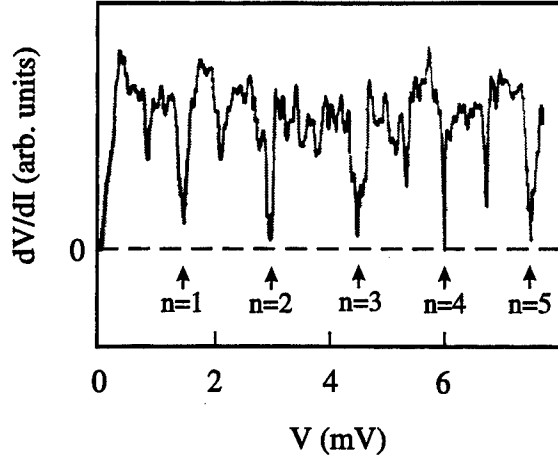


FIGURE 8. dV/dI versus V of a 10×10 array measured at a temperature $T \approx 4.5$ K. V is measured across the feeding resistors and thus includes a contribution from the bias current through these resistors. Microwave (70 GHz) with maximum power ($P = 1$) is applied. The first five integer Shapiro steps are marked by arrows.

cuss this topic in more detail in the following section, some results obtained with injection locked arrays are presented now. The coupling of array junctions to an external ac drive also reveals some important properties of the mutual interaction of the junctions.

Figure 8 shows the differential resistance dV/dI versus the array voltage measured for a certain microwave power and the frequency is 70 GHz. The differential resistance of this 10×10 array without microwave injection looks very similar to the one shown in Fig. 4 obtained for another 10×10 array. The sample is irradiated with the microwave from free space without using an antenna.

Notice that only the step $n = 4$ in Fig. 8 shows zero differential resistance as expected for complete locking. Such a behavior has also been frequently observed by others [15–17]. The finite differential resistance of the Shapiro steps has been attributed to thermally activated phase slips, thermally induced vortices, nonuniform current flow, or a spread in the critical currents of the junctions. Besides these possible microscopic reasons for nonperfect phase locking of all junctions, it is also important to look at the global behavior of the array [18]. In the following, we demonstrate that clusters of junctions, which are not locked to the external microwave irradiation, appear for finite differential resistance of the Shapiro steps.

Figure 9 shows the LTSEM voltage image of a 10×10 array, current biased at a voltage corresponding to the fourth Shapiro step. From Fig. 9(a) to 9(d) the power

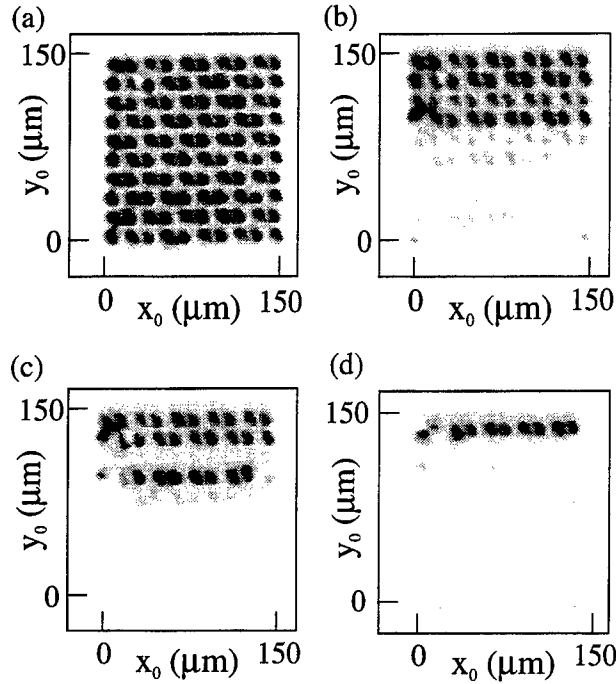


FIGURE 9. Gray value representation of the voltage image $\Delta V(x_0, y_0)$ of a 10×10 array at $T \approx 4.5$ K for different P (70 GHz). The array is dc current biased at $V \approx 6$ mV, which corresponds to the fourth Shapiro step. The array boundaries lie between 0 and 150 μm in both directions. A negative e-beam-induced signal ΔV is indicated by dark areas. (a) $P = 0$, (b) $P = 0.55$, (c) $P = 0.67$, (d) $P = 0.95$.

P of the external microwave is changed from $P = 0$ to $P = 0.95$. P is normalized to the maximum available power in our experimental set-up. In Fig. 9(a) the heating of each junction gives rise to a voltage decrease ΔV of the array. A signal from each junction can be detected. With increasing microwave power, the total number of junctions generating a voltage signal ΔV is decreasing [Figs. 9(a)–9(d)]. With $P = 1$ no voltage response from the junctions is detected.

If a junction's oscillation is locked to the external microwave field, the voltage of this junction is given by the frequency of the external source. Hence, if we slightly perturb a locked junction with the electron beam, we do not detect a voltage response. When all junctions of the array are locked to the external signal, the voltage response is zero for all junctions. Notice that the spatial distribution of the

clusters of locked junctions is stable in time, because it does not fluctuate during taking the LTSEM image which takes about three minutes. For a more detailed discussion of this experiment, see [18].

In most cases, almost whole rows of junctions are locked as can be seen in Fig. 9. The rows lie in the direction perpendicular to the direction of the dc transport current flow. This behavior is consistent with the assumption that phase locking in two-dimensional arrays of Josephson junctions is described by coherent vortex motion perpendicular to the transport current [17,19]. In some cases, we observed that all junctions of one row, but not the edge junctions, give a voltage signal. The inhomogeneous distribution of the dc and ac currents in the array, due to current-induced magnetic fields [20], may be responsible for this phenomenon.

The minimum value of dV/dI for a given Shapiro step can be tuned by the microwave power in accordance with the tunability of the number of locked junctions that can be determined from LTSEM images as those shown in Fig. 9. The number of locked junctions Δ normalized to the total number of junctions NM is determined by counting the junctions which do not show a voltage response in the LTSEM images as those shown in Fig. 9. Figure 10(b) shows the result of our measurements. The solid line in Fig. 10(b) is the fit $\Delta = a(P_t - P)^{1/2}$ with $a = 1.153 \pm 0.014$ and $P_t = 0.303 \pm 0.005$, with P_t denoting the threshold value of the normalized microwave power where the junctions start to lock.

In order to recognize the relationship to another system of oscillators, namely the laser, in Fig. 10(a) the textbook example of the dependence of the emitted laser intensity from the pump power is presented. Obviously, the coherently emitted microwave power from an array of Josephson junctions is determined by the square of the phase-locked junctions measured by Δ^2 in our case of injection locking. For comparison, we plot Δ^2 in Fig. 10(c). The solid line again shows the fit $\Delta^2 = b(P_t - P)$ with $b = 1.129 \pm 0.043$ and $P_t = 0.292 \pm 0.014$. For calculating the solid curves, the data points with $\Delta = 0$ have been omitted. If the injected microwave power P for the junction array is identified with the pump power for the laser, we observe very similar behavior for the emission of coherent radiation: there is a threshold value P_t for the injection (pump) power which has to be exceeded for the coherent emission; for $P > P_t$ the coherently emitted radiation power increases linearly with P .

For the laser it is known that the transition from incoherent to coherent emission can be identified with a non-equilibrium phase transition of the second kind, when the pump power is increased from a value below to above the threshold [21]. Now one can speculate whether the two-dimensional Josephson junction array also shows such a second-order phase transition [18]. This question is not completely answered up to now.

There are alternative quantities which can be used as the control parameter for the observation of the transition from incoherent to coherent oscillation of the array junctions. Besides the injected microwave power used above, the dc bias current can be taken [22]. In this case, we observe a similar transition as for the case presented above where the injected power has been used as control parameter and Δ as

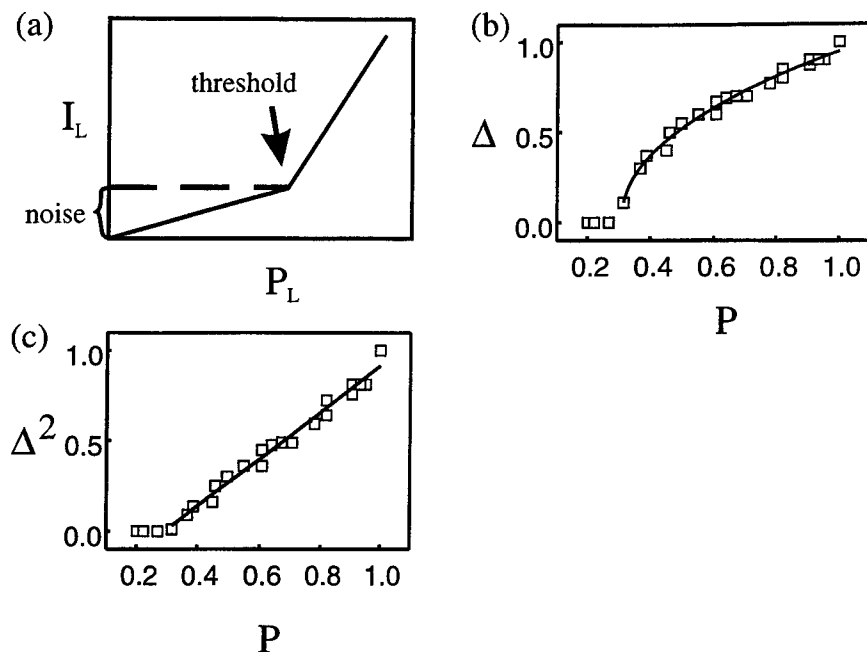


FIGURE 10. (a) Sketch of the intensity I_L of the emitted laser light as a function of the pump power (after Ref. [21]). (b) The open squares show the normalized number Δ of locked junctions, deduced from the spatially resolved measurements. The solid line shows a fit (see text). (c) The open squares show Δ^2 ; the solid line shows a linear fitting function (see text).

order parameter. Dealing with one-dimensional series arrays without microwave injection, Wiesenfeld *et al.* have shown theoretically that a current-biased array of nonidentical junctions can undergo a similar transition from incoherent oscillations to complete phase locking [23]. They also have used the dc bias current as the control parameter.

MICROWAVE EMISSION

All results shown in this section have been obtained for autonomous arrays (without external microwave irradiation). For the measurement of the emitted microwave power, we have manufactured two-dimensional arrays of Josephson junctions coupled to a detector Josephson junction via a microstripline. A sketch of the sample is shown in Fig. 3.

The value of the suppression of the critical current of the detector junction can be used as a first indication of emission from the array. This suppression is not sensitive to the degree of coherence of the radiation (wide-band detection). However, the observation of Shapiro steps in the $I - V$ curve of the detector indicates (partial)

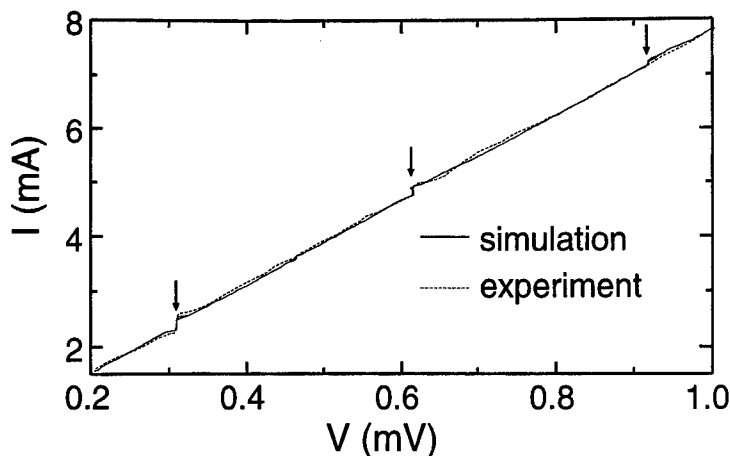


FIGURE 11. Simulated and experimental $I - V$ curves of the detector junction. The arrows point to integer Shapiro steps.

coherence. In Fig. 11 we show an example of the detector $I - V$ curve for a 10×10 array. This detector has a critical current of 0.31 mA and a shunt resistance of 0.125Ω . The emitted power can be quantitatively determined from this $I - V$ curve by numerical calculations of the curve using realistic parameters of the detector junction, and the injected microwave power as the only adjustable parameter [24]. We have performed such calculations by using the program PSCAN [25]. For the situation shown in Fig. 11 we estimate a detected microwave power of 56 nW at a frequency of 147 GHz.

For the estimation of the emitted power one has to consider various possibilities for transmission loss between the array and the detector. The main loss mechanism is expected due to non-perfect impedance matching between two neighboring elements, namely the array and the coupling stripline on the one hand, and the coupling stripline and the detector junction on the other hand. With LTSEM it is possible to measure directly the reflection coefficient at these two interfaces [24]. Figure 12 shows an example of such a measurement result for the case of a tapered coupling microstripline, indicating a pronounced standing wave inside the microstripline. Due to non-perfect impedance matching on both sides of the microstripline, the stripline acts as a resonator, and a standing wave appears if some microwave power is transmitted. Details of this imaging mode are presented in [26,27].

In brief, to measure the reflection coefficient r between array and coupling microstripline, we use the appearance of self-induced current steps in the $I - V$ curve of the detector junction. Such steps appear for resonator coupled junctions due to feed-back of the emitted radiation at the voltages corresponding to the resonance frequencies of the resonator. The shape of the steps depends on the quality

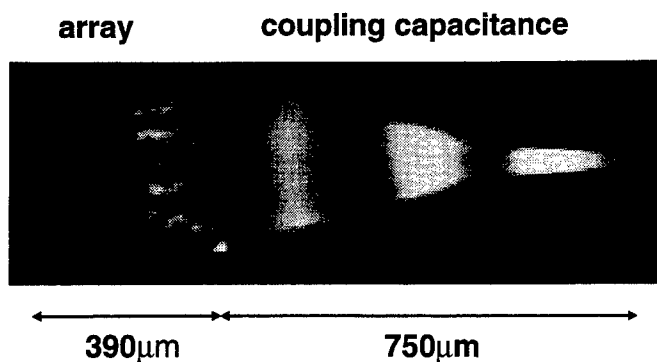


FIGURE 12. LTSEM image of the standing wave in a tapered microstripline, coupled to a 10×10 array. Bright areas indicate regions of the microstripline where the microwave surface current amplitude is high, whereas nodes of the surface current are indicated black. The brighter the image, the larger is the local microwave current amplitude.

Q of the resonator. If there is a standing wave excited inside the resonator, the electron-beam-induced local heating decreases Q . This decrement depends on the magnitude of the rf surface currents present at (x_0, y_0) : the larger these rf currents the larger is the decrement of Q and, hence, the larger is the change of the current step. The latter is measured by recording the change of the detector voltage while dc biased on a step. The impedance mismatch between coupling capacitance and detector is measured in the same way with the array using as the resonator coupled element. From such images, like that shown in Fig. 12, the voltage standing wave ratio (VSWR) of the microstripline is directly measurable, and from this the reflection coefficients for both interfaces can be determined.

For the circuit used for obtaining Fig. 11 we have estimated $r = 0.2$ for the interface between array and microstripline, and $r = 0.55$ for the interface between microstripline and detector [24]. By taking these results into account, the emitted microwave power is larger than the detected one by a factor of 2.8, and thus the array emits with a power level of about 160 nW. This power level indicates the in-phase oscillation of all junctions, as can be estimated from the maximum available power by using the Stewart-McCumber model for the array junctions.

After fabrication of the samples, for some of the arrays we have observed no coherent emission, but a suppression of the detector's critical current at 4.2 K, thus indicating incoherent emission. Theoretical considerations suggest that the parameter β_L must be small in order to observe the in-phase oscillation state in the presence of junction nonuniformities [28,29]. A simple method to decrease β_L after the fabrication of the samples is to increase the temperature above 4.2 K during the measurement but, of course, keeping it below the superconducting transition temperature of the sample (about 9 K for Nb). The higher the temperature, the

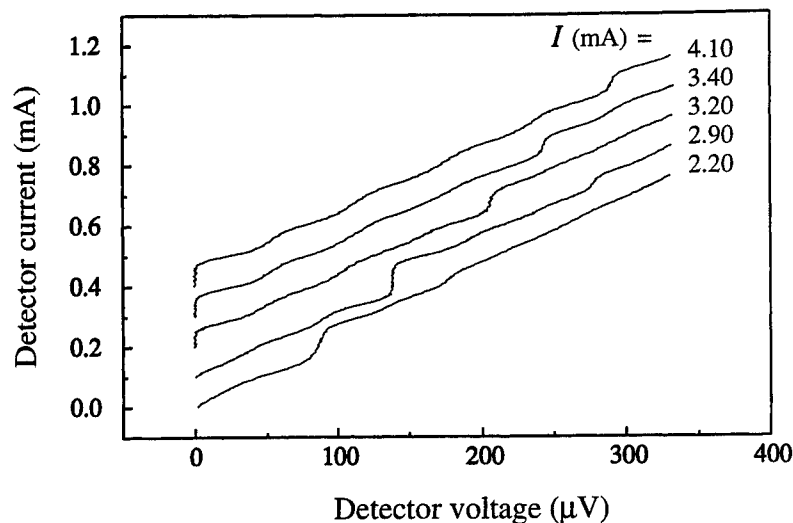


FIGURE 13. $I - V$ curves of the detector junction for different array bias currents at 6.4 K. Subsequent curves are offset by 0.1 mA.

smaller is i_c and, therefore, the smaller is β_L . From this it is expected that the coupling strength among the junctions can be tuned to a certain amount by the temperature.

This is indeed what we have found. Figure 13 shows examples for the detector $I - V$ curves when measured at a raised sample temperature [30]. For an array bias current $I = 2.90$ mA a pronounced Shapiro step is observed in the detector's $I - V$ curve corresponding to a frequency of 67 GHz. We have estimated the detected power for this bias current of the array in the same way as described above, and found a value of 57 nW which again is close to the value expected for the in-phase oscillation state [30]. In addition, we have observed that the tunability of the array improves at higher operation temperature. Similar behavior has also been reported by Cawthorne *et al.*, who measured (at constant temperature) the emitted microwave power from two-dimensional arrays having different critical current densities [31].

It is important to notice that the maximum available output power P_{max} of an array decreases with increasing temperature because $P_{max} \propto i_c^2$. Nevertheless, for this particular array, the entrainment of the coherent oscillation state due to the reduction of β_L predominates the reduction of P_{max} due to the reduction of i_c . Further studies will be performed in the near future regarding the nature of the transition from incoherent to coherent oscillations by variation of the temperature and, thus, variation of β_L .

Let us now turn to diagnostic tools in order to examine experimentally the degree of coherence of junctions' oscillations. Without special precaution regarding

the mutual interaction among the junctions or the uniformity of the junction parameters over the array, one- or two-dimensional do not show the in-phase oscillation state. Therefore, besides thorough theoretical analysis, it is mandatory to examine experimentally the degree of coherence. Up to now, coherent oscillations in one- and two-dimensional arrays of Josephson junctions have been observed in experiments making use of different methods. One can measure the power of the emitted radiation, which depends on the number of phase-locked junctions [2,24,32,33]. Another way is to measure the linewidth of the emitted radiation, which decreases as the number of phase-locked junctions increases [34,35]. However, both methods are associated with restrictions. Determining the power one has to take into account losses due to damping or reflections for non-perfect impedance matching between the array and the microwave detector (see above). On the other hand, the linewidth of the emitted radiation may be affected by resonances in the microwave coupling circuits [35].

We have introduced a new method for the detection of mutual locking [36]. The method is based on the same LTSEM imaging technique presented above in the section *Microwave Injection*, but now there is no external irradiation of the array with microwaves. However, due to the mutual coupling of the junctions, each junction in the array feels the microwave that is emitted from the other junctions, and the junction can be entrained this way. If the power of the electron beam is low enough (about $1 \mu\text{W}$, corresponding to a local temperature increase of about 0.2 K) such that the junction which is close to the e-beam focus does not lose its phase-coherence, this junction does not show a voltage response signal ($\Delta V(x_0, y_0) = 0$). On the other hand, if the focus is close to a non-locked junction for the same beam power, we are able to detect a voltage response signal ($\Delta V(x_0, y_0) \neq 0$). By applying this method to an array of junctions, we can detect those junctions which are not locked to the (partial) coherent oscillation mode.

For the experiment we have used the same circuit design as for the measurements of the emitted power (Fig. 3). Here, the detector's $I-V$ curve indicates the presence of coherent emission by the appearance of Shapiro steps. For the array investigated here, we have observed coherent radiation for some range of the bias current. Thus we can compare coherent and non-coherent states in the experiments. Figures 14(a) and 14(c) show LTSEM images for different bias currents. In Figs. 14(b) and 14(d) the corresponding $I-V$ curves of the detector junction are presented. For a bias current of the array $I = 2.17 \text{ mA}$ [Figs. 14(a) and 14(b)], no Shapiro steps in the detector $I-V$ curve are observed. The structure in the $I-V$ curve is due to resonances in the coupling circuit. The corresponding LTSEM image shows beam-induced voltage response signals of different signs and magnitude from almost all junctions. The maximum detected voltage signal $|\Delta V|$ shown in this figure is less than $0.5 \mu\text{V}$. For the two LTSEM images presented in Fig. 14 we have used the same scaling for coding the voltage response in form of gray values, therefore the two images can be directly compared to each other. Similar behavior as shown in Fig. 14(a) has been found for other samples which do not emit coherently [4,9]; those images have been attributed to vortex dynamic regimes (see section *Dynamics of*

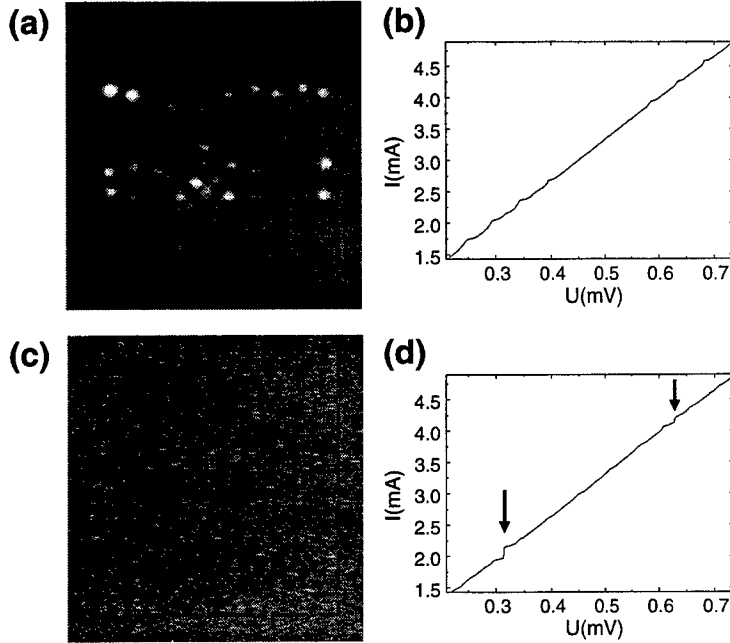


FIGURE 14. LTSEM voltage images for non-locked and mutually locked array states. A positive (negative) e-beam-induced voltage signal $\Delta V(x_0, y_0)$ is indicated by the dark (bright) areas, whereas zero signal level is shown by the areas surrounding the array. The dc bias current flows vertically through the 10×10 array. The dotted black box indicates the position of the array. The size of the array is $370 \times 370 \mu\text{m}^2$. (a) Array's bias current $I = 2.17$ mA, no coherent emission is observed. (c) $I = 1.90$ mA, almost all junctions are locked. The corresponding $I - V$ curves of the detector junction are shown in (b) and (d). (b) $I = 2.17$ mA, no Shapiro steps. (d) $I = 1.90$ mA, Shapiro steps at 0.315 mV (1^{st}) and 0.63 mV (2^{nd}), indicated by the arrows. Temperature $T \approx 4.5\text{ K}$.

Vortices above).

On the other hand, for a slightly lower bias current of 1.90 mA [Fig. 14(c) and 14(d)] Shapiro steps are clearly visible in the detector $I - V$ characteristic corresponding to a frequency of 152 GHz . Only very few junctions generate a beam-induced voltage signal. From the detector $I - V$ curve we estimate a detected microwave power of approximately 35 nW . In consideration of reflection losses during the transmission of the microwave power from the array to the detector and of the non-matched load (detector) impedance, this amount of detected power indicates a high degree of coherence in the array. A careful inspection of the junctions which are not perfectly locked [indicated by the dark signals (hardly visible) in Fig. 14(c)] shows that these junctions deviate from the others by a different value of their critical current. This can be inferred from LTSEM images taken at bias

currents at which there is no coherent emission present.

An advantage of LTSEM for the investigation of the coupling of junctions in arrays is that it allows the observation of coherent oscillating states without the need of an extra coupling circuit. Coupling structures practically always come with resonances.

Regarding the practical application of arrays of Josephson junctions as microwave radiation source, encouraging progress has been obtained during the recent years [14]. The activities can roughly be divided into two categories: one- and two-dimensional arrays of junctions. Practically all promising results have been obtained with arrays made from low temperature superconductors (mainly Nb-based). This comes from the fact that, at present, the high temperature superconducting (HTS) junctions cannot be fabricated with small margins in a large number, so that only cryoelectronic devices with the demand for only a few junctions can be realized from HTS [37]. For one-dimensional series arrays, on-chip detected power levels of $47\text{ }\mu\text{W}$ (at 394 GHz with 500 junctions) [32] or $160\text{ }\mu\text{W}$ (at 240 GHz with 1968 junctions) [33] have been attained. For a one-dimensional parallel-biased array, a detected power of $0.1\text{ }\mu\text{W}$ (at 680 GHz with 11 junctions) has been reported [38]. For the two-dimensional arrays, the power levels amount to 400 nW (at 150 GHz with a 10×10 array) [2], 150 nW (at 210 GHz with a 10×10 array) [31], or 56 nW (at 147 GHz with a 10×10 array) [24], just to name a few results. However, for a direct comparison of the maximum detected power, besides possible transmission losses between array and detector, one has to take into account the principal parameters governing the level of emitted power (provided that the in-phase oscillation state has been achieved): the number of phase-locked junctions and the critical current (or the product of critical current and normal state resistance) of the junctions. Of course, the primary goal cannot be to make maximum (incoherent) emission available, but to attain the complete in-phase oscillation state of a large number of junctions in an array, thus ensuring minimum linewidth. Furthermore, the tunability of the emitted frequency is an important requirement.

CONCLUSIONS

We have discussed some selected topics regarding the dynamics of two-dimensional arrays of Josephson junctions. For this, we have restricted to overdamped junctions where, in addition, the Josephson coupling energy predominates the charging energy, because such arrays are promising as possible coherent microwave radiation sources.

Due to the very complex nonlinear dynamics of such arrays (see, e.g., [39,40]) various dynamical modes are expected to exist. From all these modes only the in-phase mode is useful for the practical application as a microwave source. The array's dynamics for low dc bias currents (of the order of, but still larger than the array's critical current) can well be described by the propagation of individual vortices, very similar to the current-induced resistive state of a superconducting thin

film. Due to the presence of some resonator devices the coherent oscillation mode is supported and observed experimentally for a certain range of the bias current. Such a resonator can be given by the capacitance of each junction together with the inductance of the shunt resistor loop. Since the quality of this resonator is low due to the large damping determined by the shunt resistance, there is the possibility of tuning the frequency of the emitted radiation in spite of coupling the junctions to a resonator.

We have presented imaging results which demonstrate directly different vortex dynamic regimes. These vortex modes have also been found in extensive numerical simulations including all self and mutual inductances of the array. Furthermore, applying the LTSEM technique to injection locked or autonomous (intrinsically locked) arrays we have succeeded in imaging the non-locked junctions. Dealing with an external ac drive, there is a global transition from incoherent to coherent oscillations of the junctions, including a threshold value for the drive power at which the number of coherently oscillating junctions starts to grow from zero. The identification of the non-locked junctions in the mutually coupled case (without external ac drive) is very valuable for the optimization of the circuits serving as a microwave source.

For any future optimization of overdamped arrays of Josephson junctions the junctions themselves deserve further attention. As in the case of other high-frequency applications of overdamped, lumped junctions, as, e.g., rapid single flux quantum (RSFQ) circuits, it would be highly desirable to fabricate overdamped junctions without the need of external shunting. This can be accomplished by using intrinsically shunted junctions, as some species of the high critical temperature superconductor Josephson junctions, or by attaining an extremely high critical current density for the Nb-based tunnel junctions. Together with the miniaturization of the junctions and the loops of the array, a high output power together with a low value of β_L should be attainable. However, a high degree of junction uniformity across the array still remains as a key requirement.

ACKNOWLEDGMENTS

We thank G. Filatrella, W. Güttinger, T. J. Hagenaaers, D. Hoffmann, R. P. Huebener, J. V. José, M. Keck, S. G. Lachenmann, A. Laub, R. Müller, J. Openländer, R. Pfeifer, H. Preßler, P. H. E. Tiesinga, T. Träuble, and J. E. van Himbergen for collaboration and valuable discussions, as well as S. G. Lachenmann for carefully reading the manuscript. Part of the samples used for the investigations have been made available to us by S. P. Benz, P. A. A. Booij, and C. J. Burroughs from NIST in Boulder (CO); other samples have been fabricated at the PTB in Braunschweig with the help of R. Dolata, J. Niemeyer, and T. Weimann. Part of this work has been supported by the Bundesminister of Bildung, Wissenschaft, Forschung und Technologie under Contract No. 13N6436, the Forschungsschwerpunktprogramm des Landes Baden-Württemberg, and the European Commission

under the program "Human Capital and Mobility" (Contract No. CHRX-CT92-0068).

REFERENCES

1. Giovannella, C. and Tinkham, M. (eds.), *Macroscopic Quantum Phenomena and Coherence in Superconducting Networks*, Singapore: World Scientific, 1995.
2. Benz, S. P. and Burroughs, C. J., *Appl. Phys. Lett.* **58**, 2162 (1991) and *Supercond. Sci. Technol.* **4**, 561 (1991).
3. Dolata, R., Khabipov, M. I., Buchholz, F. I., Kessel, W., and Niemeyer, J., *Applied Superconductivity 1995*, Dew-Hughes, D. (ed.), London: IOP Publishing, 1995, pp. 1709–1712.
4. Lachenmann, S. G., Doderer, T., Huebener, R. P., Hagenaaars, T. J., van Himbergen, J. E., Tiesinga, P. H. E., José, J. V., *Phys. Rev. B*, scheduled to appear 1 September 1997; also available in cond-mat #9705194.
5. Huebener, R. P., *Advances in Electronics and Electron Physics*, Vol. **70**, Hawkes, P. W., (ed.), New York: Academic Press, 1988, pp. 1–78.
6. Gross, R. and Koelle, D., *Rep. Prog. Phys.* **57**, 651 (1994).
7. Doderer, T., *Int. J. Mod. Phys. B* **11**, 1979 (1997).
8. Tinkham, M., *Introduction to superconductivity*, Second Edition, New York: McGraw-Hill, 1996, ch. 6.6.
9. Lachenmann, S. G., Doderer, T., Hoffmann, D., Huebener, R. P., Booi, P. A. A., and Benz, S. P., *Phys. Rev. B* **50**, 3158 (1994).
10. Doderer, T., Lachenmann, S. G., Huebener, R. P., *Macroscopic Quantum Phenomena and Coherence in Superconducting Networks*, Giovannella, C. and Tinkham, M. (eds.), Singapore: World Scientific, 1995, pp. 317–328.
11. Hagenaaars, T. J., van Himbergen, J. E., Tiesinga, P. H. E., José, J. V., Lachenmann, S. G., *Macroscopic Quantum Phenomena and Coherence in Superconducting Networks*, Giovannella, C. and Tinkham, M. (eds.), Singapore: World Scientific, 1995, pp. 329–336.
12. Huebener, R. P., *Magnetic Flux Structures in Superconductors*, Berlin: Springer, 1979, ch. 14.
13. Booi, P. A. A. and Benz, S. P., *IEEE Trans. Appl. Supercond.* **5**, 2899 (1995).
14. Mygind, J. and Pedersen, N. F., *Macroscopic Quantum Phenomena and Coherence in Superconducting Networks*, Giovannella, C. and Tinkham, M. (eds.), Singapore: World Scientific, 1995, pp. 339–350.
15. Clark, T. D., *Phys. Rev. B* **8**, 137 (1973).
16. Leemann, Ch., Lerch, Ph., and Martinoli, P., *Physica* **126B**, 475 (1984).
17. Benz, S. P., Rzchowski, M. S., Tinkham, M., and Lobb, C. J., *Phys. Rev. Lett.* **64**, 693 (1990).
18. Lachenmann, S. G., Doderer, T., Huebener, R. P., *Phys. Rev. B* **53**, 14541 (1996).
19. Domínguez, D. and José, J. V., *Int. J. Mod. Phys. B* **8**, 3749 (1994).
20. Phillips, J. R., van der Zant, H. S. J., White, J., and Orlando, T. P., *Phys. Rev. B* **50**, 9387 (1994).

21. Haken, H., *Synergetics, An Introduction*, Third Edition, Berlin: Springer, 1983.
22. Laub, A., Augke, R., Lachenmann, S. G., Doderer, T., Keck, M., Träuble, T., Huebener, R. P., Dolata, R., and Niemeyer, J., *Czech. J. Phys.* **46**, 689 (1996).
23. Wiesenfeld, K., Colet, P., Strogatz, S. H., *Phys. Rev. Lett.* **76**, 404 (1996).
24. Keck, M., Doderer, T., Mueller, R., Pfeifer, R., Laub, A., Huebener, R. P., Traeuble, T., Dolata, R., Weimann, T., and Niemeyer, J., *IEEE Trans. Appl. Supercond.* **7**, 3407 (1997).
25. Odintsov, A. A., Semenov, V. K., and Zorin, A. B., *IEEE Trans. Mag.* **MAG-23**, 763 (1987).
26. Quenter, D., Stehle, S., Doderer, T., Krülle, C. A., Huebener, R. P., Müller, F., Niemeyer, J., Pöpel, R., Weimann, T., Ruby, R., and Barfknecht, A. T., *Appl. Phys. Lett.* **63**, 2135 (1993).
27. Quenter, D., Doderer, T., and Huebener, R. P., *J. Appl. Phys.* **80**, 3566 (1996).
28. Basler, M., Krech, W., and Platov, K. Yu., *Phys. Rev. B* **52**, 7504 (1995).
29. Basler, M., Krech, W., and Platov, K. Yu., *Phys. Rev. B* **55**, 1114 (1997).
30. Traeuble, T., Keck, M., Pressler, H., Dolata, R., Doderer, T., Weimann, T., Huebener, R. P., and Niemeyer, J., "Optimization of coherent emission from Josephson junction arrays by variation of the temperature", in *Proceedings of the Third European Conference on Applied Superconductivity 1997*, to be published.
31. Cawthorne, A. B., Barbara, P., and Lobb, C. J., *IEEE Trans. Appl. Supercond.* **7**, 3403 (1997).
32. Han, S., Bi, B., Zhang, W., and Lukens, J. E., *Appl. Phys. Lett.* **64**, 1424 (1994).
33. Booi, P. A. A. and Benz, S. P., *Appl. Phys. Lett.* **68**, 3799 (1996).
34. Bi, B., Han, S., Lukens, J. E., and Wan, K., *IEEE Trans. Appl. Supercond.* **3**, 2303 (1993).
35. Booi, P. A. A. and Benz, S. P., *Appl. Phys. Lett.* **64**, 2163 (1994).
36. Keck, M., Doderer, T., Huebener, R. P., Traeuble, T., Dolata, R., Weimann, T., and Niemeyer, J., *Appl. Phys. Lett.* **71**, 270 (1997).
37. Van Duzer, T., *IEEE Trans. Appl. Supercond.* **7**, 98 (1997).
38. Kawakami, A., Uzawa, Y., and Wang, Z., "Josephson Array Oscillator with Microstrip Resonators for Submillimeter Wave Region", in *Extended Abstracts of the Sixth Int. Superconductive Electronics Conference*, Vol. **3**, 1997, pp. 192-194.
39. Wiesenfeld, K., Benz, S. P., and Booi, P. A. A., *J. Appl. Phys.* **76**, 3835 (1994).
40. Oppenländer, J., Dangelmayr, G., and Güttinger, W., *Phys. Rev. B* **54**, 1213 (1996).

RSFQ logic devices; non-linear properties and experimental investigations

Jesper Mygind

*Department of Physics, Technical University of Denmark
DK-2800 Lyngby, Denmark¹*

Abstract. *Rapid Single Flux Quantum* (RSFQ) logic has a great potential as fast digital and high frequency analog electronics. Several Logic/Memory base elements and integrated sub-systems in the *RSFQ family* have been devised and tested since the pioneering work in the mid 1980s by K. K. Likharev's group at Moscow State University [1,2]. It is argued why the RSFQ digital circuits are superior to the *voltage state family* circuits, which were utilised in the first development of Josephson logic. Also the parameter space for operation of the 1-D RSFQ transmission line is discussed.

Presently most RSFQ circuits are made with low- T_c superconductors using the now mature whole-wafer NbAlO_x/Nb technology, which allows for large and densely packed integrated circuits. Recently, a few operational high- T_c RSFQ circuits have been reported. An important development within the last two years is the advent of general-purpose on-chip bit-by-bit verification test systems. Timing of RSFQ circuits and a few recent RSFQ "highlights" are briefly mentioned. Basically the RSFQ technology appears "ready" for widespread industrial use.

One of the key components is the RSFQ transmission line, which can both generate and transmit SFQ pulses. In order to demonstrate the importance of the fluxon dynamics we discuss a new phenomenon observed in a parallel array of identical junctions. Steps with extremely low differential resistance in the $I - V$ characteristic are found to be due to the self-induced magnetic field produced by the edge current fed to the array. The underlying mechanism is that the non-uniform field divides the moving fluxon into "domains" covering several (unit) cells. The experimental/numerical results illustrate practical and may be more fundamental limits to RSFQ electronics.

INTRODUCTION, PAST AND PRESENT

The fluxoid quantization in units of the Single Flux Quantum (SFQ, $\Phi_0 = h/2e$) in a superconducting contour is the basic physical mechanism for RSFQ

¹⁾ e-mail: myg@mips.fys.dtu.dk, URL: <http://mips.fys.dtu.dk/myg/>

electronics. The vortex (or fluxon) in a bulk type-II superconductor (*Abrikosov vortex*) has a normal conducting core and is distinctly different from the vortex inside a Josephson tunnel junction (*Josephson fluxon*), which has a partly insulating core. Propagation and storage of fluxons as quantum mechanical entities in a network consisting of Josephson junctions and superconducting interconnections is the important advantage of the RSFQ concept. In addition, the inherent low power dissipation as well as the unique combination of fast response and high energy resolution theoretically make the RSFQ circuits superior to semiconductor devices in several applications. Within the so-called *RSFQ family* [2] of logic circuits the presence or absence of a circulating current in an inductive superconducting network loop (with one or more Josephson junctions) represents a logic "one" or "zero". As discussed below RSFQ logic is expected to operate up to subterahertz frequencies. Fluxoid quantization is particularly important also for clocking and synchronisation of RSFQ circuits.

The RSFQ concept gained momentum around 1990 when some of the very active researchers from Moscow State University and Institute of Radio Engineering and Electronics (IRE) moved to the New York area (SUNY, Stony Brook and Hypres, Inc.).

Three decades of voltage state logic

The alternative Josephson logic circuit - the *voltage state family* - is fundamentally different. Here logic "one" and "zero" are given by the presence or absence of a ≈ 3 mV voltage signal. Most of the Josephson switching circuits developed over the last three decades have been of the voltage state type. The first simple circuits were made at IBM where since the late 1960s many new design concepts and inventive fabrication methods were developed. The project terminated in the early 1980s mainly because it became obvious that the lead-alloy technology and the problems with producing an operational random access memory (RAM) impede profitable competition with the rapidly growing semiconductor industry. Parallel to the IBM project several other universities and government institutes (Berkeley, NIST, Tohoku, Tokyo, Moscow, et al.) and industries (TRW, Bell, Sperry, et al.) developed their own logic circuits and junction production technologies using other strategies.

A major step towards reliable and densely packed superconducting circuits was the whole-wafer NbAlO_xNb tri-layer process, which now is a standard technology mastered by over hundred laboratories around the World. The development of the tri-layer process to a large extent was the result of the 10-year MITTI (Japan Ministry of International Trade and Industry) superconducting computer project started in 1981. A number of Japanese companies and government institutes (ETL, Fujitsu, NEC, NTT, et al.) made important progress in Josephson logics using the tri-layer process. An updated overview of Superconductor Electronics may be found in Ref. [3].

Circuit production

Hypres [4] and IRE now serve as commercial foundries for the community delivering chips with both voltage state and RSFQ based circuits. Josephson 10 V voltage standard chips with more than 20.000 junctions are routinely made with reasonable yield at Hypres using standard optical $\approx 2.5\mu\text{m}$ resolution lithography. The alternative and indeed very attractive technology based on high- T_c superconducting materials still is very young and only a few industries (Conductus, NKT, a. o.) have entered junction and circuit fabrication. Several numerical design and circuit simulation tools (PSCAN [2], JSPICE [5], MALT [6], a. o.) as well as programs able to evaluate inductances of superconducting circuits are available.

The state-of-the-art superconductor electronics make use of electron beam lithography and nanoprobe (STM, AFM, etc.) to fabricate complex circuits with sub-micron and even nanometer size junctions. This advanced technology is driven by the recent developments in optics (quantum lasers, quantum wells, etc. based on the 2-D electron gas in e. g. GaAs/AlGaAs/GaAs semiconducting structures) and electronics based on tunneling of single charge carriers (SET and SCPT, Single Electron and Single Cooper-Pair Tunneling).

RSFQ status, highlights

In spite of the theoretical superiority no commercial instrument with neither voltage state nor RSFQ Josephson logic has yet been produced. This is due to the competition from semiconductors, mainly because of their favourable cost-benefit but also the impressive continued increase in performance of silicon integrated circuits is hard to beat. Together with technological conservatism especially the irrational aversion against cooling this only leaves a small number of niches where superconductor electronics is evidently superior. Today only two applications are widely used: the SQUID (utilised for magnetometers, biomagnetism, etc.), and the SIS mixer (deployed at every millimeter wave astronomy telescope). Both are analog and rely on few junctions. Useful Josephson logic requires large scale integration with many junctions and interconnections in complex digital circuits. Compared to modern semiconductor chips even the most elaborate superconducting circuit (the abovementioned Josephson voltage standard) has a low scale of integration. Time will change this and the RSFQ concept in the authors opinion is the most promising candidate for future superconductor electronics.

Space limitations only permit a very brief discussion of RSFQ digital circuits. Reference should be made to proceedings from the major conferences in superconductivity (ASC, EUCAS, ISEC, CPEM, a. o.) which contain series of papers and updated reviews describing the recent developments. Here I will mention four applications two of which seem prone to practical realisation.

1) The RSFQ *time-to-digital converter* (TDC) [7] is a fast 14 bit (20 GHz, 50 ps) instrument dedicated to register time-of-flight (TOF) in all branches of high-energy physics (HEP) and nuclear physics, where the determination of the mass or energy of a particle relies on accurate and fast measurement of the flight path. Most modern HEP instruments already are cooled to liquid helium temperatures or below, and the low power operation of the RSFQ logic makes it far superior to semiconductor electronics. Presently the small signals from the cooled front-end detectors (Photon counters, etc.) are transmitted to the room temperature electronics (amplifiers, counters, etc.) via low-heat conducting cables. The best semiconductor TDC provides 16 ps resolution but its 6 W power consumption prevents cryogenic integration. The RSFQ TDC only dissipates 0.5 mW and can be placed directly onto the photon detectors. By integrating the clock generator (or a multiplier) with the TDC on the same chip one expects operational frequencies above 100 GHz.

2) The RSFQ *analog-to-digital converter* (ADC) has been investigated for several years and many designs have been devised [3]. It is superior to semiconductor ADCs in power dissipation, speed, dynamic range, and sensitivity. A recent counting type ADC with 2100 interferometers and junctions showed 16 bits accuracy for a 5 MHz analog signal using a 10 GHz clock [8]. The ADC occupies $4 \times 4 \text{ mm}^2$ and dissipates 0.6 mW. This is one of the remarkable demonstrations of the state-of-the art RSFQ circuits, but many new results also by other groups indicate that in the near future the RSFQ ADC is a very prominent candidate for real practical applications. Several high- T_c ADCs including DC-SFQ circuits have been successfully operated.

3) The inverse, the Josephson *digital-to-analog converter* (D/A) has been designed and used as a programmable voltage standard to synthesise metrologically accurate ac waveforms [9]. It is based on the Josephson D/A proposed by Hamilton et al. (see Ref. [10]) for programmable voltage standards. The D/A is a binary sequence of series arrays each with N resistively shunted tunnel junctions. When biased with a microwave frequency each junction generate constant-voltage steps at V_n where n is the quantum step number. The array bias determines $n = \dots, -1, 0, +1, \dots$ and thus the step number of the array. Since the number of pulses per period $1/f$ is n each array of N junctions generates an average voltage $V_N = N \cdot V_n$. This pulse quantizer holding 32 768 SNS junctions fabricated with NIST's tri-layer process in 9 independently selectable arrays on a single chip has been able to generate voltages in the range -1.2 V to +1.2 V. Instead of changing n and N the output voltage can also be controlled by changing the applied frequency. The NIST group has shown that if a pulse excitation is used instead of the sine wave the amplitude of the voltage step is independent of the pulse repetition rate below a characteristic frequency. Thus it is now possible to generate any complex waveform by gating the incoming pulse train by a long digital word generator, or visa versa knowing the digital code, the clock frequency, and N one can precisely calculate the output waveform. In metrology as with the dc Josephson voltage

standard there is a need for accurate ac voltages with known waveforms. In preliminary experiments using 1000 junctions clocked at 12 Gbits/s, a ≈ 5 mV sine wave has been synthesised at frequencies up to 1 MHz.

4) Finally, an elegant method for on-chip linewidth measurements of Josephson oscillators using RSFQ T-flip-flops (TFFs) has been devised by a group at Conductus, Inc. [11]. Measurements can be done on a single short junction but may be extended to long junctions. The oscillator junction is connected by a RSFQ transmission line (discussed below) to the first TFF. A divider circuit of eight series connected TFFs is used to divide the oscillator frequency by $2^8 = 256$. Each TFF has a Josephson storage interferometer, which (also discussed below) can only hold a single SFQ. If the TFF is in the "0" state an arriving SFQ pulse will insert a flux quantum, and if the TFF is in the "1" state the SFQ pulse will eject the existing flux quantum. Thus there will be an SFQ pulse on the output of the TFF for every other SFQ pulse on the input, so each TFF divides its input frequency by two. After division one can use a (cheaper) low frequency spectrum analyzer to measure the frequency and linewidth of the Josephson oscillator. The actual test circuit with standard NbAlO_xNb junctions was able to measure linewidths as small as 1 kHz at 20 GHz. The TFF frequency division scheme is used also for demodulation by other groups.

Fluxon dynamics, other structures

In the following we mainly consider one-dimensional circuits. Fluxon dynamics is of great importance in many other structures, and an extensive theoretical and experimental work is being done on two-dimensional arrays (frustration, commensurability, Kosterlitz-Thouless transition, row/column synchronisation, rf induced Giant Shapiro steps) [12]. The interaction between Abrikosov and Josephson vortices in stacked Josephson structures may explain many of the physical properties of the high- T_c materials.

I RSFQ VS "VOLTAGE STATE" LOGIC

RSFQ circuits consist of small (dimensions $< \lambda_J$) shunted junctions connected by superconducting electrodes. The Josephson penetration depth $\lambda_J = \sqrt{\frac{\Phi_0}{2\pi\mu_0 d J_c}}$ is the depth to which magnetic flux enters into a long (length $L > \lambda_J$, width $W < \lambda_J$) Josephson tunnel junction with current density J_c and effective magnetic thickness d . The junction parameters and in particular the inductance and other transmission line properties of the interconnects are important for the dynamics of fluxons within the RSFQ network. Below we shall follow the original ideas in the seminal review by Likharev and Semenov [2] and supplement with arguments by Feldman [13].

Elementary RSFQ cells can store, transfer, and generate an SFQ representing a data bit. The cell has one or more stable flux states and an incoming SFQ pulse may force the cell to change its state and possibly produce an outgoing SFQ pulse. When a bit is transferred it is accompanied by a picosecond voltage pulse $V(t)$ with a quantized size

$$\int V(t)dt = \Phi_0 = h/2e \approx 2mV \cdot ps \quad (1)$$

i. e. given by fundamental constants. Eq. (1) relates the voltage pulse height V_{\max} and width τ , approximately $V_{\max}\tau = \Phi_0$. The pulse width τ is a very important parameter for RSFQ circuits. In order to distinguish two SFQ pulses, say a clock pulse and a data pulse, they must arrive at a given cell with a time separation of $\approx 2\tau$, meaning that the maximum clock frequency is less than $1/2\tau$. It is a general rule that the maximum intrinsic circuit speed scales with $1/\tau$.

For an isolated small Josephson junction with critical current I_c and shunt resistance R the standard RSJ-model current biased at a current $I_b > I_c$ gives the following time dependent voltage:

$$v(\theta) = \frac{\omega^2 - 1}{i_b + \sin(\omega\tau + \phi_0)} \quad (2)$$

where the voltage $v(\theta)$ is normalized by RI_c , the bias current i_b by I_c , and time θ by $\Phi_0/(2\pi RI_c)$. The "effective" angular velocity is $\omega = (i_b^2 - 1)^{1/2}$, and ϕ_0 is an arbitrary phase angle. When the junction is biased with i_b being slightly larger than unity, Eq. (2) shows that $v(\theta)$ consists of a series of voltage spikes with maximum voltage $v_{\max} = i_b + 1 \approx 2$. The full width at half maximum is 2θ . In real units the pulse height is $2I_cR$. The pulse width is $\Phi_0/(\pi I_cR)$ and the product of these is $(2/\pi)\Phi_0$. The larger R the smaller is the width of the SFQ pulse.

The tunnel junction used in RSFQ circuits also has an inherent capacitance C and usually R is chosen so that the McCumber parameter $\beta_c = 2\pi I_c R^2 C / \Phi_0 \approx 1$. The reason is that a larger β_c value makes the junction hysteretic. A simulation [13] of the pulse shape for $\beta_c = 1$ shows a somewhat distorted pulse with an asymmetric pattern of oscillations. The product of pulse height and pulse width is slightly larger than the $\beta_c = 0$ case and approaches $\approx \Phi_0$.

For a typical cell with standard $(3.5\mu m)^2$ NbAlO_xNb junctions the minimum clock period is 10-20 ps. Theoretically [2] a 1-2 ps clock period can be obtained using submicron technology.

A basic switching in a simple *voltage state* circuit is shown in Fig. (1). A bias current I_b is supplied to the two-junction SQUID gate at $\approx 80\%$ of its critical current I_c . An applied control current I_{cont} reduces the critical current of the SQUID and it switches from the zero voltage state (logical "zero") to the

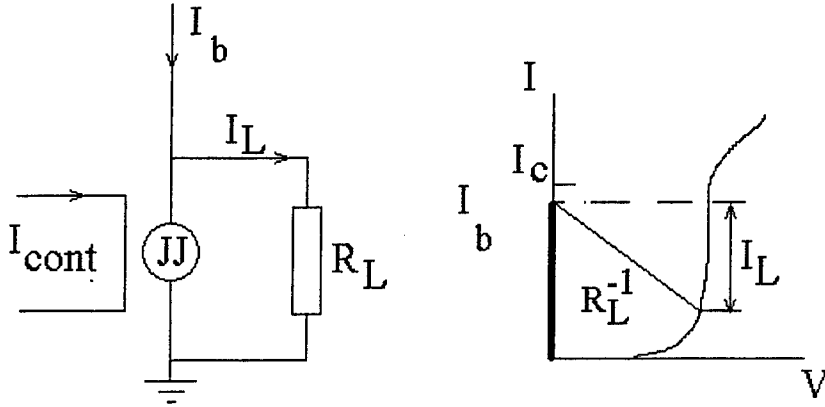


FIGURE 1. Voltage state logic. The control current I_{cont} reduces the critical current of the dc SQUID loop and it switches along the load line and becomes a high resistance. A fraction, I_L , of the bias current I_b is diverted into the load.

voltage state (logical "one"). The current I_L is delivered to the load resistor R_L here representing the transmission line to the next gate. The SQUID gate current remains positive in the "one" state and the output is non-inverted. This is a serious weakness of the voltage state family logic since many general logic operations involve inversion. A number of logic circuits rely on direct-coupled overdrive to switch between states instead of the inductive coupling shown here. Another important process is the resetting of the gate to the "zero" state. As described below this limits the switching speed of the voltage state family.

The maximum speed for the *voltage state* logic originates in the fact that the fundamental parameters for the Josephson effect are current and phase (I, ϕ) and not current and voltage (I, V). In the finite voltage state the phase is basically undefined. If we use the simple pendulum model for the small Josephson junction it is clear that in order to reset the junction from a rotating state at the voltage (given by the 1st Josephson equation)

$$V = \frac{\Phi_0}{2\pi} \frac{d\phi}{dt} \quad (3)$$

to the zero voltage state, the phase must be "recaptured" from an essentially randomly distributed phase to the phase ϕ_b given implicitly by the bias current via the 2nd Josephson equation

$$I_b = I_c \sin \phi_b \quad (4)$$

Any 2π periodic "bias" phase $\phi'_b = \phi_b + n2\pi$ will satisfy this. In the case where the initial phase is in the vicinity of the separatrix between two neighbouring (say n to $n+1$) attractors the junction will take some time to decide where to settle. If this time is long it causes a bit error. Using the simple capacitively shunted CRSJ model the *bit-error rate*, BER is given by [13]

$$BER = \frac{1}{\pi} e^{-\omega_{pb} t_0} \quad (5)$$

where t_0 is the time used to reset, and ω_{pb} is the plasma frequency, $\omega_{pb} = \omega_{p0} [1 - i_b^2]^{1/4}$, in the bias point Here $\omega_{p0} = \left[\frac{2\pi I_c}{\Phi_0 C} \right]^{1/2}$ is the maximum plasma frequency.

If we set t_0 equal to one quarter of the clock period Eq. (5) predicts a $BER \approx 1 \cdot 10^{-9}$ per reset using a 10 GHz clock rate and a standard NbAlO_xNb junction with $J_c = 1$ kA/cm². This cannot be tolerated for an integrated circuit with many junctions and therefor severely limits the applicability of the voltage state family logic.

Since the RSFQ family relies on the "natural" Josephson parameters (I, ϕ) it does not suffer from this calamity. As mentioned above clock periods of order 10 ps can routinely be achieved for a single cell. However, as described below, the inductance, and in general the transmission line properties of the interconnects may impose restrictions on operation times in extended circuits.

II INDUCTANCES IN RSFQ NETWORK

If we combine the two Josephson equations (Eq. (3) and Eq. (4)) with Faraday's induction law

$$V = -\frac{d\Phi_J}{dt} = -\frac{d(L_J I)}{dt} \quad (6)$$

(Φ_J is the magnetic flux, here formally inside the junction), and integrate we can represent the junction by the so-called *Josephson inductance*

$$L_J = L_{J0} \frac{\phi}{\sin \phi} \quad \text{with} \quad L_{J0} = \frac{\Phi_0}{2\pi I_c} \quad (7)$$

where ϕ is the phase difference across the junction.

Consider the simple RSFQ cell shown in Fig. 2 with a Josephson junction in parallel with an inductor L made out of a thick superconductor. The bias current I_b divides with I_L flowing in L and I_J in the junction. Using the vortex quantization condition (n is an integer) for the loop and that ϕ is gauge invariant we find

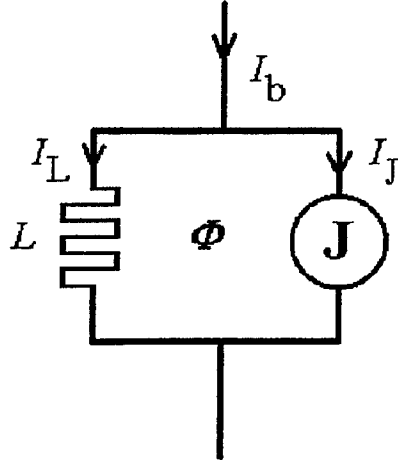


FIGURE 2. DC bias current distribution in a simple RSFQ cell consisting of a Josephson junction in parallel with an inductor.

$$\phi = 2\pi \frac{\Phi_L}{\Phi_0} - 2\pi n \quad (8)$$

where Φ_L is the magnetic flux enclosed by the loop. If no external flux is applied $\Phi_L = LI_L$ since no (real) magnetic flux is inside the junction. Eq. (8) can be rearranged to get the "effective" flux in the loop

$$\Phi_{L,\text{eff}} = LI_L - L_J I_J = n\Phi_0 \quad (9)$$

which always is an integer number of flux quanta. Knowing n and the inductances L and L_J we can calculate the currents in the two arms. This illustrates the usefulness of the Josephson inductance. The same procedure can be applied to more complex RSFQ circuits. If we represent each junction by its Josephson inductance the whole RSFQ network consists of inductances and the dc bias current will divide as in a resistive network but with the R 's replaced by L 's ($n = 0$ in Eq. (9)).

Thus, when analysing RSFQ circuits we can view the dc bias as generating an integer flux quanta background onto which we superimpose the transients. This is feasible because L_J in Eq. (7) is a slowly varying function of I_J , increasing only 16 % at $I_J = 0.8I_c$ and to $\pi/2$ at $I_J = I_c$.

The NbAlO_xNb junctions now used in RSFQ network typically an area of $(3.5\mu\text{m})^2$ and $J_c = 1000 \text{ A/cm}^2$. This gives $I_c \approx 100\mu\text{A}$, which is very appropriate since inductors with correct L are easily produced. Even more important is that the corresponding Josephson coupling energy is much larger

than $k_B T$ at helium temperatures keeping the thermally induced bit error rate, BER_T , very low.

The Josephson inductance L_J in Eq. (7) should not be confused with the small signal *incremental* Josephson inductance

$$\mathcal{L}_J = \frac{d(L_J I_J)}{dI_J} = \frac{\Phi_0}{2\pi I_c \cos \phi_b} \quad (10)$$

used in the analysis of the Josephson parametric amplifier.

For a SQUID loop the LI_c -product determines its ability to store magnetic flux. If LI_c is $\approx 1.5\Phi_0$ it can store, if LI_c is $\approx 0.5\Phi_0$ incoming flux will quickly be transmitted. In terms of the Josephson inductance a storage cell must have an $L \approx 10L_J$ while a transmission line cell only needs $L \approx 3L_J$. We return to the LI_c -product below.

III FLUXON PROPAGATION IN A 1-D JOSEPHSON ARRAY

Consider a one-dimensional structure, a transmission line for fluxons formed by a discrete array of Josephson junctions interconnected by inductances (see Ref. [14] and references herein). This transmission line is one of the basic elements in RSFQ networks. The SFQ dynamics in this structure in many ways resembles the fluxon dynamics in a long Josephson junction with periodically spaced narrow (compared to λ_J) inhomogeneities [15,16].

The scenario is illustrated in Fig. 3. The McCumber parameter β_c measures the *damping of the individual junctions*. In the perturbed sine-Gordon equation modelling the long Josephson junction (with time normalized to the reciprocal of the maximum plasma frequency ω_{p0}) the shunt damping parameter is $\alpha = 1/\sqrt{\beta_c}$. The vertical dashed line and hatched area divides the parameter space in two half-planes: $\beta_c < 1$ corresponds to overdamped (shunted, nonhysteretic) junctions; and $\beta_c > 1$ corresponds to underdamped (unshunted, hysteretic) junctions.

The vertical axis in the figure is the *discreteness parameter*, which unfortunately is defined differently in many papers and text books. Physically the parameter relates the Josephson inductance L_J (Eq. (7)) to the total inductance L of the loop that forms the primitive cell of the array. For a 2-D network of Josephson junctions the primitive cell can comprise up to four junctions, while for a parallel 1-D array, the cell is a two junction dc SQUID. The well established SQUID parameter

$$\beta_L = \frac{L}{L_J} = \frac{2\pi I_c L}{\Phi_0} \quad (11)$$

is one discreteness parameter. Ref. [12] p. 226 uses the screening parameter $\beta_m = (1/\pi)\beta_L$ where $\beta_m \leq 2/\pi$ avoids magnetic hysteresis of the SQUID.

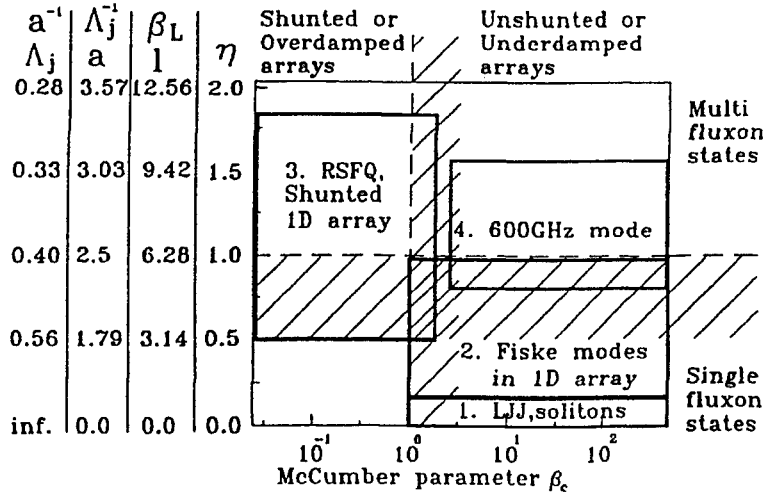


FIGURE 3. Overview of phenomena in parameter space given by the McCumber and discreteness parameters

In practice one often uses the square root, either

$$a = \beta_L^{1/2} \quad (12)$$

or

$$\Lambda_j = \beta_L^{-1/2} \quad (13)$$

This is because the product $D = x \cdot \Lambda_j = x/a$, where x is the length of the primitive cell, has the same meaning for the discrete array as the Josephson penetration depth λ_j has for the long Josephson junction. When $\Lambda_j > 1$ (or $a < 1$) D corresponds to the fluxon size, in the opposite case $\Lambda_j < 1$ there seems no physical meaning of it. The latter case, however, is typical for the RSFQ circuits (see Fig. 3), and the most convenient choice for the discreteness parameter is

$$\eta = \frac{I_c L}{\Phi_0} = \frac{\beta_L}{2\pi} = \frac{1}{2} \beta_m \quad (14)$$

The magnitude of η directly shows how many fluxons the primitive cell of the array can keep in the absence of any bias currents and magnetic fields. The horizontal dashed line at $\eta = 1$ in Fig. 3 marks the frontier between multi fluxon states and single fluxon states of the primitive cell. The application of magnetic fields and bias currents are broadening the frontier horizontally as indicated by the hatched field.

The area "1" in Fig. 3 is where the main features of continuum long Josephson junctions, like zero-field step (ZFS), Fiske steps (FS), and flux-flow steps (FFS) exist. At higher discreteness parameter values in area "2", new resonances appear due to the discreteness of an unshunted array [17-19]. These resonances can be described in the same way as it is done for quasiparticle motion in a periodic potential [17], and for these resonances both optical and acoustic dispersion relations has been found experimentally [18]. Areas "1" and "2" in Fig. 3 will not be discussed further here.

As mentioned above RSFQ circuits (area "3" in Fig. 3) are mainly build as a network of two kinds of interferometers. The first type with parameter $0.5 < \eta < 1$ is used mainly for transferring fluxons and the other with $1 < \eta < 2$ for storage of a single fluxon.

The RSFQ transmission line is one of the key components: it transfers SFQ pulses between the active elements, it provides the time delay of fluxon propagation, and it can be employed to amplify the magnetic field energy connected with the flux quantum [2]. Experimentally its high frequency properties up to several 100 GHz can be tested by rather simple dc measurements using the Josephson voltage relation (Eq. (3)).

IV THE RSFQ TRANSMISSION LINE WITH EDGE CURRENTS

In order to illustrate the importance of the fluxon dynamics in RSFQ networks we shall discuss in more detail the simple twenty-junction parallel-current-biased array. An equivalent diagram is shown in Fig. 4. When an additional current is injected to one of the edge junctions it generates SFQ pulses which propagate down the line. Unexpected steps appear in the $I - V$ curve [20] which cannot be explained by the simple two-junction interferometer model. Here we describe the formation of internal dynamical fluxon structures which together with and resonances in the connecting superconducting network may limit the maximum speed of the RSFQ logic.

A The non-resonant transmission line

A standard trilayer Nb-AlO_x-Nb technique ($J_c = 1 \text{ kA/cm}^2$) was employed to fabricate the samples. The junctions were identical (circular with diameter $5 \mu\text{m}$) with the following characteristics: Critical current $I_c = 265 \mu\text{A}$, junction resistance (including the external shunt resistance) $R = 1.75 \Omega$. The junction capacitance is estimated to 0.8 pF , giving a McCumber parameter $\beta_c = 2$. The capacitance of the overlap geometry is negligible. The inductances, $L_1 - L_{20}$, as measured with a two-junction interferometer located on the substrate close to the array, were 9.4 pH .

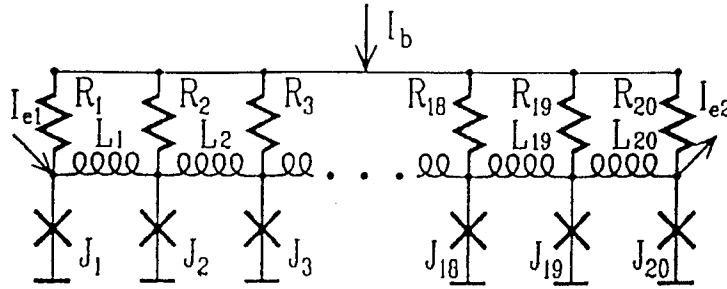


FIGURE 4. Equivalent circuit of one-dimensional array of over-damped Josephson tunnel junctions (crosses). The resistances $R_1 - R_{20}$ provide a uniform bias current. A magnetic field may be introduced by adding a current, I_h , to one of the edge currents, say I_{e1} and subtracting it from the other, I_{e2} . The array voltage, V , is measured across one of the edge junctions.

The unit cell is a two-junction interferometer sharing its junctions with the neighbouring cells. There are three bias currents supplied to the array. I_b , is a uniformly distributed dc current applied to the individual junctions through the resistances $R_1 - R_{20}$. These resistances are ten times larger than the junction shunt resistances. The current I_{e1} is fed directly to the edge junction J_1 . I_{e2} is fed directly to the edge junction J_{20} and is used only when applying a magnetic field, which is controlled by adding a dc current, I_h to I_{e1} and subtracting the same current $I_{e2} = -I_h$ at J_{20} . The array voltage, V , is measured across one of the edge junctions. The experimental $V(I_b)$ curve with fixed I_{e1} appears as a smooth curve that accurately fits to the predictions of the RSJ model for a single junction. An external magnetic field introduced by I_h does not change the shape of the $I - V$ characteristic. It means [20] that the bias current I_b is uniform and does not influence the magnetic field distribution in the array.

On the contrary, as seen in Fig. 5 an applied edge current I_{e1} significantly changes this distribution. The experimental $V(I_{e1})$ curves obtained with zero magnetic field ($I_h = 0$) for ten different fixed values of I_b shows that the parallel junction array is used as an SFQ generator. When an additional bias current is applied to the edge junction, it generates flux quanta, which propagate down the transmission line and a number of characteristic steps appear in the $I - V$ curve of the fluxon generator junction. These steps have practically zero differential resistance. The extremely small differential resistance of the steps in the junction array is interpreted [14] as being due a non-linear resonant interaction briefly described below. It is definitely not a geometrical resonance since the step voltage varies with the common bias current I_b .

(as given above), and also because the $V(I_b)$ characteristic is smooth. Furthermore the damping of the circuit is much too large for the observation of geometrical resonances.

The bias current, I_b , defines the velocity of fluxons moving through the array and influences the voltage positions of the (nearly) horizontal steps. From the experimental curves we have found that the current width, ΔI_{e1} , of the steps is given by $\Delta I_{e1} = \Phi_0/L$, where L is the inductance connecting the junctions. The numerical simulations confirmed this picture. Accordingly, a new step appears when an additional fluxon penetrates into the array. This effect is similar to the one observed for a non-symmetrically biased two-junction interferometer, where the bias current induces a magnetic field in the interferometer loop, resulting in the well-known modulation of the $I - V$ curve.

B Numerical simulations

Extensive numerical simulations have revealed [20,14] that the edge currents causes a splitting of the array into sections (domains) each having predominantly the same number of fluxons per unit cell. In fact the non-uniform magnetic field caused by the edge current penetrates into the array over a distance significantly larger than the Josephson penetration depth observed in long tunnel junctions. This is somewhat unexpected since the discreteness parameter $\eta \approx 1.3$. The first step in Fig. 5 seems to be due only to the edge current which is constant and dictates the repetition rate of the fluxon excitation. The step voltage depends on this repetition rate and on the average velocity of the fluxon. This also explains the increase of the step voltage with increasing total bias current

A more complex picture appears for higher order steps. The fluxons group themselves by a highly non-linear process in a complex pattern of "domains" that move collectively along the array. On the second step we have two domains and so forth. The domains not reaching the edges are spatially symmetric; the junction in the middle (we call it the leading junction) switches first, producing a fluxon and an antifluxon which in turn propagate in opposite directions. That means that the total fluxon number within a symmetrical domain is conserved at all times. The simulation shows that the number of domains changes as we go from one step to another, and that a variation of the edge current within the same voltage step only changes the spatial position of the leading junction in the edge domains. It looks as if there is a mutual phase-locking between the leading junctions belonging to different domains. The junctions are connected by a superconductor and therefor must be synchronized, leaving only the spatial location of the leading junction as the free parameter. LTSEM experiments [21] have confirmed this interpretation of the results.

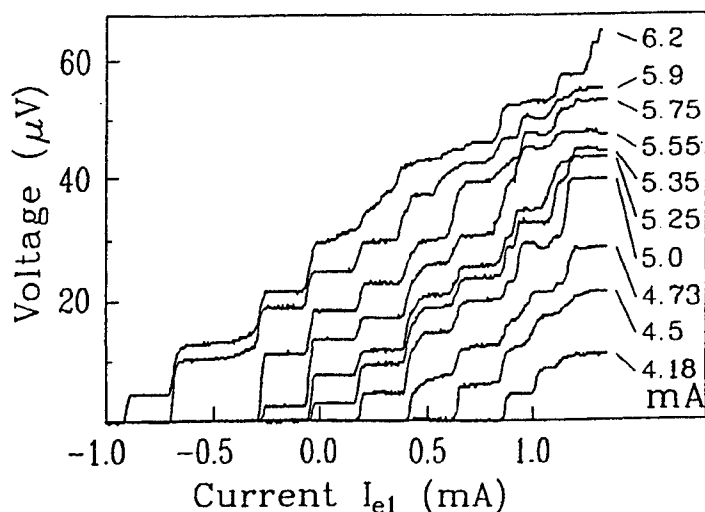


FIGURE 5. Array voltage, V , versus edge current, I_{e1} , measured for different values of the common bias current, I_b (values given in the right column) for zero external magnetic field ($I_h = 0$, $I_{e2} = 0$).

C 20-junction array with resonant interconnections

The high frequency properties of the SFQ transmission lines are vital in RSFQ logic. Unanticipated effects may deteriorate their performance such as, for example, internal resonances in the microstrip lines connecting the junctions. To elucidate this it is important to test an RSFQ circuit in the low damping limit, with all shunting resistances removed. In a supplementing experiment [22] we connected the individual 20 junctions (similar to the 20-junction parallel array described above) by short superconducting microstrip sections and found a clear 600 GHz resonator-induced step in the $I - V$ characteristics corresponding to the electromagnetic resonance in the microstrip line. In fact due to the relatively low damping (see area "4" in Fig. 3) and the strong mutual coupling the junctions phase locked. This makes the resonant transmission line a narrow linewidth oscillator. The resonant step could be tuned by applying an external magnetic field. A fine agreement was found between experiment and numerical simulations of the circuit. Recently, we have devised a method [23] to directly measure the spectral linewidth of the emitted 600 GHz radiation by integrating the oscillator with a small SIS junction used as a high-harmonic mixer. At lower frequencies an alternative would be the TFF frequency divider scheme already mentioned.

V TIMING AND CLOCKING IN RSFQ CIRCUITS

The recent progress in circuit design and fabrication makes the RSFQ family a possible candidate to first cross the 100 GHz clock scale in large scale digital applications. A comprehensive and up-to-date review of timing and clocking of RSFQ circuits is given in Ref. [24]. RSFQ logic may utilize both synchronous and asynchronous timing schemes, but synchronous clocking with an external system clock becomes increasingly inadequate as the speed of operation increases. Until now single phase synchronous clocking (every gate is clocked at the same instant) has been successfully used in virtually all RSFQ circuits. The reason why RSFQ operates so well even at high speed using this standard semiconductor synchronous clocking scheme is that the SFQ timing pulses propagate in the clock circuit in the same manner as the data flow. This calls for pipelined clocking, either counterflow or concurrent (the clock SFQ travels in the opposite or the same direction as the data SFQ) giving a positive or negative clock skew, respectively. For future larger and more complex circuits where also non-linear transmission properties become important at the minimum clock period, asynchronous or even sequential (one circuit block generates the clock SFQ for the next) timing schemes are needed. Other schemes also suited for 2-D $N \times N$ array RSFQ circuits are proposed in Ref. [24].

ACKNOWLEDGMENTS

The work in Ref. [14] and Ref. [22] was done in collaboration with V. K. Kaplunenko, T. Doderer, V. P. Koshelets, B. H. Larsen, N. F. Pedersen and A. V. Ustinov. The author thanks M. J. Feldman and R. D. Parmentier for fruitful discussions.

REFERENCES

1. K. K. Likharev, O. Mukhanov, and V. Semenov, "RSFQ logic for the Josephson junction technology," in *SQUID'85* (H. Hahlbohm and H. Lübbig., eds.), (Berlin), pp. 1103-1108, Walter de Gruyter, 1985.
2. K. K. Likharev and V. K. Semenov, "RSFQ logic/memory family: a new Josephson-junction technology for sub-terahertz clock-frequency digital systems," *IEEE Trans. Appl. Supercond.* **AS**, vol. 1, pp. 3-28, March 1991.
3. T. van Duzer, "Superconductor electronics, 1986 - 1996," *IEEE Trans. Appl. Supercond.* **AS**, vol. 7, pp. 98-112, June 1997.
4. HYPRES and Inc. *Hypres Niobium process flow and design rules* - available from HYPRES, Inc., 175 Clearbrook Road, Elmsford, NY 10523, USA.
5. S. R. Whiteley, "Josephson junctions in SPICE3," *IEEE Trans. Mag.* **MAG**, vol. 27, pp. 2902-2905, March 1991.

6. Q. P. Herr and M. J. Feldman, "Multiparameter optimization of RSFQ circuits using the method of inscribed hyperspheres," *IEEE Trans. Appl. Supercond.* **AS**, vol. 5, pp. 3327-3340, June 1995.
7. O. A. Mukhanov and S. V. Rylov, "Time-to-digital converters based on RSFQ digital counter," *IEEE Trans. Appl. Supercond.* **AS**, vol. 7, pp. 2669-2672, June 1997.
8. V. K. Semenov, Y. A. Polyakov, and D. Schneider, "Implementation of oversampling Analog-to-Digital Converter based on RSFQ logic," in *Extended Abstracts, 6th International Superconductive Electronics Conference, ISEC'97* (H. Koch and S. Knappe, eds.), no. D-6 in vol. 1, (Berlin), pp. 41-43, PTB, Braunschweig, Germany, June 1997.
9. S. P. Benz, C. A. Hamilton, and C. J. Burroughs, "Pulse-driven Josephson Digital/Analog Converter," in *Extended Abstracts, 6th International Superconductive Electronics Conference, ISEC'97* (H. Koch and S. Knappe, eds.), no. A-4 in vol. 1, (Berlin), pp. 134-136, PTB, Braunschweig, Germany, June 1997.
10. C. A. Hamilton, C. J. Burroughs, and R. L. Kautz, "Josephson D/A converter with fundamental accuracy," *IEEE Transactions on Instruments and Measurements*, vol. 44, pp. 223-225, April 1995.
11. N. B. Dubash, Y. M. Zhang, U. Ghoshal, and P. F. Yuh, "Linewidth measurements and phase locking of Josephson oscillators using RSFQ circuits," August 1996. Preprint, private communication.
12. M. Tinkham, *Introduction to Superconductivity*. New York: McGraw-Hill, 1996. Second Edition.
13. M. J. Feldman, "Digital applications of Josephson junctions," *Progress of Theoretical Physics*, vol. submitted June 1997, 1997. Supplement; Physics and Applications of Josephson Junctions.
14. V. K. Kaplunenko, J. Mygind, N. F. Pedersen, V. K. Koshelets, and T. Doderer, "Nonlinear phenomena in RSFQ logic devices," in *Nonlinear Superconducting Devices and High- T_c Materials* (R. D. Parmentier and N. F. Pedersen, eds.), (Singapore), pp. 411-436, World Scientific, 1995.
15. B. A. Malomed and A. V. Ustinov *J. Appl. Phys.*, no. 67, p. 3791, 1990.
16. B. H. Larsen, J. Mygind, and A. V. Ustinov, "Internal resonances in periodically modulated long Josephson junctions," *IEEE Trans. Appl. Supercond.* **AS**, vol. 5, pp. 2947-2950, June 1995.
17. M. Cirillo, "Inductively coupled fluxon oscillators," *J. Appl. Phys.*, vol. 58, p. 3217, 1985.
18. H. S. J. van der Zant, D. Berman, T. P. Orlando, and K. A. Delin, "One-dimensional parallel Josephson-junction arrays," *Phys. Rev. B*, vol. 49, no. 18, p. 12945, 1994.
19. M. Cirillo, B. H. Larsen, A. V. Ustinov, V. Merlo, V. A. Oboznov, and R. Leoni, "On magnetic flux dynamics in 1-D arrays of under-damped Josephson junctions," *Phys. Lett. A*, vol. 183, pp. 383-389, 1993.
20. V. K. Kaplunenko, E. B. Goldobin, M. I. Khabipov, B. H. Larsen, J. Mygind, and N. F. Pedersen, "Self-induced magnetic field effects caused by edge currents

- in parallel array of Josephson junctions," *J. Appl. Phys.*, vol. 74, pp. 5854-5858, November 1993.
21. T. Doderer, V. K. Kaplunenko, J. Mygind, and N. F. Pedersen, "Imaging of the dynamic structure in a parallel array of shunted Josephson junctions," *Phys. Rev. B*, vol. 50, pp. 7211-7214, September 1994.
 22. V. K. Kaplunenko, B. H. Larsen, J. Mygind, and N. F. Pedersen, "600 GHz resonant mode in a parallel array of tunnel junctions connected by superconducting microstrip lines," *J. Appl. Phys.*, vol. 76, pp. 3172-3176, September 1994.
 23. V. P. Koshelets, A. V. Shchukin, L. V. Filippenko, and J. Mygind, "Linewidth of frequency locked flux flow oscillators for sub-mm wave receivers," *IEEE Trans. Appl. Supercond.* AS, vol. 7, pp. 2905-2908, June 1997.
 24. K. Gaj, E. G. Friedman, and M. J. Feldman, "Timing of multi-gigahertz rapid single flux quantum digital circuits," *Journ. VLSI Signal Processing*, vol. 9, 1997. To be published.

High- T_C Josephson junction arrays and their applications

Marian Darula

Intitut für Schicht-und Ionentechnik, Forschungszentrum Jülich GmbH, 52425 Jülich, Germany

Abstract. This paper deals with the specific problems of fabrication of arrays of Josephson junctions using high- T_C superconductors. The attention is focused especially on facts, which are important for possible applications of such arrays. After introduction of the basic properties of high- T_C superconductors (HTS), which are relevant for the fabrication of HTS Josephson junctions and arrays, the main areas of possible applications are discussed in details. Namely, we focus on application of HTS arrays as voltage standards, microwave radiation sources and mixers.

INTRODUCTION

The physics of Josephson junction arrays was the object of many theoretical and experimental studies in the past decades. Several possible application areas have been addressed to. Arrays as voltage standards found already commercial application, high frequency applications are under strong investigation. However, most of the experimental work on Josephson junction arrays was done using the low T_C (Nb) superconductor technology. This, of course, limits the exploration of these devices because of the hard cooling requirements. The systems have to be cooled using liquid He or special (two stage) cryocoolers. This makes the final device too complicated and expensive and thus less attractive for customers. The discovery of the new high- T_C superconducting (HTS) materials [1] [2] with critical temperature well above 77 K (the temperature of liquid nitrogen) brought hope to overcome this cooling barrier. Indeed, the liquid nitrogen is broadly available for reasonable price. Recent strong developments in cryocooler techniques promise the availability of low cost (of the order 1000\$ and less) and reliable closed cycle cryocoolers for the temperature range around the temperature of liquid nitrogen [3]. The purpose of this paper is to discuss the possibility of realization of Josephson junction arrays using HTS technology keeping in mind the target applications. We will focus on the areas of voltage standards, high frequency applications as microwave sources and mixers. Before talking about particular applications we first address some general notes concerning HTS superconductors and Josephson junctions based on

these materials. Then the arrays are discussed in the context of each particular application.

HTS SUPERCONDUCTORS AND JOSEPHSON JUNCTIONS

Soon after discovery of the first HTS superconductor $\text{La}_{2-x}\text{Sr}_x\text{CuO}_4$ [1] with relatively low critical temperature $T_C = 38\text{K}$ several groups of materials with T_C well above the temperature of liquid nitrogen were synthesized. The compounds most frequently used in practical applications are listed in Table 1 along with the lattice constants. In Table 2 the superconducting parameters of HTS materials are listed. For comparison, the parameters for most common low T_C superconductor Nb are also listed in Table 2.

We see that the critical temperatures indeed offer the possibility to work at relatively high temperatures. However, in order to fabricate arrays of Josephson junction using these materials several technological problems have to be solved. First of all the technology for fabrication of good quality thin films of HTS materials must be available. At present, there are several standard procedures for deposition of high quality thin films. Mostly the magnetron sputtering, co-evaporation and pulsed laser deposition method are used. Details about these and other methods can be found in the review [4]. Further, the substrate used for film deposition plays a very important role since good lattice matching is required for epitaxial growth of the films. On the other hand the substrate properties should fit the proposed application, e.g. for microwave application the dielectric properties are very important. In the Table 3 the substrates commonly used for HTS thin film deposition are listed.

Once having a HTS thin film on proper substrate one can try to fabricate Josephson junctions. Unfortunately, the complicated material properties of HTS, especially the high anisotropy and the extremely small coherence length (see Table 1 and 2) do not allow to mimic simply the well developed technology of low T_C three-layer niobium superconductor-isolator-superconductor (SIS) tunnel junctions. In order to get HTS Josephson junctions it is necessary to use different procedures.

In Figure 1 some approaches, where already relatively good results were obtained, are schematically shown. More details about HTS Josephson junctions and their properties can be found in [5] [6].

TABLE 1. High T_C superconductors and their lattice constants.

Material	a (Å)	b (Å)	c (Å)
$\text{YBa}_2\text{Cu}_3\text{O}_7$ (YBCO)	3.822	3.885	11.676
$\text{Bi}_2\text{Sr}_2\text{Ca}_2\text{Cu}_3\text{O}_{10}$ (BSCCO)	3.823	3.823	37.074
$\text{Tl}_2\text{Ba}_2\text{Ca}_2\text{Cu}_3\text{O}_{10+\delta}$ (TBCCO)	3.8	3.8	35.4

The first type of HTS Josephson junction we will discuss is the so-called step-edge junction, shown schematically in Figure 1(a). Before the film deposition a steep-step in the substrate is fabricated. The film over the step grows with different crystallographic orientation and thus at the edges of the step grain boundaries are formed. This grain boundary effectively works as Josephson junction. In fact, using this technique, two junctions are created in the step area, however the technology can be controlled in such a way that the junctions have different critical currents and thus only one of them is effectively working. Another type of grain boundary HTS Josephson junction is the bicrystal junction shown in Figure 1(b). The film is deposited on a special bicrystal substrate which consists of two parts with different crystallographic orientation. The epitaxially deposited film follows the crystallographic orientation of the substrate and at the place of the crystallographic misorientation the grain boundary Josephson junction is formed. The properties of this junctions depend strongly on the angle of misorientation. Another possibility how to create the HTS Josephson junction is to use weakened bridges, Figure 1(c). A small part of the bridge is modified by ion or electron beam irradiation to change the electrical properties of this region and thus to create a weak connection between the superconductors. The common feature of the junction types discussed up to now is, that they rely on single superconducting layers. This is an advantage, because the fabrication process requires only a limited number of technological steps. Unfortunately, the properties of these junctions often do not fulfil the requirements especially with respect to reproducibility, spread in junction parameters as well as to geometrical restrictions. Therefore the HTS Josephson junctions based on more advanced multi-layer technology are under development. One typical example of this kind of junction is shown in Figure 1(d). After the deposition of a bilayer (superconductor + insulator) a flat ramp is fabricated using a special etching technique. Then a very thin (of the order of coherence length) barrier, which can be normal conducting or isolating is deposited. Finally, the structure is covered by a top superconducting layer and properly patterned. The advantage of this topology is that the interaction between the superconducting electrodes takes place in a-b direction where the coherence length is substantially larger than in c-direction (see Table 2).

In Figure 2(a) [7], curve 1 we show as an example a typical current-voltage characteristic (IVC) of a HTS Josephson junction. In this particular case it was a

TABLE 2. Superconducting properties of HTS materials. Δ_{ab} is energy gap in $a - b$ direction, Δ_c is energy gap in c direction, ξ_{ab} and ξ_c are coherence in respective direction.

Material	T_C (K)	Δ_{ab} (meV)	Δ_c (meV)	ξ_{ab} (nm)	ξ_c (nm)
YBCO	92	15-25	3-6	1.5	0.1-0.4
BSCCO	110-115	25-35	5-9	1	< 0.1
TBCCO	118	25-30	5	2	0.03
Nb	9.2	1.45	1.45	40	40

bicrystal junction on MgO substrate [7]. As a film YBCO with thickness of 200 nm was used. YBCO is the most frequently used high- T_C superconductor (all circuit shown below were made using YBCO) because of its relatively high coherence length and not very complicated procedure of film growth. We observe, that the IVC of this junction is non-hysteretic, which is typical for overdamped (shunted) junctions with very small capacitance. The ideal Josephson junction should follow the resistively and capacitively shunted junction (RCSJ) model [8]:

$$I_b = I_C \sin \phi + V_t/R_N + C dV_t/dt, V_t = \frac{\Phi_0}{2\pi} \frac{d\phi}{dt} \quad (1)$$

where I_b is biasing current of the junction, I_C is the critical current, R_N is normal resistance of junction, ϕ is phase difference across the junction, V_t is the instantaneous voltage across the junction, C is the capacitance and Φ_0 is flux quantum (2.06810^{-15} Wb). By solving (numerically) the Eqs. (1) the time dependence of V_t can be calculated. The general feature of this solution is that (for $I_b > I_C$) the voltage across the junction oscillates with a very high frequency

$$f = V/\Phi_0, \quad (2)$$

where V is time averaged voltage V_t . Because of the very high frequency of oscillation of V_t , typically in upper GHz frequency range, the value which is measured experimentally is the average voltage V . For a given biasing point I_b the average voltage V can be easily numerically calculated from solution of Eqs. (1) and the theoretical IVC can be obtained. In Figure 2(b), curve 1, the result of the calculation for experimental parameters is shown. We see that the calculation reproduce the measured curve perfectly.

One of the most striking features of Josephson junctions is their behavior in the presence of microwave radiation. The internal oscillations of Josephson junction can be synchronized (phase-locked) to the external microwave radiation which results in a constant voltage over a certain bias current interval. The typical so called Shapiro steps appear on the IVC at voltages

$$V = n\Phi_0 f_{ext} \quad (3)$$

where f_{ext} is the frequency of incident microwave radiation. This is shown on experimentally measured curves for the case of two values of microwave power, Figure 2(a), curve 2 and 3. Corresponding curves calculated using Eqs. (1) are shown in Figure 2(b), curve 2 and 3. Here we observe also an almost identical agreement between experiment and calculation. Thus, the RCSJ model is a relatively simple tool which describes the dynamics of HTS junctions well. It gives us the possibility

of theoretical predictions and allows to model even more complicated circuits based on HTS Josephson junctions.

We see on Figure 2(a) that the junction has characteristic voltage $V_C = I_C R_N$ approx. 2 mV. This quantity is important when the junction is to be operated at very high frequencies. In many application the optimal operation frequency is related to the characteristic frequency $f_C = V_C/\Phi_0$. In the ideal case V_C should be close to the gap voltage, which should be around 20 mV according to Table 2. We observe that our junction has a significantly reduced V_C which is probably caused by imperfection during the fabrication or by intrinsic properties in the barrier region. Nevertheless, even this reduced V_C is about one order of magnitude higher than typical values for overdamped Josephson junction based on classical low T_C superconductors.

The data shown on Figure 2 where measured at relatively low temperature. In order to make HTS technology attractive for application good quality junctions which operate at much higher temperatures are needed. Recently, progress was achieved in fabrication of good quality junctions working at relatively high temperatures. As an exmple we show results obtained with a grain boundary junction fabricated on bicrystal substrate out of yttria stabilized zirconia oxide (YSZ). The YBCO thin film was deposited by reactive high-oxygen-pressure co-evaporation. The junctions showed very promising properties at temperatures well above 77 K [11]. In Figure 3(a) the IVC measured at 80 K is shown. We see a substantial critical current even at relatively high temperatures and well developed Shapiro steps which follow the prediction of the RSJ model, Figure 3(b).

HTS JOSEPHSON JUNCTIONS ARRAYS FOR VOLTAGE STANDARDS

We have seen in Figure 2 that a Josephson junction under microwave radiation exhibits Shapiro steps at voltages given by Eq. (3). Since the frequency of the external microwave radiation can be usually precisely controlled and the average dc voltage is related to this frequency only via fundamental constant, the resulting voltage can be tuned with extremely high accuracy. Based on this idea precise voltage standards can be constructed. When using a single junction the voltage steps are typically in the μV range, which is too low for applications. The solution is to connect the junctions in series and thus multiply the voltages. Indeed, using arrays based on low T_C Josephson junctions commercially available voltage standards were fabricated [9]. The traditional design of a voltage standard was based on

underdamped junctions with high capacitance. Standards based on such junctions suffered from dynamical instabilities due to chaotic behavior of the underdamped junctions in presence of microwave radiation with the frequency close to junction's plasma frequency

$$f_p = \sqrt{I_C / 2\pi\Phi_0 C}. \quad (4)$$

The plasma frequency is a natural junction resonance defined by the capacitance and inductance of the junction. The modern trend in the arrays for voltage standards is to use arrays of overdamped junctions with very low capacitance. In low T_C technology a special shunting procedure for SIS junction must be used or another type of junctions like superconductor - normal metal - superconductor (SNS) junctions must be taken [10]. As we have seen in the previous paragraph, the typical HTS Josephson junction is an overdamped junction and therefore a natural candidate for voltage standard. Before discussing the suitability of HTS technology for implementation in voltage standard some important features will be discussed and demonstrated using a simple simulation based on the RCSJ model.

The general idea is to connect the junctions in series and thus add the voltages at the Shapiro step. The idea works well when the junction are identical or nearly identical. This is demonstrated for the case of the array consisting of three junctions connected in series and biased by common current in the Figure 4 (aa)-(ad). Differences in the critical currents and the normal resistances of the junctions are within a 1 % interval in this case. Clearly, a step at a voltage, which is three times the voltage of an individual junction, is obtained. The situation changes dramatically when much larger spread in junction parameters exists. Such situation is illustrated on Figure 4 (ba)-(bd) where the spread is 20 %. No steps are observed on the resulting IVC despite of the well developed steps of each junction. We see that the spread plays a crucial role when the voltage standard consisting of several hundred junctions should be constructed.

Unfortunately, high spread in both critical currents as well as in normal resistances of junctions is typical for the present stage of HTS technology. Some partial solution which reduces at least spread in normal resistances was developed by Klushin et al [12]. In this approach the bicrystal junctions are covered additionally by normal metal and thus additionally shunted. The resistance is then defined by this external shunt rather than by the intrinsic value of normal resistance. The array consisting of 108 junction fabricated using this procedure showed proper operation as it is illustrated in Figure 5 [13]. The additional effect connected with this method is the reduction of impedance of junction and the reduction of characteristic voltage V_C . This must not be necessarily the disadvantage for this

particular application since lower V_C allows to work with lower driving frequency. It is well known that in order to get Shapiro steps with optimal heights the driving frequency must be close or higher than the characteristic frequency of the junctions f_C [14].

The promising results presented here give hope that HTS arrays will find soon application as voltage standard. The voltage standard in classical meaning is a device which generates exact but only one value of voltage. Using arrays, however, there exists the possibility to get standards with variable and digital controlled voltage output. It is possible to fabricate so called programmable voltage standards or digital to analog (D/A) converters with ultimate accuracy. The circuit was invented by Hamilton *et al* [15] and it is schematically shown in Figure 6. The series array of junctions is divided into a binary sequence of segments consisting of 2^{j-1} junctions (j is the number of sequence). Each segment can be individually biased so that all junctions in the segment are at either zero voltage or at the voltage of the first Shapiro step. Thus, by changing the bias of individual segments different total voltage can be achieved with $\Delta V = \Phi_0 f_{ext}$ (f_{ext} is the frequency of external microwave radiation) resolution. The realization of a D/A converter based on a similar idea but using HTS Josephson junction arrays is in progress [13]. When connecting such a device with a digital measurement equipment (voltmeter), an instrument with fundamental accuracy could be constructed. This certainly will have strong impact on development and broad commercial application of HTS Josephson junction arrays.

HTS JOSEPHSON JUNCTION ARRAYS AS RADIATION SOURCES

In Figure 7 [16] the dependence of the generated microwave power of different sources as a function of frequency is shown for the THz and the sub-THz frequency range. We observe that with increasing frequency the available power decreases for almost all presently existing devices. Especially, above 1 THz there is a gap and oscillators which would generate substantial microwave power in this frequency band are needed.

As already mentioned in the introduction the Josephson junction is in fact an ideal voltage to frequency transducer where the frequency is related to the dc voltage of the junction via Eq. (2). For typical characteristic voltage of HTS Josephson junction $V_C \simeq 2mV$ we get a frequency of about 1 THz. Therefore, the generator

of microwave radiation based on HTS Josephson junctions is one of the potential candidates to fill the gap in THz generators. The idea of using devices based on Josephson junctions as microwave generators is not new and during several decades different type of devices utilizing low T_C superconductor (Nb) Josephson junctions were developed. The underdamped SIS junctions can be fabricated with high reproducibility and therefore they are the natural choice for fabrication of generators. Based on this type of junction the so-called flux-flow oscillators, where the microwave power is generated as a result of moving of Josephson vortices along the long Josephson junction, can be constructed. Considerable progress has been achieved in this field [17] [18] and at present the oscillator integrated with SIS mixer on one chip is available [19]. However, there is a frequency limitation for devices based on Nb due to relatively low value of superconducting gap of this material (see Table 2). Above ≈ 800 GHz a strong degradation of the performance occurs. In addition, the barrier due to strong cooling requirements exists. The HTS superconductor should have advantages with respect to both, the energy gap (see Table 2) as well as the cooling issue. Unfortunately, in HTS technology high quality SIS-type underdamped junction are not available. Therefore, alternative concepts of oscillators must be used. Already in low T_C technology, the oscillator based on arrays of discrete Josephson junctions were developed parallel to flux-flow oscillator [20]. These arrays utilize overdamped junctions and therefore they are the natural choice for realization in HTS. Before discussing different HTS array concepts some general considerations should be addressed.

The maximal power emitted from single overdamped, short (with geometrical dimension shorter than Josephson penetration depth) Josephson junction is [20]

$$P = \frac{1}{8} I_C R_N. \quad (5)$$

For a typical HTS Josephson junction with $I_C = 1\text{mA}$ and $R_N = 1\Omega$ we get from Eq. (5) $P \simeq 0.1\mu\text{W}$. Already this value is not very high and in typical experimental arrangements the microwave losses cause that the practically available power is much lower, typically on the level $p\text{W} - n\text{W}$ [21]. Another important point which requires the consideration is the issue of linewidth of microwave radiation generated from Josephson junction. For applications in receivers for the sub-THz frequency band a linewidth of the local oscillator in the kHz-MHz region is required. Since the frequency of Josephson junction is controlled by the junction's voltage any voltage fluctuation will cause the broadening of the linewidth. In the ideal case, when only the fluctuation due to thermal noise are considered the linewidth is [20]

$$\Delta f = \frac{1}{2} \left(\frac{2\pi}{\Phi_0} \right)^2 R_d^2 S_I(0), S_I(0) = \frac{2k_b T}{\pi R_N}, \quad (6)$$

where k_b is Boltzman constant, T is working temperature and R_d is differential resistance at the bias point. For typical HTS Josephson junction at 4 K we get the linewidth $\Delta f \simeq 160 MHz$. This value is of course too large for most applications. The problem of low radiation power and large linewidth can be solved, if more junctions are connected in arrays. According to simple rules the available power increases with the number of junctions and at the same time the linewidth decreases [20]. However, all this is true only if all junctions oscillate coherently, i.e. if they are mutually phase-locked. This is a not trivial issue, because the mutual phase-locking depends on several factors like topology of the arrays, the loading of arrays and also the spread in junction parameters plays important role. The problem of mutual phase-locking in different types of arrays of Josephson junction was investigated in many papers and the scientific discussion still continues. Even in the simplest case, when junction are connected in series, the situation is not trivial. For the resulting behavior of such arrays the value of the McCumber parameter of the junctions $\beta_C = 2\pi C I_C R_N^2 / \Phi_0$ is important. If the junctions are overdamped with $\beta_C = 0$ and the whole array is loaded by an inductive load stable in-phase locking is possible (i.e. all junctions oscillates with the same phase) [20]. For $\beta_C \simeq 1$ the stable in-phase locking exists also for a pure resistive load [22]. A general complex load and finit β_C causes a complicated situation where several dynamical states co-exist what in presence of thermal noise results in chaotic-like behavior [23]. Other very important requirement for stable phase-locking is the low spread in junction parameters. The requirements are here even more severe as we seen in the case of arrays for voltage standard. Depending on the array topology (series arrays, two-dimensional arrays) different, but in general relatively low spread, of the order of maximum 10-20 % is allowed.

An example of a HTS series array consisting of 23 HTS step-edge Josephson junctions is shown in Figure 8(a) [24]. The junctions are located at the places where the meander-like stripline crosses the step in substrate (shown by dashed line). The array is embedded into spiral-type antenna in order to couple the array to the environment. In a special quasi-optical microwave setup and using a conventional

receiver the radiation power from the array was measured. The receiver was tuned to the fixed frequency 12 GHz and the radiation was detected during the sweep of bias current of the array. The result for the case of array consisting of 10 junctions is shown in Figure 8(b). The radiation peaks prove the ability of the array to generate microwave radiation. However, the fact that several peaks appear indicates that the array did not operate in a phase-locked mode. Most probably the spread was too high to achieve the total phase-locking. On the other hand the same array (i.e. with the same spread) can respond well to external microwave radiation and all junction can be synchronized on the first and second Shapiro step as it is shown in the inset of Figure 8(b).

After such experiments it became clear that one simple and clear experiment is required in which the phase-locking of HTS Josephson junctions can be studied. For this experiment a circuit had to be choosed which tolerates larger spread and at the same time allowed for observation of dynamical properties using simple experimental tools. For this purpose the circuit where arrays of Josephson junction are closed into a superconducting loop, the so called multi-junction superconducting loop (MSL), was used [25] [26]. Schematically, the circuit is shown in Figure 9(a). Here, the MSL consisted of four junctions. Additional leads allowed the simultaneous measurement of the voltages of all junctions as a function of the bias current. If all voltages are the same, because of Eq. (2) the frequency of oscillations are also the same. In addition, if this occurs not only for one particular value of bias current but in some interval of bias currents (locking interval) the conclusion is evident, that the junctions oscillate not only with the same frequency but also with locked phases [20].

The result of such an experiment is shown in Figure 9(c). During sweep of bias current the voltages of junctions were simultaneously recorded. We observe in certain locking interval that the voltages are indeed the same. This indicates that phase-locking in HTS arrays is possible. The question, however, must be answered whether such circuit is able to generate radiation power. For this purpose, together with the MSL the detector junction was integrated on the same chip and connected to the MSL via a coupling structure. The design allowed to bias both, MSL and detector junction, independently. When biasing the MSL within the locking interval, radiation should be generated and this radiation should influence the detector junction. The Shapiro steps should appear on the IVC of the detector

junction at voltages which correspond to the frequency of generation of the MSL. Indeed, such steps are seen on experimental IVC of detector junction, Figure 9(d) curve 1. When the MSL was biased in the zero voltage state or outside of the locking interval the IVC of the detector junction without step was observed, Figure 9(d) curve 2, which prove that the radiation was really generated by the MSL. The operation of the MSL up to 50 K was observed.

This experiment demonstrated that HTS Josephson junction arrays can be operated in a phase-locked mode and can generate microwave radiation. However, as an unsolved problem remains the relatively large linewidth of generated radiation. It is at the present stage of HTS technology not possible to extend the design to several hundred or thousand junctions. Some other approach how to lower this linewidth must be found. The external impedance seen by the Josephson junction influences strongly the behavior of junction. Especially resonant circuits connected to the junction change the shape and character of the junction's IVC. On Figure 10 the calculated IVC of a Josephson junction connected to a LC resonant circuit is shown. At the resonant frequency we observe a strong decrease of the differential resistance. According to Eq. (6) this means that also the linewidth will decrease.

There are different ways how to integrate the arrays into resonators. There is one design which uses not only resonator feature but integrate the junctions in the way that even large spread can be tolerated. This is the so called parallel biasing scheme (PBS) [20], shown schematically in the Figure 11(a). Junctions are closed into long superconducting loops and they are biased through these loops in parallel. Due to the superconducting loop the average voltages across the junctions must be automatically the same. For high frequencies, however, the large loop inductance do not allow the microwaves to propagate through the loops and high frequency interaction between junctions similar to the case of simple series arrays occurs. The superconducting loops can be designed in the form of coplanar resonator as indicated in Figure 11(a). It is expected that the resonance should have influence on the linewidth of radiation. The circuit was fabricated using bicrystal Josephson junctions on LaAl_2O_3 substrate [27] as well as on sapphire (Al_2O_3) [28]. On the experimentally measured IVC of the PBS shown in Figure 11(b), curve 1 [27] we observe self-induced steps due to interaction of junctions with the coplanar resonators. The influence of resonators can be also seen on experimentally measured radiation from the array. Two examples of radiation curves are shown in

Figure 11(b). The curve 2 demonstrates the case when array was biased between self-resonances, in the region with relatively large differential resistance. According to Eq. (6) larger linewidth is expected what is also observed experimentally. In contrast to this case we observe strong decrease of linewidth when measurement was made in the vicinity of a resonant step as it is shown in Figure 11(b), curve 3. The maximal microwave power detected on chip from this type of array was 4 nW [27].

The PBS is a promising candidate for application as radiation source based on HTS Josephson junctions. However, still the power delivered from such array is limited. From experiments done with low T_C Josephson junction arrays it is known that one solution is the use of two-dimensional (2d) arrays of Josephson junctions [29]. Such arrays have a much more complicated dynamical behavior as series arrays but in general they should tolerate relatively large spread [30]. There were several attempts to fabricate 2d HTS arrays using different type of junctions [31] [32]. Due to topological limitations the bicrystal Josephson junctions cannot be used in this case. The example of 2d HTS arrays fabricated using step-edge junctions is shown in Figure 12 [33]. Here we see the so-called shorted 2d array, where horizontal junctions are replaced by inductors. The advantage of this design over classical XY 2d array is, that even in presence of large spread the average voltage of junctions in the row is the same. Thus, the junctions in the row are forced to oscillate with the same frequency. It remains to clear the interaction between rows. In the experimental layout additional leads to the rows allowed to measure the voltages of the rows simultaneously, and thus using DC measurement indirectly observe the rows dynamics. These leads can be also used for additional biasing of single rows and thus influence the behavior of the circuit. The typical experimental result is shown in Figure 12(c). Here, the row's voltages as a function of biasing current are shown. We see, that only two rows have the same voltages in certain bias interval, which indicates complicated behavior of the circuit. In finite magnetic field it was occasionally possible to observe weak locking of all rows, but the system was extremely sensitive to change in external magnetic field and disturbances.

It is clear that in order to operate 2d HTS arrays properly, the interaction between rows must be increased. This can be done by adopting the idea of parallel biasing for 2d arrays. The design of such an array, called a parallel biased 2d array (PBS2D), is shown in Figure 13 [33]. The rows are closed into superconducting loops which distribute in parallel the bias current to the junctions. The experimentally fabricated PBS 2D array shown in Figure 13 was coupled via a stripline to another Josephson junction, which served as a frequency and power sensitive radiation detector and allowed thus the on-chip detection of radiation from the ar-

ray. The stripline was terminated by a capacitor on one end and by a short in close vicinity of the detector junction on the other end as is shown in Figure 13(a)-(b). Similarly to PBS discussed earlier the edge loops were designed in form of coplanar resonators which give the possibility to influence the linewidth of radiation and to couple the rows electromagnetically. The photograph in Figure 13 (b) shows the structure in the stage before fabrication of the top gold coupling loop. The experimentally measured IVC of the array (Figure 13(c)) shows the self-resonant steps due to interaction with the coplanar resonators, similar to the simple parallel biased series arrays. The detector junction integrated on-chip allowed to detect the radiation generated from the array. The result of such experiment is shown in Figure 13(d), where the IVC of detector was recorded while the array was biased at different voltages. On the IVC of the detector junction clear Shapiro steps appear and the position of the steps exactly coincides with the generated frequency. This proves the proper operation of the array. The clear detector response was observed in the frequency range 90-500 GHz, which demonstrates the relatively large tunability of the array.

As it is clear from the experiments presented in this paper the problem of HTS Josephson junction microwave generators is not closed. Some promising approaches already exist, however considerable work must be done before implementation of such array in commercial applications. Nevertheless, in relatively short time since the discovery of HTS considerable progress was done in this field, and certainly, HTS Josephson junction arrays should be seriously considered as candidate for THz microwave generators.

HTS JOSEPHSON JUNCTION ARRAYS AS MICROWAVE MIXERS

As already mentioned, the array generators have perspectives for applications as local oscillators for THz receivers. An exciting idea is to connect such HTS local oscillator with HTS microwave mixer. Low T_C superconductor mixers based on SIS junction are probably the most important success of superconducting electron-

ics. Certainly, the transformation of this idea into HTS would have revolutionary impact on development in high frequency instruments. Unfortunately, as already mentioned HTS SIS type of junction is not available. The hope is connected with intrinsic Josephson effect seen in HTS monocrystals [34]. The layered nature of HTS material produces natural underdamped Josephson junctions. These intrinsic junctions are able to generate microwave power and there are already mixing experiments available [35]. However, clear SIS operation, that means the operation where the quasiparticle tunneling is explored, was not demonstrated yet and also such devices are not available in thin film technology. The alternative approach can be to use overdamped HTS junction or arrays of such junction as mixer. The idea of the Josephson mixer was developed since the discovery of Josephson effect and such mixers were investigated using low T_C materials [36] [37]. Recently, the data about implementation in HTS are available [38] [39]. In these experiments mostly single junction was used, which makes the design more simple. On the other hand arrays of HTS junction can bring some advantages. Especially, the impedance matching can be improved when series array are used. Konopka *et al* [40] made mixing experiments using series HTS array. On Figure 14 [40] the result of such mixing experiment is shown. We see the response at intermediate frequency of 3.5 GHz when the array was irradiated by two microwave sources. One source was 3rd harmonic of Gunn oscillator and second source was 2nd harmonic of backward-wave oscillator at 291 GHz. The appearance of the peak at the intermediate frequency demonstrated the ability of such an array to convert down microwave signals and the temperature dependence suggests the ability to operate at higher temperatures. As an open question remains the sensitivity of such a mixer and how the spread in junction parameters influence the performance of the array.

Not without importance is the exciting idea to use such arrays in the so-called self mixing mode, where the array plays the role of local oscillator and mixer at the same time. This would lead to an enormous simplification of the whole receiver design. The demonstration of self mixing using HTS was already made on the level of single junctions [41], the transfer into array is in progress.

CONCLUSIONS

In this paper we addressed some application areas of Josephson junction arrays based on high- T_C (HTS) superconductors. In particular, we discussed the possibility of construction of voltage standards, high frequency radiation sources and mixers using HTS arrays. The aim of the paper was to give a picture about problems and available solutions in this field. We showed, that in the case of voltage standards the real industrial application can come soon, while high frequency sources and mixers need still more investigation. Although, the basic solutions for principal problems already exist. HTS Josephson junction arrays are examples, how exciting physics can be converted into practical and useful devices.

ACKNOWLEDGEMENTS

The author would like to thank all coworkers, who contributed to this paper. Especially he would like to thank Stephan Beuven, who fabricated and experimentally investigated HTS MSL, 2d, and PBS2d arrays. The thank is addressed also to Janusz Konopka who did nice work on series arrays, Gerhardt Kunkel for data on PBS series arrays and Alexander M. Klushin and Clemens Weber for material concerning HTS voltage standard. The work could not be done also without very fruitful discussion and practical help from Oliver Harnack, Hermann Kohlstedt, Stefan Benacka and Paul Seidel.

REFERENCES

1. Bednorz J.G., and Müller K.A., *Z. Phys. B* **64**, 189 (1986).
2. Wu M.K. et al, K.A., *Phys. Rev. Lett.* **58**, 908 (1987).
3. Wolf S.A., Patten F.W. in: *Proceedings of the 10th Anniversary HTS Workshop on Physics, Materials and Applications* Eds: Batlogg B. et al, Singapore: World Scientific, 1996, pp.58-62.
4. Stoessel C.H., Bunshah R.F., Prakash S., and Fetterman H.R., *Journal of Superconductivity* **6**, 1 (1993).
5. Gross R., Alff L., Beck A., Froehlich O.M., Koelle D., Marx A., *IEEE Trans. on Appl. Superconductivity* **7**, 2929 (1997).
6. Seidel P., in: *Nonlinear Superconducting devices and High- T_C Materials* Eds: Parmentier R.D., Pedersen N.F., Singapore: World Scientific, 1995, pp. 19-36.
7. Strbik V., Harnack O., Chromik S., Darula M., and Benacka S, will be published in *Proceedings of 3rd European Conference on Applied Superconductivity* Enschede, (1997).
8. Van Duzer T., and Turner C.W., *Principles of Superconductive Devices and Circuits* Elsevier North Holland, Inc., 1981, pp.170.
9. Hamilton C.A., Burroughs C.J., Benz S.P., *IEEE Trans. on Appl. Superconductivity* **7**, 3756 (1997).
10. Hamilton C.A., Benz S.P., Burroughs C.J., and Harvey T.E., *IEEE Trans. on Appl. Superconductivity* **7**, 2472 (1997).
11. Weber C., Klushin A.M., Darula M., Semerad R., Prusseit W., and Kohlstedt H., submitted to *Applied Superconductivity* (1997).
12. Klushin A.M., Prusseit W., Sodtke E., Borovitskii S.I., Amatuni L.E., and Kohlstedt H., *Appl. Phys. Lett.* **69**, 1634 (1996).
13. Klushin A.M., Borovitskii S.I., Weber C., Sodtke E., Semerad R., Prusseit W., Gelikonova V.D., and Kohlstedt H., will be published in *Proceedings of 3rd European Conference on Applied Superconductivity* Enschede, (1997).
14. Likharev K.K., *Dynamics of Josephson Junctions and Circuits*, New York: Gordon and Breach Science Publisher 1986, ch. 11, pp. 332-341.
15. Hamilton C.A., Burroughs C.J., and Kautz R.L., *IEEE Trans. Instrum. Meas.* **44**, 223 (1995).

16. Kordos P., unpublished
17. Koshelets V.P., Shitov S.V., Shchukin A.V., Filipenko L.V., and Mygind J., *IEEE Trans. on Appl. Superconductivity* **7**, 2905 (1997).
18. Pedersen N.F., Ustinov A.V., *Supercond. Sci. Technol.* **8**, 389 (1995).
19. Koshelets V.P., Shitov S.V., Filipenko L.V., Baryshev A.M., Luinge W., Golstein H., Van de Stadt H., Gao Jian-R., and de Graauw T., *IEEE Trans. on Appl. Superconductivity* **7**, 3589 (1997).
20. A. K. Jain, K. K. Likharev, J. E. Lukens, and J. E. Sauvageau, *Phys. Rep.* **109**, 309, (1984).
21. Amatuni L., Glyantsev V.N., Herrmann K, Klushin A., Harnack O., Beuven S., and Darula M., *Czechoslovak Journal of Physics* **46**, 1285 (1996).
22. Hadley P., Beasley M.R., Wiesenfeld K., *Appl. Phys. Lett.* **52**, 1619 (1988).
23. Tsang K.Y., Wiesenfeld K., *Appl. Phys. Lett.* **56**, 495 (1990).
24. Konopka J., Wolff I., Beuven S., Siegel M., and Braginski A.I., *IEEE Trans. on Appl. Superconductivity* **5**, 3263 (1995).
25. Darula M., Beuven S., Siegel M., Darulova A., Seidel P., *Appl. Phys. Lett.* **67**, 1618 (1995).
26. Beuven S., Harnack O., Amatuni L., Kohlstedt H., and Darula M., *IEEE Trans. on Appl. Superconductivity* **7**, 2591 (1997).
27. Kunkel G., Ono R.H., and Klushin A.M., *Supercond. Sci. Technol.* **9**, A1 (1996).
28. Kunkel G., Hechtfisher G., Frommberger M., Veit K., Kleiner R., Müller P., Prusseit W., Kinder H., Frechland L., Daalmans G., Ono R.H., *IEEE Trans. on Appl. Superconductivity* **7**, 3339 (1997).
29. S. P. Benz and C. J. Burroughs, *Appl. Phys. Lett.* **64**, 2163 (1994).
30. M. Darula, P. Seidel, J. von Zameck Glyscinski, A. Darulova, F. Busse, and S. Benacka, in *Applied Superconductivity*, ed. H. C. Freyhardt, DGM Informationsgesellschaft, Oberursel, 1993.
31. Ovsyannikov G.A., Ivanov Z.G., Mygind J., Pedersen N.F., *Physica C* **241**, 228 (1995).
32. Reintsema C.D., *IEEE Trans. on Appl. Superconductivity* **5**, 3259 (1995).
33. Beuven S., Harnack O., Darula M., submitted to *Applied Superconductivity* (1997).
34. Kleiner R., Steinmeyer F., Kunkel G., and Müller P., *Phys. Rev. Lett.* **68**, 2394 (1992).
35. Hechtfisher G., Walkenhorst W., Kunkel G., Schlenga K., Kleiner R., Müller P., Johnson H.L., *IEEE Trans. on Appl. Superconductivity* **7**, 2723 (1997).
36. Taur Y., Claassen J.H., Richards P.L., *IEEE Trans. on Microwave Theory and Techniques* **22**, 1005 (1974).
37. Schoelkopf R.J., Zmuidzinas J., Phillips T.G., LeDuc H.G., and Stern J.A., *IEEE Trans. on Microwave Theory and Techniques* **43**, 977 (1995).
38. Shimakage H., Uzawa Y., Tonouchi M., and Wang Z., *IEEE Trans. on Appl. Superconductivity* **7**, 2595 (1997).
39. Harnack O., Darula M., Andoh M., Beuven S., and Kohlstedt H. submitted to *Applied Superconductivity* (1997).
40. Konopka J., Wolff I., Beuven S., Siegel M., *IEEE Trans. on Appl. Superconductivity* **5**, 2443 (1995).
41. Harnack O., Darula M., Beuven S., Amatuni L., and Kohlstedt H., *J. of Low Temp. Phys.* **106**, 463 (1997).

TABLE 3. Substrates used for deposition of HTS thin films.

Substrate	Lattice constant (\AA)	ϵ_r
SrTiO ₃	3.790	300
LaAlO ₃	3.793	24
MgO	4.213	10
NdGaO ₃	3.837	23
YSZ	5.140	29
Al ₂ O ₃	3.48	9.3

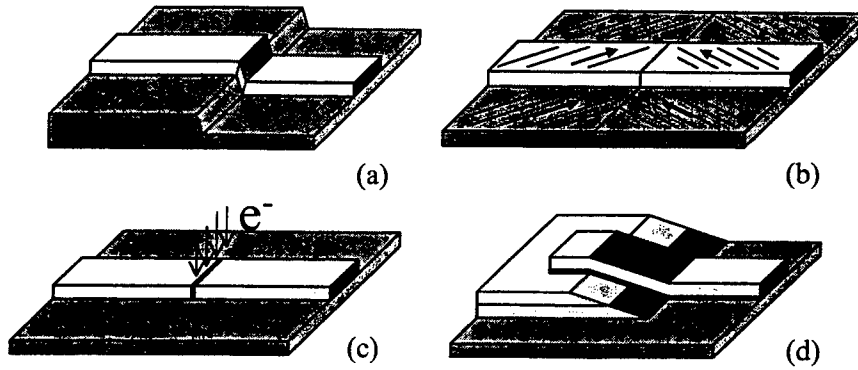


FIGURE 1. HTS Josephson junctions.

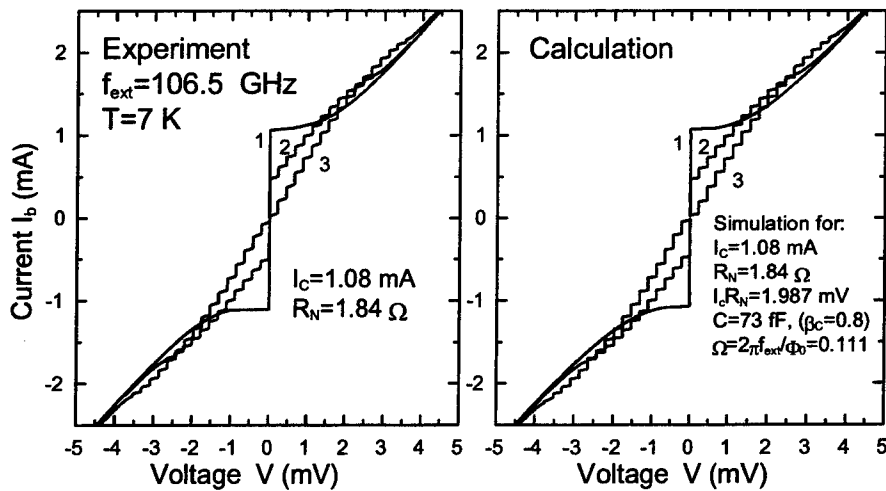


FIGURE 2. (a) Current-voltage characteristic (IVC) of HTS Josephson junctions without external microwave radiation (curve 1) and two values of microwave radiation (curve 2 and 3). (b) Theoretical fit using RCSJ model.

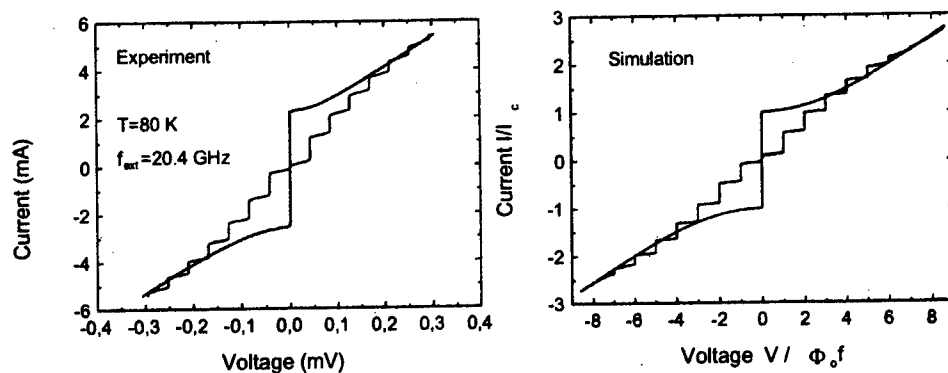


FIGURE 3. (a) IVC of HTS Josephson junctions measured at 80 K. (b) Theoretical fit using RCSJ model (with $C = 0$).

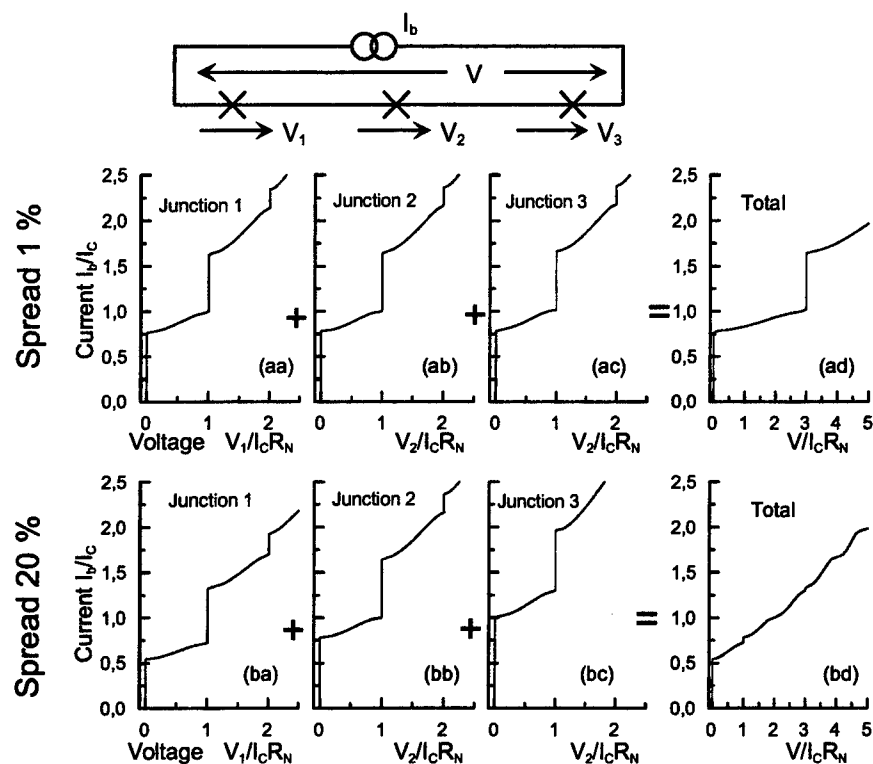


FIGURE 4. Shapiro steps in the series array of three junctions. (aa)-(ad) the spread in I_c and R_N is 1%, (ba)-(bd) the spread is 20%.

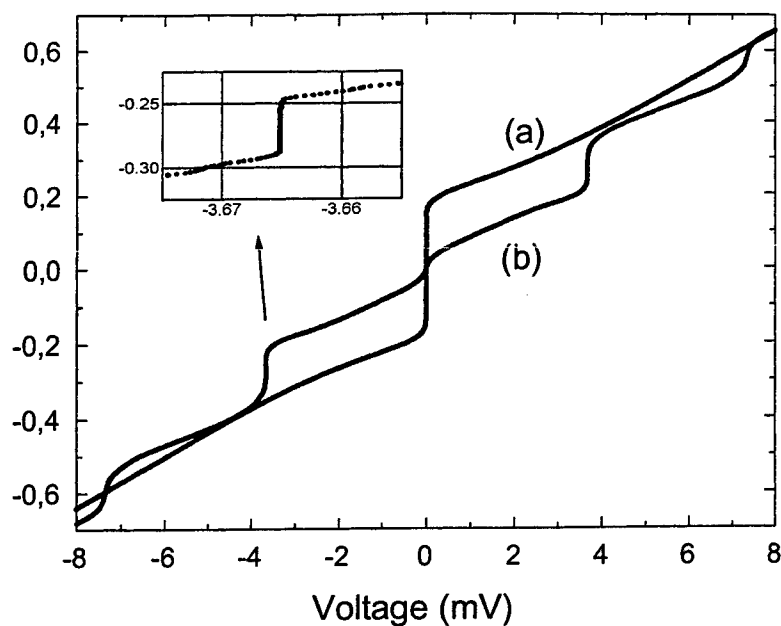


FIGURE 5. IVC of series array of 108 junctions at 83 K, (a) without and (b) with microwave power at 16.4 GHz. The inset shows an enlarged portion of curve (b), demonstrating step height and steepness.

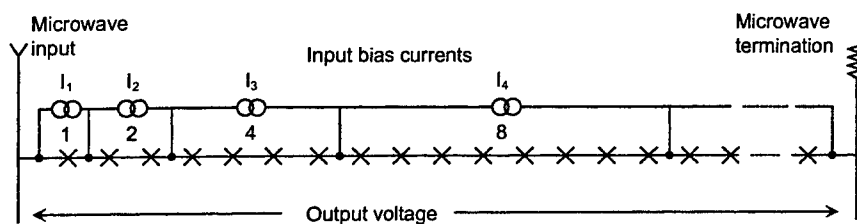


FIGURE 6. A programmable Josephson array voltage standard.

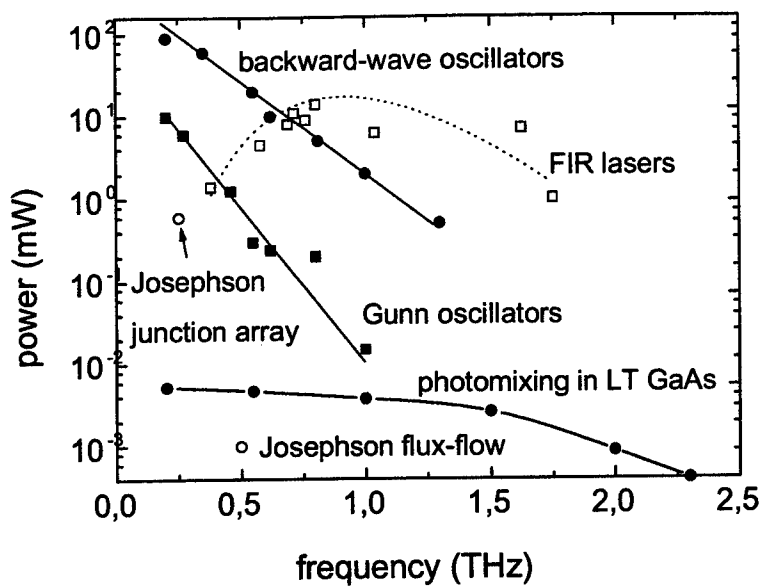


FIGURE 7. Dependence of emitted power of THz microwave generators.

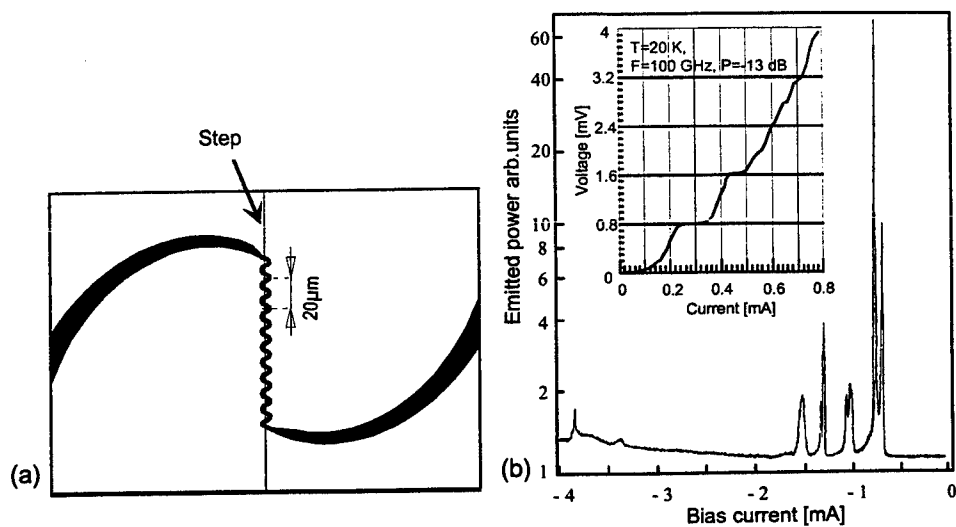


FIGURE 8. (a) Topology of series array of HTS Josephson junctions. (b) Microwave emission from 10 HTS step-edge array measured at 12 GHz.

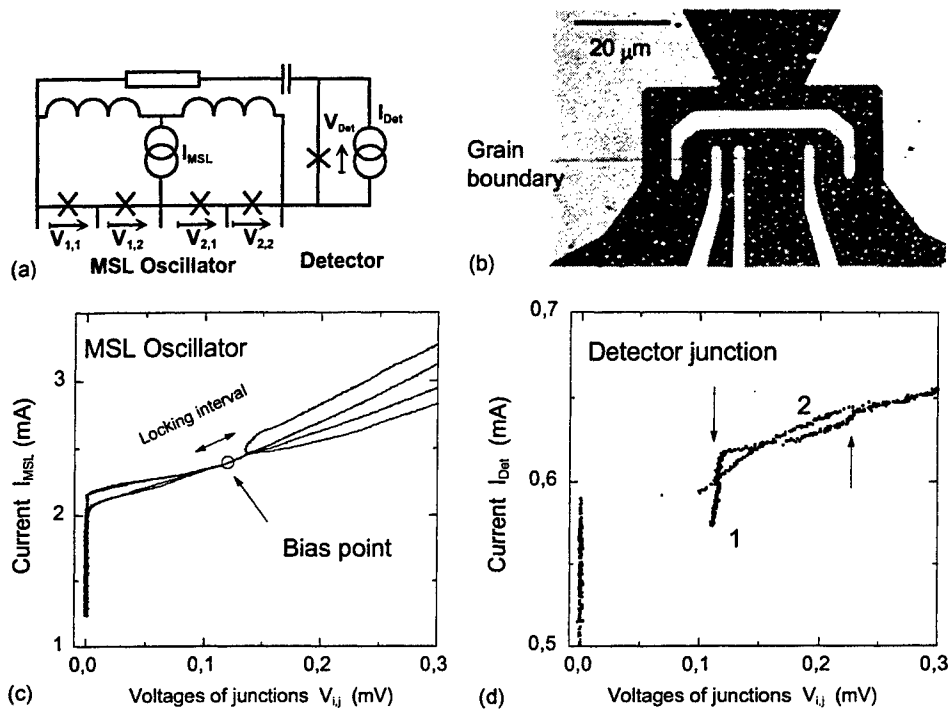


FIGURE 9. Multi-junction superconducting loop (MSL) connected to the detector junction. (a) The circuit scheme, (b) the photograph of the MSL (the array part) fabricated using bicrystal Josephson junctions. (c) Dependence of voltages of all MSL's junctions as a function of bias current. (d) Curve 1 - the response of detector junction when MSL was biased at the phase-locking conditions, curve 2 - the IVC of detector when MSL was "switched-off" (biased at zero voltage state).

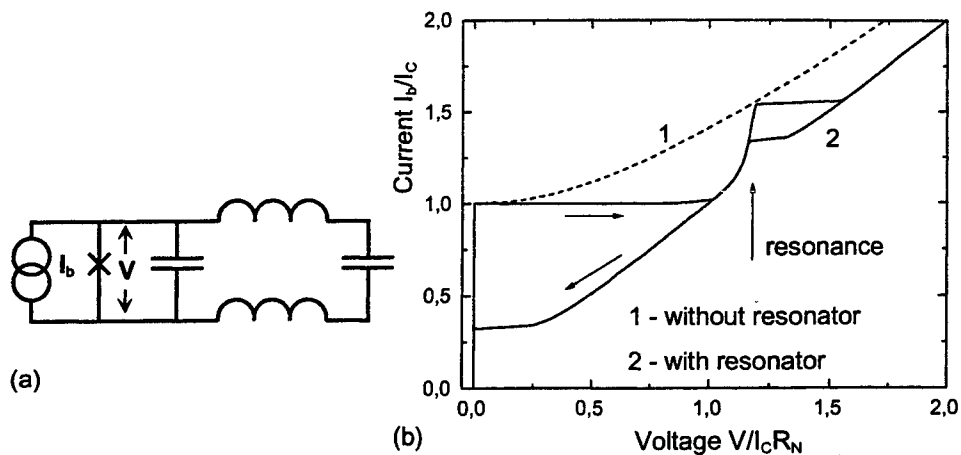


FIGURE 10. (a) Josephson junction connected to resonant circuit and its IVC (b).

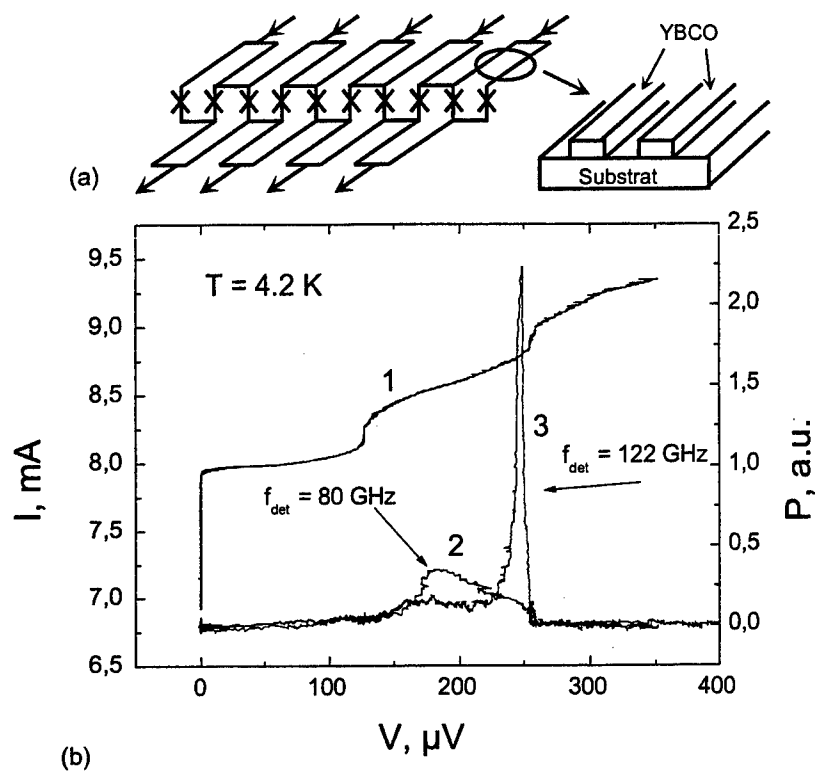


FIGURE 11. (a) Scheme of parallel biased series array with coplanar resonator. (b) Curve 1 - IVC of the array, curve 2 and curve 3 - the radiation from the array at 80 and 122 GHz. The measurements were made at 4.2 K

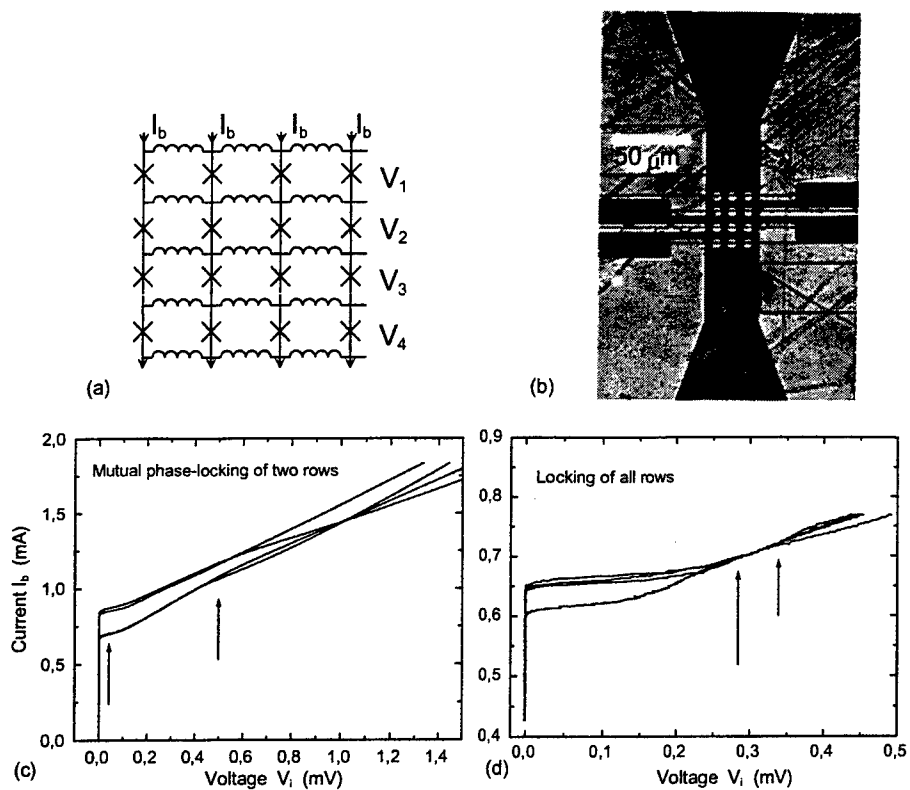


FIGURE 12. (a) Scheme of shorted 2d arrays. (b) Photograph of the circuit. (c) Dependence of voltages of rows as a function of bias current in zero magnetic field, (d) in finite magnetic field. The measurements were made at 4.2 K

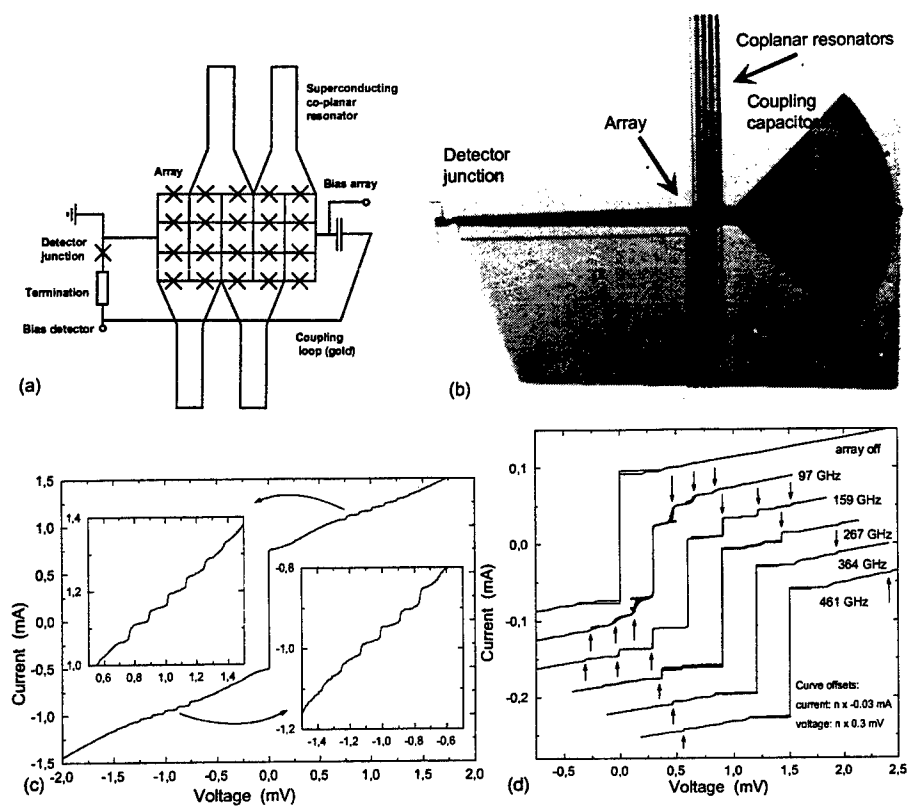


FIGURE 13. (a) Circuit scheme of parallel biased 2d array, (b) photograph of the circuit. (c) IVC of array, (d) response of detector junction when array biased at different voltage. The measurements were made at the temperature 10 K.

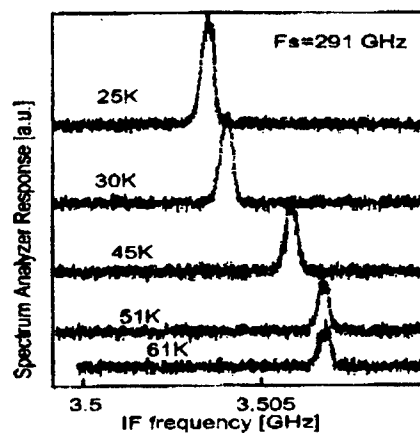


FIGURE 14. Intermediate frequency spectral lines for mixing of 3rd harmonic of Gunn oscillator and 2nd harmonic of BWO at 291 GHz.

II. ARRAYS IN CLASSICAL REGIME: CRITICAL PROPERTIES

Confinement and Quantization Effects in Mesoscopic Superconducting Structures

V. V. Moshchalkov, V. Bruyndoncx, E. Rosseel, L. Van Look, M. Baert, M. J. Van Bael, T. Puig¹, C. Strunk² and Y. Bruynseraede

*Laboratorium voor Vaste-Stoffysica en Magnetisme, Katholieke Universiteit Leuven,
Celestijnenlaan 200 D, B-3001 Leuven, Belgium*

Abstract. We have studied quantization and confinement effects in nanostructured superconductors. Three different types of nanostructured samples were investigated: individual structures (line, loop, dot), 1-dimensional (1D) clusters of loops and 2D clusters of antidots, and finally large lattices of antidots. Hereby, a crossover from individual elementary "plaquettes", via clusters, to huge arrays of these elements, is realized. The main idea of our study was to vary the boundary conditions for confinement of the superconducting condensate by taking samples of different topology and, through that, modifying the lowest Landau level $E_{LLL}(H)$. Since the critical temperature versus applied magnetic field $T_c(H)$ is, in fact, $E_{LLL}(H)$ measured in temperature units, it is varied as well when the sample topology is changed through nanostructuring. We demonstrate that in all studied nanostructured superconductors the shape of the $T_c(H)$ phase boundary is determined by the confinement topology in a unique way.

I INTRODUCTION

A Confinement and Quantization

"Confinement" and "quantization" are two closely interrelated definitions: if a particle is "confined" then its energy is "quantized", and vice versa. According to the dictionary, to "confine" means to "restrict within limits", to "enclose", and even to "imprison". A typical example, illustrating the relation between confinement and quantization, is the restriction of the motion of a particle by an infinite potential well of size L_A . Due to the presence of an infinite potential $U(x)$ (Fig. 1) for $x < 0$ and $x > L_A$, the wave function $\Psi(x)$ describing the particle is zero outside the well: $\Psi = 0$ for $x < 0$ and $x > L_A$ and, in the region with $U(x) = 0$ ($0 \leq x \leq L_A$),

¹⁾ Present address: Institut de Ciència de Materials de Barcelona, 08193 Bellaterra, Spain

²⁾ Currently at: University of Basel, Institute for Physics, CH-4056 Basel, Switzerland

the solutions of the one-dimensional Schrödinger equation correspond to standing waves with an integer number n of half wavelengths λ along L_A : $n \lambda_n/2 = L_A$. This simple constraint results in the well-known quantized energy spectrum

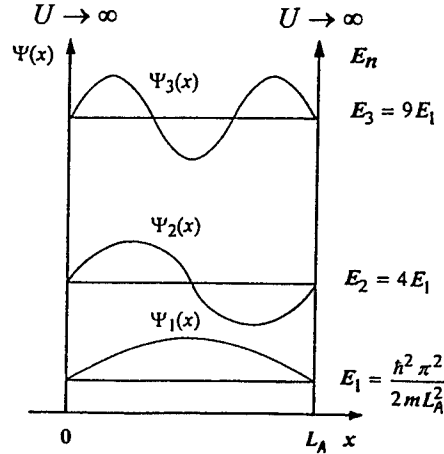


FIGURE 1. Confinement and quantization of the motion of a particle by an infinite potential well with size L_A for $n = 1, 2$ and 3 .

$$E_n = \frac{\hbar^2 k_n^2}{2m} = \frac{\hbar^2 (2\pi/\lambda_n)^2}{2m} = \frac{\hbar^2 \pi^2}{2m L_A^2} n^2 \quad (1)$$

Here k_n is the wave number and m is the free electron mass. To have an idea about the characteristic energy scales involved and their dependence upon the confinement length L_A , we have calculated (see Table 1) the energies E_1 (Eq. (1)) for electrons confined by an infinite potential well with the sizes 1 \AA , 1 nm and $1 \mu\text{m}$.

TABLE 1. Confinement by the infinite potential well

Confinement length L_A	Energy E_1	Temperature T
1 \AA	40 eV	$4 \times 10^5 \text{ K}$
1 nm	0.4 eV	$4 \times 10^3 \text{ K}$
$1 \mu\text{m}$	$0.4 \mu\text{eV}$	4 mK

B Nanostructuring

Recent impressive progress in nanofabrication has made it possible to realize the whole range of confinement lengths L_A : from $1 \mu\text{m}$ (photo- and e-beam lithography), via 1 nm to 1 \AA (single atom manipulation) and, through that, to control the

confinement energy (temperature) from a few mK higher up to far above room temperature (Table 1).

This progress has stimulated dramatically the experimental and theoretical studies of different nanostructured materials and individual nanostructures. The interest towards such structures arises from the remarkable principle of "quantum design", when quantum mechanics can be efficiently used to tailor the physical properties of nanostructured materials.

Nanostructuring can also be considered as a sort of artificial modulation. We can identify then the main classes of nanostructured materials using the idea of their modification along one-, two- or three-axes, thus introducing 1-dimensional (1D)-, 2D- or 3D- artificial modulation (Fig. 2). The 1D or "vertical" modulation repre-

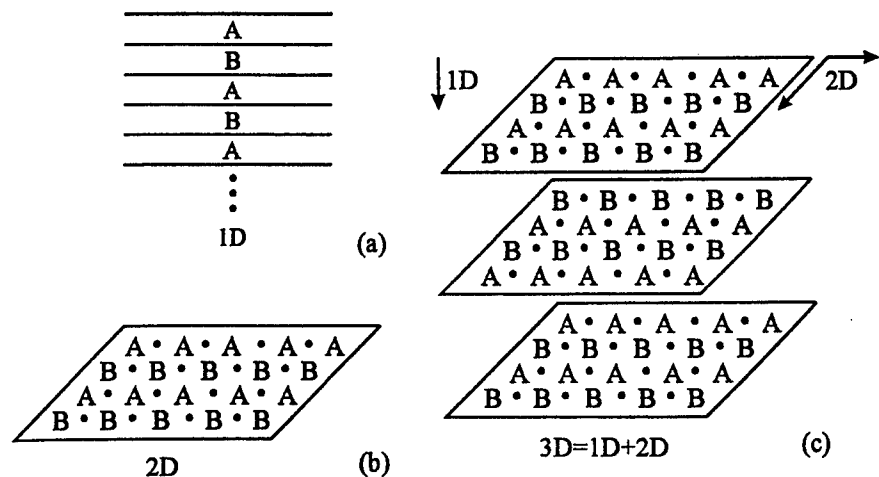


FIGURE 2. Schematic presentation of the vertical modulation in superlattices or multilayers (a), of the horizontal modulation achieved by a lateral repetition of elements A and B (b) and of the $1D+2D=3D$ artificial modulation (c).

sents then the class of superlattices or multilayers (Fig. 2a) formed by alternating individual films of two (A, B) or more different materials on a stack. Some examples of different types of multilayers are superconductor/insulator (Pb/Ge, WGe/Ge,...), superconductor/metal (V/Ag,...), superconductor/ferromagnet (Nb/Fe, V/Fe,...), ferromagnet/metal (Fe/Cr, Cu/Co,...), etc.

The "horizontal" (lateral) superlattices (Fig. 2b) correspond to the 2D artificial modulation achieved by a lateral repetition of one (A), two (A,B) or more elements. As examples, we should mention here antidot arrays or antidot lattices, when A=microhole ("antidot"), or arrays and lateral superlattices consisting of magnetic dots.

If the 2D lateral modulation is applied to each individual layer of a multilayer or superlattice, then we deal with the $1D+2D=3D$ artificial modulation (Fig. 2c).

For example, if arrays of antidots are made in a multilayer, then we have a system with 3D artificial modulation which combines 2D lateral "horizontal" with the 1D "vertical" modulation.

Finally, macroscopic nanostructured samples, with a huge number N of repeated elementary "plaquettes" (A,B,...), are examples of very complicated systems if the confined charge carriers or flux lines are strongly interacting with each other and the relevant interaction is of a long range. In this case the essential physics of such systems can be understood much better if we use clusters of elements ($N \simeq 10$), instead of their huge arrays ($N \rightarrow \infty$) (Fig. 3). These clusters, occupying an

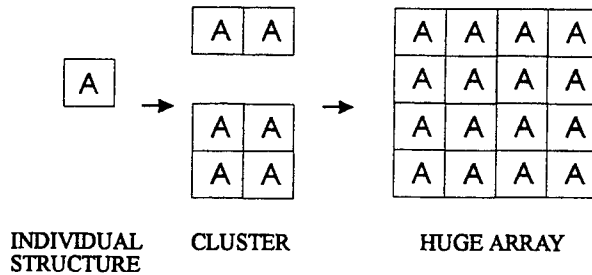


FIGURE 3. Schematic presentation of an individual structure, a cluster and a huge array.

intermediate place between individual nanostructures ($N = 1$) and nanostructured materials ($N \rightarrow \infty$), are very helpful model objects to study the interactions between flux lines or charge carriers confined by elements A. The "growth" of clusters on the way from an individual object A to a huge array of A's can be done either in a 1D or 2D fashion (Fig. 3), thus realizing 1D chains or 2D-like clusters of elements A.

C Confining the Superconducting Condensate

The nanostructured materials and individual nanostructures, introduced in the previous section, can be prepared using the modern facilities for nanofabrication. It is worth, however, first asking ourselves a few simple questions like: why do we want to make such structures, what interesting new physics do we expect, and why do we want to focus on superconducting (and not, for example, normal metallic) nanostructured materials?

First of all, by making nanostructured materials, one creates an artificial potential in which charge carriers or flux lines are confined. The size L_A of an elementary "plaquette" A, gives roughly the expected energy scale in accordance with Table 1, while the positions of the elements A determine the pattern of the potential modulation. The concentration of charge carriers or flux lines can be controlled by varying a gate voltage (in 2D electron gas systems) [1] or the applied magnetic field (in superconductors) [2]. In this situation, different commensurability effects

between the fixed number of elements A in an array and a tunable number of charge or flux carriers are observed.

Secondly, modifying the sample topology in nanostructured materials creates a unique possibility to impose the desired boundary conditions, and thus almost "impose" the properties of the sample. A Fermi liquid or a superconducting condensate confined within such materials will be subjected to severe constraints and, as a result, the properties of these materials will be strongly affected by the boundary conditions.

While a normal metallic system should be considered quantum-mechanically by solving the Schrödinger equation:

$$\frac{1}{2m} (-i\hbar \vec{\nabla} - e\vec{A})^2 \Psi + U \Psi = E \Psi, \quad (2)$$

a superconducting system is described by the two coupled Ginzburg-Landau (GL) equations:

$$\frac{1}{2m^*} (-i\hbar \vec{\nabla} - e^*\vec{A})^2 \Psi_s + \beta |\Psi_s|^2 \Psi_s = -\alpha \Psi_s \quad (3)$$

$$\vec{j}_s = \vec{\nabla} \times \vec{h} = \frac{e^*}{2m^*} [\Psi_s^* (-i\hbar \vec{\nabla} - e^*\vec{A}) \Psi_s + \Psi_s (i\hbar \vec{\nabla} - e^*\vec{A}) \Psi_s^*], \quad (4)$$

with \vec{A} the vector potential which corresponds to the microscopic field $\vec{h} = \text{rot} \vec{A} / \mu_0$, U the potential energy, E the total energy, α a temperature dependent parameter changing sign from $\alpha > 0$ to $\alpha < 0$ as T is decreased through T_c , β a positive temperature independent constant, m^* the effective mass which can be chosen arbitrarily and is generally taken as twice the free electron mass m .

Note that the first GL equation (Eq. (3)), with the nonlinear term $\beta |\Psi_s|^2 \Psi_s$ neglected, is the analogue of the Schrödinger equation (Eq. (2)) with $U = 0$, when making a few substitutions: $\Psi_s \leftrightarrow \Psi$, $e^* \leftrightarrow e$, $-\alpha \leftrightarrow E$ and $m^* \leftrightarrow m$. The superconducting order parameter Ψ_s corresponds to the wave function Ψ in Eq. (2). The effective charge e^* in the GL equations is $2e$, i.e. the charge of a Cooper pair, while the temperature dependent GL parameter α

$$-\alpha = \frac{\hbar^2}{2m^* \xi^2(T)} \quad (5)$$

plays the role of E in Schrödinger equation. Here $\xi(T)$ is the temperature dependent coherence length:

$$\xi(T) = \frac{\xi(0)}{\sqrt{1 - \frac{T}{T_{c0}}}}. \quad (6)$$

The boundary conditions for interfaces normal metal-vacuum and superconductor-vacuum are, however, different (Fig. 4):

$$\Psi\Psi^*|_b = 0 \quad (7)$$

$$(-i\hbar\vec{\nabla} - e^*\vec{A})\Psi_s|_{\perp,b} = 0 \quad (8)$$

i.e. for normal metallic systems the density is zero, while for superconducting systems, the gradient of Ψ_s (for the case $\vec{A} = 0$) has no component perpendicular to the boundary. As a consequence, the supercurrent cannot flow through the boundary. The nucleation of the superconducting condensate is favored at the superconductor/ vacuum interfaces, thus leading to the appearance of superconductivity in a surface sheet with a thickness $\xi(T)$ at the third critical field $H_{c3}(T)$.

For bulk superconductors the surface-to-volume ratio is negligible and therefore superconductivity in the bulk is not affected by a thin superconducting surface layer. For nanostructured superconductors with antidot arrays, however, the boundary conditions (Eq. (8)) and the surface superconductivity introduced through them, become very important if $L_A \leq \xi(T)$. The advantage of superconducting materials in this case is that it is not even necessary to go to nm scale (like for normal metals), since for L_A of the order of $0.1-1.0 \mu m$ the temperature range where $L_A \leq \xi(T)$, spreads over $0.01 - 0.1 K$ below T_c due to the divergence of $\xi(T)$ at $T \rightarrow T_{c0}$ (Eq. (6)).

In principle, the mesoscopic regime $L_A \leq \xi(T)$ can be reached even in bulk superconducting samples with $L_A \sim 1 cm - 1 m$, since $\xi(T)$ diverges. However, the temperature window where $L_A \leq \xi(T)$ is so narrow, not more than $\sim 1 nK$ below T_{c0} , that one needs ideal sample homogeneity and perfect temperature stability.

In the mesoscopic regime $L_A \leq \xi(T)$, which is quite easily realized in (perforated) nanostructured materials, the surface superconductivity can cover the whole available space occupied by the material, thus spreading superconductivity all over the sample. It is then evident that in this case surface effects play the role of bulk effects.

Using the similarity between the linearized GL equation (Eq. (3)) and the Schrödinger equation (Eq. (2)), we can formalize our approach as follows: since the parameter $-\alpha$ (Eqs. (3) and (5)) plays the role of energy E (Eq. (2)), then *the highest possible temperature $T_c(H)$ for the nucleation of the superconducting state in presence of the magnetic field H always corresponds to the lowest Landau level $E_{LLL}(H)$ found by solving the Schrödinger equation (Eq. (2)) with "superconducting" boundary conditions (Eq. (8)).*

Figure 5 illustrates the application of this rule to the calculation of the upper critical field $H_{c2}(T)$: indeed, if we take the well-known classical Landau solution for the lowest level in bulk samples $E_{LLL}(H) = \hbar\omega/2$, where $\omega = e^*\mu_0 H/m^*$ is the cyclotron frequency. Then, from $-\alpha = E_{LLL}(H)$ we have

$$\frac{\hbar^2}{2m^* \xi^2(T)} = \frac{\hbar\omega}{2} \Big|_{H=H_{c2}} \quad (9)$$

and with the help of Eq. (5), we obtain

$$\mu_0 H_{c2}(T) = \frac{\Phi_0}{2\pi \xi^2(T)} \quad (10)$$

with $\Phi_0 = h/e^* = h/2e$ the superconducting flux quantum.

In nanostructured superconductors, where the boundary conditions (Eq. (8)) strongly influence the Landau level scheme, $E_{LLL}(H)$ has to be calculated for each different confinement geometry. By measuring the shift of the critical temperature $T_c(H)$ in a magnetic field, we can compare the experimental $T_c(H)$ with the calculated level $E_{LLL}(H)$ and thus check the effect of the confinement topology on the superconducting phase boundary for a series of nanostructured superconducting samples. The transition between normal and superconducting states is usually very sharp and therefore the lowest Landau level can be easily traced as a function of applied magnetic field. Except when stated explicitly, we have taken the midpoint of the resistive transition from the superconducting to the normal state, as the criterion to determine $T_c(H)$.

In this paper we present the systematic study of the influence of the confinement geometry on the superconducting phase boundary $T_c(H)$ in a series of nanostructured samples. We begin with individual nanostructures of different topologies (lines, loops, dots) (Section II) and then focus on "intermediate" systems: clusters of loops fabricated in the form of a 1D chain of loops (Section III.A) or 2D antidot clusters (Section III.B). Finally, we move on to huge arrays of antidots in Section IV where we report on the $T_c(H)$ boundary for superconducting films with antidot lattices. The main emphasis of the paper is on the demonstration of the importance of the confinement geometry for the superconducting condensate and on the related quantization phenomena in nanostructured superconductors through the study of the phase boundaries $T_c(H)$.

II INDIVIDUAL STRUCTURES: LINE, LOOP AND DOT

We begin this section by presenting the experimental results on the $T_c(H)$ phase boundary of individual superconducting mesoscopic structures of different topology. Simultaneously, we have kept other parameters of these samples, like material from which they are made (Al), the width of the lines ($w = 0.15 \mu m$) and the film thickness $t = 25 nm$ the same for all three structures, thus directly relating the differences in $T_c(H)$ to topological effects. The magnetic field H is always applied perpendicular to the structures.

A Line

In Fig. 6a the phase boundary $T_c(H)$ of a mesoscopic line is shown. The solid line gives the $T_c(H)$ calculated from the well-known formula [3]:

$$T_c(H) = T_{c0} \left[1 - \frac{\pi^2}{3} \left(\frac{w \xi(0) \mu_0 H}{\Phi_0} \right)^2 \right] \quad (11)$$

which, in fact, describes the parabolic shape of $T_c(H)$ for a thin film of thickness w in parallel magnetic field. Since the cross-section, exposed to the applied magnetic field, is the same for a film of thickness w in a parallel magnetic field and for a mesoscopic line of width w in a perpendicular field, the same formula can be used for both [4]. Indeed, the solid line in Fig 6a is a parabolic fit of the experimental data with Eq. (11) where $\xi(0) = 110 \text{ nm}$ was obtained as a fitting parameter. The coherence length obtained using this method, coincides reasonably well with the dirty limit value $\xi(0) = 0.85(\xi_0 \ell)^{1/2} = 132 \text{ nm}$ calculated from the known BCS coherence length $\xi_0 = 1600 \text{ nm}$ for bulk Al [5] and the mean free path $\ell = 15 \text{ nm}$, estimated from the normal state resistivity ρ at 4.2 K [6].

We can use also another simple argument to explain the parabolic relation $T_c(H) \propto H^2$: the expansion of the energy $E(H)$ in powers of H , as given by the perturbation theory, is [7]:

$$E(H) = E_0 + A_1 L H + A_2 S H^2 + \dots \quad (12)$$

where A_1 and A_2 are constant coefficients, the first term E_0 represents the energy levels in zero field, the second term is the linear field splitting with the orbital quantum number L and the third term is the diamagnetic shift with S , being the area exposed to the applied field.

Now, for the topology of the line with a width w much smaller than the Larmor radius $r_H \gg w$, any orbital motion is impossible due to the constraints imposed by the boundaries onto the electrons inside the line. Therefore, in this particular case $L = 0$ and $E(H) = E_0 + A_2 S H^2$, which immediately leads to the parabolic relation $T_c \propto H^2$. This diamagnetic shift of $T_c(H)$ can be understood in terms of a partial screening of the magnetic field H due to the non-zero width of the line [8].

B Loop

The $T_c(H)$ of the mesoscopic loop, shown in Fig. 6b, demonstrates very distinct Little-Parks (LP) oscillations [9] superimposed on a monotonic background. A closer investigation leads to the conclusion that this background is very well described by the same parabolic dependence as the one which we just discussed for the mesoscopic line [4] (see the solid line in Fig. 6a). As long as the width of the strips w , forming the loop, is much smaller than the loop size, the total shift of $T_c(H)$

can be written as the sum of an oscillatory part, and the monotonic background given by Eq. (11) [4,10]:

$$T_c(H) = T_{c0} \left[1 - \frac{\pi^2}{3} \left(\frac{w \xi(0) \mu_0 H}{\Phi_0} \right)^2 - \frac{\xi^2(0)}{R^2} \left(n - \frac{\Phi}{\Phi_0} \right)^2 \right] \quad (13)$$

where $R^2 = R_1 R_2$ is the product of inner and outer loop radius, and the magnetic flux threading the loop $\Phi = \pi R^2 \mu_0 H$. The integer n has to be chosen so as to maximize $T_c(H)$ or, in other words, selecting $E_{LLL}(H)$.

The LP oscillations originate from the fluxoid quantization requirement, which states that the complex order parameter Ψ_s should be a single-valued function when integrating along a closed contour

$$\oint \vec{\nabla} \varphi \cdot d\mathbf{l} = n 2\pi \quad n = \dots, -2, -1, 0, 1, 2, \dots \quad (14)$$

where we have introduced the order parameter as $\Psi_s = |\Psi_s| \exp(i\varphi)$. Fluxoid quantization gives rise to a circulating supercurrent in the loop when $\Phi \neq n\Phi_0$, which is periodic with the applied flux Φ/Φ_0 .

Using the sample dimensions and the value for $\xi(0)$ obtained before for the mesoscopic line (with the same width $w = 0.15 \mu m$), the $T_c(H)$ for the loop can be calculated from Eq. (13) without any free parameter. The solid line in Fig. 6b shows indeed a very good agreement with the experimental data. It is worth noting here that the amplitude of the LP oscillations is about a few mK - in qualitative agreement with the simple estimate given in Table 1 for $L_A \simeq 1 \mu m$.

Another interesting feature of a mesoscopic loop and other mesoscopic structures is the unique possibility they offer for studying nonlocal effects [11]. In fact, a single loop can be considered as a 2D artificial quantum orbit with a *fixed radius*, in contrast to Bohr's description of atomic orbitals. In the latter case the stable radii are found from the quasiclassical quantization rule, stating that only an integer number of wavelengths can be set along the circumference of the allowed orbits. For a superconducting loop, however, supercurrents must flow, in order to fulfil the fluxoid quantization requirement (Eq. (14)), thus causing oscillations of the critical temperature T_c versus magnetic field H .

In order to measure the resistance of a mesoscopic loop, electrical contacts have, of course, to be attached to it, and as a consequence the confinement geometry is changed. A loop with attached contacts and the same loop without any contacts are, strictly speaking, different mesoscopic systems. This "disturbing" or "invasive" aspect can now be exploited for the study of nonlocal effects [11]. Due to the divergence of the coherence length $\xi(T)$ at $T = T_{c0}$ (Eq. (6)) the coupling of the loop with the attached leads is expected to be very strong for $T \rightarrow T_{c0}$.

Fig. 7 shows the results of these measurements. Both "local" (potential probes across the loop V_1/V_2) and "nonlocal" (potential probes aside of the loop V_1/V_3 or V_2/V_4) LP oscillations are clearly observed. For the "local" probes there is an unexpected and pronounced increase of the oscillation amplitude with increasing

field, in disagreement with previous measurements on Al microcylinders [10]. In contrast to this, for the "nonlocal" LP effect, the oscillations rapidly vanish when the magnetic field is increased.

When increasing the field, the background suppression of T_c (Eq. (11)) results in a decrease of $\xi(T)$. Hence, the change of the oscillation amplitude with H is directly related to the temperature-dependent coherence length. As long as the coherence of the superconducting condensate protuberates over the nonlocal voltage probes, the nonlocal LP oscillations can be observed.

On the other hand, the importance of an "arm" attached to a mesoscopic loop, was already demonstrated theoretically by de Gennes in 1981 [12]. For a perfect 1D loop (vanishing width of the strips) adding an "arm" will result in a decrease of the LP oscillation amplitude, what we observed indeed at low magnetic fields, where $\xi(T)$ is still large. With these experiments, we have proved that adding probes to a structure considerably changes both the confinement topology and the phase boundary $T_c(H)$.

C Dot

The Landau level scheme for a cylindrical dot with "superconducting" boundary conditions (Eq. (8)) is presented in Fig. 8. Each level is characterized by a certain orbital quantum number L where $\Psi_s = |\Psi_s| \exp(\mp i L \varphi)$ [13]. The levels, corresponding to the sign "+" in the argument of the exponent are not shown since they are situated at energies higher than the ones with the sign "-". The lowest Landau level in Fig. 8 represents a cusp-like envelope, switching between different L values with changing magnetic field. Following our main guideline that $E_{LLL}(H)$ determines $T_c(H)$, we expect for the dot the cusp-like superconducting phase boundary with nearly perfect linear background. The measured phase boundary $T_c(H)$, shown in Fig. 6b, can be nicely fitted by the calculated one (Fig. 8), thus proving that $T_c(H)$ of a superconducting dot indeed consists of cusps with different L 's [14]. Each fixed L describes a giant vortex state which carries L flux quanta Φ_0 . The linear background of the $T_c(H)$ dependence is very close to the third critical field $H_{c3}(T) \simeq 1.69 H_{c2}(T)$ [15]. Contrary to the loop, where the LP oscillations are perfectly periodic, the dot demonstrates a certain aperiodicity [16], in very good agreement with the theoretical calculations [14,17].

III CLUSTERS OF LOOPS AND ANTIDOTS

A 1D Clusters of loops

After the description of the confinement effects of several individual superconducting structures (A = line, loop, dot) we are ready to move further on to clusters of elements A (Fig. 3) on our way from "single plaquette" samples to materials

nanostructured by introducing huge arrays of elements A. First we take $A = \text{loop}$ and consider one-dimensional multiloop structures: "bola", double and triple loop Al structures. Figure 9 shows a AFM image of the structures. For these geometries some interesting theoretical predictions have been made, for which no experimental verification has been carried out up to now (see more in Ref. [18]). The loops in all three structures have the same dimensions, thus leading to the same magnetic field period $\mu_0 \Delta H = 1.24 \text{ mT}$. The strips forming the structures are $0.13 \mu\text{m}$ wide and the film thickness $t = 34 \text{ nm}$. In all the experimental data we show, the parabolic background (Eq. (11)) is already subtracted in order to allow for a direct comparison with the theory. In the temperature interval where we measured the $T_c(H)$ boundary, the coherence length $\xi(T)$ is considerably larger than the width w of the strips. This makes it possible to use the one-dimensional models for the calculation of $E_{LLL}(H)$ and thus $T_c(H)$. The basic idea is to consider $|\Psi_s| = \text{constant}$ across the strips forming the network and to allow a variation of $|\Psi_s|$ only along the strips. In the simplest approach $|\Psi_s|$ is assumed to be spatially constant (London limit (LL)) [19,20], in contrast to the de Gennes-Alexander (dGA) approach [12,21,22], where $|\Psi_s|$ is allowed to vary along the strips. In the latter approach one imposes:

$$\sum_n \left(i \frac{\partial}{\partial x} + \frac{2\pi}{\Phi_0} A_{\parallel}(x) \right) \Psi_s(x) = 0 \quad (15)$$

at the points where the current paths join. The summation is taken over all strips connected to the junction point. Here, x is the coordinate defining the position on the strips, and A_{\parallel} is the component of the vector potential along x . Eq. (15) is often called the generalized first Kirchhoff law, ensuring current conservation [22]. The second Kirchhoff law for voltages in normal circuits is now replaced by the fluxoid quantization requirement (Eq. (14)), which should be fulfilled for each closed contour around a loop.

In Figs. 10-12 the phase boundaries of the three structures are shown. The dashed lines are the phase boundaries obtained with the LL, while the solid lines give the results from the dGA approach. As we discussed in Section II.B for a mesoscopic loop, attaching contacts modifies the confinement topology, so that the amplitude of the local LP oscillations is lowered at low magnetic fields. Here as well, the inclusion of the leads reduces the amplitude of the oscillations. The dash-dotted line in Figs. 10-12 give the result of the dGA calculation where the presence of the leads has been included. The values for $\xi(0)$ obtained from the fits agree within a few percent with the $\xi(0)$ values found independently from the monotonic background of $T_c(\Phi)$ (see Eq. (11)).

First, in Fig. 10, we consider the mesoscopic "bola" - two loops connected by a wire. Fink *et al.* [22] showed that, in the complete magnetic flux interval, the spatially symmetric solution, with equal orientation of the supercurrents in both loops, has a lower energy than the antisymmetric solution. Coming back to the similarity between a mesoscopic loop and a hydrogen atom, we discussed in Section II.B, we can then compare the bola with a H_2 molecule, where the symmetric and the

antisymmetric solutions correspond to singlet and triplet states, respectively. In fact, $T_c(\Phi)$ of the bola is the same as for a single loop provided that the length of the strip connecting the two loops is short, as confirmed by the LP oscillations observed in the experimental $T_c(\Phi)$ (Fig. 10).

In what follows we will focus on the phase boundaries of the double (Fig. 11) and the triple loop (Fig. 12). To facilitate the discussion we divide the flux period in two intervals: flux regime I for $\Phi/\Phi_0 < g$ or $\Phi/\Phi_0 > (1 - g)$ and flux regime II for $g < \Phi/\Phi_0 < (1 - g)$. In the flux regime I the phase boundaries, predicted by the different models, are nearly identical. Near $\Phi/\Phi_0 = 1/2$ (flux regime II), however, clear differences are found between the dGA approach and the LL. The dGA result fits better the experimental data with respect to the crossover point g between regimes I and II, and the amplitude of the T_c oscillations. Using the dGA approach we have calculated the spatial modulation of $|\Psi_s|$ and the supercurrents for different values at the $T_c(\Phi)$ boundary. In the flux regime I $|\Psi_s|$ varies only slightly and therefore the results of the LL and the dGA models nearly coincide. The elementary loops have an equal fluxoid quantum number (and consequently an equal supercurrent orientation) for both the double and the triple loop geometry. For the double loop this leads to a cancellation of the supercurrent in the middle strip, while for the triple loop structure the fluxoid quantization condition (Eq. (14)) results in a different value for the supercurrent in the inner and the outer loops. As a result, the common strips of the triple loop structure carry a finite current.

In the flux regime II, qualitatively different states are obtained from the LL and the dGA approach: the states calculated within the dGA approach have strongly modulated $|\Psi_s|$ along the strips. This is most severe for the double loop: Ψ_s shows a node ($|\Psi_s| = 0$) in the center of the common strip, the phase φ having a discontinuity of π at this point. This node is a one-dimensional analog of the core of an Abrikosov vortex, where the order parameter also vanishes and the phase shows a discontinuity. In Fig. 13 the spatial variation of $|\Psi_s|$ along the strips is shown for $\Phi/\Phi_0 = 0.36$ close to the crossover point g . The dashed curve gives $|\Psi_s|$ in flux regime I, which is quasi-constant. The strongly modulated solution, which goes through zero in the center, is indicated by the solid line. Although there exists a finite phase difference across the junction points of the middle strip, no supercurrent can flow through the strip due to the presence of the node. This node is predicted to persist when moving below the phase boundary into the superconducting state [23,24]. Already in 1964 Parks [25] anticipated that, in a double loop, "a part of the middle link will revert to the normal phase", and that "this in effect will convert the double loop to a single loop", giving an intuitive explanation for the maximum in $T_c(\Phi)$ at $\Phi/\Phi_0 = 1/2$. Such a modulation of $|\Psi_s|$ is obviously excluded in the LL, where the loop currents have an opposite orientation and add up in the central strip, thus giving rise to a rather high kinetic energy. An extra argument in favor of the presence of the node is given by the much better agreement for the crossover point g when the presence of the leads is taken into account in the calculations (see dash-dotted line in Fig. 11).

For the triple loop structure the modulation of $|\Psi_s|$ is still considerable in flux

regime II, but it does not show any nodes. Therefore the supercurrent orientations can be found from the fluxoid quantum numbers $\{n_i\}$, obtained from integrating the phase gradients along each individual loop. When passing through the crossover point between flux regime I and regime II only the supercurrent in the middle loop is reversed, while increasing the flux above $\Phi/\Phi_0 = 1/2$ implies a reversal of the supercurrent in all loops.

Surprisingly, the behavior of a microladder with a linear arrangement of m loops appears to be qualitatively different for even and for odd m in the sense that m determines the presence or absence of nodes in the common strips. For an infinitely long microladder $|\Psi_s|$ was found to be spatially constant below a certain $\Phi < \Phi_c$ [26], which is analogous to the states we find in flux regime I. For fluxes $\Phi > \Phi_c$ modulated $|\Psi_s|$ states, with an incommensurate fluxoid pattern, were found. At $\Phi/\Phi_0 = 1/2$, nodes appear at the center of every second common (transverse) branch.

B 2D clusters of antidots

As a 2D intermediate structure between individual elements A and their huge arrays (Fig. 3), we have studied the superconducting micro-square with a 2×2 antidot cluster. In this case A = "antidot". The micro-square with the 2×2 antidot cluster consists of a $2 \times 2 \mu m^2$ superconducting square with four antidots (i.e. square holes of $0.53 \times 0.53 \mu m^2$). A Pb/Cu bilayer with 50 nm of Pb and 17 nm of Cu was used as the superconducting film for the fabrication of this structure. The thin Cu layer was deposited on the Pb to protect it from oxidation and to provide a good contact-layer for the wire-bonding to the experimental apparatus. An AFM image of the Pb/Cu 2×2 antidot cluster, is shown in Fig. 14 together with a reference sample (i.e. a Pb/Cu micro-square of $2 \times 2 \mu m^2$ without antidots). The Pb(50 nm)/Cu(17 nm) bilayer behaves as a Type II superconductor with a $T_{c0} = 6.05$ K, a coherence length, $\xi(0) \approx 35$ nm and a dirty limit penetration depth, $\lambda(0) \approx 76$ nm. The $T_c(H)$ measurements on the reference sample revealed characteristic features originating from the confinement of the superconducting condensate by the dot geometry (see Section II.C). The additional features observed in the $T_c(H)$ phase boundary of the antidot cluster can therefore be attributed to the presence of the antidots.

The experimental $T_c(H)$ phase boundary is shown in Fig. 15. It was measured by keeping the sample resistance at 10% of its normal state value and varying the magnetic field and temperature [27]. Strong oscillations are observed with a periodicity of 26 G and in each of these periods, smaller dips appear at approximately 7.5 G, 13 G and 18 G. The parabolic background superimposed on $T_c(H)$ can again be described by Eq. (11).

Defining a flux quantum per antidot as $\Phi_0 = h/2e = BS$, where $B = \mu_0 H$ and S is an effective area per antidot cell ($S = 0.8 \mu m^2$), the minima observed in the magnetoresistance and the $T_c(H)$ phase boundary at integer multiples of 26 G can

be correlated with a magnetic flux quantum per antidot cell, $\Phi = n\Phi_0$. The ones observed at 7.5 G, 13 G and 18 G correspond to the values $\Phi/\Phi_0=0.3, 0.5$ and 0.7 .

The solutions obtained from the London model (LL) define a phase boundary which is periodic in Φ with a periodicity of Φ_0 . Within each parabola $\Delta T_c = \gamma(\Phi/\Phi_0)^2$, where the coefficient γ characterizes the effective flux penetration through the unit cell. The γ -value is determined by the combination of λ and the effective size of the current loops. In Fig. 16, the first period of this phase boundary, $\Delta T_c(\Phi) = T_{c0} - T_c(\Phi)$ versus Φ/Φ_0 is shown. Note that there are six parabolic solutions given by a different set of flux quantum numbers $\{n_i\}$, each one defining a specific vortex configuration. In Fig. 16a, this is indicated by the numbers shown inside the schematic drawings of the antidot cluster. Note that some vortex configurations are degenerate.

From all these possible solutions, for each particular value of Φ/Φ_0 , only the branch with a minimum value of $\Delta T_c(\Phi)$ is stable (indicated with a solid line in Fig. 16a). Note that for the phase boundary, calculated within the 1D model of 4 equivalent and properly attached squares, no fitting parameters were used since the variation of $T_c(\Phi)$ was calculated from the known values for ξ and the size. One period of the phase boundary of the antidot cluster is composed of five branches and in each branch a different stable vortex configuration is permitted. For the middle branch ($0.37 < \Phi/\Phi_0 < 0.63$), the stable configuration is the *diagonal* vortex configuration (antidots with equal n_i at the diagonals) instead of the *parallel* state (dashed line in Fig. 16a).

The net supercurrent density distribution circulating in the antidot cluster for different values of Φ/Φ_0 has been determined using the same approach. Circular currents flow around each antidot. For the states $n_i=0$ and $n_i=1$ currents flow in the opposite direction, since currents corresponding to $n_i=0$ must screen the flux to fulfil the fluxoid quantization condition (Eq. (14)), whereas for $n_i=1$ they have to generate flux. At low values of Φ/Φ_0 , currents are canceled in the internal strips and screening currents only flow around the cluster. When we enter the field range corresponding to the second branch of the phase boundary, a vortex ($n_i=1$) is pinned around one antidot of the cluster (see Fig. 16a). At the third branch, the second vortex enters the structure and is localized in the diagonal. In the fourth branch of the phase boundary the third vortex is pinned in the antidot cluster. And finally, the current distribution for the fifth branch is similar to that of the first branch although currents flow in opposite direction.

Figure 16c shows the first period of the measured phase boundary $T_c(\Phi)$ after subtraction of the parabolic background. For all measured samples, the first period of the experimental phase boundary is composed of five parabolic branches with minima at $\Phi/\Phi_0 = 0, 0.3, 0.5, 0.7, 1$. If we compare it with the theoretical prediction given in Figure 16a, the overall shape can be reproduced although the experimental plot has two major peaks at $\Phi/\Phi_0 = 0.2$ and 0.8 whereas the theoretical curve only predicts cusps around these positions.

The agreement between the measured and the calculated $T_c(\Phi)$ is improved if we assume that the coefficient γ can be considered as a fitting parameter. This seems

to be feasible if we take into account the simplicity and limitation of the used 1D model. Due to the relatively large width of the strips forming the 2×2 cluster, the sizes of the current loops can change since they are "soft" in this case and not defined very precisely.

As a result, the coefficient γ can not be treated as a known constant. If we use it as a free parameter (Fig. 16b) then the curvature of all parabolae forming $T_c(H)$ can be changed and the calculated $T_c(H)$ curve becomes closer to the experimental one though the amplitude of the maxima at $\Phi/\Phi_0 = 0.2$ and 0.8 is still lower than in the experiment (Fig. 16c). The discrepancy in the description of the amplitude of the maxima at $\Phi/\Phi_0 = 0.2$ and 0.8 could also be related to the pinning of vortices by the antidot cluster when potential barriers between different vortex configurations may appear. At the same time, the achieved agreement between the positions of the measured and calculated minima of the $T_c(H)$ curves confirms that the observed effects are due to fluxoid quantization and formation of certain stable vortex configurations at the antidots.

IV SUPERCONDUCTING FILMS WITH AN ANTIDOT LATTICE

Laterally nanostructured superconducting films having regular arrays of antidots are convenient model objects to study the effects of the confinement topology on the $T_c(H)$ phase boundary in two different regimes. The first (or "collective") regime corresponds to the situation where all elements A, forming an array, are coupled.

From the experimental $T_c(H)$ data on antidot clusters we expect for films with an antidot lattice, higher critical fields at $\Phi = n\Phi_0$, which is in agreement with the appearance of the $T_c(H)$ cusps at $\Phi = n\Phi_0$ in superconducting networks [28]. Here, the flux Φ is calculated per unit cell of the antidot lattice.

On the other hand, by applying sufficiently high magnetic fields, the individual circular currents flowing around antidots, can be decoupled and the crossover to a "single object" behaviour could be observed. In this case the relevant area for the flux is the area of the antidot itself and we deal with surface superconductivity around an antidot.

Figure 17 shows the critical field for a Pb(50 nm) sample with a square antidot lattice (period $d = 1 \mu m$ and the antidot size $a = 0.4 \mu m$). The $T_c(H)$ boundary is determined at 10% of the normal state resistance, R_n . In this graph two distinct periodicities are present.

Below ~ 8 mT cusps are found with a period of 2.07 mT, corresponding to one flux-quantum per lattice cell. These cusps or "collective oscillations" [29] are reminiscent of superconducting wire networks [28] and arise from the phase correlations between the different loops which constitute the network. These cusps are obtained by narrowing the minima at $n\Phi_0$ with increasing size N of the $N \times N$ antidot cluster (see the sharpening of the minima at $\Phi = 0, \Phi_0$ in Fig. 18; note that the phase boundary in the $N \rightarrow \infty$ case has a similar shape as the lowest energy level of

the Hofstadter butterfly [2,31]). An important observation is that the amplitude of these "collective" oscillations depends upon the choice of the resistive criterion. This is similar to the case of Josephson junction arrays and weakly coupled wire networks [30] where phase fluctuations dominate the resistive behavior. The inset of Fig. 17 shows the first collective period, measured using three different criteria. As the criterion is lowered the cusps become sharper and the amplitude increases well above the prediction based on the mean field theory for strongly coupled wire networks [28]. At the same time, cusps appear at rational fields $\Phi/\Phi_0=1/4, 1/3, 1/2, 2/3$ and $3/4$ arising from the commensurability of the vortex structure with the underlying lattice.

Above ~ 8 mT, the collective oscillations die out and "single object" cusps appear, having a periodicity which roughly corresponds to one flux quantum Φ_0 per antidot area, a^2 . These cusps are due to the transition between localized superconducting edge states [29] having a different angular momentum L . These states are formed around the antidots and are described by the same orbital momentum introduced in Section II.C for dots.

Figure 19 shows the same critical field as shown in Fig. 17, but normalized by the upper critical field H_{c2} of a plain film without antidots, $\mu_0 H_{c2} = \Phi_0/2\pi\xi^2(T)$ ($\xi(0) = 36$ nm). The dashed line is the calculation of the reduced critical field for a plain film with a single circular antidot with radius $R = 0.24$ μm . The positions of the cusps correspond reasonably well to the experimental ones, taking into account that the model only considers a single hole. From this comparison, an effective area $\pi R^2 = 0.187$ μm^2 is determined which is close to the experimental value $a^2 = 0.16$ μm^2 .

From Figures 17 and 19 it is possible to show that the transition from the network regime to the "single object" regime takes place at a temperature T^* given by the relation $w \approx 1.6 \xi(T^*)$, (where w is the width of the superconducting region between two adjacent antidots).

Experiments on systems with other antidot sizes demonstrate that the a/d ratio determines the relative importance of the "collective regime" and changes the cross-over temperature T^* . The relation $w \approx 1.6 \xi(T^*)$, seems nevertheless to hold reasonably well and is similar to the transition from bulk nucleation of superconductivity to surface nucleation in a thin superconducting slab parallel to the magnetic field [15], which happens at a temperature T_{cr} satisfying $w = 1.8 \xi(T_{cr})$.

Comparing the bulk $H_{c2}(T)$ curve with the $T_c(H)$ boundary for films with an antidot lattice, we clearly see a qualitative difference between the two, caused by the lateral micro-structuring. In the network limit, $T_c(H)$ can be related to the lowest E_{LLL} level in the Hofstadter butterfly [2,31] with pronounced cusps at $n\Phi_0$ and the substructure within each period. Reducing the size of the antidot, we are modifying $T_c(H)$ substantially but the cusps at $n\Phi_0$ are still clearly seen [32].

Finally, by introducing antidot lattices we stabilize the novel flux states, which can be briefly characterized as follows. For relatively large antidots sharp cusp-like magnetization anomalies appear at the matching fields H_m . These anomalies are caused by the formation of the multi-quanta vortex lattices at each subsequent H_m

[33–36]. The multi-quanta vortex lattices make possible a peaceful coexistence of the flux penetration at the antidots and the presence of a substantial superfluid density in the space between them. This leads to a very strong enhancement of the critical current density in films with an antidot lattice. For smaller antidots the vortices are forced to occupy the interstitial positions after the saturation of the pinning sites at antidots [36–38]. This leads to the formation of the novel composite flux-line lattices consisting from the interpenetrating sublattices of weakly pinned interstitial single-quantum vortices and multi-quanta vortices strongly pinned by the antidots. When the interstitial flux-line lattice melts, it forms the interstitial flux-liquid coexisting with the flux solid at the antidots.

V CONCLUSIONS

We have carried out a systematic study of and quantization phenomena in nanostructured superconductors. The main idea of this study was to vary the boundary conditions for confining the superconducting condensate by taking samples of different topology and, through that, to modify the lowest Landau level $E_{LLL}(H)$ and therefore the critical temperature $T_c(H)$. Three different types of samples were used: (i) individual nanostructures (lines, loops, dots), (ii) clusters of nanoscopic elements - 1D clusters of loops and 2D clusters of antidots, and (iii) films with huge regular arrays of antidots (antidot lattices). We have shown that in all these structures, the phase boundary $T_c(H)$ changes dramatically when the confinement topology for the superconducting condensate is varied. The induced $T_c(H)$ variation is very well described by the calculations of $E_{LLL}(H)$ taking into account the imposed boundary conditions. These results convincingly demonstrate that the phase boundary in $T_c(H)$ of nanostructured superconductors differs drastically from that of corresponding bulk materials. Moreover, since, for a known geometry $E_{LLL}(H)$ can be calculated a priori, the superconducting critical parameters, i.e. $T_c(H)$, can be controlled by designing a proper confinement geometry. While the optimization of the superconducting critical parameters has been done mostly by looking for different materials, we now have a unique alternative - to improve the superconducting critical parameters of *the same material* through the optimization of *the confinement topology* for the superconducting condensate and for the penetrating magnetic flux.

ACKNOWLEDGMENTS

The authors would like to thank A. López and V. Fomin for fruitful discussions and R. Jonckheere for the electron beam lithography. We are grateful to the Flemish Fund for Scientific Research (FWO), the Flemish Concerted Action (GOA), the Belgian Inter-University Attraction Poles (IUAP) and the European Human Capital and Mobility (HCM) research programs for the financial support. E. Rosseel is a Research Fellow of the Belgian Interuniversity Institute for Nuclear

Sciences (I.I.K.W.), and L. Van Look of the European project JOVIAL. M. Baert is a Postdoctoral Fellow supported by the Research Council of the K.U.Leuven.

REFERENCES

1. K. Ensslin, and P. M. Petroff, *Phys. Rev. B* **41**, 12307 (1990); H. Fang, R. Zeller, and P. J. Stiles, *Appl. Phys. Lett.* **55**, 1433 (1989); R. Schuster *et al.*, *Phys. Rev. B* **49**, 8510 (1994).
2. B. Pannetier, J. Chaussy, R. Rammal, and J. C. Villegier, *Phys. Rev. Lett.* **53**, 1845 (1984).
3. M. Tinkham, *Phys. Rev.* **129**, 2413 (1963).
4. V. V. Moshchalkov, L. Gielen, C. Strunk, R. Jonckheere, X. Qiu, C. Van Haesendonck, and Y. Bruynseraede, *Nature* **373**, 319 (1995).
5. P. G. de Gennes, *Superconductivity of Metals and Alloys*, Benjamin, New York, 1966.
6. J. Romijn, T. M. Klapwijk, M. J. Renne, and J. E. Mooij, *Phys. Rev. B* **26**, 3648 (1982).
7. H. Welker, and S. B. Bayer, *Akad. Wiss.* **14**, 115 (1938).
8. M. Tinkham, *Introduction to Superconductivity*, McGraw Hill, New York, 1975.
9. W. A. Little, and R. D. Parks, *Phys. Rev. Lett.* **9**, 9 (1962); R. D. Parks, and W. A. Little, *Phys. Rev.* **133**, A97 (1964).
10. R. P. Groff, and R. D. Parks, *Phys. Rev.* **176**, 567 (1968).
11. C. Strunk, V. Bruyndoncx, V. V. Moshchalkov, C. Van Haesendonck, Y. Bruynseraede, and R. Jonckheere, *Phys. Rev. B* **54**, R12701 (1996).
12. P.-G. de Gennes, *C. R. Acad. Sci. Ser. II* **292**, 279 (1981).
13. V. V. Moshchalkov, X. G. Qiu, and V. Bruyndoncx, *Phys. Rev. B* **55**, 11793 (1996).
14. D. Saint-James, *Phys. Lett.* **15**, 13 (1965); O. Buisson, P. Gandit, R. Rammal, Y. Y. Wang, and B. Pannetier, *Phys. Lett. A* **150**, 36 (1990).
15. D. Saint-James, *Phys. Lett.* **16**, 218 (1965).
16. V. V. Moshchalkov, L. Gielen, M. Baert, V. Metlushko, G. Neuttiens, C. Strunk, V. Bruyndoncx, X. Qiu, M. Dhallé, K. Temst, C. Potter, R. Jonckheere, L. Stockman, M. Van Bael, C. Van Haesendonck, and Y. Bruynseraede, *Physica Scripta* **T55**, 168 (1994).
17. R. Benoist, and W. Zwerger, *Z. Phys. B* **103**, 377 (1997).
18. V. Bruyndoncx, C. Strunk, V. V. Moshchalkov, C. Van Haesendonck, and Y. Bruynseraede *Europhys. Lett.* **36**, 449 (1996).
19. S. Alexander, and E. Halevi, *J. Phys. (Paris)* **44**, 805 (1983).
20. C. C. Chi, P. Santhanam, and P. E. Blöchl, *J. Low Temp. Phys.* **88**, 163 (1992).
21. S. Alexander, *Phys. Rev. B* **27**, 2820 (1983).
22. H. J. Fink, A. López, and R. Maynard, *Phys. Rev. B* **26**, 5237 (1982).
23. C. Ammann, P. Erdös, and S. B. Haley, *Phys. Rev. B* **51**, 11739 (1995).
24. J. I. Castro, and A. López, *Phys. Rev. B* **52**, 7495 (1995).
25. R. D. Parks, *Science* **146**, 1429 (1964).
26. J. Simonin, D. Rodrigues, and A. López, *Phys. Rev. Lett.* **49**, 944 (1982).
27. T. Puig, E. Rosseel, M. Baert, M. J. Van Bael, V. V. Moshchalkov, and Y. Bruynseraede, *Appl. Phys. Lett.* **70**, 3155 (1997).
28. B. Pannetier, in *Quantum coherence in mesoscopic systems*, edited by B. Kramer, (Plenum Press, New York, 1991).

29. A. Bezryadin, and B. Pannetier, *J. Low Temp. Phys.* **98**, 251 (1996);
A. Bezryadin *et al.*, *Phys. Rev. B* **51**, 3718 (1995).
30. M. Giroud *et al.*, *J. Low Temp. Phys.* **87**, 683 (1992); H. S. J. van der Zant, *Phys. Rev. B* **50**, 340 (1994).
31. D. R. Hofstadter, *Phys. Rev. B* **14**, 2239 (1976).
32. E. Rosseel, T. Puig, M. J. Van Bael, V. V. Moshchalkov, and Y. Bruynseraede, *to be published in the proceedings of the $M_2S - HTSC - V$ conference*, Beijing, China, 1997.
33. M. Baert, V. V. Metlushko, R. Jonckheere, V. V. Moshchalkov, and Y. Bruynseraede, *Phys. Rev. Lett.* **74**, 3269 (1995).
34. M. Baert, V. V. Metlushko, R. Jonckheere, V. V. Moshchalkov, and Y. Bruynseraede, *Europhys. Lett.* **29**, 157 (1995).
35. V. V. Moshchalkov, M. Baert, V. V. Metlushko, E. Rosseel, M. J. Van Bael, K. Temst, R. Jonckheere, and Y. Bruynseraede, *Phys. Rev. B* **54**, 7385 (1996).
36. A. Bezryadin, and B. Pannetier, *J. Low Temp. Phys.* **102**, 73 (1996).
37. E. Rosseel, M. Van Bael, M. Baert, R. Jonckheere, V. V. Moshchalkov, and Y. Bruynseraede, *Phys. Rev. B* **53**, R2983 (1996).
38. K. Harada, O. Kamimura, H. Kasai, T. Matsuda, A. Tonomura, and V. V. Moshchalkov, *Science* **274**, 1167 (1996).

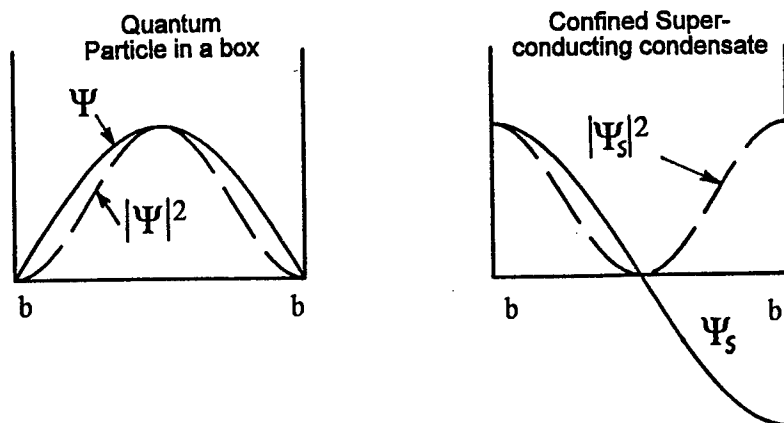


FIGURE 4. Boundary conditions for interfaces normal metal-vacuum and superconductor-vacuum.

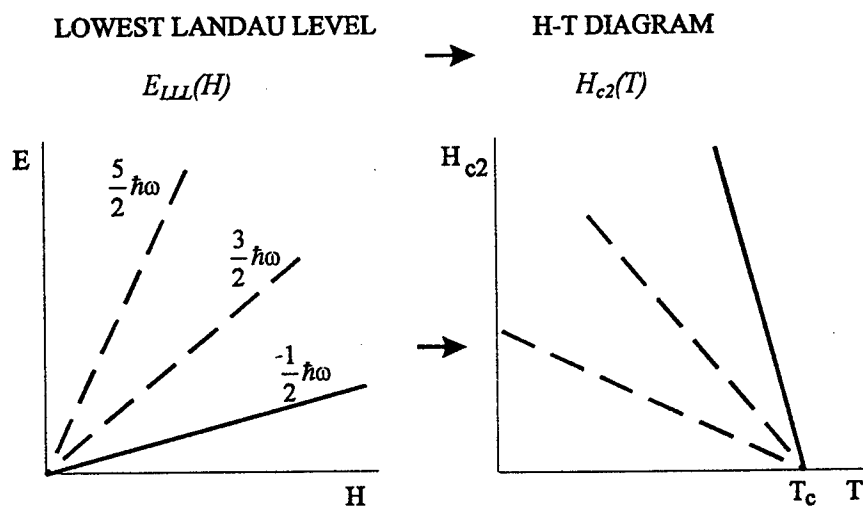


FIGURE 5. Landau level scheme for a particle in a magnetic field. From the lowest Landau level $E_{LLL}(H)$ the second critical field $H_{c2}(T)$ is derived (solid line).

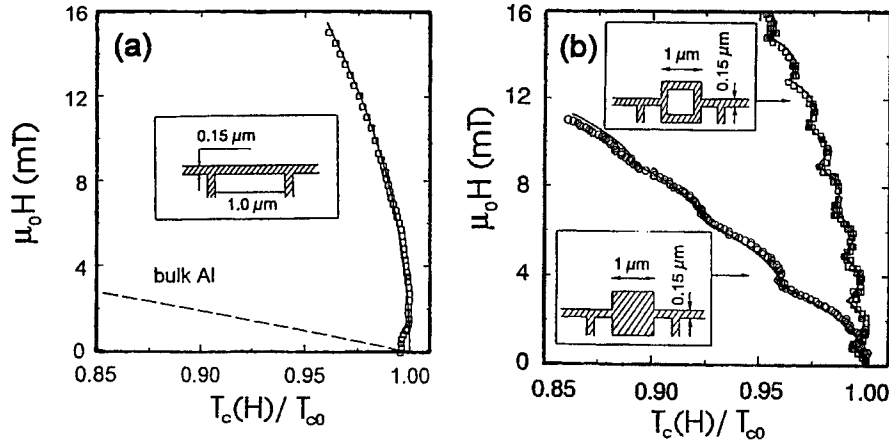


FIGURE 6. The measured superconducting/normal phase boundary as a function of the reduced temperature $T_c(H)/T_{c0}$ for a) the line, and b) the loop and the dot. The solid line in (a) is calculated using Eq. (11) with $\xi(0) = 110 \text{ nm}$ as a fitting parameter. The dashed line represents $T_c(H)$ for bulk Al.

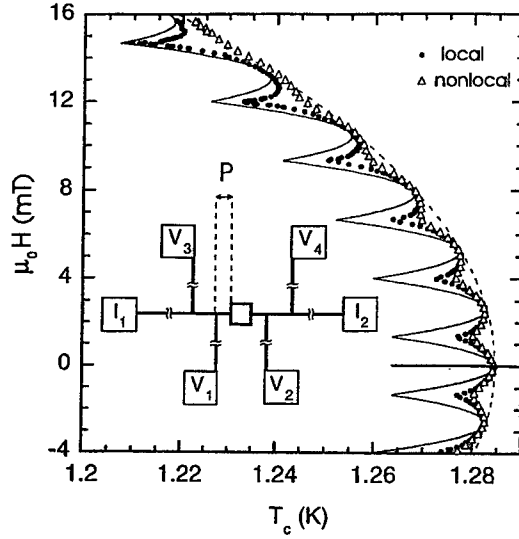


FIGURE 7. Local (V_1/V_2) and nonlocal phase boundaries (V_1/V_3 or V_2/V_4) $T_c(H)$. The measuring current is sent through I_1/I_2 . The solid and dashed lines correspond to the theoretical $T_c(H)$ of an isolated loop and a one-dimensional line, respectively. The inset shows a schematic of the structure, where the distance $P = 0.4 \text{ } \mu\text{m}$.

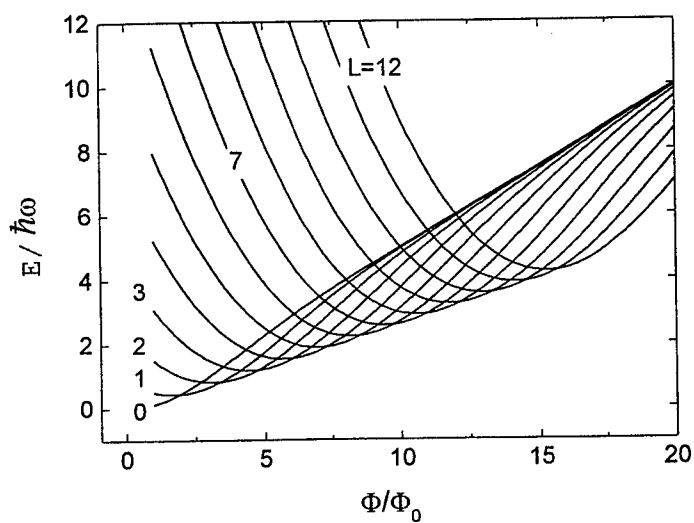


FIGURE 8. Energy level scheme versus normalized flux Φ/Φ_0 for a superconducting cylinder in a parallel magnetic field. The cusp-like $H_{c3}(T)$ line is formed due to the change of the orbital quantum number L .

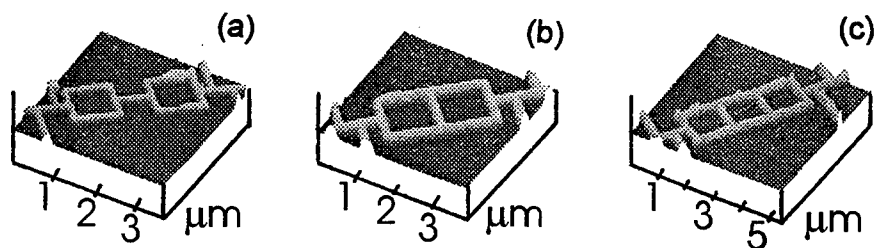


FIGURE 9. AFM micrographs of the studied structures: a) the bola, b) the double loop, and c) the triple loop.

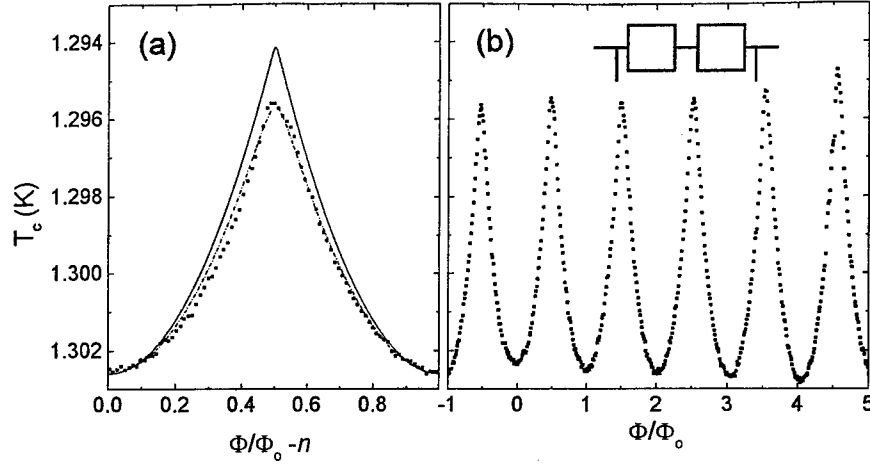


FIGURE 10. Experimental $T_c(\Phi)$ data for the **bola** with the parabolic background (Eq. (11)) subtracted. The dots are the experimental data points, while the lines correspond to the different theoretical results as explained in the text. a) Single period of $T_c(\Phi)$, b) A few periods of the experimental $T_c(\Phi)$ curve.

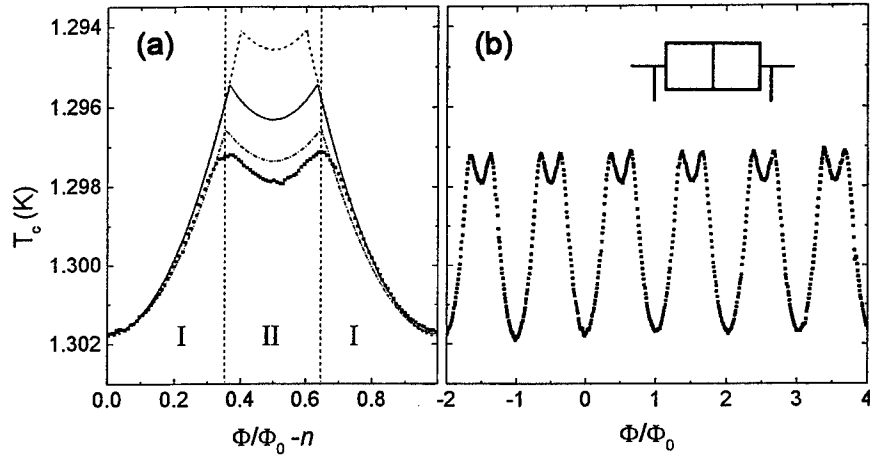


FIGURE 11. Experimental $T_c(\Phi)$ data for the **double loop** with the parabolic background (Eq. (11)) subtracted. The dots are the experimental data points, while the lines correspond to the different theoretical results as explained in the text. a) Single period of $T_c(\Phi)$, b) A few periods of the experimental $T_c(\Phi)$ curve.

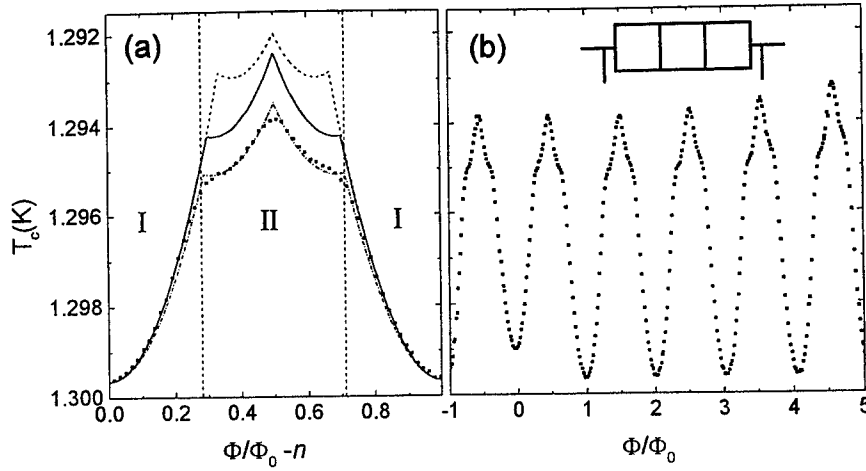


FIGURE 12. Experimental $T_c(\Phi)$ data for the triple loop with the parabolic background (Eq. (11)) subtracted. The dots are the experimental data points, while the lines correspond to the different theoretical results as explained in the text. a) Single period of $T_c(\Phi)$, b) A few periods of the experimental $T_c(\Phi)$ curve.

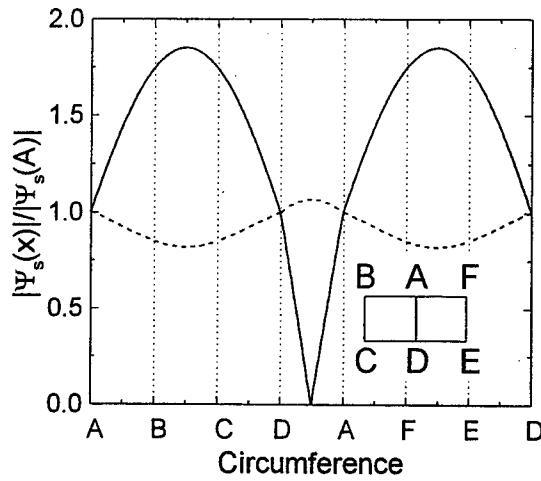


FIGURE 13. Calculated variation of $|\Psi_s|$ along the circumference of the double loop, at the phase boundary ($\Phi/\Phi_0 = 0.36$). The dashed line is the solution with $|\Psi_s|$ nearly spatially constant, while the solid line is the state with a node in the center of the strip connecting points A and D.

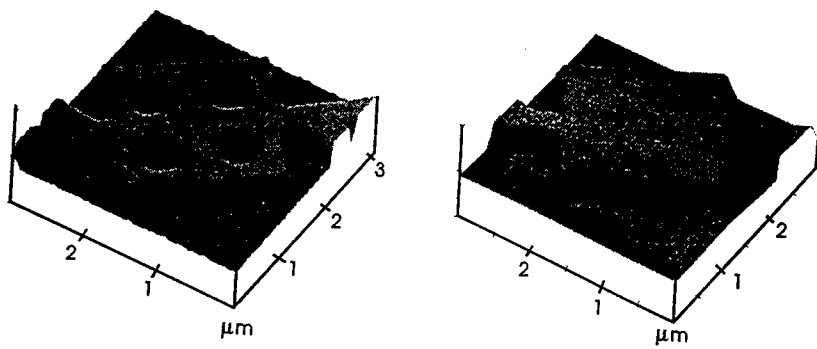


FIGURE 14. AFM image of the Pb/Cu 2×2 antidot cluster (on the left) and of the reference sample (on the right).

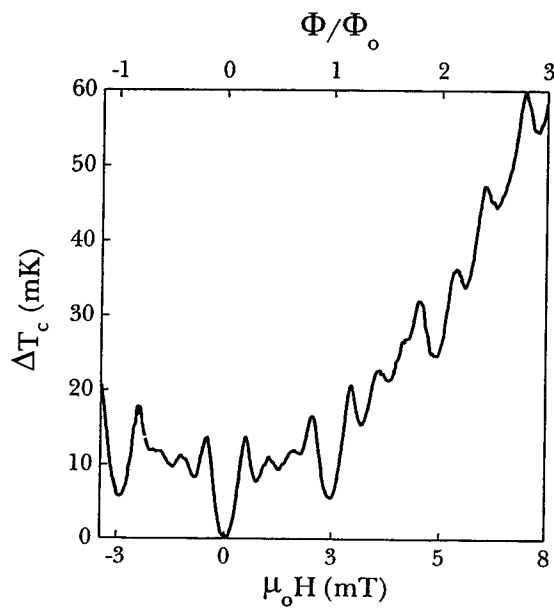


FIGURE 15. Experimental phase boundary, $\Delta T_c(H)$ for the Pb/Cu 2×2 antidot cluster.

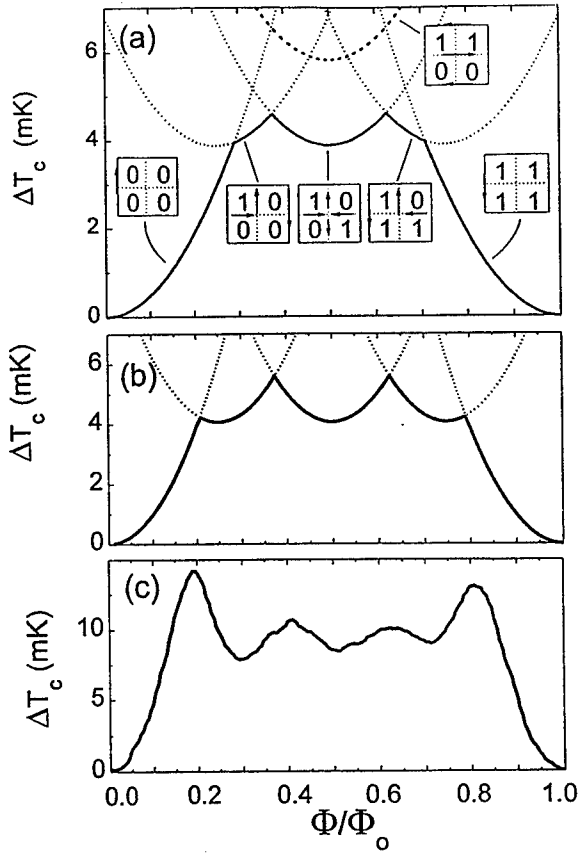


FIGURE 16. (a) Theoretical phase boundary, $T_c(\Phi/\Phi_0)$, calculated in the London limit of the Ginzburg-Landau theory without any fitting parameter (solid line). All possible parabolic solutions are represented by dotted lines. The dashed line indicates the non-stable *parallel* configuration. The schematic representation of the $\{n_i\}$ quantum numbers at the antidots and characteristic current flow patterns for each parabolic branch are also sketched. (b) The $T_c(\Phi/\Phi_0)$ phase boundary, calculated as in Fig. 16a, but with the curvature " γ " of the parabolae taken as a free parameter. The γ -value was increased by a factor of two with respect to its calculated value used in Fig. 16a. (c) First period of the measured phase boundary shown in Fig. 15 after subtraction of the parabolic background.

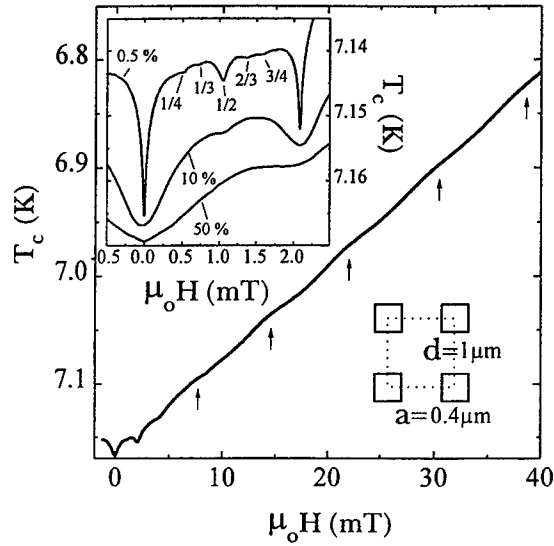


FIGURE 17. Critical field of a Pb(50nm) film measured at 10% R_n , with $d = 1\mu\text{m}$, $a = 0.4\mu\text{m}$. The inset shows a zoom of the first cusp at different criteria 50% R_n , 10% R_n and 0.5% R_n .

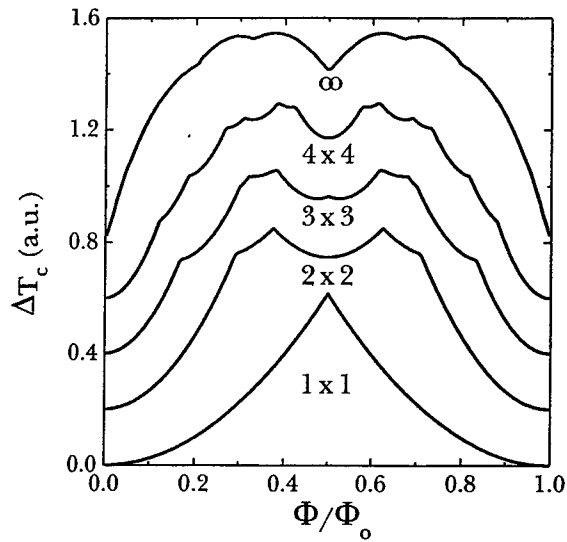


FIGURE 18. Calculations of the first $T_c(H)$ period for an $N \times N$ antidot system ($N = 1, 2, 3, 4, \infty$) in the London limit.

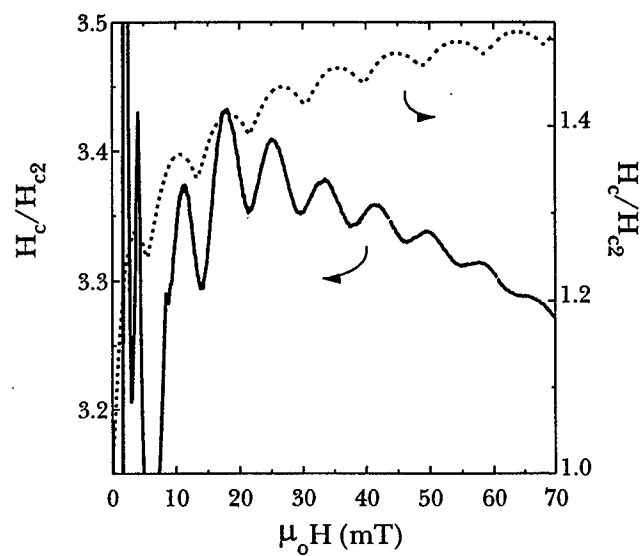


FIGURE 19. The critical field of Fig. 17 normalized by $\Phi_0/2\pi\xi^2(T)$ versus the applied field. The dashed line (right axis) shows the theoretical result for a single circular hole with a radius $R = 0.24 \mu m$.

Vortex unbinding in 2D classical JJ arrays

Petter Minnhagen

*Dept. of Theor. Physics
Umeå University
901 87 Umeå, Sweden.
<minnhagen@tp.umu.se>*

Abstract. Vortices for 2D superfluids are introduced and are described in terms of a 2D Coulomb gas. The 2D classical JJ array is modeled by a 2D XY-model and a mapping between the XY-model and the Coulomb gas is given. The physical properties of a JJ array are then given in terms of the corresponding Coulomb gas properties. First aspects of the Kosterlitz-Thouless vortex unbinding transitions are reviewed. Consequences for the resistance as well as the frequency dependent conductivity are described. Next the vortex unbinding induced by an external current is considered with Consequences for the non-linear IV-characteristics. Finally some effects of a perpendicular magnetic field are discussed in terms of an interplay between free vortices and bound vortex pairs.

I INTRODUCTION

Two-dimensional (2D) classical Josephson junction arrays, superconducting films and ^4He -films are physical realizations of 2D superfluids with the same generic vortex physics. [1] This vortex physics gives characteristic features to the response of the system in certain regions of the parameter space and the present lectures are aiming at describing such characteristic features. We will start by defining what a vortex is and how the vortex physics for the various realizations are related. This will take us to the 2D Coulomb gas model for vortex physics and to a description of the JJ array in terms of the Coulomb gas model. We can roughly think of the vortex physics as the interplay between bound vortex pairs and free vortices. In fact the transition from the superfluid state to the normal state for a 2D superfluid is driven by thermally created vortices: below the transition there are only bound vortex pairs whereas at the transition the pairs start to unbind so that above the transition there are both bond pairs and free vortices present. This is the

Kosterlitz-Thouless transition [2] and consequences for the resistive transition and the complex conductivity will be described. It is possible to induce pair breaking also below the transition by imposing a current. This current induced pair breaking gives rise to a non-linear IV-characteristics where the vortex physics is reflected in the non-linear IV-exponent. Some ideas about this are reviewed together with results from simulations. Another way of inducing free vortices below the transition is by imposing a perpendicular magnetic field. The resulting complex conductivity obtained from numerical simulations is discussed together with an interpretation in terms of free vortices and bound vortex pairs.

II VORTEX

A 2D superfluid can be described in terms of a complex order parameter $\psi(\mathbf{r}) = |\psi(\mathbf{r})|e^{i\theta(\mathbf{r})}$ where \mathbf{r} is the position vector in the 2D plane and $|\psi(\mathbf{r})|^2 = \rho(\mathbf{r})$ is the (areal) mass density of superfluid particles (for a superconductor the superfluid particle is just a Cooper pair). The gradient of the phase $\theta(\mathbf{r})$ is related to the superfluid velocity. The simplest case is the neutral superfluid for which the relation is just

$$\mathbf{v}_s(\mathbf{r}) = \frac{\hbar}{m^*} \nabla \theta(\mathbf{r}) \quad (1)$$

where m^* is the mass of the superfluid particle.

The order parameter has a unique value at each point \mathbf{r} . This means that the value of θ at a point is unique up to a multiple of 2π . Consequently the line integral around a closed loop $\oint \nabla \theta(\mathbf{r}) \cdot d\mathbf{l}$ has likewise to be a multiple of 2π . If the line integral (in the anti-clockwise direction) for an arbitrary small closed loop around the point \mathbf{r}_0 is 2π , then there is an elementary vortex with vorticity $s = 1$ positioned at this point. Since $\psi(\mathbf{r}_0)$ must have a unique value, this means that $|\psi(\mathbf{r})|$ and the density of the superfluid particles $\rho(\mathbf{r})$ has to vanish at \mathbf{r}_0 . Thus an elementary vortex with vorticity $s = 1$ is associated with a point where the order parameter is zero and around which a closed loop integral is 2π . Likewise if the loop integral is -2π there is an elementary vortex of vorticity $s = -1$.

Let us consider a single vortex with vorticity $s = 1$ at the origin. By symmetry $\psi(\mathbf{r})$ only depends on the distance r from the origin so that for any line integral around a circle with radius r we have $2\pi r \nabla \theta(r) = 2\pi$. Consequently $|\nabla \theta(r)| = 1/r$ and the magnitude of superfluid velocity around the vortex center is $v_s(r) = \hbar/(m^*r)$, as inferred from eq.(1). The energy associated with this vortex is the kinetic energy $E_{\text{kin}} = \int dr^2 \rho(r) v_s^2(r)/2$ stored in the mass current around the vortex center. E_{kin} can be estimated by

$$\frac{E_{\text{kin}}}{k_B T} = \frac{\rho_0}{K_B T} \left(\frac{\hbar}{m^*} \right)^2 \frac{1}{2} \int_{r_0}^L 2\pi r dr \frac{1}{r^2} = \frac{1}{T C G} \frac{1}{2} \ln L/r_0$$

where ρ_0 is the mass density in the absence of the vortex, the small distance cut off r_0 reflects the fact that the mass density $\rho(r)$ vanishes as the vortex center is approached, and the large distance cut off L is the linear size of the system. The ratio between the energy for a vortex and the thermal energy $k_B T$ is what appears in the Boltzmann factor and this ratio determines the probability for the spontaneous creation of a vortex at a finite temperature. The parameter T^{CG} where

$$T^{CG} = \frac{k_B T}{2\pi\rho_0(\frac{\hbar}{m^*})^2} \quad (2)$$

can be interpreted as an effective dimensionless temperature for the vortices. [1] The energy for a single vortex obviously diverges with the system size. This means that it is not possible to spontaneously create a single vortex by a thermal fluctuation. However, if we instead consider two vortices of opposite vorticity a distance a from each other then the mass current from the one vortex at a distance larger than of the order of a from its center destructively interferes with the mass current from the other. Consequently the kinetic energy of such a vortex-antivortex pair can be estimated as the kinetic energy of two single vortices where the mass flow vanishes for distances much larger than a . Thus a serves as a large distance cut off so that

$$\frac{E_{\text{kin}}}{k_B T} = \frac{1}{T^{CG}} \ln \frac{a}{r_0} \quad (3)$$

Hence vortex-antivortex pairs can be spontaneously created by thermal fluctuations. Eqs (2) and (3) forms the basis for the Coulomb gas analogy of vortex fluctuations: The potential $V(r)$ outside a charge at the origin is given by Poisson's equation $\nabla^2 V(r) = -2\pi s \delta(\mathbf{r})$ where s is the charge. This gives $\hat{V}(k) = 2\pi/k^2$ which in two dimensions corresponds to a logarithmic interaction. Thus we can interpret $\ln a/r_0$ as the Coulomb energy associated with two particles separated a distance a and with charge $s = 1$ and $s = -1$, respectively. This correspondence between Coulomb gas charges and vortices can be made very precise: [1] The superfluid density $\rho(r)$ vanishes smoothly at the vortex center so that a vortex is characterized by a particular vortex core structure. This means that the corresponding Coulomb particle has a particular single charge distribution given by [3]

$$n_v(r) = s \frac{1}{2\pi r} \frac{d}{dr} \left(\frac{\rho(r)}{\rho_0} \right)$$

where $s = \pm 1$ is the total charge of the Coulomb particle. A general vortex configuration corresponds to a Coulomb charge density

$$n(r) = \sum_i s_i n_v(\mathbf{r} - \mathbf{r}_i)$$

where $s_i(\mathbf{r}_i)$ is the vorticity (position of the center) of vortex i . The kinetic energy of the mass flow corresponding to the vortex configuration is given by the Coulomb self-energy

$$\frac{1}{2} \int \frac{d^2k}{(2\pi)^2} \hat{n}(\mathbf{k}) V(\mathbf{k}) \hat{n}(-\mathbf{k})$$

In addition to the kinetic mass flow energy of a vortex there is an energy associated the depletion of the superfluid density towards zero at the center of a vortex. This energy corresponds to a constant energy E_c for each Coulomb particle. [1]

So far we have discussed the Coulomb gas analogy of vortices for a neutral superfluid. What happens for a charge superfluid like a superconducting film? In this case the flow of the superfluid particles (the Cooper pairs) induces a magnet flux in the 3D space. Each vortex is associated with a flux quantum $\Phi_0 = 2\pi\hbar c/|e^*|$ penetrating the superconducting film perpendicular to the plane of the film. The magnetic flux is largest through the vortex center and falls off from the center on a length scale given by the perpendicular magnetic penetration length

$$\Lambda \equiv \frac{2\lambda^2}{d} = \frac{1}{2\pi} \left(\frac{m^*c}{e^*} \right)^2 \rho_0^{-1}$$

where λ is the usual London penetration length and d is the thickness of the thin film. [4] Λ is typically a macroscopic length and is in practice often larger than the sample size. The only modification caused by the induced magnetic field in the description of Coulomb charge analogy of the vortex is that the Coulomb self-energy for a vortex configuration becomes

$$\frac{1}{2} \int \frac{d^2k}{(2\pi)^2} \hat{n}(\mathbf{k}) \hat{V}_\Lambda(\mathbf{k}) \hat{n}(-\mathbf{k})$$

where the logarithmic Coulomb interaction is replaced by $V_\Lambda(r)$ which is cut off for distances larger than Λ . However, since Λ is in practice a macroscopic length, V_Λ can be replaced by the Coulomb interaction $V(r)$. Consequently, the Coulomb gas analogy of vortex fluctuation for all practical purposes also applies to a 2D superconductor. [1]

III THE COULOMB GAS MODEL

The energy for a neutral ($\sum_i s_i = 0$) configuration of N vortices is in the Coulomb charge analogy given by

$$E_N = NE_c + \frac{1}{2} NU(0) + \frac{1}{2} \sum_{i \neq j} s_i s_j U(r_{ij})$$

$$\begin{aligned}
&= NE_c + \frac{1}{2} \sum_{i \neq j} s_i s_j (U(r_{ij}) - U(0)) \\
&\approx NE_c - \frac{1}{2} \sum_{i \neq j} s_i s_j \ln \frac{r_{ij}}{r_0}
\end{aligned}$$

where $\hat{U}(\mathbf{k}) = \hat{n}_v(\mathbf{k})\hat{V}(\mathbf{k})\hat{n}_v(-\mathbf{k})$ is the effective particle interaction and $\frac{1}{2}U(0) \approx \ln L/r_0$ is the self-energy for a particle which diverges with the size of the system L . The probability for the occurrence of a vortex configuration is given by the Boltzmann factor $\exp(-E_N/T^{CG})$. Non-neutral configurations have vanishing probability since $E_N \propto U(0) \sum_i s_i$ which for a non-neutral configuration diverges with the system size. The grand partition function for vortex fluctuations is consequently given by the corresponding one for a neutral Coulomb gas

$$Z = \sum_{N=0}^{\infty} \frac{(e^{-E_c/T^{CG}})^N}{(\frac{N}{2})!(\frac{N}{2})!} \prod_i \frac{\int d^2 r_i}{\Delta} e^{-\frac{1}{T^{CG}} \sum_{i \neq j} s_i s_j (U(r_{ij}) - U(0))} \quad (4)$$

where Δ is the phase space division of a particle. This phase space division is related to the size of the particle so that $\Delta \propto r_0^2$.

For a superconducting film it is often the case that a phenomenological Ginzburg-Landau (GL) description applies to good approximation. In this case the Coulomb gas analogy of vortex fluctuations turns into the specific Ginzburg-Landau Coulomb gas (GLCG) model where E_c and $U(r)$ are unique. The extension of the vortex core is given by the GL coherence length ξ i.e. $r_0 = \xi$. In this case the vortex properties are only a function of the two variables T^{CG} and ξ so that all sample specific properties are absorbed into these two effective variables. [1]

Static thermodynamic properties caused by the vortex fluctuations are obtainable from the Coulomb gas partition function Z . A particularly important quantity is the charge density correlation function

$$\hat{g}(k) = \frac{1}{\Omega} \langle \hat{n}(\mathbf{k}) \hat{n}(-\mathbf{k}) \rangle$$

where Ω is the (2D) volume and $\langle \rangle$ denotes the thermal average. The charge density correlation function is in turn related to the static dielectric function $\hat{\epsilon}(\mathbf{k})$ by

$$\frac{1}{\hat{\epsilon}(k)} = 1 - \frac{\hat{V}(k)}{T^{CG}} \hat{g}(k) \quad (5)$$

In the absence of vortex fluctuations the superfluid density is given by $\rho_0(T)$ which is in general temperature dependent. The vortex fluctuations renormalize ρ_0 into [5,6]

$$\rho = \frac{\rho_0}{\hat{\epsilon}(k=0)}$$

and the phase transition from the superconducting state $\rho > 0$ to the normal state $\rho = 0$ consequently corresponds to a Coulomb gas transition from a $1/\hat{\epsilon}(k=0) > 0$ phase to a $1/\hat{\epsilon}(k=0) = 0$ phase.

The vortex fluctuations also cause dynamical effects on the properties of the superconductor caused by the motion of the vortices. This motion can for a superconducting film often to good approximation be described by a Langevin equation of the form [7]

$$\frac{d\mathbf{r}(t)}{dt} = \frac{D}{T_{CG}} \mathbf{F}_{\text{tot}} + \eta(t) \quad (6)$$

where $\mathbf{r}(t)$ is the position of a vortex, \mathbf{F}_{tot} is the total force acting on it, D is a vortex diffusion constant, and $\eta(t)$ is a random force obeying

$$\langle \eta^\alpha(t) \eta^\beta(t') \rangle = 2D \delta_{\alpha\beta} \delta(t - t')$$

where α and β denote Cartesian coordinates. Consequently both the static and dynamic properties of the vortex fluctuations can be obtained within a Coulomb gas analogy. In particular the complex conductivity $\sigma(\omega)$ for the superconductor is given by $\sigma(\omega) = \left(\frac{e^*}{m^*}\right)^2 \rho_0 \tilde{\sigma}(\omega)$ where [7,1]

$$\tilde{\sigma}(\omega) = -\frac{1}{i\omega \hat{\epsilon}(0, \omega)} \quad (7)$$

Here $\hat{\epsilon}(\mathbf{k}, \omega)$ is the \mathbf{k} and ω dependent complex dielectric function.

IV XY-MODEL

Let us discretize the order parameter $\psi(\mathbf{r})$ by putting it on a lattice (for convenience a square lattice). The discretized version is then $\psi_j = |\psi_j| e^{i\theta_j}$ where the index j denotes the lattice points. We simplify further by neglecting the variations of the magnitude of the order parameter and take $|\psi_j| = |\psi|$ to be a constant. The energy for a superconductor is given by (compare section 2)

$$2\pi \left(\frac{\hbar}{m^*}\right)^2 \rho_0 \int d^2r \frac{(\nabla \theta(\mathbf{r}))^2}{2}$$

In the discretized version this energy takes the form

$$H_{XY} = J \sum_{\langle ij \rangle} U(\Phi_{ij} = \theta_i - \theta_j) \quad (8)$$

where $J = 2\pi(\frac{\hbar}{m^*})^2|\psi|^2$ and the sum is over nearest-neighbour pairs. The lattice constant is taken to be one so that $\Phi_{ij} = \theta_i - \theta_j$ corresponds to $\nabla\theta$. The function $U(\Phi)$ has to be equal to $\Phi^2/2$ for small Φ in order to yield the correct continuum limit and in addition $U(\Phi)$ has to be a periodic function of 2π since the phase angle θ_i for each lattice point is only defined up to a multiple of 2π . A possible choice for $U(\Phi)$ is

$$U(\Phi) = 1 - \cos(\Phi)$$

With this particular choice the model becomes the usual 2D XY-model or the planar rotator model. This form of the interaction would *e.g.* arise if each lattice point was a small superconducting island which was Josephson coupled to its nearest-neighbours. In this sense the 2D XY-model is an approximate model for a JJ array. The coupling energy for a Josephson junction is $\frac{\hbar}{2e}i_c(T)$, where i_c is the critical current of the junction, so the XY-coupling can also be expressed as $J = \frac{\hbar}{2e}i_c(T)$.

However, from the point of view of vortex fluctuations any $U(\Phi)$ fulfilling the necessary requirements stipulated above will do. For example the sequence

$$U(\Phi) = \frac{2}{p^2} \left[1 - \cos^{2p^2}\left(\frac{\Phi}{2}\right) \right] \quad (9)$$

will do for any value $p \geq 1$ where $p = 1$ corresponds to the usual XY-model. The practical point with such a flexibility is that the vortex density increases with increasing p . [8] Since the characteristic of vortex fluctuations depends on the vortex density, it may well be the case that the vortex characteristic for a particular JJ array is better described by an XY-model with a $p \neq 1$.

The resistively shunted Josephson(RSJ)-model is a dynamical version of the Josephson junction coupled array which from the point of view of the vortices corresponds to the Coulomb gas with Langevin dynamics. Another possible dynamics is a Langevin equation for the phase at each lattice point sometimes termed a TDGL(time-dependent Ginzburg-Landau)-type dynamics

$$\frac{d\theta_i(t)}{dt} = -\Gamma \frac{\partial H_{XY}}{\partial \theta_i} + \eta_i(t) \quad (10)$$

where Γ is a constant which determines the relaxation and $\eta_i(t)$ is a fluctuating noise associated with each lattice point such that

$$\langle \eta_i(t) \eta_j(t') \rangle = \Gamma T \delta(t - t')$$

This dynamics is easier to numerically simulate than the full RSJ-dynamics. The basic feature of the vortex dynamics is believed to be very similar for these two types of dynamics. [9]

The discrete XY-model can be mapped to the Coulomb gas model just as the continuum model in the preceding section. The closest mapping is obtained by

observing that $U' = \frac{\partial U(\Phi)}{\partial \Phi}$ corresponds to $\nabla \Phi$. [10] More precisely $\rho_0 \propto \langle U'' \rangle$ so that the Coulomb gas temperature is given by

$$T^{CG} = T/[2\pi J \langle U'' \rangle]$$

and the Coulomb gas charge n_l , corresponding to the elementary plaquette l , is given by the directed sum (corresponding to a line integral) over the four links $\langle ij \rangle$ making up the square [10]

$$n_l \equiv \frac{T^{CG}}{T} \sum_{\langle ij \rangle \in l} U'.$$

This means that the Coulomb gas particle corresponding to a vortex has a charge which is spread over several lattice spacings.

The dielectric function is given by

$$\text{Re} \left[\frac{1}{\hat{\epsilon}(k, \omega)} \right] = \frac{1}{\hat{\epsilon}(k, 0)} + \frac{2\pi\omega T^{CG}}{T^2} \int_0^\infty dt \sin \omega t \hat{G}(k, t) \quad (11)$$

$$\text{Im} \left[\frac{1}{\hat{\epsilon}(k, \omega)} \right] = -\frac{2\pi\omega T^{CG}}{T^2} \int_0^\infty dt \cos \omega t \hat{G}(k, t) \quad (12)$$

where

$$\frac{1}{\hat{\epsilon}(k, 0)} = 1 - \frac{2\pi T^{CG}}{T^2} \hat{G}(k, 0)$$

and $\hat{G}(k, t)$ is related to the charge density correlation function $g(r, t) = \frac{1}{\Omega} \langle n(r, t) n(0, 0) \rangle$ by

$$\hat{G}(k, t) \equiv \left(\frac{T}{T^{CG}} \right)^2 \frac{\hat{g}(k, t)}{k^2}$$

For the lattice models $\hat{G}(k, t)$ is given by [11]

$$\hat{G}(k, t) = \frac{1}{\Omega} \langle \hat{F}(\mathbf{k}, t) \hat{F}(-\mathbf{k}, t) \rangle$$

where $\hat{F}(\mathbf{k})$ is the 1D Fourier transform

$$\hat{F}(k, t) = \sum_m F_m e^{ikm},$$

m labels the rows of the lattice, and finally

$$F_m(t) = \sum_{\langle ij \rangle \in m} U'(\Phi_{ij}(t))$$

where the sum is over all the links making up the row m .

V VORTEX UNBINDING

The phase transition for the 2D Coulomb gas is reflected in the static dielectric function as follows: For small k one has [1]

$$\frac{1}{\hat{\epsilon}(k)} = \frac{1}{\tilde{\epsilon}} \frac{k^2}{k^2 + \lambda_s^{-2}}$$

where λ_s is the screening length caused by free charges. The condition for the high (low) temperature phase is $1/\hat{\epsilon}(0) = 0 (> 0)$ (see section 3). Thus λ_s is finite (infinite) in the high (low) temperature phase *i.e.* free charges are present (not present) in the high (low) temperature phase. In this sense the low temperature phase only contains bound dipole pairs and the phase transition can be interpreted as a charge unbinding transition. In the low temperature phase we have $1/\hat{\epsilon}(0) = 1/\tilde{\epsilon}$ and $\tilde{\epsilon}$ can be interpreted in terms of the polarization due to bound dipole pairs.

The charge density correlation function is given by

$$g(r) = -2\langle n^+(r)n^-(0) \rangle + \langle n^+(r)n^+(0) \rangle + \langle n^-(r)n^-(0) \rangle$$

where $n^\pm(-)(\mathbf{r})$ is the particle density for positive (negative) charges at a point \mathbf{r} . The energy needed to create a pair of opposite (equal) charges separated a distance r is $2E_c + U(0) - (+)U(r)$ in the absence of all other particles so that $\langle n^+(r)n^-(0) \rangle \propto \exp[(2E_c + U(0) - U(r))/T^{CG}]$ and similarly for equal charges. The presence of the other particles can approximately be taken into account by replacing $U(0)$ with the linear screened interaction $\tilde{U}_L(\mathbf{k}) = \tilde{U}(\mathbf{k})/\hat{\epsilon}(\mathbf{k})$. Thus $g(r)$ can be approximated by [12,13]

$$g(r) = -2\Delta^{-2}e^{-2E_c/T^{CG}} 2e^{\frac{1}{\tilde{\epsilon}\tilde{r}\tilde{c}\tilde{\sigma}}[U_L(r)-U_L(0)]} \left[1 - e^{-\frac{2}{\tilde{\epsilon}\tilde{r}\tilde{c}\tilde{\sigma}}U_L(r)}\right] \quad (13)$$

Below the phase transition the screening length vanishes and eq.(13) reduces to (since $U_L(r) - U_L(0) \approx \frac{1}{\tilde{\epsilon}} \ln r/r_0$ and $U_L(0) = \infty$)

$$g(r) \propto -e^{\frac{1}{\tilde{\epsilon}\tilde{r}\tilde{c}\tilde{\sigma}} \ln r/r_0} \propto \left(\frac{r_0}{r}\right)^{\frac{1}{\tilde{\epsilon}}} \quad (14)$$

Thus the correlations fall off like power laws in the low temperature phase. From eqs.(5) and (14) we get the connection

$$\frac{1}{\hat{\epsilon}(0)} = 1 + \frac{\pi^2}{T^{CG}} \int_0^\infty dr'(r')^3 g(r') \approx 1 - |const| \int_0^\infty dr'(r')^{3-\frac{1}{\tilde{\epsilon}\tilde{r}\tilde{c}\tilde{\sigma}}}$$

The last integral diverges for large r if $T^{CG} > 1/4\tilde{\epsilon}$ and consequently the low temperature phase requires $T^{CG} < 1/4\tilde{\epsilon}$. The phase transition at $T_c^{CG} = 1/4\tilde{\epsilon}$ is the Kosterlitz-Thouless (KT) transition [2,1] and the critical behaviour can

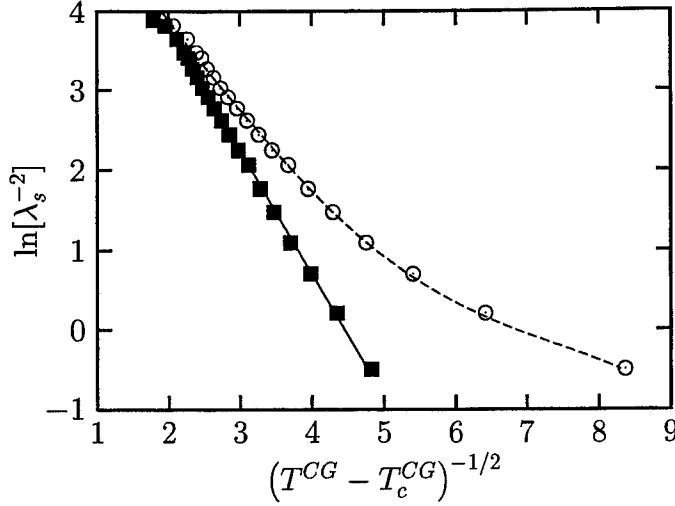


FIGURE 1. Comparison between simulations of the 2D Coulomb gas and the critical behaviour of λ_s in eq.(15): the data for λ_s^{-2} (open circles) should fall on straight line for small enough values of λ_s^{-2} or equivalently large enough values of $(T^{CG} - T_c^{CG})^{-1/2}$. However, the values of λ_s^{-2} reached in the simulations are not small enough to be within the critical region. If T_c^{CG} is treated as a free parameter then the data can be made to fall on a straight line as is demonstrated by the solid squares, but this is a spurious feature and does not represent the true critical behaviour. (From ref. [16].)

be obtained from Kosterlitz renormalization group equations. [14] In particular λ_s diverges as

$$\lambda_s \propto e^{\frac{\text{const}}{\sqrt{T^{CG} - T_c^{CG}}}} \quad (15)$$

when T^{CG} approaches the transition from above.

Eqs (13) and (5) together with $\hat{U}_L(k) = \hat{U}(k)/\hat{\epsilon}(k)$ form a self-consistent set of equations which can be solved numerically. [12,13] From these equations the width of the critical region can be estimated and this width is found to be extremely narrow ($0.95 < T^{CG}/T_c^{CG} < 1.05$) [15] which makes the critical properties very hard (if not impossible) to observe in real systems like JJ arrays. For example to be inside the critical region λ/r_0 has to be larger than of the order of 200. If r_0 is given by the lattice distance this implies scales corresponding to 200 junctions. Such scales are usually in practice masked by other length scale effects coming from *i.e.* finite sample size, finite Λ , as well as tiny but non-vanishing currents and magnetic fields. [1]

Figure 1 illustrates the divergence of λ_s at the KT transition obtained from simulations for the 2D Coulomb gas: [16] $\ln \lambda_s^{-2}$ is plotted against $1/\sqrt{T^{CG} - T_c^{CG}}$ and the data (filled dots) should according to eq. (15) fall on a straight line for large $1/\sqrt{T^{CG} - T_c^{CG}}$. This critical behaviour is not reached in the simulations. However, one may note that if T_c^{CG} was used as a free parameter (instead of being independently determined) then lowering it by 13% would bring the data for $\ln \lambda_s^{-2}$ in fig. 1 on a straight line (open circles). The flux flow resistance R is proportional to the density of free vortices, n_F , which is proportional to λ_s^{-2} , so experimentally one measures R . [1] Since it is often in practice hard to determine T_c^{CG} with the required precision, T_c^{CG} is often used as a free parameter when analyzing resistance data. A straight line like the one obtained in fig. 1 is then taken as evidence of a critical KT-behaviour. As demonstrated by the example in fig. 1, this is usually not the correct conclusion. Nevertheless, the resistive drop at the transition can often be tied to the vortex-unbinding scenario through the GLCG-model. This connection manifestate itself in the existence of a unique resistance scaling curve for samples which are describable within the GL-phenomenology. [1]

The interplay between bound pairs and free vortices is also reflected in the complex conductivity $\sigma(\omega)$ which is proportional to $i/\omega\hat{\epsilon}(0,\omega)$ (compare eq.(7)). The diffusion of free vortices give rise to a usual Drude form of the vortex response

$$Re\left(\frac{1}{\hat{\epsilon}(0,\omega)}\right) = \frac{\omega^2}{\omega^2 + \sigma_0^2} \quad (16)$$

$$Im\left(\frac{1}{\hat{\epsilon}(0,\omega)}\right) = -\frac{\sigma_0\omega}{\omega^2 + \sigma_0^2} \quad (17)$$

where $\sigma_0 = D/\lambda_s^2$ is the corresponding Coulomb gas conductivity at zero frequency. However, when the bound vortex pairs dominate the response it is instead well described by the response function [1,17,11,16]

$$Re\left(\frac{1}{\hat{\epsilon}(0,\omega)}\right) = \frac{1}{\tilde{\epsilon}} \frac{\omega_0}{\omega + \omega_0} \quad (18)$$

$$Im\left(\frac{1}{\hat{\epsilon}(0,\omega)}\right) = -\frac{1}{\tilde{\epsilon}} \frac{2}{\pi} \frac{\omega\omega_0 \ln \omega/\omega_0}{\omega^2 - \omega_0^2} \quad (19)$$

where ω_0 is a characteristic frequency which decreases with decreasing temperature and vanishes at the transition. Thus, as the temperature is increased from the transition, the response gradually crosses over from a bound pair dominated response to a free particle response because the vortex unbinding

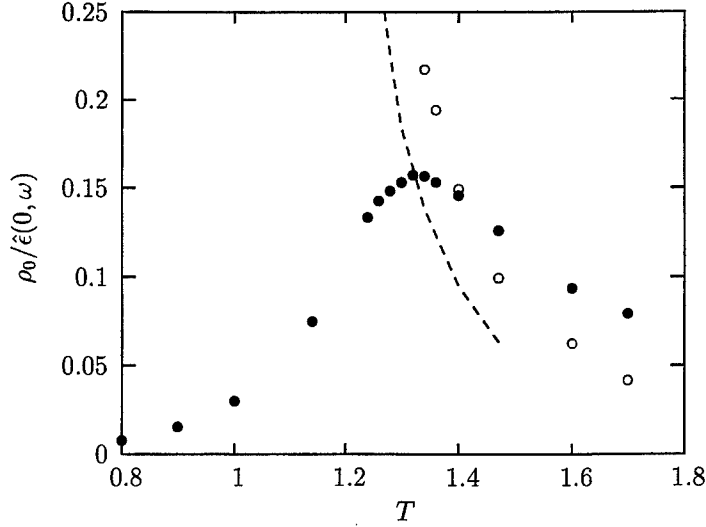


FIGURE 2. Demonstration of the peak ratio $2/\pi$ for the response function $1/\hat{\epsilon}(0, \omega)$ obtained from simulations for a 2D XY-model with TDGL dynamics. The figure shows the real part (open circles) and absolute value of the imaginary part (filled circles) of $\rho_0/\hat{\epsilon}(0, \omega)$ for a fixed frequency ω as a function of the "real" temperature T . The broken curve is $2/\pi$ times the real part and cuts the imaginary part precisely at the maximum. (From ref. [11].)

causes the proportion of free particles to gradually increase relative to the bound vortex pairs. A manifestation of this vortex unbinding effect is contained in the peak ratio (PR) where $PR = |Im(1/\hat{\epsilon}(0, \omega_{\max})/Re(1/\hat{\epsilon}(0, \omega_{\max}))|$ and ω_{\max} is the frequency for which $|Im(1/\hat{\epsilon}(0, \omega)|$ has a maximum. For the free particle response this ration is 1 whereas it is $2/\pi$ for the vortex pair response. Figure 2 shows a simulation for a 2D XY-model for a fixed ω as a

function of "real" temperature T : [11] the imaginary part has a maximum for a certain T and, as seen from eqs (19) and (17), this maximum corresponds to $\omega/\omega_0(T) = 1$ ($\omega/\sigma_0(T) = 1$) for pair (free particle) dominated response. This means that at the T , corresponding to the maximum as a function of T for fixed ω , we have $\omega_{\max} = \omega$. The example in fig. 2 corresponds to $PR = 2/\pi$ which means that at this ω the peak in T occurs at a T which is close enough to the transition for the pairs to completely dominate the response. A higher ω moves the peak to a higher T where the proportion of free vortices is higher and consequently the peak ratio becomes larger, *i.e.* the peak ratio increases from $2/\pi$ towards 1 with increasing ω as a consequence of the vortex unbinding. [11]

VI IV-CHARACTERISTICS

A finite applied current I gives rise to a Lorentz force proportional to I which corresponds to an applied electric field \mathcal{E} in the Coulomb gas analogy. This Lorentz force induces vortex unbinding. The energy associated with a pair, as a function of separation r , can then be estimated (in the Coulomb language) with $E(r) = \frac{1}{\epsilon} \ln r/r_0 - \frac{1}{\epsilon} \mathcal{E}r$ which has a maximum at $r_{\max} = \mathcal{E}^{-1} \propto I^{-1}$. For separations larger than r_{\max} the Lorentz force wins and the pair unbinds. The pair breaking rate may then be estimated as an escape over barrier rate *i.e.* [7]

$$\Gamma_+ \propto e^{-\frac{1}{\epsilon T^{CG}} \ln r_{\max}/r_0} \propto \mathcal{E}^{\frac{1}{\epsilon T^{CG}}}$$

If we assume a simple two particle recombination process then the recombination rate Γ_- goes as the square of the density of free vortices n_F and the steady state condition $\Gamma_+ = \Gamma_-$ implies $n_F \propto \Gamma_+^{\frac{1}{2}} \propto \mathcal{E}^{\frac{1}{2\epsilon T^{CG}}}$. The voltage between two points in a superconductor is just proportional to the flow of flux quanta passing between the points or, in other words, the voltage is proportional to the current of Coulomb gas charges I_{CG} . The velocity of a vortex is proportional to the force acting on it. Thus the contribution from the free vortices to I_{CG} is proportional to $\mathcal{E} \mathcal{E}^{\frac{1}{2\epsilon T^{CG}}}$ so that $V \propto I^a$ where the exponent a is given by $a = \frac{1}{2\epsilon T^{CG}} + 1$. [7] Figure 3 shows the result from simulations of the 2D Coulomb gas for fixed particle density n_p . [16] The data for a does not fall on the line $a = \frac{1}{2\epsilon T^{CG}} + 1$ but on the line $a = \frac{1}{\epsilon T^{CG}} - 1$. A heuristic argument for the exponent found in fig. 3 considers the stretching of a pair to the breaking point at r_{\max} . [18]

At the moment a pair breaks it has already contributed to the transport of Coulomb gas charge over the length r_{\max} so that the corresponding contribution to the Coulomb gas current I_{CG} is proportional to $r_{\max} \Gamma_+ \propto \mathcal{E}^{-1} \mathcal{E}^{\frac{1}{\epsilon T^{CG}}} = \mathcal{E}^{\frac{1}{\epsilon T^{CG}} - 1}$ *i.e.* $a = \frac{1}{\epsilon T^{CG}} - 1$ in agreement with fig. 3. [18,19] The simulations also suggests that $I_{CG} \propto n_p^b$ for small n_p where the exponent b is approximately $1 - (2 + 5.1\epsilon T^{CG})^{-1}$. [20] Since Γ_+ is expected to be proportional to n_p in a canonical ensemble, the pair stretching mechanism ($\propto \Gamma_+$) suggests $b = 1$ whereas the free particle mechanism ($\propto \Gamma_+^{\frac{1}{2}}$) suggests $b = 1/2$. The exponent b found in the simulations falls between these two values and depends on T^{CG} . This points towards a somewhat more involved connection between the induced vortex unbinding and the IV exponent.

Precisely at the KT transition condition $1/\epsilon T^{CG} = 4$, the data in fig. 3 as well as the two exponents $a = \frac{1}{2\epsilon T^{CG}} + 1$ and $a = \frac{1}{\epsilon T^{CG}} - 1$ agree on the value $a=3$. This value is also obtained from a dynamical scaling argument which links the exponent a to the dynamical critical exponent z through the relation $a = 1 + z$. [21] For conventional relaxation type dynamics one expects $z = 2$ which gives $a = 3$. Thus the result that $a = 3$ precisely at the KT transition seems to be particularly robust.

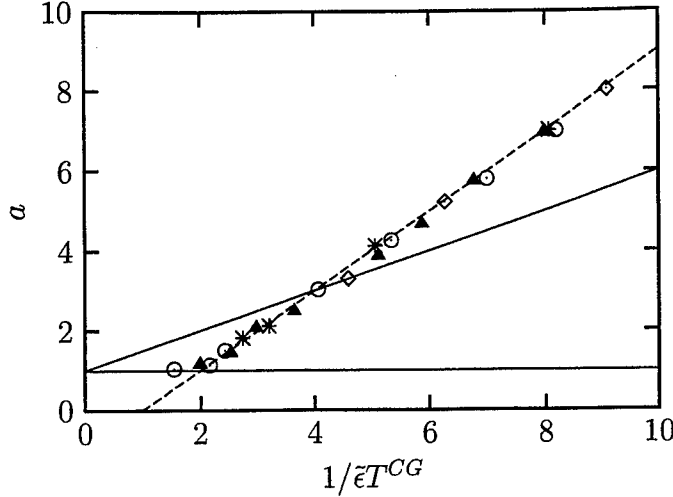


FIGURE 3. The non-linear IV exponent a obtained from simulations of the 2D Coulomb gas model with Langevin dynamics. The data points are for four different densities n_p and are plotted against $1/(\epsilon T^{CG})$. The broken straight line is $a = \frac{1}{\epsilon T^{CG}\sigma} - 1$ whereas the full drawn straight line is the AHNS prediction $a = \frac{1}{2\epsilon T^{CG}\sigma} + 1$. The data clearly suggest $a = \frac{1}{\epsilon T^{CG}\sigma} - 1$. (From ref. [16].)

VII EFFECT OF FRUSTRATION

Applying a magnetic field perpendicular to the JJ array gives another way of changing the proportion between bound vortex pairs and free vortices. Since each vortex is associated with an elementary flux Φ_0 , the magnetic field corresponds to an induced density of vortices f/p where f is the frustration defined as the magnetic flux per elementary plaquette of the JJ array imposed by the applied magnetic field and p is the area of the plaquette. Let us focus on the low temperature phase where, for $f = 0$, there are only bound vortex pairs. Let us further choose the temperature T so low that there are in fact very few bound pairs present but where T is still higher than the melting of the flux lattice formed by a small applied magnetic field.

For a small frustration we expect, at such a T , to get a response dominated by the free vortices which are induced by the magnetic field. Figure 4 shows a simulation for the XY-model (with TDGL dynamics) in this situation and as seen the response is indeed of the Drude form given by eqs (16) and (17) with $PR=1$. [22] What happens as the frustration is increased? First of all the T^{CG} increases with increasing f because the "bare" superfluid density ρ_0

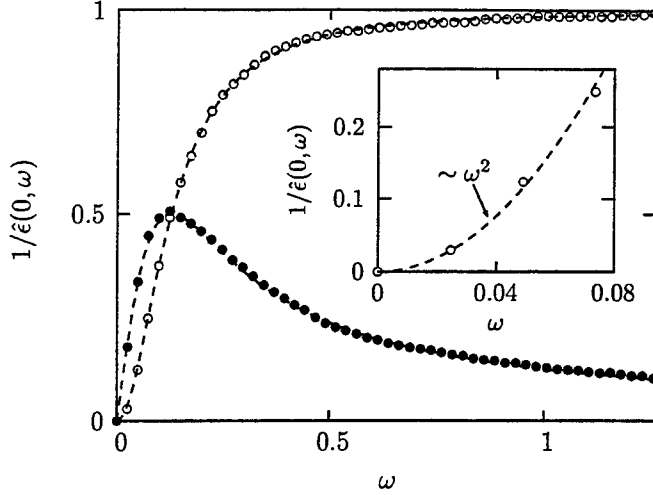


FIGURE 4. The dielectric function $1/\tilde{\epsilon}(0, \omega)$ obtained from TDGL-simulations of the XY-model on a triangular lattice with $f = 1/64$ and $T^{CG} = T_c^{CG}/3$. The open circles correspond to $\text{Re}[1/\tilde{\epsilon}]$ and the filled circles $|\text{Im}[1/\tilde{\epsilon}]|$. The broken curves are a fit to the Drude form given by eqs (16) and (17). The inset shows that the leading behaviour of $\text{Re}[1/\tilde{\epsilon}]$ for small ω is proportional to ω^2 . (From ref. [22].)

Reprinted with kind permission of Elsevier Science - NL, Sara Burgerhartstraat 25, 1055 KV Amsterdam, The Netherlands.

decreases with f . A larger T^{CG} means more vortex pair fluctuations which makes the response more pair like. However, the simulations suggests that there is something more striking: even if the simulations are done at a constant T^{CG} there is a dramatic cross over to a pair like response with increasing f . This is illustrated in fig. 5 which shows the same simulation as in fig. 4 for the same T^{CG} but at a higher frustration. As seen the response is now very pair like and well described by eqs (18) and (19) with $\text{PR} \approx 2/\pi$. [22] Thus the simulations suggest that an increasing f induces more vortex pair correlations which pushes the response towards the pair like one.

VIII FINAL REMARKS

We have discussed effects of vortex pair unbinding caused by changing the temperature T , the externally imposed current I and the frustration f . Some of these effects are directly accessible to experiments like the peak ratio related to the complex conductivity described in connection with fig. 2 [11,17] and similarly the f -dependence of the complex conductivity $\sigma(\omega)$ discussed in connection with figs 4 and 5. [11,22,23] Other effects should in practice be

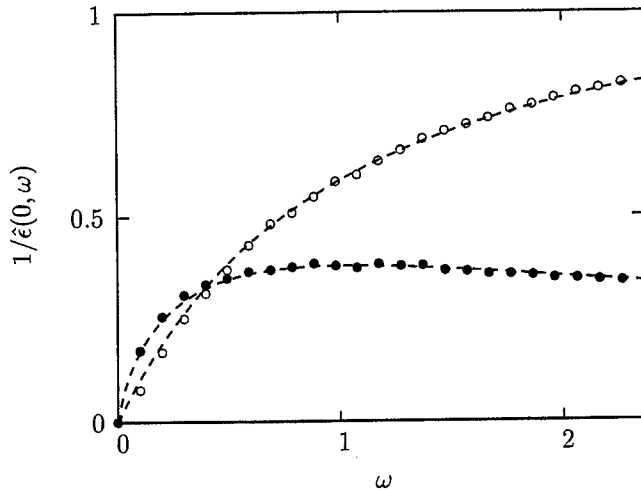


FIGURE 5. Same simulations as in fig. 4 but at a larger $f = 1/8$. The broken c curves are a fit to the bound pair response form given by eqs (18) and (19). (From ref. [22].)

Reprinted with kind permission of Elsevier Science - NL, Sara Burgerhartstraat 25, 1055 KV Amsterdam, The Netherlands.

extremely hard (if not impossible) to observe like the KT critical behaviour for the resistance described in connection with fig. 1. Some requires that the Coulomb gas temperature T^{CG} can be determined as a function of T like in the expressions for the non-linear IV characteristics discussed in connection with fig. 3. This is also possible since $T^{CG} \propto 1/\rho_0(T)$ and $Im(\omega\sigma(\omega) \propto \rho_0/\hat{\epsilon}(0, \omega))$ and $\sigma(\omega)$ can be measured. [23]

So to sum up there are many aspects of vortex pair unbinding in connection with JJ arrays. A lot has been done so far, but quite a lot is not yet well understood in particular concerning the dynamical aspects of vortex unbinding. So here is work remaining for the future and much more information can no doubt be obtained from experiments and simulations.

REFERENCES

1. For a more detailed review see Minnhagen P., *Rev. Mod. Phys.* **59**, 1001 (1987)
2. Kosterlitz J. M. and Thouless D. J., *J. Phys. C* **5** L124 (1972); Kosterlitz J. M. and Thouless D. M., *J. Phys. C* **6**, 1181 (1973); Berezinskii V. L., *Zh. Eksp. Teor. Fiz.* **61**, 1144 (1972) (*Sov. Phys. JETP* **34**, 610 (1972)).
3. Minnhagen P. and Nylén M., *Phys. Rev. B* **31**, 5768 (1985).

4. Pearl J., *Appl. Phys. Lett.* **5**, 65 (1964); Pearl J. in *Low Temperature Physics-LT9*, edited by J. G. Daunt, D.O. Edwards, F.J. Milford, and M. Yagub (Plenum, New York) 1965, pp. 566.
5. Nelson D. R. and Kosterlitz J. M., *Phys. Rev. Lett.* **39**, 1201(1977).
6. Minnhagen P. and Warren G. G., *Phys. Rev. B* **24**, 2526 (1981).
7. Ambegaokar V., Halperin B I., Nelson D. R., and Siggia E. D., *Phys. Rev. Lett.* **40**, 783 (1978) and *Phys. Rev. B* **21**, 1806 (1980).
8. Domany E., Schick M., and Swendsen R., *Phys. Rev. Lett.* **52**, 1535 (1984).
9. Capezzali M., Beck H., and Shenoy S., *Phys. Rev. Lett.* **78**, 523 (1997).
10. Olsson P., *Phys. Rev. B* **46**, 14598 (1992); *Ph.D. Thesis*, Umeå University, 1992.
11. Jonsson A. and Minnhagen P., *Phys. Rev. B* **55**, 9035 (1997).
12. Minnhagen P., *Phys. Rev. B* **32**, 3088 (1985).
13. Minnhagen P. and Wallin M., *Phys. Rev B* **40**, 5109 (1989).
14. Kosterlitz J.M., *J. Phys. C* **7**, 1046 (1974).
15. Minnhagen P. and Olsson P., *Phys. Rev. B* **45** , 10557 (1992).
16. Holmlund K. and Minnhagen P., *Phys. Rev. B* **54**, 523 (1996).
17. Wallin M., *Phys. Rev. B* **41**, 6575 (1990).
18. Bormann D., *Phys. Rev. Lett.* **78**, 519 (1997).
19. Minnhagen P., Westman O., Jonsson A., and Olsson P., *Phys. Rev. Lett.* **74**, 3672 (1995).
20. Holmlund K. and Minnhagen P., preprint (1997).
21. Dorsey A., *Phys. Rev. B* **43**, 7575 (1991).
22. Jonsson A. and Minnhagen P., *Physica C* **277**, 161 (1997).
23. Théron R., Simond J-B., Leemann Ch., Beck H., Martinoli P., and Minnhagen P., *Phys. Rev. Lett.* **71**, 1246 (1993).

Critical properties of classical Josephson junction arrays ¹

Jorge V. José

Instituto de Física, Universidad Nacional Autónoma de México, Apdo. postal 20-364, 01000 México D. F.

Physics Department and Center for the Interdisciplinary Research on Complex Systems, Northeastern University, Boston Massachusetts 02115 USA ²

Abstract. In this lecture notes I briefly review results on the equilibrium critical properties of models of classical Josephson junction arrays (JJA). The calculational approaches involve Monte Carlo and Langevin dynamical simulations. Specifically, we mention results from: (i) Monte Carlo results on the critical properties of the classical two-dimensional frustrated and unfrustrated XY models. (ii) Equilibrium dynamical critical properties from Langevin calculations of the unfrustrated JJA. In particular its magnetic flux noise spectra, which favorably compares with experimental results.

INTRODUCTION

This is a brief review that deals with different aspects of the equilibrium critical and dynamical properties of Josephson-junction arrays (JJA). These arrays have been extensively studied in the last few years [1]. Modern photolithographic techniques have allowed the fabrication of these arrays with tailor made properties. They were initially fabricated as true model systems to study the Berezinskii-Kosterlitz-Thouless (BKT) phase transition [2,3].

Evidence for the BKT vortex unbinding scenario has been found experimentally in superfluid helium [4], thin superconducting films [5] and Josephson junction arrays (JJA) [6,7]. The XY-model exhibits the BKT transition and Josephson junction arrays are an experimental realization of this model. They can be fabricated with a high degree of uniformity, and have controllable parameters that make them an ideal model system to study the critical behavior of the BKT transition. In addition, it allows for a direct comparison with dynamical simulations, like the one we discuss in this work. Earlier experimental studies of the BKT transition in arrays focused on the I - V characteristics [6,7]. In this experimental setup the

¹⁾ To appear in "1997 Euroschool, Siena, Italy, Superconductivity in Networks and Mesoscopic Structures" Eds. C. Giovannella and C. Lambert, AIP, 1998

²⁾ Permanent address

system is driven by an external current and is consequently not in equilibrium. Other experiments have been concerned with probing properties using the two-coil technique [8]. This also involves applying an external drive to the system and is generally confined to measuring the response at a specific frequency.

One of the main motivation for the work described here [10] is the experimental work by Shaw *et al.* [9]. They have measured the magnetic flux noise S_Φ generated by the equilibrium fluctuations in the vortex density, which is directly related to the vortex noise S_V . The importance of this work lies in the fact that it employs, basically, a non-invasive probe to measure the equilibrium dynamics associated with the BKT transition, in clear contrast with the experiments done before. The flux noise has a low frequency $\omega \ll \omega_\xi$ white-noise part and for $\omega \gg \omega_\xi$ a power-law behavior $S_\Phi \sim \omega^{-\alpha}$, where ω_ξ is a characteristic frequency and $\alpha \approx 1$. Similar but less extensive measurements have been performed earlier by Lerch *et al.* [11] below T_{BKT} . The frequency dependence, in particular the observed value of α , is different from predictions of phenomenological theories by Ambegaokar *et al.* (AHNS) [12] and Minnhagen [13], and other numerical results *et al.* [14]. The value of the exponent $\alpha = 1$ indicates that the critical vortex density fluctuations are of a $1/\nu$ -noise type (here ν denotes the frequency). A number of phenomenological models have been proposed to explain these observations (see e.g. [15]). The occurrence of $1/\nu$ -noise in these systems is not well understood and it is still the subject of intense research. In Josephson-junction arrays $1/\nu$ -noise from vortices is unexpected in view of previous theoretical analyses [12,13].

To set up the stage I start this paper with a brief introduction to the critical properties of the X-Y model and the fully frustrated XY model, FFXMM. The latter model has been the source of many studies and it is still not fully understood.. Then we will move to discuss the dynamical critical properties of the XY model, using the Langevin dynamics that is the appropriate one for the arrays. Here we find some interesting surprises that agree in many respects with the Shaw *et al.* results. The surprise is that a time-dependent Ginzburgh-Landau model gives better results than the RSJ model, that has been assumed to be the correct model for overdamped JJA.

CRITICAL PROPERTIES THE ZERO AND FULL FRUSTRATION XY MODELS

We start by considering results from Monte Carlo studies of the critical properties of the 2-D XY model at zero and full frustration in a square lattice. We obtained the critical exponents of the models from explicit calculations of the thermodynamic and correlation functions for the spin and chiral (frustration) degrees of freedom [16].

The critical behavior of the fully frustrated 2-D XY model has been studied extensively, both theoretically [2,3] and experimentally [1]. The model is defined by the Hamiltonian

$$H = - \sum_{\langle \vec{r}, \vec{r}' \rangle} E_J \cos(\theta(\vec{r}) - \theta(\vec{r}') + f(\vec{r}, \vec{r}')), \quad (1)$$

where $\theta(\vec{r})$ is the angle at site \vec{r} , with $\vec{r} = (ia_o, ja_o)$, i, j integers and a_o the lattice spacing; $\langle \vec{r}, \vec{r}' \rangle$ stands for a sum over nearest-neighbor lattice sites, and E_J is the exchange constant. In the JJA case in a homogeneous transverse magnetic field, the bond variables $f(\vec{r}, \vec{r}')$ are given by the line integral $f(\vec{r}, \vec{r}') = \frac{2\pi}{\Phi_0} \int_{\vec{r}}^{\vec{r}'} \vec{A} \cdot d\vec{l}$, with \vec{A} the magnetic vector potential. The frustration parameter, f , is defined by $2\pi f = \sum_{\mathcal{P}} f(\vec{r}, \vec{r}') = \frac{2\pi}{\Phi_0} \oint_{\mathcal{P}} \vec{A} \cdot d\vec{l}$, with \mathcal{P} a plaquette. The uniformly frustrated model is periodic in f with period one, and with reflection symmetry about $f = 1/2$. The XYM corresponds to the unfrustrated $f = 0$ case, while the fully frustrated case to $f = 1/2$. The effect of f in this case is to produce alternate rows with ferro- and antiferromagnetic couplings, while the couplings along the columns are all ferromagnetic. Each plaquette has one antiferromagnetic and three ferromagnetic bonds, or vice versa, leading to a ground state that has a two-fold degeneracy with half-integer vortices of opposite circulation or chirality [17]. Thus, the system displays two symmetries: the underlying continuous $U(1)$ Abelian symmetry for the phases and a discrete Z_2 or Ising-like symmetry associated with the chiral degrees of freedom, leading to the possibility of true long-range order in two dimensions. In contrast, the unfrustrated 2-D XY model (XYM) only possesses a continuous $U(1)$ Abelian symmetry: its low temperature phase is characterized by quasi-long range order rather than true long-range order. In spite of the many experimental and theoretical studies of the FFXYM, there are several questions that remain to be resolved. For example, it is not clear whether one phase transition exists at the critical temperature T_c which is a combination of a Berezinskii-Kosterlitz-Thouless (BKT) type transition for the $U(1)$ symmetry plus an Ising-like transition for the Z_2 symmetry, or whether there are two successive phase transitions at critical temperatures $T_{U(1)}$ and T_{Z_2} . Even the order in which they may occur is controversial. More importantly the nature of the transitions, as characterized by their critical properties, is not yet fully understood. In the XYM the nature of the BKT phase is characterized by the approximate analytic expression for the spin-spin correlation functions. However, unlike in the XYM case, it has been very difficult to calculate the correlation functions for the FFXYM analytically. All the studies carried out previously have mostly concentrated on calculating thermodynamic quantities in which it is difficult to separate the Z_2 from the $U(1)$ contributions.

The purpose of our work was to fill this gap by explicitly calculating the $U(1)$ and Z_2 correlation functions. One further complication is that at present there is no available analytic theory for the $f \neq 0$ case that could suggest what form these correlation functions should have and we needed to make an *ansatz* for them. Generally, we assumed that they decay exponentially or algebraically with distance. We used different statistical measures to test for the two possibilities. When our MC results for the correlation functions were consistent with an exponential decay we extracted a correlation length $\xi(T)$, while if they were consistent with a power law decay we extracted the corresponding $\eta(T)$ exponent. In the case that $\xi(T)$ diverged

at T_c from above it could diverge as a power law or with the BKT form $\xi(T) \sim \exp(B(T - T_c)^{-\nu})$. In the $f = 0$ case the critical exponent $\nu(f = 0) = 1/2$. In the low temperature phase of the XYM the correlation function decays algebraically with distance r as $\sim r^{-\eta}$, where the η exponent is a continuous function of T and takes the universal value $\eta(f = 0, T_{BKT}) = 1/4$. In addition, other MC simulations have provided an accurate evaluation of the $f = 0$ XYM critical exponents [18]. The high statistics estimates for $f = 0$ are $\nu = 0.4695(1)$ and $\eta = 0.235$, with the critical temperature $T_{BKT} = 0.8953$ [18].

In order to understand the nature of the phase transitions in the FFXYM we studied a variety of quantities, several of which separately describe each particular symmetry. The thermodynamic quantities calculated were: the helicity modulus, Υ , the square of both the staggered chiral magnetization, \mathcal{M}_s^2 , and susceptibility, χ_s^2 . We also carried out an extensive analysis of the gauge invariant $U(1)$ correlation function, $g_{U(1)}(r)$ and their corresponding even and odd coherence lengths. These calculations allowed us to extract the $U(1)$ critical temperature, $T_{U(1)}$, and its critical exponents ν and η . For the Z_2 freedoms we calculated the chiral correlation function, $g_\chi(r)$, and its corresponding coherence length, ξ_χ , which allowed us to estimate the critical exponent ν_χ and the critical temperature T_{Z_2} . Our result for the exponent ν_χ is in very good agreement with the MC transfer matrix calculation [19].

Exponents

We will now outline the main results of our study. We begin by discussing the helicity modulus $\Upsilon(T)$. Previous studies of the FFXYM and the fully frustrated Coulomb gas have indicated the possibility that the jump in $\Upsilon(T)$ may be different from the universal XYM result. To further shed light onto this problem we studied $\Upsilon(T)$ as a function of temperature for different lattice sizes and carried out a finite size analysis of $\Upsilon_{U(1)} = \Upsilon(T = T_{U(1)})$ obtained from runs for $L = 8, 16, 32$ with 250K MCS and $L = 60$ with 200K MCS. We note that at low temperatures the finite size effects are almost negligible, however, they become important in the critical region. We performed a finite size analysis of Υ at the critical temperature $T_{U(1)} = 0.44$, found from a high temperature analysis of the correlations. The simulations were carried out in lattices of size $L = 8, 16, 24, 32, 48, 60, 72, 84$, and 96 and extrapolated to infinite lattices giving the result,

$$\Upsilon_{U(1)} = 0.37(1). \quad (2)$$

This result suggests that for the lattice sizes and statistics of our simulations, the jump in the helicity modulus for the FFXYM is about 23% below the XYM result. Note, however, that one cannot rule out the possibility of a smaller value of $\Upsilon_{T_{U(1)}}$ for larger lattices. Nonetheless, we do not believe that the trend would change significantly from the result given here.

We also studied the staggered magnetization M_{stagg} due to the supercurrents circulating around the plaquettes as a function of T for $L = 16$ and 32 . It is non-zero at low temperatures and drops sharply at about $T = 0.42$. We note that finite size effects are almost negligible for these lattice sizes. The behavior of M_{stagg} as a function of temperature suggests that it may be considered as an order parameter for the $U(1)$ phase transition. Note, however, that the chirality is defined in terms of the direction of the circulating currents about the plaquettes and thus M_{stagg} can also be thought of as an order parameter for chirality.

We calculated the staggered chiral magnetization \mathcal{M}_s . However, \mathcal{M}_s oscillates too irregularly between positive and negative values, thus it was more convenient instead to study \mathcal{M}_s^2 and its fluctuations χ_s^2 . \mathcal{M}_s^2 goes to unity at low temperatures and it decays sharply to zero close to the critical region. We note that χ_s^2 displays an asymmetric behavior close to $T_{Z_2} (\approx 0.42$ for $L = 60$), where it has a sharp maximum. This indicates that the critical exponents for χ_s^2 above and below T_{Z_2} should be different. For $T > T_{Z_2}$ we fitted the MC data to $\mathcal{M}_s^2 \sim (-\epsilon_{Z_2})^{2\beta}$, and $\chi_s^2 \sim (\epsilon_{Z_2})^{-2\gamma}$ while for $T \leq T_{Z_2}$ χ_s^2 was fitted to $\chi_s^2 \sim (-\epsilon_{Z_2})^{-2\gamma'}$. We extracted the critical exponents 2β , 2γ and $2\gamma'$ by a straight line fits to $\ln(\mathcal{M}_s^2)$ vs $\ln(\epsilon_{Z_2}(L))$ and $\ln(\chi_s^2)$ vs $\ln(|\epsilon_{Z_2}(L)|)$ for temperatures within 10% from the estimated $T_{Z_2}(L)$. Here we used the notation $\epsilon_{Z_2} = (T - T_{Z_2})/T_{Z_2}(L)$, with $T_{Z_2}(L)$ the temperature at which \mathcal{M}_s^2 goes steeply to zero and χ_s^2 shows a maximum for a given L . The exponents obtained for the largest lattice were

$$2\beta = 0.1936(35), \quad 2\gamma' = 1.025(79), \quad \text{and} \quad 2\gamma = 1.82(13). \quad (3)$$

These exponents clearly differ from the corresponding 2-D Ising model exponents $2\beta = 1/4$, $2\gamma = 2\gamma' = 7/2$. We note that our chiral order parameter exponent does agree with the value $2\beta = 0.20(2)$ obtained from MC transfer-matrix studies of the FFXYM [19].

We now discuss our MC results for the gauge invariant phase correlation functions obtained from simulations in lattices from $L=16$ up to $L=240$, with periodic boundary conditions. To reduce finite size effects the lattice sizes at each temperature were chosen such that $L/\xi \geq 5$. We note that $g_{U(1)}(r)$ has an oscillatory behavior with period $1/2$ which comes from the Aharonov-Bohm phase factors [16]. At higher temperatures we find that the oscillatory behavior disappears, as one would expect. As the critical temperature is approached from above the oscillations increase in amplitude and saturate below $T_{U(1)}$. This oscillatory behavior led us to separate the correlation functions into two components; one for the odd and one for the even lattice sites, with their corresponding coherence lengths ξ_o and ξ_e . The MC data for the zero momentum correlation functions was fitted to the periodic version of the *ansatz* given in for $T \geq T_{U(1)}$. This procedure incorporates the periodic boundary conditions due to the finiteness of the lattice. We carried out unconstrained non-linear 3-parameter fits to the data to obtain $\xi(T)$, $\eta(T)$ and the coefficient A for the odd and even correlation functions. We fitted the MC data

to the linear functions $\ln(g(r)) = \ln A + \ln[r^{-\eta}e^{-r/\xi} + (L-r)^{-\eta}e^{-(L-r)/\xi}]$, varying η until a minimum for χ^2 was reached. As one gets closer to the critical temperature from above, the coherence length increases exponentially and one needs longer simulations and larger lattices in order to get statistically reliable data. Furthermore, the fitting parameter $\eta(T)$ increases and oscillates rapidly, for both the odd and the even lattices so that an estimate of $\eta(T_{U(1)})$ was not attempted. We also found that as the temperature decreases, A_o decreases while A_e increases, both slowly. Far from the critical region we got reliable results for ξ_o and ξ_e using lattices of size $L \leq 60$. In the determination of the critical exponents and the critical temperature it is crucial how one fits the data. We first tried a 4-parameter unconstrained non-linear fit to the MC data of the BKT type obtaining the results,

$$\nu_e = 0.3133(57), \quad \text{and} \quad \nu_o = 0.3005(6), \quad (4)$$

which are close to $1/3$. We then fixed the values $\nu_e = \nu_o = 1/3$, and carried out a 3-parameter fit to the data for both lattices. The quality of the fits improved and hence we could surmise that the correct value of this exponent may indeed be $1/3$.

As an additional test of the reliability of the results for $T_{U(1)}$ and ν , we carried out a finite size scaling analysis of the data for ξ_o and ξ_e . For a finite system, assuming periodic boundary conditions, the usual $T > T_{U(1)}$ finite size scaling *ansatz* for a BKT transition is $\xi(T, L) \sim L F_\xi(L^{-1} \exp(B_\xi \epsilon^{-\nu}))$, with F_ξ the scaling function, not known *a priori*, which must satisfy the conditions $F_\xi(x) = 0$, as $x \rightarrow 0$, $F_\xi(x) < \infty$, as $x \rightarrow \infty$. The idea is to find the set of parameters B , ν and $T_{U(1)}$ for which the data for different temperatures and lattice sizes fall onto one curve. Fixing $\nu = 1/3$, we varied the values of B and $T_{U(1)}$ about their values obtained in the previous fits. We found that as we moved away from those values in the increasing or decreasing directions, the data became more scattered. However, very close to the values found from the previous fits the data fell very close to a unique curve. The values for which the data collapsed approximately onto the universal curve were $B_e = 1.045$, $B_o = 0.999$, and $T_{U(1)}^e = 0.440$, $T_{U(1)}^o = 0.442$. These numbers are in rather good agreement with the values found in the previous fits. We also calculated η_e and η_o at the average critical temperature $T_{U(1)} \equiv \frac{1}{2}(T_{U(1)}^o + T_{U(1)}^e)$ obtained from the high temperature analyses for lattices with $L = 32, 40, 48, 60, 72, 84$ and 96 . However, the η 's do seem to reach the asymptotic values

$$\eta_o(T_{U(1)}) = 0.1955(3) \quad \text{and} \quad \eta_e(T_{U(1)}) = 0.1875(3). \quad (5)$$

On the other hand for the XYM we obtained

$$\eta_o(T_{U(1)}) = 0.2521(3) \quad \text{and} \quad \eta_e(T_{U(1)}) = 0.2480(3), \quad (6)$$

assuming the exponential fits to the correlations.

Let us now turn to the discussion of the correlation functions for the chiral degrees of freedom. Our study was less detailed than in the $U(1)$ case, mainly concentrating

on the temperature region above T_{Z_2} . Prior information about the chiral critical exponents is available so that we can compare our results to them. The calculation of the zero momentum chiral correlation functions was less demanding than in the $U(1)$ case since one expects that ξ_χ diverges algebraically, that is $\xi_\chi \sim (\epsilon_{Z_2})^{-\nu_\chi}$. The analysis of $g_\chi(r)$ followed a similar logic to that of the $U(1)$ study. The results obtained from different fits gave

$$A_\chi = 0.36(3), \quad \text{and} \quad T_{Z_2} = 0.432(9), \quad \text{for} \quad \nu_\chi = 0.760, \quad (7)$$

with $\chi^2 = 9.7 \times 10^{-2}$. Our result for ν_χ agrees quite well with finite size scaling analysis that gave $\nu_\chi = 0.85(3)$, as well as with the MC transfer matrix calculations [19]. The advantage of the finite size scaling analysis is that ν_χ was obtained from a one parameter fit without needing a precise value for T_{Z_2} , as in our analysis. Therefore it appears that the ν_χ and T_{Z_2} values obtained here from the nonlinear fits may in fact be very close to the correct ones. It is important to emphasize that the T_{Z_2} found here is consistent with the temperature at which \mathcal{M}_s^2 fell to zero, and χ_s^2 displayed a sharp maximum. In summary, our numerical analysis of the chiral degrees of freedom led to the critical exponents

$$2\beta = 0.1936(35), \quad 2\gamma = 1.025(79), \quad 2\gamma = 1.82(13), \quad \text{and} \quad \nu_\chi = 0.875(35). \quad (8)$$

These results strongly indicate that the Z_2 phase transition is not an Ising-like transition as had been suspected from previous thermodynamics studies of this model. Note that in our calculations the difference between the T_{Z_2} and $T_{U(1)}$, is about 7%, which may not be considered as different within the size of our estimated errors. Equivalently, one cannot rule out the possibility that in improved numerical simulations and closer to the critical point this difference may disappear.

In this section we have briefly reviewed results from extensive MC calculations of the FFXYM [16]. We have explicitly analyzed the separate contributions from the $U(1)$ and Z_2 freedoms. We have extracted the $U(1)$ and Z_2 critical exponents from direct calculations of their corresponding correlation functions and selected thermodynamic properties. We found compelling quantitative evidence that the $U(1)$ and Z_2 critical exponents are clearly different from those of the usual 2-D XY and Ising models. We have tested our results using several consistency checks. There are no other calculations of the $U(1)$ exponents to which to compare our results. However, a reanalysis of the experimental data lead to an η exponent that is clearly different from the XYM result and that agrees with the one found in our calculations [20].

LANGEVIN DYNAMICAL EQUATIONS OF MOTION

Josephson-junction arrays consist of superconducting islands that are Josephson-coupled either by proximity effect (SNS) or through an insulation barrier (SIS). Typically, these islands are arranged in regular two-dimensional lattice structures,

e.g. square or triangular. The amplitude of the order parameter can be assumed to be constant in time and the same for all islands since there are no significant spatial variations in the SNS arrays. Each island is then characterized by the order parameter phase θ . The supercurrents carried for each junction in the array is given by $I_s(\mathbf{r}, \mathbf{r}') = I_c \sin(\theta(\mathbf{r}) - \theta(\mathbf{r}') - 2\pi f(\mathbf{r}, \mathbf{r}'))$. Here \mathbf{r} and \mathbf{r}' denote the coordinates of neighbor islands, I_c is the critical current of the junction. When one applies a voltage across a junction, or applies a bias current that exceeds the critical current, resistive currents will flow in the junction, and the phase difference will change in time. The voltage $V(\mathbf{r}, \mathbf{r}', t)$ across a Josephson junction is Josephson's relation:

$$V(\mathbf{r}, \mathbf{r}', t) = \frac{\hbar}{2e} \frac{d}{dt} (\theta(\mathbf{r}, t) - \theta(\mathbf{r}', t) - 2\pi f(\mathbf{r}, \mathbf{r}', t)). \quad (9)$$

The dynamics of a classical JJA is governed by a set of coupled single-junction equations, if necessary supplemented by Maxwell's equations when screening is important [21–23]. Obviously, the model is also appropriate to describe junctions that are explicitly shunted by a resistor. Shunting underdamped SIS junctions with resistors is a way to make these junctions overdamped. The charging of the junction capacitance is described in terms of a shunt capacitor. The general RCSJ equation then divides the total current $I(\mathbf{r}, \mathbf{r}')$ through the junction in three parts: the capacitive current, the resistive current and the Josephson current:

$$I(\mathbf{r}, \mathbf{r}') = \frac{\hbar C}{2e} \frac{d^2}{dt^2} (\theta(\mathbf{r}, \mathbf{r}') - 2\pi f(\mathbf{r}, \mathbf{r}')) + \frac{\hbar}{2e R_n} \frac{d}{dt} (\theta(\mathbf{r}, \mathbf{r}') - 2\pi f(\mathbf{r}, \mathbf{r}')) + I_c \sin[\theta(\mathbf{r}, \mathbf{r}') - 2\pi f(\mathbf{r}, \mathbf{r}')]. \quad (10)$$

Here C is the junction capacitance and $\theta(\mathbf{r}, \mathbf{r}')$ is defined as the phase difference $\theta(\mathbf{r}) - \theta(\mathbf{r}')$. The arguments \mathbf{r} and \mathbf{r}' refer to nearest-neighbor islands. To describe the effect of non-zero temperature, a white noise term must be added to Eq. (10). It is convenient to write the RCSJ model in dimensionless units, in which it takes the following form:

$$i(\mathbf{r}, \mathbf{r}') = \beta_c (\ddot{\theta}(\mathbf{r}, \mathbf{r}') - 2\pi \ddot{f}(\mathbf{r}, \mathbf{r}')) + \dot{\theta}(\mathbf{r}, \mathbf{r}') - 2\pi \dot{f}(\mathbf{r}, \mathbf{r}') + \sin[\theta(\mathbf{r}, \mathbf{r}') - 2\pi f(\mathbf{r}, \mathbf{r}')]. \quad (11)$$

Here the dots represent time derivatives. The currents are expressed in units of the junction critical current I_c ; time is measured in units of the characteristic time $1/\omega_c = \hbar/(2eR_n I_c)$, and $\beta_c = (\omega_c/\omega_p)^2$ is the Stewart-McCumber parameter, with the plasma frequency ω_p defined as $\omega_p^2 = 2eI_c/\hbar C$. Kirchhoff's law of current conservation holds at every island in the array: $\sum_{\mathbf{a}} i(\mathbf{r}, \mathbf{r} + \mathbf{a}) = i_{\text{ext}}(\mathbf{r})$, where the summation runs over all nearest neighbor islands $\mathbf{r} + \mathbf{a}$. These conditions provide the coupling of the individual junction equations (11) into a set of equations that describes the array. If we use the conservation conditions to eliminate the variables $i(\mathbf{r}, \mathbf{r}')$ in (11), we obtain

$$\sum_{\mathbf{r}'} G^{-1}(\mathbf{r}, \mathbf{r}') D_t \theta(\mathbf{r}') \equiv \sum_{\mathbf{a}} D_t (\theta(\mathbf{r}) - \theta(\mathbf{r} + \mathbf{a})) \quad (12)$$

$$= i_{\text{ext}}(\mathbf{r}) - \sum_{\mathbf{a}} \sin(\theta(\mathbf{r}, \mathbf{r} + \mathbf{a}) - 2\pi f(\mathbf{r}, \mathbf{r} + \mathbf{a})). \quad (13)$$

Here we defined $D_t \equiv \beta_c \partial_t^2 + \partial_t$ and $G^{-1}(\mathbf{r}, \mathbf{r}')$ is the inverse two-dimensional lattice Green function. We assume that in the coupled set (13), the magnetic field that enters via the variables $f(\mathbf{r}, \mathbf{r}')$ is only due to an *externally applied* uniform magnetic field, thus neglecting here the magnetic fields induced by the currents flowing in the array. As mentioned above the dynamical properties of the driven arrays studied in SNS experiments have been successfully explained in numerical simulations using the RSJ dynamics. The RSJ dynamics is obtained from some microscopic considerations. On the other hand, the time-dependent Ginzburg Landau (TDGL) dynamics is proposed to describe the SNS JJA dynamics as a purely phenomenological theory of the relaxation of the order parameter $\theta(\mathbf{r})$. The TDGL approach has been used by Martinoli *et al.* [24,25] to interpret the results of linear-response experiments on Josephson-junction arrays. TDGL dynamics has also extensively been used in numerical investigations of the dynamics of the XY-model [14]. Since one of our aims was a critical re-examination of both RSJ and TDGL models, we decided to study them both at the same time. The dynamical equations of motion in the overdamped case needed for the analysis of the experiments for both models are then.

$$\sum_{\mathbf{r}'} G^{-1}(\mathbf{r}, \mathbf{r}') \partial_t \theta(\mathbf{r}', t) = -\Gamma \left(\frac{\partial H}{\partial \theta(\mathbf{r})} + \nabla \cdot \boldsymbol{\eta}_1(\mathbf{r}) \right), \quad \text{RSJ} \quad (14)$$

$$\partial_t \theta(\mathbf{r}, t) = -\Gamma \left(\frac{\partial H}{\partial \theta(\mathbf{r})} + \eta_2(\mathbf{r}) \right). \quad \text{TDGL} \quad (15)$$

The magnitude of the thermal noise is determined by the microscopic dissipation mechanisms using the Fluctuation-Dissipation theorem. For RSJ dynamics we add fluctuating *currents* η_1 to the bonds, whereas for TDGL dynamics we add thermal noise η_2 to the islands.

$$\begin{aligned} \langle \eta_1(\mathbf{r}, \mathbf{r} + \mathbf{a}, t) \eta_1(\mathbf{r}', \mathbf{r}' + \mathbf{a}', t') \rangle &= 2T \delta(\mathbf{a}, \mathbf{a}') \delta(\mathbf{r}, \mathbf{r}') \delta(t - t'), \\ \langle \eta_2(\mathbf{r}, t) \eta_2(\mathbf{r}', t') \rangle &= 2T \delta(\mathbf{r}, \mathbf{r}') \delta(t - t'). \end{aligned}$$

Note that the two sets of equations have very different mathematical properties. The RSJ involves the Green function that makes the explicit calculations much harder to do than in the TDGL model. However, in the equilibrium limit the macroscopic properties, like the helicity modulus, for both models are essentially the same, as would be required from the principles of statistical mechanics. However, the equilibrium dynamical properties are significantly different as we see in the following subsections.

Flux noise

In the paper by Shaw *et al.* [9] they assume that the time-dependence of the magnetic flux correlation function in time $S_\Phi \sim \langle \Phi(t)\Phi(0) \rangle$ is essentially the vortex density correlation in time, $S_V \sim \langle N(t)N(0) \rangle$. Here Φ is the magnetic flux through the SQUID and N the vorticity within the SQUID. We therefore assume that the magnetic flux noise S_Φ is equivalent to the vortex noise S_V . In the experiment the SQUID occupies a smaller area than the area of the array. For that reason we replace the SQUID used in experiments by pseudo-SQUIDS, that is we consider vortex fluctuations in an $l \times l$ part of the array. More explicitly, the net vorticity in part i of the array is

$$N_i^i(t) = \sum_{(l \times l)_i} n(\mathbf{R}, t). \quad (16)$$

The vorticity of a plaquette \mathbf{R} is given by:

$$2\pi n(\mathbf{R}) = \sum_{\mathcal{P}(\mathbf{R})} (\theta(\mathbf{r}, t) - \theta(\mathbf{r}', t)). \quad (17)$$

Here $\mathcal{P}(\mathbf{R})$ denotes an anticlockwise sum around the plaquette \mathbf{R} and the phase difference $\theta(\mathbf{r}, t) - \theta(\mathbf{r}', t)$ is taken between $-\pi$ and $+\pi$. Given the vorticities N_i^i in part i of the array, we calculate the time-correlation function, and average this correlation function over all the \mathcal{N}_i different pseudo-SQUIDS:

$$g_i^V(t) \equiv \frac{1}{\mathcal{N}_i} \sum_i \left(\langle N_i^i(t) N_i^i(0) \rangle - \langle N_i^i(0) \rangle^2 \right). \quad (18)$$

The time-average $\langle \cdot \rangle$ is defined as follows:

$$\langle A(t) A(0) \rangle \equiv \frac{1}{N_t - t} \sum_{t'}^{N_t - t} A(t + t') A(t'). \quad (19)$$

Here N_t is the number of time-averaging steps. The technical advantage of the pseudo-SQUID approach is that since one averages over $\mathcal{N}_i = L_x L_y / l^2$ different and independent realizations of g_i^V . For example using $l = 4$ reduces the statistical error approximately an order of magnitude compared to $l = 32$. We have also calculated the correlations $g_i^a(t)$ of the fluctuations of the absolute vorticities $N_a(t)$, that is instead of the net vorticity one takes the sum of positive and negative vortices. We determined the vortex noise S_V as the Fourier transform of the time correlations g_i^V of the net vorticity N_i within a part of the system consisting of $l \times l$ plaquettes

$$S_V(\omega) = \int dt e^{i\omega t} \langle N_i(t) N_i(0) \rangle. \quad (20)$$

This method of calculating S_V has two advantages over the method used previously [14]. We evaluate S_V directly, using a definition in terms of the vorticity

itself, instead of using a derived quantity. Our method faithfully represents the experimental procedure and allows us to study the dependence of S_V on the effective SQUID size l .

To gain further insight in the nature of the vortex dynamics we have also considered the spatial vortex configurations and followed the spatially-resolved vortex dynamics in real time. We find that single vortices hardly move on the time scales considered and that for $T > T_{BKT}$ the spatial configurations are dominated by clusters consisting of vortices and antivortices in neighboring plaquettes. In view of these results it is possible that the vortex clusters are a natural candidate for explaining the $1/\nu$ spectrum in arrays. We therefore analyzed the behavior of vortex clusters. We have calculated the cluster distribution function and the time correlations in the number of clusters. We find that the number of vortices that are part of a cluster increases with temperature, and that clusters, depending on their net vorticity and size, relax differently and with a different characteristic time. We have compared the α obtained here to one from a system without clusters. In the latter we find for low temperatures $\alpha \approx 1.5$. For that reason we suggest that the measured α can be connected to the dynamics of vortex clusters.

Thermodynamic results

We start comparing the results for the helicity modulus calculated by Langevin dynamics to the Monte Carlo results. As discussed before, in the MC calculations it was found that the universal jump in Υ slowly converges with the system size to the universal value $2T_{BKT}/\pi$. The value we obtain here for $L = 64$ using the dynamical equations is $\Upsilon(T = 0.90) = 0.63(5)$, which is approximately the same as the one $\Upsilon(T = 0.9035) = 0.623(2)$ obtained for $L = 60$ in Ref. [16].

We have also calculated the spin-spin correlation function $g_\theta \equiv \langle \cos(\theta(\mathbf{r}) - \theta(\mathbf{r}')) \rangle$ for the RSJ and TDGL dynamics with both full periodic boundary conditions and semi-periodic boundary conditions (i.e. free in one direction). The algorithm for calculating g_θ is $O(L)$ slower than the time-integration step itself. We used the complete spin wave expression $Ar^{-\eta}$ to fit $g_\theta(r)$, [16]. Here A is already determined and the number of fitting parameters is reduced by one. We have fitted the results for g_θ to six different functions. The results for Υ and $g_\theta(r)$ for the RSJ and TDGL dynamics are identical within the statistical error.

Above T_{BKT} free vortices appear in the system and the phase correlations decay exponentially with a correlation length: $\xi(T) = \xi_0 \exp\left(\frac{b}{(T - T_{BKT})^\nu}\right)$, with $\nu = \frac{1}{2}$. This expression is only valid for low vortex densities or large ξ . However, in practice numerical and experimental results can be fitted to this form for somewhat higher vortex densities.

We have calculated the static correlation function $g_\theta(r)$ above T_{BKT} and found rather good fits to the expected results. For T close to T_{BKT} the statistical error in g_θ for large separation $r > 10$ is visible. The points for $T = 1.08$ oscillate above

the fitting curve. The resulting error in the coherence length ξ , that is determined as a fitting parameter, can be as large as 10% for $T < 1.08$. For $T > 1.12$ the error is smaller than 5%. We fit the Kosterlitz-Thouless prediction to the $\xi(T)$ obtained from the g_θ -fits. The results for TDGL and RSJ dynamics in this case are slightly different: $\xi_0 = 0.230(1)$, $b = 1.45(1)$ and $T_{BKT} = 0.935(1)$ (TDGL) and $\xi_0 = 0.274(30)$, $b = 1.41(10)$ and $T_{BKT} = 0.917(10)$ (RSJ). These differences are mainly due to the differences in the values of $\xi(T)$ obtained for the dynamics below $T < 1.12$. The quoted error estimates are obtained by determining the change in the fitting parameters when one removes a point $\xi(T)$ from the data. The RSJ fit (11 points) is less robust than the TDGL fit (22 points). One can compare these fitting parameters with the ones obtained from Monte Carlo calculations [16] that obtain: $\xi_0 = 0.2050$, $b = 1.6113$, $T_{BKT} = 0.9035$ and $\nu = 0.4797$. There the exponent ν was also a fitting parameter, while here we fixed it to $\nu = 0.5$. The agreement is reasonable, given the fact that in their study they calculated $\xi(T)$ for temperatures closer to the critical temperature T_{BKT} and larger system sizes (up to 240×240).

Dynamic equilibrium results

The dynamical critical exponents are obtained from a scaling analysis of the data that we describe in this subsection. Based on the work by Shaw *et al.* [9] one expects the vortex noise to be a scaling function of the relevant frequency scale $\omega_\xi \sim \xi(T)^{-z}$ and the lengths $\xi(T)$, array size L , SQUID size l and the vertical distance d between the SQUID and the array. In Ref. [9] the following form is proposed:

$$S_\Phi(\omega) = \xi^{\beta'} \mathcal{F}(\omega/\omega_\xi, L/\xi, l/\xi, d/\xi). \quad (21)$$

The scaling function corresponding to \mathcal{F} in the time domain is:

$$g_l^Y(t) = \xi^\beta \mathcal{G}(t/\tau_\xi, L/\xi, l/\xi, d/\xi). \quad (22)$$

When $L > l \gg \xi$ there is no L or l dependence and therefore g_l^Y can be written as $\xi^\beta \mathcal{G}(t/\xi^z)$. We perform our scaling analysis in the time domain. In this domain we have an estimate for the statistical errors and we can weigh the data points accordingly in the scaling procedure. We only use data with $l > \xi$. Data for larger l has usually large statistical errors, that increase when the temperature gets closer to T_{BKT} . Therefore only data with $\xi < 8$ is included. We collapse curves onto \mathcal{G} using a nonlinear fit procedure, where we show that the data collapses for TDGL and RSJ dynamics. One notes that the function \mathcal{G} for TDGL is different from the one for RSJ dynamics. We have collapsed the data for $l = 16$ and $l = 32$ for TDGL and $l = 16$ for RSJ. The statistical error in the $l = 32$ data sets for RSJ dynamics was too large to yield a reasonable collapse. In the plots of the data collapse the statistical errors become visible for $t > 10$. Shaw *et al.* [9] defined a

characteristic frequency ω_ξ at the intersection of the critical part of the spectrum with the white noise plateaus in a log-log plot. We did the same but by scaling in the time t -domain. The numerical value of ω_ξ itself will not be the same, but the dependence on $\xi(T)$ is the same. The value of z is obtained from scaling over only a limited ξ -range $\xi = 2 - 6.4$. We do obtain distinctly different results for the two dynamics,

$$z \approx 2.2(4) \quad \quad \quad TDGL \quad \quad \quad (23)$$

and

$$z \approx 0.90(5) \quad \quad \quad RSJ \quad \quad \quad (24)$$

Note the significant difference between the two results, with TDGL closer to the experimental value but the RSJ results clearly off. We have also collapsed the data for $l = 4$ and 8 . This gives lower values for z .

We found that the vortex noise S_V is flat for $\omega \gg \omega_\xi$, and a straight line, $S_V \sim \omega^{-\alpha}$ for $\omega \gg \omega_\xi$ (where ω_ξ is a characteristic frequency). The flat part of the spectrum is characteristic of white noise and indicates that the vortex fluctuations are uncorrelated. For that time scale g_l^V is approximately zero. The high frequency power-law part is the critical portion of the spectrum. For the TDGL case the exponent

$$\alpha_{TDGL} = 0.748(2) \quad \text{for } T = 0.84 \quad \text{and} \quad \alpha_{TDGL} = 0.916(2) \quad \text{for } T = 1.12. \quad (25)$$

We obtained the exponent α by fitting the apparent straight part of the curve to a line. Adding points to, or removing points from the fit changes the exponent α by an amount typically not exceeding 0.05 . For curves with a critical spectrum spanning only a small frequency range or with large statistical errors this effect can be larger. The quoted errors are obtained from the variances of the fit itself and do not involve the aforementioned effects. For the highest ω -value in our simulations the curve deviates from a straight line. There is a divergence in the analytic form for $g_l^V(t)$ for small t , because $\omega^{-\alpha}$ is non-integrable. In our simulations we obtained a finite $g_l^V(0)$. The $\omega^{-\alpha}$ behavior can therefore not persist up to the highest frequency.

The RSJ results are almost linear over the entire time range and the cosine-transform yields an $\omega^{-\alpha}$ dependence over approximately 2 decades, with

$$\alpha_{RSJ} \approx 1.17. \quad (26)$$

Comparing this to the behavior of $g_l^V(t)$ one finds that initially g_l^V decays slowly almost like $\log t$ but then dies out faster for larger times. This behavior leads to the characteristic low frequency white-noise plateau in S_V . For TDGL dynamics we find a slightly lower value for α_{RSJ} .

CONCLUSIONS

We now give a vortex interpretation of the dynamic calculation results. Thermally excited vortex pairs screen the interaction between two separate members of a given pair. When the vortices in a pair are separated over a distance larger than ξ they are free. There are free vortices and pairs in the array, but there are also neutral and non-neutral clusters consisting of more than two vortices. In g_l^V we measure the net charge present within a SQUID. The presence of clusters influences the time correlations; clusters of different charge and size decay to other clusters on a different time scale and with a different functional form. We made this idea a bit more quantitative by studying the average number of clusters P_c of a specific size c and the time correlations g_c in the number of clusters of a specific size.

Close to T_{BKT} we find that the vortex configurations consists mainly of small vortex pairs. For a higher temperature the fraction of small pairs decreases and more single vortices appear. At $T = 1.20$ the fraction of single vortices, $P_{1\pm}$, saturates and the fraction of larger charged clusters $P_{3\pm}$, $P_{5\pm}$ and so on, increases. The fraction of larger neutral clusters also increases. The statistical error in these quantities is estimated to be approximately 1%. The actual number of vortices $\langle cN_c \rangle$ in larger clusters grows even faster.

We also determined g_c for clusters consisting of two or more vortices. Non-neutral clusters of different size $c = 1+$, $3+$ and $5+$ relax on different time scales and contribute with a different weight $W_l(c, c)$ to g_l^V . The weight $W_l(c, c)$ depends on temperature via P_c . It is also clear that g_2 decays faster and in a different way than g_{3+} . The presence of larger clusters reduces the decay time of a unit of net vorticity and when more vortices are part of a cluster, g_l^V decays faster. The scaling of τ_ξ with ξ is related to the vortex density increment (and ξ decreases), so there are more clusters. In animations of the spatial vortex configuration versus time we have seldomly observed a vortex moving more than one plaquette. The clusters, however, change on a faster time scale. To study the noise created by "free" vortices alone, we have simulated a system with a small frustration $f = 0.02$. Due to this frustration there is, even at low temperatures, a finite number of vortices in the sample. In this situation there are no large clusters and pairs that will influence the relaxation of vorticity fluctuations.

With increasing temperature vortex-antivortex pairs and other clusters will enter the system. The exponent α then decreases with temperature to $\alpha \approx 1$. Therefore, when there are only single vortices in the system, we obtain a critical spectrum consistent with diffusive decay of vortex density fluctuations, and hence diffusive motion of vortices. When there are pairs and clusters present in the system, the spectrum is inconsistent with a simple diffusive vortex motion. This suggests that pairs and clusters are somehow responsible for the observed value of α . When there are clusters in the system there is an additional mechanism for the transport of vorticity. Clusters can change in size, of charge and shape. From the animations of the spatially-resolved vortex dynamics, and more quantitatively from the time-correlation functions g_c we calculated, we find that this indeed happens on a faster

time scale than vortex jumps. These combined processes of vorticity transport can be interpreted as the motion of effective vortices (renormalized by clusters). The (fractional) random walk of independent vortices can be directly connected to the vortex noise that is measured by a SQUID. The *vortex* random walk is characterized by a Hurst exponent H_V , that gives $\alpha = 1 + H_V$. For a regular random walk $H_V = \frac{1}{2}$. A fractional random walk, $H_V \neq \frac{1}{2}$, corresponds to anomalous diffusion. Théron *et al.* [24] find non-Drude behavior of the vortex dynamics in the array for $T < T_{BKT}$ and in a small magnetic field f . They interpret this behavior as a sign of anomalous vortex diffusion. For the same parameter regime we obtain $\alpha = 1.0-1.5$, also indicating anomalous vortex diffusion. If the two types of anomalous vortex diffusion are the same needs to be studied in more detail.

Next we consider an analytic way of thinking about the results obtained here. Schönfeld [28] gave an explanation for the $1/\nu$ -noise, with a low-frequency white-noise component. Such a spectrum can be obtained from independent vortex fluctuations, $N(t)$, that relax according to a $t^{-1/2}$ statistical law, and decays fast enough for longer times. The occurrence times of these fluctuations are distributed in a Poisson-like fashion. The $t^{-1/2}$ relaxation can be obtained from a one-dimensional diffusion equation. Our numerical results for g_l^V can be also be fitted to a Bessel function K_0 form:

$$g_l^V \sim K_0(\Omega t) \propto e^{-\Omega t} \int_0^\infty d\tau e^{-2\Omega\tau} [\tau(\tau+t)]^{-1/2}. \quad (27)$$

When the ergodic theorem is valid, this gives for the fluctuations themselves:

$$N_l(t) \propto \frac{1}{\sqrt{t}} e^{-\Omega t}. \quad (28)$$

which is precisely the form suggested in the work by Schönfeld. This suggests that the flux noise is generated by independent vortex fluctuations diffusing across the boundary of the SQUID.

A derivation of the particular form of g_l^V based on the microscopic vortex dynamics is presently lacking and remains a challenge for the future. Further experimental work may elucidate the precise functional form of g_l^V based on the possibilities suggested in this paper.

There are, however, still a number of questions to be answered in this problem that need further analysis.

ACKNOWLEDGMENTS

We thank all collaborators of the work reviewed in this lecture notes. The Monte Carlo work was done with G. Ramirez and the dynamic work with P. Tiesinga, J. van Himbergen and T. Hagenaars. Many more details on the dynamics can be found in Tiesinga's Ph.D. thesis. This work has been partially supported by *NSF* grant DMR-9521845.

REFERENCES

1. For a review of superconducting networks see *Proceedings of the 2nd CTP Workshop on Statistical Physics: KT Transition and Superconducting Arrays*, Edited by D. Kim, et al. (Min Eum Sa, Seoul, Korea, 1993). *Macroscopic quantum phenomena and coherence in superconducting networks*. Edited by C. Giovannella and M. Tinkham. World Scientific Co., Singapore, 1995)
2. V. L. Berezinskii, Zh. Teor. Fiz. **61**, 1144 (1971). [Soviet Physics JETP **32**, 493 (1971)]. J. M. Kosterlitz and D. J. Thouless, J. Phys. **C6**, 1181 (1973); J. M. Kosterlitz, J. Phys. **C7**, 1046 (1974).
3. J. V. José, L. P. Kadanoff, S. Kirkpatrick, and D. R. Nelson, Phys. Rev. **B16**, 1217 (1977).
4. D.J. Bishop and J.D. Reppy, Phys. Rev. B **22**, 5171 (1980).
5. A.F. Hebard and A.T. Fiory, Phys. Rev. Lett. **44**, 291 (1980).
6. J. Resnick, et al Phys. Rev. Lett. **47**, 1542 (1981).
7. R.F. Voss and R.A. Webb, Phys. Rev. B **25**, 3446 (1982).
8. Ch. Leemann, Ph. Lerch, G.-A. Racine and P. Martinoli, Phys. Rev. Lett. **56** 1291 (1986).
9. T.J. Shaw, Phys. Rev. Lett. **76**, 2551 (1996).
10. P. H. E. Tiesinga, et all. *ibid* **78**, 519 (1997), and P. H. E. Tiesinga Ph. D. Thesis University of Utrecht (1996).
11. Ph. Lerch, Ch. Leemann, R. Therón and P. Martinoli, Helv. Phys. **65**, 389 (1992).
12. V. Ambegaokar, B.I. Halperin, D.R. Nelson and E.D. Siggia, Phys. Rev. B **21**, 1806 (1980).
13. P. Minnhagen, Rev. Mod. Phys. **59**, 1001 (1987).
14. A. Jonsson and P. Minnhagen, Phys. Rev. Lett. **73**, 3576 (1994); J. Houlrik, A. Jonsson and P. Minnhagen, Phys. Rev. B **50**, 3953 (1994). M. Wallin, Phys. Rev. B **41**, 6575 (1990).
15. K-H Wagenblast and R. Fazio "Flux noise near KTB transition" (preprint)
16. G. Ramírez-Santiago and J.V. José, Phys. Rev. Lett. **68**, 1224 (1992); Phys. Rev. **B49**, 9567 (1994).
17. S. Teitel and C. Jayaprakash, Phys. Rev. **B27**, 598 (1983); *ibid* Phys. Rev. Lett. **51**, 1999 (1983).
18. R. Gupta and C. F. Baillie, Phys. Rev. **45**, 2883 (1992).
19. E. Granato and M. P. Nightingale, Phys. Rev. **B48**, 7438 (1993).
20. J. V. José, G. Ramírez-Santiago and H. S. J. van der Zant, Physica B **195-196**, 1671 (1994).
21. J.R. Phillips, et all. Phys. Rev. B **47**, 5219 (1993).
22. D. Domínguez and J.V. José, Int. J. Mod. Phys. B **8**, 3749 (1994).
23. J. C. Ciria and C. Giovannella (in this Proceedings)
24. R. Therón, et all. Phys. Rev. Lett. **71**, 1246 (1993).
25. See also A. Jonsson and P. Minnhagen, Phys. Rev. Lett. **73**, 3576 (1994); J. Houlrik, A. Jonsson and P. Minnhagen, Phys. Rev. B **50**, 3953 (1994).
26. C.T. Rogers, K.E. Myers, J.N. Eckstein and I. Bozovic, Phys. Rev. Lett. **69** 160 (1992).

-
27. Ph. Lerch, Ch. Leemann, R. Therón and P. Martinoli, *Helv. Phys.* **65**, 389 (1992).
 28. H. Schoenfeld, *Z. Naturforsch. Teil A* **10**, 291 (1955). See also M.J. Bukingham, *Noise in electronic devices and systems*. Ellis Horwood Limited Publishers, Chichester, West Sussex, England (1983).

III. ARRAYS IN QUANTUM REGIME: VORTEX PROPERTIES AND APPLICATIONS

Particle-like aspects of vortices in Josephson arrays

H.S.J. van der Zant

*Department of Applied Physics and DIMES, Delft University of Technology, Lorentzweg 1, 2628
CJ Delft, The Netherlands*

Abstract. Vortices in Josephson-junction arrays are bosonic quantum mechanical particles with repulsive interactions which move in a known periodic potential. Freedom in choosing the array geometry and junction parameters allows for manipulation of single massive vortices and quantum vortex experiments. High-energetic vortices are not affected by the periodic potential and can move ballistically in a force-free environment. Quantum vortices tunnel through the barriers of the periodic potential. They may exhibit Bloch oscillations analogous to conduction electrons in semiconductor superlattices.

I INTRODUCTION

For a long time, it has been known that vortices in long continuous Josephson junctions behave like relativistic particles [1]. As their name already implies long Josephson junctions are long and their length is generally too large to allow for quantum fluctuations in the vortex position. Discrete Josephson arrays consist of superconducting islands which are coupled to each other by Josephson junctions. With present day technology these junctions can be made so small that charging effects become important: tunneling of a charge Q from an island is prevented unless an energy of the order of the charging energy, E_C , is available.

The phases of the order parameter (ϕ) on each island define the vortex. Around the vortex center, the junction phase differences of any closed contour add up to 2π . The characteristic energy scale for the coupling between ϕ 's on adjacent islands is the Josephson coupling energy E_J . There is a competition between E_C and E_J because ϕ and Q are non-commuting variables: $\Delta Q \Delta \phi \geq e$. In the classical regime ($E_J \gg E_C$), ϕ is well defined (i.e., the vortex position is well defined) and there are large fluctuations in Q . In the opposite regime ($E_C \gg E_J$) charges are localized and fluctuations in ϕ are large (vortices are delocalized). It is this competition between E_C and E_J that leads to the quantum mechanical nature of vortices.

A great advantage of arrays is that they can be made in different geometries. A few examples are shown in Fig. 1: a 1D Josephson ring, a 2D array in a square

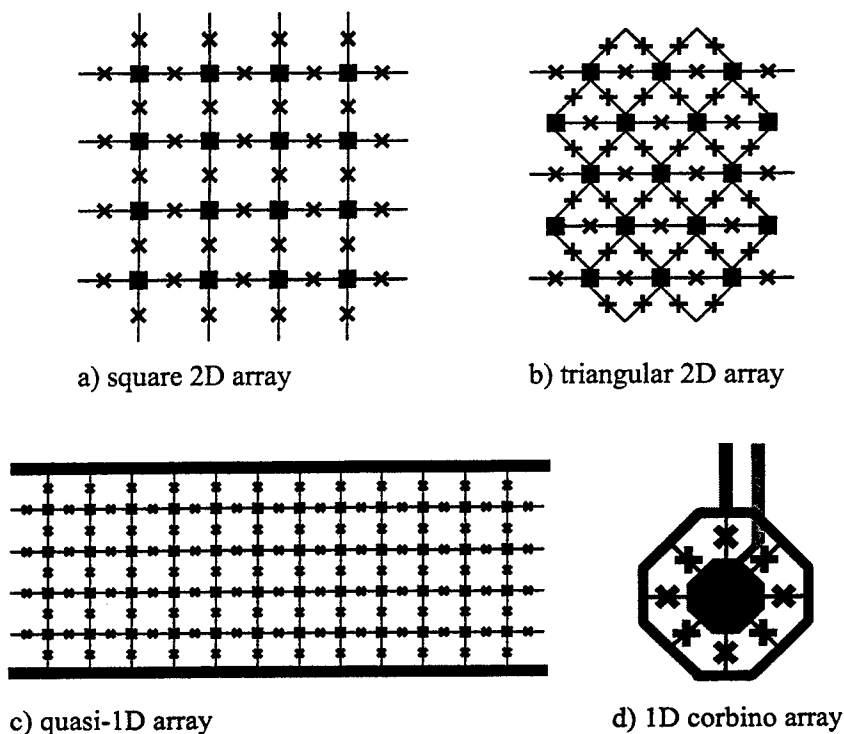


FIGURE 1. Various Josephson-junction arrays. The crosses represent the Josephson junctions. The black square are the superconducting islands; black lines superconducting strips.

or triangular geometry and a quasi-1D array. When performing experiments on quantum arrays, the environment of the arrays is of crucial importance. Arrays are usually connected to the outside world by superconducting strips (wires) which are then connected through bond wires, special micro-wave filters and coaxial cables to the measuring equipment. The superconducting wires form transmission lines with impedances of the order of 100Ω for relevant frequencies [2].

These low impedances prevent the observation of quantum effects in Josephson rings. Junctions can be decoupled from the environment by placing high-ohmic resistors in the leads within a distance of order μm or by using high-ohmic junctions themselves. For example, the quasi-1D array shown in Fig. 1c is an interesting system for the study of quantum effects. Under influence of a current, quantum vortices move in the middle row which is decoupled from the

environment by the junctions in the outer rows.

The dynamics of quantum vortices will be discussed in the second part of this paper. We will first discuss the classical dynamics of Josephson arrays. The discrete nature of Josephson arrays introduces new phenomena in the dynamics that are absent in continuous superconducting systems. In arrays, there can be an energy barrier for vortex motion from one cell to the next. Vortices are then subject to a periodic potential similar to electrons in solids. In a discrete system, the dispersion relation is periodic in the wave vector k . This periodicity enables a coupling between moving vortices and the linear modes in the arrays (spinwaves or the oscillatory motion of the junction phase around its equilibrium position). We will calculate the vortex mass and discuss the damping vortices experience. The coupling to spinwaves plays a crucial role but does not prevent ballistic vortex motion in discrete Josephson arrays.

The concepts we introduce in the first part of this paper are applicable to arrays with arbitrary shape but we will in particular concentrate on the arrays shown in Fig. 1 as they are most widely studied. We will discuss the properties of single vortices and not their collective response. For instance we will not treat the Kosterlitz-Thouless-Berezinskii phase transition in classical arrays associated with the unbinding of vortex and antivortex pairs at the transition. Likewise, part II will not contain a detailed discussion on quantum phase transitions in Josephson arrays. A recent overview on the latter subject can be found elsewhere [3].

II CLASSICAL VORTEX DYNAMICS

In Josephson arrays, damping occurs through ohmic dissipation inside the junctions and is characterized by the McCumber parameter $\beta_c = 2\pi I_c C R_e^2 / \Phi_0$, where R_e is the effective damping resistance, I_c the junction critical current, C its capacitance and where Φ_0 is the flux quantum $h/2e$. In arrays made of underdamped tunnel junctions dissipation can be extremely low ($\beta_c \gg 1$). At high temperatures, R_e is equal to the normal-state junction resistance R_n but at low temperatures the R_e of tunnel junctions is determined by the much higher subgap resistance. As a consequence, the electric energy stored in the junction capacitors when vortices move, can no longer be neglected. This electric energy acts like a kinetic energy term, thereby defining a vortex mass [4]. In the next two subsections, we will calculate the vortex mass and derive the equation of motion for a single vortex. We will first discuss some general details of niobium and aluminum tunnel-junction arrays.

Aluminum arrays at Delft used for the study of (semi-)classical vortex dynamics are typically built of junctions of size 1 by $1 \mu\text{m}^2$ with $C \approx 100$ fF and $0.1 \text{ k}\Omega < R_n < 1 \text{ k}\Omega$. For aluminum at low temperatures, the $I_c R_n$ product equals 0.32 mV. Nowadays, niobium arrays are made commercially [5] and are also available for the study of the underdamped, classical dynamics of vortices. Presently, the smallest reliable niobium junctions are 3 by $3 \mu\text{m}^2$. Typical junction parameters are $C = 340$ fF and R_n values ranging from 10 to 100Ω . For niobium the

$I_c R_n$ product at low temperatures equals 1.9 mV. Thus, for the niobium arrays the junction critical current is considerably higher than in aluminum arrays. The main consequence of this higher critical current is that in niobium arrays self-field effects can no longer be neglected.

In 2D, the self-inductive effects are parameterized by λ_\perp which is the ratio of the Josephson inductance of a junction $L_J = \Phi_0/2\pi I_c$ to the self-inductance of a cell $L_0 \approx \mu_0 p$. In units of the lattice parameter p , $\lambda_\perp = L_J/L_0$ is the penetration depth. There are two general types of self-field effects [6]. First, there are self-inductance effects which are short-ranged and caused by the self-inductance of the cell loop. It turns out that the cell-to-cell energy barrier is dominated by these short-range interactions. Second, there are mutual-inductive effects which have a longer range. For example, the current distribution in the middle of a current-driven 2D array changes from an exponential fall-off for self-inductances to an algebraic fall-off when the mutual inductances between all cell pairs are included.

In the purely 1D case (Fig. 1d), self-fields always play a role since the superconducting wires connecting the junctions act like inductors. In 1D, the penetration depth Λ_J is the square root of the penetration depth in 2D, i.e., $\Lambda_J = \sqrt{L_J/L_0}$. In addition, long-range interactions are not as important. One can to a good approximation only consider self-inductances when replacing Λ_J by an effective $\Lambda_{J,eff}$ [7].

A Vortex mass

Moving vortices lead to phase changes across junctions. They therefore result in voltage differences V_i between islands. Islands in Josephson arrays are not only capacitively coupled to each other by the junction capacitors C but also to a far away ground plane by C_0 . Both C and C_0 contribute to the electric energy, a moving vortex induces. In fabricated arrays, however, C_0 is generally orders of magnitude smaller than C so that the main contribution to the electric energy comes from the junctions:

$$E_{el} = \frac{1}{2}C \sum_i V_i^2 = \frac{1}{2}C \left(\frac{\Phi_0}{2\pi}\right)^2 \sum \left(\frac{\Delta\phi}{\Delta t}\right)^2 \quad (1)$$

where the sum is over all the junctions in the array.

In a quasi-static approach this sum can be calculated by comparing the phase differences across each junction at times t and $t + p/u$: $\Delta\phi = \Delta\phi_{t+p/u} - \Delta\phi_t$. Here, u is the averaged vortex velocity. The electric energy then acts like a kinetic energy term and the proportionality factor defines the vortex mass:

$$E_{el} = \frac{1}{2}M_v u^2 \quad \text{with} \quad M_v = \frac{h^2}{32\pi^2 p^2} E_C^{-1} \sum (\Delta\phi_{t+p/u} - \Delta\phi_t)^2, \quad (2)$$

where $E_C = e^2/2C$. The problem of calculating the vortex mass is now reduced to finding the phase differences across junctions at times t and $t + p/u$. Equation (2)

is a general result which can be applied to various array geometries if the phase configuration around a vortex is known.

In large 2D Josephson arrays with a single vortex situated at (x_0, y_0) , the phase on island (x, y) can be approximated by $\phi_{x,y} = \arctan[(y - y_0)/(x - x_0)]$. This arctan-approximation is valid for arrays in which self-field effects are small. Assuming that this arctan-phase configuration remains the same when the vortex moves through the array, numerical evaluation of the phase differences in a large 2D square array yields $\sum (\Delta\phi_{t+p/u} - \Delta\phi_t)^2 = 2\pi^2$. With Eq. (2), one obtains

$$M_v = \frac{h^2}{16p^2} E_C^{-1}. \quad (3)$$

Note, that in this calculation half of the vortex mass is due to the junction the vortex crosses; the other half comes from all the other junctions in the array. For a triangular array, a similar calculation can be done and the vortex mass is twice the mass of a square array.

It has been shown [8] that near array edges the vortex mass vanishes when it approaches a free boundary of the array. These boundary effects are, however, negligible if the vortex is a few lattice spacings away from the edge. One can also include self-field effects. Currents now extend over a distance λ_\perp from the vortex center so that the arctan approximation can no longer be used. As the vortex is effectively reduced in size, the sum of the V_i 's can be restricted to those junctions which are λ_\perp from the vortex center. The result is a smaller vortex mass and its decrease with decreasing λ_\perp is given in Ref. [9]. As $\lambda_\perp \rightarrow 0$, $M_v \rightarrow 0$. The vortex mass is also dependent on the E_J/E_C ratio. It vanishes at the superconductor-to-insulator (SI) transition but to a good approximation has the value given in Eq. (3) for arrays with $E_J/E_C > 1$ [10].

In a 1D array with N junctions, the vortex phase configuration is given by $\phi_x = 4 \arctan[\exp((x - x_0)/\Lambda_J)]$, where x_0 denotes the position of the vortex center in units of p . For $\Lambda_J < N$, the vortex has a kink-like shape, which extends over a distance of the order of Λ_J ; for $\Lambda_J > N$ the vortex is spread out equally over the whole system with $\phi_{x+1} - \phi_x \approx 2\pi/N$. Therefore, $\Delta\phi_{t+p/u} - \Delta\phi_t = 2\pi/N$ and $M_v = h^2/(8E_C(Np)^2)$ for $\Lambda_J > N$. For $1 < \Lambda_J < N$ the sum can be computed numerically or in a continuum approximation. We find that the sum over the phase differences squared is equal to $8/\Lambda_J$ [11]. Hence,

$$M_v = \frac{h^2}{4\pi^2 p^2 \Lambda_J} E_C^{-1} \text{ for } 1 < \Lambda_J < N. \quad (4)$$

In other geometries, the phase configuration of a vortex is not exactly known. It can in principle be calculated. However, since a substantial part of the mass is determined by the junction the vortex crosses, Eq. (3) can be used as a estimate for the quasi-static vortex mass in these cases.

B Equation of motion for a single vortex

A vortex in a Josephson array moves under influence of a Lorentz force $\Phi_0 I/p$ in a direction perpendicular to the current flow. A phenomenological damping term and the periodic lattice potential $U(x)$ provide additional forces. The equation of motion can therefore be written as:

$$M_v \ddot{x} + \eta \dot{x} = -\frac{dU}{dx} + \frac{\Phi_0 I}{p}, \quad (5)$$

where x is the vortex position, I is the applied current per junction and where η is the viscosity coefficient. In a Bardeen-Stephen like model η can be calculated. The total power loss is the sum of all the resistive losses in the junctions: $\sum V_i^2/R_e$. Assuming R_e to be identical for all junctions, the sum in the total power is the same as in the calculation of the vortex mass. For example, $\eta = \Phi_0^2/2R_e p^2$ for a large square 2D array.

Neglecting interactions with array edges and with each other, vortices are only subject to the periodic lattice potential: $U(x) = \frac{1}{2}\gamma E_J \sin(2\pi x/p)$. Here, γ is the energy barrier in units of E_J a vortex has to overcome when moving from one cell to the next. In large 2D arrays with no self fields, $\gamma = 0.2$ in a square geometry and in a triangular geometry the barrier is about a factor five lower, $\gamma = 0.043$ [12]. Inclusion of self-field effects can be done and γ increases dramatically for $\lambda_\perp < 1$ [6]. In contrast, there is no energy barrier in 1D arrays if $\Lambda_J > 1$ [7].

The problem of vortex dynamics in Josephson arrays can directly be mapped onto the problem of the phase difference across a single junction: vortices in arrays produce the same dynamics as a single junction with a critical current per junction of $\gamma I_c/2$, a McCumber parameter $\beta_{c,v} = \gamma\beta_c$ and a plasma frequency $\omega_{p,v} = \sqrt{\gamma}\omega_p$. The dynamics can be visualized as that of a massive particle moving in a washboard potential. For the junction problem motion is in artificial ϕ -space; for the vortex problem motion is in real space.

Just as in single junctions, hysteresis at low voltages is seen in the measured array I - V characteristic when $\beta_{c,v} > 1$ as is illustrated in Fig. 2. This figure is measured on a square, aluminum 2D array [13] and the depinning current is close to the expected value of $\gamma/2I_c = 0.1I_c$ per junction. We do not observe, however, a RCSJ-like I - V characteristic. Above the depinning current, the I - V is almost a straight line with a slight bending in the direction of the voltage axis opposite to what is expected from the analogy with the single junction problem. This is also seen in simulations on the properties of a single vortex in a 2D array with periodic boundaries [14]. In that paper, a nonlinear viscosity coefficient was introduced which described the simulated data very well.

For currents well above depinning (above 50 μ A in Fig. 2), hysteresis is commonly seen in underdamped arrays. At high currents the flux-flow state becomes unstable and the I - V enters a row-switched state. In this row-switched state, rows of junctions across the whole array width start to oscillate coherently [15]: all phases rotate continuously in time with a phase shift between them.

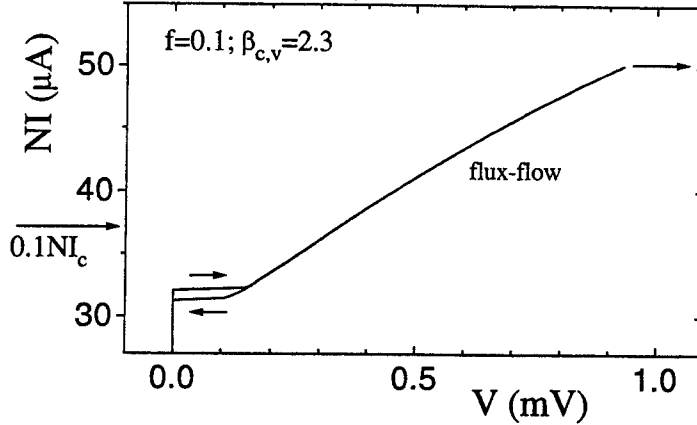


FIGURE 2. A current-voltage characteristic of a 2D square, aluminum array measured at low temperatures in a magnetic field of $0.1 \Phi_0$ applied per cell ($f = 0.1$). The arrow at the left indicates the expected depinning current of $0.1NI_c$ with N the number of junctions perpendicular to the direction of the current flow. For small voltages hysteresis is seen. The flux-flow region is found above the depinning current but below the current at which row switching sets in (arrow at the left).

One should realize that the curve in Fig. 2 was recorded at an applied magnetic flux of $0.1 \Phi_0$ per cell ($f = 0.1$). The frustration index f is a measure of the number of vortices in the array. On average there is approximately one vortex per $1/f$ cells. Thus at $f = 0.1$, the average distance between vortices is only three cells. At such a short distance, vortices will interact with each other. The influence of these vortex-vortex interactions on measured I - V characteristics is not known in detail.

Additional evidence for massive vortices is found in simulations on the influence of free boundaries on vortex motion [16]. The numerical calculations show that a vortex may be reflected at the boundary, thereby changing its sign (i.e., it becomes an antivortex). This behavior is qualitatively explained with the model (Eq. (5)) of a massive vortex interacting logarithmically with the image vortices outside the array. The authors also note that the way in which vortex inertia manifests itself depends on the dynamical situation considered. Changes in the applied current may induce oscillations in the phases (spinwaves) which introduce a new dissipation mechanism for the vortex (to be discussed in the next subsection).

C Coupling to spinwaves

In arrays with free boundaries, energy barriers for vortex entry exist near the array edges [17]. These barriers are not present in a ring geometry. This fact

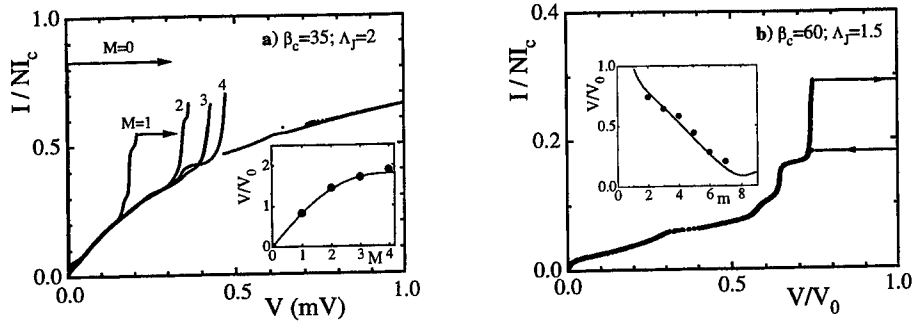


FIGURE 3. a: Experimental I - V curves corresponding to the five possible situations with M kinks trapped in a ring of $N = 8$ junctions. Inset: voltage position of main steps versus M . Curve is the predicted voltage position according to a sinusoidal dispersion relation. b: Enlarged view of the curve with $M = 1$ taken at a slightly lower temperature. Inset: voltage position of the substructure versus m . Curve is theoretical prediction (no fit parameters used).

makes the Josephson ring an ideal system for a quantitative comparison with the theory presented in the previous subsection.

Figure 2 plots I - V curves of a niobium Josephson ring cooled down in different applied magnetic fields. Cooling down in a field of about M flux quanta Φ_0 corresponds to trapping *exactly* M vortices in the ring, i.e., the number of vortices in the ring can only be an integer. When the ring is cooled through T_c in zero field, the I - V curve shows a critical current and jumps to the gap voltage at $0.84N I_c$. When cooling through T_c with $M = 1$ applied to the ring, the critical current vanishes and a current step appears near $V = 200 \mu\text{V}$. The jump to the gap voltage now occurs at $I_{max} = 0.55N I_c$. The absence of a depinning current for the curve with $M = 1$ in Fig. 3a is consistent with the absence of a lattice potential in the equation of motion for $\Lambda_J > 1$. With $M = 2, 3$, and 4 applied to the ring, the voltage position of the steps increases to about $350, 430$, and $480 \mu\text{V}$ respectively.

In contrast to the experiments on continuous Josephson rings [18], the voltages of the steps shown in Fig. 3a are not proportional to M . This is a direct consequence of the discrete nature of the Josephson array. The voltage positions map out the dispersion relation of the array. In a discrete system the dispersion relation bends near the Brillouin zone edges making the differences in voltage positions smaller for larger values of M . This bending is clearly visible in the inset of Fig. 3a. In this inset the voltage is normalized to $V_0 = \Phi_0 \omega_0 / 2\pi$ with $\omega_0 = 1/\sqrt{L_0 C}$.

We now turn to the $M = 1$ case, i.e., to the case of a Josephson ring with one vortex trapped in it. In Fig. 3a, one clearly sees that the $M = 1$ step contains smaller steps. These steps are enlarged in Fig. 3b. For high Λ_J^2 (high temperatures; not shown in the figure) the I - V curve is smooth indicating a continuous acceleration of the vortex. In this high Λ_J regime, the I - V curve can quantitatively

be described by the equation of motion as discussed in the previous subsection if one includes the relativistic nature of the vortex [11]. However, as Λ_J^2 approaches 1, substructure becomes visible in the I - V characteristic and in Fig. 3b six resonant steps are present. The substructure does not follow from our vortex model (Eq. (5)).

The substructure is caused by a phase locking between the propagating vortex and the linear waves (spinwaves) it excites in its wake [19,20]. Damping is low in Josephson systems and as a consequence small-amplitude oscillations in the junction phases generated by the moving vortex, have not died out when the kink passes by again. The possible ringing frequencies of these small-amplitude oscillations are the lattice eigenfrequencies. By matching the circulation frequency of the kink (which is proportional to the voltage position of the step) to an integer multiple m of ringing periods, the resonant voltages can be calculated. As illustrated in the inset of Fig. 3b, this model explains the positions of the resonant steps very well.

The coupling to linear waves can be viewed as an additional source of damping for the vortex. On a resonant step, further increases of the current do not lead to further increases in the vortex velocity. Instead, the energy is consumed in amplifying the linear waves.

Spinwave damping also determines the effective viscosity in the flux-flow regime of 2D highly underdamped, aluminum arrays [21]. Experiments showed that vortices, when driven with a *large current*, experience more damping than can be explained by ohmic dissipation alone. In a simple semi-quantitative model, the effective viscosity due to coupling to spinwaves was calculated. The result is $\eta_{pl} = \frac{1}{c} \frac{\Phi_0^2}{2S} \frac{1}{\sqrt{L_J/C}}$ where the constant c equals π for a square array and $c = 3\pi$ for a triangular array. When comparing this viscosity coefficient to the Bardeen-Stephen viscosity coefficient, one sees that the more underdamped the arrays are, the more dominant the damping due to energy lost in the wake of the vortex becomes. This result, however, is obtained from the measurement on the flux flow resistance and one should be careful with applying this result more generally. The situation might be different when this transport current is absent and vortices move at low velocities (see next subsection).

D Ballistic vortex motion

If vortices are massive particles, they should keep on moving if the current were to be turned off suddenly. In an experiment, this idea can be realized by accelerating vortices up to a high velocity u_0 so that their kinetic energy is much larger than the lattice potential. With Eq. (5) one finds that $u_0/p \approx \Phi_0 I / p^2 \eta$ if one neglects the lattice potential. Then, these fast moving vortices can be launched into a force-free environment where voltage probes can be used to detect their path through this region. The criterion $E_{kin} \geq E_{pot}$ translates into a minimum vortex velocity

$$\frac{u_{0,min}}{p} = \frac{\sqrt{\gamma}\omega_p}{\pi} . \quad (6)$$

Note, that for a 1D system with $\Lambda_J > 1$, $\gamma \approx 0$ so that the minimum vortex velocity is small.

The vortex velocity, on the other hand, can not be chosen arbitrarily large. Fast moving vortices can trigger row switching in the array. Simulations [22] indicate that in 2D arrays the vortex velocity must be limited to $u/p < \omega_p$. In 1D arrays $u/p < \pi\omega_0/4$ [20] (see also Fig. 3).

Another limitation comes from coupling to spinwaves. In 2D arrays, there is a threshold vortex velocity (u_{th}) below which this coupling is weak. In a continuum approximation [23,24], it has been shown that a moving vortex only couples to spinwaves above $u_{th}/p \approx 0.1\omega_p$. With Eq. (6), this indicates that ballistic motion is possible in triangular arrays just above depinning. In a recent paper, Fazio et al. [10] treat the charge transfer as a discrete process. The result is a stiffer spinwave spectrum and a reduction of spinwave dissipation even for classical arrays with large E_J/E_C . Their calculations show that there is wider window for ballistic motion with $u_{th}/p \approx 0.5\omega_p$.

With no current applied and for high-energetic vortices, Eq. (5) reduces to $M_v \dot{u} + \eta u = 0$, indicating that the vortex velocity decreases exponentially in time as $u_0 \exp[-M_v t/\eta]$. A mean free vortex path can be defined as

$$\frac{\lambda_{free}}{p} = \frac{u_0 M_v}{p\eta} = \alpha \frac{I}{I_c} \beta_c , \quad (7)$$

with $\alpha = 1/\pi$ for a square 2D array and $\alpha = \pi\Lambda_J/4$ for a 1D array. The factor $\alpha I/I_c$ is typically of order 0.1 so that at high temperatures with $R_e = R_n$, $\lambda_{free} \approx p$. At low temperatures with $R_e \gg R_n$ (the corresponding β_c can be high as 10^7), $\lambda_{free} \gg p$.

Ballistic vortex motion has not only been observed in long continuous junctions [25], where there are no energy barriers and no spinwave coupling, but also in discrete 1D arrays [26] and in 2D aluminum arrays [27]. Here, we discuss the experiment with 2D arrays. The sample consists of two 2D arrays which are connected by a narrow channel of 20 cells long and 7 cells wide as shown in Fig. 4a. Superconducting banks on both side of the channel confine the vortices in the channel. To reduce the influence of the lattice potential, arrays and channel are made in a triangular geometry.

In one array, vortices generated by a small magnetic field, are accelerated up to a high velocity. Some of these high-energetic vortices will enter the channel and will then be launched into the detector array. There is no driving current applied to this array. A set of voltage probes around the detector array is used to detect the places where vortices leave the force-free environment. (The voltage measured across two probes is proportional to the number of vortices passing the probes per unit time.) At high temperatures, vortices move diffusively and voltages are observed between all voltage probes. At low temperatures, subgap damping is extremely low and the

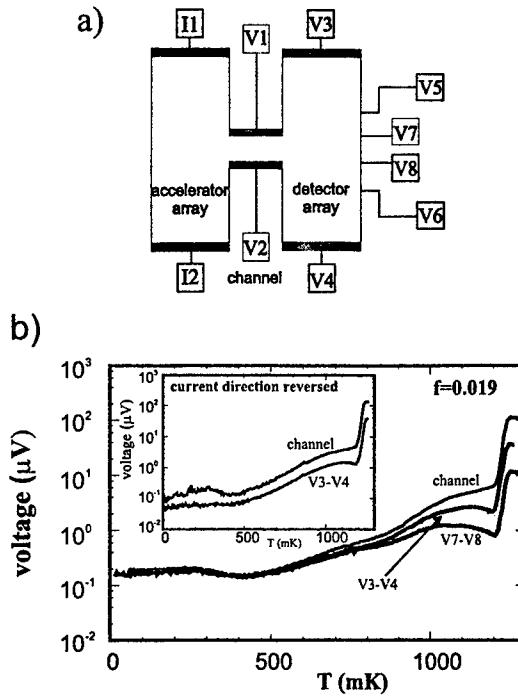


FIGURE 4. a) Special sample lay-out to measure ballistic vortices. b) Voltage across different voltage probes. At low temperatures, the voltage across the two probes opposite from the channel is almost equal to the voltage across the channel: all vortices that go through the channel leave the array between V7 and V8. Inset: with reversed current direction vortices are accelerated in the opposite direction and no ballistic motion is observed.

voltage measured between the two probes situated just opposite to the channel is almost equal to the channel voltage. Vortices cross the second array in a narrow beam (see Fig. 4b).

This ballistic vortex motion is observed for small applied magnetic fields ($0.01 < f < 0.025$) and for currents just above depinning. For high magnetic fields, vortex-vortex interactions start to play a role when more than one vortex is in the channel at the same time and for too high currents coupling to spinwaves starts to play a role.

III QUANTUM VORTEX DYNAMICS

If vortices are massive particles that move ballistically, one has to think of them as quantum mechanical objects. Like an electron, a vortex in a periodic potential will also have a Bloch wave function with momentum $p = \hbar k$ and thus a wavelength of h/uM_v . At present, many experiments have verified the concept of a quantum vortex [3,28–32]. In this paper we will discuss the macroscopic quantum tunneling of vortices [3] and their motion in a periodic potential [29–31] in more detail. We will not discuss the observation of vortex interference in a hexagon-shaped array [32] and the predicted persistent motion of quantum vortices in corbino arrays [33]. We will start this chapter with some general considerations.

In a classical description vortices oscillate in the minima of the washboard potential with frequency $\omega_{p,v}$. In quantum arrays, these oscillations are quantized. To estimate when quantum fluctuations in the vortex position become important, we compare the zero-point energy $\frac{1}{2}\hbar\omega_{p,v} = \frac{1}{2}\sqrt{8\gamma E_J E_C}$ to the energy barrier $U_{bar} = \gamma E_J$. The two energies are equal if $E_J/E_C = \sqrt{2/\gamma}$. In this quantum vortex regime, the zero-point fluctuations are large enough to allow for quantum tunneling of vortices (next subsection).

These fluctuations also influence the depinning current in the array. We found [35] that the depinning currents in quantum arrays are substantially lower than the expected value of $0.1NI_c$. The Chalmers group [28] has reported a similar observation. Like in single junctions [34], quantum depinning should also show up as a saturation of the array critical current distribution as temperature is lowered. In Delft, we have tried to measure this effect but found a more complicated behavior than in single junctions [35].

The quantum nature of vortices becomes more prominent as the ratio E_J/E_C is decreased. There is, however, a limit to decreasing this ratio. In zero magnetic field depending on their E_J/E_C ratio, arrays at low temperature are either superconducting or insulating. Experiments [3,36] show that in square 2D arrays this S-I transition occurs at $E_J/E_C \approx 0.6$ in agreement with theoretical predictions [37]. When a magnetic field is applied to arrays with $E_J \approx E_C$, a collective quantum S-I transition involving a Bose condensation of vortices can occur. Arrays which are in the superconducting state at zero magnetic field can be driven into the insulating state by a magnetic field of only 1 Gauss [3,38]. At low magnetic fields, vortices are pinned and the array is in the superconducting state. For higher fields a critical vortex density is reached at which they Bose condense. The vortex superfluid now leads to an infinite resistance.

Arrays in which charging effects are important are made of aluminum with a shadow evaporation technique. For the study of quantum vortex effects, arrays typically have junctions of size 0.1 by $0.1 \mu\text{m}^2$. Their capacitance C is 1 fF. The charging energy $E_C = e^2/2C$ then corresponds to a temperature of 0.9 K. At low temperatures, the Josephson coupling energy is given by $E_J/k_B = \Phi_0 I_c / 2\pi k_B = 7.2 R_n^{-1}$ K when the normal-state resistance R_n is expressed in $\text{k}\Omega$. Quantum vortex

arrays have $1 \text{ k}\Omega < R_n < 15 \text{ k}\Omega$. In low-capacitance arrays supercurrents flowing around the vortices induce a negligible magnetic field so that self-field effects can be neglected; the penetration depth λ_1 is larger than the array sizes.

A Macroscopic quantum tunneling of vortices

In Fig. 5, we plot the resistance per junction (linear response) as a function of temperature for two square arrays; a classical array in (a) and a quantum array in (b). The resistance of the classical array decreases exponentially all the way down to the lowest temperatures. The slopes define the barrier for this thermally activated process: $R \propto \exp[-U_{bar}/k_B T] = \exp[-\gamma/\tau]$. In contrast, the resistance of the quantum array levels off at a certain normalized temperature τ_{cr} below which it remains constant. We denote this constant value with R_c . Above τ_{cr} , again thermally activated behavior is observed.

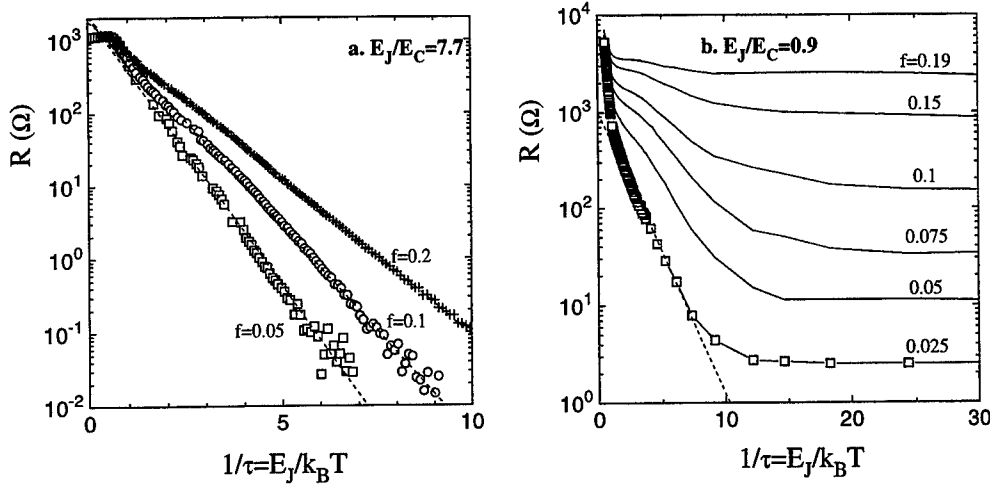


FIGURE 5. Zero-bias resistance per junction versus the inverse normalized temperature measured for two different square arrays.

From the analogy with the single-junction problem, the tunnel rates and hence R_c can be estimated. In the moderate damping regime [34] one finds:

$$R_c \approx 140 R_q f \sqrt{s} e^{-s} \quad (8)$$

where s is given by

$$s = \frac{7.2 U_{bar}}{\hbar \omega_{p,v}} \left(1 + \frac{0.87}{\sqrt{\beta_{c,v}}} \right). \quad (9)$$

Here, $R_q = h/4e^2 = 6.45 \text{ k}\Omega$. Since $\hbar\omega_{p,v} = \sqrt{8\gamma E_J E_C}$, s is proportional to $\sqrt{E_J/E_C}$.

An estimate for τ_{cr} can be obtained by equating s to γ/τ . Neglecting the term with $\beta_{c,v}$, the result is:

$$1/\tau_{cr} = \frac{2.5}{\sqrt{\gamma}} \sqrt{\frac{E_J}{E_C}}. \quad (10)$$

With E_J of the order of E_C , $1/\tau_{cr}$ is typically somewhat larger than 2.5 in agreement with the data of Fig. 5.

We have compared the measured values of R_c with the estimates (Eq. (8,9)) and found that the tunnel rates in the measurements are lower than expected even when taking R_n as the resistance determining $\beta_{c,v}$. The measured values of R_c are about a factor $\exp[4]$ too small. A smaller R_c is consistent with a single vortex model in which the vortex mass is an order of magnitude larger than the one calculated in the quasi-static approximation. It is likely that vortices do not move as rigid objects and calculations have shown that the dynamic band mass of a vortex can be an order of magnitude larger [39].

A surprising result is that the array in Fig. 5a doesn't show a sign of quantum tunneling. Our simple argument given above indicates that for this array the zero-point energy is of order $0.2E_J$. The absence of quantum tunneling is explained by the fact that in Fig. 5a the measured energy barriers are of order E_J , instead of $0.2E_J$. We have studied the thermally activated behavior in other arrays as well and found a systematic increase of the measured energy barriers with decreasing E_J/E_C ratio as shown in Fig. 6. At $E_J/E_C = 2$, however, there is sudden decrease with about $2E_J$ in the measured energy barriers. Quantum tunneling is observed in the small region from $E_J/E_C = 2$ down to the S-I transition.

We believe that the observed dependence of the measured energy barriers with E_J/E_C has something to do with coupling to the oscillatory junction modes: the dashed line in Fig. (6) represents a barrier of $0.2E_J + \hbar\omega_p$, i.e., the predicted energy barrier for a large array plus the plasma energy of a single junction. For $E_J/E_C < 2$, an energy of $\hbar\omega_p$ can no longer be transferred to the junction because $\hbar\omega_p$ is larger than $2E_J$, the maximum energy a single junction can absorb. This would then explain the sudden decrease of the measured energy barrier near $E_J/E_C = 2$. Since the precise mechanism behind this coupling is unclear, we can not be sure that the single-vortex model accounts for our experimental data. We can not exclude the possibility of collective tunneling.

B Quantum vortex transport in a periodic 1D potential

Electrons in metals move in the periodic potential created by the positively charged ions. The electron wave functions overlap and energy bands are formed. A constant electric field accelerates electrons, but in the absence of scattering,

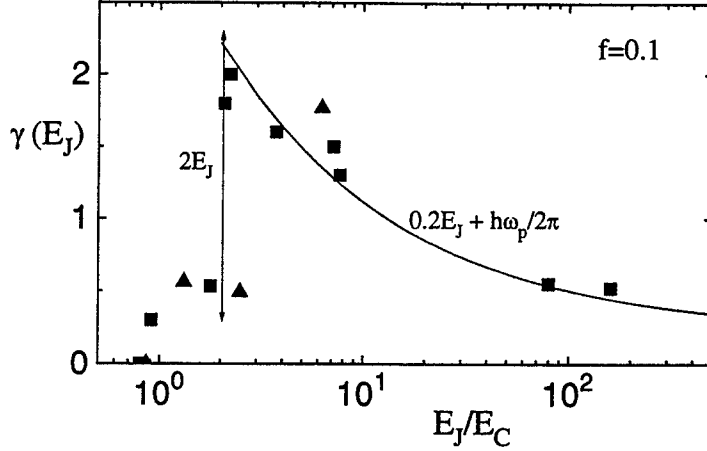


FIGURE 6. Measured energy barriers in units of E_J as a function of the E_J/E_C ratio for square (solid squares) and triangular (solid triangles) 2D arrays. Around $E_J/E_C = 2$, a sudden decrease by an amount of $2E_J$ is found in the measured energy barriers. The S-I transition for this value of applied magnetic field ($f = 0.1$) occurs at $E_J/E_C \approx 0.9$, slightly above the zero-field value of 0.6.

electrons would be Bragg reflected at the zone edges. Electrons then undergo an oscillatory motion in space (Bloch oscillations). No charge would be transported. In metals scattering takes place before the electrons can reach the zone edge. Bloch oscillations do not appear and charge is transported. In semiconductor superlattices [40] Bloch oscillations have recently been observed because of the larger superlattice period and because of less scattering in the controlled fabricated structures.

Vortices in a periodic potential should also form energy bands. We will consider the geometry of Fig. 1c. For low densities, vortices move in the middle row only experiencing a 1D sine potential. For a free vortex the energy depends quadratic on the wave vector k : $E(k) = \hbar^2 k^2 / 2M_v$. The quasi-static vortex mass is approximately given by the value in Eq. (3) so that $E(k) = 2E_C (p/\pi)^2 k^2$. At the Brillouin zone edge $k = \pi/p$, the energy is equal to $2E_C$. In a periodic potential, energy gaps open up at the zone edges. The gap is equal to the Fourier coefficient of the lattice potential [41]. For a sine potential $\frac{1}{2}\gamma E_J \sin(2\pi x)$, the gap is therefore γE_J . Thus, vortices in arrays form energy bands with a bandwidth of order E_C and an energy gap of $\frac{1}{2}\gamma E_J$ as is illustrated in Fig. 7.

If a small constant force ($= \Phi_0 I / p$) is applied to the vortex, the wave vector will change linearly in time because $\Phi_0 I / p = \hbar dk / dt$. In the absence of damping, the vortex will always reach the Brillouin zone edge where it will be Bragg reflected. This Bragg reflection results in an oscillatory motion in k -space. On average the vortex velocity ($= \hbar^{-1} dE(k) / dk$) is zero due to the periodicity of the bands. The time it takes the vortex to complete one oscillation follows from $\Delta t = \Delta k / <$

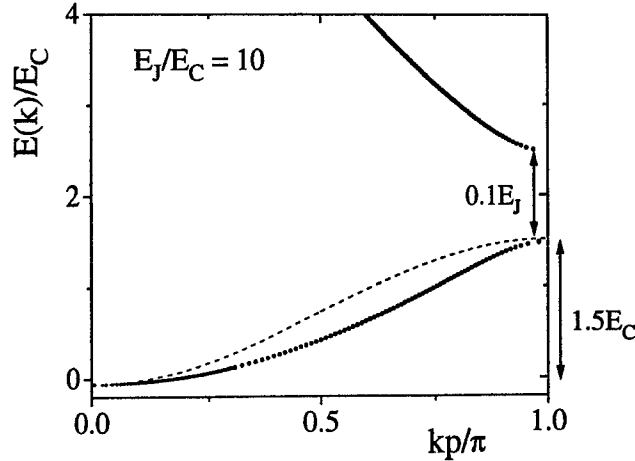


FIGURE 7. Schematic drawing of the energy bands for a vortex moving in a quasi-1D Josephson array. Dots: numerical calculated energy bands starting from Schrödinger's equation with a cosine potential [42]. The dashed line shows the first band of a cosinusoidal dispersion relation with the same band width.

$dk/dt > 0$ with $\Delta k = 2\pi/p$. The corresponding Bloch oscillation frequency (ν_B) is:

$$\nu_B = \frac{I}{2e} . \quad (11)$$

The Bloch frequency increases linearly with increasing bias current. When biasing an array with 1000 junctions with currents of order μA 's, Bloch frequencies will be of the order of 1-10 GHz.

The amplitude of the Bloch oscillation can be estimated from combining the equations given in the previous paragraph ($\Phi_0 I/p = \hbar dk/dt$ and $dx/dt = \hbar^{-1} dE(k)/dk$). If the bandwidth is $2E_C$, the result is:

$$\frac{x}{p} = \frac{E_C}{E_J} \frac{I_c}{2\pi I} . \quad (12)$$

Since $E_C \approx E_J$ and I_c/I is typically 100, the Bloch oscillations extend over 10 cells.

What will be the characteristic feature of Bloch oscillating vortices in a dc current-voltage characteristic? For very small bias, there will be a small supercurrent because vortices need to overcome the energy barriers near the array edges. Just above the depinning current, vortices start to move but even the smallest amount of dissipation will prevent the occurrence of Bloch oscillations. Thus, an increase of the current will yield an increase of the measured voltage across the array. However, when increasing the current even more at some point the dissipation is not strong enough to prevent the vortices from reaching the zone edges. Bloch

oscillations are now possible. In the I - V characteristic a sudden decrease of the voltage is then expected with a negative differential resistance: the oscillating vortices do not contribute to the net transport of vortices through the array. In Delft, I - V characteristics with a negative differential resistance have been measured in quasi-1D quantum arrays [29]. The data indicate a more complicated picture than our single-vortex model presented here. In the experiment, vortex-vortex interactions seem to play a role as well. To date, it has been impossible to measure the response of one vortex in the array.

When the periodicity of the underlying lattice is distorted, the spatial extent of the vortex wave functions will be reduced. This phenomenon is called Anderson localization [43]. In one-dimension, localization is strong even with weak disorder. Anderson localization of quantum vortices in disordered arrays has recently been reported [30]. The arrays have vertical rows with larger junctions. The larger junctions create additional energy barriers for vortex motion. If the spacing between rows is equal, a superlattice is obtained with a new cell given by the distance between the rows and the array width. In these arrays, vortex wave functions are still extended since at the lowest temperatures a finite, temperature independent resistance remains. Vortices are mobile and tunnel through the energy barriers of the array. Disorder is introduced by changing the distance between adjacent rows with the larger junctions. A dramatic difference is found in the resistive behavior. When lowering temperature, the resistance monotonically decreases. There is no leveling off as observed for the arrays with a superlattice. The vortices in the disordered array are localized. For high vortex densities, however, the response is not so different. Vortex-vortex interaction have led to a delocalization of the vortices due to their repulsive interaction.

These vortex-vortex interactions also play a dominant role in the transition to a Mott insulator [31]. In a periodic potential vortices localize when their density is commensurate with the 1D lattice potential. This transition is due to a collective effect associated with vortex-vortex interactions.

IV ACKNOWLEDGMENT

Discussions with Rosario Fazio, Hans Mooij, Terry Orlando, Anne van Otterlo, Alexander van Oudenaarden, Gerd Schön, Steven Strogatz and Shinya Watanabe are gratefully acknowledged. Work supported by the Dutch Foundation for Fundamental Research on Matter (FOM).

REFERENCES

1. D.J. Bergmann, E. Ben-Jacob, Y. Imry and K. Maki, Phys. Rev. B **27** (1983) 3345.
2. M.H. Devoret and H. Grabert, in *Single charge tunneling* (Plenum Press, New York, 1992) page 8.

3. H.S.J. van der Zant, W.J. Elion, L.J. Geerligs and J.E. Mooij, Phys. Rev. B **54** (1996) 10081.
4. S.E. Korshunov, Physica B **152** (1988) 261; A.I. Larkin, Yu. N. Ovchinnikov, and A. Schmid, *ibid.* 266; U. Eckern and A. Schmid, Phys. Rev. B **39** (1989) 6441.
5. HYPRES, Inc., Elmsford, NY 10523.
6. J.R. Phillips, H.S.J. van der Zant, J. White and T.P. Orlando, Phys. Rev. B **47** (1993) 5219.
7. R.D. Bock, J.R. Phillips, H.S.J. van der Zant, J. White and T.P. Orlando Phys. Rev. B **49** (1994) 10009.
8. T.P. Orlando, J.E. Mooij and H.S.J. van der Zant, Phys. Rev. B **43** (1991) 10218.
9. T.P. Orlando, H.S.J. van der Zant, J.R. Phillips, J. White, E. Trias and A.E. Duwel, in *Macroscopic Quantum Phenomena and Coherence in Superconducting Arrays*, eds. C. Giovannella and M. Tinkham (World Scientific, Singapore, 1995) page 175.
10. R. Fazio, A. van Otterlo and G. Schön, Europhys. Lett. **25** (1994) 453.
11. H.S.J. van der Zant, T.P. Orlando, S. Watanabe and S.H. Strogatz, Physica B **203** (1994) 490.
12. C.J. Lobb, D.W. Abraham and M. Tinkham, Phys. Rev. B **27** (1983) 150.
13. H.S.J. van der Zant, F.C. Fritschy, T.P. Orlando and J.E. Mooij, Phys. Rev. Lett. **66** (1991) 2531.
14. T.J. Hagenaars, P.H.E. Tiesinga, J.E. van Himbergen and J.V. José, Phys. Rev. B **50** (1994) 1143.
15. H.S.J. van der Zant, C.J. Muller, L.J. Geerligs, C.J.P.M. Harmans and J.E. Mooij, Phys. Rev. B **38** (1988) 5154; J.R. Phillips, H.S.J. van der Zant and T.P. Orlando, Phys. Rev. B **50** (1994) 9380.
16. T.J. Hagenaars, J.E. van Himbergen, J.V. José and P.H.E. Tiesinga, Phys. Rev. B **53** (1996) 2719.
17. H.S.J. van der Zant, H.A. Rijken and J.E. Mooij, J. Low. Temp. Phys. **79** (1990) 289.
18. A. Davidson, B. Dueholm and N.F. Pedersen, J. Appl. Phys. **60** (1986) 1447; A.V. Ustinov, T. Doderer, R.P. Huebener, N.F. Pedersen, B. Mayer and V.A. Oboznov, Phys. Rev. Lett. **69** (1992) 1815.
19. A.V. Ustinov, M. Cirillo, and B.A. Malomed, Phys. Rev. B **47** (1993) 8357.
20. H.S.J. van der Zant, T.P. Orlando, S. Watanabe and S.H. Strogatz, Phys. Rev. Lett. **74** (1995) 174.
21. H.S.J. van der Zant, F.C. Fritschy, T.P. Orlando and J.E. Mooij, Phys. Rev. B **47** (1993) 295.
22. P. A. Bobbert, Phys. Rev. B **45** (1992) 7540.
23. U. Geigenmüller, C.J. Lobb and C.B. Whan, Phys. Rev. B **47** (1993) 348.
24. U. Eckern and E.B. Sonin, Phys. Rev. B **47** (1993) 505.
25. A. Matsuda and T. Kawakami, Phys. Rev. Lett. **51** (1983) 694.
26. A. Fujimaki, K. Nakajima and Y. Sawada, J. Appl. Phys. **61** (1987) 5471.
27. H.S.J. van der Zant, F.C. Fritschy, T.P. Orlando and J.E. Mooij, Europhys. Lett. **18** (1992) 343.
28. C.D. Chen, P. Delsing, D.B. Haviland, Y. Harada and T. Claeson, Phys. Rev. B **54** (1996) 9449.

29. A. van Oudenaarden, S.J.K. Várdy and J.E. Mooij, Czechoslovak Journal of Physics **46 Suppl. S2** (1996) 707.
30. A. van Oudenaarden, S.J.K. Várdy and J.E. Mooij, Phys. Rev. Lett. **77** (1996) 4257.
31. A. van Oudenaarden and J.E. Mooij, Phys. Rev. Lett. **76** (1996) 4947.
32. W.J. Elion, J.J. Wachters, L.L. Sohn and J.E. Mooij, Phys. Rev. Lett. **71**, 2311 (1993).
33. B.J. van Wees, Phys. Rev. Lett. **65** (1990) 225; T.P. Orlando and K.A. Delin, Phys. Rev. B **43** (1991) 8717; Z. Hermon, A. Stern and E. Ben-Jacob, Phys. Rev. B **49** (1994) 9757.
34. J.M. Martinis, M.H. Devoret and J. Clarke, Phys. Rev. B **35** (1987) 4682.
35. H.S.J. van der Zant, unpublished work.
36. L.J. Geerligs, M. Peters, L.E.M. de Groot, A. Verbruggen and J.E. Mooij, Phys. Rev. Lett. **63** (1989) 326.
37. R. Fazio and G. Schön, Phys. Rev. B **43** (1991) 5307.
38. H.S.J. van der Zant, F.C. Fritschy, W.J. Elion, L.J. Geerligs and J.E. Mooij, Phys. Rev. Lett. **69** (1992) 2971; C.D. Chen, P. Delsing, D.B. Haviland, Y. Harada and T. Claeson, Phys. Rev. B **51** (1995) 15645.
39. U. Geigenmüller, in *Macroscopic Quantum Phenomena*, eds. T.D. Clarke et al. (World Scientific, Singapore, 1991) page 131.
40. J. Feldman et al., Phys. Rev. B **46** (1992) 7252; C. Waschke et al., Phys. Rev. Lett. **70** (1993) 3319.
41. C. Kittel, *Introduction to Solid State Physics* (John Wiley & Sons, New York, 1986) Chapter 7.
42. A. van Oudenaarden et al., to be published in Phys. Rev. B.
43. P.W. Anderson, Phys. Rev. **109** (1958) 1492.

Single-Electron Tunneling Devices

P. Hadley

*Department of Applied Physics and DIMES, Delft University of Technology, PO Box 5046, 2600
GA Delft, The Netherlands*

Abstract. Single-electron tunneling devices can detect charges much smaller than the charge of an electron. This enables phenomenally precise charge measurements and it has been suggested that large scale integration of single-electron devices could be used to construct logic circuits with a high device packing density. Here the operation of the two basic types of single-electron tunneling transistors is reviewed. The applications of single-electron tunneling in precision measurements and in general purpose computation is discussed. Particular attention is paid to the characteristics of single-electron tunneling transistors in the superconducting state.

Introduction

Single-electron tunneling (SET) devices can monitor and manipulate the motion of individual electrons.¹⁻⁵ These devices lie at the intersection of two major research trends: mesoscopic physics and the miniaturization of electronic circuits. Much of the original motivation for the studying of SET devices came from mesoscopic physics. Mesoscopic physics is the study of artificially constructed systems that exhibit quantum behavior. Sometimes the systems that are fabricated are called artificial atoms because the devices that are produced behave in many ways like atoms. Mesoscopic physicists often study the electrical transport through a small island of metal or semiconductor (also called a quantum dot) by weakly attaching leads to the island. The capacitance of these islands can be so small that adding a single electron to the island causes the voltage to jump significantly. By adding electrons to the island of a SET transistor one can investigate the quantum mechanical level spacing in the island,⁶⁻⁸ the spin splitting of the quantum mechanical levels in a magnetic field,^{9,10} the interaction of electrons on the island, the modulation of the shot noise due to the Coulomb blockade,¹¹ and how electrical transport through the island is coupled to the electromagnetic environment.¹² The physics of electrical transport through a island is more complex if either the leads or the island itself is superconducting. In that case, current can flow due to the motion of Cooper pairs or due to the motion of normal electrons, or due to a combination of both.

Another important research trend that has focused attention on SET devices is the miniaturization of electronic circuits. The information technologies that are be-

coming increasingly important in our society are advancing so quickly because we keep finding ways to manufacture circuits more cheaply. Powerful computers have become widely available for a reasonable price. One of the essential ingredients to the success of the information technologies is the miniaturization of electronic circuits. As the circuits are made smaller, more devices can be manufactured simultaneously, resulting in cheaper circuits. The smaller the circuits are made, the smaller the amount of charge that is used to represent a bit. It is necessary to reduce the amount of charge that represents a bit because in the commonly used logic schemes, the amount of energy that is dissipated when a bit is manipulated is related to the charge that represents the bit times the voltage level. The power dissipated by a circuit is one of the factors limiting the miniaturization of electronic circuits. The smallest amount of charge that can be used to represent a bit is a single electron. Therefore SET devices have been investigated where bits are represented by individual electrons or just a few electrons. These circuits can be made very small and dissipate little power making them potentially useful for dense integrated circuits. Quite a number of logic schemes using SET devices have been proposed. To understand how these devices work, we will begin with the simplest components of SET circuits, the single-electron tunneling transistors.

Single Electron Tunneling Transistors

The most widely studied SET device is the capacitively coupled SET transistor. It consists of a metallic island that is coupled to three electrodes as shown in Fig. 1. Two of the leads are coupled to the island via high resistance tunnel junctions and the third lead (the gate) is capacitively coupled to the island. The transistor shown was fabricated in a Au/SiO₂/Al three layer process.¹³ Since aluminum is a superconductor, this device can be operated either in the superconducting state or in the normal state where the superconductivity is suppressed by applying a magnetic field. SET transistors can be made using a wide variety of metals, semiconductors, or conducting polymers.

The electrical characteristics of the capacitively coupled SET transistor are shown in Fig. 2. The current that flows through the two tunnel junctions can be modulated by changing the charge on the gate. Two current-voltage curves are shown for this device in the normal state and two curves in the superconducting state. In the normal state, on the curve labeled $q = 0$, no current flows until there is a finite voltage across the two junctions. This is known as the Coulomb blockade. The origin of the blockade has to do with the finite energy that is necessary to add an extra electron to the island. The Coulomb blockade is maximized any time the charge on the gate is an integer multiple of the charge of an electron, e . The Coulomb blockade can be suppressed by adjusting gate charge to $(n + \frac{1}{2})e$, where

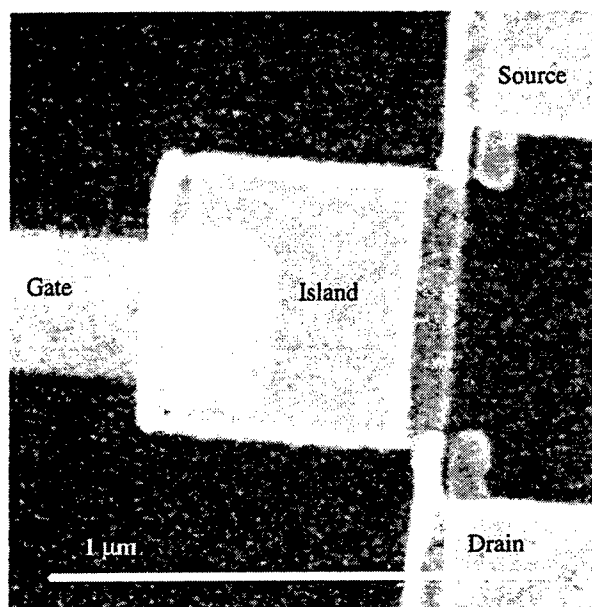


FIGURE 1 A SEM photo of a capacitively coupled SET transistor. First gold layer was deposited on an oxidized Si substrate and this was patterned by liftoff to form the gate. Next SiO was deposited to electrically isolate the gate and the island. Finally the aluminum source, drain, and island were defined by liftoff. The two tunnel junctions at the corners where the island meets the source and the drain were defined by shadow evaporation. (Courtesy of Erik Visscher)

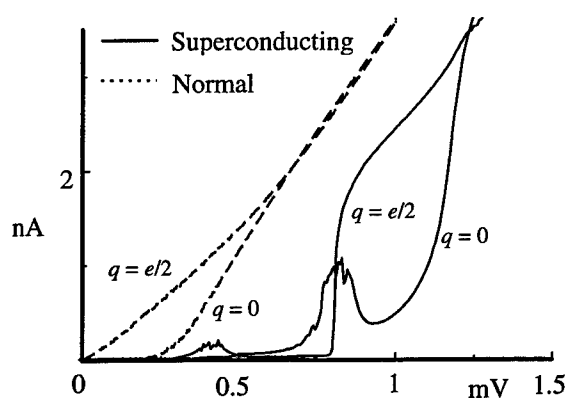


FIGURE 2. The current - voltage characteristics for the same SET transistor in the normal state and in the superconducting state.

n is an integer. When the Coulomb blockade is suppressed, the curve labeled $q = e/2$ is observed. In the superconducting state, hardly any current flows through the device below a bias voltage of $4\Delta/e$ even when the Coulomb blockade is suppressed. Here Δ is the superconducting gap.

A SET transistor can be used to measure charge either in the normal state or in the superconducting state. Typically, the SET transistor is voltage biased at a point where there is a large modulation of the current as a function of the gate charge. The charge that is to be measured is coupled to the gate and the current through the gate is monitored. By this means charges much smaller than the charge on an electron can be measured. The charge resolution that can be achieved is about $10^{-4} e/\sqrt{\text{Hz}}$ at 10 Hz. SET transistors offer by far the best charge resolution of any of the available charge measurement devices. The charge resolution of the SET transistor is better in the superconducting state due to the larger current modulation at the optimum bias point.¹⁴

People familiar with superconducting electronics may be puzzled by the lack of a supercurrent in Fig. 2. If the tunnel junctions were larger so that they had a resistance of about 1Ω , a supercurrent would flow through the two tunnel junctions in series. This supercurrent would not be sensitive to the charge on the gate. Such large tunnel junctions exhibit the Josephson effects in the superconducting state and behave like resistors in the normal state. As the junctions are made smaller, the resistance of the junctions increases and their capacitances decrease. The first significant deviation from large junction behavior occurs when the junction resistance exceeds about 100Ω . This has to do with the impedance of the environment in which the junction is embedded. The environment usually consists of the leads which act as either an antenna or a transmission line and transport high frequency radiation away from the junction. From the junction's point of view, the environmental impedance can often be modeled as an ohmic resistor with a value of about 100Ω . (see Fig. 3) The impedance of the environment is in parallel with the junction and can be neglected if the junction impedance is much lower than the impedance of the environment. In the large junction limit, the impedance of the junction is typically 1Ω and thus the impedance of the environment can be safely neglected. When the impedance of the junction exceeds about 100Ω , the environment effectively shunts the junction at high frequencies and it cannot be neglected. This results in additional high frequency damping which is sometimes reflected in the measured dc characteristics. An excellent discussion of these effects is given in the second edition of *Introduction to Superconductivity* by M. Tinkham.¹⁵ For any devices with impedances larger than 100Ω the high frequency damping of a low impedance environment should be kept in mind.

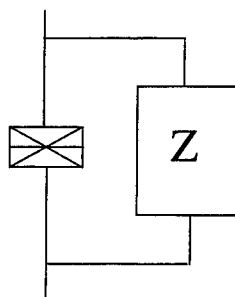


FIGURE 3. A superconducting tunnel junction and the impedance of the environment it sees at high frequencies. A typical environment has an impedance of $100\ \Omega$. If the junction resistance is much less than $100\ \Omega$, the effect of the environment can be ignored. For junctions with impedances larger than $100\ \Omega$, the environment increases the high frequency damping.

As junctions are made still smaller another qualitative change in the behavior of the junctions occurs when the resistance of the junctions approaches the quantum resistance $h/e^2 = 25\ \text{k}\Omega$, familiar from the quantum Hall effect. This resistance marks the transition where the dynamics of a superconducting junction can better be described by the motion individual electrons and Cooper pairs than by the motion of individual vortices. Since the voltage across a superconducting junction is the number of vortices that pass by per second and the current is the number of electrons that pass by per second, the resistance is the ratio of the number of vortices that pass by to the number of electrons that pass by. For resistances much below the quantum resistance many electrons pass through the junction for every vortex that goes by. In this regime, the circuit can best be described in terms of the motion of individual vortices. When the resistance is much higher than the quantum resistance, many vortices pass through the junction for every electron that passes by. Here the circuit can best be described in terms of the motion of individual electrons and Cooper pairs.

When the resistance of the junctions in a circuit is approximately equal to $25\ \text{k}\Omega$, the circuit must be analyzed quantum mechanically. When this is done for a SET transistor one finds that the current that flows onto the island and the charge on the island are noncommuting variables. One consequence of this is that the supercurrent can be modulated by changing the charge on the gate. It is possible to use the modulation of the supercurrent to measure the charge on the gate. Charge measurements can be made more quickly when the supercurrent is monitored than when the quasiparticle current is monitored because the output impedance is lower.¹⁶ As the resistance is increased further, the supercurrent is suppressed. For junctions with resistances more than $100\ \text{k}\Omega$, the current that flows is primarily

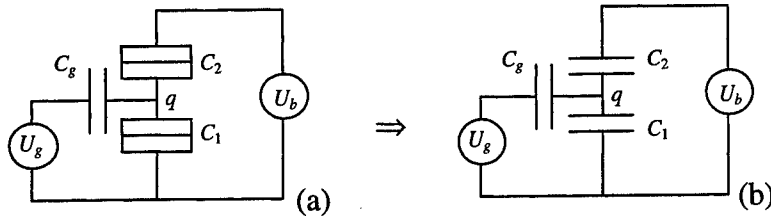


FIGURE 4. If the tunnel junctions resistances are much larger than the quantum resistance then the voltages across the tunnel junctions in circuit (a) can be approximated by solving for the voltages across the equivalent system of capacitors in circuit (b).

due to quasiparticles and the current-voltage characteristics has the form shown in Fig. 2.

For resistances much larger than the quantum resistance it is possible calculate the Coulomb blockade region by first ignoring tunneling and treating the circuit as a system of capacitors (see Fig. 4). When this is done, the voltages across the two junctions can be determined.

$$V_1 = \frac{1}{C_\Sigma} (q + C_g U_g + C_2 U_b)$$

$$V_2 = \frac{1}{C_\Sigma} ((C_\Sigma - C_2) U_b - q - C_g U_g)$$

Here q is the charge on the island and C_Σ is the total capacitance, $C_\Sigma = C_1 + C_2 + C_g$. The charge on the island can be decomposed into an integer times the charge of an electron plus an offset charge, $q = ne + q_0$. The offset charge is due to the polarization of the island by charged defects in the vicinity of the island. A current will flow through a SET transistor in the normal state if the voltage across one of the junctions exceeds $e/(2C_\Sigma)$. The condition that $|V_1| < e/(2C_\Sigma)$ and $|V_2| < e/(2C_\Sigma)$ corresponds to a different diamond shaped region in the $U_b - U_g$ plane for every value of n . This is shown in the stability diagram of Fig. 5a. The Coulomb blockade occurs inside the diamonds. The periodicity of the stability diagram is e/C_g along the U_g axis. In the superconducting state, the condition that no significant quasiparticle current flow is $|V_1| < e/(2C_\Sigma) + 2\Delta$ and $|V_2| < e/(2C_\Sigma) + 2\Delta$. This results in the stability diagram shown in Fig. 5b.

Measurements of the current through a superconducting SET transistor are shown in Fig. 6. The most prominent feature in the figure is the zigzag pattern across the top which indicates the onset of significant quasiparticle current flow through the SET transistor. This zigzag pattern follows the top of the overlapping diamonds

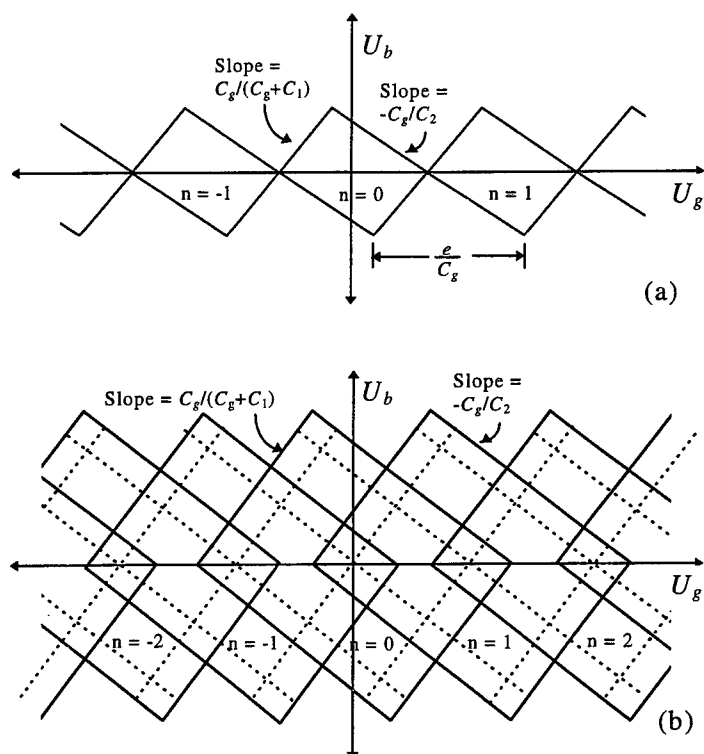


FIGURE 5. (a) The stability diagram for a capacitively coupled SET in the normal state. The Coulomb blockade occurs inside the diamonds. The periodicity along the U_g axes is e/C_g . (b) The stability diagram for the same SET transistor in the superconducting state. In the superconducting state the diamonds overlap. The dotted lines indicate where resonant Cooper pair tunneling can take place. For convenience the offset charge, q_0 , was taken to be zero in these figures. A nonzero offset charge displaces the stability diagrams along the U_g axis.

shown in Fig. 5b. The periodicity of the pattern along the gate voltage axis can be used to calculate the gate capacitance and the slopes that form the zigzag pattern can be used to calculate the capacitances of the two junctions using the formulas given in Fig. 5b.

The isolated current peaks at a bias voltage of about 0.4 mV are due to the $3e$ processes described by Maassen van den Brink.¹⁷ The intersecting ridges of cur-

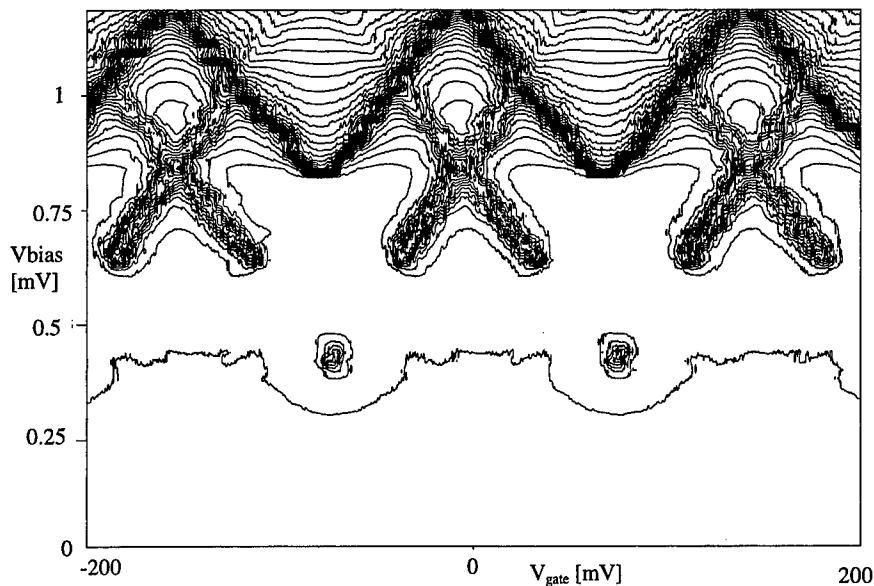


FIGURE 6. Contour plot of the current through a superconducting SET transistor as a function of the bias voltage and the gate voltage. The current varies from 0 to 3 nA.

rent are due to the Josephson - quasiparticle cycle.¹⁸ Both of these processes involve the tunneling of quasiparticles and Cooper pairs and fall on the dotted lines given in Fig. 5b.

One of the difficulties with using a capacitively coupled SET transistor is adjusting for the offset charge.¹⁹ There are charged defects in the vicinity of the island that act like an extra gate and give the charge on the island a random offset. In circuits consisting of just a small number of SET transistors, one can compensate for the offset charges by coupling a gate to each island. This solution is impractical for circuits consisting of more than a few SET transistors. The effect of the offset charges can be seen in Fig. 7a where the offset charge changed suddenly while a SET transistor was being measured in the normal state. The abrupt change in current at -0.25 mV was caused by a change of the offset charge. It is not uncommon for offset charges to change on the time scale of hours or days. Offset charges can

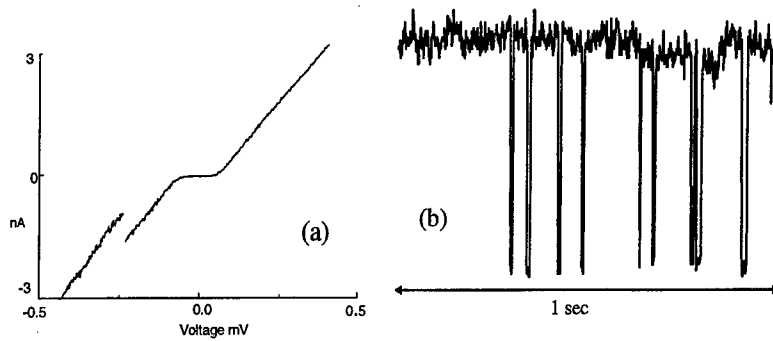


FIGURE 7. (a) The current - voltage characteristic of a capacitively coupled SET transistor in the normal state. At a gate voltage of -0.25 mV the offset charge suddenly changed. (b) The time dependence of the current for a rapidly oscillating offset charge.

also fluctuate more rapidly. A rapidly fluctuating offset charge is shown in Fig 7b. The existence of fluctuating offset charges makes the behavior of SET transistors somewhat unpredictable. This makes it difficult to design reliable circuits using capacitively coupled SET transistors.

Another sort of transistor which is not sensitive to offset charges is the resistively coupled SET transistor. This also consists of a metallic island connected to two leads via tunnel junctions but in this case the control terminal is resistively coupled to the island. To insure that the charge on the island is well defined, the resistor must have a resistance greater than the quantum resistance. The stability diagram for a resistively coupled SET transistor is shown in Fig. 8 for the super-

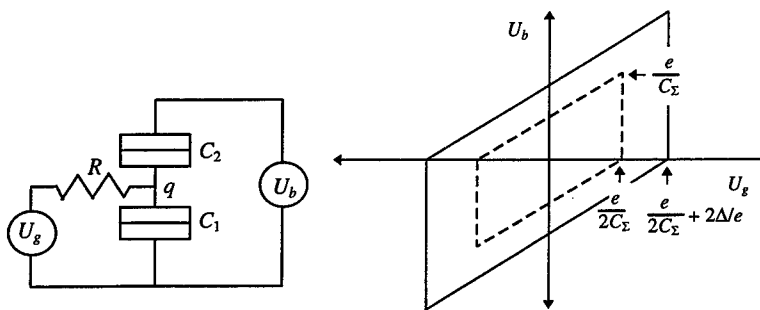


FIGURE 8. The schematic of a resistively coupled SET transistor and its stability diagram. The dashed line in the stability diagram identifies the region where the Coulomb blockade exists in the normal state and the solid line indicates the region where no significant quasi-particle current flows in the superconducting state.

conducting state and the normal state. The region where no significant current flows is determined again by neglecting tunneling and requiring that the voltages across the two tunnel junctions satisfy $|V_1| < e/(2C_\Sigma)$ and $|V_2| < e/(2C_\Sigma)$ in the normal state and $|V_1| < e/(2C_\Sigma) + 2\Delta$ and $|V_2| < e/(2C_\Sigma) + 2\Delta$ in the superconducting state. Unlike a capacitively coupled SET transistor, the characteristics of a resistively coupled SET transistor are not a periodic function of the gate voltage and are not dependent on the offset charge. It is therefore easier to design circuits using the resistively coupled SET transistor.

Measurements using SET transistors

Because of their charge sensitivity, SET transistors are very well suited for making precision charge measurements. Many measurements have been made studying charge transport in the SET transistors themselves. By adding electrons to the island of a SET transistor one can investigate the quantum mechanical level spacing in the island, the spin splitting of the quantum mechanical levels in a magnetic field, the interaction of electrons on the island, the coupling of states in the leads to states in the island, the modulation of the shot noise due to the Coulomb blockade, and how electrical transport through the island is coupled to the electromagnetic environment. SET transistors are also very sensitive to applied radiation.²⁰ Photon assisted tunneling has been observed and the absorption of individual photons of microwave radiation can be detected.

SET transistors have been capacitively coupled to a variety of systems so that the charge motion of those systems could be observed. Metallic SET transistors have been coupled to semiconductor quantum dots to monitor the charge fluctuations in the quantum dot.²¹ They have been coupled to superconducting particles where it is possible to observe whether the particle has an odd number or an even number of electrons on it.¹⁰ An even number of electrons has a lower energy because all of the electrons can pair to form Cooper pairs. When the number of electrons is odd one must remain unpaired which increases the energy by the superconducting gap Δ . This odd-even energy difference can be observed even when the particle contains a billion electrons. SET transistors have also been scanned over semiconductors to measure fluctuations in the dopant distribution.²² The spatial resolution of these measurements was 100 nm and the charge resolution was $0.01 e$. Fundamental measurements such as an experiment to make a more accurate measurement of the fine structure constant have been proposed.²³ Furthermore, it is possible to use SET transistors to monitor the occurrence of unlikely higher order tunnel events which occur at sub zA currents.

One of the potential applications of SET devices is a fundamental current standard. In such a device, a known current is established by transferring individual electrons through the device with a frequency f . This results in a current $I = ef$. A number of different schemes for doing this have been proposed which include modulating the gates coupled to the islands in a series array of tunnel junctions,^{24,25} modulating the tunnel barriers in a semiconducting quantum dot,²⁶ transferring Cooper pairs in a superconducting circuit,²⁷ and using surface acoustic waves to transport individual electrons.²⁸ The most intensively studied current standard is called an electron pump. It consists of a number of tunnel junctions in series with a gate connected to each island between the junctions. By modulating the gates successively one can draw a single electron through the array of tunnel junctions. The accuracy that has been achieved with this current standard is 15 parts per billion.²⁹

All of the measurements that have been described so far have been made at very low temperatures, typically 0.1 K. This is partly because the SET transistors only work at low temperatures and partly because the phenomena that was being studied with SET transistors only manifest themselves at low temperature. The necessity for very low temperatures is not a great problem for fundamental measurements but it is a problem for applications in general purpose computation which will be discussed in the next section.

SET logic and memories

The small size and low power dissipation of SET circuits makes them potentially useful for the information technology industry. Quite a number of logic schemes have been presented. Some of the schemes are very similar to CMOS where bits are represented by voltage levels.³⁰⁻³³ Figure 9 shows two CMOS-like inverters constructed from SET transistors where the complementary nature of the logic can be seen. Other logic schemes resemble superconducting single flux quantum logic.¹ In this case, bits are represented by the presence or the absence of individual electrons. Some logic schemes contain elements that act like electron pumps for moving charge around.³⁴ One scheme is based on the phaselocking of single-electron tunneling oscillations to an ac signal³⁵ and other logic schemes have a neural net architecture.³⁶ Several schemes are based on the bistability of certain element where the electrons can exist in two configurations which have an equivalent energy.^{37,38} Reversible logic elements³⁹ as well as the more typical irreversible logic schemes have been proposed.

One practical problem that all of the SET logic schemes face is the necessity for low temperature operation. The problem is that if the energy that is necessary to add an electron to the island of a SET transistor is smaller than the characteristic

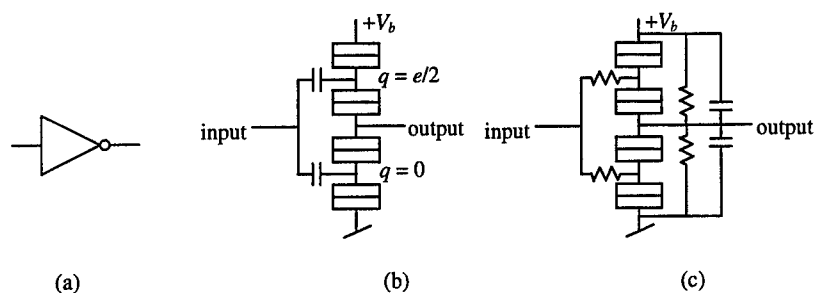


FIGURE 9. (a) The schematic of an inverter. (b) A SET inverter realized with capacitively coupled SET transistors. The offset charges q are specified to insure proper inverter operation. (c) A SET inverter realized with resistively coupled SET transistors.

thermal energy $k_B T$, then the Coulomb blockade will be washed out by thermal fluctuations. The path that must be followed to make circuits that operate at higher temperatures is clear; the dimensions of the devices must be reduced. This will decrease the capacitances and increase the amount of energy that is necessary to add an electron to the island of a SET transistor. In the last few years there has been considerable progress in fabricating smaller devices. A large international effort in nanofabrication is underway that will eventually make molecular-scale devices a reality. It is not yet clear whether the mass production of molecular-scale devices will be economically competitive but it is clear that the devices will become available in the next few years. When SET circuits are scaled down to molecular dimensions, they will function at room temperature. This shrinking of the circuit dimensions has a number of consequences both desirable and undesirable. As the size and the capacitance of the devices decrease, the operating temperature, the operating voltage, and the device packing density increase. These are desirable consequences of the shrinking of SET devices. However, as the dimensions decrease, the electric fields, the current densities, the energy dissipated per switching event, and the power dissipated per unit area all increase. These are undesirable consequences of shrinking.

Another practical problem that many of the logic schemes face is that of offset charges. Most of the logic schemes simply will not work if the offset charges are not somehow eliminated. It is not just the fluctuations of the offset charges that is a problem. Even stationary random offset charges completely disrupt the operation of most logic schemes. The prospects for eliminating the offset charges seem rather dim. It is therefore important to focus on logic schemes which are offset-charge independent.

Exactly how SET devices will contribute to the enterprise of general purpose computation remains unclear. No SET logic scheme is presently threatening to

overthrow the semiconductor industry standard CMOS technology. However, different schemes are continuously being proposed and one of these may prove to be superior in some ways to mainstream semiconductor devices. In any case, miniaturization will likely remain an important aspect of dense integrated circuits and single electron effects will almost certainly play a role in devices with very small dimensions.

A separate issue from using SET circuits for logic is the applicability of SET circuits for memories. Right now the memories seem more promising than the logic. Two memories in particular are worth mentioning. The first is an offset-charge independent DRAM cell which was described by Likharev and Korotkov.⁴⁰ In their circuit, a bit is represented by the presence or absence of a charge of a few electrons which is stored on an island. The charge on the island is monitored by a SET transistor. When the memory cell is read, the circuit is biased so that any charge on that may be on the island is removed. If there was charge on the island when the memory cell is read, the current through the SET transistor undergoes oscillations as each electron tunnels off the island. If there was no charge stored on the island there are no oscillations of the current. The oscillations of the current through the SET transistor occur for any value of the offset charge.

Another type memory called a single-electron MOS memory (SEMM) is also based on the motion of individual electrons.^{41,42} This device is very similar to a conventional floating gate MOS memory. The charge on a floating gate modulates the conduction through a channel nearby the gate. The gate is made so small that even if one electron is added to the floating gate, the conduction through the channel changes appreciably.

Conclusions

Single-electron tunneling devices are contributing to our understanding of how charge is transported in tunnel junction circuits and how to treat circuits quantum mechanically. It is likely that SET circuits will make a lasting impact in the field of precision measurements either as a fundamental standard of capacitance, or a fundamental current standard, or both. A great number of SET logic schemes are being proposed but it is not yet clear if any of them will be competitive with semiconductor circuits. SET memories that should work at very high packing densities have been proposed. The realization of these memories will have to wait for fabrication technologies that can produce them at those densities.

Acknowledgments

Support from Esprit project 22953, CHARGE, is gratefully acknowledged.

References

1. D.V. Averin and K. K. Likharev, "Single-electronics: A correlated transfer of single electrons and Cooper pairs in systems of small tunnel junctions," in *Mesoscopic Phenomena in Solids*, eds. B.L. Altshuler, P. A. Lee, and R. A. Webb, Elsevier (1991).
2. M. H. Devoret, D. Esteve, and C. Urbina, "Single Electron transfer in metallic nanostructures," *Nature* 360 p. 547 (1992).
3. H. Grabert and M. H. Devoret, Eds., *Single Charge Tunneling*, Plenum Press, London (1991).
4. K. K. Likharev, "Physics and possible applications of single-electron devices," *FED Journal* 6 p. 5 (1995). <http://hana.physics.sunysb.edu/set/pubs.html>
5. M. I. Lutwyche, and Y. Wada, "Estimate of the ultimate performance of the single-electron transistor," *J. Appl. Phys.* 75 p. 3654 (1994).
6. A. T. Johnson, L. P. Kouwenhoven, W. de Jong, N. C. van der Vaart, and C. J. P. M. Harmans, "Zero-dimensional states and single electron charging in quantum dots," *Physical Review Letters* 69 p. 1592 (1992).
7. D. C. Ralph, C. T. Black, and M. Tinkham, "Spectroscopy measurements of discrete electronic states in single metal particles," *Phys. Rev. Lett.* 74 3241 (1995).
8. S. Tarucha, D. G. Austing, T. Honda, R. J. van der Hage, and L. P. Kouwenhoven, "Shell filling and spin effects in a few electron quantum dot," *PRL* 77 p. 3613 (1996).
9. N. C. van der Vaart, A. T. Johnson, L. P. Kouwenhoven, D. J. Maas, W. de Jong, M. P. de Ruyter van Steveninck, A. van der Enden, and C. J. P. M. Harmans, "Charging effects in quantum dots at high magnetic field," *Physica B* 189 p. 99 (1993).
10. C. T. Black, D. C. Ralph, and M. Tinkham, "Spectroscopy of the superconducting gap in individual nanometer-scale aluminum particles," *Phys. Rev. Lett.* 76 688 (1996).
11. H. Birk, M.J.M. de Jong, and C. Schonenberger, "Shot noise suppression in the single-electron tunneling regime," *Phys. Rev. Lett.* 75 p. 1610 (1995).
12. G. -L. Ingold, P. Wyrowski, and H. Grabert, "Effect of the electromagnetic environment on the single electron transistor," *Zeitschrift für Physik* 85 p. 443 (1991).
13. E. H. Visscher, S. M. Verbrugh, J. Lindeman, P. Hadley, and J. E. Mooij, "Fabrication of multilayer single-electron tunneling devices," *Applied Physics Letters* 66 p. 305 (1995).
14. A. N. Korotkov, "Charge sensitivity of superconducting single-electron transistor," *Appl. Phys. Lett.* 69, p. 2593 (1996).
15. M. Tinkham, *Introduction to Superconductivity*, McGraw-Hill (1996).
16. A. B. Zorin, "Quantum-limited electrometer based on single Cooper pair tunneling," *PRL* 76 p. 4408 (1996).
17. A. Maassen van den Brink, A. A. Odintsov, P. A. Bobbert, G. Schön, "Coherent Cooper pair tunneling in systems of Josephson junctions: effects of quasiparticle tunneling and of the electromagnetic environment," *Zeitschrift für Physik* 85 p. 459 (1991).
18. T. A. Fulton, P.L. Gammel, D. J. Bishop, L. N. Dunkleberger, and G. J. Dolan, "Observation of combined Josephson and charging effects in small tunnel junction circuits," *Phys. Rev. Lett.* 63 p. 1307 (1989).
19. A.B. Zorin, F.-J. Ahlers, J. Niemeyer, T. Weimann, H. Wolf, V.A. Krupenin, and S.V. Lotkhov, "Background charge noise in metallic single-electron tunneling devices," *Physical Review B* 53, p. 13682 (1996).
20. J. M. Hergenrother, J. G. Lu, M. T. Touminen, D. C. Ralph, and M. Tinkham, *Phys. Rev. B* 51, p. 9407 (1995).
21. D. Berman, N.B. Zhitenev, R.C. Ashoori, H.I. Smith and M.R. Melloch, "The Single-Electron Transistor as a Charge Sensor for Semiconductor Applications," to be published in the *Journal of Vacuum Science and Technology B*.
22. M. J. Yoo, T. A. Fulton, H. F. Hess, R. L. Willett, L. N. Dunkleberger, R. J. Chichester, L. N. Pfeiffer, K. W. West, "Scanning single-electron transistor microscopy: Imaging individual charges," *Science* 276 p. 579 (1997).

23. Alan F. Clark, Neil M. Zimmerman, Edwin R. Williams, A. Amar, Dian Song, F. C. Wellstood, C. J. Lobb, and R. J. Soulen, Jr., "Application of Single Electron Tunneling: Precision Capacitance Ratio Measurements", *Appl. Phys. Lett.* 66, 2588 (1995).
<http://www.eeel.nist.gov/811/femg/set.html>
24. L. J. Geerligs, V.F. Anderegg, P.A.M. Holweg, J. E. Mooij, H. Pothier, D. Esteve, C. Urbina, and M. H. Devoret, "Frequency locked turnstile device for single electrons," *Phys. Rev. Lett.* 64 p. 2691 (1990).
25. H. Pothier, P. Lafarge, C. Urbina, D. Esteve, and M. H. Devoret, "Single electron pump based on charging effects," *Europhys. Lett.* 17 p. 249 (1992).
26. L. P. Kouwenhoven, A. T. Johnson, N. C. van der Vaart, and C. J. P. M. Harmans, "Quantized current in a quantum dot turnstile using oscillating tunnel barriers," *Physical Review Letters* 67 p. 1626 (1991).
27. L.J. Geerligs, S.M. Verbrugh, P. Hadley, J.E. Mooij, H. Pothier, P. Lafarge, C. Urbina, D. Esteve, and M.H. Devoret, "Single Cooper pair pump," *Zeitschrift für Physik B* 85 p. 349-355 (1991).
28. V. I. Talyanskii, J. M. Shilton, M. Pepper, E. H. Linfield, D. A. Ritchie, and C.J.B. Ford, "Single electron transport in one-dimensional channel by high-frequency surface acoustic waves," *Proceedings of the Workshop on Fundamental aspects of applications of single electron devices*, p. 19 (1997).
29. Mark W. Keller, John M. Martinis, Neil M. Zimmerman, and Andrew H. Steinbach, "Accuracy of Electron Counting Using a 7-Junction Electron Pump", *Appl. Phys. Lett.* 69, 1804 (1996).
30. Tucker, J. R., "Complementary digital logic based on the Coulomb blockade," *J. Appl. Phys.* 72 p. 4399 (1992).
31. Nobuyuki Yoshikawa, Yasuyuki Jingui, Hiroshi Ishibashi, and Masanori Sugahara, "Complementary digital logic using resistively coupled single-electron transistor," *Jpn J. Appl. Phys.* 35, p. 1140 (1996).
32. R. H. Chen, A. N. Korotkov, and K. K. Likharev, "Single-electron transistor logic," *Appl. Phys. Lett.* 68 p. 1954 (1996). <http://hana.physics.sunysb.edu/set/pubs.html>
33. A. N. Korotkov, R. H. Chen, and L. K. Likharev, "Possible performance of capacitively coupled single-electron transistors in digital circuits," *J. Appl. Phys.* 78, p. 2520 (1995).
<http://hana.physics.sunysb.edu/set/pubs.html>
34. M.G. Ancona, "Design of computationally useful single-electron digital circuits," *J. Appl. Phys.* 79, p. 526 (1996).
35. T. Ohshima, and R.A. Kiehl, "Operation of bistable phase-locked single-electron tunneling logic elements," *J. Appl. Phys* 80 p. 912 (1996).
36. M.J. Goossens, J.H. Ritskes, C.J.M. Verhoeven, and A.H.M. van Roermund, "Neural networks with periodic single-electron tunneling transistors," *Proceedings of the 1997 European Conference on Circuit Theory and Design (ECCTD'97)*, p. 937-941 (1997).
37. A. N. Korotkov, "Wireless single-electron logic biased by alternating electric field," *Appl. Phys. Lett.* 67 p. 2412 (1995). <http://hana.physics.sunysb.edu/set/pubs.html>
38. P. D. Tougaard and C. S. Lent, "Logical devices implemented using quantum cellular automata," *J. Appl. Phys.* 75 p. 1818 (1994).
39. K. K. Likharev, and A. N. Korotkov, "Single-Electron Parametron: Reversible Computation in a Discrete State System," *Science* 273, p. 763 (1996).
<http://hana.physics.sunysb.edu/set/pubs.html>
40. Likharev, K. K., and A. N. Korotkov, "Ultradense hybrid SET/FET dynamic RAM: Feasibility of background-charge-independent room-temperature single-electron digital circuits," *Proceedings of ISDRS'95* (1995). <http://hana.physics.sunysb.edu/set/pubs.html>
41. K. Yano, T. Ishii, T. Kobayashi, F. Murai, and K. Seki, "Room-temperature single-electron memory," *IEEE Transactions on Electron Devices* 41, p. 1628, (1994).
42. Lingjie Guo, Effendi Leobandung, and Stephen Y. Chou, "A silicon single-electron transistor memory operating at room temperature," *Science* 275, p. 649 (1997).

IV. ARRAYS IN QUANTUM REGIME: CRITICAL PROPERTIES

Quantum Phase Transitions in Josephson Junction Arrays

Rosario Fazio⁽¹⁾ and Gerd Schön⁽²⁾

⁽¹⁾*Istituto di Fisica, Università di Catania & INFM, viale A. Doria 6, 95129 Catania - Italy*

⁽²⁾*Institut für Theoretische Festkörperphysik, Universität Karlsruhe, D76128 Karlsruhe, Germany*

Abstract. In this chapter we review the quantum phase transitions and transport properties of low-capacitance Josephson junction arrays. We will present the models and introduce the relevant topological excitations. The phase diagram depends in a very rich way on various control parameters. We will discuss the universality or absence of universality of the transport properties at the quantum phase transition.

I INTRODUCTION

Josephson junctions arrays (JJA) are ideal model systems to study a variety of non-conventional phase transitions [1–3]. In the last years, due to the development of the microfabrication techniques, it became possible to fabricate Josephson arrays whose junctions are of submicron size. In these systems the competition of single electron effects [4] with the Josephson effect, leads to a number of quantum phase transitions with a very rich phase diagram. In this chapter we review some theoretical aspects of quantum critical phenomena in these systems. This topic will be also touched in the chapter of J.V. Josè while a review on experiments is given in the chapters of H. van der Zant and P. Delsing.

In JJA it is important to distinguish between local and global superconductivity. When cooling the sample, each island of the array becomes superconducting (develops a nonvanishing gap Δ) at a critical temperature T_c . However, dissipation-less conduction requires phase coherence of the superconducting order parameter $\Delta e^{i\phi_i}$ across the whole system. This can set in at a much lower temperature T_J , which defines the superconducting transition temperature. Alternatively, if the junctions are submicron size, the low temperature phase of the array may be insulating even though each island is superconducting [5–7].

The two characteristic energy scales in the system are the Josephson energy E_J which is associated to the tunneling of Cooper pairs between neighboring islands and the charging energy $E_C = e^2/2C$ (where C is the geometrical capacitance of

the junction) which is the energy cost to add an extra electron charge to a neutral island. The electrostatic energy inhibits the fluctuations of the charge due to tunneling; equivalently, it enhances the quantum fluctuations of the phases ϕ 's of the superconducting order parameters of the islands. If $E_J \gg E_C$ the system turns superconducting at low temperatures since the fluctuations of the ϕ_i 's are weak and the system is globally phase coherent. We will refer to the $E_J/E_C \rightarrow \infty$ limit as the *classical* case (in the classical limit JJA's are a physical realization of the two dimensional XY-model). In the opposite limit, $E_J \ll E_C$, the array becomes a Mott insulator since the charges Q_i in each islands are localized (Coulomb blockade of Cooper pairs) while strong quantum fluctuations of ϕ_i prevent the system to reach long range phase coherence. At a critical ratio of these coupling energy a superconductor-insulator (SI) transition occurs. It has been observed experimentally by the groups of Delft and Goteborg [5–7].

In the classical limit vortices are the topological excitations which determine the (thermo)dynamic properties of JJA. Deep in the quantum limit ($E_J \ll E_C$) the charges on each island are the relevant degrees of freedom. Vortices and charges play a dual role and many features of JJA can be observed in the two limits if the role of charges and vortices are interchanged [12,13].

Many of the properties discussed here, are also observed in granular superconductors [8] and ultra thin superconducting films [9–11]. In granular systems disorder plays a crucial role, while this is virtually absent in JJAs, or it can be introduced in a controlled way. In ultra-thin films it is believed that pre-formed Cooper pairs exist and that phase fluctuations, which can be controlled by varying the film thickness, drive the system through the SI transition.

It is well established that in classical arrays an applied magnetic field leads to frustration [16], with similar effects predicted for quantum JJAs [14,15]. In a quantum JJA an applied gate voltage relative to the ground plane V_x introduces a *charge frustration*. The combination of charge frustration and finite-range Coulomb interaction leads to the appearance of various Mott insulating phases [17]. They are characterized by crystal-like configurations (with a lattice constant which depends on V_x) of the charges on the islands. In addition a new phase, characterized by the coexistence of off-diagonal (superconducting) and diagonal (charge-crystalline) long range order, occurs. This phase is known as *supersolid*. The combination of charge *and* magnetic frustration may lead to qualitatively new effects [25]. The most striking prediction is that for certain ratios of the magnetic to charge frustration the JJA is in a Quantum Hall phase [26].

In quantum phase transitions the dynamics and thermodynamics are intimately interconnected. Hence rather peculiar transport properties are expected close to the SI transition. One of the most striking predictions in this respect is that at the transition the conductance is finite and universal [27,28]. Since the original prediction of a metallic behavior at zero temperature for two-dimensional superconductors there has been a substantial interest in the actual value of the universal conductance, and in the possibility of non-universal corrections [29].

This chapter is organized as follows. In the next section the models which are

used to study quantum JJA will be introduced. Although different in many details, all those models have similar phase diagrams. In section III some theoretical tools to study the phase diagram are briefly discussed: the mean field approximation, the coarse graining approach to derive a Ginzburg-Landau effective free energy, and the Villain transformation which leads to a description in terms of charges and vortices. These approaches capture most of the essential physics. The subsequent section is devoted to a description of the phase diagram including the case when there is charge and/or magnetic frustration. Since the number of parameters which can be varied is rather large, the phase diagram is discussed only in some limiting cases. The last section is devoted to a discussion of the transport properties close to the SI transition. In this chapter we will not discuss the effects of disorder. This may lead to an additional glass transition [39–41] as it will be discussed by J.V. Josè in this volume.

II THE MODELS

A quantum JJA consists of metallic islands (which undergo a superconducting transition of the BCS type at a transition temperatures T_c) which are connected by tunnel junctions. Each island has a capacitance to each of the other islands, to the ground and to any neighboring metallic region (such as gates or leads). The electrostatic energy of the system is entirely specified by the capacitance matrix C_{ij} [42] and the charge configuration $Q_i \equiv 2eq_i$ of each island (q_i being an integer number). Moreover, as known from the classical arrays, the Josephson coupling across the junctions introduces another contribution to the energy. Since at low temperatures the fluctuations of the amplitude of the order parameter can be ignored, the only relevant dynamical variables are the phases ϕ_i of each island, and the charge. Both are canonically conjugated variables [43]

$$[\phi_i, Q_j] = 2e i \delta_{ij}$$

Thus the relevant physics is captured by the following model, frequently defined as the Quantum Phase Model (QPM)

$$H_{\text{QPM}} = \sum_{i,j} (q_i - q_x) U_{ij} (q_j - q_x) - E_J \sum_{\langle i,j \rangle} \cos(\phi_i - \phi_j - A_{ij}) . \quad (1)$$

The Coulomb interaction is described by the matrix $U_{ij} = e^2 C_{ij}^{-1}$. The simplest, sufficiently realistic, model for the capacitance matrix C_{ij} includes only the ground capacitance C_0 and the junction capacitance C , with the corresponding energy scales $E_C = e^2/2C$ and $E_0 = e^2/2C_0$. The range of the electrostatic interaction between Cooper pairs is, in units of the lattice spacing, $\lambda = \sqrt{C/C_0}$. A control (external) voltage V_x applied to the ground plane enters via the induced charge $Q_x = 2eq_x = \sum_j C_{ij} V_x$ (a homogeneous situation is considered here). When tuning V_x different charge configurations minimize the electrostatic energy. It suppresses

tunneling (Coulomb blockade) except at degeneracy points. A perpendicular magnetic field with vector potential \mathbf{A} enters the QPM in the standard way through $A_{ij} = 2e \int_i^j \mathbf{A} \cdot d\mathbf{l}$. The relevant parameter which describes the magnetic frustration is $f = (1/2\pi) \sum A_{ij}$, where the summation runs over an elementary plaquette.

The QPM accounts only for Cooper pair tunneling, in some case one has to take into account the tunneling of quasiparticles and/or the flow of Ohmic current through the substrate or between the junctions. These effects will be discussed in the section devoted to the transport properties.

In the case of strong *on-site* Coulomb interaction $U_{ii} = U_0$ and very low temperatures only few charge states are important. If the gate voltage is tuned close to a degeneracy, the relevant physics is captured by considering only two adjacent charge states of each island, and the QPM is equivalent to an anisotropic XXZ spin-1/2 Heisenberg model [20]

$$H_S = -h \sum_i S_i^z + \sum_{i,j} S_i^z U_{ij} S_j^z - E_J \sum_{\langle i,j \rangle} (e^{iA_{ij}} S_i^+ S_j^- + e^{-iA_{ij}} S_i^- S_j^+) . \quad (2)$$

The operators S_i^z , S_i^+ , S_i^- are the spin-1/2 operators, S_i^z being related to the charge on each island ($q_i = S_i^z + \frac{1}{2}$), and the raising and lowering S_i^\pm operators corresponding to the "creation" and "annihilation" operators $e^{\pm i\phi_j}$ of the QPM. The "external" field h is related to the external charge by

$$h = (q_x - 1/2) \sum_j U_{ij} .$$

Various magnetic ordered phases of the XXZ Hamiltonian correspond to the different phases in the QPM. Long range order in $\langle S^+ \rangle$ indicates superfluidity in the QPM while long range order in $\langle S^z \rangle$ describes order in the charge configuration.

There is yet another closely related model which is mostly used in the context of superconductivity in ultrathin films, the Bose-Hubbard model [39]

$$H = \frac{1}{2} \sum_i n_i U_{ij} n_i - \mu \sum_i n_i - \frac{t}{2} \sum_{\langle ij \rangle} (b_i^\dagger b_j + h.c.) \quad (3)$$

where b^\dagger, b are the creation and annihilation operators for bosons and $n_i = b_i^\dagger b_i$ is the number of bosons. Again U_{ij} describes the Coulomb interaction between bosons, μ is the chemical potential, and t the hopping matrix element. The connection between the Bose-Hubbard model and the QPM is easily seen by writing the field b_i in terms of amplitude and phase and then approximating the amplitude by its average, i.e. $b_i \sim e^{i\phi_i}$. The hopping term is then associated with the Josephson tunneling while the chemical potential plays the same role as the external charge in the QPM. This mapping becomes more accurate as the average number of bosons per sites increases.

The three models are equivalent in the sense that they belong to the same universality class (they lead to the same Ginzburg-Landau effective free energy). However, the non-universal features like the location of the phase transitions depend quantitatively on the specific choice of the model.

III ANALYTIC TOOLS

A Mean Field

The mean field approximation consists in approximating the Hamiltonian of eq.(1) by [44,45]

$$H_{\text{MF}} = \frac{1}{2} \sum_{i,j} q_i U_{ij} q_j - z E_J \langle \cos(\phi) \rangle \sum_j \cos(\phi_j)$$

where z is the coordination number in the lattice and $\psi \equiv \langle \cos(\phi) \rangle$ is the order parameter. It has to be calculated self-consistently according to

$$\langle \cos(\phi) \rangle = \text{Tr} \{ \cos(\phi_i) \exp(-\beta H_{\text{MF}}) \} / \text{Tr} \{ \exp(-\beta H_{\text{MF}}) \} .$$

Close to the transition point, the thermal average on the r.h.s can be evaluated by expanding in powers of ψ . To third order, a Ginzburg-Landau type equation arises:

$$\left[1 - z E_J \int_0^\beta d\tau \langle \cos \phi_i(\tau) \cos \phi_i(0) \rangle_{ch} \right] \psi + \left(\frac{z E_J}{U_0} \right)^3 \mathcal{B} \psi^3 = 0 \quad (4)$$

Here the average $\langle \dots \rangle_{ch}$ is performed over the eigenstates of the charging part of the Hamiltonian only and the quantity \mathcal{B} entails the four point phase correlation. If the charging term is absent, the phase-phase correlator in Eq. (4) is one and we recover the classical result $\beta_{cr} z E_J = 2$. Due to the charging effects the phase starts to fluctuate and the critical temperature is depressed. The correlator is easy to evaluate. For instance in the self-charging limit $U_{ij} = U_0 \delta_{ij}$ at $T = 0$ it is ($U_0 \equiv 8E_0$ only if the junction capacitance is zero).

$$\langle \cos \phi_i(\tau) \cos \phi_i(0) \rangle_{ch} = (1/2) \exp\{-(U_0/2)\tau(1 - \tau/\beta)\} .$$

As a result the SI transition at zero temperature occurs at

$$2z E_J = U_0 .$$

For larger values of the charging energy the array does not acquire phase coherence even at zero temperature. The full phase diagram will be described in details in the next section.

Similar types of mean field approaches can be used to study the effect of frustration in these systems. In this case, however, a nontrivial space dependence of the order parameter may arise.

B Coarse-Graining approach

By using the coarse-graining approximation it is possible to go from the microscopic models introduced in the previous section to a Ginzburg-Landau effective free energy which depend only on the order parameter [47,48]. Since the transition in this case is governed by quantum fluctuations, the order parameter will depend both on space and (imaginary)-time [49].

The coarse-graining proceeds in two steps:

- An auxiliary field $\psi(x, \tau)$ (which has the meaning of an order parameter) is introduced through a Hubbard-Stratonovich transformation. The partition function is then expressed as a path integral over ψ .
- The assumption that the order parameter is small close to the transition allows a subsequent cumulant expansion to obtain the usual (polynomial) GL effective free energy. The coefficients depend on the details of the microscopic model.

The partition function of the QPM is given by

$$Z = \text{Tr}\{e^{-\beta H_{\text{QPM}}}\} = Z_{\text{ch}} \langle T_{\tau} e^{-\int_0^{\beta} d\tau H_J(\tau)} \rangle \quad (5)$$

where the subscripts ch and J indicate the charging and Josephson part to the Hamiltonian of Eq.(1). Applying the Hubbard-Stratonovich transformation to the Josephson term we get

$$\begin{aligned} & \exp \left\{ \frac{E_J}{2} \int_0^{\beta} d\tau \sum_{\langle i,j \rangle} e^{i\phi_i} e^{-i\phi_j} + h.c. \right\} \\ & \sim \int \mathcal{D}\psi^* \mathcal{D}\psi \exp \left\{ - \int_0^{\beta} d\tau \sum_{\langle i,j \rangle} (E_J)_{ij}^{-1} \psi_i^*(\tau) \psi_j(\tau) + \int_0^{\beta} d\tau \sum_i [\psi_i^*(\tau) e^{i\phi_i(\tau)} + h.c.] \right\} \end{aligned} \quad (6)$$

Here we introduced a matrix $(E_J)_{ij}$ which is equal to E_J if ij are nearest neighbors and zero otherwise. Now the partition function can be written as

$$Z = Z_{\text{ch}} \int \mathcal{D}\psi^* \mathcal{D}\psi \exp \{-F[\psi]\} \quad (7)$$

where the effective free energy F is defined as

$$F = - \int_0^{\beta} d\tau \sum_{ij} (E_J)_{ij}^{-1} \psi_i^*(\tau) \psi_j(\tau) - \ln \left\langle - \int_0^{\beta} d\tau \sum_i [\psi_i^*(\tau) e^{i\phi_i(\tau)} + h.c.] \right\rangle_{\text{ch}}. \quad (8)$$

After truncation of higher order terms and a gradient expansion, the effective free energy reads

$$F = \int d^2r \, d\tau d\tau' \psi^*(r, \tau) \left\{ \frac{1}{2E_J} \left[1 + \frac{1}{4} \left(\frac{\vec{\nabla}}{i} + \frac{2e}{\hbar} \vec{A} \right)^2 \right] - g(\tau - \tau') \right\} \psi(r, \tau') + \kappa \int d^2r \, d\tau |\psi(r, \tau)|^4. \quad (9)$$

The dynamics of the field ψ is governed by the phase-phase correlator

$$g(\tau) = \langle \exp\{i\phi_i(\tau) - i\phi_i(0)\} \rangle_{\text{ch}},$$

while κ depends on a 4-point phase correlator. The effect of a magnetic field and frustration can be introduced in the standard way by the replacement $\nabla \rightarrow \nabla + 2e\vec{A}$.

In the mean field approximation the phase transition is obtained for

$$\frac{1}{2E_J} = \int_0^\beta d\tau g(\tau). \quad (10)$$

which coincides with the results of the previous section. In the coarse graining approach, however, a systematic treatment of the fluctuations is possible.

C Duality Transformations

In this section we derive some properties of quantum JJA using dual transformations [50–53]. We follow closely the derivation given in Ref. [12]. Our starting point is the partition function expressed in terms of the Euclidean action [4],

$$Z = \prod_i \int_0^{2\pi} d\phi_i^{(0)} \sum_{\{m_i=0,\pm 1,\dots\}} \int_{\phi_i^{(0)}}^{\phi_i^{(0)}+2\pi m_i} D\phi_i(\tau) \exp[-S\{\phi\}]. \quad (11)$$

Here the path integration is carried out with the boundary conditions

$$\phi_i(0) = \phi_i^{(0)}; \quad \phi_i(\beta) = \phi_i^{(0)} + 2\pi m_i, \quad (12)$$

with β being the inverse temperature. These non-trivial boundary conditions express the fact that the charges of the grains are integer multiples of $2e$ [4]. The Euclidean effective action $S\{\phi\}$ has the form

$$S[\phi] = \int_0^\beta d\tau \left\{ \frac{C_0}{8e^2} \sum_i (\dot{\phi}_i)^2 + \frac{C}{8e^2} \sum_{\langle ij \rangle} (\dot{\phi}_i - \dot{\phi}_j)^2 - E_J \sum_{\langle ij \rangle} \cos(\phi_i - \phi_j) \right\}. \quad (13)$$

The first two terms are easily recognized to be charging energy expressed in terms of voltages ($\phi = 2eV_i$). It is clear that when the Josephson energy is either much larger or much smaller than the charging energy, the properties of the array are governed either by vortices or charges. It is therefore useful to express the action of the system in terms of these degrees of freedom. Vortex degrees of freedom have been

introduced in the classical limit by means of the Villain transformation [54]; the quantum problem requires some additional steps [12]. We introduce the lattice with spacing ϵ in time direction; this spacing is of order of inverse Josephson plasmon frequency, $\epsilon \sim (8E_J E_C)^{1/2}$. In the Villain approximation one replaces

$$\exp \left\{ -\epsilon E_J \sum_{\langle ij \rangle, \tau} [1 - \cos(\phi_{i,\tau} - \phi_{j,\tau})] \right\} \rightarrow \sum_{\{\mathbf{m}_{i\tau}\}} \exp \left\{ -\frac{\epsilon E_J}{2} \sum_{i,\tau} |\nabla \phi_{i\tau} - 2\pi \mathbf{m}_{i\tau}|^2 \right\}.$$

A resummation of the expression on the r.h.s. yields

$$\sum_{\{\mathbf{J}_{i\tau}\}} \exp \left\{ -\frac{1}{2\epsilon E_J} \sum_{i,\tau} |\mathbf{J}_{i\tau}|^2 - i\mathbf{J}_{i\tau} \nabla \phi_{i\tau} \right\}.$$

After this step the Gaussian integration over the phases can be performed, with the result

$$Z = \sum_{q_{i\tau}} \sum_{\mathbf{J}_{i\tau}} \exp \left\{ -\epsilon \sum_{i,j,\tau} q_{i\tau} U_{ij} q_{j\tau} - \frac{1}{2\epsilon E_J} \sum_{i,\tau} |\mathbf{J}_{i\tau}|^2 \right\}. \quad (14)$$

The summation is constrained by the continuity equation,

$$\nabla \mathbf{J}_{i\tau} - \dot{q}_{i\tau} = 0.$$

Here and in the following the time derivative stands for a discrete derivative $\dot{f}(\tau) = \epsilon_\mu^{-1}[f(\tau + \epsilon_\mu) - f(\tau)]$. The constraint is satisfied by the parameterization [55]

$$J_{i\tau}^{(\mu)} = n^{(\mu)} (\mathbf{n} \nabla)^{-1} \dot{q}_{i\tau} + \epsilon^{(\mu\nu)} \nabla_\nu A_{i\tau},$$

where $A_{i\tau}$ is an unconstrained integer-valued scalar field. The operator $(\mathbf{n} \nabla)^{-1}$ is the line integral on the lattice (in Fourier space it has the form $i(k_x + k_y)^{-1}$), while $\epsilon^{(\mu\nu)}$ is the antisymmetric tensor.

With the use of the Poisson resummation (which requires introducing a new integer scalar field $v_{i\tau}$) the partition function can be written as a sum over two integer valued fields defined on the space-time lattice, the charges $q_{i\tau}$ and vorticities $v_{i\tau}$,

$$Z = \sum_{q_{i\tau}, v_{i\tau}} \exp -S\{q, v\}.$$

The effective action is

$$S\{q, v\} = \int_0^\beta d\tau \sum_{ij} \left\{ 2e^2 q_{i\tau} U_{ij} q_{j\tau} + \pi E_J v_{i\tau} G_{ij} v_{j\tau} + i q_{i\tau} \Theta_{ij} \dot{v}_{j\tau} + \frac{1}{4\pi E_J} \dot{q}_{i\tau} G_{ij} \dot{q}_{j\tau} \right\}. \quad (15)$$

It describes two coupled Coulomb gases. The charges interact via the inverse capacitance matrix. The interaction among the vortices is described by the kernel

G_{ij} , which is obtained as the Fourier transform of k^{-2} . At large distances $r_{ij} \gg a$ between the sites i and j it depends logarithmically on the distance

$$G_{ij} = \frac{1}{2} \ln \left(\frac{a}{r_{ij}} \right).$$

The charges and vortices are coupled in the dynamical theory as described by the third term. Here

$$\Theta_{ij} = \arctan \left(\frac{y_i - y_j}{x_i - x_j} \right)$$

describes the phase configuration at the site i if a vortex is placed at the site j . The coupling has a simple physical interpretation: a change of vorticity at site j produces a voltage at site i which is felt by the charge at this location. The last term $\dot{q}G\dot{q}$ represents a spin-wave contribution to the charge correlation function.

The effective action (15) shows a high degree of symmetry between vortex and charge degrees of freedom. In particular, in the limit $C_0 \ll C$ the inverse capacitance matrix has the same functional form as the kernel describing the vortex interaction, $e^2 C_{ij}^{-1} = E_C G_{ij} / \pi$, and the charges and vortices are (approximately) dual. The duality is broken by the last term $\dot{q}G\dot{q}$. This term is "irrelevant" for the phase transitions, i.e. it merely shifts the transition point. However, it has important implications for the dynamical behavior.

Recently the same duality transformations has been applied to double layers [13]. They will be reviewed by J.V. Josè in this volume.

IV THE PHASE DIAGRAM

The phase diagram in quantum JJA depends sensitively on the exact model considered. Moreover in the presence of charge and/or magnetic frustration the boundaries changes and new phases appear. This section is organized in small subsections which briefly describe the main features of the phase diagram in various limiting cases.

A Long range Coulomb interaction, $C \gg C_0$

At transition temperature the vortex-unbinding KTB transition, from the superconducting to the resistive phase, is shifted by quantum fluctuations to values below the transition temperature T_J of the classical array (with $E_C = 0$). In the case $C_0 = 0$ the shift of the transition temperature is [56]

$$T_J = \frac{\pi E_J}{2} - \frac{E_C}{6}. \quad (16)$$

If $C \gg C_0$ another phase transition occurs at finite temperature [57]. In this limit charges interact logarithmically. Hence they undergo a charge-unbinding KTB transition, which now separates an insulating low-temperature phase from a conducting

high-temperature phase. In the limit of weak Josephson coupling the charge-KTB transition occur at a temperature [12]

$$T_C = \frac{E_C}{\pi} - 0.31 \frac{(E_J)^2}{E_C}.$$

Hence the array has three different phases. Upon increasing the charging energy the system undergoes first a superconducting - resistive transition and then a resistive - insulating transition. At $T = 0$ there is a direct superconducting - insulator transition which occurs at a critical point

$$\frac{E_J}{E_C} \sim \frac{2}{\pi^2}$$

At this critical point the system is self-dual with respect to interchanging of charges and vortices. The duality is strict only in the ideal case of vanishing self-capacitance and the absence of the spin-wave duality breaking term in eq. (15). The phase diagram corresponding to this case is shown in Fig.(1). Experimental evidence of this behavior has been found van der Zant *et al.* [6,58].

B Short range Coulomb interaction, $C \ll C_0$

In this case the phase boundary can be obtained using the mean field theory. The phase - phase correlator needed in Eq. (10) can be easily calculated for a general capacitance matrix [46]. In Fig. 2 we show the phase diagram for the self-charging model ($C = 0$) as a function of the external charge q_x at zero temperature. As a function of q_x a lobe structure appears. A finite external charge lowers the energy cost to transfer Cooper pairs between neighboring grains, increasing the regime of the superconducting phase. At the degeneracy points the superconducting phase extends to down to arbitrary small Josephson couplings.

For finite-range Coulomb interaction, further insulating phases are stable, and the phase diagram becomes rather rich. In this case not only Mott-insulating phases with the same integer filling of each island are allowed, but new lobes with crystal-like structure of the filling, e.g. $q_i = 0$ or 1 arise. The simplest is a checkerboard pattern with alternating filling of neighboring islands. In general, with increasing external charge, a sequence of inhomogeneous charge configurations minimizes the energy. Since the Mott-insulating lobes are incompressible (there is a gap in the excitation spectrum), the average charge $\langle q \rangle$ is pinned to a fractional value in the whole lobe. In Fig.3 a schematic phase diagram is shown, where on-site U_0 and nearest neighboring U_1 Coulomb interaction are taken into account. In this case the only fractional filling which can occur is the checkerboard configuration with $\langle q \rangle = 1/2$. At finite temperature the thermal occupation of higher charges states smears the lobe structure [46,59].

The combined effect of Josephson coupling and finite range interaction with charge frustration leads to the possibility of new phases, called *supersolids*. The

concept of supersolids dates back to the early 70's when Andreev and Lifshitz [18] proposed that vacancies in a quantum crystal might undergo a Bose-Einstein condensation without destroying the crystal order. In such a phase the superfluid order and the crystalline order coexist.

The exciting possibility of a supersolid phase in Josephson junction arrays and Bose-Hubbard systems has been extensively investigated in recent years. Loosely speaking, the supersolid phase is located in an intermediate region around the half-filling lobe. A simple way to understand its existence is to focus on a region close to the phase boundary at $q_x \sim 1/2$. In this case there will be a finite density of vacancies. They have bosonic character and therefore have the possibility to Bose condense. In a limited range of parameters they can become superfluid (and therefore are able to move freely through the system) without being able to destroy completely the crystal order (since they have a low density).

There are various methods to study the supersolid phase in JJA. We follow here a variational approach discussed in Ref. [60] (valid only at zero temperature). The idea is to consider a variational wave function of the Gutzwiller type, as discussed in early treatments of spin [61] and Bose-Hubbard [62] models. It is convenient to write down the variational ground state using as a basis the charge on each island ($|q_i\rangle$). For simplicity we choose it as a product of single-site wave functions

$$|G_0\rangle = Z^{-1} \prod_{n=1}^{\infty} \sum_{[n_i]} e^{-k_i(q_i - m_i)^2/2} |q_i\rangle, \quad (17)$$

where k_i and m_i are variational parameters, and Z is a normalization constant. In the limit of zero charging energy, each island of the array has a fixed phase ϕ , this corresponds to a coherent superpositions of charge states, i.e. $k_i = 0$ in the variational wave function. In the case of non-zero charging energy, states in which the islands have non-zero charge are suppressed. This effect is controlled by the variational parameter k . The other variational parameter m fixes the average charge on each island.

The variational parameters are determined by minimizing the energy expectation value $E_{\text{QPM}} = \langle G_0 | H_{\text{QPM}} | G_0 \rangle$. The various phases are determined by evaluating the average of the superconducting order

$$\psi_i = \langle G_0 | e^{i\phi_i} | G_0 \rangle,$$

and the structure factor (which signals crystal order)

$$S(\pi, \pi) = \frac{1}{N^2} \langle G_0 | \sum_{n=a,j} (-1)^{|i-j|} q_i q_j | G_0 \rangle.$$

A finite $S(\pi, \pi)$ corresponds to a checkerboard arrangement of the charges on the islands. Due to discrete sums required in the evaluation of the expectation values the calculation should be done numerically. Results are shown in Fig. 4.

V TRANSPORT PROPERTIES

In two dimensions at the SI transition at $T = 0$ the conductance has been predicted to be finite and universal [27,28]. This is quite striking since a metallic behavior should be present even in the absence of dissipation. This effect is entirely due to the presence of collective modes which become critical at the transition point. The prediction of a metallic behavior at zero temperature created a lot of interest both on the experimental and the theoretical side. The universal conductance in a model with no disorder was considered in Ref. [30] by means of $1/N$ expansion [63] and Monte Carlo simulations and in Ref. [37] by means of an ϵ -expansion [63]. The dirty boson system and the transition to the Bose glass phase (including the case of long-range Coulomb interaction) was extensively studied in [35,31]. Wen employed a scaling theory of conserved currents at anisotropic critical points [64] identifying many universal amplitudes. One of these amplitudes in two dimensions reduces to the universal conductance σ^* . The finite frequencies properties close to the transition point were analyzed by means of the $1/N$ expansion [33,34]. On the numerical side, besides the Monte Carlo simulations, exact diagonalization calculation [36] were employed to evaluate the universal value of the conductivity σ^* .

The simplest way to evaluate the conductivity is to use the Ginzburg-Landau formulation of Eq.(9) in imaginary time and then to continue the result analytically to real times. The conductivity in the linear response regime can be determined from the functional derivatives of the partition function. Noticing that the current is the derivative of the free energy with respect to the vector potential and that the electric field is the time derivative of the vector potential (with a negative sign), the conductivity is expressed as

$$\sigma_{ab}(\omega_\mu) = \frac{\hbar}{\omega_\mu} \int d^2r d\tau \frac{\delta^2 \ln Z}{\delta A_a(r, \tau) \delta A_b(0)} |_{\vec{A}=0} e^{i\omega_\mu \tau}. \quad (18)$$

Using Eq.(9), the longitudinal conductivity $\sigma_{aa}(\omega_\mu)$ can be expressed in terms of two- and four-point Green's functions. In the absence of a magnetic field we have [30]

$$\sigma(\omega_\mu) = \frac{4\pi}{R_Q \omega_\mu} \left[\int \frac{d^3q}{(2\pi)^3} \langle \psi_{\vec{q}}^* \psi_{\vec{q}} \rangle - 2 \int \frac{d^3q d^3p}{(2\pi)^6} q_x p_x \langle \psi_{\vec{q}-\frac{\vec{k}}{2}}^* \psi_{\vec{p}+\frac{\vec{k}}{2}}^* \psi_{\vec{p}-\frac{\vec{k}}{2}} \psi_{\vec{q}+\frac{\vec{k}}{2}} \rangle \right] \quad (19)$$

where the $\vec{q} = (q_x, q_y, \omega_\nu)$ are vectors in the 3-dimensional space-time, $\vec{k} = (0, 0, \omega_\mu)$ and $R_Q = h/4e^2$. There are various approaches to evaluate these correlators. The most straightforward is the Gaussian approximation which turns out to be the first term in a $1/N$ expansion [30]. Evaluating the correlators with the quadratic part of the free energy one gets

$$\sigma(\omega_\mu) = \frac{1}{R_Q \omega_\mu} \frac{1}{\beta} \sum_\nu \int dk k^3 G(k, \omega_\nu) [G(k, \omega_\nu) - G(k, \omega_\nu + \omega_\mu)],$$

where $G(k, \omega_\mu) = [\epsilon + k^2 + \zeta \omega_\mu^2]^{-1}$. Performing the k -integrals and the analytical continuation to real frequencies, the real and imaginary parts of the conductivity are

$$\Re \sigma(\omega) = \frac{\pi}{8R_Q} \left(1 - \frac{\omega_c^2}{\omega^2}\right) \Theta(\omega_c^2 - \omega^2) \quad (20)$$

$$\Im \sigma(\omega) = \frac{1}{8R_Q} \left[-\frac{2\omega_c}{\omega} \left(1 - \frac{\omega_c^2}{\omega^2}\right) \ln \left| \frac{\omega - \omega_c}{\omega + \omega_c} \right| \right] \quad (21)$$

The threshold is $\omega_c = 8U_0\sqrt{(1 - E_J/U_0)}$ (in the case of on-site interaction). It vanishes at the SI transition thus leading to a finite d.c. ($\omega \rightarrow 0$) conductivity,

$$\sigma^* = \frac{\pi}{8} \frac{4e^2}{h}. \quad (22)$$

Corrections to the next order in the $1/N$ expansion correct the Gaussian result by roughly 30% yielding $\sigma^* \sim 0.251\sigma_Q$. Another powerful method for evaluating critical quantities is the ϵ -expansion [63]. In order to set up the ϵ -expansion one should move away from two-dimensions and consider systems with $d - 1$ spatial dimensions. Eq. (19) should be rewritten accordingly (i.e. the three-dimensional vectors should be replaced by d -dimensional ones). This approach allows also to obtain the scaling form of the frequency dependent conductance (for more details the interested reader is referred to Ref. [37]). In two dimension, to order ϵ^2 , the universal conductance is

$$\sigma^* = 0.315 \frac{4e^2}{h}. \quad (23)$$

slightly larger than the result of the Monte Carlo simulation of Ref. [30].

The question arises how a system of bosons can have a dissipative dynamics at zero temperature. A look at the available experiments shows indeed a finite conductance at zero temperature, however, its value appears not to be universal. The origin of the dissipative dynamics may be Ohmic shunts or quasi-particle tunneling between the islands, which been studied extensively in the past (see e.g. Ref. [67]). Pair breaking processes are another mechanism for damping. These processes are present in inhomogeneous films if the order parameter is locally suppressed, or due to Andreev scattering at the boundaries of the grains. Dissipation may arise also due to electronic degrees of freedom, which can be introduced in the model of Eq.(1) by means of what is know as the 'local damping' model. Local damping changes the universality class of the SI transition [29], it also has been known to influence the low frequency dispersion of the vortex response in classical arrays [65,66].

In the presence of Ohmic shunts the effective Euclidean action (13)) for the array gets the additional contribution

$$S_{LD}[\phi] = \frac{1}{2} \int_0^\beta d\tau d\tau' \sum_{ij} \alpha_{ij}(\tau - \tau') [\phi_i(\tau) - \phi_j(\tau')]^2 . \quad (24)$$

For Ohmic baths the Fourier transform of the kernel is $\alpha_{ij}(\omega_\mu) = |\omega_\mu|(\alpha_0 + \alpha_1 k^2)/2\pi$. In this general expression shunts to the ground ($\alpha_0 = R_Q/R_0$) and shunts between the islands ($\alpha_1 = R_Q/R$) are accounted for. The shunts break the 2π -periodicity in the phase variables since they allow for continuous charge fluctuations. The *local* Ohmic damping (the term proportional to α_0) correlates the phase of a single island at different times. In proximity-coupled arrays, which consist of superconducting islands on top of a metallic film, the model with local damping is appropriate to describe the flow of normal electrons into the substrate. This process induces a dissipation for the phase ϕ_i , rather than for the phase difference $\phi_i - \phi_j$ as in the resistively shunted junctions (RSJ) model. The number of Cooper pairs in each island is allowed to decay in the presence of a local damping, whereas the RSJ model describes only charge transfer between neighboring islands.

By going over the same steps outlined in the section on the coarse graining, it is possible to obtain also in this case an effective Ginzburg-Landau free energy. The only difference is that now the phase-phase correlator $g(\tau)$ has to be evaluated including the local damping term. For small frequencies the Fourier transform reads (for more details see Ref. [29])

$$g(\omega_\mu) = g(0) - \eta |\omega_\mu|^s - \zeta \omega_\mu^2 \quad \text{with } s = \frac{2}{\alpha} - 1 . \quad (25)$$

The coefficients η and ζ can be determined from the phase correlator, their value is not important for our purposes. Using this expression for $g(\omega_\mu)$, the free energy (9) contains a *non-Ohmic* dissipative term ($\propto |\omega_\mu|^s$) (reducing to Ohmic, or 'velocity proportional' damping only in the special case $s = 1$). This means that an *Ohmic* damping in the quantum phase model yields a *non-Ohmic* dynamics for the coarse-grained order-parameter.

The phase boundary in the saddle point approximation is shown in the inset of Fig. 5. Increasing damping shifts the phase boundary to smaller values of E_J . At $T = 0$ a quantum phase transition is ruled out beyond the critical value $\alpha = 2$. The value of the d.c. conductivity *at the transition* is displayed in Fig. 4. The non-dissipative transition has a *finite basin of attraction*: $0 \leq \alpha_0 \leq 2/3$. Here the dissipation is an irrelevant operator, and the transition is characterized by $z = 1$ and a universal critical conductivity. However, for stronger damping $\alpha_0 > 2/3$ a new universality class describes the transition, with a *damping dependent* conductance σ^* and $z = 2/s$ as observed experimentally.

ACKNOWLEDGMENTS

We thank L. Amico, R. Baltin, C. Bruder, G. Falci, G. Giamontina, A. van Otterlo, K.-H. Wagenblast, G.T. Zimanyi and D. Zappalà for valuable collaboration on these

topics. The financial support of INFM under the PRA-QTMD, the SFB 195 of the DFG, the Programma Vigoni, and EU TMR programme (Contract no. FMRX-CT 960042) is acknowledged.

REFERENCES

1. Proceedings of the NATO Advanced Research Workshop on *Coherence in superconducting networks*, J.E. Mooij and G.Schön Eds., Physica B **152** (1988).
2. J.E. Mooij and G. Schön in *Single Charge tunneling* H. Grabert and M.H. Devoret Eds., NATO ASI series Vol.294 (Plenum, NY 1992), p. 275.
3. Proc. of the Conference on *Macroscopic quantum phenomena and coherence in superconducting networks* C. Giovannella and M. Tinkham Eds., World Scientific (Singapore, 1995).
4. G. Schön and A.D. Zaikin, Phys. Rep. **198**, 237 (1990).
5. L.J. Geerligs, M. Peters, L.E.M. de Groot, A. Verbruggen, and J.E. Mooij, Phys. Rev. Lett. **63**, 326 (1989).
6. H.S.J. van der Zant, L.J. Geerligs, and J.E. Mooij, Europhys. Lett. **19**, 541 (1992).
7. C.D. Chen, P. Delsing, D.B. Haviland, Y. Harada, and T. Claeson, Phys. Rev. B **50**, 3959 (1995).
8. R. Yagi, T. Tamaguchi, H. Kazawa and S. Kobayashi, J. Phys. Soc. Jpn. **65**, 36 (1996). Very recently the same group has studied the SI transition also in JJA, R. Yagi, T. Tamaguchi, H. Kazawa and S. Kobayashi, J. Phys. Soc. Jpn. **66**, 2429 (1997).
9. D.B. Haviland, Y. Liu, and A.M. Goldman, Phys. Rev. Lett. **62**, 2180 (1989).
10. A. Hebard and M. Palaan, Phys. Rev. Lett. **65**, 927 (1990).
11. S.L. Sondhi, S.M. Girvin, J.P. Carini, and S. Shahar, Rev. Mod. Phys. **69**, 315 (1997).
12. R. Fazio and G. Schön, Phys. Rev. B **43**, 5307 (1991).
13. Ya. Blanter and G. Schön, Phys. Rev. B **53**, 14534 (1996). Ya. Blanter, R. Fazio and G. Schön, Nucl. Phys. B **58**, 79 (1997).
14. R.S. Fishman, and D. Stroud, Phys. Rev. B **37**, 1499 (1987).
15. A. Kampf and G. Schön, Phys. Rev. B **37**, 5954 (1988).
16. S. Teitel and C. Jayaprakash, Phys. Rev. B **27**, 598 (1983); S. Teitel and C. Jayaprakash, Phys. Rev. Lett. **51**, 1999 (1983); T.C. Halsey, Phys. Rev. B **31**, 5728 (1985); W. Y. Shih and D. Stroud, Phys. Rev. B **30**, 6774 (1984); W. Y. Shih and D. Stroud, Phys. Rev. B **28**, 6575 (1983); D. Ariosa, A. Vallat and H. Beck, J. Phys. France **51**, (1990).
17. C. Bruder, R. Fazio, and G. Schön, Phys. Rev. B **47**, 342 (1993).
18. A.F. Andreev, I.M. Lifshitz, Sov. Phys. JETP **29**, 1107 (1969).
19. H. Matsuda and T. Tsuneto, Suppl. Prog. Theor. Phys. **46**, 411 (1970).
20. K.S. Liu and M.E. Fisher, J. Low Temp. Phys. **10**, 655 (1973).
21. E. Roddick and D.H. Stroud, Phys. Rev. B **48**, 16600 (1993); E. Sørensen and E. Roddick, Phys. Rev. B **53**, 8867 (1995).
22. A. van Otterlo, K-H. Wagenblast, Phys. Rev. Lett. **48**, 16600 (1994).

23. R.T. Scalettar, G.G. Batrouni, A.P. Kampf, G.T. Zimanyi Phys. Rev. B **51**, 8467 (1995).
24. E. Frey and L. Balents, Phys. Rev. B **55**, 1050 (1997).
25. L. Amico, G. Falci, R. Fazio, and G. Giaquinta, Phys. Rev. B **55**, 1100 (1997).
26. A. Stern Phys. Rev. B **50**, 10092 (1994).; A.A. Odintsov and Yu. N. Nazarov, Phys. Rev. B **51**, 1133 (1995).; M.Y. Choi Phys. Rev. B **50**, 10088 (1994).
27. M.P.A. Fisher, G. Grinstein and S.M. Girvin, Phys. Rev. Lett. **64**, 587 (1990).
28. X.G. Wen and A. Zee, Int.J.Mod.Phys. B **4**, 437 (1990).
29. K.-H. Wagenblast, A. van Otterlo, G.T. Zimanyi and G. Schön, Phys. Rev. Lett. **78**, 1779 (1997); *ibid.* **79**, 2730 (1997).
30. M.-C. Cha, M.P.A. Fisher, S.M. Girvin, M. Wallin, A.P. Young, Phys. Rev. B **44**, 6883 (1991).
31. E.S. Sørensen, M. Wallin, S.M. Girvin, and A.P. Young, Phys. Rev. Lett. **69**, 828 (1992).
32. M. Wallin, E.S. Sørensen, S.M. Girvin, and A.P. Young, Phys. Rev. B **45**, 13136 (1992).
33. A. van Otterlo, K.-H. Wagenblast, R. Fazio, and G. Schön, Phys. Rev. **48**, 3316 (1993).
34. A.P. Kampf and G. T. Zimanyi, Phys. Rev. **47**, 279 (1993).
35. G.G. Batrouni, B. Larson, R.T. Scalettar, J. Tobochnik, and J. Wang, Phys. Rev. B **48**, 9628 (1993).
36. K. Runge, Phys. Rev. B **49**, 12115 (1994).
37. R. Fazio and D. Zappalà, Phys. Rev. B **53**, R8883 (1996).
38. K. Damle and S. Sachdev, cond-mat.9705206
39. M.P.A. Fisher, B. P. Weichman, G. Grinstein, and D. S. Fisher, Phys. Rev. B **40**, 546 (1989).
40. G. G. Batrouni, R. T. Scalettar, and G. T. Zimanyi, Phys. Rev. Lett. **65**, 1765 (1990).
41. W. Krauth and N. Trivedi, Europhys. Lett. **14**, 627 (1991).
42. J. D. Jackson, *Classical Electrodynamics*, John Wiley & Sons, 1975.
43. P.W. Anderson, *Lectures on the Many Body Problem*, Caianiello Ed., Academic Press (New York, 1964), p.113.
44. K.B. Efetov Sov. Phys. JETP **51**, 1015 (1980).
45. E. Simanek, Phys. Rev. B **23**, 5762 (1982).
46. C. Bruder, R. Fazio, A. Kampf, A. van Otterlo and G. Schön, Physica Scripta **T42**, 159 (1992).
47. S. Doniach, Phys. Rev. B **24**, 5063 (1981).
48. J.G. Kissner and U. Eckern, Z. Phys. **B91**, 155 (1993)
49. J.A. Herz, Phys. Rev. B **14**, 1165 (1976).
50. J. V. José, L. P. Kadanoff, S. Kirkpatrick, and D. R. Nelson, Phys. Rev. B **16**, 1217 (1977).
51. L. P. Kadanoff, J. Phys. A **11**, 1399 (1978).
52. R. Savit, Rev. Mod. Phys. **52**, 453 (1980).
53. B. Nienhuis, in: *Phase transitions and critical phenomena*, Vol. 11, ed. by C. Domb and J. L. Lebowitz (Academic Press, London, 1987)., p.1.

54. J. Villain, *J. Physique* **36**, 581 (1975).
55. S. Elitzur, R. Pearson, and J. Shigemitsu, *Phys. Rev. D* **19**, 3638 (1979).
56. J. V. José and C. Rojas, *Physica B* **203**, 481 (1994).
57. J.E. Mooij, B.J. van Wees, L.J. Geerligs, M. Peters, R. Fazio, and G. Schön, *Phys. Rev. Lett.* **65**, 315 (1990).
58. R. Yagi, T. Tamaguchi, H. Kazawa and S. Kobayashi, *J. Phys. Soc. Jpn.* **66**, 2429 (1997).
59. B.-J. Kim, J. Kim, S.-Y. Park and M.Y. Choi, cond-mat 9704176
60. A. van Otterlo, K.-H. Wagenblast, R. Baltin, C. Bruder, R. Fazio, and G. Schön, *Phys. Rev.* **52**, 16176 (1995).
61. D.A. Huse and V. Elser, *Phys. Rev. Lett.* **60**, 2351 (1988).
62. W. Krauth, D. Caffarel, and J.-P. Bouchard, *Phys. Rev.* **45**, 3137 (1992).
63. C. Itzykson and J.-M. Drouffe, *Statistical Field Theory*, Cambridge University Press (1989).
64. X.G. Wen, *Phys. Rev. B* **46**, 2655 (1992).
65. H. Beck, *Phys. Rev. B* **49**, 6153 (1994).
66. S.E. Korshunov, *Phys. Rev. B* **50**, 13616 (1994).
67. S. Chakravarty, G.-L. Ingold, S. Kivelson, and G.T. Zimanyi, *Phys. Rev. B* **37**, 3283 (1988) and references therein.

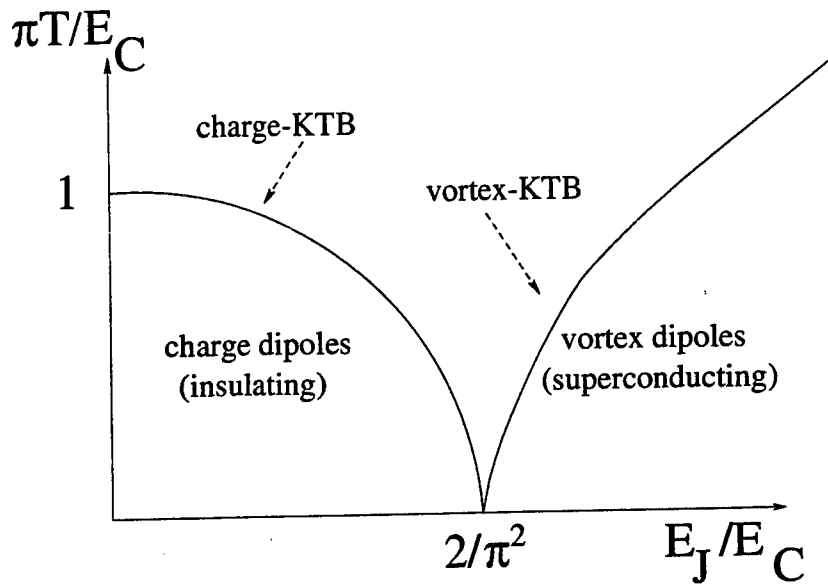


FIGURE 1. The phase diagram for a quantum JJA in the limit of long range (logarithmic) interaction between charges.

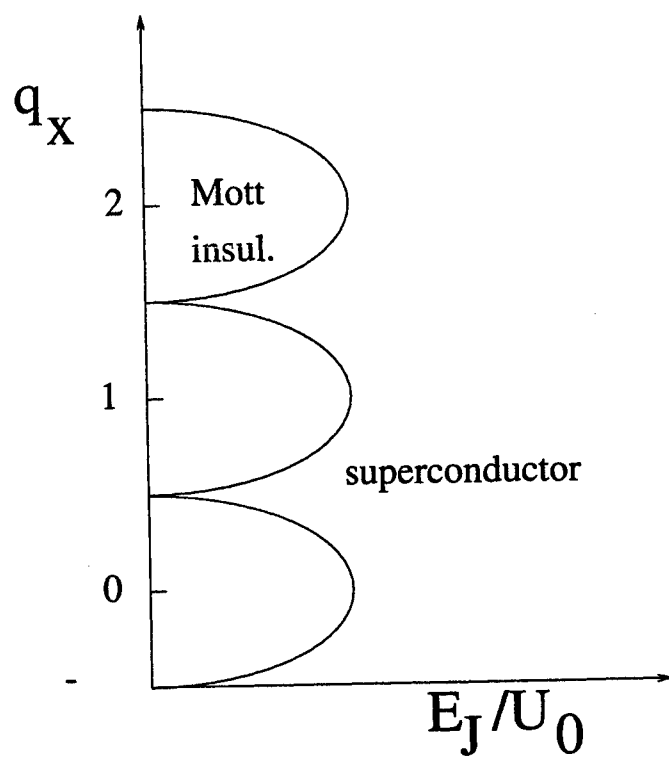


FIGURE 2. The $T = 0$ phase diagram in the limit of on-site interaction as a function of the charge frustration. At the values of q_x for which two charge states are degenerate, the superconducting phase extends to arbitrary small Josephson coupling.

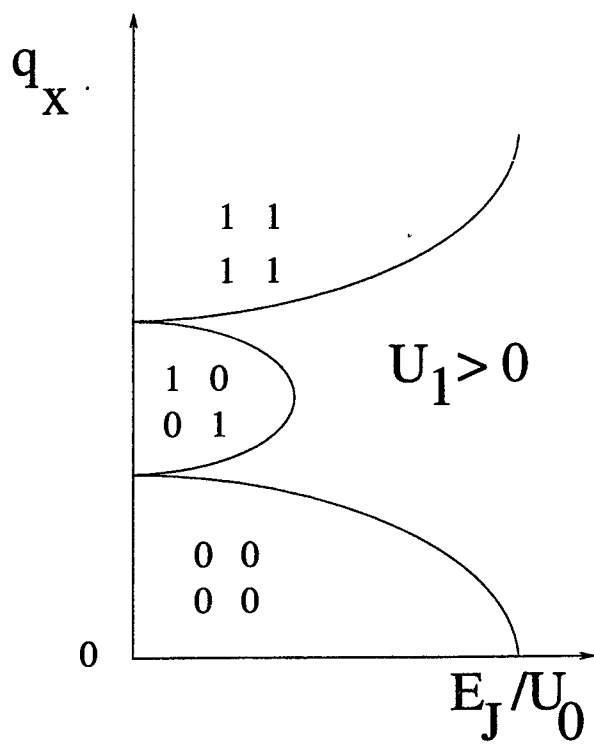


FIGURE 3. The same as in Fig. 2 including a small rearest neighbor charging term U_1 . Around $q_x = 1/2$ the half-integer lobe appears.

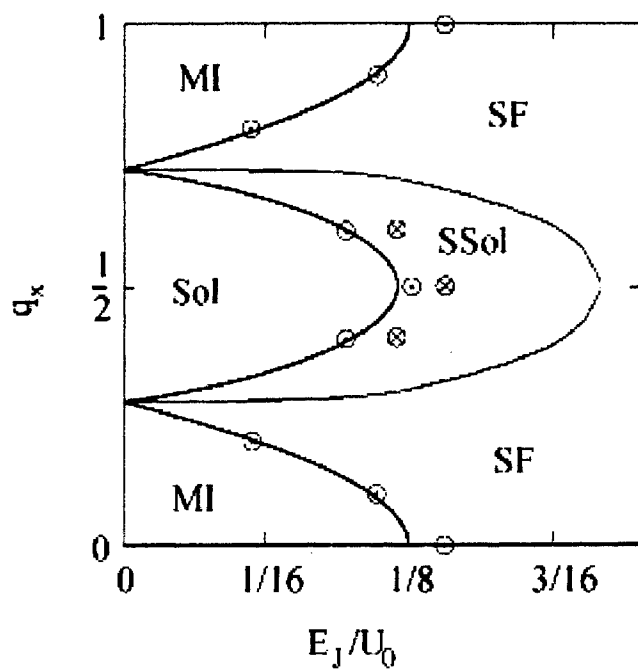


FIGURE 4. The phase diagram as obtained from the variational calculation. Mi= Mott insulator, Sol = solid (with a checkerboard structure), SF = superfluid, SSol = supersolid. ($U_1/U_0 = 0.2$)

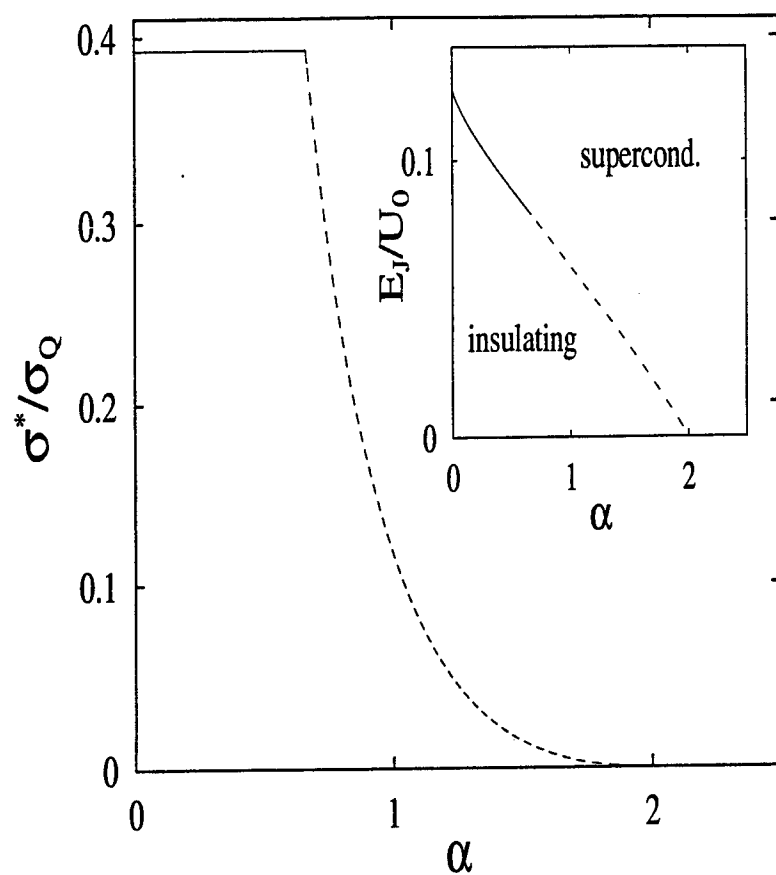


FIGURE 5. The critical conductance as a function of the strength of the local damping. In the inset the SI phase boundary in the presence of dissipation.

Phase transitions in arrays of ultrasmall two-dimensional Josephson junction arrays¹

Jorge V. José

Instituto de Física, Universidad Nacional Autónoma de México, Apdo. postal 20-364, 01000 México D. F.

Physics Department and Center for the Interdisciplinary Research on Complex Systems, Northeastern University, Boston Massachusetts 02115 USA²

Abstract. We briefly review results from extensive semi-classical analytic and quantum Monte Carlo studies of a model of ultrasmall Josephson junction arrays (JJA). Specifically, we mention results: (i) Close to the renormalized semi-classical critical temperature and its successful comparison to experiment. (ii) The existing renormalization-group, self-consistent harmonic approximation and QMC evidence for a low temperature quantum induced phase transition in zero magnetic field.

INTRODUCTION

Josephson junction arrays (JJA) have been the source of many experimental and theoretical studies in the last few years [1]. This interest has been due in part because JJA represent experimental realizations of the two-dimensional XY model. Furthermore, due to the recent advances in sub-micrometer technology it has been possible to fabricate relatively large arrays of ultrasmall SIS (superconductor-insulator-superconductor) Josephson junctions [2-5]. These arrays can have junctions with areas that can vary from a few microns to submicron sizes, with effective capacitances that can be smaller than a few femto Farads ($\text{fF} = 10 \times 10^{-15}$ Farads). Under these circumstances the electric field between the areas that form the junctions has to be quantized. The nature of the possible order present in these devices depends on the competition between the Josephson energy E_J , that tries to establish long range phase coherence, and the charging energy E_c that disrupts this

¹⁾ To appear in "1997 Euroschool, Siena, Italy, Superconductivity in Networks and Mesoscopic Structures" Eds. C. Giovannella and C. Lambert, AIP, 1998

²⁾ Permanent address

order. The relevant parameter to study this competition is

$$\alpha_m = \frac{E_{C_m}}{E_J}, \quad (1)$$

with E_{C_m} and E_J the charging and Josephson energies, respectively, and C_m the mutual capacitance of a junction. In this paper we briefly present the results of work done in collaboration with C. Rojas (more details are given in [6] and in his Ph.D. thesis [7]). We have studied the phase coherence of models of JJA that quantitatively represent the experimentally fabricated devices, including the specific experimental values for α [3]. For the most part the experimental systems have been two-dimensional, but quasi-three-dimensional samples have also been fabricated. Here quasi- means two layers of JJA capacitively coupled at each lattice site [8]. From the type of junctions fabricated there are two main contributions to the charging energy. The charging energy associated with adding a single charge to a superconducting island is given by $E_{C_s} = e^2/2C_s$, whereas the corresponding energy necessary to transfer a charge from an island to a nearby one is $E_{C_m} = e^2/2C_m$, with e the electronic charge. For the Delft experiments, the self capacitances were typically on the order $C_s \sim 3 \times 10^{-17}$ F, while the mutual capacitances were $C_m \sim 1 \times 10^{-15}$ F. This means that C_m is two orders of magnitude larger than C_s .

The resulting phase diagram as a function of temperature vs α_m , for zero and full frustration, is shown in Fig. (1). For small α_m there is a superconducting phase in which the Cooper pair charges are delocalized, while on the right hand side the system has localized vortices and thus it is an insulator. In the following sections we discuss aspects of this phase diagram that have been obtained in experiment and compared to our renormalization group (RG) and Quantum Monte Carlo simulations.

TWO-DIMENSIONAL MODEL

The appropriate model Hamiltonian representing the JJA is

$$\hat{H} = \hat{E}_C + \hat{E}_J = \frac{q^2}{2} \sum_{\vec{r}_1, \vec{r}_2} \hat{n}(\vec{r}_1) \mathbf{C}^{-1}(\vec{r}_1, \vec{r}_2) \hat{n}(\vec{r}_2) + E_J \sum_{\langle \vec{r}_1, \vec{r}_2 \rangle} [1 - \cos(\hat{\phi}(\vec{r}_1) - \hat{\phi}(\vec{r}_2))], \quad (2)$$

where $q = 2e$; $\hat{\phi}(\vec{r})$ is the quantum phase operator, $\hat{n}(\vec{r})$ is its canonically conjugate number operator which measures the excess number of Cooper pairs in the \vec{r} island. These operators satisfy the commutation relations [9] $[\hat{n}(\vec{r}_1), \hat{\phi}(\vec{r}_2)] = -i\delta_{\vec{r}_1, \vec{r}_2}$. The matrix $\mathbf{C}^{-1}(\vec{r}_1, \vec{r}_2)$ is the electric field Green function and its inverse, $\mathbf{C}(\vec{r}_1, \vec{r}_2)$, is the geometric capacitance matrix, which must in principle be obtained from solving the Poisson equation subject to the appropriate boundary conditions. This is not easy to do in general and typically this matrix is approximated, both theoretically and

in the experiments, by diagonal plus nearest neighbor contributions: $C(\vec{r}_1, \vec{r}_2) = (C_s + zC_m)\delta_{\vec{r}_1, \vec{r}_2} - C_m \sum_{\vec{d}} \delta_{\vec{r}_1, \vec{r}_2 + \vec{d}}$, where the vector \vec{d} runs over nearest neighboring islands, and z is the coordination number.

Here we are interested in calculating the thermodynamic properties of the model defined by $\hat{\mathcal{H}}$. The quantity of interest is the partition function $Z \equiv \text{Tr} \{e^{-\beta \hat{\mathcal{H}}}\}$. The trace is taken either over the phase variables, $\hat{\phi}$, or over the charge number operators, \hat{n} . To evaluate the partition function we used its path integral representation [14]. This means that we add one more dimension to the problem, the imaginary time dimension τ , with a range $\tau \in [0, \beta \hbar]$, where $\hbar = h/2\pi$, with h Planck's constant and $\beta = 1/k_B T$, where T is the absolute temperature and k_B Boltzmann's constant. At zero temperature we have a three-dimensional system, while at finite temperatures it is quasi-three dimensional. To evaluate the partition function in this representation we discretize the imaginary time axis in L_τ slices with spacing $\epsilon = \frac{\beta \hbar}{L_\tau}$.

To write a convenient expression for the partition function in the imaginary time representation we use the Poisson summation formula and obtain the explicit form [6]

$$Z = \prod_{\tau=0}^{L_\tau-1} \sqrt{\det[C]} \prod_{\vec{r}} \int_0^{2\pi} \sqrt{\frac{L_\tau}{2\pi\beta q^2}} d\phi(\vec{r}, \tau) \sum_{m(\vec{r}, \tau)=-\infty}^{\infty} \exp \left[-\frac{1}{\hbar} S[\{\phi\}, \{m\}] \right]. \quad (3)$$

Here we defined the action

$$\begin{aligned} \frac{1}{\hbar} S[\{\phi\}, \{m\}] = & \sum_{\tau=0}^{L_\tau-1} \left[\frac{\beta}{L_\tau} H_J(\{\phi(\tau, \vec{r})\}) + \frac{L_\tau}{2\beta q^2} \sum_{\vec{r}_1, \vec{r}_2} [\phi(\tau+1, \vec{r}_1) - \phi(\tau, \vec{r}_1) + 2\pi m(\tau, \vec{r}_1)] \times \right. \\ & \times C(\vec{r}_1, \vec{r}_2) [\phi(\tau+1, \vec{r}_2) - \phi(\tau, \vec{r}_2) + 2\pi m(\tau, \vec{r}_2)] \left. \right] + \\ & + O(1/L_\tau^2), \end{aligned} \quad (4)$$

where the important quantization condition $\phi(L_\tau, \vec{r}) = \phi(0, \vec{r})$ is implicit. Now, to recover the quantum solutions at low temperatures, where we expect novel things to occur, we need to take the continuum limit in the imaginary time direction, which means taking an L_τ very large. This is what makes the QMC computer simulations of this problem difficult and that's why we need to have alternative analytic ways to check the numerical results wherever possible. We discuss this in more detail in the following sections.

WKB-RG ANALYTIC STUDY

Our approach here is to perturb the physics described by $H_J(\{\phi(\vec{r}, \tau)\})$, in the limit when the charging energy is small. When $\alpha = 0$, H_J describes the physics of the classical 2-D XY model [10,11]. In this case we have the BKT scenario that

depends on the thermal nucleation of vortex-antivortex pairs (VAP). The density of VAP increases exponentially as the temperature rises until they unbind at the critical temperature $T_{\text{BKT}}(\alpha = 0) = T_{\text{BKT}}^{(0)} = (\pi E_J / 2k_B)$. The BKT scenario is best understood in terms of a renormalization group (RG) analysis [10,11]. The RG flow diagram is obtained from a perturbation expansion in powers of the vortex pair density $y = y_0 e^{-\frac{\pi^2}{2}K}$. Here $K = \beta E_J$ and y_0 is the initial condition for the bare vortex pair density. In the standard BKT picture there is a line of fixed points for $0 \leq T \leq T_{\text{BKT}}^{(0)}$, with algebraically decaying correlation functions. In the self-capacitive model, at $T = 0$, one can map the problem to an anisotropic three-dimensional XY model, which must have a standard phase transition at a critical value of α_s^c . Around the $T = 0$ critical point α_s^c , one expects to have exponentially decaying correlation functions while at α_s^c the correlations must decay algebraically. The important question is then: How do we go from the BKT regime, with algebraic decaying correlation functions to the very low temperature exponentially decaying one? There must be a discontinuity in going from one limit ($\alpha_s = 0, T \neq 0$) to the other one ($\alpha_s \neq 0, T = 0$). Below we discuss the evidence we have found, including a possible experimental candidate, that there may indeed be a quantum induced phase transition (QUIT) at low temperatures.

The situation when $C_s = 0$ and $C_m \neq 0$ is actually quite different. In that case the $T = 0$ limit can be approximately represented by two coupled three-dimensional XY models, one describing the phase degrees of freedom and the other the charges. As a function of α_m we can go from a phase dominated region, with a 3-D type XY model critical properties to one dominated by a 3-D Coulomb gas. There is not much known about the critical properties, and in particular the correlation function behavior, of the two coupled 3D XY models. So, strictly speaking, we can not state what kind of crossover we should expect when going from $T = T_{\text{BKT}}(\alpha_m, \alpha_s)$ to $T = 0$. Some understanding of the physics in this limit can be obtained by using the Villain transformation, both for the charging energy term and for the phase contribution [12]. The Villain approximation is, however, valid only in a restricted range of α values which do not cover the full experimental range. One could conjecture, however, that the properties of the Villain approximated models is in the same universality class as the full coupled XY models, which is in fact the case when $\alpha = 0$ [11], but this needs to be explicitly shown. Furthermore, the general case treated here where both $C_s \neq 0$ and $C_m \neq 0$ is more complicated since the effective Coulomb gas in the insulating phase has a finite screening length. All these issues need to be studied further.

To find the corrections to the BKT scenario due to the charging effects we carry out a semiclassical or WKB analysis of the model. This was originally done for the self-capacitive model in Ref. [13]. Here we follow a similar approach for the mutual capacitance dominated regime, except that technically the problem is more demanding.

To evaluate the partition function in the SC to N, or small α regime, we notice that we can extend the range of integration of the phases in Eq. (3) from $[0, 2\pi]$

to $[-\infty, \infty]$, while at the same time all but one of the summations over the set of $\{m\}$'s can be eliminated. The resulting expression for the partition function, in the $L_\tau \rightarrow \infty$ limit, then reads

$$Z = \sqrt{\det[C]} \int_0^{2\pi} \prod_{\vec{r}} \sqrt{\frac{L_\tau}{2\pi\beta q^2}} d\phi(\vec{r}, 0) \sum_{m(\vec{r})=-\infty}^{\infty} \int_{-\infty}^{\infty} \prod_{\tau=0}^{L_\tau-1} \sqrt{\det[C]} \prod_{\vec{r}} \sqrt{\frac{L_\tau}{2\pi\beta q^2}} d\phi(\vec{r}, \tau) \times \exp \left[-\frac{1}{\hbar} \int_0^{\beta\hbar} d\tau L_E \right], \quad (5)$$

where the Euclidean Lagrangian is

$$L_E = \frac{1}{2} \left(\frac{\hbar}{q} \right)^2 \sum_{\langle \vec{r}_1, \vec{r}_2 \rangle} \frac{d\phi}{d\tau}(\vec{r}_1, \tau) C(\vec{r}_1, \vec{r}_2) \frac{d\phi}{d\tau}(\vec{r}_2, \tau) + H_J(\{\phi\}). \quad (6)$$

The boundary condition now reads

$$\phi(\vec{r}, \beta\hbar) = \phi(\vec{r}, 0) + 2\pi m(\vec{r}), \quad (7)$$

where the $\{m(\vec{r})\}$'s are the winding numbers. We note that since the Lagrangian is invariant under the transformation $\phi(\vec{r}, 0) \rightarrow \phi(\vec{r}, 0) + 2\pi l(\vec{r})$ for all integers $\{l(\vec{r})\}$, we can extend the limits of integration over $\phi(\vec{r}, 0)$ to $[-\infty, \infty]$, the difference coming only from an overall multiplicative constant. Now that the limits of Eq. (5) are all from $[-\infty, \infty]$ we can make the following change of variable [14]

$$\phi(\tau, \vec{r}) = \frac{2\pi}{\beta\hbar} m(\vec{r}) \tau + \bar{\phi}(\vec{r}) + \phi_f(\vec{r}, \tau). \quad (8)$$

Here $\phi_f(\vec{r}, \tau)$ represents the quantum fluctuations of the path about its mean value $\bar{\phi}(\vec{r})$. These quantum fluctuations become larger than the thermal ones as α increases or as the temperature decreases. This means that we would need to take higher order harmonics in the Fourier series into account when the quantum effects are not relatively small. Because of the periodicity in Eq (7), $\phi_f(\vec{r}, \tau)$ can be expanded in the Fourier series

$$\phi_f(\tau, \vec{r}) = (\beta\hbar)^{-1/2} \sum_{k=1}^{\infty} [\phi_k(\vec{r}) e^{i\omega_k \tau} + C.C.], \quad (9)$$

where the $\omega_k = 2\pi k/\beta\hbar$ are the Bose Matsubara frequencies. Substituting Eqs. (8) and (9) in Eq. (5), expanding the Josephson term up to second order in $\phi_k(\vec{r})$, i.e. up to order $O(q^2)$ or equivalently to $O(\alpha)$, we obtain an effective action for the classical variables $\bar{\phi}(\vec{r})$ after evaluating the integrals. In obtaining the effective action we note that once the integrations over the $\phi_k(\vec{r})$'s are carried out, the partition function still includes a summation over the $m(\vec{r})$'s. In the semiclassical limit the contributions to the partition function from configurations with $m(\vec{r})$ different from zero are exponentially small, so that we can safely take $m(\vec{r}) = 0$ for

all \vec{r} . A most important property of the Josephson Hamiltonian H_J is that it is a periodic function of its argument. This implies that in the expansion the second order derivative with respect to the argument in H_J is proportional to H_J itself. Specifically, for the cosinusoidal form of H_J we have $H_J'' = -H_J + \text{constant}$. This important property of H_J allows us to write the effective partition function as a 2-D classical XY model with an effective coupling constant. The effective partition function to this order of approximation is³

$$Z_{eff} = \int \prod_{\vec{r}} \frac{d\vec{\phi}(\vec{r})}{2\pi} \exp[-\beta_{eff} H_J(\vec{\phi})], \quad (10)$$

where the effective inverse temperature is given by

$$\beta_{eff} = \beta - \frac{(q\beta)^2}{12} [\mathbf{C}^{-1}(0) - \mathbf{C}^{-1}(\vec{d})]. \quad (11)$$

Note that we have explicitly used the fact that $\mathbf{C}(\vec{r}_1, \vec{r}_2) = \mathbf{C}(|\vec{r}_1 - \vec{r}_2|)$, valid for a periodic lattice, so that we can Fourier transform the capacitance matrix.

Once we have a Hamiltonian which is just like the 2-D classical XY model, we can write down the corresponding effective RG recursion relations to lowest order in x as

$$\frac{dK}{dl} = 4\pi^3 K^2 \tilde{y}^2 \frac{(1-xK)^2}{(2Kx-1)}, \quad (12)$$

$$\frac{d\tilde{y}}{dl} = [2 - \pi K(1-xK)]\tilde{y}. \quad (13)$$

In writing these equations we defined the variables

$$x = \frac{q^2}{12E_J} [\mathbf{C}^{-1}(0) - \mathbf{C}^{-1}(\vec{d})], \quad (14)$$

$$\tilde{y} = \exp[-\frac{\pi^2}{2} K(1-xK)] \equiv \exp[-\frac{\pi^2}{2} K_{eff}]. \quad (15)$$

The variable x is the α parameter when the capacitance matrix is not just the self or the mutual capacitance. The RG equations are solved using as initial conditions $K_{eff}(l=0) \equiv K_{eff}^0$ and $\tilde{y}(l=0) \equiv \tilde{y}_0$. As written, the RG equations are valid for an arbitrary ratio between the self and the mutual capacitances. We first notice that in the $x=0$ limit the RG equations reduce to the standard Kosterlitz RG equations [10,11], as they should. The form of the vortex density \tilde{y} is most important. As

³⁾ We must note that in obtaining the effective partition function we assumed that the phases took values between $[-\infty, \infty]$, whereas in the classical XY model the phases are constrained to lie in the $[0, 2\pi]$ range. Following this route makes the derivation of the effective action more direct. However, in the small α regime of interest here the differences between the two ranges for the phases can be shown to be exponentially small.

mentioned above, $\tilde{y}(x = 0)$ grows exponentially with temperature. When $x \neq 0$ and as a function of temperature, \tilde{y} exhibits a low temperature minimum. This is shown in the discontinuous line in Fig. 2. This behavior for \tilde{y} is easy to understand physically. At high temperatures the difference between \tilde{y} and y is very small. However, below the minimum the increase in the vortex pair density is due to nucleation of VAP via quantum phase slips. Of course, we need to remember that we have done a perturbative calculation in x and therefore we may not be on safe ground when \tilde{y} starts increasing again at low temperatures. Nevertheless, as often happens with WKB derived results, the fact that the perturbative analysis shows a low temperature instability is likely to be true. In fact we also have found numerical evidence for the low temperature instability in our QMC calculations [15].

The RG equations have two nontrivial fixed points, one that corresponds to the effective BKT thermal fluctuations driven transition, and the other that corresponds to the QUantum fluctuations Induced transition (QUIT) [13,15].

The RG level curves in the (\tilde{y}, K) phase space, to lowest order in x , result from solving Eq. (15) and

$$\pi x K - \pi \ln K - \frac{2}{K} + 2\pi^3 \tilde{y}^2 = A, \quad (16)$$

for different initial conditions. Figure 2 shows the RG flows for different initial conditions starting with different values for (\tilde{y}_0, K^0) along the discontinuous line in the figure. Each RG flow line corresponds to a different temperature with the arrows indicating the direction of increasing l . We clearly see from the figure that we can divide the temperature axis into three different regions. In the region between $[K_{QUIT}^{-1}, K_{BKT}^{-1}]$, as the value of l increases we eliminate VAP, with the unusual property that the vortex density can initially grow for a while before tumbling to the critical line $\tilde{y} = 0$. This means that in this region at $l = \infty$ there are no VAP with infinite separation, i.e. unbounded. Below K_{QUIT}^{-1} , as l increases, the RG trajectories grow away from the $\tilde{y} = 0$ line, non monotonically, indicating that the perturbation expansion in \tilde{y} is no longer valid. If we associate the instability in the perturbation theory with the normal state behavior, one could say then that this behavior is characteristic of a reentrant phase transition, i.e. going from N to SC to N. This is certainly the case in the high temperature regime but not necessarily so at low temperatures. The single line that divides the two types of behaviors mentioned above is the separatrix that determines the critical temperature. This is the line with the highest temperature for which we can touch the $\tilde{y} = 0$ line. The corresponding separatrix value of the constant $A = A_c$ is determined from the condition that it passes through the point $(K_{BKT}^{-1}, \tilde{y} = 0)$. This leads to the result that the critical point is obtained from solving the equation,

$$\pi x K_c - \pi \ln K_c - \frac{2}{K_c} 2\pi^3 \exp\{-\pi^2 K_c(1 - x K_c)\} = A_c(x), \quad (17)$$

where $A_c(x)$ is obtained from $A_c(x) = 2\pi x K_c - \pi - \pi \ln K_c$, and K_c is the solution to the equation $2 = \pi x K_c(1 - x K_c)$. We'll come back to the problem of determining

K_{BKT}^{-1} in the next section, where we make a comparison with the experimental results. It is known, however, that the determination of T_{BKT} using the RG equations is not quantitatively exact, since the RG analysis is explicitly derived for the Villain action. In comparing with experiment in the next section we will take this into account. Here we present the corrections to the classical results to the leading order in x , which give the correct qualitative trends. Specifically, expanding in powers of x we find that T_{BKT} and T_{QUIT} are given by

$$T_{BKT} \approx T_{BKT}^{(0)} - \frac{E_J}{k_B} x + O(x^2), \quad (18)$$

$$T_{QUIT} \approx \frac{E_J}{k_B} x + O(x^2). \quad (19)$$

Notice that these equations are applicable not only in 2-D, for if the system described by Eq. (10) has a transition point at some K_{eff}^c then the equation $K_{\text{eff}}^c = K - xK^2$ has two solutions for K , which are the ones implied in Eq. (13). Moreover, notice that the results to the first order in x are independent of the specific value of $T_{BKT}^{(0)}$. This means that if we consider the finite magnetic field case, the corresponding critical temperature will be $T_c(B) \approx T_c^{(0)}(B) - (E_J/k_B)x + O(x^2)$. Furthermore, we notice that, to the lowest order in x , the T_{QUIT} must be the same with and without a field. This fact will be compared with the experiments in the next section.

The explicit leading order calculation of the correction to the BKT critical temperature in the asymptotic limits in which either the self or the mutual capacitance dominates results in

$$\frac{T_{BKT}}{T_{BKT}^{(0)}} = \begin{cases} 1 - \frac{4}{3\pi} \frac{E_{C_s}}{E_J} + O\left[\left(\frac{E_{C_s}}{E_J}\right)^2\right], & \text{if } C_s \gg C_m \\ 1 - \frac{4}{3z\pi} \frac{E_{C_m}}{E_J} + O\left[\left(\frac{E_{C_m}}{E_J}\right)^2\right], & \text{if } C_s \ll C_m \end{cases} \quad (20)$$

here z is the coordination number of the array, and for a square array in two dimensions, $z = 4$.

QUANTUM MONTE CARLO APPROACH

To carry out our QMC calculations, we tried different methods but ended up settling with the standard Metropolis algorithm since we needed to update not only the phases but the integers given in the partition function Z (Eqs. (3), (4)) together with the quantum boundary conditions. The advantage of this approach is that it is general enough to be used over all ranges of α_m covered in the phase diagram. We then have a set of angles $\phi(\tau, \vec{r}) \in [0, 2\pi)$, located at the nodes of a three-dimensional cubic lattice, with two space dimensions, L_x and L_y , and one imaginary time dimension, L_τ . The quantum periodic boundary condition appears from the trace condition in Z , and we also took periodic boundary conditions along

the spatial directions. The link variables $m(\tau, \vec{r})$ are defined in the bonds between the lattice sites along the τ -direction and they can take any integer value.

As the phases are updated we restrict their values to the interval $[0, 2\pi)$, so that if after an update a $\phi(\tau, \vec{r})$ is outside this interval, we carry out the transformations,

$$\begin{array}{ll|ll} \text{if } \phi(\tau, \vec{r}) < 0, \text{ then} & & \text{if } \phi(\tau, \vec{r}) > 2\pi, \text{ then} & \\ \phi(\tau, \vec{r}) \rightarrow \phi(\tau, \vec{r}) + 2\pi, & & \phi(\tau, \vec{r}) \rightarrow \phi(\tau, \vec{r}) - 2\pi, & \\ m(\tau, \vec{r}) \rightarrow m(\tau, \vec{r}) + 1, & & m(\tau, \vec{r}) \rightarrow m(\tau, \vec{r}) - 1, & \\ m(\tau + 1, \vec{r}) \rightarrow m(\tau + 1, \vec{r}) - 1. & & m(\tau + 1, \vec{r}) \rightarrow m(\tau + 1, \vec{r}) + 1. & \end{array} \quad (21)$$

From Eq.(4), we see that the action is invariant under these transformations. Moreover, the shifts in the column and individual phase moves are adjusted to keep the acceptance rates in the range $[0.2, 0.3]$.

When α_m is small, the fluctuations of the phases along the imaginary time axis as well as the fluctuations in the m 's are suppressed by the second term in Eq. (4). Attempts to change a phase variable have a very small success rate. Therefore we implemented two kinds of Monte Carlo moves in the phase degrees of freedom. In one sweep of the array we update $L_x \times L_y$ imaginary time columns, by shifting all the phases along a given column by the same angle. This move does not change the second term in Eq. (4), and thus it probes only the Josephson energy [15]. To account for phase fluctuations along the imaginary time axis, which become more likely as (α_m/T) increases, we also make local updates of the phases along the columns. We did check on the reliability of this procedure by comparing with our RG-WKB and self-consistent harmonic approximation results [6]. Another aspect of the implementation of the MC algorithm is the order in which we visit the array. This is relevant for the optimization of the computer code for different computer architectures. In a scalar machine we used an algorithm that updates column by column in the array. For a vector machine we used the fact that for local updates, like the ones we used, the lattice can be separated into four sublattices in a checkerboard-like pattern. This partition is done in such a way that each of the sublattices can be updated using a long vector loop without problems of data dependency. Using this last visiting scheme, the cpu time grows sublinearly with the size of the array. One of the problems that this type of visiting scheme has in a vector machine, like the Cray C90, is that the array's dimensions have to be even, and this produces memory conflicts. We have not made attempts to optimize this part of the code.

We also replaced the $U(1)$ symmetry of the phases by the subgroup $Z(N)$, with $N = 5000$ [15]. This allows the use of integer arithmetic for the values of the phase variables, and to store lookup tables for the Josephson cosine part of the Boltzmann factors. This can not be done for the charging energy part of the Boltzmann factors, except in the $C_m = 0$ case where the m 's can be summed up in a virtually exact form. In the latter case we can also store lookup tables using the following definition of an effective potential V_{eff} ,

$$\exp \left[- \left(\frac{L_\tau C_s}{q^2 \beta} \right) V_{\text{eff}}(\phi) \right] = \sum_{m=-\infty}^{\infty} \exp \left[- \frac{1}{2} \left(\frac{L_\tau C_s}{q^2 \beta} \right) (\phi + 2\pi m)^2 \right]. \quad (22)$$

These sums can be evaluated numerically to any desired accuracy.

We calculated thermodynamic averages after we made N phase updates and M of the m updates through the whole lattice. Typically, for α_m small we used $N = 4$ and $M = 1$. In the opposite limit we used $N = 1$ and $M = 8, 10, \dots$. This is so because our local updating algorithms for the m 's have serious decorrelation time problem, due to the long range interaction among the charges. We typically found that in order to get reasonably small statistical errors, we needed to perform, in most cases, about $N_{\text{meas}} = 2^{12} = 4096$ measurements of the thermodynamical quantities, other times we made up to $N_{\text{meas}} = 2^{13} = 8192$ measurements.

High temperature results

In this section we present some of our quantum Monte Carlo results at high temperatures. In this limit the results are quite reliable since essentially $\beta\hbar \ll 1$ and thus the quantum fluctuations act mostly to renormalize the classical results, as originally discussed many years ago [13]. A proper way to measure the long range phase coherence in the model is by calculating the helicity modulus, which is defined by $\Upsilon = \left. \frac{\partial^2 F}{\partial A_{\vec{r}, \vec{r}+\hat{z}}^2} \right|_{A=0}$. Here $e^{-\beta F} = Z$, defines free energy F , and A denotes a twist of the phases along the \hat{z} direction, so that Υ gives the response of the system to this twist. We calculated the Υ in the small α_m region and the inverse dielectric constant ϵ^{-1} in the large α_m regime, and both quantities in the intermediate region.

Most of the calculations we performed used the capacitances values from experiment. These were the **only** external parameters used in the calculations. In particular, the ratio between the self and mutual capacitance was kept fixed around the values $C_s/C_m \approx 0.01$ and 0.03 , with the bulk of the calculations carried out for 0.01 . We found that in the case of the helicity modulus both values give essentially the same results. Almost all of the calculations were done by lowering the temperature, in order to reduce the chances for the system to be trapped in metastable states [16]. Our results are given in Fig. (1). There we see that the experimental and numerical results are indeed quantitatively close in the $f = 0$ case and have the correct qualitative trend in the $f = 1/2$ case.

We have also carried out WKB renormalization group calculations valid for $\beta\hbar \ll 1$, and they agree quite well in the small α_m regime of Fig. (1) as well. The WKB-RG results are in principle only valid for $\beta\hbar \ll 1$. However a persistent property of the results is the evidence for a low temperature instability. We discuss this possibility next.

Low temperature results

As we mentioned above, motivated by the WKB-RG results, there has been an extensive search for what has been called a **QUIT** (QUantum Induced Transition). Originally this prediction was made for the case where the capacitive matrix only has a self-capacitive term. This means that there is only a superconducting phase in the T -vs- α phase diagram. For the specific type of fabricated samples it was then necessary to consider the case where both C_s and C_m were included and with C_m being larger than C_s by two orders of magnitude. We carried out the corresponding WKB-RG calculations and again they led to the possibility of having a low temperature QUIT. An important aspect of the analytic results is that to leading order in α_m the $T_{QUIT} \sim \alpha_m$, independent of an applied magnetic field. This means that T_{QUIT} for zero for $f = 1/2$ fields to leading order in α must be the same. This result is important since to test the existence of a QUIT in a field, as was tried in Ref. [16] much lower temperatures had to be simulated. Here we concentrate in the $f = 0$ case to keep things clearer, for the $f = 1/2$ case has its own special excitations that may confuse the T_{QUIT} issue. Our approach was then to calculate Υ for relatively large values of α_m so as to enhance the possibility of seeing the transition but this implied that much larger lattices and runs had to be carried out. In Fig. (2) we show typical results for Υ for fixed values of α but varying L_τ . There we see that there is a reentrant type behavior for Υ but it shows that as L_τ increases the reentrant temperature decreases. The important question is what happens in the $L_\tau \rightarrow \infty$ limit. In Fig. (3) we show the $L_\tau \rightarrow \infty$ for one $\alpha_m = 2.0$. There we see that the extrapolated $\Upsilon(L_\tau \rightarrow \infty)$ gives evidence for $T_{QUIT}(\alpha_m = 2.0) \neq 0$ the same is true for a calculation with $\alpha_m = 2.25$, however for $\alpha_m = 2.5$ the extrapolated value for T_{QUIT} becomes negative indicating that it must be zero. The conclusion we draw from these calculations is that there is a critical value for α_m below which there is a finite QUIT and above which it disappears. We also carried out a self consistent harmonic approximation analytic (SCHA) analysis to carefully study the important dependence on L_τ . We did find quantitative agreement between our analytic SCHA results and those obtained from our QMC analysis thus given further validity to the results obtained. Therefore we conclude that our evidence points to the existence of a QUIT for the system where the mutual capacitance dominates. There is some evidence for a low temperature instability as well in the experiments but it is not yet conclusive [3]. More experimental and theoretical work is needed to ascertain the real existence of this QUIT.

COMPARISON TO EXPERIMENT

We now move on to a brief discussion of how we obtained the results presented in Fig. 1. As mentioned before, in trying to find quantitative correspondence between experiment and theory it is important to ascertain the validity of the theoretical models employed to study the arrays. We have carried out two different types of

checks. One based on the RG analysis described in the previous sections and the other from a nonperturbative quantum Monte Carlo calculation [6]. We discuss the RG analysis here and only briefly mention the QMC results, with more details left for other publications [6,7].

As mentioned before, it is known that the RG equations do not lead to quantitatively exact results for the critical temperatures. They do, of course, lead to the correct universal critical exponents. However, what has so far been measured experimentally is the phase boundary between the SC and the N phases. We then need a consistent way to compare the RG results with the experimental results.

We first note that the phase diagram of Fig. 1 is plotted as a function of $\alpha_m = \frac{E_{Cm}}{E_J}$, since experimentally α_s is three orders of magnitude smaller. We can then write $K_{eff} = K(1 - xK)$ with $C_S = 0$ as

$$K_{eff} = K - \frac{\alpha_m}{6} K^2. \quad (23)$$

Next we set the critical temperature for the classical model to be the one obtained in classical MC simulations (e.g. [20]) $1/K_c^{(0)} \approx 0.93$, so that the critical temperature $T_c(\alpha_m)$ of the actual model is given by the equation

$$k_B T_c(\alpha_m) = \frac{1}{2K_c^{(0)}} \left[1 + \sqrt{1 - \frac{2\alpha_m}{3} K_c^{(0)}} \right]. \quad (24)$$

To lowest order in α_m this equation gives

$$T_c(\alpha) = T_c(0) - \frac{\alpha_m}{6}, \quad (25)$$

whereas the maximum value of α_m for which there is a physical solution is $\alpha_m = \frac{3}{2} k_B T_c(0) \approx 1.4$. The results obtained from this analysis are shown as a discontinuous line in Fig. 1. By following this approach we see that for $\alpha_m \leq 1$ the RG result is actually quite good when compared to the experimental and the MC results.

We also have extended our previous QMC calculations to the case when the off-diagonal capacitance is dominant. The results are shown in Fig. 1 by the crosses, including their error bars. It is clear from these results that the correspondence between experiment and QMC results is excellent, up to nonperturbative values of α_m . This leads us to the conclusion that the model studied here does provide a good representation of the experimental system, at least in the SC to N regime. In the next section we will briefly discuss what happens in the insulating region to normal region.

The discussion presented above dealt with the SC to N phase boundary. What about evidence for a QUIT? In this regard we note that in the experimental results of Ref. [3] there are results for a sample with a nominal $\alpha_m = 1.67$ for which there is a double type of reentrant behavior. The low temperature glitch seen in

the resistance versus temperature diagram occurs at $T' = 40mK$. Moreover the latter instability is also characterized by an increase in noise fluctuations in the IV characteristics measured in this sample. If we assume that what is seen at T' is related to the QUIT, using Eq.(24) and the parameter values of the experiment we get a $T_{QUIT} = 33mK$, rather close to the experimental value. Furthermore when the same experiment is repeated in a small magnetic field the low temperature instability is found at the same temperature, i.e.; $T'(f = 0) = T'(f = 0.08)$. This result is also consistent with Eq. (24) which also leads to a T_{QUIT} independent of f at leading order in α_m . These results may just be coincidental and more work needs to be done to conclusively connect the T_{QUIT} with the low temperature instability already seen in the Delft experiments.

INSULATING TO NORMAL CROSS OVER

As mentioned in the introduction, as α_m increases there is a SC to I transition at finite temperature. In the $\alpha_s = 0$ case, the insulating phase has been modeled as a two-dimensional Coulomb gas of charges with a possible BKT charge unbinding transition [21,22,12]. This situation has been studied extensively, in particular in Ref. [12]. Here we ask if there is an equivalent QUIT in the insulating phase at low temperatures. If we draw an analogy to the quantum induced vortices in the SC phase one could also imagine that the number of free dipoles in the arrays could increase due to quantum fluctuations. However, as we show below the vortices and charges are not dual to each other in that sense.

The calculation described here aims at finding the leading correction to the charging Hamiltonian due to Josephson junction fluctuations. We then expand the Josephson contribution to Z as

$$\exp \left[-\frac{1}{\hbar} \int_0^{\beta\hbar} d\tau H_J(\tau) \right] \approx 1 - \frac{1}{\hbar} \int_0^{\beta\hbar} d\tau H_J(\tau) + \frac{1}{2\hbar^2} \int_0^{\beta\hbar} \int_0^{\beta\hbar} d\tau d\tau' H_J(\tau) H_J(\tau') + \dots \quad (26)$$

As before, we use Eqs. (12) and (13), but this time we integrate out both $\phi_f(\tau, \vec{r})$ and $\phi(\vec{r})$, which leaves us with an effective action for the $\{m\}$'s,

$$Z \approx Z_\phi \prod_{\vec{r}} \sum_{m(\vec{r})=-\infty}^{\infty} \exp \left[-\frac{1}{4\tilde{K}_{\text{eff}}} \sum_{\vec{r}, \vec{d}} \left(m(\vec{r} + \vec{d}) - m(\vec{r}) \right)^2 \right], \quad (27)$$

where we have assumed that $C_s \ll C_m$. The function Z_ϕ does not contain the $\{m\}$ variables, and the effective coupling constant \tilde{K}_{eff} is

$$\tilde{K}_{\text{eff}}^{-1} = \tilde{K}^{-1} \left[1 + \left(\frac{2\pi^2}{\alpha_m} \right)^2 g(\tilde{K}) \right], \quad (28)$$

given as a function of $\tilde{K} = (\beta E_{C_m})/2\pi$. As in the vortex dominated case, we have ended up with a Coulomb gas problem but with a renormalized coupling constant. The function $g(\tilde{K})$ determines the importance of the zero point fluctuations of the phases on the charge dominated phase. The function $g(\tilde{K})$ is defined as

$$g(\tilde{K}) = \int_0^{1/2} dt [1 - \cos(2\pi t)] \exp \left[-\frac{(2\pi)^2}{z} \tilde{K} t(1-t) \right]. \quad (29)$$

For a BKT type phase transition we have $\tilde{K}_{eff} = K_{BKT}^c = 2/\pi$ [12]. It is important here to see if, within this approximation, the system shows a QUIT or a reentrant transition. We then need to study the number of solutions to this equation. From the fact that $K_{BKT}^c \sim O(1)$ we can see that for any value of $1/\alpha_m$ the function $g(\tilde{K})$ has only one solution for \tilde{K}_c . This means that, to this order of approximation, **there is no QUIT** in the charge dominated phase in this model.

A question that immediately arises is: Why is there a difference between the vortex and charge dominated phases, in particular in view of the duality between the two phases extensively studied in [12]? The reason is that the duality is not exact since there is a term in the action, obtained using the Villain approximation, that breaks this symmetry. If one includes this term we then see that the cost of producing quantum fluctuations in the vortices is bounded from above whereas the corresponding cost in the charge dominated phase is unbounded. In our calculation we have kept these contributions intact.

CONCLUSIONS

We have briefly presented results from a thorough study of the α_m vs. T phase diagram for an array of ultrasmall Josephson junctions in zero and $f = 1/2$ external magnetic fields. One of our main goals was to perform different calculations for these arrays using experimentally realistic parameters. For convenience of calculation we derived a path integral formulations of the quantum partition function of the JJA. In the small α_m limit we used a WKB-RG approximation to find the first order correction in α_m to the classical partition function. The result of this calculation was an effective classical partition function of a 2-D XY model, where the coupling constant is modified by the quantum fluctuations. Our quantitative comparison between our $f = 0$ calculations and experiment was excellent and only needed as adjustable parameter the capacitance ratios given by experiment. The results for the $f = 1/2$ agreed only qualitatively though. In the low temperature limit we provided evidence for the existence of a *QUIT*, and still more experimental and theoretical work is needed to further elucidate the properties and reality of the *QUIT*. One of the conclusions from these calculations is that the general trend of the Monte Carlo results for the helicity modulus can be traced to the degree of discretization along the imaginary time axis.

We also performed some Monte Carlo calculations of the inverse dielectric constant of the 2-D Coulomb gas, in order to find the conducting to insulating phase

boundary. We found that the present Monte Carlo path integral implementation of our model does not allow us to make fully reliable calculations of this quantity. Our results for this transition are only qualitative. The reason for this is that in the simulations we have to update simultaneously phases and the charges that have long range interactions. Further technical improvements are needed in order to make solid quantitative statements about the insulating phase.

Finally, these type of systems hold the promise of leading to a great variety of novel experimentally observable phenomena. There are other possibilities not discussed here, like that of two arrays capacitively coupled [24,23], in which there is a vortex-charge interaction of gauge nature that deals with the interplay of quantum-classical effects, and may lead to a possible quantum Hall effect either in the gas of charges or that of vortices.

ACKNOWLEDGMENTS

This work has been partially supported by *NSF* grant DMR-9521845.

REFERENCES

1. For a review of superconducting networks see *Proceedings of the 2nd CTP Workshop on Statistical Physics: KT Transition and Superconducting Arrays*, Edited by D. Kim, et al. (Min Eum Sa, Seoul, Korea, 1993). *Macroscopic quantum phenomena and coherence in superconducting networks*. Edited by C. Giovannella and M. Tinkham. World Scientific Co., Singapore, 1995)
2. H. S. J. van der Zant, *et al. ibid.*, **69**, 2971 (1992).
3. H. S. J. van der Zant, Ph. D. Thesis, Delft (1991) and preprint (1996).
4. T. S. Tighe, *et al.*, Phys. Rev. **B47**, 1145 (1993).
5. C. D. Chen, *et al.* Physica Scripta **T42**, 182 (1992).
6. C. Rojas, J. V. José, Phys. Rev. **B54**, 12361 (1996)
7. C. Rojas, Ph.D. thesis, Northeastern University, 1996.
8. L. L. Sohn, et al., Physica **B194-196**, 125 (1994).
9. P. W. Anderson, in *Lectures in The Many Body Problem*, edited by E. R. Caianiello, (Academic, New York, 1964), Vol. 2.
10. V. L. Berezinskii, Zh. Teor. Fiz. **61**, 1144 (1971). [Soviet Physics JETP **32**, 493 (1971)]. J. M. Kosterlitz and D. J. Thouless, J. Phys. **C6**, 1181 (1973); J. M. Kosterlitz, J. Phys. **C7**, 1046 (1974).
11. J. V. José, L. P. Kadanoff, S. Kirkpatrick, and D. R. Nelson, Phys. Rev. **B16**, 1217 (1977).
12. R. Fazio and G. Schön, Phys. Rev. **B43**, 5307 (1991).
13. J. V. José, Phys. Rev. **B29**, 2836 (1984)
14. L. S. Schulman, *Techniques and applications of path integration* New York: Wiley, (1981).
15. Jacobs, J. V. José, M. A. Novotny, and A. M. Goldman, Phys. Rev. **B38**, 4562 (1988); L. Jacobs, J. V. José, M. A. Novotny, and A. M. Goldman, Europhys. Lett. **3**, 1295 (1987); L. Jacobs, J. V. José, and M. A. Novotny, Phys. Rev. Lett. **53**, 2177 (1984)
16. J. Mikalopas, et al, Phys. Rev. B **50**, 1321 (1994).
17. C. Rojas and J. V. José, and A. M. Tikofsky Bull. Am. Phys. Soc. **40**, 68, B11-7 (1995).
18. Ya. M. Blanter and F. Schön, Phys. Rev. **B53**, 14534 (1996).
19. L.J. Geerlings, *et al.*, Phys. Rev. Lett. **63**, 326(1989) and Ref. 1, p. 212.
20. G. Ramírez-Santiago and J.V. José, Phys. Rev. Lett. **68**, 1224 (1992); Phys. Rev. **B49**, 9567 (1994).
21. N. Yoshioka, *et al.*, Jpn. J. Appl. Phys. **26**, 949 (1987). A. Widom and S. Badjou, Phys. Rev. **37**, 7915 (1988).
22. J. E. Mooij *et al.*, Phys. Rev. Lett. **65**, 645 (1990).
23. C. Rojas and J. V. José, and A. M. Tikofsky Bull. Am. Phys. Soc. **40**, 68, B11-7 (1995).
24. Ya. M. Blanter and F. Schön, Phys. Rev. **B53**, 14534 (1996).

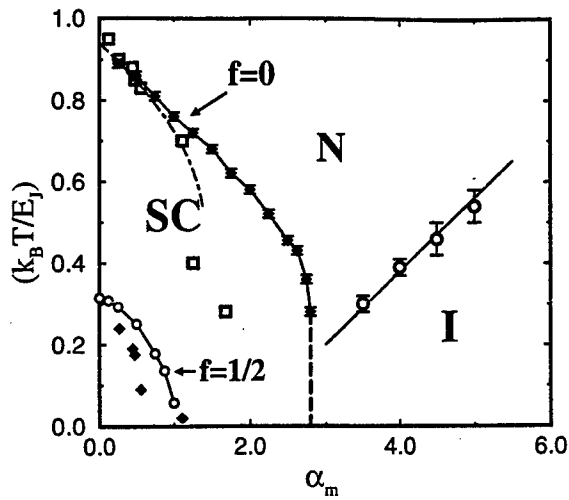


FIGURE 1. Temperature vs. quantum parameter α_m phase diagram, for zero magnetic field and for full frustration $f = 1/2$. SC stands for superconducting, N for normal and I for insulating phases. The experimental results are denoted by squares. The quantum Monte Carlo results are denoted by crosses ($f=0$) and circles ($f=1/2$) joined by continuous lines as guides to the eye. The QMC results include the statistical error bars in the calculations.

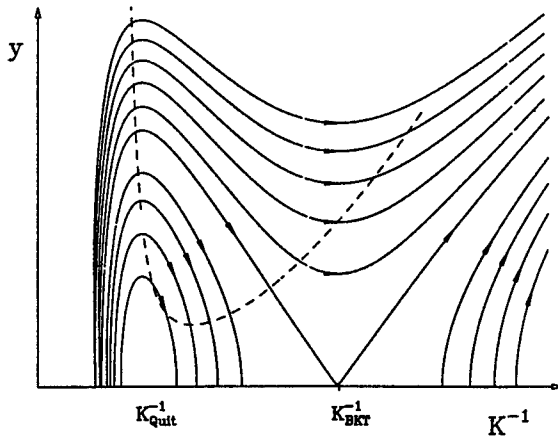


FIGURE 2. Renormalization group flow diagram. The discontinuous line indicates the vortex pair density as a function of temperature. See text for a discussion of the analysis of this diagram.

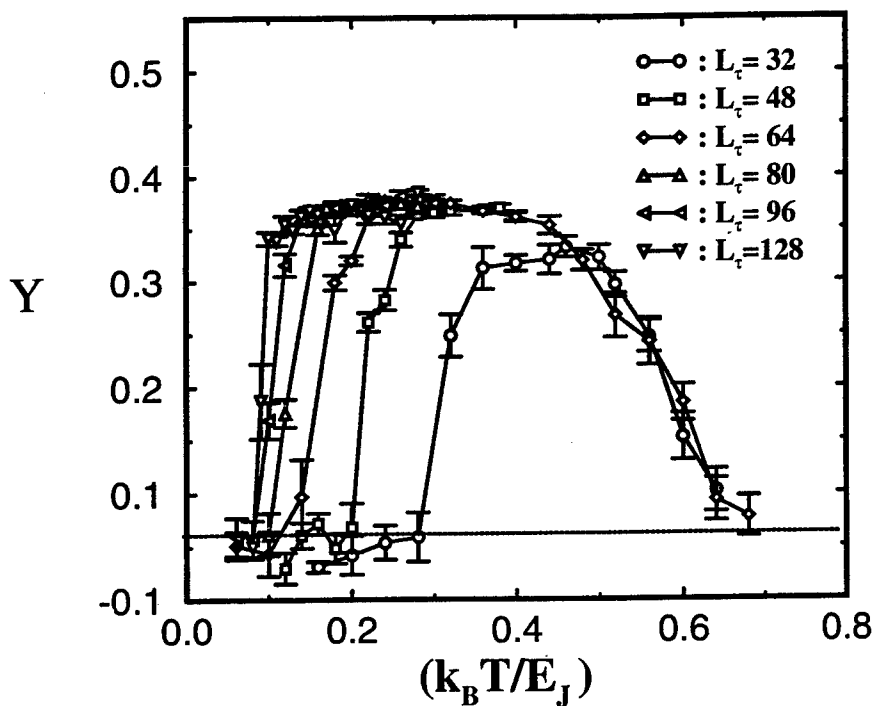


FIGURE 3. Υ vs temperature for $\alpha_m = 2.5$, $L_x = L_y = 20$. At this value of α_m the drop in the helicity modulus at low temperatures yields essentially $\Upsilon = 0$. This abrupt drop is probably due to having a finite L_τ . Note that the decrease of the Υ as T is lowered tends to a nonzero T_{QUIT} temperature (see text for more details)

Two-dimensional arrays of low capacitance tunnel junctions: general properties, phase transitions and Hall effect

P. Delsing*, C.D. Chen[†]*, D.B Haviland*, T. Bergsten*
and T. Claeson*

* *Department of Microelectronics and Nanoscience,
Chalmers University of Technology and Göteborg University, S-412 96, Göteborg Sweden*
[†] *Institute of Physics, Academia Sinica, Nankang, Taipei 11529, Taiwan*

Abstract. We describe transport properties of two-dimensional arrays of low capacitance tunnel junctions, such as the current voltage characteristic and its dependence on external magnetic field and temperature. We discuss several experiments in which the small capacitance of the junctions plays an important role, and we also describe the methods for fabrication and measurements.

In arrays where the junctions have a relatively large charging energy, (*i.e.* when they have a low capacitance) and a high normal state resistance, the low bias resistance increases with decreasing temperature and eventually at very low temperature the whole array may become insulating even though the electrodes in the array are superconducting. This transition to the insulating state can be described by thermal activation, characterized by an activation energy. We find that for certain junction parameters the activation energy oscillates with magnetic field with a period corresponding to one flux quantum per unit cell.

In an intermediate region where the junction resistance is of the order of the quantum resistance and the charging energy is of the order of the Josephson coupling energy, the arrays can be tuned between a superconducting and an insulating state with a magnetic field. We describe measurements of this magnetic-field-tuned superconductor insulator transition, and we show that the resistance data can be scaled over several orders of magnitude. Four arrays follow the same universal function provided we use a modified scaling parameter. We find a critical exponent close to unity, in good agreement with the theory.

At the transition the transverse (Hall) resistance is found to be very small in comparison with the longitudinal resistance. However, for magnetic field values larger than the critical value, we observe a substantial Hall resistance. The Hall resistance of these arrays oscillates with the applied magnetic field. Features in the magnetic field dependence of the Hall resistance can qualitatively be correlated to features in the derivative of the longitudinal resistance, similar to what is found in the quantum Hall effect.

I INTRODUCTION

The electrical transport in two-dimensional (2D) arrays of small Josephson tunnel junctions can be described either in terms of charges or in terms of vortices [1,2]. Transport of charge generates a current which acts as a driving force for the vortices. The charge transport may be obstructed by a large charging energy, $E_C \equiv e^2/2C$, C being the capacitance of the individual junction. On the other hand, transport of vortices generates a voltage which acts as a driving force for the charges. The vortex transport may be hindered if the Josephson coupling energy is large. At low temperature the Josephson coupling energy is given by $E_J \equiv (R_Q/R_N)/(\Delta/2)$, where R_N is the normal state resistance of the individual junctions, $R_Q \equiv h/4e^2 \approx 6.45 \text{ k}\Omega$ is the quantum resistance, and Δ is the superconducting energy gap of the electrodes.

Adding a single charge to an electrode in the array gives rise to an electrostatic potential distribution which is sometimes referred to as a charge soliton [3]. A missing charge gives rise to the counterpart, an anti-soliton. The charge solitons can move in the array by single-charge tunnel events. When the electrodes are superconducting, both Single Electron Solitons (SES) and Cooper Pair Solitons (CPS) can exist. An exact calculation of the potential distribution in a 49×47 junction array assuming only nearest neighbor coupling, is shown in Fig. 1, for two different cases: A single electron in the center of the array, giving rise to a SES, and the fundamental excitation, a soliton/anti-soliton pair at adjacent electrodes. The size of the soliton is given by $\sqrt{C/C_0}$ as long as $C > C_0$. C_0 is the capacitance between an electrode in the array and infinity. However if C is of the order of C_0 the nearest neighbor approach is not a good approximation [4].

On the other hand, due to the existence of a macroscopic phase of the super-

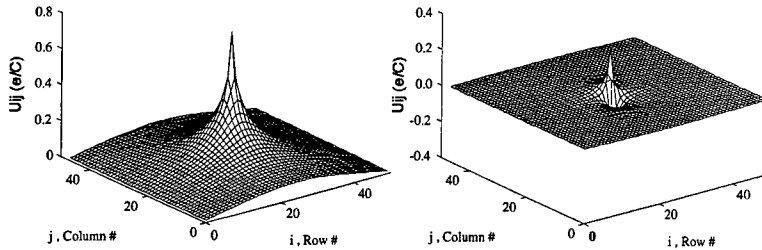


FIGURE 1. The exact solution for the potential distribution U_{ij} in a 49×47 junction array, where the ratio between the junction capacitance and the self capacitance of each electrode is 400. The current leads are connected at $i = 1$ and $i = 49$ a) A single electron in the center of the array giving rise to a single electron soliton. b) The fundamental excitation, a soliton/anti-soliton pair at neighboring sites.

conductor, a vortex, *i.e.* a phase winding of 2π , with an associated magnetic flux quantum $\Phi_0 \equiv h/2e$, can exist in a loop of the array. In a two-dimensional (2D) array of small Josephson tunnel junctions the duality between charges and vortices is especially pronounced. Therefore it is a very suitable object to study the dynamics of both charges and vortices.

The arrays which have high junction resistance, $R_N \gg R_Q$ and large charging energy, $E_C \gg E_J$, become insulating at low temperature due to the Coulomb blockade [5,6], regardless of whether the electrodes are superconducting or normal.

In the opposite limit, $R_N \ll R_Q$ and $E_C \ll E_J$, superconductivity prevails and the resistance goes to zero at low temperature. In this limit where the Josephson energy dominates, vortices act as classical or quasi-classical particles and there is a large number of papers describing such systems theoretically [7-10] as well as experimentally [11-17]. With normal electrodes and $R_N \gg R_Q$ the array goes insulating at low temperature while in the opposite limit $R_N \ll R_Q$, the array stays resistive even down to very low temperature.

In this paper we will concentrate on the arrays where the charging energy is comparable to or larger than the Josephson coupling energy, and where the junction resistance is of the order of or larger than R_Q . Throughout this paper, we will refer to an array with normal electrodes as being in the N-state, and to an array with superconducting electrodes as being in the S-state.

If the interaction between the charges (or vortices) is logarithmic, the transition to the insulating (superconducting) state would be of the Kosterlitz-Thouless-Berezinskii (KTB) type [18,19]. As the temperature is increased, an insulating 2D array can undergo a charge unbinding transition [20] at some transition temperature, which results in a conductive state. Likewise, a superconducting array can undergo a vortex unbinding transition to a resistive state. It has been shown that the superconducting transition can be described as a vortex unbinding, KTB transition [11]. In more recent years there has also been a lot of interest in arrays where the dynamics is best described in terms of charges [20-27]. In several papers there has been a discussion whether the observed transition to the insulating state can be described as a KTB transition as well [20,24,25]. In a paper by Tighe et al. [25] it was pointed out that the transition could be well described by thermal activation of charge solitons. Comparing results of three different groups [20,24,25], they found an activation energy $E_a \approx \frac{1}{4}E_C$ in the N-state, a value which can be theoretically justified. They also suggested that in the S-state at $B = 0$, E_a should be $\frac{1}{4}E_C + \Delta_0$, where $2\Delta_0$ is the superconducting energy gap at $B = 0$ and $T = 0$. An interesting new result is that of Kanda and Kobayashi [27] where they find a thermal activation behavior at higher temperatures but a stronger dependence at lower temperature in the N-state. An interesting theoretical development in this field is a recent paper by Feigelman et al. [28], where they treat the possibility of parity effects 2D arrays. In section IV we will describe measurements where we have investigated the transition to the insulating state extensively.

For arrays in the intermediate regime ($R_N \approx R_Q$ and $E_C \approx E_J$) which just barely go superconducting, a small magnetic field can drastically change the low

bias resistance and in fact drive the array into the insulating state [29]. In a theoretical description of this effect [30], the field induced excess vortices drive the system from a vortex glass superconducting phase into a Bose-condensed insulating phase. The zero-magnetic-field KTB vortex-unbinding transition is replaced by a field-tuned vortex-delocalization transition. A superconductor-insulator(SI) transition can also be driven by other external variables such as electric field [31,32] or dissipation [33]. In Section V we show experiments on the magnetic-field-tuned superconductor-insulator transition. The zero bias resistance, R_o , was measured as a function of temperature and frustration. The frustration, f is defined as the magnetic field normalized to B_o , where B_o is the field corresponding to one flux quantum per unit cell in the array. The scaling curves demonstrate how R_o , plotted as a particular function of T and f , display a transition from insulator to superconductor. According to theory the resistance at the critical frustration f_c should be universal and equal to R_Q . From the data of four different arrays we find a value which is of the order of R_Q but sample dependent. We can also deduce a dynamic exponent close to unity, which is in agreement with the theory [30].

Right at the critical frustration, the Hall resistance is very small compared with the longitudinal resistance, indicating a small Hall effect at the SI transition. However for frustration values larger than the critical frustration the Hall resistance can be relatively large. Hall measurements in both conventional superconductors [34,35] and high- T_c superconductors [36,37] have shown a sign reversal of the Hall resistivity in the vicinity of the superconducting transition temperature T_c , where the samples are in a mixed state. Hall measurements have also been performed on disordered superconductors near the superconductor-to-insulator transition [38]. In Section VI we present the frustration dependence of the longitudinal resistance R_{0xx} and the Hall resistance R_{0xy} . Both the longitudinal and Hall resistance are periodic functions of the magnetic field, and the Hall resistance changes sign at several magnetic fields within one period. We also describe the dc measurements of longitudinal voltage V_x and the Hall voltage V_y as a function of bias current I_x .

II SAMPLE FABRICATION AND MEASUREMENTS

The arrays are fabricated on unoxidized silicon substrates, using a combination of photo- and electron-beam-lithography and an angle evaporation technique. Aluminum is used for both top and bottom electrodes. The number of junctions in each row, N , is the same as the number of junctions in each column, with N ranging between 10 and 168. Therefore, the array resistance equals the individual junction resistance, assuming a homogeneous array.

The samples are made in two steps. First a gold contact pattern is made with conventional photo lithography, and then the actual array is made with electron-beam lithography. The contact pattern contains a large number of $7 \times 7 \text{ mm}^2$ chips distributed over a 2 inch wafer area, each with 16 contact pads leading to a central area of $160 \times 160 \mu\text{m}^2$. A double metal layer of 20 nm chromium-nickel and 80 nm

gold is evaporated and the redundant metal is lifted off in acetone. The chromium-nickel film makes the gold stick better to the surface.

A double layer e-beam resist consisting of a ~ 210 nm thick bottom layer of P(MMA/MAA) copolymer is spun onto the wafer and a ~ 60 nm thick top layer of PMMA(950k) is used. The chip is mounted in an e-beam lithography instrument and the central area of each chip is exposed using the array pattern. A current of 20-30 pA corresponding to a beam size of about 10 nm is used. The beam voltage is 50 kV and the area dose is 160-200 $\mu\text{C}/\text{cm}^2$.

Each chip is then developed in two different developers: first for ~ 10 -20 s in the PMMA developer which consists of a 1:3 mixture of toluene and isopropanol, then for 20-40 s in the copolymer developer which consists of a 1:5 mixture of ethyl-cellosolve-acetate (ECA) and ethanol. As an alternative the nontoxic mixture of 5-10 % water in isopropanol can be used to develop both layers in one step, with a development time of 1-2 minutes.

After development, the resist mask contains an undercut pattern with suspended bridges [39,40] which will be used to form the junctions. By depositing bottom and top electrodes from different angles the overlap can be controlled. The base and top electrodes are evaporated from tungsten boats, while the substrate holder is tilted at two different angles ($\sim \pm 15^\circ\text{C}$) to give the desired overlap. Before the top electrode is deposited, a tunnel barrier is formed by introducing 0.01-0.1 mbar of oxygen to the chamber for 3-10 minutes, by adjusting the oxidation parameters we get the desired junction resistance.

A drawback with the angle evaporation technique is that a relatively large junction is formed in series with the small tunnel junction, see Fig. 3. The effect of this larger junction can in most cases be neglected, if its area is much larger than the area of the smaller junction. This is easy to make, but this requirement limits the minimum unit cell size of the array, which in turn decreases the soliton size.

The fabrication procedure results in junctions with normal state resistances in the range 4 to 150 k Ω , capacitances of the order of 1 fF, and $\Delta_0 \approx 200 \mu\text{V}$ per junction. The typical unit cell size is of the order of $A_{\text{cell}} \approx 1 \mu\text{m}^2$. These values are deduced from the IV -characteristics, assuming an offset voltage of $V_{\text{off}} = Ne/2C$ (for a discussion of the offset value see Ref. [25]). The Josephson coupling energies of the individual junctions are determined [41] from R_N and Δ_0 . The superconducting transition temperature T_c for the aluminum is in the range of 1.35 to 1.60 K.

The self capacitance of each electrode C_0 depends on the size of the electrode and the size of the array, and can be estimated to be of the order 10-20 aF for the smaller arrays (#2 and #3) and about 2 aF for the other arrays. This results in a soliton size in the range of 11 to 35, measured in units of the lattice spacing.

The most important parameters of the 2D arrays described in this paper are listed in Table 1. The arrays are divided into 3 groups. Arrays #1-3 show a decreasing resistance for decreasing temperature, and are referred to as the "superconducting" arrays. They have a low resistance, $R_N < R_Q$ and a relatively large Josephson coupling energy, $E_J/E_C > 1$.

Arrays #4-8 show also go superconducting at low temperature, but they display

the magnetic field tuned SI transition, and are referred to as the "intermediate" arrays. They have $R_N \approx R_Q$ and $E_J/E_C \approx 1$.

Arrays #9-15 show an increasing resistance for decreasing temperature, and are referred to as the "insulating" arrays. They have a high resistance, $R_N > 15 \text{ k}\Omega$ and a relatively small Josephson coupling energy, $E_J/E_C < 0.5$.

The arrays are mapped onto a so called quasi-Schmid diagram [42,43] in Fig. 2, showing the E_J/E_C and the R_Q/R_N parameters of each array. The E_J/E_C and R_Q/R_N values in the range 0 to ∞ are scaled onto the horizontal and vertical axes in the range 0 to 2, using the function $f(z)=2z/(1+z)$. The diagonal line represents $\Delta_0 = 2E_C$, *i.e.* where the charging energy for a Cooper-pair is equal to $2\Delta_0$. The dotted line represents the border to the insulating region predicted by Fazio and Schön [2]. The dashed line corresponds to a Stewart MacCumber parameter of $\beta_c \equiv (\pi^2/2)(E_J/E_C)(R_N/R_Q)^2 = 1$. Above this line a classical Josephson junction (in the upper right part of the diagram) shows hysteresis [44,45].

Our classification of the "insulating" arrays roughly agrees with the classification suggested by Fazio and Schön [2] shown as a dashed line in Fig. 2. However, a few of the arrays (#9-11) which show "insulating" behavior fall slightly outside the insulating area predicted by Fazio and Schön.

TABLE 1. Parameters for the 15 arrays. The resistance R_N , the capacitance C , and the superconducting energy gap $2\Delta_0$, were deduced from the *IV*-curves. The charging energy E_C , and the Josephson coupling energy E_J , were calculated from these values. B_0 is the magnetic field corresponding to one flux quantum per unit cell. Λ is the soliton size measured in units of the lattice spacing. E_{aN} is the activation energy for normal electrodes.

#	N	R_N (k Ω)	B_0 (G)	Λ	E_J/k_B (K)	E_C/k_B (K)	Δ_0/E_C	E_{aN}/E_C	E_J/E_C
1	112	3.98	10.4	35	1.82	0.37	6.08	0.56	4.91
2	20	4.08	10.4	16	1.78	0.36	6.12	0.66	4.93
3	10	4.49	10.4	11	1.62	0.38	5.98	0.70	4.25
4	146	7.54	16.3	19	0.95	0.60	3.64	-	1.57
5	168	10.7	16.3	23	0.68	0.55	3.97	-	1.24
6	146	12.5	16.3	27	0.57	0.72	3.04	-	0.80
7	168	13.5	16.3	27	0.53	0.59	3.71	-	0.90
8	146	13.5	16.3	29	0.56	0.73	3.25	0.24	0.77
9	146	24.4	16.3	22	0.33	1.22	2.05	0.24	0.27
10	80	35.4	27.6	23	0.21	0.88	2.62	0.25	0.24
11	80	38.0	27.6	22	0.194	0.92	2.49	0.24	0.21
12	100	49.3	43.1	24	0.159	1.27	1.91	0.26	0.12
13	100	59.7	43.1	23	0.132	1.35	1.82	0.25	0.10
14	80	88.4	27.6	21	0.090	1.09	2.27	0.28	0.08
15	100	151	43.1	20	0.057	1.75	1.52	0.31	0.03

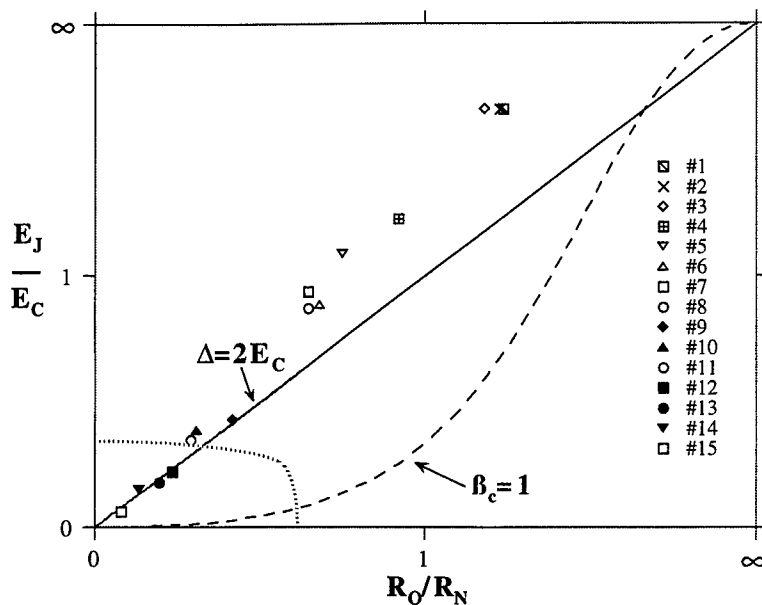


FIGURE 2. A $T = 0$ phase diagram showing the E_J/E_C and the R_Q/R_N parameters for the measured arrays. The diagonal line represents $\Delta_0 = 2E_C$. The dotted line represents the border to the insulating region predicted by Fazio and Schön. The dashed line corresponds to a Stewart MacCumber parameter of $\beta_c = 1$.

In Section IV, we will concentrate on the "insulating" arrays, but we will also present the N-state properties of the "superconducting" arrays. The N-state may be thought of as lying on the x-axis of the diagram in Fig. 2. Sections V and VI will discuss the "intermediate" arrays.

Fig. 3 shows a typical sample, and the inset shows the probe layout for the Hall measurements. There are four Hall probe pairs situated at $1/6$, $1/3$, $1/2$ and $5/6$ the distance between the ends of the array. Each Hall probe is actually an array of 3×3 junctions, with the outer side shorted by a strip from which the Hall voltage is taken. In this way we can reduce the influence on the sample behavior arising from the presence of the voltage probes, and we are less sensitive to local defects possibly occurring in the probe. The resistance of the probe arrays is presumably similar to that of the array itself. This resistance is much smaller than the input impedance of our voltage amplifiers.

The measurements are performed in a dilution refrigerator which is situated in an electrically shielded room. A magnetic field up to about 1400 G is applied perpendicular to the substrate. The magnetic field needed to produce one magnetic flux quantum per unit cell, B_0 , varied between 10.4 G and 43.1 G for the different arrays. This is much less than the critical magnetic field, B_c (~ 800 G), which was

needed to bring the aluminum electrodes into the N-state.

All measurements are made with the biasing and the measurement circuitry symmetric with respect to ground. The current-voltage (IV)-characteristics of the arrays are recorded at temperatures down to about 25 mK. The threshold voltages are deduced from the IVC measured as the voltage at which the current has dropped to two times the noise level (going from large bias). The rms current-noise determined at low voltage is typically of the order of 0.1 pA or less.

For the insulating arrays we deduce the zero bias resistance R_0 from the IV -characteristics. For the “superconducting” and “intermediate arrays”, R_0 can also be measured with an ac-technique using lock-in amplifiers, with excitation currents in the range 0.01-3 nA, and frequencies of the order of 10 Hz.

The longitudinal voltage V_x is measured at the superconducting strips at the ends of the array, and the Hall voltage V_y is measured on the probes located on opposite sites of the array. The Hall data presented here were measured from the probes located in the center of the array, see the inset of Fig. 3

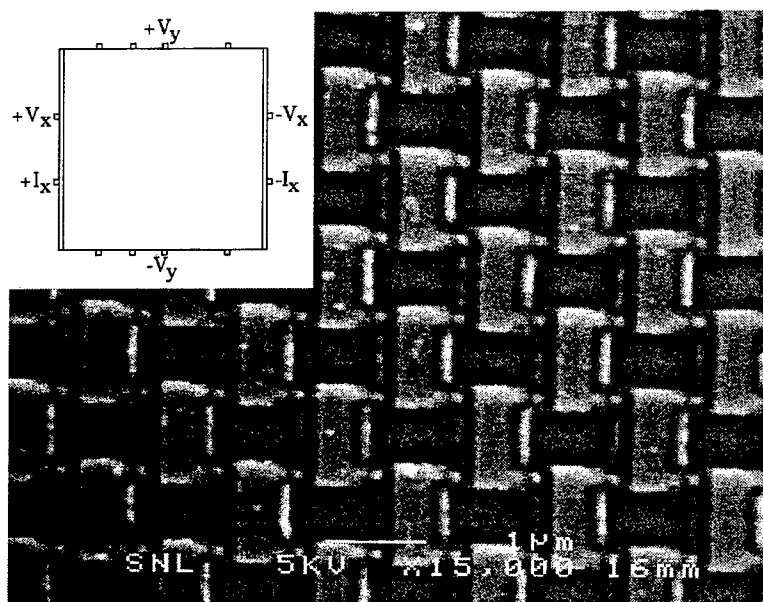


FIGURE 3. A SEM picture of a part of an array. Each island measures 0.5 by 1 μm , the overlap between neighboring islands defines the tunnel junction. The insert shows the probe layout. Each Hall probe consists of 3×3 junctions, the junctions are identical to the junctions in the array.

III CURRENT VOLTAGE CHARACTERISTICS

The large scale IV -characteristics of the arrays are very similar for the 11 arrays and they resemble the IV -characteristics of a single high resistance Josephson junction. In the S-state there is a sharp rise in the conductance at a voltage $\sim N \cdot 2\Delta_0/e$. At high voltages the IV -characteristics are linear and there is the usual offset voltage which is due to the Coulomb blockade [5,6]. In the N-state the gap feature disappears but the offset voltage remains.

For low bias in the S-state, the IV -characteristics differ drastically for the different arrays. Qualitative similarities can be found between these IV -curves and those of single junctions biased through high impedance resistors [46]. Arrays #1-8 show a supercurrent-like feature at low bias, and R_0 decreases for decreasing temperature. Arrays #9-15 show a Coulomb blockade feature at low bias, and R_0 increases for decreasing temperature.

A The threshold voltage

The threshold voltage V_t is the voltage at which solitons can be injected into the array. According to theory [3], the threshold voltage for injection of SESs in the N-state should be

$$V_{tN} = 2 \left(1 - \frac{2}{\pi} \right) \frac{E_C}{e} \Lambda \quad (1)$$

for a symmetrically biased array with $C \gg C_0$. It is important to make the distinction between symmetric and asymmetric (one side grounded) bias of the array, since the latter gives a factor of two lower threshold voltage. However, it has been shown by Middleton and Wingreen [47] that the background charges modify the picture and that the threshold voltage actually scales with the length of the array if the effect of random background charges is taken into account.

In the N-state, all arrays show Coulomb blockade feature at low temperature and low bias, but the threshold is smeared. However there is no sharp threshold voltage in the N-state for most of the arrays. Only for array #15, which has the largest R_N , we can deduce a threshold voltage of about 0.25 mV (see Fig. 4). Note that the onset of current occurs at a substantially higher voltage for intermediate magnetic fields. For those fields however the onset was more gradual. A similar behavior was observed in all of the "insulating" arrays.

All of our arrays were symmetrically biased and for array #15 we get a theoretical value of $V_{tN} = 2.3$ mV, according to Eq. 1. The fact that the measured value is substantially lower than the theoretically predicted one, is consistent with the picture that quantum fluctuations effectively lower the energy barrier for injection of charge [26].

In the S-state there was a sharp threshold for all the "insulating" arrays, except for arrays #10 and #11. V_t is shown as a function of B for four of the arrays in

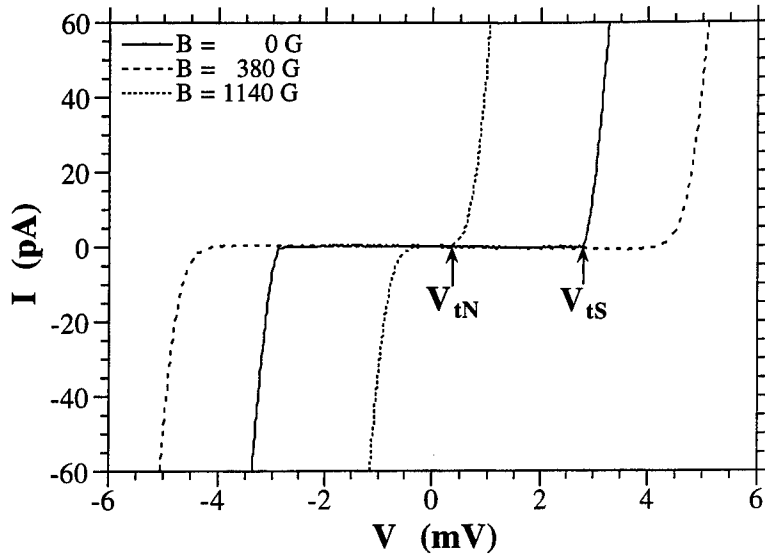


FIGURE 4. The IV -characteristics of sample #15 at different values of magnetic field. In the S-state ($B=0$ G), the threshold is $V_{tS} = 2.75$ mV, while in the N-state ($B = 1140$ G), the threshold is $V_{tN} = 0.25$ mV. Note that the onset of current occurs at an even larger voltage for an intermediate value of B .

Fig. 5. For several of the arrays V_t oscillates with B , demonstrating that Cooper pair solitons are injected at low magnetic fields. The period of oscillation corresponds to one flux quantum per unit cell and agrees well with the B_0 values of the different arrays. The oscillations in V_t correspond to the oscillations in activation energy, described in Section IV, and the oscillation peaks in V_t and E_a occur at the same B values (compare Figs. 8 and 5). For increasing magnetic field the threshold voltage increases and peaks at a field in the range of 250 to 450 G, which is well below the critical field B_c for the electrodes. V_t then decreases rapidly at larger B .

The threshold voltage in the S-state has, to our knowledge, not been described theoretically in the literature. However, following the arguments in Ref. [3], and neglecting the Josephson coupling energy, we can estimate V_t for two different situations. For direct injection of Cooper pair solitons, we get a threshold voltage which is two times higher than the value for single electron solitons, $V_{tS2e} = 2V_{tN}$. The other possibility is that a Cooper-pair is broken up and then a single electron is injected. Then the threshold would be $V_{tSe} = V_{tN} + \Lambda 4\Delta_0/e$ for the case of symmetric bias. For all our arrays $V_{tS2e} < V_{tSe}$ at $B = 0$, and therefore we would expect injection of Cooper pairs to be responsible for the threshold.

This agrees well with our observation of the oscillating V_t at low magnetic field. The increase of V_t with increasing magnetic field can be understood in the following way. Since Δ , and thereby E_J , decreases with increasing magnetic field it becomes

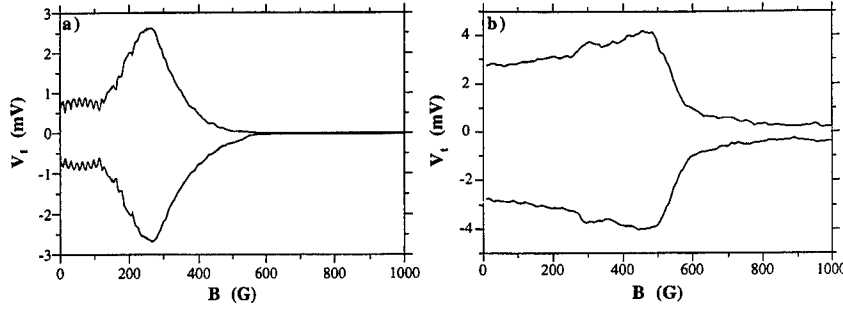


FIGURE 5. The positive and negative threshold voltages as a function of B for two of the arrays at $T \approx 25$ mK, a) #9 At low magnetic field V_t oscillates with one flux quantum per unit cell, showing that Cooper pair solitons are injected. b) #15.

harder to inject Cooper-pairs, and therefore V_t increases. At some magnetic field the threshold for single electrons will become equal to that for Cooper-pairs ($V_{tS2e} = V_{tSe}$) and we would expect a crossover from Cooper-pair injection to single electron injection. This is observed in all the samples as a peak in V_t at magnetic fields in the range 250 to 450 G. Beyond this crossover V_{tSe} decreases as a function of increasing B , due to the decreasing Δ .

To get a more quantitative description, other effects depending on the array size and the background charge, as well as co-tunneling and the Josephson coupling, would have to be included. The fact that the observed values at $B = 0$ are generally lower than the "theoretical" value V_{tS2e} , can possibly be explained if the Josephson coupling energy is taken into account. A step in this direction is a recent paper on 1D-arrays where the threshold dependence on E_J is discussed [48]. The current above the threshold has been analyzed using scaling theory by Rimberg et al. [49].

B Hall voltages

In an array which is strongly superconducting there is no Hall voltage since the Hall probes would be shorted. In an array with a strong Coulomb blockade the whole array is insulating and therefore the Hall probes are effectively disconnected, and no Hall voltage can be measured. Therefore it is not surprising that it is only the "intermediate" arrays which show some Hall voltage. In Fig. 6a we see the $I_x V_x$ characteristics for sample #5 which shows a sharp dip in the current before entering the flux-flow regime, characterized by I being proportional to V . The $I_x V_y$ curve, shown in Fig. 6b, displays a very similar feature, but the Hall voltage is about two orders of magnitude smaller. As the current is reversed, the Hall voltage changes sign as expected.

In the flux-flow regime, both V_x and V_y increases linearly with applied current

until the longitudinal voltage reaches the sum gap voltage of the entire array ($N \cdot 2\Delta_0 \approx 63 \text{ mV}$). At this point, the Hall voltage reaches a maximum of about 0.2 mV and then starts to fluctuate, gradually decreasing almost to zero. At still higher currents, the Hall voltage displays rich structure, which can also be seen in the derivative of V_x with respect to I_x .

At very high currents, when V_x is on the normal resistance branch of the $I_x - V_x$ curve, the Hall voltage V_y also increases linearly with the applied current, with slope 2.1Ω . Because this slope is a small fraction of R_N (0.02% for array #5 and 0.1% for array #7) we conclude that small non-uniformities exist in the array. For array #7, the Hall voltage as a function of bias current shows very similar behavior to that of array #5.

IV THE INSULATING TRANSITION

The zero bias resistance was measured as a function of both temperature and magnetic field. All arrays showed an "insulating" behavior in the N-state, meaning that R_0 increased as a function of decreasing temperature. Over a fairly wide range of temperature the $R_0(T)$ dependence was exponential as can be seen in Fig. 7, indicating thermal activation of charge solitons. However, R_0 saturates and is no longer temperature dependent at the lowest temperatures, (beyond the range displayed in Fig. 7). This saturation has been discussed in Ref. [26] and here we will concentrate on the thermal activation.

In the S-state, R_0 increased even more rapidly as a function of decreasing temperature for the "insulating" arrays. The R_0 versus T curves can be divided into three temperature regions (see Fig. 7). i) In a temperature range below 500 mK , R_0

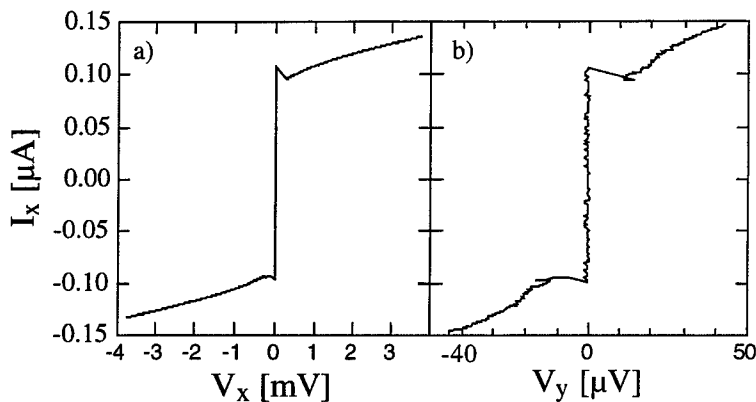


FIGURE 6. The longitudinal voltage V_x (a), and the Hall voltage V_y (b) measured as a function of bias current for sample #5 at $T \approx 20 \text{ mK}$, and $f \approx 0$. Note that at low bias V_x and V_y are very similar

increases exponentially with decreasing temperature, and an activation energy can be defined. ii) At higher temperatures the dependence was not purely exponential due to the temperature dependence of the superconducting gap. iii) For the lowest temperatures R_0 became larger than $1\text{ G}\Omega$ (not shown in the figure), and could not be measured accurately with our experimental setup.

In a temperature interval roughly between 200 mK and 500 mK, R_0 for the "insulating" arrays could be fitted by a thermal activation dependence over the whole magnetic field range, such that

$$R_0(B, T) = b \cdot \exp \frac{E_a(B)}{k_B T} \quad (2)$$

where E_a is the activation energy and b is a constant. It should be noted that there is a region of magnetic field slightly below B_c where the superconducting gap goes to zero in the temperature interval where the fit is made to determine E_a . Therefore, the $\ln(R_0)$ vs. $1/T$ plots are not perfectly linear at those magnetic fields. However the Arrhenius law (2) is still a fair approximation.

The fact that we do not observe a KTB charge unbinding transition in these arrays is not altogether surprising. It was shown by Zaikin and Panyukov [50], that

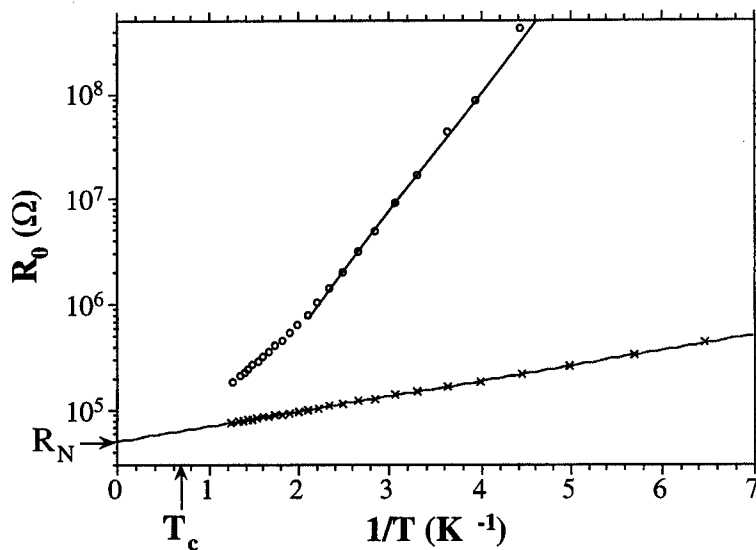


FIGURE 7. The zero bias resistance R_0 for array #10, vs. $1/T$ for $B = 0\text{ G}$, S-state (\circ), and for $B = 1400\text{ G}$, N-state (\times). Note the very good fit to the thermal activation Arrhenius dependence for the N-state. The resulting slope is very close to $\frac{1}{4}E_C$ and the extrapolation to infinite temperature ends up right at R_N . At low temperature the data in the S-state can also be fitted to an Arrhenius dependence with a slope close to $\frac{1}{4}E_C + \Delta_0$.

the effect of offset charges will effectively cut off the logarithmic interaction between the charges. Also, the finite size of our samples is probably a limiting factor.

In the N-state, E_a was found to be close to $\frac{1}{4}E_C$ (see Table 1), and b was very close to R_N , for all the "insulating" arrays. This value of E_a agrees well with that of Tighe et al. [25]. If the conduction is caused by thermal activation of single electron solitons we expect that $E_a = \frac{1}{4}E_C$ in the N-state. The energy required to create a soliton anti-soliton pair starting from an uncharged array, i.e. the tunneling of a single charge, is the so called core energy $E_{core} = e^2/4C = \frac{1}{2}E_C$ for single electrons, and four times as high $E_{core} = 2E_C$ for Cooper-pairs. Similarly to thermal activation in other systems the activation energy becomes half of the core energy.

We next consider the S-state case, where we can imagine two alternative transport mechanisms. On one hand, we can calculate the energy needed to brake up a Cooper pair and to create a SES pair. We would expect $E_{core} = \frac{1}{2}E_C + 2\Delta_0$ and therefore, $E_a = \frac{1}{4}E_C + \Delta_0$ if the charge transport was entirely due to SESs, created from broken Cooper pairs. If on the other hand, we assume that only CPSs are activated, we would expect the activation energy to be four times higher (because of the $2e$ charge) than for SESs in the N-state, so that $E_a = E_C$. This picture is of course a bit naive because the Josephson coupling energy is not taken into account. Nevertheless, if this simple picture holds, we would expect that for arrays with $\Delta_0/E_C < \frac{3}{4}$, thermal excitation of SESs would always be advantageous, and we would expect $E_a = E_C + \Delta(B)$. If on the other hand $\Delta_0/E_C > \frac{3}{4}$, we would expect a crossover from activation of CPSs to activation of SESs as Δ is suppressed by the magnetic field. All the "insulating" arrays had $\Delta_0/E_C > \frac{3}{4}$, and we thus expect the crossover behavior with magnetic field.

Our observations suggest a somewhat more complicated picture. As we enter the S-state, by lowering the magnetic field below B_c , E_a increases for all the "insulating" arrays. At zero magnetic field, we find that E_a is equal to or smaller than $\frac{1}{4}E_C + \Delta_0$ but larger than E_C , for all seven arrays. In Fig. 8 the magnetic field dependence of E_a is shown for two of the arrays, and it is compared to $\frac{1}{4}E_C + \Delta(B)$, which is represented by a dashed line. Here, Δ_0 is measured for each array and the form of the function $\Delta(B/B_c)/\Delta_0$ is also determined from the measurements [26].

From our simple picture outlined above we would expect the ratio Δ_0/E_C to be important. We find that for arrays with a ratio Δ_0/E_C less than 2, (arrays #12,13, and 15), $E_a(B)$ has a behavior which is very close to $\frac{1}{4}E_C + \Delta(B)$, as can be seen for array #13 in Fig. 8a. Arrays #12 and #15 show a very similar behavior. Tighe et al. [25] have also obtained the same result at $B = 0$ for arrays where the ratio Δ_0/E_C was less than 2. However, for the other arrays #9-11, and #14, where Δ_0/E_C was larger than 2, $E_a(B)$ is lower than $\frac{1}{4}E_C + \Delta(B)$. This can be seen in Fig. 8b, for array #9. It is obvious that the ratio Δ/E_C is important. We find that the critical value is about 2.

In several arrays, we observe oscillations in $E_a(B)$. The period of oscillation corresponds to one flux quantum per unit cell (see the inset of Fig. 8b). The period

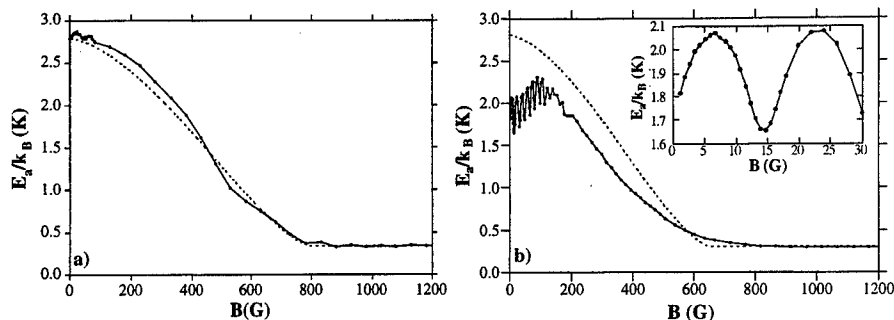


FIGURE 8. The activation energy E_a , as a function of magnetic field B for two of the arrays. At high magnetic field (in the N-state), E_a is close to $\frac{1}{4}E_C$. The dashed lines corresponds to $\frac{1}{4}E_C + \Delta(B)$. a) Array #13. Note the good agreement between the experimental data and the dashed line. b) Array #9. Note the oscillations, the period correspond to one flux quantum per unit cell, the amplitude is roughly equal to E_J .

agrees very well with the B_0 values, determined from geometry. The oscillations show that the Josephson coupling affects the activation energy. The oscillations are observed in all arrays where the measurements were taken with sufficiently small steps of the magnetic field. The amplitude of the oscillations is roughly E_J . Arrays with a large E_J also showed an increase of (the average of) E_a with increasing B resulting in a peak at 100 to 200 G (Fig. 8b).

These effects can be understood since the creation of CPS/antiCPS pairs should be dependent on the Josephson coupling. For a weaker Josephson coupling, it should be harder to create CPS/anti-CPS pairs and E_a should increase. The Josephson coupling $E_J \cos(\Phi/\Phi_0)$ is affected in two ways by the magnetic field. At low field the cosine part is affected, resulting in an oscillating E_a with maxima where $(B = n + \frac{1}{2})B_0$, n being an integer. The oscillations of E_a demonstrate clearly that at least part of the current at low bias is carried by Cooper-pair solitons. At higher magnetic field the increasing E_a with increasing B may be explained by a decreasing Δ , and thereby also a decreasing E_J . At even higher fields Δ/E_C becomes smaller than 2 so that SES creation dominates, and thus E_a decreases with increasing field

In summary, our results for the N-state agree well with thermal activation behavior, and an activation energy of $\frac{1}{4}E_C$ for single electron solitons can be extracted. For the S-state we find that as long as $\Delta/E_C < 2$, pairs of SESs are created by breaking up Cooper pairs so that $E_a = \frac{1}{4}E_C + \Delta(B)$. For larger values, $\Delta/E_C > 2$, pairs of CPSs are responsible for a substantial part of the charge transport and E_a oscillates as a function of temperature.

TABLE 2. Parameters and scaling exponents for four of the arrays which showed the superconductor insulator transition. The variables are defined in the text.

#	E_J/E_C	T_{KTB} (K)	f_c	$z_B \nu_B$	R_{0xx}^* (k Ω)	R_{oxy}^* (Ω)
4	1.57	0.70 ± 0.04	0.122 ± 0.012	4.75 ± 0.5	2.45 ± 0.15	-
5	1.24	0.46 ± 0.04	0.039 ± 0.007	8.20 ± 1.0	1.23 ± 0.10	28 ± 5
6	0.80	0.44 ± 0.05	0.047 ± 0.005	1.47 ± 0.2	2.20 ± 0.15	-
7	0.90	0.35 ± 0.04	0.034 ± 0.010	4.45 ± 0.5	1.61 ± 0.15	34 ± 5

V THE MAGNETIC FIELD TUNED SUPERCONDUCTOR INSULATOR TRANSITION

As mentioned previously arrays which are superconducting a low temperature can display a vortex-unbinding KTB [18] transition to a resistive state above a certain critical temperature T_{KTB} . In zero magnetic field, the theory for KTB vortex-unbinding gives a relation between the superconducting correlation length ξ and the transition temperature T_{KTB} . The correlation length is determined by a control parameter which, for example, can be the disorder of the system. A Josephson junction array can be described by the classical 2D-XY model and can be associated to the KTB transition in continuous films [12]. In the presence of disorder, the conductivity at low temperature is governed by variable-range hopping (VRH) [51] and ξ should scale with T_{KTB} . In a highly disordered film, the long-range vortex-pair order is destroyed, and T_{KTB} is substantially suppressed compared with that of a disorder-free film. Provided that the transition between insulator and superconductor is continuous, right at a critical disorder, ξ should diverge and T_{KTB} should vanish. If the disorder is smaller than but close to the critical disorder, Fisher [30] predicted, based on the analogy of VRH of vortices to VRH of electrons, that ξ should diverge as $(B - B_c)^{-\nu_B}$ with exponent $\nu_B \geq 2/d = 1$, where $d=2$ is the dimension of the system. The scaling theory developed for the zero field case implies a power law dependence of T_{KTB} on ξ , *i.e.* $T_{KTB} \sim \xi^{-z_B}$, with an exponent z_B of unity. Furthermore, the dual transformation suggests a $T = 0$, $B = B_c$ fixed point where the magnitude of the resistivity (vector sum of the longitudinal and transverse components of the resistivity) should also be universal and equal to R_Q .

Experiments on homogeneous thin films in zero magnetic field demonstrated a SI transition by changing the film thickness. The transition was found to occur when the film sheet resistance was close to a critical value of R_Q [52]. A magnetic field tuned transition was found for films close to the critical resistance [38,53,55-57] and agreement with the scaling theory [30] was obtained. In Josephson junction arrays, a SI transition can be achieved by changing the junction normal state resistance

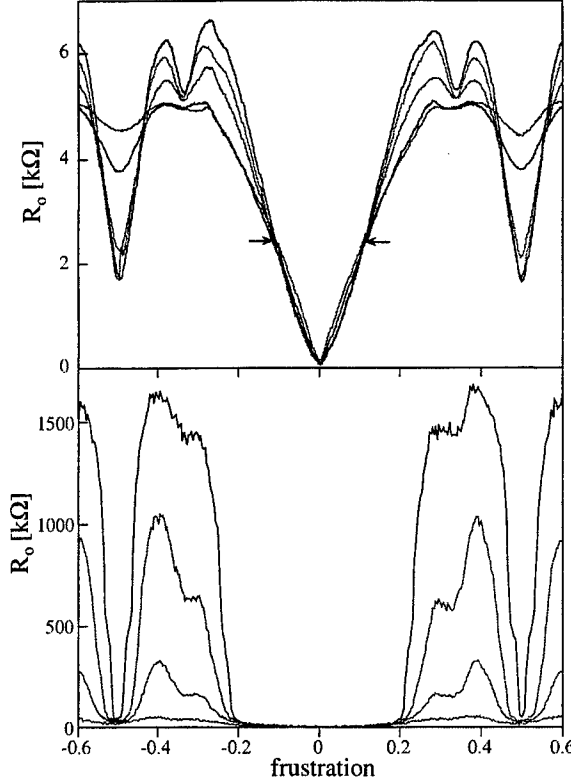


FIGURE 9. Linear resistance R_o at zero bias as a function of frustration for a) array #4 measured at several temperatures (from the top, 20, 200, 400, 600, 700 mK). At $f = f_c \approx 0.12$, dR_o/dT changes sign and, $R_o^* \approx 2.4$ kΩ. b) array #6 at low temperatures (from the top 50, 70, 90, 125 mK).

R_N and the junction capacitance C [23,30]. The transition is found to occur near a critical point at $R_N \approx R_Q$ and $E_J/E_C \approx 1$. We therefore expect a magnetic-field-tuned SI transition for arrays near the critical point. However, there is a major difference between a uniform film and a regular array in the presence of an external magnetic field. In the former case the vortices form an Abrikosov (triangular) lattice in the ground state [58] whereas in the latter case the vortices are pinned in a periodic potential, imposed by the array lattice [59]. The array lattice results in a ground state energy which is an oscillatory function of the applied magnetic field with period $\Delta f = 1$ [59]. The ground state energy is not only periodic, but has minima at rational frustrations, *i.e.* $f = 1/2, 1/3, 2/3$, etc. From one point of view, frustration is simply proportional to magnetic field and should be related to B in the scaling theory [30]. From another point of view, frustration can be considered as introducing defects from the ordered lattice at rational f values, in which case the

KTB transition under consideration is the melting of the vortex lattice. We thus expect that the f value can act as a control parameter for the SI transition, and the scaling theory can be applied, provided one accepts that the correlation length diverges at some critical value of f as $(f - f_c)^{-\nu_B}$. Experimentally, we find that the SI transition occurs at $f = n \pm \delta$ and $n + 1/2 \pm \epsilon$ (where n is an integer and $\delta, \epsilon \ll 1$), and that the scaling analysis is applicable to both cases.

The important parameters are listed in Table 2. The charging energies E_C were judged from the offset voltage of the IV -characteristics at large bias. B_o was about 16 G for all the intermediate arrays. For sample #6 the superconducting mean-field-transition temperature, $T_c = 1.51$ K, was measured on an aluminum wire which was fabricated on the same chip as the array. The KTB transition temperature T_{KTB} could be deduced from the onset of the linear dependence of $R_o(f)$ [17], the values are listed in Table 2. This method of deducing T_{KTB} has been confirmed both theoretically [18,60] and experimentally [53,61].

$R_o(f)$ for sample #4 at $T < T_{KTB}$ is depicted in Fig. 9. Below a critical frustration $f_c \approx 0.12$, the resistance is lower for lower temperature, indicating a superconducting transition. Above f_c , the resistance is higher for lower temperature, implying an insulating transition. The resistance at f_c , R_o^* , can be identified from Fig. 9a and is about 2.4 k Ω .

Fig. 9b illustrates the $R_o(f)$ dependence for sample #6 at low temperatures. While arrays #4 and #5 do not show a resistance higher than their normal resistances R_N at any f in the accessible temperature range, the resistance of arrays #6 and #7 in the most insulating case (at $f \approx 0.4$) are much greater than their R_N . Remarkably, the resistance of array #6 changes by more than five orders of magnitude going from $f \approx 0$ to $f \approx 0.27$ at 15 mK. The IV characteristics measured in the superconducting state and in the insulating state for array #6 are displayed in Fig. 10. In the superconducting state, the array exhibits clear Josephson-like current, with $R_o(f \approx 0) \approx 130 \Omega$, whereas in the insulating state, the array shows an insulating behavior with $R_o(f \approx 0.27) > 37 \text{ M}\Omega$ and a back-bending feature in the IV characteristics similar to the behavior of higher resistance arrays ($R_N \approx 17 \text{ k}\Omega$) reported earlier [21,23]. This feature is easily smeared by increasing temperature, resulting in a drastic decrease in the measured R_o in the insulating phase as seen in Fig. 9b. $R_o(T)$ curves for array #6 in the range $0 < f < 0.27$ are shown as an inset of Fig. 10. The flattening-off of the resistance at non-zero frustrations at low temperatures is attributed to a finite size effect, explained within the context of the (vortex) VRH picture [62]. In this picture, the hopping range increases at low temperature. When the hopping length becomes larger than the sample size, a temperature-independent resistance is expected. This flattening-off behavior was also reported in Refs. [29,26] and can be shown to depend on the sample size [17].

To appreciate the scaling theory, all the data from both the superconducting and the insulating sides should collapse onto a single curve when plotting the resistances against the scaling variable $|f - f_c| \cdot T^{-1/z_B \nu_B}$. This is done using both f_c and $z_B \nu_B$ as free parameters. The curves were determined by minimization of the mean square deviation from an averaged curve on the insulating branch. The scaling

was performed in the temperature range $50 \text{ mK} < T < T_{KTB}$ and in the frustration range $0 < f < 0.2$. The scaling parameters as well as R_0^* are listed in Table 1. Scaling curves for arrays #4 and #6 are shown in Fig. 11. All data point in the insulating branch collapse onto the same trend. For the superconductor transition the low temperature points deviate from the general trend due to the finite size effect.

The form of the scaling curves are very similar in the different cases, in fact it is possible to make the curves from all four arrays overlap by offsetting the graphs slightly in the x and the y direction. The different offsets in the y direction demonstrates that the zero temperature fix point is different for the different arrays and that we get sample dependent values of R_0^* . The offset in the x -direction shows an interesting, and unpredicted, linear dependence on the E_J/E_C ratio. This is shown in Fig. 12 where x_c is plotted versus the E_J/E_C ratio. x_c is the x -value at which the superconducting transition extrapolates to zero resistance. Disregarding the low temperature points on the superconducting side, we find that we can describe all the data of the four arrays with a single formula (Eq. 3), where the scaling parameter deduced from theory is normalized to the E_J/E_C ratio.

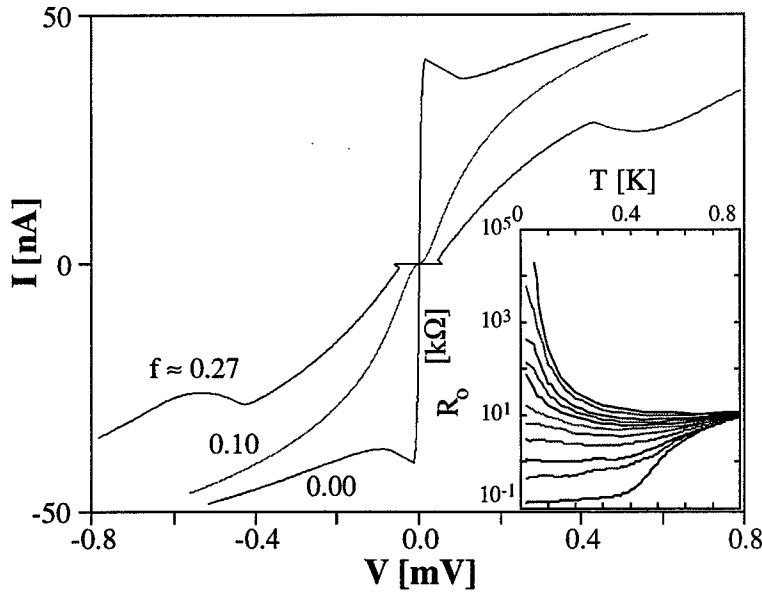


FIGURE 10. Magnetic field dependence of on the IV characteristics of array #6 taken at 15 mK. In the superconducting state ($f \approx 0$, $R_0 \approx 132 \Omega$) it shows a clear supercurrent whereas in the insulating state ($f \approx 0.27$, $R_0 \approx 37.2 \text{ M}\Omega$) it exhibits a back-bending feature. The zero bias resistances differ by more than five orders of magnitude, while the change in magnetic field is only 4.4 G. The inset shows $R_0(T)$ for the same array for $0 < f < 0.27$.

$$R_0(f, T) = R_0^* \cdot F\left(\frac{E_C}{E_J} \cdot \frac{|f - f_c|}{T^{1/z_B \nu_B}}\right) \quad (3)$$

Here F is a universal function describing both the insulating transition and the superconducting transition, and R_0^* is a nonuniversal, sample dependent parameter.

We find, similar to Hebard and Paalanen [53], that the quality of the scaling is more sensitive to f_c than to $z_B \nu_B$. Using an improper f_c value may cause large discrepancies at the left side of the plot and slightly shift R_0^* , whereas an improper $z_B \nu_B$ degrades the scaling but does not change R_0^* . Note that the scaling analysis is limited to low f values by the commensurability between the applied flux and the array lattice. The theory predicts that the transition temperature should scale with the correlation length as $T_{KTB} \sim \xi^{-z_B}$. This, together with the fact that ξ depends on the critical frustration as $f_c \sim \xi^{-2}$, leads to the relation $f_c \sim T_{KTB}^{2/z_B}$. Fitting f_c and T_{KTB} for the four samples as shown in the inset of Fig. 11b, we can deduce $z_B = 1.05$. This can be compared to the theoretically predicted value of unity [30].

In the case of $f=1/2$ the region of sample parameters where the phase transition is observable shifts to lower R_N and larger E_J/E_C . For array #4 we find $f_c = 0.5 \pm \epsilon$, with $\epsilon = 0.055 \pm 0.001$ and R_0^* is 4.33 ± 0.15 k Ω . The scaling is shown as an inset in Fig. 11a, the frustration range was $0.5 < f < 0.6$. For array B, we find

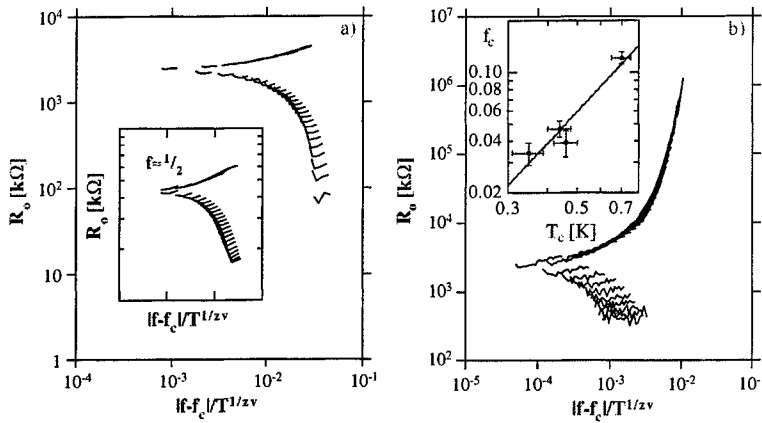


FIGURE 11. R_0 as a function of the scaling parameter $|f - f_c| \cdot T^{-1/z_B \nu_B}$ for array #4 and array #6, $0 < f < 0.2$. The data collapse onto one curve: the upper part for the insulating transition and the lower part for the superconducting transition. The low temperature points on the superconducting side deviate from the general trend due to the finite array size. a) Sample #4. The inset shows the scaling for array #4 close to full frustration, $0.5 < f < 0.6$. b) Sample #6. The inset shows a log-log plot of the critical frustrations f_c as a function of the Kosterlitz-Thouless transition temperature T_c for the four measured samples. The critical exponent $z_B \approx 1.05$ can be obtained from the relation $f_c \sim T_{KTB}^{2/z_B}$.

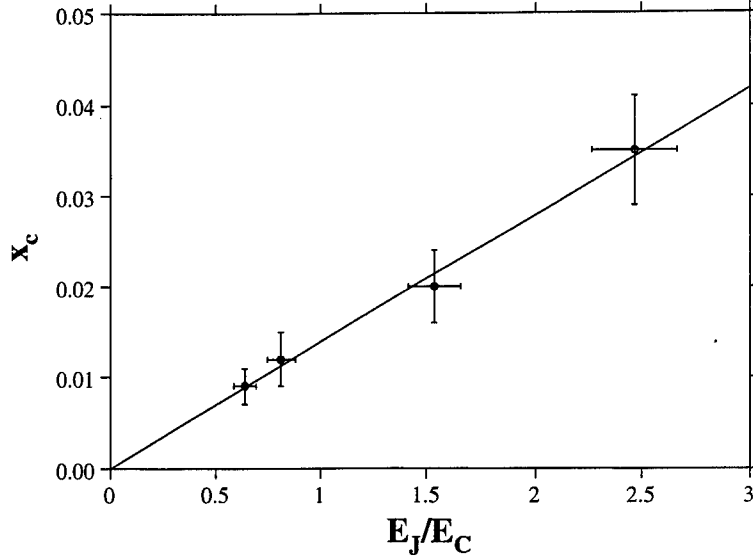


FIGURE 12. The critical x -value, x_c versus the E_J/E_C value for the four arrays #4-7. Our data shows a clear linear dependence which is not predicted by theory

$\epsilon = 0.030 \pm 0.003$ and $R_o^* \approx 5.40 \pm 0.15 \text{ k}\Omega$. Arrays #6 and #7 have a larger R_N and a smaller E_J/E_C ratio, it is thus not surprising that the $R_o(f)$ curves at various temperatures do not cross near $f = 1/2$.

Returning to the S-I transition at f close to zero, the scaling curves for all four arrays exhibit similar bifurcation shape, but with a different R_o^* . As other measurements on 2D arrays [29,54] and on superconducting films [55,56] also showed a different R_o^* , we conclude that R_o^* is non-universal and sample dependent. According to theory [30] the vector sum of the longitudinal resistance R_{oxx} (previously R_o) and the Hall resistance R_{oxy} should be universal and equal to R_Q at $f = f_c$. To check this prediction, we performed measurements of R_{oxy} for arrays #5 and #7. Four pairs of Hall voltage probes allow us to check the spread of the junction parameters in an array, which is found to be within 3%. $R_{oxy}(f)$ shows a rich structure, the details will be published elsewhere. For both arrays R_{oxy} is of the order of 30Ω , see Table 2. The sum of R_{oxx}^{*2} and R_{oxy}^{*2} is thus smaller than R_Q^2 for both arrays. It should be noted that the smallness of R_{oxy}^* compared with R_{oxx}^* agrees well with recent experiments on thin films [38]. The Hall angle at the transition, is about 1.2° for both arrays.

In the thin film case [38] a critical field was found also for the R_{oxy} data. In our case the linear region in the I_x vs. V_y characteristics is very small at finite f , which limits the excitation current and, consequently, the resolution in R_{oxy} . Therefore it is hard to determine the crossing point in the $R_{oxy}(f)$ curves at $T < T_c$ for both array #5 and #7. Nevertheless, the frustration above which the $R_{oxy}(f)$ curves at

various T start to deviate from each other seems to be very close to f_c . This is in contrast to the case of disordered films [38] where the "critical field" at which all $R_{xy}(f)$ curves cross is higher than B_c and is associated with the suppression Δ . This is evidently not the case for 2D arrays, since the field needed for suppression of Δ of our arrays is about 800 G [26], which is much greater than the critical field ($=f_c B_0$) of a few G.

VI THE HALL EFFECT

Superconducting films can, to some extent, be modeled as a 2D array of Josephson junctions, and understanding their transport behavior can be reduced to the problem of vortex dynamics. Many interesting phenomena occurring in superconducting films can also be seen in 2D Josephson junction arrays. In fact, the phenomena can be more easily modeled in the latter system because complications due to the (often unknown) microstructures do not exist, and phenomenological parameters such as the junction normal state resistance, R_N , Josephson coupling energy E_J , and charging energy E_C , can be independently determined. However, there is a major difference between a uniform film and a regular array in the presence of an external magnetic field. In the former case the vortices form an Abrikosov (triangular) lattice in the ground state whereas in the latter case the vortices are pinned in the periodic potential imposed by the array lattice [59]. The array lattice of loops of area A , results in a ground state energy which is an oscillatory function of the frustration. The ground state energy is not only periodic, but has minima at rational frustrations, *i.e.* $f = 1/2, 1/3, 2/3$, etc. [59]. In the vicinity of these rational frustrations, the dynamics is dominated by the motion of "defect" vortices [16] and the vorticity of the majority defect is reversed upon passing through these rational frustrations.

The frustration dependence of R_{xx} and R_{xy} for sample #7 at various temperatures is shown in Fig. 13. R_{xx} is an oscillatory function of the applied magnetic field with period $\Delta f = 1$ and minima at rational frustrations, $f = 1/2, 1/3$ and $2/3$ as can be seen in Fig. 13. There is a critical frustration, $f_c \approx 0.034$, below which the resistance decreases as the temperature is lowered, and above which the resistance increases as the temperature is lowered. The longitudinal resistance at f_c , $R_{0xx}^* = 1.61 \text{ k}\Omega$, can be identified from an expanded view of Fig. 13a around $f = f_c$, as well from a scaling analysis on these curves which we have discussed in detail in Section V, see also Ref. [63].

The Hall resistance R_{0xy} as a function of frustration is shown in Fig. 13 where we see that it also oscillates with the applied field having the same period $\Delta f = 1$. At $f = 0$, R_{0xy} is zero, and $R_{0xy}(f)$ has a very small negative slope. As the frustration is increased, R_{0xy} goes through a minimum, increasing to $R_{0xy}^* = 34 \Omega$ at $f = f_c$. Thereafter it rapidly increases, reaching a maximum value at $f \approx 0.23$. As the frustration is increased further, R_{0xy} starts to decrease and at $f > 2/5$, it becomes negative. At $f \approx 0.45$, R_{0xy} reaches a local minimum and starts to

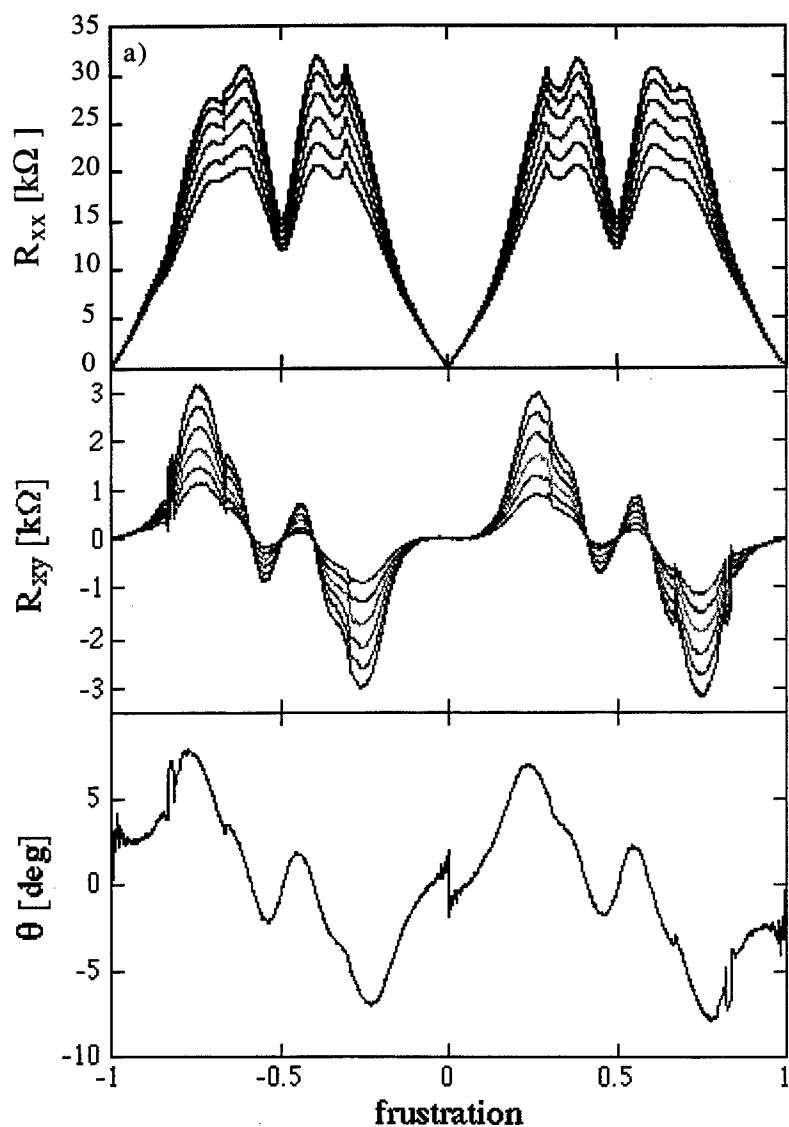


FIGURE 13. (a) The longitudinal resistance R_{0xx} and (b) the Hall resistance R_{0xy} , and (c) the Hall angle θ , as functions of frustration. R_{0xx} , and R_{0xy} are shown for various temperatures (from the top at $f \approx 0.25$, $T = 20, 75, 100, 125, 150, 175$ mK). R_{0xx} is symmetric at $f = 0$ and $f = \pm 1/2$ whereas R_{0xy} changes sign upon passing through these frustrations. The data are for sample #7

increase to zero at $f = 1/2$. $R_{0xy}(f)$ is anti-symmetric about $f = 0$ and locally anti-symmetric about $f = 1/2$. In the raw data a small symmetric part arises due to sample non-uniformities. This symmetric part can be removed by taking $(R_{0xy}(f) - R_{0xy}(-f))/2$. The removed symmetric part looks identical to, but is only 3% of, R_{0xx} . The data shown in Fig.13 has the symmetric part removed. The difference in shape at $f = 0$ and $f = \pm 1$ is not understood although it is reproducible for $-1.2 < f < +1.2$.

The R_{0xx} and R_{0xy} data can be combined to generate a third plot of the Hall angle $\Theta \equiv \arctan(R_{0xy}/R_{0xx})$ which is shown in Fig. 13 at $T = 20$ mK. Comparing our results to those of van Wees et al. [13] we find a much larger Hall angle. Furthermore they did not observe an anti-symmetric R_{0xy} versus f curve. This is probably because their array was in the classical limit $E_J \gg E_C$, whereas ours were in the quantum limit $E_J \approx E_C$ where a finite R_{0xy} has been predicted [30,64]

The Hall angle can be interpreted as the angle between the vortex velocity vector \vec{V}_v and a unit vector perpendicular to the direction of current flow \vec{J} . The moving vortices generates an electric field given by

$$\vec{E} = -q_v n_v \phi_0 \vec{V}_v \times \hat{z} \quad (4)$$

with $q_v = \pm 1$ describing the vorticity, n_v the area density of vortices, and \hat{z} the unit vector perpendicular to the plane of the array. Vortex motion in the direction of $J \times z$ creates a field E parallel to the transport current J . The force on a moving vortex is the Magnus force [65]

$$\vec{F} = n_s e \phi_0 (\vec{V}_s - \vec{V}_v) \times \hat{z} \quad (5)$$

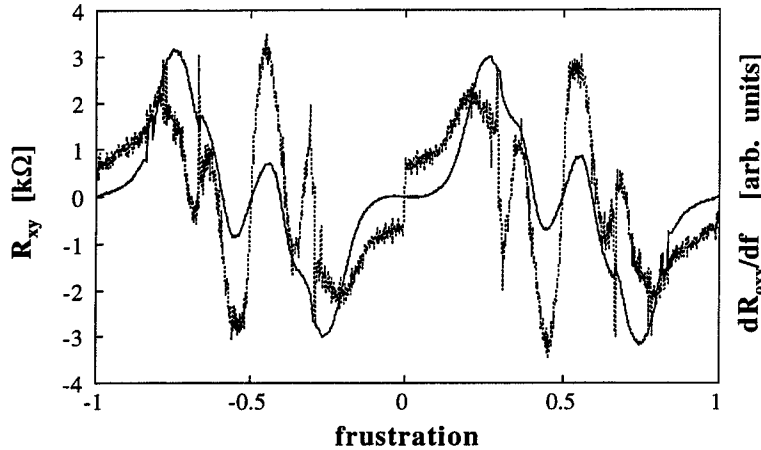


FIGURE 14. A comparison of R_{0xy} (solid curve) and dR_{0xx}/df (dotted curve) for sample #7 at $T = 20$ mK, plotted with arbitrary scale. Both curves show a similar behavior, minima and maxima occur at the same values of frustration

where n_s is the superfluid electron density and $\vec{V}_s = \vec{J}/n_s e$ is the superfluid velocity. Due to this force, there is a component of vortex motion parallel to the applied current which produces a transverse field in the $-\vec{J} \times \hat{z}$ direction.

In two dimensional regular arrays, the field \vec{E} at irrational frustrations is generated by the motion of "defect" or vacancy vortices. From Eq. 4, it is clear that the sign change in the vorticity is responsible for the sign reversal of R_{0xy} in the vicinity of $f = 1/2$, because the defects have opposite vorticity to the field induced vortices.

We find that the structures in $R_{0xy}(f)$ can be correlated to structure dR_{0xx}/df as shown in Fig. 14. The correlation is most clear in the vicinity of $f = 1/2$. This is similar to what is found in the Quantum Hall effect in two dimensional electron gases (2DEGs), where $R_{0xx}(B) \propto dR_{0xy}/dB$. That we find traces of the opposite derivative law is probably related to the fact that our system is described in terms of vortices rather than in terms of electrons as the QHE in 2DEGs.

VII CONCLUSIONS

Based on the parameters of the tunnel junction we find that we can divide the properties of the 2D arrays into three different categories: i) Those which are dominated by the Coulomb blockade and go insulating at low temperature, ii) those which are dominated by the Josephson effect and go superconducting at low temperature, and iii) the intermediate arrays which just barely become superconducting at low temperature, but can be made insulating by applying a magnetic field.

We find that the transition for the insulating arrays can be well described by thermal activation of charge solitons both when the electrodes are normal and when they are superconducting. When the electrodes are in the normal state we find thermal activation of single electron solitons, with an activation energy $E_a \approx \frac{1}{4}E_C$. When the electrodes are in the superconducting state we find a much larger E_a . For arrays with $\Delta_0/E_C < 2$, the activation energy is simply $\frac{1}{4}E_C + \Delta(B)$ indicating that Cooper pairs are broken up and that pairs of single electron solitons are created. When $\Delta_0/E_C > 2$, the activation energy oscillates with B at low magnetic field, demonstrating that Cooper pair solitons are created. The amplitude of these oscillations is roughly equal to E_J and the period corresponds to one flux quantum ($h/2e$) per unit cell.

The threshold voltage for the insulating arrays also oscillates at low magnetic field demonstrating that Cooper pair solitons are injected at low field. For increasing magnetic field the average threshold voltage increases, due to the decreasing E_J . In the region 250 to 450 Gauss we observe a peak in the threshold voltage which is interpreted as a crossover from Cooper pair soliton injection to single electron soliton injection.

We have observed a frustration-tuned superconductor-insulator phase transition in several of the "intermediate" arrays. A small applied magnetic field of 4.4 G can change the zero-bias resistance of an array by more than 5 orders of magnitude.

We show scaling curves for both $f=0$ and $f=1/2$. The results for our four samples show a dynamic critical exponent of 1.05, in good agreement with the theory of the field-tuned S-I transition. Our data indicate a sample dependent R_Q^* . Moreover, we have measured the Hall resistance at f_c , which is much smaller than R_Q .

For frustration values larger than the critical value the Hall resistance is substantially larger and has a rich structure as a function of applied magnetic field. Reversal of the sign of the Hall resistance appears at several frustrations, which can be attributed to the change of sign of the "defect" vortices. We find that the structure in $R_{0xy}(f)$ is similar to the derivative $dR_{0xx}(f)/df$.

ACKNOWLEDGEMENTS

We gratefully acknowledge fruitful discussions with S.M. Girvin, M. Jonson, J. E. Mooij, A. A. Odintsov, R. Shekhter, G. Schön, A. Stern, M. Tinkham and H. van der Zant. Our samples were made in the Swedish Nanometer Laboratory. We would also like to acknowledge the financial support from the Swedish SSF, TFR and NFR, and the Wallenberg Foundation.

REFERENCES

1. J.E. Mooij, and G. Schön *Single Charge Tunneling*, Proc. NATO ASI **294**, ed. H. Grabert and M. Devoret, (Plenum, New York, 1992)
2. R. Fazio, and G. Schön, *Phys. Rev.* **B43**, 5307 (1991)
3. N.S. Bakhvalov, G.S. Kazacha, K.K. Likharev, and S.I. Serdyukova, *Physica* **B173**, 319 (1991)
4. C. B. Whan, J. White, and T. P. Orlando *Appl. Phys. Lett.* **68**, 2996 (1996)
5. D.V. Averin, and K.K. Likharev, in *Mesoscopic Phenomena in Solids*, ed. B. Al'tshuler, P. Lee and R. Webb, (Elsevier, Amst., 1991) p. 173
6. *Single Charge Tunneling, Coulomb Blockade Phenomena in Nanostructures*, ed. H. Grabert and M. Devoret, (Plenum, New York, 1992)
7. *Percolation Localization, and Superconductivity*, Proc. NATO ASI **109**, ed. A. M. Goldman and S. A. Wolf (1986)
8. *Coherence in Superconducting Networks*, Proc. NATO ASI, *Physica* **B152** ed. J.E. Mooij, and G. Schön (1988)
9. *Macroscopic Quantum Phenomena and Coherence in Superconducting Networks*, ed. C. Giovannella and M. Tinkham (World Scientific, Singapore, 1995)
10. P. Minnhagen *Rev. Mod. Phys.* **59**, 1001 (1987)
11. R.F. Voss, and R.A. Webb, *Phys. Rev.* **B25**, 3446 (1983)
12. C. J. Lobb, D. W. Abraham and M. Tinkham, *Phys. Rev. B* **27**, 150 (1983).
13. B.J. van Wees, H. S. J. van der Zant, and J. E. Mooij, *Phys. Rev.* **B35**, 7291 (1987)
14. T.S. Tighe, A.T. Johnson, and M. Tinkham, *Phys. Rev.* **B44**, 10286 (1991)
15. H. S. J. van der Zant, F. C. Fritschy, T. P. Orlando and J. E. Mooij, *Phys. Rev.* **B47**, 295 (1993)

16. M. S. Rzchowski, S. P. Benz, M. Tinkham and C. J. Lobb, *Phys. Rev.* **B42**, 2041 (1990)
17. C. D. Chen, P. Delsing, D. B. Haviland, Y. Harada and T. Claeson, *Phys. Rev. B* **54**, 9449 (1996).
18. J.M. Kosterlitz, and D.J. Thouless, *J Phys.* **C6**, 1181 (1973)
19. V.L. Berezinskii, *Sov. Phys. JEPT* **34**, 610 (1972)
20. J.E. Mooij, B.J. van Wees, L.J. Geerligs, M. Peters, R. Fazio, and G. Schön, *Phys. Rev. Lett.* **65**, 645 (1990)
21. L.J. Geerligs, and J.E. Mooij, *Physica* **B152**, 212 (1988)
22. L.J. Geerligs, M. Peters, L.E.M. de Groot, A. Verbruggen, and J.E. Mooij, *Phys. Rev. Lett.* **63**, 326 (1989)
23. C.D. Chen, P. Delsing, D.B. Haviland, and T. Claeson, *Phys. Scripta* **T42**, 182 (1992)
24. P. Delsing, C.D. Chen, D.B. Haviland, and T. Claeson, in *Single-Electron Tunneling and Mesoscopic Devices*, ed. H. Koch and H. Lübbig, (Springer, Heidelberg, 1992) p. 137
25. T.S. Tighe, M.T. Tuominen, J.M. Hergenrother, and M. Tinkham, *Phys. Rev.* **B47**, 1145 (1993)
26. P. Delsing, C.D. Chen, D.B. Haviland, Y. Harada, and T. Claeson, *Phys. Rev.* **B50**, 3959 (1994)
27. A. Kanda and S. Kobayashi *Czech. J. Phys.* **46**, 703 (1996)
28. M.V. Feigel'man, S.E. Korshunov, A.B. Pugachev *JETP-Lett.* **65**, 566 (1997)
29. H. S. J. van der Zant, F. C. Fritschy, W. J. Elion, L. J. Geerligs and J. E. Mooij, *Phys. Rev. Lett.* **69**, 2971 (1992).
30. M. P. A. Fisher, *Phys. Rev. Lett.* **65**, 923 (1990).
31. C. Bruder, R. Fazio, A. Kampf, A. van Otterlo and G. Schön, *Phys. Scripta* **T42**, 159 (1992)
32. P. Lafarge, J. J. Meindersma, J. E. Mooij, *Macroscopic Quantum Phenomena and Coherence in Superconducting Networks*, (World Scientific, Singapore, 1995) p.94
33. A. J. Rimberg, T. R. Ho, C. Kurdak J, Clarke, K. L. Campman and A. C. Gossard, *Phys. Rev. Lett.* **78**, 2632 (1997)
34. J. M. Graybeal, J. Luo and W. R. White, *Phys. Rev.* **B49**, 12923 (1994)
35. A. W. Smith, T. W. Clinton, C. C. Tsuei and C. J. Lobb, *Phys. Rev.* **B49**, 12927 (1994)
36. A. V. Samoilov, Z. G. Ivanov and L. G. Johansson, *Phys. Rev.* **B49**, 3667 (1994)
37. J. M. Harris, N. P. Ong and Y. F. Yan, *Phys. Rev. Lett.* **71**, 1455 (1993)
38. M. A. Paalanen, A. F. Hebard and R. R. Ruel, *Phys. Rev. Lett.* **69**, 1604 (1992).
39. J. Niemeyer *PTB Mitteilungen* **84**, 251 (1974)
40. G. J. Dolan *Appl. Phys. Lett.* **31**, 337 (1977)
41. V. Ambegaokar, and A. Baratoff, *Phys. Rev. Lett.* **10**, 486 (1963), and **11**, 104(E) (1963)
42. A. Schmid, *Phys. Rev. Lett.* **51**, 1506 (1983)
43. Strictly speaking this is not a Schmid Diagram since there one plots the damping term, which is determined by the tunneling resistance. For energies below the gap energy this is different from R_N .

-
44. W. C. Stewart, *Appl. Phys. Lett.* **12**, 277 (1968)
 45. D. E. MacCumber, *J. Appl. Phys.* **39**, 3113 (1968)
 46. D. B. Haviland, L. S. Kuzmin, P. Delsing, K. K. Likharev, and T. Claeson, *Z. Phys.* **B85**, 339 (1991)
 47. A. A. Middelton and N. S. Wingreen, *Phys. Rev. Lett.* **71**, 3198 (1993).
 48. D. B. Haviland and P. Delsing, *Phys. Rev.* **B54**, R6857 (1996)
 49. A. J. Rimberg, T. R. Ho, and Clarke, *Phys. Rev. Lett.* **74**, 4714 (1995)
 50. A. D. Zaikin and S. V. Panyukov *Czech. J. Phys.* **46**, 629 (1996)
 51. M. P. A. Fisher, P. B. Weichman, G. Grinstein and D. S. Fisher, *Phys. Rev. B* **40**, 546 (1989).
 52. D. B. Haviland, Y. Liu and A. M. Goldman, *Phys. Rev. Lett.* **62**, 2180 (1989).
 53. A. F. Hebard and M. A. Paalanen, *Phys. Rev. Lett.* **65**, 927 (1990).
 54. H.S.J van der Zant, W.J. Elion, L.J. Geerligs, J.E. Mooij *Phys. Rev. B* **54**, 10081 (1996).
 55. G. T. Seidler, T. V. Rosenbaum and B. W. Veal, *Phys. Rev. B* **45**, 10162 (1992).
 56. S. Tanda, S. Ohzeki and T. Nakayama, *Phys. Rev. Lett.* **69**, 530 (1992).
 57. W. Wu and P.W. Adams *Phys. Rev. Lett.* **74**, 610 (1995).
 58. M. Tinkham, *Introduction to Superconductivity*, (McGraw-Hill, New York, 1976)
 59. T. C. Halsey, *Phys. Rev. B* **31**, 5728 (1985).
 60. B. I. Halperin and D. R. Nelson, *J. Low Temp. Phys.* **36**, 1165 (1979).
 61. S. Martin, A. T. Fiory, R. M. Fleming, G. P. Espinosa and A. S. Cooper, *Phys. Rev. Lett.* **62**, 677 (1989).
 62. M. P. A. Fisher, T. A. Tokuyasu and A. P. Young, *Phys. Rev. Lett.* **66**, 2931 (1991)
 63. C. D. Chen, P. Delsing, D. B. Haviland, Y. Harada and T. Claeson, *Phys. Rev. B* **51**, 15645 (1995).
 64. A. van Otterlo, K. H. Wagenblast, R. Fazio, and G. Schön, *Phys. Rev.* **B48**, 3316 (1993)
 65. P. Ao and D. J. Thouless, *Phys. Rev. Lett.* **70**, 2158 (1993)

V. TRANSPORT AND PROXIMITY EFFECT IN MESOSCOPIC STRUCTURES

Methods of quasiclassical Green's functions in the theory of transport phenomena in superconducting mesoscopic structures

A.F.Volkov* and V.V.Pavlovskii†

* *School of Physics and Chemistry, Lancaster University, Lancaster LA1 4YB and Institute of Radioengineering and Electronics of the Russian Academy of Sciences, Mokhovaya str.11, Moscow 103907, Russia*

† *Institute of Physics and Technology of the Russian Academy of Sciences, Nakhimovskii Avenue 34, Moscow 117218, Russia*

Abstract. A short introduction to the theory of matrix quasiclassical Green's functions is given and possible applications of this theory to transport properties of mesoscopic superconducting-normal metal (S/N) structures are considered. We discuss a simplified version of these equations in the diffusive regime and in the case of a weak proximity effect. These equations are used for the calculation of the conductance of different S/N structures and for analysis of kinetic phenomena in these structures. We discuss the subgap conductance measured in SIN tunnel junctions and the mechanism of a nonmonotonic dependence of the conductance of a N wire on temperature T and voltage V , observed in an S/N structure.

Long-range, phase-coherent effects are studied in a 4-terminal S/N/S structure under conditions when the Josephson critical current is negligible (the distance between superconductors is much larger than the coherence length in the normal wire). It is shown that the Josephson effects may be observed in this system if a current I , in addition to a current I_1 in the S/N/S circuit, flows through the N electrode.

1. Introduction

The progress of nanotechnology over the last few years has made it possible to produce conducting nanostructures in which new physical phenomena have been observed. Specifically, hybrid structures consisting of superconductors (S) and normal conductors (N) have been created using metal films [2-5] or semiconductor layers [1,6-8] as the normal conductors. The transport properties of these S/N structures have turned out to be quite unusual. First, the subgap conductance (zero-bias anomaly) has been observed in SIN tunnel junctions at low temperatures ($T < 100$ mK) [1] (see also [7,8]). Second, conductivity oscillations have been observed in these mesoscopic structures in a magnetic field H (i.e., in structures with dimensions less than the phase-breaking length L_φ). Oscillations of the con-

ductivity of the N channel appeared if the structure contained superconducting or normal loops [2–6]. Moreover, for an N channel in contact with superconductors a nonmonotonic dependence of the conductivity on the temperature T and voltage V has been observed at $T \ll T_c$ [5]. The main experimental facts have been explained in recent theoretical works (see review articles [23,24]). It was established that the proximity effect plays the main role in the transport properties. For example, the conductivity of an N channel in the structure shown in Fig.1 changes as a result of the contribution of the condensate induced by the proximity effect. Since the condensate is induced by both superconductors in a nonlocal manner, interference appears and a term $-\delta R \cos \varphi$, which depends on the phase difference φ between the superconductors, arises in the resistance of the N channel [9–11]. The phase difference increases with the magnetic field H , and this results in oscillations of the conductivity of the N channel in a magnetic field. The nonmonotonic dependence of the resistance R of an N channel on T and V has also been explained [12–15] (see also the theoretical works in the Conference Proceedings in Ref. [14]). The nonmonotonic dependence of the resistance $R(T, V)$ of a point contact ScN (c is a constriction) was first obtained theoretically in Ref. [16].

New effects have also been predicted in theoretical work devoted to S/N structures. For example, in Refs. [14,17] it was shown that the critical Josephson current I_c in a structure of the type displayed in Fig.1 depends on the voltage V_S between the S and N conductors, changing sign (π -contact) if V_S exceeds a certain value. In addition, it has been shown that the Josephson effect also arises in the case when current flows only through one S/N boundary. Several different configurations of S/N structures were studied in Ref. [18], determining that under certain conditions the current-voltage characteristics of the S/N structures have descending segments ($dI/dV < 0$).

An important circumstance was noted in Ref. [19] (see also the works in Ref. [14]). It was shown that the local conductivity of an N channel changes over distances from the S/N boundary which can be much greater than the coherence length $\xi_N = \sqrt{D/2\pi T}$ (D is the diffusion coefficient). Important consequences follow from this fact. For example, phase coherence effects in the conductivity of an N channel remain even if the distance $2L_1$ between the superconductors is much greater than ξ_N . This means that the conductivity oscillations in the structure shown in Fig.1b will also be observed in the case of a negligibly low critical current I_c . The oscillation conservation effect is due to fact that as T increases, I_c decreases exponentially ($I_c \sim \exp(-2L_1/\xi_N(T))$), and δR decreases slowly ($\delta R \sim T^{-1}$) [20,35].

In these lectures we discuss briefly the method of quasiclassical Green's functions and apply this method to the study of transport phenomena in mesoscopic S/N structures. We restrict ourselves to the dirty limit where the mean free path l is essentially less than geometric dimensions of the system and the coherence length, but exceeds significantly the Fermi wave length k_F (quasiclassic approximation). We will consider mostly a weak proximity effect, when the amplitude of the condensate induced in the normal metal is small compared to the condensate amplitude

in the superconductors S. This case occurs if the S/N interface resistance is larger than the resistance of the normal conductor N. Results obtained for this case remain qualitatively valid in case when these resistances are comparable.

In the next Section we present the main necessary equations for the Green's functions and a general expression for the current in the N channel in which a condensate is present due to proximity effect. In Section 3 we will give formulas describing the subgap conductance of tunnel S/I/N junctions and discuss a possible physical interpretation of this conductance. In Section 4 we will consider the conductance of a N channel attached to two superconductors and obtain a formula describing, in particular, the oscillatory behaviour of the conductance in an applied magnetic field H . Also a nonmonotonic dependence of the conductance on temperature T and on bias voltage V will be analysed. The possibility of observing Josephson-like effects in a S/N/S mesoscopic structure (see Fig.1b) will be considered in Section 5. We will show that zero voltage between superconductors may exist in some interval of the current through the S/N interfaces and Shapiro-steps may be observed even in absence of the real Josephson coupling between superconductors when the distance

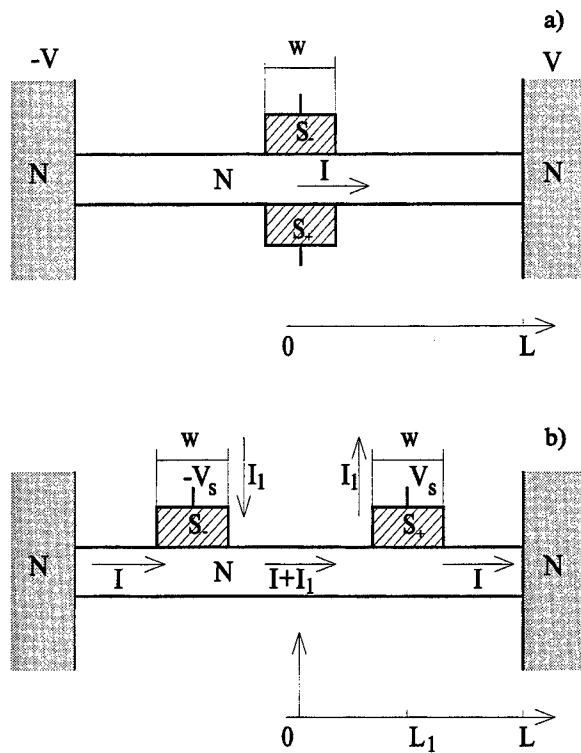


FIGURE 1. Schematic diagram of the system considered

separating superconductors exceeds essentially the coherence length

$$2L_1 \gg \xi_N(T) = \sqrt{D/2\pi T}. \quad (1)$$

It is important that these effects arise only in the case when a current I flows along the N channel and the dissipation takes place [21,35].

2. Basic equations for quasiclassical Green's functions

The Green's function technique is a powerful tool for the theoretical study of different phenomena in superconductors and superconducting structures. In the case of superconducting systems, we need to introduce condensate Green's functions of the type $\langle \psi_\uparrow(1) \psi_\downarrow(2) \rangle$, therefore all the Green's functions have a matrix form. For example, the retarded (advanced) Green's functions are defined as follows [22,23]

$$\hat{G}^{R(A)} = \pm \theta(t_{1(2)} - t_{2(1)}) (\hat{G}^>(1,2) - \hat{G}^<(1,2)) \quad (2)$$

Here $\hat{G}^<$ and $\hat{G}^>$ are

$$\begin{aligned} \hat{G}_{\alpha\beta}^> &= -i \langle \psi_\alpha(1) \psi_\beta^+(2) \rangle (-1)^{\alpha+1}, \\ \hat{G}_{\alpha\beta}^< &= i \langle \psi_\beta^+(2) \psi_\alpha(1) \rangle (-1)^{\alpha+1} \end{aligned} \quad (3)$$

We introduced here spin indices in the Nambu-space: $\psi_1(1) = \psi_\uparrow(1)$, $\psi_2(1) = \psi_\downarrow^+(1)$. As is well known, the functions $\hat{G}^{R(A)}$ describe the excitation spectrum of the system. In order to describe nonequilibrium processes, one needs to know the distribution functions which are related to the Green's function \hat{G} introduced by Keldysh. It is convenient to define a supermatrix $\check{G}(1,2)$ elements of which are the matrices $\hat{G}^{R(A)} = (\check{G}(1,2))_{11,(22)}$ and $\hat{G} = (\check{G})_{12}$. The element $(\check{G})_{21}$ is the zero matrix.

In the quasiclassical approximation all components of the Green's functions $\check{G}_{ex}(1,2)$ are integrated over the variable $\xi_p = (p - p_F)v_F$ and in the corresponding equation for $\check{G}_{ex}(1,2)$ an expansion is carried out in the parameters $(p_F d)^{-1}$, $(p_F l)^{-1}$ or $(p_F \xi_N)^{-1}$, where d is the thickness of the S or N films, ξ_N is the coherence length in the N conductor and l is the mean free path. The quasiclassical Green's functions are defined by the relation [22,23]

$$\check{G}(\vec{p}/p, \vec{r}; t_1, t_2) = (i/\pi) \int d\xi_p \check{G}_{ex}(\vec{p}, \vec{r}; t_1, t_2) \quad (4)$$

The subscript "ex" means exact (nonquasiclassical) Green's functions. Therefore the quasiclassical Green's functions $\check{G}(1,2)$ depends on the angle of momentum on the Fermi surface, on the coordinate \vec{r} , and on two times.

In what follows we need an equation for the supermatrix $\check{G}(1,2)$ only in the N conductor, having the form

$$D\nabla (\check{G}\nabla\check{G}) + i\epsilon [\check{\sigma}_z, \check{G}] = 0. \quad (5)$$

where $\check{\sigma}_z$ is a diagonal supermatrix elements of which are the Pauli matrix $\hat{\sigma}_z$. Eq.(5) may be averaged over the thickness of the N film d . Performing the averaging, we obtain

$$D\partial_x (\check{G}\partial_x \check{G}) + i\epsilon [\check{\sigma}_z, \check{G}] = \epsilon_b \theta(x_S) [\check{G}_S, \check{G}]. \quad (6)$$

where the coefficient ϵ_b is a characteristic energy which is proportional to the transmission of the S/N boundary: $\epsilon_b = \rho D / 2R_{b2} d$, R_{b2} is the resistance of a unit area of the S/N boundary; ρ and d are the resistivity and thickness of the N film.

When deriving Eq. (6), the boundary condition

$$D (\check{G}\partial_z \check{G}) = (\epsilon_b d_N) [\check{G}, \check{G}_S] \quad (7)$$

was used. Here the z-axis is normal to the plane of the S/N interface. The boundary conditions for the quasiclassical Green's functions \check{G} have been derived in the general case by Zaitsev [25] and have been reduced to the simple form (7) by Kupriyanov and Lukichev [26] in the dirty case. In the case of a good S/N contact, condition (7) is reduced to the continuity of the Green's functions at the S/N interface: $\check{G} = \check{G}_S$. In the case of a poor contact ($\epsilon_b \rightarrow 0$), condition (7) gives the same result for the current through the S/N interface as obtained with the aid of the tunneling Hamiltonian method. However, for a S/N contact with an arbitrary barrier transparency condition (7) is not applicable. The point is that when deriving Eq. (7) Kupriyanov and Lukichev [26] restricted themselves to the Legendre polynomials of the zeroth and first orders in the expansion of the angle-dependent Green's function \check{G} . Meanwhile, one can easily show that all the Legendre harmonics are excited near the S/N (or N/N') interface. They decay to zero (except the Legendre polynomials of the zeroth and first order) over the mean free path away from the interface. In order to obtain a correction of the next order in ϵ_b to condition (7), one has to solve an integral equation (see Ref. [27]). In the case of the S/N interface with an arbitrary barrier transparency, the problem of boundary conditions for the quasiclassical Green's functions becomes complicate (boundary conditions and their applicability are discussed in detail in the Raimondi's Lecture Notes).

Eq.(6) must be solved in the normal conductor for a particular geometry (see, for example, Fig.1) with boundary conditions at $x = \pm L$. In the case of normal reservoirs the condensate functions $\hat{F}^{R(A)}(\pm L)$ are equal to zero and $\hat{G}^{R(A)}(\pm L) = \pm \hat{\sigma}_z$. In the case of superconducting reservoirs the boundary conditions for the retarded (advanced) Green's functions are

$$\hat{G}^{R(A)}(\pm L) = G^{R(A)} \hat{\sigma}_z + \hat{F}_{S\pm}^{R(A)} \quad (8)$$

where $G^{R(A)} = \epsilon / \xi_\epsilon^{R(A)}$, $\hat{F}_{S\pm}^{R(A)} = \Delta / \xi_\epsilon^{R(A)} (\pm i \hat{\sigma}_x \sin \phi + i \hat{\sigma}_y \cos \phi)$, $\xi_\epsilon^{R(A)} = \sqrt{(\epsilon \pm i\Gamma)^2 - \Delta^2}$, Γ is a damping in the excitation spectrum in superconductor, 2ϕ is the phase difference between superconductors. Eq.(8) is valid if the voltage

between superconductors $2V$ is much less than Δ/e . We assume that there is no barrier between the N conductor and reservoirs.

The Keldysh function \hat{G} describes the kinetic properties of the system and is related to distribution functions

$$\hat{G} = \hat{G}^R \hat{f} - \hat{f} \hat{G}^A \quad (9)$$

where $\hat{f} = f_o \hat{1} + f \hat{\sigma}_z$ is a matrix distribution function. The function f_o enters an expression for the supercurrent (in a superconductor it determines the energy gap), and the function f determines the quasiparticle current (in a superconductor it describes the charge-imbalance and the electric field; see, for example [28]). In reservoirs the functions f_o and f are supposed to have equilibrium form

$$f_o(\pm L) = [\tanh((\epsilon + eV)\beta) + \tanh((\epsilon - eV)\beta)]/2, \quad (10)$$

$$f(\pm L) \equiv \pm F_N(\epsilon) = \pm [\tanh((\epsilon + eV)\beta) - \tanh((\epsilon - eV)\beta)]/2, \quad (11)$$

where $\beta = (2T)^{-1}$.

If the functions $\hat{G}^{R(A)}$ and \hat{G} are known, one can easily find a relation between the applied voltage $2V$ and the current I in the N conductor. The expression for the current is [22,23]

$$I = (\sigma d/8) Tr \hat{\sigma}_z \int d\epsilon (\hat{G}^R \partial_x \hat{G} - \hat{G} \partial_x \hat{G}^A) \quad (12)$$

Eqs.(6) and (12) can be simplified significantly in the case of a weak proximity effect when the amplitudes of the condensate functions in the N conductor $\hat{F}^{R(A)}$ are small. Then the retarded (advanced) Green's functions in the N conductor have the form

$$\hat{G}^{R(A)} = G^{R(A)} \hat{\sigma}_z + \hat{F}^{R(A)} \quad (13)$$

where $G^{R(A)} \approx \pm[1 + (F^{R(A)})^2/2]$ and $|F^{R(A)}| \ll 1$. When obtaining the relation between $\hat{G}^{R(A)}$ and $\hat{F}^{R(A)}$, we employed the normalization condition [22,23]

$$(G^{R(A)})^2 \hat{1} + (\hat{F}^{R(A)})^2 = \hat{1}, \quad (14)$$

where $\hat{1}$ is a unit matrix.

The equation for the condensate functions $\hat{F}^{R(A)}$ follows from Eq.(6) and the expression (14)

$$\partial_{xx} \hat{F}^{R(A)} - (k_b^{R(A)})^2 \hat{F}^{R(A)} = -k_b^2 w [\hat{F}_{S+}^{R(A)} \delta(x - L_1) + \hat{F}_{S-}^{R(A)} \delta(x + L_1)] \quad (15)$$

where $k_b^2 = 2\epsilon_b/D$, $(k_b^{R(A)})^2 = (\pm 2i\epsilon + \gamma)/D$, w is the width of the S/N interface in the x-direction and is supposed to be much less than L and $\xi_N(T)$. We introduce here the depairing rate γ in the N conductor which determines the phase-breaking

length $L_\phi = \sqrt{D/\gamma}$. Once the functions $\hat{F}^{R(A)}$ are known from a solution of the linear equation (15), we can find the conductance of the N film.

Let us consider for example the system shown in Fig.1. Writing down Eq.(6) for the matrix element (12), we arrive at the equation outside the S/N interface

$$D\partial_x [\hat{G}^R \partial_x \hat{G} + \hat{G} \partial_x \hat{G}^A] + i\epsilon [\hat{\sigma}_z, \hat{G}] = 0. \quad (16)$$

Multiplying Eq.(16) by $\hat{\sigma}_z$ and calculating the trace, we obtain after the first integration

$$(\partial_x f) [1 - m_-] = J(\epsilon). \quad (17)$$

Here $J(\epsilon)$ is an x -independent constant and

$$m_- = (1/8)Tr (\hat{F}^R - \hat{F}^A)^2 \quad (18)$$

is a function which describes the condensate contribution to the N film conductance. The left side of Eq.(17) stems from the first term in the square brackets in Eq.(16) provided that the condensate functions are small. Therefore, according to Eq.(12), the current I is an integral from the "partial current" J

$$I = (\sigma d/2) \int d\epsilon J(\epsilon) \quad (19)$$

Solving Eq.(17) with boundary conditions (11), we can find a relationship between the current and voltage $I(V)$. In the next Sections we will analyse the conductance of S/N mesoscopic systems.

3. Subgap conductance in SIN junctions

In this Section the subgap conductance in superconductor/insulator/normal metal (S/I/N) tunnel junctions will be discussed. As is well known from conventional theory for S/I/N junctions, the subgap conductance should exponentially decrease with decreasing temperature T (see, for example, Ref. [29]). However, experiments on Nb/n+InGaAs contacts have established that a peak in conductance appears at zero-bias if the temperature becomes low enough ($T \ll \Delta$), and the magnitude of this peak at low temperatures ($T \approx 50$ mK) is comparable with the conductance in the normal state [1]. This contact can be considered as a tunnel S/I/N junction. A Schottky barrier at the interface plays the role of the insulating layer I. An explanation for anomalous transparency of the SIN junction at low voltages and temperatures ($T, eV \ll \Delta$) was suggested in Refs. [9,30-34]. According to the interpretation proposed in Ref. [32], the subgap conductance is due to a component of the current which, in the case of a SIS Josephson junction, gives the so-called interference current. This component can be presented in the form

$$I_{int} = -(8R_b)^{-1} \int d\epsilon \cdot F_N(\epsilon, V) (F^R + F^A) (F_S^R + F_S^A), \quad (20)$$

where $F_N(\varepsilon, V)$ is defined in Eq. (11); $F_S^{R(A)} = \Delta / ((\varepsilon \pm i\Gamma)^2 - \Delta^2)^{1/2}$ are the condensate, retarded (advanced) Green's functions in the superconductor. This formula can be obtained from the general expression for the current (12) and from Eq.(6) in which we have to put $\theta(x_S) = 1$. If the energy ε is small, $F^R = F^A \approx -i$. In the case of a S/I/N junction, $F^{R(A)}$ are the condensate functions in the N electrode. To zero order in the barrier transmittance (i.e., in R_b^{-1}), they are equal to zero. If the proximity effect is taken into account, they differ from zero and in the case of a planar S/I/N junction they have the form (see, for example, Ref. [32])

$$F^{R(A)} = \begin{cases} \pm \varepsilon_b / (\varepsilon \pm i\gamma), & \gamma > \varepsilon_b \\ \varepsilon_b / [(\varepsilon \pm i\gamma)^2 - \varepsilon_b^2]^{1/2}, & \gamma < \varepsilon_b \end{cases} \quad (21)$$

This formula can be obtained from Eq.(6) in the case of weak and strong proximity effect. It is seen from Eq.(21) that $F^{R(A)}$ are small if $\varepsilon_b \ll \varepsilon, \gamma$, where ε is determined either by temperature T or voltage V . In the opposite limit when ε and γ are small compared with ε_b , $F^{R(A)}$ are not small, and the differential conductance normalized by R_b^{-1} , $S = R_b dI/dV$, calculated from Eq.(20) for $T=0$ and $V=0$ is not small either. The integrand in Eq.(20) is not zero if $|\varepsilon| < \Delta$ because $F^R = F^A$ at $|\varepsilon| < \Delta$ and $F^R = -F^A$ at $|\varepsilon| > \Delta$. This means that the current given by Eq.(1) is caused by the charge-transfer mechanism of the same type as Andreev reflection processes. The second important circumstance leading to the subgap conductance is related to an anomalous proximity effect when the amplitude of the condensate functions $F^{R(A)}$ at small energies ε is not small.

The density-of-states (DOS) in the N electrode is changed drastically in the case of the strong proximity effect: the DOS is zero at $|\varepsilon| < \varepsilon_b$ and the DOS = $\varepsilon / \sqrt{\varepsilon^2 - \varepsilon_b^2}$ in the interval $\Delta \gg |\varepsilon| > \varepsilon_b$. In a one-dimensional S/I/N junction the DOS has a quasigap at $|\varepsilon| < \varepsilon_b$. In both cases of a planar or one-dimensional S/I/N junctions the zero-bias, zero-temperature conductance coincides with it's value in the normal state [32].

4. Conductance of the Andreev interferometer

Consider the system shown in Fig.1 (the Andreev interferometer). In order to calculate the normalized differential conductance of the N channel $S = R_N dI/dV$ in the presence of a phase difference between superconductors, we must solve Eq.(17) taking into account the boundary condition (11). The function m_- is small by assumption. Therefore the expression for J may be presented in the form

$$J(\varepsilon) = F_N(\varepsilon, V) [1 - \langle m_- \rangle] / L \quad (22)$$

where $\langle m_- \rangle = (1/L) \int_0^L dx \cdot m_-^2$. Substituting (22) into Eq.(19), we can obtain an expression for S . Here we present the formula for a deviation of the normalized differential conductance from it's value in the normal state R_N : $\delta S \equiv (2L/\sigma d) dI/dV - 1$. We obtain

$$\delta S = -(1/2) \int d\epsilon \cdot \beta \cdot F'_N(\epsilon, V) \langle m_- \rangle, \quad (23)$$

where $F'_N(\epsilon, V) = [\cosh^{-2}(\epsilon + eV)\beta + \cosh^{-2}(\epsilon - eV)\beta]/2$. By virtue of the definition of $\langle m_- \rangle$ (see Eqs.(18)), we can write $\langle m_- \rangle$ in the form

$$\langle m_- \rangle = Tr \left\langle \left(\hat{F}^R \right)^2 + \left(\hat{F}^A \right)^2 - 2\hat{F}^R \hat{F}^A \right\rangle / 8 \quad (24)$$

The first two terms in (24) determine a change in the DOS of the N channel due to the condensate (this term reduces the conductance), and the last, so-called anomalous, term leads to an increase of the conductance.

As it is seen from Eq.(23), in order to find the conductance, we need to solve Eq.(15) for the condensate functions $\hat{F}^{R(A)}(x)$. In this Section we present here the solution for the geometry shown in Fig.1a.

$$\hat{F}^{R(A)}(x) = i\hat{\sigma}_y F_S^{R(A)} r \left[\theta^{R(A)} \cosh \theta^{R(A)} \right]^{-1} \sinh \left[k^{R(A)} (L - |x|) \right] \cdot \cos \varphi \quad (25)$$

Here $r = k_0^2 L w$ is the ratio of the N channel resistance to the S/N resistance, $\theta^{R(A)} = k^{R(A)} L$. Calculating $\langle m_- \rangle$ we find

$$\langle m_- \rangle = (r^2/8) \left\{ Re [\sinh(2\theta)/2\theta - 1] / (\theta \cosh \theta)^2 - [\sinh(2\theta_1)/2\theta_1 - \sin(2\theta_2)/2\theta_2] / |\theta \coth \theta|^2 \right\} (1 + \cos 2\varphi) \quad (26)$$

where $\theta = \theta_1 + i\theta_2$. The first term in (26) determines a contribution to the conductance due to a change in the DOS, and the second term is related to the anomalous term ($\hat{F}^A \hat{F}^R$). In Fig.2 we show the dependence δS_{DOS} (first term contribution) and the $\delta S_{an}(V)$ dependence (anomalous term contribution) at $T = 0$. It is seen that $\delta S_{DOS}(V)$ is negative and $\delta S_{an}(V)$ is positive. The total change in the conductance $\delta S(V) = \delta S_{DOS}(V) + \delta S_{an}(V)$ is shown by the solid line. This quantity increases with increasing V from zero, reaches a maximum at $V_m \approx \epsilon_L/e$, and decays to zero with further increase of V (here $\epsilon_L = D/L^2$ is the so-called Thouless energy).

As follows from (23) and (26), the conductance δS oscillates with increasing the phase difference. In Fig.2 we also plot the temperature dependence of the zero-bias conductance. Both curves, $\delta S(V)$ at $T = 0$ and $\delta S(T)$ at $V = 0$ are similar. Note that nonmonotonous temperature dependence of the conductance was obtained earlier in Ref. [16] where a short ScN contact was analyzed (here c means a constriction).

5. Dissipative Josephson-like effects in S/N/S structures

In this Section we discuss a possibility to observe Josephson-like effects in mesoscopic S/N/S structures (see Fig.1b) with negligible Josephson coupling between superconductors, i.e., when the inequality (1) is fulfilled [21,35]. Following the same steps as in Section 2, we obtain instead of Eq.(17)

$$(1 - m_-(x)) \partial_x f = \begin{cases} J + J_1 - J_S, & 0 < x < L_1 \\ J, & L_1 < x < L \end{cases} \quad (27)$$

In what follows the function m_- plays the most important role.

The current on the segment $(0, L_1)$ is determined by Eq.(19) if J is replaced by $J + J_1$. The quantity J_S , the superconducting "current", is constant over the segment (L_1, L) and $(0, L_1)$ and is equal to

$$J_S = (1/4) Tr \hat{\sigma}_z (\hat{F}^R \partial_x \hat{F}^R - \hat{F}^A \partial_x \hat{F}^A) \quad (28)$$

The integral of J_S (28) over the energy is exponentially small if the condition (1) is satisfied. As follows from Eq. (6), the constant J_1 , is related with the Green's function and distribution function in the superconductor. It can be written in the form [11]

$$J_1 = J_q + \tilde{J}_S, J_q = (\rho/d_N \Re_b) [F_S(\epsilon) - f(L_1)] \quad (29)$$

Here $\Re_b = R_{b2}/w [\nu_N \nu_S + (1/8) Tr (\hat{F}^R + \hat{F}^A) (\hat{F}_S^R + \hat{F}_S^A)]^{-1}$ is the resistance of the S/N boundary per unit length in the y direction and ν_N, ν_S - are the density of states in the N and S conductors. It can be shown that for $V_{N,S}$ which are small compared with T/e , the "supercurrent" \tilde{J}_S , flowing throw the S/N boundary equals J_S . The distribution function F_S is the equilibrium function, i.e., it is identical to the function in Eq. (11), if V_N is replaced by V_S (we measure voltages from the point 0, where the voltage is equal to zero). Using the fact that m_- is small, we can integrate Eq. (27) and find the relation of J and J_q with F_N and F_S (see the boundary condition (11)). We obtain the normal currents

$$\begin{aligned} (d_N/\rho) J &= \frac{\Re_b F_N + \Re_1 (F_N - F_S)}{\Re_b \Re + \Re_1 \Re_2}, \\ (d_N/\rho) J_1 &\approx J_q (d_N/\rho) = \frac{\Re_2 F_S + \Re_1 (F_S - F_N)}{\Re_b \Re + \Re_1 \Re_2} \end{aligned} \quad (30)$$

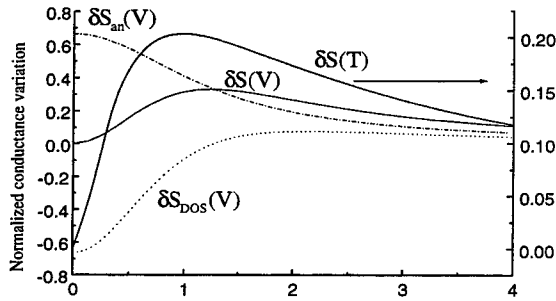


FIGURE 2. Normalized conductance δS vs. normalized voltage eV/ϵ_L at $T = 0$ and vs. normalized temperature T/ϵ_L at $V = 0$ for the structure shown in Fig.1a.

Here \mathfrak{R}_b is determined in Eq. (29); the quantity $\mathfrak{R} = \mathfrak{R}_1 + \mathfrak{R}_2$, $\mathfrak{R}_{1,2} = R_{1,2} (1 + \langle m_- \rangle)$ can be termed the partial resistance. The spatial average $\langle m_- \rangle_{1,2}$ on the segments $(0, L_1)$ and (L_1, L) gives a decrease in the resistances on account of proximity effect ($\langle m_- \rangle$ is negative). All resistances in Eq. (30) depend on the difference of the phases φ and on the energy; they can be represented in the form $\mathfrak{R}_b = R_b - \delta R_b \cos \varphi$ and $\mathfrak{R}_{1,2} = R_{1,2} - \delta R_{1,2} \cos \varphi$. The corrections to the resistances δR_b and $\delta R_{1,2}$ are small in the case of a weak proximity effect. The quantities R_b and $R_{1,2}$, depend, generally speaking, on the energy ϵ (for example, ν_S depends on ϵ). We assume, for simplicity, that these quantities do not depend on the energy. This is valid if it is assumed that the superconductors are gapless (the results remain qualitatively the same in the case of superconductors with a gap). Then, integrating Eq. (30) over energies, we obtain on the left-hand side the currents I and I_1 (see Eq. (19)). Eliminating V_N from the two equations obtained, we find for V_S

$$V_S = \hbar \partial_t \varphi / 2e = I_1 [R_b + R_1 - (\delta R_b + \delta R_1) \cos 2\varphi] + I (R_1 - \delta R_1 \cos 2\varphi) \quad (31)$$

Here we employed the Josephson relation; R_b is the resistance of the S/N boundary, which in the case of zero-gap superconductors is approximately equal to its value in the normal state. The resistance R_1 is also approximately equal to $\rho L_1 / d_N$ (the φ -independent correction arising from $\langle m_- \rangle$ is small and unimportant). Integrating Eq. (31), we obtain a relation between the average voltage \bar{V}_S and the fixed currents I and I_1 .

$$\bar{V}_S = \sqrt{[(I + I_1) R_1 + I_1 R_b]^2 - [(I + I_1) \delta R_1 + I_1 \delta R_b]^2} \quad (32)$$

The function $\bar{V}_S(I_1)$ is displayed in Fig.3 for different currents I . One can see that for $I \neq 0$ this dependence is identical to the current-voltage characteristic of a standard Josephson contact. In this case the critical current is

$$I_c = I \frac{\delta R_1 R_b - \delta R_b R_1}{(R_b + R_1)^2} \quad (33)$$

Therefore I_c increases in proportion to the current I . We shall show below that the correction δR_1 decreases slowly with increasing temperature ($\delta R_1 \sim T^{-1}$), and the correction δR_b is small if the condition (1) is satisfied. Therefore, for $R_b \gg R_1$, we obtain $I_c \simeq I \delta R_1 / R_b$. The maximum current I is limited by the condition that Joule heating be small and by the condition $eV_N \simeq eIR \ll T$. In the opposite case δR_1 decreases as V_N increases. If the condition (1) is not satisfied and a finite Josephson coupling exists between the superconductors, then it is easy to show that the critical current of the structure equals $I_c^* = \sqrt{I_c^2 + I_{cJ}^2}$, where I_{cJ} is the critical Josephson current. An expression for I_{cJ} can be easily obtained with the aid of Eq. (28). This expression is presented in Ref. [20]. The equilibrium phase difference φ_0 for $I_1 + IR_1 / (R_b + R_1) = 0$ equals $2\varphi_0 = -\arcsin(I_c / I_c^*)$.

To determine δR_1 and δR_b it is necessary to find the condensate functions $\hat{F}^{R(A)}$. For $|x| < L_1$ the solution of Eq.(15) has the form

$$\hat{F}^{R(A)}(x) = F_S^{R(A)} [i\hat{\sigma}_y \cos(\varphi) P_y \cosh(kx) + i\hat{\sigma}_x \sin(\varphi) P_x \sinh(kx)]^{R(A)} \quad (34)$$

Here $F_S^{R(A)}$ is the amplitude of the condensate functions in the superconductors. In the zero-gap case $F_S^{R(A)} = \pm \Delta / (\epsilon \pm i\gamma_S)$, where γ_S is the frequency of spin-flip collisions with impurities. The functions $P_{x,y}$ equal:

$$P_x = b \sinh \theta_2 / (\sinh \theta + b \sinh \theta_1 \sinh \theta_2),$$

$$P_y = b \sinh \theta_2 / (\cosh \theta + b \cosh \theta_1 \sinh \theta_2),$$

$b = \rho w / (R_{b2} d_N) k$, $k^{R(A)} = \sqrt{\mp 2i\epsilon/D}$, $\theta = \theta_1 + \theta_2$, $\theta_{1,2} \equiv \theta'_{1,2} + i\theta''_{1,2} = kL_{1,2}$. Once the functions $\hat{F}^{R(A)}$ are known, the interference correction δR_1 to the resistance can be calculated:

$$\delta R_1 = -R_1 \int_0^\infty d\epsilon \beta \cdot \cosh^{-2}(\epsilon\beta) \langle m_-(x, \varphi) - m_-(x, \pi/2) \rangle_1 \quad (35)$$

With the aid of the expressions for $\langle m_- \rangle_1$ and for $\hat{F}^{R(A)}$ (see Eq. (34)), we find

$$\delta R_1 / R_1 = \int_0^\infty d\epsilon \beta \cdot \cosh^{-2}(\epsilon\beta) M(\epsilon), \quad (36)$$

where $M(\epsilon) = (1/8) \left\{ |F_S|^2 \left[|P_y|^2 [\sinh(2\theta'_1)/2\theta'_1 + \sin(2\theta''_1)/2\theta''_1] - |P_x|^2 [\sinh(2\theta'_1)/2\theta'_1 - \sin(2\theta''_1)/2\theta''_1] \right] + \text{Re} F_S^2 [P_y^2 (\sinh(2\theta_1)/2\theta_1 + 1)] \right\}$

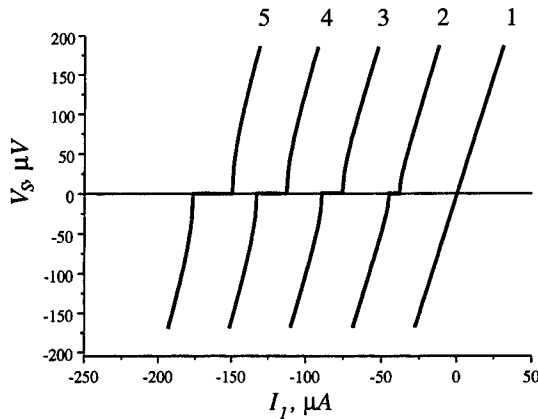


FIGURE 3. V_S versus the current I_1 for the following values of the current: 1 - 0, 2 - $250\mu\text{A}$, 3 - $500\mu\text{A}$, 4 - $750\mu\text{A}$, 5 - 1mA . Here $\delta R_1 = 0.1R_1$, $R_b = 5R_1$, $R_1 = 1\Omega$.

$-P_x^2 (\sinh(2\theta_1)/2\theta_1 - 1)]\}$. The temperature dependence of δR_1 is displayed in Fig.4. One can see that for $T > \epsilon_{L_1} = D/(2L_1)^2$ the quantity δR_1 decreases as T^{-1} with increasing temperature. As noted in Refs. [15,18], the slow decrease of $\delta R_1(T)$ is due to the so-called anomalous term $F_R F_A$ in $\langle m_- \rangle_1$. The special role of this term, which is nonanalytic both in the upper and lower planes of ϵ , was noted in Ref. [36].

The Josephson current I_S is determined by the integral of J_S (28), over all energies, i.e., the integral of products of either advanced or retarded Green's functions. It can be calculated by closing the integration contour in the upper (lower) half plane of ϵ and switching to summation over the Matsubara frequencies $\omega_n = \pi T(2n+1)$. For such energies the functions $F^{R(A)}$ decay exponentially over distances $k^{-1}(\omega_n) \leq \xi_n(T)$ away from the S/N boundary. Therefore the current I_S will be exponentially small ($I_S \sim \exp(-2L_1/\xi_N(T))$). The function $I_S(T)$ for the structure shown in Fig.1b is presented in Ref. [20]. Similar arguments are also applicable to the calculation of δR_b , since for $T < \gamma_S$ the functions F_S^R and F_S^A can be assumed to be equal and independent of the energy. At the same time, the function $F^R F^A$, appearing in the expression for δR_1 , decreases over a small (compared with T) energy $\epsilon_{L_1} = D/(2L_1)^2$ and makes a nonzero contribution. For such energies the characteristic decay length of $F^{R(A)}(x)$ is of the order L_1 , i.e., of the order of the distance between the superconductors.

In order to observe long-range Josephson effects, the critical current I_c must exceed the fluctuation current Te/\hbar : $I_c \gg Te/\hbar$. On the other hand, the ordinary Josephson effect is negligible if the condition $\epsilon_{L_1} \ll T$ is fulfilled. Combining these inequalities, we obtain the condition

$$TR_b R_1 / (\delta R_b R_Q) \ll \epsilon_{L_1} \ll T \quad (37)$$

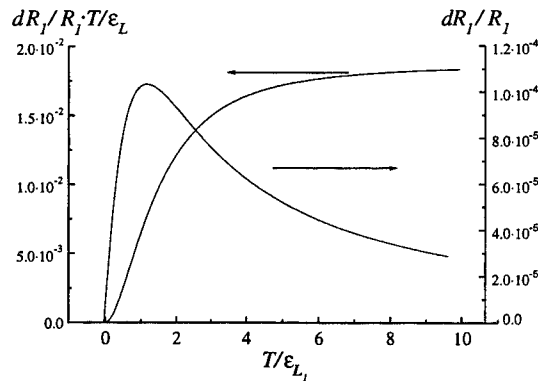


FIGURE 4. Interference correction δR_1 to the resistance as a function of temperature in the case $L_1 = 0.5L$, $R/R_b = 0.4$, $\gamma/\epsilon_L = 100$, $\Delta/\epsilon_L = 30$.

which should be satisfied for observation of the effects under consideration. Here $R_Q = \hbar/e^2 \approx 3k\Omega$, and we took into account that a maximal value of I is determined by the relation $eIR \leq \epsilon_{L_1}$. Otherwise δR_1 decreases with increasing I . The first inequality of (37) means that the zeroth Shapiro step on the $I_1(V_S)$ curve is absent at $I = 0$. If the second inequality of (37) is not fulfilled, then the critical current is not zero at $I = 0$ (ordinary Josephson effect). In this case the effective critical current I_c^* should first increase with increasing I and then decrease when I exceeds ϵ_{L_1}/eR .

6. Conclusion

In conclusion we note that, as one can see from Fig.4, the correction δR_1 to the resistance of the normal channel caused by the proximity effect depends on the temperature T in a nonmonotonic way: it is equal to zero at $T = 0$ (the bias voltage is zero as well), reaches a maximum at $T \approx \epsilon_{L_1}$ and decays to zero at higher T . Such behavior of $\delta R_1(T)$ is related, as noted in [15], to different dependencies of two contributions to δR_1 on the energy ϵ . One contribution which increases the N channel resistance is connected with a decrease of the density-of-states in the normal channel, which is described by the last term in $M(\epsilon)$ (see Eq. (36)). Another contribution (anomalous) which diminishes the resistance of the normal channel is described by the first two terms in $M(\epsilon)$. This contribution exactly compensates a contribution due to a change in the density-of-states of the normal channel at $\epsilon = 0$ and dominates at $\epsilon \neq 0$. At $T > T_c$ it leads to the Maki-Thompson contribution to the paraconductivity. Mathematically, compensation of the two contributions at $\epsilon = 0$ arises because at $\epsilon = 0$ $F^R = F^A$ and m_- in Eq. (35) tends to zero. The nonmonotonic behavior of δR has been observed in an experiment [5]. It would be interesting to observe the long-range Josephson effect experimentally.

This work was supported by the Russian Fund for Fundamental Research (Project 96-02-16663a), by the Russian Grant on high T_c Superconductivity (Project 96053), and by CRDF Project (RP1-165). This support is gratefully acknowledged.

REFERENCES

1. A.Kastalsky *et al.*, Phys. Rev. Lett., **67**,1326 (1991); A.W.Kleinsasser and A.Kastalsky, Phys. Rev. **B47**, 8361 (1993).
2. V.T. Petrashov, V.N. Antonov, P. Delsing, and T. Claeson, Phys. Rev. Lett.**70**, 347, (1993); Phys. Rev. Lett. **74**,5268 (1995).
3. H. Pothier, S. Gueron, D. Esteve, and M.H. Devoret, Phys. Rev. Lett. **73**, 2488 (1994).
4. P.G.N. Vegvar, T.A. Fulton, W.H. Mallison, and R.E. Miller, Phys. Rev. Lett. **73**, 1416(1994).
5. H. Courtois, Ph. Grandit, D. Mailly, and B. Pannetier, Phys. Rev. Lett. **76**, 130 (1996); D. Charlat, H. Courtais, Ph. Grandit, D. Mailly, A.F. Volkov, and B. Pannetier, Phys. Rev. Lett. **77**, 4950 (1996).
6. H. Dimoulas, J.P. Heida, B.J. van Wees *et al*, Phys. Rev. Lett. **74**, 602 (1995); S.G. den Hartog, C.M.A. Kapteyn, V.J. van Wees, *at all*, Phys. Rev. Lett. **76**, 4592, 1996.
7. C. Nguen, H. Kroemer, and E.L. Hu, Phys. Rev. Lett., **69**, 2847 (1992).
8. W. Poirier, D. Mailly, and M. Sanquer, in *Proceedings of the Conference on Correlated Fermions and Transport in Mesoscopic Systems*, Les Arcs, France, 1996.
9. F.W. Hekking and Yu.V. Nazarov, Phys. Rev. Lett. **71**,1525 (1993); Phys. Rev. **B49**, 6847 (1994).
10. A.V. Zaitsev, Phys. Lett. **A194**, 315 (1994).
11. A.F. Volkov and A.V. Zaitsev, Phys. Rev. **B53**, 9267(1996).
12. Yu.V. Nazarov and T.H. Stoof, Phys. Rev. Lett. **76**,823 (1996)
13. A.F. Volkov, N. Allsopp, and C.J. Lambert, J. Phys. Cond. Matter **8**, 45(1996).
14. A.F. Volkov and V.V. Pavlovskii, in *Proc. of the Conference on Correlated Fermions and Transport in Mesoscopic Systems*, LesArcs, France, 1996.
15. A.A.Golubov, F.Wilhelm, and A.D.Zaikin, Phys.Rev. **B55**, 1123 (1996).
16. S.N. Artemenko, A.F. Volkov, and A.V. Zaitsev, Solid State Comm. **30**, 771 (1979).
17. A.F. Volkov, Phys. Rev. Lett. **74**,4730(1995); JETP Lett, **61**,565 (1995).
18. A.V. Zaitsev, JETP Lett. **61**, 771(1995).
19. F. Zhou, B.Z. Spivak, and A. Zyuzin, Phys. Rev. **B52**, 4467(1995)
20. A.F. Volkov and H. Takayanagi, Phys. Rev. Lett. **76**, 4026 (1996)
21. A.F. Volkov and V.V. Pavlovskii, Sov. Phys. JETP Lett. **64**, 670 (1996).
22. A.I. Larkin and Yu.N. Ovchinnikov, in *Nonequilibrium Superconductivity*, ed. by D.N. Langenberg and A.I. Larkin (Elsevier, Amsterdam, 1986), p.493.
23. C.J. Lambert and R.Raimondi, J. Phys. Cond. Matter (to appear)(1997).
24. C.W.J.Beenakker, Rev.Mod.Phys. **69**, 731 (1997)
25. A.V. Zaitsev, Zh. Eksp. Teor. Fiz. **86**, 1742 (1984) [Sov. Phys. JETP **59**, 1015 (1984)].
26. M.Yu. Kupriyanov and V.F. Lukichev, Zh. Eksp. Teor. Fiz. **94**, 139 (1988) [Sov. Phys. JETP **67**, 1163 (1988)].
27. C.J. Lambert, R. Raimondi, V. Sweeney, and A.F. Volkov, Phys. Rev. **B55**, 6015 (1997).

28. S.N.Artemenko and A.F. Volkov, Sov.Phys.Uspekhi, **22**, 295 (1979)
29. J.R.Schriffer, *Theory of Superconductivity*, (Benjamin, New York, 1964).
30. A.V.Zaitsev, Sov. Phys JETP Lett. **51**, 41 (1990); Physica **C185-189**, 2539(1991).
31. A.F.Volkov, A.V.Zaitsev, and T.M.Klapwijk, Physica **C210**, 21 (1993).
32. A.F.Volkov, JETP Lett. **55**, 746 (1992); Phys. Lett. **A174**,144 (1993); *ibid.* **187**, 404 (1994); in *Proceedings of the NATO Workshop on Mesoscopic Superconductivity* [Physica **B203**,267 (1994)].
33. C.W.J. Beenakker, Phys. Rev. **B46**, 12841 (1992); I.K.Marmorkos, C.W.J. Beenakker, and R.A. Jalabert, *ibid.* **48**, 2811 (1993).
34. B.J. van Wees, P. de Vries, P. Magnee, and T.M.Klapwijk, Phys. Rev. Lett. **69**, 510 (1992).
35. A.F.Volkov and H.Takayanagi, Phys. Rev. (in press) (1997).
36. L.P. Gor'kov and G.M. Eliashberg, Zh. Eksp. Teor. Fiz. **56**, 1297 (1969) [Sov. Phys. JETP **29**, 698 (1969)].

Boundary Conditions in the Theory of Superconductivity

Roberto Raimondi

Dipartimento di Fisica "E. Amaldi", Terza Università degli Studi di Roma, Via della Vasca Navale 84, I-00146, Roma, Italy

Abstract. In these Lecture Notes I discuss the boundary conditions for the quasiclassical Green's functions in the theory of superconductivity.

I INTRODUCTION

The quasiclassical Green's functions are a powerful method for investigating equilibrium and nonequilibrium superconductivity [1]. They can be used when the length scale a over which the macroscopic physical quantities of interest vary is much greater than the typical atomic scale λ_F , the electron wavelength. In hybrid structures, due to the electron reflection occurring at the boundaries between different metals, macroscopic quantities do not vary slowly in the quasiclassical sense and the set of equations for the quasiclassical Green's functions needs to be complemented by appropriate boundary conditions that tell how to match the quasiclassical Green's functions on the different sides of a boundary once the scattering properties of the boundary are known. The derivation of such boundary conditions was done by Zaitsev [2] in a general form, valid both in the clean and dirty limits. Successively, Kupriyanov and Lukichev [3] obtained in the dirty limit simpler boundary conditions which are strictly valid in the case of small transparency of the boundary. This dirty limit form of the boundary conditions has played a considerable role in recent years in the analysis of electrical transport properties in hybrid superconducting structures [4]. Recently, new effective boundary conditions, valid in the dirty limit, have been derived by means of a perturbative expansion in the boundary transparency [5].

These Lecture Notes are organized as follows. In the next Section, in order to illustrate the general ideas, I consider the normal case when no superconductivity is present. In this case the derivation of the boundary conditions necessary for example to evaluate the conductance of a normal disordered wire are derived. In Section III, I introduce the formalism to be used in the general case when superconductivity is present and derive the set of quasiclassical Green's functions needed

in the presence of interface boundaries. In Section IV, the derivation of the boundary conditions for the quasiclassical Green's functions is given. Section V deals with the important limit of dirty systems where the boundary conditions acquire a particularly simple expression. A few examples are then shown for the purpose of illustration. In Section VI, finally, I address new recent developments aiming to go beyond the small transparency limit of the boundary conditions for dirty systems along with some physical consequences.

II THE NORMAL CASE

As anticipated in the Introduction, it is useful to start by considering the simple situation of a disordered normal metallic wire of length L and cross section S , attached to two normal macroscopic electrodes. The two electrodes must be thought of as large electronic reservoirs in statistical equilibrium. The dimensions of the wire are in the mesoscopic domain, i.e., the typical length scales are less than the phase coherence breaking length. To compute the physical properties of the wire, like, for example, the electrical conductance, one can use the quasiclassical approximation which is valid when the length scale over which the macroscopic quantities vary is much greater than the typical atomic length scale. This is done by solving the Boltzmann kinetic equation for the electron distribution function. In the electrodes the distribution function is the equilibrium Fermi function which provides the appropriate boundary conditions at the two ends of the wire. Let $f(\mathbf{r}, \mathbf{k}, t)$ be the distribution function in the wire. In the case of weak s-wave impurity scattering, in the absence of external fields and in time independent situations, the Boltzmann equation for the distribution function integrated over the modulus of the momentum, $f(\mathbf{r}, \mu) = N_0 \int dE f(\mathbf{r}, \mathbf{k})$, $E = \hbar^2 k^2 / 2m$, reads [6]

$$l\mu\partial_z f(z, \mu) = \langle f(z, \mu) \rangle - f(z, \mu) \quad (1)$$

where N_0 is the non-interacting single-particle density of states per spin and $l = v_F \tau$ is the mean free path with τ the scattering time. $\mu = \cos(\theta) = k_z / k_F$ is the component of the momentum parallel to the wire. The symbol $\langle \dots \rangle$ indicates the solid angle average $\int d\Omega / (4\pi) (\dots) = \int_0^{2\pi} d\phi / (2\pi) \int_0^\pi (d\theta/2) \sin(\theta) (\dots) = (1/2) \int_{-1}^1 d\mu (\dots)$. In writing eq.(1), we have made the assumption that f depends only on the longitudinal coordinate z ($-L/2 < z < L/2$), perpendicular to the boundary plane, as suggested by the one-dimensional character of the problem. It is customary to divide f in symmetric and antisymmetric components with respect to the reversal of the direction of the momentum

$$f_s(z, \mu) = (f(z, \mu) + f(z, -\mu))/2, \quad f_a(z, \mu) = (f(z, \mu) - f(z, -\mu))/2. \quad (2)$$

The current is then written solely in terms of the antisymmetric part

$$j = 2eN_0 v_F S \langle \mu f_a(0, \mu) \rangle \quad (3)$$

ans has been evaluated at $z = 0$ for the sake of definiteness. Eq.(1) can then be written for both f_s and f_a to read

$$l\mu\partial_z f_s = -f_a \quad (4)$$

$$l\mu\partial_z f_a = < f_s > - f_s \quad (5)$$

and the boundary conditions at the wire ends are

$$f_s(\pm L/2, \mu) = f_{R,L}, \quad (6)$$

where $f_{R,L} \equiv \int dE (\exp(E - eV_{R,L}) + 1)^{-1}$, and $\mu_{R,L} = eV_{R,L}$, $V_R - V_L$ is the applied bias. The solution of eqs.(4-5) is $f_s = (f_R - f_L)(z/L) + (f_R + f_L)/2$, $f_a = -\mu(f_R - f_L)(l/L)$ and one obtains the standard Drude formula for the electrical conductance of the wire

$$G_D = \frac{\sigma S}{L} \quad (7)$$

where $\sigma = 2e^2 N_0 v_F l / 3$.

Consider now the situation when a boundary separating two metals is present. This can be modelled, for example, as a potential barrier, say, at $z = 0$, with given reflection and transmission coefficients, R and T . To solve the Boltzmann equation in this case, one needs to specify the boundary conditions for f_s and f_a at the interface separating the two regions of the wire. By means of counting arguments, it is almost evident that

$$f(z = 0^-, \mu) = Rf(z = 0^-, -\mu) + Tf(z = 0^+, \mu), \quad (8)$$

which in terms of f_s and f_a can be rewritten as

$$f_a(z = 0^-) = f_a(z = 0^+) \equiv f_a(z = 0) \quad (9)$$

$$f_s(z = 0^+) - f_s(z = 0^-) = \frac{2R}{T} f_a(z = 0). \quad (10)$$

As expected physically, the function f_a is continuous across the boundary, meaning the conservation of the current, while the symmetric part undergoes a jump. The eqs.(4-5) together with the boundary conditions (6,9-10) can then be solved to get the current in the system. As a simple illustration of the boundary condition (10), consider the case when a tunnel junction is between the two electrodes. This corresponds to the case when the left and right regions of the wire are at equilibrium. The tunnel junction conductance is then easily obtained by inserting eq.(10) into eq.(3) for the current

$$G_T = e^2 N_0 v_F < \frac{\mu T}{R} >. \quad (11)$$

III EQUATIONS OF MOTION

A systematic way to deal with nonequilibrium problems in quantum field theory is provided by the Keldysh technique [7], which introduces a matrix Green's function

$$\check{G} = \begin{pmatrix} \hat{G}^R & \hat{G} \\ 0 & \hat{G}^A \end{pmatrix}. \quad (12)$$

where the diagonal and off-diagonal blocks contain information about the spectrum of the elementary excitations and their distribution function, respectively. The various elements of the "check" Green's function, \check{G} , are themselves "hat" matrices in the Nambu space to take into account the normal and the anomalous Green's functions [1]. The quasiclassical approximation is usually carried out by eliminating the small scale information contained in \check{G} , and deriving an equation for the quasiclassical Green's function \check{g} , which is the Green's function integrated over the energy. In the presence of a boundary between contiguous metals, the passage from \check{G} to \check{g} requires some care, as we now show. To be specific, I consider, as in Section II, a boundary at $z = 0$ and with the regions $z < 0$ and $z > 0$, labelled by the index $i = 1, 2$, respectively. The position vector is $\mathbf{r} = (z, \rho)$, with ρ the two-dimensional vector lying in the boundary plane (x-y plane). The Green's function depends both on space and time arguments, $\check{G}(z, \rho, t; z', \rho', t')$. The quasiclassical approximation does not involve the time variables and in the following, to keep the notation simple, I will not explicitly show the time dependence. To further simplify the treatment, it is useful to assume that all variations parallel to the boundary plane will be slow in the quasiclassical sense, so that the Green's function will feel the presence of the boundary only through the longitudinal coordinates z, z' . It is then convenient to go to the quasiclassical description for the transverse coordinates, ρ, ρ' in the standard way. This amounts to Fourier transform with respect to the relative coordinate $\rho - \rho'$ and consider the variation of \check{G} as function of the center-of-mass coordinate $\rho_c = (\rho + \rho')/2$ and transverse momentum k_{\parallel} . We are then left with $\check{G}(z, z'; \rho_c, k_{\parallel}) \equiv \check{G}(z, z')$, and the Dyson equation of motion for the Green's function can be written as

$$(\check{H} + \frac{1}{2m} \frac{\partial^2}{\partial z^2} + \mu_z - U)\check{G}(z, z') = \check{1}\delta(z - z') \quad (13)$$

where $\mu_z = k_z^2/2m = \mu - k_{\parallel}^2/2m$ and

$$\check{H} = (i\tau_z \frac{\partial}{\partial t} + i\mathbf{v}_{\parallel} \cdot \frac{\partial}{\partial \rho} - \Phi + \check{\Delta} - \check{\Sigma}). \quad (14)$$

Here $\check{\Sigma}$ indicates the self-energy as usual. $\check{\Delta}$ is the self-consistent pairing field and Φ is the electrical potential. The symbol U indicates the potential due to the boundary and may be considered to be appreciably different from zero near the boundary on a length scale δ . More precisely, the conditions $\delta \gg \lambda_F$ and $\delta \approx \lambda_F$ describe smooth

and sharp boundaries. The "check" identity symbol includes a delta function in the time variables, $\check{1} \equiv \check{1}\delta(t-t')$. Finally, $\check{\tau}_z$ is block diagonal in the "check" space with elements the Pauli matrix $\hat{\tau}_z$. In the spirit of the quasiclassical approximation, we write the Green's function, for example for $z, z' < 0$ ($i = 1$), in the form

$$\check{G} = \check{G}_{11}^1 \exp[ik_{z,1}(z-z')] + \check{G}_{22}^1 \exp[-ik_{z,1}(z-z')] + \check{G}_{12}^1 \exp[ik_{z,1}(z+z')] + \check{G}_{21}^1 \exp[-ik_{z,1}(z+z')] \quad (15)$$

where the rapidly oscillating parts have been explicitly separated. The length scale over which \check{G}_{nk}^1 varies is of the order of l, ξ , where l is the mean free path and ξ is the correlation length, which is equal to $v_F/\bar{\epsilon}$ and $\sqrt{D/\bar{\epsilon}}$ in the clean and dirty cases, respectively. Here $\bar{\epsilon}$ is $\max\{E, T, \Delta, V\}$ where E is the energy, T the temperature, Δ the energy gap, and V the voltage across the system. The above form of the Green's function is valid not too close to the boundary for $z < -\delta$ or $z > \delta$ where the potential U vanishes. By inserting the Green's function in the form (15) in the equation of motion (13), it is easy to see that, for $z \neq z'$,

$$(\check{H} + i(-1)^{n+1}v_{z,i}\frac{\partial}{\partial z})\check{G}_{nk}^i(z, z') = \check{0}. \quad (16)$$

The point $z = z'$ must be handled with care. From the Dyson equation (13) one has that

$$\frac{\partial}{\partial z}\check{G}(z+0^+, z) - \frac{\partial}{\partial z}\check{G}(z-0^+, z) = \check{1}2m \quad (17)$$

which translated in terms of \check{G}_{nk}^i becomes

$$\check{G}_{nk}^i(z+0^+, z) - \check{G}_{nk}^i(z-0^+, z) = \check{1}\frac{(-1)^{n+1}}{iv_{z,i}}\delta_{nk} \quad (18)$$

i.e., the functions \check{G}_{nk}^i with equal indices are discontinuous. By making the identification

$$\check{g}_i(z, z', k_{z,1}) = \begin{cases} 2|v_{z,i}|i\check{G}_{11}^i - \text{sign}(z-z') & k_{z,i} > 0 \\ 2|v_{z,i}|i\check{G}_{22}^i + \text{sign}(z-z') & k_{z,i} < 0 \end{cases} \quad (19)$$

one sees that, when $z = z'$, \check{g}_i is the usual quasiclassical Green's function [2]. In fact, from eq.(16) and its conjugate, it is direct to show that \check{g}_i obeys the usual quasiclassical equation. Note that the sign functions have been appositely introduced to make the \check{g}_i 's continuous at $z = z'$. The effect of the electron reflection and transmission occurring at the boundary is described by the Green's function \check{G}_i

$$\check{G}_i(z, z', k_{z,i}) = \begin{cases} 2|v_{z,i}|i\check{G}_{12}^i & k_{z,i} > 0 \\ 2|v_{z,i}|i\check{G}_{21}^i & k_{z,i} < 0. \end{cases} \quad (20)$$

In general one can derive an equation of motion for \check{G}_i to be used together with the equation for \check{g}_i . This can be done easily by using again eq.(16) and its conjugate. However, in practice, one is interested to evaluate physical quantities far away from the interface, where the contribution made by \check{G}_i is vanishingly small. For this reason, we do not derive such an equation explicitly, as it is never used and conclude the present section by illustrating some useful consequences of the equation of motion (16) to be used in the next Section. If one defines the function \check{P}_{nk}^i [2], [8]

$$\check{P}_{nk}^i(z, z_1, z_2) = \check{G}_{nn}^i(z_1, z) \check{G}_{nk}^i(z, z_2) \quad (21)$$

it is direct to show that

$$iv_{z,i} \frac{\partial}{\partial z} \check{P}_{nk}^i(z, z_1, z_2) = 0. \quad (22)$$

Furthermore for $|z - z_{1,2}| \rightarrow \infty$, all \check{G}_{nk}^i vanish, so that, by keeping in mind that \check{P}_{nk}^i does not depend on z , one concludes that for $z < z_1, z_2$ or $z > z_1, z_2$, \check{P}_{nk}^i must be identically zero. In going to the quasiclassical description, one sets $z_1 = z_2$, so that z is always outside the interval (z_1, z_2) . Finally, by setting $z = z_1$, one obtains

$$\check{g}_i(k_i) \check{G}_i(k_i) = (-1)^i \text{sgn}(k_i) \check{G}_i(k_i), \quad (23)$$

and the usual normalization condition¹

$$\check{g}_i \check{g}_i = \check{1}. \quad (24)$$

IV THE BOUNDARY CONDITIONS

In this Section, I address the problem of deriving the boundary conditions for the quasiclassical Green's function \check{g}_i . This involves essentially two steps. First, by means of the scattering theory, I derive the boundary conditions for the full quantum mechanical Green's function. Secondly, by going to the quasiclassical description and by eliminating \check{G}_i I will derive effective boundary conditions for \check{g}_i . The problem to be solved is that of connecting the Green's function in the region j to the Green's function in the region i , where $i, j = 1, 2$. Near the boundary, the most important terms in the equation of motion are the kinetic energy and the scattering potential U and one may write the Green's function in terms of the scattering states

$$G(\underline{r}_i, \underline{r}_j) = \sum_{p, p', \sigma, \sigma'} A_{\sigma, \sigma'}^{ij}(p, p', \Sigma) \frac{\exp[ik_{i, \sigma}^p(E)z_i + ik_{j, \sigma'}^{p'}(E)z_j]}{\sqrt{v_{(i, \sigma, p)}(E)v_{(j, \sigma', p')}(E)}}, \quad (25)$$

¹⁾ It is worth to note that the argument given here has allowed to give a more mathematically sound and physically transparent base to the normalization condition $\check{g}^2 = \check{1}$ commonly used in the quasiclassical theory. A more extended discussion can be found in the paper by Shelankov [8].

where Σ is equal to the sign of $(z_i - z_j)$. Here p labels all transverse quantum numbers, $\sigma = +1$ for a right-going (or right-decaying) wave and $\sigma = -1$ for a left-going (or left-decaying) wave). The quantities $A_{\sigma,\sigma'}^{ij}(p, p', \Sigma)$ do not depend on z_i, z_j , though in general depend on ρ_i, ρ_j , with $\underline{r}_{i(j)} = (\rho_{i(j)}, z_{i(j)})$. The potential barrier may be represented by a transfer matrix T satisfying

$$\begin{pmatrix} O' \\ I' \end{pmatrix} = T \begin{pmatrix} I \\ O \end{pmatrix}, \quad (26)$$

where O (I) refer to vectors of outgoing (incoming) plane-wave amplitudes on the left and O' , (I') to corresponding amplitudes on the right, each plane-wave being divided by the square root of its longitudinal group velocity to ensure unitarity of the scattering matrix s . Whereas T connects plane wave amplitudes in the left lead to amplitudes in the right lead, the scattering matrix s -matrix connects incoming amplitudes to outgoing amplitudes and satisfies (cf. Lambert's Lecture Notes in these Proceedings)

$$\begin{pmatrix} O \\ O' \end{pmatrix} = s \begin{pmatrix} I \\ I' \end{pmatrix} \quad (27)$$

Once T is known, the s -matrix can be constructed. Indeed we have

$$s = \begin{pmatrix} r & t' \\ t & r' \end{pmatrix}, T = \begin{pmatrix} T_{11} & T_{12} \\ T_{21} & T_{22} \end{pmatrix} = \begin{pmatrix} (t^\dagger)^{-1} & r'(t')^{-1} \\ -(t')^{-1}r & (t')^{-1} \end{pmatrix} \quad (28)$$

For $\underline{r}_i \neq \underline{r}_j$ and a fixed value of Σ , the matrix $A_{\sigma,\sigma'}^{ij}$ with matrix elements $A_{\sigma,\sigma'}^{ij}(p, p', \Sigma)$ satisfy relations of the form of equation (26). First consider the form of the Green's function when $z_j < z_i$ and $j = 1$. When viewed as a function of z_i , one has

$$T(E, H) \begin{pmatrix} A_{++}^{11} & A_{+-}^{11} \\ A_{-+}^{11} & A_{--}^{11} \end{pmatrix} = \begin{pmatrix} A_{++}^{21} & A_{+-}^{21} \\ A_{-+}^{21} & A_{--}^{21} \end{pmatrix} \quad (29)$$

On the other hand, when viewed as a function of z_j , using the conjugate equation for the Green's function (which involves the time reversed Hamiltonian), one obtains for $i = 2$,

$$\begin{pmatrix} A_{++}^{22} & A_{+-}^{22} \\ A_{-+}^{22} & A_{--}^{22} \end{pmatrix} = T(E, H^*) \begin{pmatrix} A_{++}^{21} & A_{+-}^{21} \\ A_{-+}^{21} & A_{--}^{21} \end{pmatrix} \quad (30)$$

Hence after eliminating the off-diagonal terms, A_{+-}^{21} , etc., we obtain the general boundary condition relating the Green's functions on the left of the scatterer, to the Green's functions on the right:

$$T(E, H) \begin{pmatrix} A_{++}^{11} & A_{+-}^{11} \\ A_{-+}^{11} & A_{--}^{11} \end{pmatrix} = \begin{pmatrix} A_{++}^{22} & A_{+-}^{22} \\ A_{-+}^{22} & A_{--}^{22} \end{pmatrix} T^t(E, H^*)^{-1}. \quad (31)$$

Equation (31) is a generalisation of Zaitsev's boundary condition to the case of a non-planar barrier [4], which in general may contain impurities and break time-reversal symmetry. ² If time reversal symmetry holds one can show that

²) A similar argument with $z_j > z_i$ yields an identical result and therefore the boundary condition is independent of the choice of Σ .

$$T^{-1t}(E, H^*) = \begin{pmatrix} 0 & 1 \\ -1 & 0 \end{pmatrix} T(E, H) \begin{pmatrix} 0 & -1 \\ 1 & 0 \end{pmatrix}, \quad (32)$$

and eq.(31) becomes

$$T(E, H) \begin{pmatrix} -A_{+-}^{11} & A_{++}^{11} \\ -A_{--}^{11} & A_{+-}^{11} \end{pmatrix} = \begin{pmatrix} -A_{+-}^{22} & A_{++}^{22} \\ -A_{--}^{22} & A_{+-}^{22} \end{pmatrix} T(E, H) \quad (33)$$

By multiplying eq.(33) by T^{-1} and exploiting the cyclic permutation of the trace, one obtains a first boundary condition

$$\text{Tr}(A_{+-}^{11} - A_{+-}^{22}) = \text{Tr}(A_{+-}^{22} - A_{+-}^{11}). \quad (34)$$

All other boundary conditions can be expressed as traces over the matrices $A_{\sigma\sigma'}^{ij}$. Indeed multiplying both sides of (33) by each of the matrices

$$\begin{pmatrix} 0 & 0 \\ 0 & T_{22}^{-1} \end{pmatrix}, \begin{pmatrix} T_{11}^{-1} & 0 \\ 0 & 0 \end{pmatrix}, \begin{pmatrix} 0 & 0 \\ T_{12}^{-1} & 0 \end{pmatrix}, \begin{pmatrix} 0 & T_{21}^{-1} \\ 0 & 0 \end{pmatrix} \quad (35)$$

and taking the trace of the resulting four equations yields

$$\text{Tr}[A_{+-}^{11} - A_{+-}^{22}] = -\text{Tr}[T_{22}^{-1}T_{21}A_{++}^{11} + T_{12}T_{22}^{-1}A_{--}^{22}] = \text{Tr}[rA_{++}^{11} - r'A_{--}^{22}] \quad (36)$$

$$\text{Tr}[A_{+-}^{11} - A_{+-}^{22}] = -\text{Tr}[T_{11}^{-1}T_{12}A_{--}^{11} + T_{21}T_{11}^{-1}A_{++}^{22}] = \text{Tr}[r^\dagger A_{--}^{11} - r'^\dagger A_{++}^{22}] \quad (37)$$

$$\text{Tr}[A_{+-}^{11} + A_{+-}^{22}] = \text{Tr}[-T_{12}^{-1}T_{11}A_{++}^{11} + T_{22}T_{12}^{-1}A_{++}^{22}] = \text{Tr}[r^{\dagger-1}A_{++}^{11} + r'^{-1}A_{++}^{22}] \quad (38)$$

$$\text{Tr}[A_{+-}^{11} + A_{+-}^{22}] = \text{Tr}[-T_{21}^{-1}T_{22}A_{--}^{11} + T_{11}T_{21}^{-1}A_{--}^{22}] = \text{Tr}[r^{-1}A_{--}^{11} + r'^{-1}A_{--}^{22}] \quad (39)$$

Subtracting (36) from (37) yields, in view of (34),

$$\text{Tr}[rA_{++}^{11} - r^\dagger A_{--}^{11}] = \text{Tr}[r'A_{--}^{22} - r'^\dagger A_{++}^{22}] \quad (40)$$

and subtracting (38) from (39) yields

$$\text{Tr}[r^{\dagger-1}A_{++}^{11} - r^{-1}A_{--}^{11}] = \text{Tr}[r'^{\dagger-1}A_{--}^{22} - r'^{-1}A_{++}^{22}] \quad (41)$$

Adding (36) to (37) and (38) to (39) yields

$$\text{Tr}[A_{+-}^{11} + A_{+-}^{11}] - \text{Tr}[A_{+-}^{22} + A_{+-}^{22}] = \text{Tr}[rA_{++}^{11} + r^\dagger A_{--}^{11}] - \text{Tr}[r'A_{--}^{22} + r'^\dagger A_{++}^{22}] \quad (42)$$

and

$$\text{Tr}[A_{+-}^{11} + A_{+-}^{11}] + \text{Tr}[A_{+-}^{22} + A_{+-}^{22}] = \text{Tr}[r^{\dagger-1}A_{++}^{11} + r^{-1}A_{--}^{11}] \quad (43)$$

$$+\text{Tr}[r'^{-1}A_{++}^{22} + r'^{-1}A_{--}^{22}].$$

If there is translational invariance in the boundary plane, writing, for each value of the transverse momentum \mathbf{k}_\parallel , $t = t' = |t| \exp i\theta$, $r = |r| \exp i\phi$, $r' = -|r| \exp i(2\theta - \phi)$, and by making the identification, valid close to the boundary, $A_{\sigma\sigma}^{ii} = \check{G}_{i\sigma}$ and $A_{\sigma-\sigma}^{ii} = \check{g}_{i\sigma}$, one obtains from either of equations (40) and (41)

$$\check{G}_{1a} = \check{G}_{2a}, \quad (44)$$

from (42) and (43),

$$\check{g}_{1s} - \check{g}_{2s} = |r|(\check{G}_{1s} + \check{G}_{2s}), \quad (45)$$

$$\check{g}_{1s} + \check{g}_{2s} = \frac{1}{|r|}(\check{G}_{1s} - \check{G}_{2s}), \quad (46)$$

and from (34)

$$\check{g}_{1a} = \check{g}_{2a}, \quad (47)$$

where

$$\check{G}_{1s,a} = [\check{G}_{1+} \exp i\phi \pm \check{G}_{1-} \exp -i\phi]/2, \quad (48)$$

$$\check{G}_{2s,a} = [\check{G}_{2+} \exp i(\phi - 2\theta) \pm \check{G}_{2-} \exp i(2\theta - \phi)]/2 \quad (49)$$

and

$$\check{g}_{is,a} = [\check{g}_{i+} \pm \check{g}_{i-}]/2. \quad (50)$$

The antisymmetric functions $\check{g}_a = \check{g}_{1a} = \check{g}_{2a}$ and $\check{G}_a = \check{G}_{1a} = \check{G}_{2a}$ are continuous across the boundary, while the symmetric ones \check{g}_{is} and \check{G}_{is} experience a jump determined by the transparency of the barrier. The size of the jump vanishes for perfectly transmitting interfaces. As noted at the end of Section III, in practice, one would like to obtain boundary conditions involving only the Green's functions \check{g}_i . The boundary conditions for the antisymmetric components are already decoupled with respect to the \check{g}_a and \check{G}_a . To decouple the symmetric components, we express the generalized normalization conditions of eqs.(23-24) in terms of the symmetric and antisymmetric parts to yield

$$\begin{aligned} \check{g}_{is}\check{G}_{is} + \check{g}_a\check{G}_a &= (-1)^i\check{G}_a \\ \check{g}_{is}\check{G}_a + \check{g}_a\check{G}_{is} &= (-1)^i\check{G}_{is} \end{aligned} \quad (51)$$

and

$$\check{g}_{is}\check{g}_{is} + \check{g}_a\check{g}_a = \check{1}, \quad \check{g}_{is}\check{g}_a + \check{g}_a\check{g}_{is} = 0. \quad (52)$$

By manipulating equation (51) one obtains

$$\check{g}_{1s}\check{G}_{1s} + \check{g}_{2s}\check{G}_{2s} = \check{g}_a(\check{g}_{1s}\check{G}_{1s} - \check{g}_{2s}\check{G}_{2s}) \quad (53)$$

which is the extra condition to be used together with equations (45-46). By means of equations (45-46) one expresses \check{G}_{2s} and \check{G}_{1s} in terms of \check{g}_{1s} and \check{g}_{2s} and substitute in equation (53) so that the final boundary condition reads [2]

$$\check{g}_a \left[R(1 - \check{g}_a\check{g}_a) + (T/4)(\check{g}_{1s} - \check{g}_{2s})^2 \right] = (T/4)(\check{g}_{2s}\check{g}_{1s} - \check{g}_{1s}\check{g}_{2s}) \quad (54)$$

where $R = |r|^2$, $T = 1 - R$ are the reflection and transmission coefficient of the barrier. To conclude this Section, I consider the normal case, when the Green's function reduces to a two-by-two matrix

$$\check{g} = \begin{pmatrix} 1 & g \\ 0 & -1 \end{pmatrix} \quad (55)$$

with $g = 2f$, f being the usual distribution function entering the Boltzman kinetic equation. By observing that

$$[\check{g}_{1s}, \check{g}_{2s}] = 4 \begin{pmatrix} 0 & f_{1s} - f_{2s} \\ 0 & 0 \end{pmatrix}; \quad (\check{g}_{1s} - \check{g}_{2s})^2 = 0; \quad \check{g}_a^2 = 0 \quad (56)$$

the boundary condition (54) assumes the form (10) of Section II.

V THE DIRTY LIMIT

In this Section, I show how the effective boundary conditions, derived in the previous Section can be considerably simplified in the dirty limit. For the sake of completeness I first briefly recall how one goes from the general case to the dirty limit. One starts from the quasiclassical equation for \check{g} [1]

$$\partial_T \{\check{\tau}_z, \check{g}\} + v_F \hat{k} \cdot \partial_{\mathbf{R}} \check{g} - i\epsilon [\check{\tau}_z, \check{g}] + i [\check{\Sigma}, \check{g}] = 0, \quad (57)$$

where the square and curly brackets indicate the commutator and the anticommutator, respectively. In eq.(57), $\mathbf{R} = (\mathbf{r} + \mathbf{r}')/2$, $T = (t + t')/2$ and ϵ is the Fourier transformed variable with respect to $t - t'$. In the presence of an isotropic scattering impurity potential, the self-energy in the self-consistent Born approximation reads

$$\check{\Sigma} = -\frac{i}{2\tau} < \check{g} >, \quad (58)$$

and one expands \check{g} in spherical harmonics keeping only the s- and p-wave terms

$$\check{g}(\mu) = \check{g}_0 + \mu \check{g}_1 \quad (59)$$

with \check{g}_0 and \check{g}_1 not depending on μ and $\mu\check{g}_1 \ll \check{g}_0$. By inserting equation (59) in equation (57), \check{g}_1 is expressed in terms of \check{g}_0

$$\check{g}_1 = -l\check{g}_0\partial_{\mathbf{R}}\check{g}_0 \quad (60)$$

and for \check{g}_0 one obtains a diffusion-like equation

$$D\partial_{\mathbf{R}}\check{g}_0\partial_{\mathbf{R}}\check{g}_0 + i\epsilon[\check{\tau}_z, \check{g}_0] - \partial_T\{\check{\tau}_z, \check{g}_0\} = 0 \quad (61)$$

with $D = v_F l \tau / 3$ the diffusion coefficient and $l = v_F \tau$ the mean free path. Kupriyanov and Lukichev [3] have shown that by assuming

$$T(\check{g}_{1s} - \check{g}_{2s}) \ll (\check{g}_{1s} + \check{g}_{2s}), \quad T(\check{g}_{1s} - \check{g}_{2s})^2 \ll R, \quad (62)$$

in the dirty limit, the boundary condition (54) reduces to

$$\check{g}_a = (T/4R)[\check{g}_{1s}, \check{g}_{2s}]. \quad (63)$$

In the next Section, I will show that eq.(63) is strictly valid in the low transparency limit, $T \ll 1$ (in which limit the conditions (62) are clearly satisfied), and modified boundary conditions result by a perturbative expansion in the boundary transparency. In the dirty limit, $\check{g}_a = -\mu l \check{g}_s \partial_{\mathbf{R}} \check{g}_s$ and equation (47) yields

$$l\check{g}_{1s}\partial_{\mathbf{R}}\check{g}_{1s} = l\check{g}_{2s}\partial_{\mathbf{R}}\check{g}_{2s}, \quad (64)$$

which after multiplying equation (63) by μ and taking the angular average yields

$$l\check{g}_{1s}\partial_{\mathbf{R}}\check{g}_{1s} = \frac{3}{4} < \mu T / R > [\check{g}_{2s}, \check{g}_{1s}]. \quad (65)$$

By defining a conserved "super" current \check{I} one finally arrives at the following boundary condition

$$\check{I} = \frac{\sigma}{e} \check{g}_{2s} \partial_{\mathbf{R}} \check{g}_{2s} = \frac{G_T}{2e} [\check{g}_{2s}, \check{g}_{1s}]. \quad (66)$$

Equation (66) is the desired boundary condition to be used together with the diffusion equation (61) in the presence of boundaries [3].

I now consider two simple applications of the formula (66), i.e., the case of a S-I-S and S-I-N structures, where I indicates an insulating thin layer or a tunnel junction. The physical current is obtained from the Keldysh component of equation (66)

$$[\check{g}_2, \check{g}_1]_k = \hat{g}_2^R \hat{g}_1 + \hat{g}_2 \hat{g}_1^A - \hat{g}_1^R \hat{g}_2 - \hat{g}_1 \hat{g}_2^A$$

where we have dropped the subscript "s" (the "a" component has now disappeared). The normalization condition, $\check{g}\check{g} = \check{1}$, allows us to choose

$$\hat{g}_{1,2} = \hat{g}_{1,2}^R \hat{f}_{1,2} - \hat{f}_{1,2} \hat{g}_{1,2}^A$$

where the matrix \hat{f} can be taken to be diagonal

$$\hat{f}_{1,2} = f_{1,2}^0 \hat{\tau}_0 + f_{1,2}^z \hat{\tau}_z.$$

As a result, multiplying by $\hat{\tau}_z$ and taking the trace, yields

$$j = \frac{G_T}{16e} \int_{-\infty}^{\infty} d\epsilon \text{Tr}(\hat{\tau}_z(f_1^0 \hat{I}_a + f_2^0 \hat{I}_b + f_1^z \hat{I}_c + f_2^z \hat{I}_d)) \quad (67)$$

where

$$\hat{I}_a = [\hat{g}_2^R(\hat{g}_1^R - \hat{g}_1^A) - (\hat{g}_1^R - \hat{g}_1^A)\hat{g}_2^A], \quad \hat{I}_b = -[\hat{g}_1^R(\hat{g}_2^R - \hat{g}_2^A) - (\hat{g}_2^R - \hat{g}_2^A)\hat{g}_1^A]$$

$$\hat{I}_c = [\hat{g}_2^R(\hat{g}_1^R \hat{\tau}_z - \hat{\tau}_z \hat{g}_1^A) - (\hat{g}_1^R \hat{\tau}_z - \hat{\tau}_z \hat{g}_1^A)\hat{g}_2^A],$$

$$\hat{I}_d = -[\hat{g}_1^R(\hat{g}_2^R \hat{\tau}_z - \hat{\tau}_z \hat{g}_2^A) - (\hat{g}_2^R \hat{\tau}_z - \hat{\tau}_z \hat{g}_2^A)\hat{g}_1^A].$$

Due to the normalization condition $\hat{g}^{R(A)} \hat{g}^{R(A)} = \hat{1}$, we have

$$\hat{g}^{R(A)} = \mathbf{g}^{R(A)} \cdot \boldsymbol{\tau} \equiv \sum_{i=1}^3 g_i^{R(A)} \tau_i$$

where $\mathbf{g}^{R(A)} = (iF^{R(A)} \sin(\phi), iF^{R(A)} \cos(\phi), G^{R(A)})$ and ϕ is the phase of the superconducting order parameter. Hence

$$j = \frac{G_T}{8e} \int_{-\infty}^{\infty} d\epsilon (I_J + I_{PI}) \quad (68)$$

where

$$I_J = i \sin(\phi_1 - \phi_2) [f_2^0 (F_2^R - F_2^A)(F_1^R + F_1^A) + f_1^0 (F_2^R + F_2^A)(F_1^R - F_1^A)]$$

and

$$I_{PI} = [(G_1^R - G_1^A)(G_2^R - G_2^A) + \cos(\phi_1 - \phi_2)(F_2^R + F_2^A)(F_1^R + F_1^A)](f_1^z - f_2^z).$$

In equation (68), I_J is the Josephson current, while I_{PI} is sometimes referred to as quasi-particle (first term) and interference or Andreev (second term) currents. To see this, consider first the case of a superconducting-insulating-superconducting (S-I-S) junction, with no applied bias. In this case, $f_i^z = 0$ ($i = 1, 2$), and $f_1^0 = f_2^0 = \tanh(\epsilon/2T)$ by assuming that the two superconductors are at equilibrium. By recalling that for a bulk superconductor

$$F^{R(A)} = \frac{\Delta}{\sqrt{(\epsilon \pm i0^+)^2 - \Delta^2}}$$

one obtains for the current

$$j = \frac{G_T}{2e} \int_{-\infty}^{\infty} d\epsilon \tanh(\epsilon/2T) \text{Im} \frac{\Delta^2}{(\epsilon \pm i0^+)^2 - \Delta^2} = G_T \frac{\pi\Delta}{2e} \tanh(\Delta/2T) \quad (69)$$

which coincides with the standard result of the tunneling theory. As a second illustration of the formula (68), consider the case of a normal metal-insulating-superconducting (N-I-S) junction. In this case there is no Josephson current ($\phi_1 = \phi_2$), though the anomalous Green's function F may be different from zero even in the normal region due to the proximity effect. If the distribution functions $f_{1,2}^z$ have their equilibrium form,

$$f_{1,2}^z = \frac{1}{2} (\tanh((\epsilon + eV_{1,2})/2T) - \tanh((\epsilon - eV_{1,2})/2T))$$

the current through the junction becomes

$$j = \frac{G_T}{2e} \int_{-\infty}^{\infty} d\epsilon (f_1^z - f_2^z) M_{12} \quad (70)$$

where

$$M_{12} = \frac{1}{4} ((G_1^R - G_1^A)(G_2^R - G_2^A) + (F_2^R + F_2^A)(F_1^R + F_1^A)).$$

At $T = 0$, this reduces to

$$I = G_T M_{12}|_{\epsilon=0} (V_1 - V_2). \quad (71)$$

Equation (71) shows that conductance of the tunnel junction is renormalized by a term M_{12} which depends on the amount of superconducting pairing on the two sides of the junction. In the limit of normal systems, $M_{1,2} = 1$, and one recovers the conductance of the normal state (cf. eq(11)). It is worth to note that the above equation has been extensively used during the last five years to analyze the transport properties of hybrid superconducting structures (cf. Ref. [4] for more details).

VI BEYOND THE SMALL BARRIER TRANSPARENCY LIMIT

One of the key features allowing a substantial simplification of the boundary conditions in the dirty limit is that the angular dependence of the quasiclassical Green's function \tilde{g} can be taken into account by keeping only the first two terms in an expansion in Legendre polynomials $P_n(\mu)$ (cf. eqs.(59-60)). In the presence of a boundary, due to the fact that the scattering coefficients, R and T , depend on μ , one should, in principle, keep all the terms in the expansion in Legendre polynomials. However, all terms $n \geq 2$ in the expansion of \tilde{g} decay exponentially over a distance l , and it would be desirable to obtain a matching condition at the

boundary involving only the lowest term ($n = 0$) in the expansion. In this Section we show how to obtain this beyond the small barrier transparency limit, by using an expansion in the small parameter $r^{-1} = T/2R$ [5]. By assuming that $r \gg 1$, eq.(54) can be cast in the form

$$\check{b}(0, \mu) \approx \frac{1}{2r\mu} [\check{g}_{2s}, \check{g}_{1s}] \left(1 - \frac{1}{2r} (\check{g}_{2s} - \check{g}_{1s})^2 \right) \quad (72)$$

where we introduced the function $\check{b} = \check{g}_a/\mu$. Eq.(72) is valid up to terms of the order r^{-2} . We proceed by writing \check{g}_s and \check{b} as the sum of a fast decaying and an asymptotic part

$$\check{g}_s = \check{g}_{s\infty} + \delta\check{g}_s, \quad \check{b} = \check{b}_\infty + \delta\check{b} \quad (73)$$

where we assume $\delta\check{g}_s \ll \check{g}_{s\infty}$. By multiplying eq.(72) by μ^2 and using the representation (73), we perform the angle average of eq.(72) to obtain

$$\begin{aligned} \frac{1}{3}\check{b}_\infty = [\check{g}_{2s\infty}, \check{g}_{1s\infty}] & \left(\langle \frac{\mu}{2r} \rangle - \langle \frac{\mu}{4r^2} \rangle (\check{g}_{2s\infty} - \check{g}_{1s\infty})^2 \right) \\ & + \langle \frac{\mu}{2r} ([\check{g}_{2s\infty}, \delta\check{g}_{1s}] + [\delta\check{g}_{2s}, \check{g}_{1s\infty}]) \rangle. \end{aligned} \quad (74)$$

In obtaining eq.(74) it has been used the fact that the quantity $\langle \mu^2 \check{b} \rangle$ does not depend on the spatial coordinate (see the equation of motion below) and one can perform the angular average in the asymptotic region. Here $\delta\check{g}_{2s,1s} = \delta\check{g}_{2s,1s}(0^\pm)$. The problem is then reduced to the calculation of the functions $\delta\check{g}_{2s,1s}$. We start by writing the equation for \check{g} in the space interval $0 < |z| \ll \xi_{N,S}$. It is then sufficient to retain only the gradient term and the collision integral in the self-consistent Born approximation for the impurity scattering. As a result the equation for \check{g} reads [1]

$$2\mu\check{g}' = \check{g} < \check{g} > - < \check{g} > \check{g} \quad (75)$$

where for brevity $\check{g}' \equiv l\partial_z$. By rewriting eq.(75) in terms of \check{b} and \check{g}_s we get

$$2\mu^2\check{b}' = \check{g}_s < \check{g}_s > - < \check{g}_s > \check{g}_s \quad (76)$$

$$2\check{g}'_s = \check{b} < \check{g}_s > - < \check{g}_s > \check{b} \quad (77)$$

together with the conditions deriving from the normalization condition $\check{g}\check{g} = \check{1}$,

$$\check{g}_s\check{g}_s = 1, \quad \check{g}_s\check{b} + \check{b}\check{g}_s = 0. \quad (78)$$

Using the expansion (73) we obtain the equations for the deviations $\delta\check{b}$ and $\delta\check{g}_s$ in the form

$$\mu^2\delta\check{b}' = -\check{g}_{s\infty}(\delta\check{g}_s - < \delta\check{g}_s >) \quad (79)$$

$$\delta \check{g}'_s = -\check{g}_{s\infty} \delta \check{b} \quad \check{g}'_{s\infty} = -\check{g}_{s\infty} \check{b}_\infty. \quad (80)$$

where we have used the relations

$$\delta \check{b} \check{g}_{s\infty} + \check{g}_{s\infty} \delta \check{b} = 0, \quad \check{g}_{s\infty} \delta \check{g}_s + \delta \check{g}_s \check{g}_{s\infty} = 0 \quad (81)$$

$$\check{g}_{s\infty} \check{g}_{s\infty} = 1 \quad (82)$$

which follow from (78). From eqs.(79-80) we finally get the equation for $\delta \check{b}$

$$\mu^2 \delta \check{b}'' - \delta \check{b} = - < \delta \check{b} > + \check{B}_0 \delta(z/l). \quad (83)$$

One can easily check that the matrix \check{B}_0 is connected to the Fourier component $\delta \check{b}_{q_0}$ (where $q_0 \equiv 0$) by

$$\check{B}_0 = < \delta \check{b}_{q_0} > - \delta \check{b}_{q_0}. \quad (84)$$

From eq.(83) we find the Fourier components

$$\delta \check{b}_q = m_q \left(\frac{q^2}{1 - < m_q >} < m_q \mu^2 \check{B}_0 > - \check{B}_0 \right) \quad (85)$$

and the value of $\delta \check{b}(0, \mu)$ at $z = 0$ reads

$$\begin{aligned} \delta \check{b}(0, \mu) &\equiv \check{b}(0, \mu) - \check{b}_\infty = \\ &- \int_{-\infty}^{\infty} \frac{dq}{2\pi} m_q \left(\frac{q^2}{1 - < m_q >} < m_q \mu^2 \delta \check{b}_{q_0} > - \delta \check{b}_{q_0} \right). \end{aligned} \quad (86)$$

To close the above equation, we need to connect $\check{b}(0, \mu)$ and \check{b}_∞ . To lowest order in r^{-1} , the boundary condition (74) yields

$$\begin{aligned} \check{b}(0, \mu) &\approx (2r\mu)^{-1} [\check{g}_{2s\infty}, \check{g}_{1s\infty}], \\ \check{b}_\infty &\approx 3 < \mu/2r > [\check{g}_{2s\infty}, \check{g}_{1s\infty}]. \end{aligned} \quad (87)$$

which when substituted into (86) yields the equation

$$\begin{aligned} \check{b}_\infty \left(\frac{1}{3\mu r < \mu/r >} - 1 \right) = \\ - \int_{-\infty}^{\infty} \frac{dq}{2\pi} m_q \left(\frac{q^2}{1 - < m_q >} < m_q \mu^2 \delta \check{b}_{q_0} > - \delta \check{b}_{q_0} \right). \end{aligned} \quad (88)$$

If we seek the solution in the form

$$\delta\check{b}_{q_0} = -\chi(\mu)\check{b}_\infty \quad (89)$$

then the function χ satisfies the integral equation

$$\frac{1}{3\mu r < \mu/r >} - 1 = -\frac{\chi(\mu)}{2\mu} + \int_0^1 d\mu_1 \mathcal{K}(\mu, \mu_1) \chi(\mu_1) \quad (90)$$

where

$$\mathcal{K}(\mu, \mu_1) = \int_{-\infty}^{\infty} \frac{dq}{2\pi} m_q(\mu) m_q(\mu_1) \frac{q^2 \mu_1^2}{1 - < m_q >}.$$

Details concerning the numerical solution of the above integral equation may be found in Ref. [5]. In the following I will confine the discussion to the qualitative consequences of the modified boundary conditions and the actual numerical solution will not be needed. The Fourier component $\delta\check{b}_{q_0}$ is related to $\delta\check{g}_{1s,2s}$ by integrating eq.(80) from $-\infty$ to 0 and from 0 to ∞ , to yield

$$\delta\check{g}_{2s} = \check{g}_{2s\infty} \delta\check{b}_{q_0}/2, \quad \delta\check{g}_{1s} = -\check{g}_{1s\infty} \delta\check{b}_{q_0}/2. \quad (91)$$

Substituting eqs.(91), (89), and (87) into eq.(74) we finally obtain

$$\begin{aligned} \frac{\check{b}_\infty}{3} &= [\check{g}_{2s\infty}, \check{g}_{1s\infty}] \left(< \frac{\mu}{2r} > - < \frac{\mu}{4r^2} > (\check{g}_{2s\infty} - \check{g}_{1s\infty})^2 \right) \\ &+ 3 < \frac{\mu\chi}{2r} > < \frac{\mu}{2r} > [\check{g}_{1s\infty}, \check{g}_{2s\infty} \check{g}_{1s\infty} \check{g}_{2s\infty}]. \end{aligned} \quad (92)$$

The above equation is the effective boundary condition for the matrix \check{g} in the dirty limit. The first term in (92) coincides with the boundary condition obtained in Ref. [3]. As a simple application of the above boundary condition, we now derive an expression for the Josephson current. To this end we rewrite eq.(92) in the following way

$$\frac{1}{3}\check{b} = A[\check{g}_2, \check{g}_1] + B[\check{g}_2, \check{g}_1]\{\check{g}_2, \check{g}_1\} \quad (93)$$

where we have identified the symmetric part \check{g}_s with the Green's function \check{g} and dropped the ∞ suffix. The constants A and B can be read off from eq.(92)

$$A = < \mu/r > - 2 < \mu/4r^2 >, \quad B = < \mu/4r^2 > - 3 < \mu\chi/2r > < \mu/2r >.$$

In deriving eq.(93) we have made use of the normalization condition $\check{g}\check{g} = \check{1}$. The current through the junction is determined by the formula

$$I = -\frac{\sigma}{16el} \int_{-\infty}^{\infty} d\epsilon \text{Tr}(\hat{\tau}_z \hat{b}) \quad (94)$$

where \hat{b} is the appropriate Keldysh component of the "check" matrix \check{b} . In the absence of a voltage across the junction, the Keldysh component of the supermatrix \check{g} reduces to

$$\hat{g} = f_0(\hat{g}^R - \hat{g}^A) \quad (95)$$

where $f_0 = \tanh(\epsilon/2T)$ is the equilibrium distribution function. The Keldysh component of the product of the commutator and the anticommutator reads

$$([\check{g}_2, \check{g}_1]\{\check{g}_2, \check{g}_1\})_k = [\hat{g}_2^R, \hat{g}_1^R]\{\check{g}_2, \check{g}_1\}_k + [\check{g}_2, \check{g}_1]_k\{\hat{g}_2^A, \hat{g}_1^A\} \quad (96)$$

with the Keldysh component of the commutator

$$[\check{g}_2, \check{g}_1]_k = f_0([\hat{g}_2^R, \hat{g}_1^R] - [\hat{g}_2^A, \hat{g}_1^A]) \quad (97)$$

and of the anticommutator

$$\{\check{g}_2, \check{g}_1\}_k = f_0(\{\hat{g}_2^R, \hat{g}_1^R\} - \{\hat{g}_2^A, \hat{g}_1^A\}). \quad (98)$$

The current in eq.(94) can be written then as the sum of three terms

$$I_A = -iI_{0,A}\sin(\phi_1 - \phi_2) \int_{-\infty}^{\infty} d\epsilon f_0(F_1^R F_2^R - F_1^A F_2^A), \quad (99)$$

$$I_B^{(1)} = -iI_{0,B}2\sin(\phi_1 - \phi_2)$$

$$\int_{-\infty}^{\infty} d\epsilon f_0(F_1^R F_2^R G_1^R G_2^R - F_1^A F_2^A G_1^A G_2^A), \quad (100)$$

and

$$I_B^{(2)} = -iI_{0,B}\sin(2(\phi_1 - \phi_2))$$

$$\int_{-\infty}^{\infty} d\epsilon f_0((F_1^R F_2^R)^2 - (F_1^A F_2^A)^2). \quad (101)$$

In the above formulae $I_{0,A} = (eN_0v_F/2)A$, $I_{0,B} = (eN_0v_F/2)B$. By using the expression for $G^{R(A)}$ and $F^{R(A)}$ at equilibrium and assuming that the gap Δ is equal on both sides of the junction, we obtain, at $T = 0$, the following result for the current

$$I = \frac{eN_0v_F\Delta\pi}{2} [(2A + B)\sin(\phi) - B\sin(2\phi)] \quad (102)$$

where $\phi = \phi_2 - \phi_1$. Note that by confining ourselves to the lowest order in r^{-1} , we would obtain for the Josephson current the standard result of tunneling theory (cf. eq.(69)). Allowance for higher order terms in the barrier transparency leads then to higher harmonics in the current phase relation. This result has a simple physical interpretation. We know that in the case of a superconductor - normal metal - superconductor structure, the Josephson effect manifests itself with a triangular shape of the current - phase relation. For this case the Fourier decomposition has an infinite number of harmonics. Hence it is clear that higher order terms in the r^{-1} expansion must possess harmonics of higher order.

REFERENCES

1. A I Larkin and Y N Ovchinnikov *Nonequilibrium superconductivity* edited by D N Langenberg and A I Larkin (North-Holland, Amsterdam, 1986) and references therein.
2. A V Zaitsev *Sov. Phys. JETP* **59**, 863 (1984).
3. M Y Kuprianov and V F Lukichev *Sov. Phys. JETP* **64**, 139 (1989).
4. C J Lambert and R Raimondi, cond-mat/9708056.
5. C J Lambert, R Raimondi, V Sweeney, and A F Volkov *Phys. Rev. B* **55**, 6015 (1997).
6. For an introduction to the Boltzmann equation see for example N. W. Ashcroft and N. D. Mermin *Solid State Physics* 1976, Chap.13 and 17. In particular eq.(16.13) and (16.18) are a convenient starting point to derive eq.(1).
7. L V Keldysh *Sov. Phys. JETP* **20**, 1018 (1965).
8. A L Shelankov *J. L. T. Phys.* **60**, 29 (1984).

Phase-coherent transport in hybrid superconducting nanostructures.

C.J. Lambert

School of Physics and Chemistry, Lancaster University, Lancaster LA1 4YB, U.K.
August 26, 1997

Abstract. These lectures provide an overview of the multiple scattering approach to quasi-particle transport in phase-coherent superconducting nanostructures, with particular emphasis on dc electrical conduction. Several paradigms of phase-coherent transport are discussed, including zero-bias anomalies, reentrant and long range proximity effects, Andreev interferometers and superconductivity-induced conductance suppression.

I INTRODUCTION

These lectures will review the multiple scattering approach to phase-coherent quasi-particle transport in hybrid superconducting nanostructures. In a phase-coherent normal-superconducting (N-S) structure, the phase of quasi-particles as well as Cooper pairs is preserved and transport properties depend in detail on the quasi-particle states produced by elastic scattering from inhomogeneities and boundaries. A key physical phenomenon, which arises in the presence of superconductivity is the possibility that an electron can coherently evolve into a hole and vice versa. This phenomenon, known as Andreev scattering [Andreev 1964], occurs without phase breaking and is describable by a variety of theoretical techniques. The effect of superconductivity on transport across a N-S interface is of course an old subject. In lowest order, the classical tunneling Hamiltonian approach ignores Andreev scattering and predicts that the dc conductance G is proportional to the density of states. Later [Shelankov 1980, Blonder, Tinkham and Klapwijk (BTK) 1982, Blonder and Tinkham 1983, Shelankov 1984] it was pointed out that the contribution to the sub-gap conductance from Andreev scattering can be significant and a theory of a clean N-I-S interface was developed, which showed that for a delta-function barrier, there is indeed a marked deviation from tunneling theory, but as the barrier strength is increased, the result of classical tunneling theory is recovered. BTK theory applies to a one-dimensional N-I-S

system or, by summing over all transverse wavevectors, to 2 or 3 dimensional systems with translational invariance in the plane of the barrier and yields for the current I through the contact

$$I = (2e/h)\Omega \int_{-\infty}^{\infty} dE (f(E - eV) - f(E))(1 + A(E) - B(E)) \quad (1)$$

where $A(E)$ and $B(E)$ are Andreev and normal reflection coefficients listed in table II of [Blonder et al 1982], $f(E)$ the Fermi function and Ω a measure of the area of the junction. In the presence of disorder or other inhomogeneities, this must be replaced by the more general expressions outlined in sections II and IV below.

Prior to 1991, experiments on N-I-S point contacts had been in broad agreement with BTK theory, exhibiting a conductance minimum at zero voltage $V = 0$ and a peak at $eV \approx \Delta$, where Δ is the superconducting energy gap. However in the experiment of Kastalskii et al. [1991], the dc current through a Nb-InGaAs contact is measured as function of the applied voltage. At the interface, depending on the semiconductor doping level, a Schottky barrier naturally forms so that the system behaves like a superconductor-insulator-normal (S-I-N) structure. (An exception to this is InAs, which does not form a Schottky barrier at an N-S interface.) According to BTK theory, as the barrier strength increases the sub-gap conductance should vanish. In contrast, the experiment revealed an excess sub-gap conductance at low bias, whose value was comparable with the conductance arising when the superconducting electrode is in the normal state. This zero bias anomaly (ZBA) was later observed by Nguyen et al. [1992] in an experiment involving InAs-AlSb quantum wells attached to superconducting Nb contacts and by using high transmittance Nb-Ag (or Al) contacts of varying geometry, Xiong et al. [1993] were able to observe the evolution from BTK to ZBA behaviour. In an experiment by Bakker et al. [1994] involving a silicon-based two-dimensional electron gas (2DEG) contacted to two superconducting electrodes, a gate voltage was also used to control the strength of the ZBA and in [Magnee et al 1994] an extensive study of the ZBA in Nb/Si structures was performed. Since these early experiments, a great deal of effort has been aimed at observing Andreev scattering in ballistic 2DEGs, including [van Wees et al 1994, Dimoulas et al 1995, Marsh et al 1994, Takayanagi and Akazaki 1995(a), Takayanagi, Toyoda and Akazaki 1996(a)]

Kastalskii et al [1991] attributed the excess conductance to a non-equilibrium proximity effect, in which superconductivity is induced in the normal electrode, giving rise to an excess pair current. Initially this phenomenon was seen as separate from Andreev reflection, but subsequent theoretical developments have shown that the distinction between the proximity effect and Andreev reflection is artificial. As will become clear later, the ZBA arises from an interplay between Andreev scattering and disorder-induced scattering in the normal electrode. Andreev scattering is sensitive to the breaking of time

reversal symmetry and as a consequence the conductance peak is destroyed by the introduction of a magnetic field.

Zero bias anomalies constitute the first of a small number of paradigms of phase-coherent transport in hybrid N-S structures. A second paradigm is the observation of re-entrant [van Wees et al 1994, Charlat et al 1996] and long-range [Courtois et al 1996] behaviour signalled by the appearance of finite-bias anomalies (FBAs) in the conductance of high-quality N-S interfaces. At high temperatures $T > T^*$ and bias-voltages $V > V^*$, where for a N-metal of length L and diffusion coefficient D , $k_B T^* = eV^* = \sqrt{(D/L^2)}$, both the ZBA and FBA conductance peaks decay as $1/\sqrt{T}$ and $1/\sqrt{V}$. For a clean interface there also exists a conductance maximum at V^* , T^* and therefore at low-temperature and voltage a re-entrance to the low-conductance state occurs. An interesting feature of this phenomenon is the long-range nature of the effect, which typically decays as a power-law in L^*/L , where $L^* = \sqrt{(D/eV)}$. This behaviour is in sharp contrast with the exponential decay of the Josephson effect and has been observed in a number of experiments. In a T-shaped Ag sample with Al islands at different distances from the current-voltage probes [Petrashov et al 1993(b)], a long-range proximity effect was observed, in which the influence of the island extended over length scales greater than the thermal coherence length L^* . Similar behaviour was also observed [Petrashov et al 1994] in ferromagnetic-superconductor hybrids made from Ni-Sn and Ni-Pb. In an experiment involving a square Cu loop in contact with 2 Al electrodes Courtois et al [1996] clearly identified both the short- and long-range contributions to phase-coherent transport. In this interferometer experiment, they observed a phase-periodic conductance decaying as a power-law in $1/T$, in parallel with a Josephson current which decays exponentially with L/L_T .

The above re-entrance phenomenon is also observed in a third paradigm of phase-coherent transport, which arises when a normal metal is in contact with two superconductors, with order parameters phases ϕ_1 and ϕ_2 , whose difference $\phi = \phi_1 - \phi_2$ can be varied by some external means. Prior to the experimental realisation of these structures, the electrical conductance of such Andreev interferometers was predicted to be an oscillatory function of ϕ . Spivak and Khmel'nitskii [1982] and Al'tshuler and Spivak [1987] identified a high temperature ($T \gg T^*$), weak localisation contribution to the conductance of a disordered sample, whose amplitude of oscillation was less than or of order $2e^2/h$. For an individual sample, the period of oscillation was found to be 2π , but for the ensemble average a period of π was predicted. Nakano and Takayanagi [1991] and Takagi [1992] examined a clean interferometer in one-dimension and again predicted a 2π -periodic conductance with an amplitude of oscillation less than or of order $2e^2/h$. Lambert [1993] examined a disordered conductor in the low-temperature limit ($T \ll T^*$) and identified a new contribution to the ensemble averaged conductance with a periodicity

of 2π . This 2π periodicity is a consequence of particle-hole symmetry, which also guarantees that at zero temperature and voltage, the conductance should possess a zero phase extremum [Lambert 1994]. Prior to experiments on such devices, the generic nature of this prediction was confirmed in numerical simulations [Hui and Lambert 1993(a)] encompassing the ballistic, diffusive and almost localised regimes and in a tunnelling calculation of the ensemble averaged conductance by Hekking and Nazarov [1993].

The first experimental realisations of Andreev interferometers came almost simultaneously from three separate groups. In March of 1994, de Vegvar et al [1994] showed results for a structure formed from two Nb electrodes in contact with an Al wire. They found a small oscillation $10^{-3}(2e^2/h)$ with a sample specific phase in the 2π periodic component, suggesting that the ensemble averaged conductance should have a periodicity of π , in agreement with Spivak and Khmel'nitskii [1982]. However in contrast with all subsequent experiments, no zero phase extremum was observed. In April/May of that year, Pothier et al [1994] produced an interferometer involving two tunnel junctions, which showed a 2π -periodic conductance, with a zero phase maximum and a low-bias, low-temperature amplitude of oscillation of order $10^{-2}(2e^2/h)$, which decayed with increasing temperature. In May 1994, van Wees et al [1994], [see also Dimoulas et al 1995] produced the first quasi-ballistic InAs 2DEG interferometer, with high transparency N-S interfaces. This experiment showed the first re-entrant behaviour in which the amplitude of oscillation δG varied from $\delta G \approx -0.08(2e^2/h)$ at zero voltage, (where a minus sign indicates a zero phase minimum and a + sign a zero-phase maximum) passes through zero at a bias of order 0.1mV, reaches a maximum at a bias of order V^* and then decays to zero at higher voltages. (For a detailed study see [den Hartog et al, 1996]). Unlike the Josephson current which decays exponentially with T/T^* , these conductance oscillations decayed only as a power-law.

The first experiment showing an amplitude of oscillation greater than $2e^2/h$ was carried out by Petrashov et al [1995]. Here, silver or antimony wires in the shape of a cross, make two separate contacts with superconducting Al and the phase difference between the contacts is varied using either an external field applied to a superconducting loop or by passing a supercurrent through the Al. The amplitude was found to be $\delta G \approx 100(2e^2/h)$ for Ag and $3.10^{-2}(2e^2/h)$ for Sb, and exhibited a periodicity of 2π . In this experiment, the phase difference ϕ was varied both by passing a magnetic flux through an external superconducting loop and by passing a supercurrent through a straight section of the superconductor, thereby emphasising that precise the manner in which the order parameter phase is controlled is not important. These experiments were crucial in demonstrating that in metallic samples, the ensemble averaged conductance is the relevant quantity and therefore a quasi-classical description is relevant. It is perhaps worth mentioning that with hindsight, an earlier experiment reporting large-scale oscillations in a sample with two superconducting islands [Petrashov et al 1993(a)] can be

regarded a precursor to these interferometer experiments. However the phase of the islands was not explicitly controlled, making an interpretation of the 1993 experiments more difficult.

A fourth and more recent paradigm of phase-coherent transport is the appearance of negative multi-probe conductances in structures where Andreev transmission of quasi-particles is a dominant process [Allsopp et al 1994]. The first experiments reporting this behaviour were carried out by Hartog et al [1996], using a diffusive InAs 2DEG. These probe individual coefficients in the current-voltage relations and demonstrate fundamental reciprocity relations arising from time-reversal and particle-hole symmetry.

Finally a fifth paradigm is the suppression of electrical conductance by superconductivity in metallic systems without tunnel barriers. Experimentally this phenomenon has been observed in several structures, involving both non-magnetic (ie Silver) and magnetic (ie Nickel) N-components in contact a superconductor via clean interfaces. In the experiment of Petrashov and Antonov [1991] the conductance of a Ag wire on which several Pb islands are deposited, decreases by 3% when the islands become superconducting, this corresponding to a conductance decrease of $\delta G \approx 100 (2e^2/h)$. These experiments reveal two regimes: as the field decreases below H_{c2} , an initial resistance increase occurs. The resistance remains field insensitive until a lower field is reached (corresponding to the order of a flux quantum through the sample), at which point a further conductance suppression occurs. In the experiment by Petrashov et al [1993b] involving a T-shaped Ag sample with Al islands at different distances from the current-voltage probes, a superconductivity induced change in the resistance by up to 30% was observed, but it was found that for different samples, the resistance could either increase or decrease. Although superconductivity-induced conductance suppression in metallic samples was predicted a number of years ago [Hui and Lambert, 1993(b)] these experiments at first sight appeared to conflict with quasi-classical theories, which universally predict that the normal-state, zero-temperature, zero-bias conductance G_N is identical the conductance G_{NS} in the superconducting state. This effect is addressed in [Hui and Lambert 1993b, Claughton et al 1995, Wilhelm et al 1997, Seviour et al 1997].

The main aim of these lectures is to review the multiple scattering theory of dc electrical conductance of phase-coherent hybrid N-S structures. For this reason we shall not discuss thermodynamic phenomena such as the Josephson effect in any detail, despite the fact that ground-breaking experiments using clean [Takayanagi and Akazaki, 1995(b,c,d)] superconducting quantum S-2DEG-S point contacts show quantization of the critical current as predicted by Furasaki et al [1991] and for shorter junctions by Beenaker and van Houten [1991]. There are several notable theoretical papers addressing Andreev scattering in such structures, including [van Wees et al 1991, Bagwell 1992, Furasaki et al 1994, Gusenheimer and Zaikin 1994, Zyuzin 1994, Hurd and Wendin 1994 and 1995, Bratus et al 1995, Chang et al 1995, Koyama,

Takane and Ebisawa 1995 and 1996, Levy Yeyati et al 1996, Martin-Rodero 1996, Wendin and Shumeiko 1996, Reidel et al 1996, Volkov and Takayanagi 1996(b)]. Similarly to restrict the length of these lectures, recent theories of thermoelectric coefficients [Bagwell and Alam 1992, Claughton and Lambert 1996] and shot noise will not be discussed, nor will we discuss work on coulomb effects in superconducting islands [Eiles et al 1993, Lafarge et al 1993, Tuominen et al 1992 and 1993, Hergenrother et al 1994, Black et al 1996, Hekking et al 1993].

While Andreev interference effects are generic phenomena, their manifestation in a given experiment is sensitive to many parameters. For the purpose of these lectures, it is therefore convenient to adopt a simple classification of experimental arrangements sketched in figure 1. The generic structure shown in figure 1a represents our first class of N-S-N hybrids and has many realisations. For convenience, we distinguish these from a second class of N-S hybrids of the kind shown in figure 1b and 1c, in which the superconductor effectively forms part of an external reservoir and is not simply part of the scattering region. Figure 1d indicates a third class of N-SS'-N structures, involving two (or more) separate superconductors S and S', with respective order parameter phases ϕ , ϕ' . As noted above, transport properties of such Andreev interferometers are periodic functions of the phase difference $\phi - \phi'$. Figure 1e shows a fourth class of S-N-S' structures, in which two superconducting reservoirs are connected to a normal scattering region. In this case, the structure forms a Josephson junction and in contrast with all other structures shown in figure 1, in the linear response limit, the dc conductance measured between the superconducting reservoirs is identically zero. In this case, the relevant dc quantity is the current-phase relation and the associated critical current. Clearly one could also measure the Josephson current between the two superconductors in the N-SS'-N structure of figure 1c and therefore the above classification is intended to label the measurement being made, rather than the device being measured. Structures of the form 1e will not be discussed.

For the most part, the theoretical descriptions discussed below have finessed problems of self-consistency, by computing measured quantities as a function of the superconducting order parameter pairing field $f_{\sigma\sigma'}(\mathbf{r}) = \langle \psi_{\sigma}(\mathbf{r}) \psi_{\sigma'}(\mathbf{r}) \rangle$ induced by making contact with a piece of superconductor. As an example, figure 1a shows a normal mesoscopic scattering region in contact with a superconducting island which plays the role of an externally controllable source of $f_{\sigma\sigma'}(\mathbf{r})$, in much the same way that the coils of a magnet are an external source of magnetic field. The coils are not of primary interest and in many cases, neither is the superconductor. It is assumed that parameters characterizing the superconductor are given and the key question is how does superconductivity influence transport through the scattering region. Of course once the influence of superconductivity is understood, transport properties can be used to probe the symmetry and spatial structure of the order parameter, as suggested by Cook et al. [1996]. Furthermore, in the presence of large currents which

modify the order parameter, a complete self-consistent treatment is necessary, as described for example in [Bruder 1990, Hara et al 1993, Barash et al 1995, Canizares and Sols 1995, Chang et al 1995, Martin and Lambert 1995 and 1996, Riedel et al 1996].

II THE MULTIPLE SCATTERING APPROACH TO DC TRANSPORT IN SUPERCONDUCTING HYBRIDS.

A Fundamental current-voltage relations.

In this section I review the multi-channel current-voltage relations for a disordered phase-coherent scatterer connected to normal reservoirs, obtained for two normal probes by [Lambert 1991] and extended to multi-probes by [Lambert Hui and Robinson, 1993]. To avoid time-dependent order parameter phases varying at the Josephson frequency, which would render a time-independent scattering approach invalid, these are derived under the condition that all superconductors share a common condensate chemical potential μ . The derivation of the fundamental current-voltage relation presented in [Lambert 1991] follows closely the multi-channel scattering theory developed during the 1980s for non-superconducting mesoscopic structures [Buettiker 1986, Buot 1993]. In the normal state, this approach yields, for example, the multi-channel Landauer formula [Landauer 1970] for the electrical conductance

$$G = (2e^2/h)T_0, \quad (2)$$

where T_0 is the transmission coefficient of the structure. Historically the above formula was not accepted without a great deal of debate and contradicts the corresponding expression used by practitioners of quasi-classical theories, where the alternative expression

$$G = (2e^2/h)(T_0/R_0) \quad (3)$$

is employed, with (in one-dimension) R_0 the reflection coefficient. In fact the above two expressions refer to different measurements and the crucial lesson from the debate surrounding these equations is that transport coefficients such as the electrical conductance are secondary quantities. More fundamental are the current-voltage relations describing a given mesoscopic structure.

Equations (2) and (3) are not valid in the presence of Andreev scattering, because charge transport and quasi-particle diffusion are no longer equivalent. For example when a quasi-particle Andreev reflects at an N-S interface, the energy and probability density of the excitation are reflected back into the

normal conductor, whereas a charge of $2e$ is injected into the superconductor. Thus charge flows into the superconductor, even though the excitation does not and as a consequence, a current-voltage relation should be used, which takes into account this charge-energy separation. For a scattering region connected to L normal reservoirs, labelled $i = 1, 2, \dots, L$, it is convenient to write this in the form

$$I_i = \sum_{j=1}^N A_{ij}, \quad (4)$$

where I_i is the current flowing from reservoir i and the coefficients A_{ij} will be discussed in detail below. In the linear-response limit, this reduces to

$$I_i = \sum_{j=1}^L a_{ij}(v_j - v), \quad (5)$$

The above expressions describe reservoirs at voltages v_i , $i = 1, 2, \dots, L$, connected to a scattering region containing one or more superconductors with a common condensate chemical μ and relates the current I_i from reservoir i to the voltage differences $(v_j - v)$, where $v = \mu/e$. The $L = 2$ formula describes a wide variety of experimental measurements and underpins many subsequent theoretical descriptions of disordered N-S interfaces and inhomogeneous structures. For this reason, after discussing the relationship between the coefficients A_{ij} , a_{ij} and the scattering matrix, we shall examine the two-probe formula in some detail and illustrate its application to some generic experimental measurements.

B Relationship between the generalised conductance matrix and the s-matrix.

The $L = 2$ analysis of [Lambert 1991] is based on the observation that in the absence of inelastic scattering, dc transport is determined by the quantum mechanical scattering matrix $s(E, H)$, which yields scattering properties at energy E , of a phase-coherent structure described by a Hamiltonian H . If the structure is connected to external reservoirs by open scattering channels labelled by quantum numbers n , then this has matrix elements of the form $s_{n,n'}(E, H)$. The squared modulus of $s_{n,n'}(E, H)$ is the outgoing flux of quasi-particles along channel n , arising from a unit incident flux along channel n' . Adopting the notation of [Lambert, Hui and Robinson 1993], we consider channels belonging to current-carrying leads, with quasi-particles labelled by a discrete quantum number α ($\alpha = +1$ for particles, -1 for holes) and therefore write $n = (l, \alpha)$, where l labels all other quantum numbers associated with the leads. With this notation, the scattering matrix elements $s_{n,n'}(E, H) =$

$s_{l,l'}^{\alpha,\beta}(E, H)$ satisfy the unitarity condition $s^\dagger(E, H) = s^{-1}(E, H)$, the time-reversibility condition $s^t(E, H) = s(E, H^*)$ and if E is measured relative to the condensate chemical potential $\mu = ev$, the particle-hole symmetry relation $s_{l,l'}^{\alpha,\beta}(E, H) = \alpha\beta[s_{l,l'}^{-\alpha,-\beta}(-E, H)]^*$. (For convenience we adopt the convention of including appropriate ratios of channel group velocities in the definition of s to yield a unitary scattering matrix.)

For a scatterer connected to external reservoirs by L crystalline, normal leads, labelled $i = 1, 2, \dots, L$, it is convenient to write $l = (i, a)$, $l' = (j, b)$, where $a(b)$ is a channel belonging to lead $i(j)$. With this notation, the quantities entering the current-voltage relation are of the form

$$P_{ij}^{\alpha,\beta}(E, H) = \sum_{a,b} |s_{(i,a),(j,b)}^{\alpha,\beta}(E, H)|^2 = \text{Trace} [s_{ij}^{\alpha,\beta}(E, H) \{s_{ij}^{\alpha,\beta}(E, H)\}^\dagger], \quad (6)$$

which is an expression for the coefficient for reflection ($i = j$) or transmission ($i \neq j$) of a quasi-particle of type β in lead j to a quasi-particle of type α in lead i . For $\alpha \neq \beta$, $P_{ij}^{\alpha,\beta}(E, H)$ is an Andreev scattering coefficient, while for $\alpha = \beta$, it is a normal scattering coefficient. Since unitarity yields

$$\sum_{\beta b j} |s_{(i,a),(j,b)}^{\alpha,\beta}(E, H)|^2 = \sum_{\alpha a j} |s_{(i,a),(j,b)}^{\alpha,\beta}(E, H)|^2 = 1, \quad (7)$$

where i and j sum over all leads containing open channels of energy E , this satisfies

$$\sum_{\beta j} P_{ij}^{\alpha,\beta}(E, H) = N_i^\alpha(E), \quad \text{and} \quad \sum_{\alpha i} P_{ij}^{\alpha,\beta}(E, H) = N_j^\beta(E), \quad (8)$$

where $N_i^\alpha(E)$ is the number of open channels for α -type quasi-particles of energy E in lead i , satisfying $N_i^+(E) = N_i^-(-E)$. Similarly particle-hole symmetry yields

$$P_{ij}^{\alpha,\beta}(E, H) = P_{ij}^{-\alpha,-\beta}(-E, H) \quad (9)$$

and time reversal symmetry

$$P_{ij}^{\alpha,\beta}(E, H) = P_{ji}^{\beta,\alpha}(E, H^*). \quad (10)$$

Having introduced the scattering coefficients $P_{ij}^{\alpha,\beta}(E, H)$, the coefficients A_{ij} of the fundamental formula (4) are given by

$$A_{ij} = (2e/h) \sum_{\alpha} (\alpha) \int_0^\infty dE \{ \delta_{ij} N_i^\alpha(E) f_i^\alpha(E) - \sum_{\beta} P_{ij}^{\alpha,\beta}(E, H) f_j^\beta(E) \}, \quad (11)$$

with $f_j^\alpha(E) = \{\exp[(E - \alpha(ev_j - \mu))/k_b T] + 1\}^{-1}$ the distribution of incoming α -type quasi-particles from lead j .¹

¹ It is perhaps worth noting that in [Lambert 1991], the following notation is employed $N_p(E) = N_1^+$, $\tilde{R}_{pp} = P_{11}^{++}(E, H)/N_p(E)$, $\tilde{R}_{hp} = P_{11}^{-+}(E, H)/N_p(E)$ etc.

Equation (4) yields the current-voltage characteristics of a given structure at finite voltages, provided all scattering coefficients are computed in the presence of a self-consistently determined order parameter and self-consistent values of all other scattering potentials. At finite temperature, but zero voltage, where $v_i - v \rightarrow 0$, it reduces to equation (5), with a_{ij} given by

$$a_{ij} = (2e^2/h) \int_{-\infty}^{\infty} dE \left[-\frac{\partial f(E)}{\partial E} \right] [N_i^+(E) \delta_{ij} - P_{ij}^{++}(E, H) + P_{ij}^{-+}(E, H)], \quad (12)$$

where $f(E)$ is the Fermi function and equation (9) has been used. At finite voltages, but zero-temperature, it reduces to

$$A_{ij} = (2e/h) \int_0^{(ev_i - \mu)} dE [\delta_{ij} N_i^+(E) + P_{ij}^{-+}(E, H) - P_{ij}^{++}(E, H)]. \quad (13)$$

Finally at finite voltages, the differential of equation (4) with respect to v_j (with μ and all other potentials held constant) yields

$$\partial I_i / \partial v_j = a_{ij}, \quad (14)$$

where at finite temperature,

$$a_{ij} = (2e^2/h) \sum_{\alpha} (\alpha) \int_0^{\infty} dE \left\{ \delta_{ij} N_i^{\alpha}(E) \left[-\alpha \frac{\partial f_i^{\alpha}(E)}{\partial E} \right] - \sum_{\beta} P_{ij}^{\alpha\beta}(E, H) \left[-\beta \frac{\partial f_j^{\beta}(E)}{\partial E} \right] \right\}. \quad (15)$$

and at zero temperature,

$$a_{ij} = [2e^2/h] [\delta_{ij} N_i^+(E_i) + P_{ij}^{-+}(E_j, H) - P_{ij}^{++}(E_j, H)]. \quad (16)$$

where $E_i = ev_i - \mu$.

It is worth noting that replacing E by $-E$ and utilizing the particle-hole symmetry relation (9) allows equation (12) to be rewritten in the form

$$a_{ij} = (2e^2/h) \int_{-\infty}^{\infty} dE \left[-\frac{\partial f(E)}{\partial E} \right] [N_i^-(E) \delta_{ij} - P_{ij}^{--}(E, H) + P_{ij}^{+-}(E, H)], \quad (17)$$

which demonstrates that particles and hole are treated on an equal footing in equations (12) and (17). Furthermore in view of the symmetries (9), (10) the reciprocity relation $a_{ij}(H) = a_{ji}(H^*)$ is satisfied.

C Two probe formulae in more detail.

While the above notation is convenient for arbitrary L , it perhaps obscures the simplicity of the final result and therefore in the literature, several alternative notations have been employed. For the case of $L = 2$ normal probes, where the scattering matrix has the structure

$$S(E, H) = \begin{pmatrix} r(E) & t'(E) \\ t(E) & r'(E) \end{pmatrix}, \quad (18)$$

it is convenient to write $s_{11}^{\alpha\beta}(E, H) = r_{\alpha\beta}(E)$, $s_{22}^{\alpha\beta}(E, H) = r'_{\alpha\beta}(E)$, $s_{21}^{\alpha\beta}(E, H) = t_{\alpha\beta}(E)$ and $s_{12}^{\alpha\beta}(E, H) = t'_{\alpha\beta}(E)$. With this notation, the sub-matrices r, t, r', t' have the form

$$r(E) = \begin{pmatrix} r_{++}(E) & r_{-+}(E) \\ r_{-+}(E) & r_{--}(E) \end{pmatrix}, \quad \text{etc.}, \quad (19)$$

The matrix $r_{\alpha\beta}$ ($r'_{\alpha\beta}$) is a matrix of amplitudes describing the reflection of β -type quasi-particles from reservoir 1 (2) into α -type quasi-particles travelling back into reservoir 1 (2). Similarly $t_{\alpha\beta}$ ($t'_{\alpha\beta}$) is a matrix of amplitudes describing the transmission of β -type quasi-particles from reservoir 1 (2) into α -type quasi-particles of reservoir 2 (1).

Using these sub-matrices, the $L = 2$ current-voltage relation can be written

$$\begin{pmatrix} I_1 \\ I_2 \end{pmatrix} = \begin{pmatrix} a_{11} & a_{12} \\ a_{21} & a_{22} \end{pmatrix} \begin{pmatrix} v_1 - v \\ v_2 - v \end{pmatrix}, \quad (20)$$

where

$$\begin{pmatrix} a_{11} & a_{12} \\ a_{21} & a_{22} \end{pmatrix} = \int_{-\infty}^{\infty} dE \left(-\frac{\partial f(E)}{\partial E} \right) \begin{pmatrix} N_1^+(E) - R_0(E) + R_a(E) & T_a'(E) - T_0'(E) \\ T_a(E) - T_0(E) & N_2^+(E) - R_0'(E) + R_a'(E) \end{pmatrix}, \quad (21)$$

with

$$\begin{pmatrix} R_0(E) \\ T_0(E) \\ R_a(E) \\ T_a(E) \end{pmatrix} = \begin{pmatrix} P_{11}^{++}(E, H) \\ P_{21}^{++}(E, H) \\ P_{11}^{--}(E, H) \\ P_{21}^{--}(E, H) \end{pmatrix} = \begin{pmatrix} \text{Trace } \{r_{++}(E)r_{++}^\dagger(E)\} \\ \text{Trace } \{t_{++}(E)t_{++}^\dagger(E)\} \\ \text{Trace } \{r_{-+}(E)r_{-+}^\dagger(E)\} \\ \text{Trace } \{t_{-+}(E)t_{-+}^\dagger(E)\} \end{pmatrix} \quad (22)$$

and

$$\begin{pmatrix} R_0'(E) \\ T_0'(E) \\ R_a'(E) \\ T_a'(E) \end{pmatrix} = \begin{pmatrix} P_{22}^{++}(E, H) \\ P_{12}^{++}(E, H) \\ P_{22}^{--}(E, H) \\ P_{12}^{--}(E, H) \end{pmatrix} = \begin{pmatrix} \text{Trace } \{r'_{++}(E)r_{++}'^\dagger(E)\} \\ \text{Trace } \{t'_{++}(E)t_{++}'^\dagger(E)\} \\ \text{Trace } \{r'_{-+}(E)r_{-+}'^\dagger(E)\} \\ \text{Trace } \{t'_{-+}(E)t_{-+}'^\dagger(E)\} \end{pmatrix}. \quad (23)$$

Similarly the zero temperature differential conductance (16) becomes

$$a_{ij} = [2e^2/h][\delta_{ij}N_i^+(E_i) + R_a(E_j) - R_0(E_j)]. \quad (24)$$

D Applications of the two-probe conductance matrix.

As noted in [Lambert 1991], the two-probe current-voltage relation (20) can be used to derive generalisations of both (2) and (3). To further illustrate the versatility of the two-probe theory, we now apply it to some typical experimental measurements. For convenience in what follows, we set $2e^2/h$ equal to unity.

Example 1. The normal limit.

Consider the structure of figure 1a, where a scattering region containing superconducting inclusions is connected to normal reservoirs at potentials v_1 , v_2 . In the normal limit, the condensate potential v must disappear from the fundamental current-voltage relation (4). As shown below, this occurs, because in the absence of Andreev scattering, unitarity of the scattering matrix implies that $a_{11} = -a_{12} = -a_{21} = a_{22} = T_0$. Hence equation (20) reduces to

$$I_1 = -I_2 = T_0(v_1 - v_2), \quad (25)$$

which is simply the Landauer formula (2).

Example 2. Experiments where $\mu_2 = \mu$.

Figure 1b shows an experiment in which the superconductor and reservoir 2 are held at the same potential. In this case, equation (20) yields

$$\frac{I_1}{(v_1 - v)} = a_{11} = \int_{-\infty}^{\infty} dE - \frac{\partial f(E)}{\partial E} [N_1^+(E) - R_0(E) + R_a(E)]. \quad (26)$$

This experimental configuration is of the type used in tunneling experiments, aimed at probing the proximity effect in the vicinity of an N-S boundary [Gueron et al 1996]. This result describes any of the structures shown in figure 1, provided $\mu_2 = \mu$ and is a generalization to disordered and inhomogeneous structures of the boundary conductance formula derived by [Blonder, Tinkham, Klapwijk 1982].

Example 3. Experiments where $a_{12} = a_{21} = 0$.

An example of such an experiment is shown in figure 1c, where under sub-gap conditions, the presence of a long superconductor (of length greater than the superconducting coherence length) prevents the transmission of quasi-particles from reservoir 1 to reservoir 2 and vice versa. In this case, combining the unitarity condition $N_1^+(E) = R_0(E) + R_a(E)$ with equation (20) yields

$$\frac{I_1}{(v_1 - v)} = a_{11} = \int_{-\infty}^{\infty} dE \left(-\frac{\partial f(E)}{\partial E} \right) [2R_a(E)]. \quad (27)$$

In common with the current-voltage relation from which it derives, equation (27) is valid in the presence of disorder and inhomogeneities and in the presence of an arbitrary number of superconducting inclusions of arbitrary geometry.

Example 4. Experiments where $I_1 = -I_2 = I$.

Such a situation is illustrated in figure 1a. In this case, inverting equation (20) yields

$$\begin{pmatrix} v_1 - v \\ v_2 - v \end{pmatrix} = \frac{1}{d} \begin{pmatrix} a_{22} & -a_{12} \\ -a_{21} & a_{11} \end{pmatrix} \begin{pmatrix} I \\ -I \end{pmatrix}, \quad (28)$$

where $d = a_{11}a_{22} - a_{12}a_{21}$. Hence the two-probe conductance $G = I/(v_1 - v_2)$ takes the form

$$G = \frac{d}{a_{11} + a_{22} + a_{12} + a_{21}}. \quad (29)$$

As an example of this formula, we note that in the zero-temperature limit, where all quantities are evaluated at zero energy, equation (29) can be written [Lambert 1993, Lambert, Hui and Robinson 1993]

$$G = T_0 + T_a + \frac{2(R_a R'_a - T_a T'_a)}{R_a + R'_a + T_a + T'_a}. \quad (30)$$

For a symmetric scatterer, where primed quantities equal unprimed quantities, this reduces to $G = T_0 + R_a$, whereas in the absence of transmission between the reservoirs, the resistance G^{-1} reduces to a sum of two resistances $G^{-1} = (1/2R_a) + (1/2R'_a)$. It should be noted that a combination of particle-hole symmetry and unitarity yield at $E = 0$, $T_0 + T_a = T'_0 + T'_a$ and therefore equation (30) is symmetric under an interchange of primed and unprimed coefficients.

Example 5. Experiments where $I_2 = 0$.

As a final example, consider the experiment sketched in figure 1d where reservoir 2 acts as a voltage probe, with $I_2 = 0$. In this case equation (20) yields for the ratio of the voltages

$$\frac{(v_2 - v)}{(v_1 - v)} = -\frac{a_{21}}{a_{22}}, \quad (31)$$

where from equation (21), the coefficient a_{22} is positive. In contrast, the coefficient a_{21} is necessarily negative for a normal system, but in the presence of Andreev scattering can have arbitrary sign. Hence superconductivity can induce voltage sign-reversals which are not present in the normal limit. This feature was first predicted within the context of negative four-probe conductances [Allsopp et al 1994] and has been confirmed in recent experiments by the Groningen group [Hartog et al 1996].

E The Bogoliubov - de Gennes equation.

The above formulae relate measurable quantities to scattering matrix elements and therefore to end this section we briefly introduce the Bogoliubov - de Gennes equation [de Gennes 1989], which forms a basis for computing the scattering matrix s . The Bogoliubov - de Gennes equation arises during the diagonalization of the mean-field BCS Hamiltonian, which for a non-magnetic, spin-singlet superconductor takes the form

$$H_{eff} = E_0 + \int d\mathbf{r} \int d\mathbf{r}' \left(\psi_{\uparrow}^{\dagger}(\mathbf{r}) \psi_{\downarrow}(\mathbf{r}) \right) H(\mathbf{r}, \mathbf{r}') \begin{pmatrix} \psi_{\uparrow}(\mathbf{r}') \\ \psi_{\downarrow}^{\dagger}(\mathbf{r}') \end{pmatrix}, \quad (32)$$

where E_0 is a constant, $\psi_{\sigma}(\mathbf{r})$ and $\psi_{\sigma}^{\dagger}(\mathbf{r})$ are field operators, destroying and creating electrons of spin σ at position \mathbf{r} and

$$H(\mathbf{r}, \mathbf{r}') = \begin{pmatrix} \delta(\mathbf{r} - \mathbf{r}') H_0(\mathbf{r}) & \Delta(\mathbf{r}, \mathbf{r}') \\ \Delta^*(\mathbf{r}, \mathbf{r}') & -\delta(\mathbf{r} - \mathbf{r}') H_0^*(\mathbf{r}) \end{pmatrix}. \quad (33)$$

To each positive eigenvalue E_n of H , with eigenvector $\underline{\Psi}_n(\mathbf{r}) = \begin{pmatrix} u_n(\mathbf{r}) \\ v_n(\mathbf{r}) \end{pmatrix}$ satisfying

$$\int d\mathbf{r}' H(\mathbf{r}, \mathbf{r}') \begin{pmatrix} u_n(\mathbf{r}') \\ v_n(\mathbf{r}') \end{pmatrix} = E_n \begin{pmatrix} u_n(\mathbf{r}) \\ v_n(\mathbf{r}) \end{pmatrix}, \quad (34)$$

there exists a corresponding negative eigenvalue $-E_n$ with eigenvector $\underline{\Psi}_{-n}(\mathbf{r}) = \begin{pmatrix} -v_n^*(\mathbf{r}) \\ u_n^*(\mathbf{r}) \end{pmatrix}$. Consequently \hat{H}_{eff} is diagonalized by the transformation

$$\begin{pmatrix} \psi_{\uparrow}(\mathbf{r}) \\ \psi_{\downarrow}^{\dagger}(\mathbf{r}) \end{pmatrix} = \sum_{n>0} \begin{pmatrix} u_n(\mathbf{r}) & -v_n^*(\mathbf{r}) \\ v_n(\mathbf{r}) & u_n^*(\mathbf{r}) \end{pmatrix} \begin{pmatrix} \gamma_{n\uparrow} \\ \gamma_{n\downarrow}^{\dagger} \end{pmatrix}, \quad (35)$$

where to avoid overcounting, only one of $\underline{\Psi}_n(\mathbf{r})$ or $\underline{\Psi}_{-n}(\mathbf{r})$ is included in the sum over n .

It should be noted that whereas the Bogoliubov - de Gennes equation (34) refers to a model in which the variable \mathbf{r} varies continuously, in a tight-binding model, the corresponding Bogoliubov - de Gennes equation is

$$\begin{aligned} E\psi_i &= \epsilon_i\psi_i - \gamma \sum_{\delta} \psi_{i+\delta} + \Delta_i\phi_i \\ E\phi_i &= -\epsilon_i\phi_i + \gamma^* \sum_{\delta} \phi_{i+\delta} + \Delta_i^*\psi_i \end{aligned} \quad (36)$$

where ψ_i (ϕ_i) indicates the particle (hole) wavefunction on site i and $i + \delta$ labels a neighbour of i .

As discussed in [Hui and Lambert 1990] and [Lambert, Hui and Robinson 1993], for a scattering region connected to two crystalline normal leads, the

Bogoliubov-de Gennes equation may be solved by means of a transfer matrix method, which yields a transfer matrix T satisfying

$$\begin{pmatrix} O' \\ I' \end{pmatrix} = T \begin{pmatrix} I \\ O \end{pmatrix}, \quad (37)$$

where O (I) refer to vectors of outgoing (incoming) plane-wave amplitudes on the left and O' , (I') to corresponding amplitudes on the right, each plane-wave being divided by the square root of its longitudinal group velocity to ensure unitarity of s . Whereas T connects plane wave amplitudes in the left lead to amplitudes in the right lead, the s -matrix connects incoming amplitudes to outgoing amplitudes and satisfies

$$\begin{pmatrix} O \\ O' \end{pmatrix} = s \begin{pmatrix} I \\ I' \end{pmatrix} \quad (38)$$

Once T is known, the s -matrix can be constructed. Indeed if s is written as

$$s = \begin{pmatrix} r & t' \\ t & r' \end{pmatrix}, \quad (39)$$

then T has the form

$$T = \begin{pmatrix} T_{11} & T_{12} \\ T_{21} & T_{22} \end{pmatrix} = \begin{pmatrix} (t^\dagger)^{-1} & r'(t')^{-1} \\ -(t')^{-1}r & (t')^{-1} \end{pmatrix}, \quad (40)$$

from which the following inverse relation is obtained,

$$s = \begin{pmatrix} -T_{22}^{-1}T_{21} & T_{22}^{-1} \\ (T_{11}^\dagger)^{-1} & T_{12}T_{22}^{-1} \end{pmatrix}. \quad (41)$$

An alternative method of evaluating coefficients in the above current-voltage relations is provided by the recursive Green's function method, which uses Gaussian elimination to compute the Green's function on sites located at the surface of the interface between external normal leads and the scatterer. Given the surface Green's function, scattering coefficients can be obtained from generalised Fisher-Lee relations [Fisher and Lee 1982], derived by [Takane and Ebisawa 1992(a)] and later rederived in [Lambert 1993, Lambert, Hui and Robinson 1993]. This recursive technique is identical to the "decimation" method employed by [Lambert and Hui 1990] and is essentially an efficient implementation of Gaussian elimination.

A third method of evaluating the coefficient R_a was derived by [Beenakker 1992] for the case where there is perfect Andreev reflection at the boundary of the superconductor. The resulting formula expresses R_a in terms of scattering properties of the normal state and facilitates the application of random matrix theory to N-S structures [Beenakker 1997].

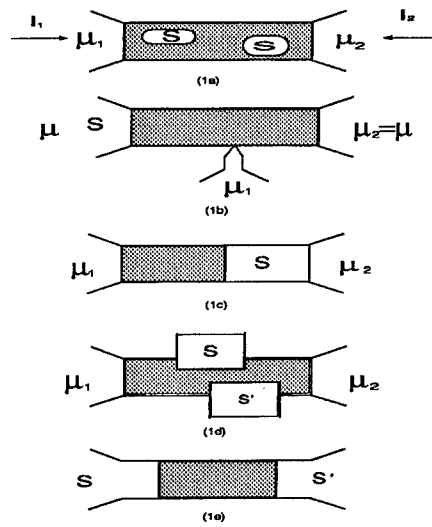


FIGURE 1. Various generic experimental arrangements used in measuring dc transport in superconducting hybrids. The grey area indicates a phase-coherent normal region, whereas superconductive parts are marked by a S. The widening open parts at the ends represent the reservoirs.

REFERENCES

1. Allsopp N K, Hui V C, Lambert C J and Robinson S K 1994 J. Phys.: Condens. Matter **6** 10475
2. Al'tshuler B L and Spivak B Z 1987 Sov. Phys. JETP **65** 343
3. Andreev A F 1964 Sov. Phys. JETP **19** 1228
4. Bagwell P F 1992 Phys. Rev. **46** 12573.
5. Bagwell P F and Alam M A 1992 Workshop on Physics and Computation PhysComp '92 (IEEE Computer Society Press, Los Alamos, CA)
6. Bakker S J, van der Drift E and Klapwijk T M 1994 Phys. Rev. B **49** 13275
7. Barash Y S, Galaktionov A V and Zaikin A D 1995 Phys. Rev. B **52** 665
8. Beenakker C W J and Van Houten H 1991 Phys. Rev. Lett. **66** 3056
9. Beenakker C W J 1992 Phys. Rev. B **46** 12841
10. Beenakker C W J 1997 Rev. Mod. Phys. to appear
11. Black C T, Ralph D C and Tinkham M 1996 Phys. Rev. Lett. **76** 688
12. Blonder G E, Tinkham M and T.M. Klapwijk T M 1982 Phys. Rev. B. **25** 4515
13. Blonder G E and Tinkham M 1983 Phys. Rev. B. **27** 112
14. Bratus E N, Shumeiko V S, and Wendin G 1995 Phys. Rev. Lett. **74** 2110
15. Bruder C 1990 Phys. Rev. B **41** 4017
16. Buettiker M 1986 Phys. Rev. Lett. **57** 1761
17. Buot F 1993 Phys. Reports **234** 73
18. Cañizares J S and Sols F 1995 J. Phys. Condens. Matter **7** L317
19. Chang L, Chaudhuri S and Bagwell P F 1996 Phys. Rev. B **54** 9399
20. Charlat P, Courtois H, Gandit Ph, Mailly D, Volkov A F and Pannetier B 1996 Phys. Rev. Lett. **77** 4950 and 1996 Czech J. Phys. **46** 3107
21. Claughton N R and Lambert C J 1995a Phys. Rev. B **51** 11635
22. Claughton N R and Lambert C J 1996 Phys. Rev. B **53** 1
23. Cook P M A, Raimondi R and Lambert C J, 1996 Phys. Rev. B **54** 9491
24. Courtois H, Gandit Ph, Mailly D and Pannetier B 1996 Phys. Rev. Lett. **76** 130
25. de Gennes P G 1989 *Superconductivity of Metals and Alloys* Addison-Wesley. New York
26. Dimoulas A , Heida J P, van Wees B J and Klapwijk T M 1995 Phys. Rev. Lett. **74** 602
27. Eiles T M, Martinis J M, and Devoret M H 1993 Phys. Rev. Lett. **70** 1862
28. Fisher D S and Lee P A 1981 Phys. Rev. B **23** 6851
29. Furusaki A, Takayanagi H and Tsukada M 1991 Phys. Rev. Lett. **67** 132
30. Günsenheimer U and Zaikin A D 1994 Phys. Rev. B **50** 6317
31. Hara J, Ashida M and Nagai K 1993 Phys. Rev. B **47** 11263
32. den Hartog S G, Kapteyn C M A, van Wees B J, Klapwijk T M, and Borghs G 1996 Phys. Rev. Lett. **77** 4954 see also Phys. Rev. Lett. **76** 4592 (1996)
33. Hekking F W J, Glazman L I, Matveev K A and Shekhter R 1993 Phys. Rev. Lett. **70** 4138

34. Hekking F W J and Nazarov Y V 1993 Phys. Rev. Lett. **71** 1625
35. Hergenrother J M, Tuominen M T and Tinkham M 1994 Phys. Rev. Lett. **72** 1742
36. Hui V C and Lambert C J 1990 J. Phys.: Condensed Matter **2** 7303
37. Hui V C and Lambert C J 1993a Europhys. Lett. **23** 203
38. Hui V C and Lambert C J 1993b J. Phys.: Condensed Matter **5** L651
39. Hurd M and Wendin G 1994 Phys. Rev. B **49** 15258
40. Hurd M and Wendin G 1995 Phys. Rev. B **51** 3754
41. Kastalsky A, Kleinsasser A W, Greene L H, Milliken F P and Harbison J P 1991 Phys. Rev. Lett. **67** 3026
42. Koyama Y, Takane Y and Ebisawa H 1995 J. Phys. Soc. Jpn. **64** 1466
43. Koyama Y, Takane Y and Ebisawa H 1996 J. Phys. Soc. Jpn. **65** 683
44. Lafarge P, Joyez P, Esteve D, Urbina C and Devoret M H 1993 Phys. Rev. Lett. **70** 994
45. Lambert C J 1991 J. Phys.: Condensed Matter **3** 6579
46. Lambert C J 1993 J. Phys.: Condensed Matter **5** 707
47. Lambert C J, Hui V C and Robinson S J 1993 J. Phys.: Condens. Matter **5** 4187
48. Lambert C J 1994 Physica B **203** 201
49. Landauer R 1970 Philos. Mag. **21** 863
50. Levy Yeyati A, Martin-Rodero A and Cuevas J C 1996 J. Phys.: Condens. Matter **8** 449
51. Magnée P H C et al, 1994 Phys. Rev. B **50** 4594
52. Martin-Rodero A, Levy Yeyati A and Garcia-Vidal F J 1996 Phys. Rev. B **53** R8891
53. Marsh A M, Williams D A and Ahmed H 1994 Phys. Rev. B **50** 8118
54. Martin A and Lambert C J 1995 Phys. Rev B **24** 17999
55. Martin A and Lambert C J 1996 J. Phys. Condens. Matter **8** L731
56. Nakano H and Takayanagi H 1991 Solid State Comm. **80** 997
57. Nguyen C, Kroemer H and Hu E L 1992 Phys. Rev. Lett. **69** 2847
58. Petrashov V T, Antonov V N, Delsing P and Claeson R 1993a Phys. Rev. Lett. **70** 347
59. Petrashov V T, Antonov V N, Maksimov S V and Shaikhaidarov R Sh 1993b JETP Lett. **58** 49
60. Petrashov V T, Antonov V N, Maksimov S V and Shaikhaidarov R Sh 1994 JETP Lett. **59** 551
61. Petrashov V, Antonov V N, Delsing P and Claeson T 1995 Phys. Rev. Lett. **74** 5268
62. Pothier H, Guéron S, Esteve D and Devoret M H, 1994 Phys. Rev. Lett. **73** 2488; Pothier H, Guéron S, Esteve D and Devoret M H 1994 Physica B **203** 226
63. Riedel R A, Chang L and Bagwell P 1996 Phys. Rev. B **54** 16082
64. Seviour R, Leadbeater M and Lambert C J 1997, (preprint)
65. Shelankov A L 1980 JETP Lett. **32** 111; 1984 Sov. Phys. Solid State **26** 981
66. Shelankov A L 1985 J. Low Temp. Phys. **60** 29

67. Spivak B Z and Khmel'nitskii D E 1982 JETP Lett **35** 413
68. Takagi S 1992 Solid State Comm. **81** 579
69. Takayanagi H and Akazaki T 1995a Phys. Rev. B **52** R8633
70. Takayanagi H, Akazaki T and Nitta J 1995b Phys. Rev. Lett. **75** 3533
71. Takayanagi H and Akazaki T 1995c Jpn. J. Appl. Phys. **34** 4552
72. Takayanagi H and Akazaki T 1995d Jpn. J. Appl. Phys. **34** 6977
73. Takayanagi H, Toyoda E and Akazaki T 1996 Czech. J. of Physics **46** 2507
74. Takagaki Y and Takayanagi H 1996 Phys. Rev. B **53** 14530
75. Takane Y and Ebisawa H 1992a J. Phys. Soc. J. **61** 1685
76. Tuominen M T, Hergenrother J M, Tighe T S and Tinkham M 1992 Phys. Rev. Lett. **69** 1997
77. Tuominen M T, Hergenrother J M, Tighe T S and Tinkham M 1993 Phys. Rev. B **47** 11599
78. van Wees B J, Lenssen K.-M. H. and Harmans C. J. P. M. 1991 Phys. Rev. B **44** 470
79. van Wees B J, Dimoulas A, Heida J P, Klapwijk T M, Graaf W.v.d. and Borghs G, 1994 Physica **B203** 285
80. de Vegvar P G N, Fulton T A, W.H. Mallison W H and Miller R E 1994 Phys. Rev. Lett. **73** 1416
81. Volkov A F and Takayanagi H 1996 Phys. Rev. B **53** 15162
82. Wendin G and Shumeiko V S 1996 Phys. Rev. B **53** R6006
83. Wilhelm F K, Zaikin A D and Courtois H 1997 cond-mat/9705225
84. Zyuzin A y 1994 Phys. Rev. B **50** 323

Experiments on Proximity Effect

P. Charlat, H. Courtois and B. Pannetier

*Centre de Recherches sur les Très Basses Températures, C.N.R.S., in convention with
Université Joseph Fourier,
F-38042 Grenoble, France*

Abstract. Long-range correlations are induced in a "non-interacting" metal by the presence of a superconducting interface. We review in this lecture recent experiments on proximity effect in metallic structures at mesoscopic length scale. Transport measurements in Aharonov-Bohm loop geometry clearly demonstrate that interference effects on low energy electrons persist far beyond the normal metal coherence length. We also discuss finite bias conductance measurements. It is shown that the conductance of a Normal metal - Superconductor hybrid structure is strongly dependent on the energy distribution in the electron reservoirs. For simplicity we focus on high transparency S-N interfaces (no tunnel junction) and diffusive metallic wires.

INTRODUCTION

The study of proximity effects in normal metal - superconductor structures has attracted a considerable interest in the last years [1-3]. The rapid development in nanofabrication is certainly one of the main driving forces. At the same time new theoretical concepts from mesoscopic physics have lead to major progresses in the understanding of this subject. The renewal of interest on proximity effect in the nineties comes after two important periods: the first one, in the "sixties" [4] follows the discovery of the BCS theory. Due to the limitation in the technology, however, the experimental studies were restricted to the investigation of metallic thin film configurations. A second interesting period, in the seventies, was dealing with non-equilibrium effects in superconductors [5] where charge imbalance and non equilibrium distribution functions were investigated. These ideas are fully relevant in the most recent results. The proximity effect also appears as an essential elementary constituent of Josephson SNS Junction arrays.

Pioneer works on proximity effect go back to 1932 when Holm and Meissner reported observation of zero resistance between pressed contacts in a SNS geometry [6]. It was realized that a supercurrent can flow in a normal metal of thickness much larger than a tunneling distance. Later J. Clarke [7] measured a large critical current in a Pb-Cu-Pb sandwich with a copper layer thickness of $0.55\mu\text{m}$. Magnetic measurements revealed the existence of a Meissner current in thick CuNb wires,

demonstrating that a supercurrent persists up to $50\mu\text{m}$ at millikelvin temperatures [8] in pure metallic copper. Theoretical studies of this effect started in 1961 with the work of Cooper [9]. The so-called Cooper limit refers to the limit of a good electrical contact between a N film and a S film that are thin and pure enough. In this limit, an effective interaction constant was derived from their relative thicknesses. More detailed theories were developed later by Werthamer [10], de Gennes [11] and MacMillan [12] who introduced the important length and energy scales. Detailed reviews on both experimental and theoretical works have been given by Deutscher and de Gennes [4] and A. Gilabert [13]. During this period, the main experimental concern was the superconducting transition temperature of thin N-S layers and their excitation spectra. Critical temperature measurements and tunneling spectra were extensively studied in evaporated thin films, in particular by the Orsay Group on Superconductivity [14]. The occurrence of a finite gap in the N layer was observed although not fully conclusive [15]. Later convincing evidences for the existence of an energy gap in the excitation spectrum of a normal metal in proximity with a superconductor were given by electronic specific heat experiments of a set of Ag-Pb-Ag sandwiches [16]. A very nice activation behaviour was obtained. The magnitude of the gap was found to decrease with increasing the thickness of the silver film. Ultrasonic attenuation experiments in Cu-Pb sandwiches [17] also revealed the existence of a gap. However the characteristic energy scale in the N metal was not recognized.

With the developement of modern techniques such as nano-lithography or scanning tunnel microscopy more precise studies of length or shape dependence has become accessible. The present approach of the physics of proximity circuits follows the point of view of mesoscopic physics with strong emphasis on phase-sensitive effects. This point of view will be taken in this lecture. We will stress the characteristic lengths and energy scales in a diffusive metal. The fundamental cut-off length scale is the phase memory length L_ϕ . It determines the practical coherence length of single electron states. On the other hand the important energy scale is given by the correlation energy or Thouless energy $E_c = \hbar D/L^2$ (Here D is the diffusion coefficient and L is the length of the sample). E_c is a characteristic energy scale for single electron effects. The time needed by an electron to diffuse to the boundary of the sample is \hbar/E_c . It is interesting to note that it is this energy scale which determine both the energy gap and the critical current in the N metal as will be discussed in this lecture. The term "induced superconductivity in the normal metal" could be misleading: there is no interaction and no condensed state in the normal metal. A superconductor-like behaviour is observed only because correlations are induced far into the N metal by the coherent reflexion at the N-S boundary. The energy level separation is much smaller than E_c and only plays a role in nanoscopic grains [18].

In this lecture we will discuss simple experimental situations: submicron metallic wires (Cu) where electron-electron interaction can be neglected. We will consider the diffusive regime and restrict to "mesoscopic" samples, *i.e.* samples with size smaller than the phase memory length. On the other hand we assume perfect in-

interface (no tunnel junction). We will see that this simplified situations leads to very subtle phenomena. Because of long-range coherence of the electronic wavefunction, non-local effects are highly important. In the so-called "4-probes" experimental configuration for conductance measurements, scattering processes occurring into the leads may be significant, even far away from the mesoscopic structure.

We will first recall the main relevant features of the Andreev reflexion at the N-S interface. We then discuss the conductance measurement with introduction of the important notion of spectral conductance. We then discuss briefly a few practical experimental points and present experiments which illustrate important features of the proximity effect: non monotoneous conductance and magnetoconductance periodic oscillations in Aharonov-Bohm geometry. The paper ends with a short discussion on supercurrent and density of states.

BASIC PHENOMENON: ANDREEV REFLEXION

The basic process in proximity effect is the Andreev reflexion [19] which describes the boundary conditions for electron states at the normal-superconductor interface.

Due to the non-zero superconducting energy gap Δ , pure electron and hole states are forbidden in the S electrode: only pair or quasiparticle states exist in S (Fig1). Therefore the S interface behaves as a particular "mirror" that reflects low energy ($\epsilon < \Delta$) electronic states with special rules. These rules follow from the famous Bogoliubov-de Gennes equations [20] for an inhomogeneous BCS superconductor:

$$i\hbar\partial_t \begin{bmatrix} \phi_e \\ \phi_h \end{bmatrix} = \begin{bmatrix} H_0 - \mu & \Delta \\ \Delta^* & -H_0^* + \mu \end{bmatrix} \begin{bmatrix} \phi_e \\ \phi_h \end{bmatrix} \quad (1)$$

Here H_0 is the kinetic hamiltonian describing independent electron states in the disordered metal. μ is the chemical potential of the superconductor, ϕ_e and ϕ_h are the electron and hole components of the electronic wavefunction and Δ is the space dependent pair potential. This equation is valid in both limit: homogeneous BCS superconducting state (uniform Δ) and normal state ($\Delta = 0$). If the N-S interface is defined as a discontinuous jump of the pair potential from 0 to Δ ,

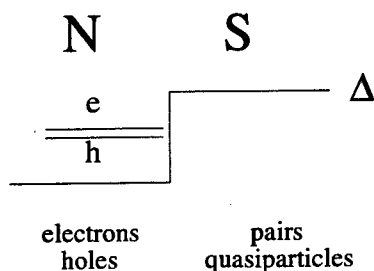


FIGURE 1. Andreev reflexion: Electrons and holes are eigenstates in N. The origin of proximity effect is e-h correlations induced in N by the pair potential which only exists in S.

the continuity conditions of the wavefunction leads to the boundary conditions at the N-S interface. An excellent introduction to the physics of Andreev reflexion is given in the famous Blonder, Tinkham, Klapwijk (BTK) paper [21]. Let us simply summarize the significant features of this process:

retroreflected hole: The reflexion is not specular. Rather, an incoming electron incident from the N side is retroreflected as a hole. As results a pair is transferred into S. The reverse process also takes place. For ideal contact (no tunnel barrier between N and S) the reflexion of low energy electrons $\epsilon < \Delta$ is total. For low barrier transparency, this process becomes negligible since the simultaneous transfer of two electrons is a process of higher order [22] in the tunneling matrix elements.

electron-hole phase coherence: One of the most important consequences of the Andreev process is the phase correlation between the incident electron and the reflected hole. The phases are correlated as results of the pairing interaction in S where the electron and hole wavefunctions are evanescent. The phase shift received by the hole writes $e^{i \arccos \epsilon / \Delta} e^{-i \phi}$. The first contribution reduces to $i\pi/2$ at low energy. The second contribution comes from the macroscopic phase ϕ of the superconducting order parameter. Aways from the interface, an additional phase shift appears because the electron and hole (energy ϵ counted from the Fermi energy) have slightly different wavenumbers. In the diffusive limit, the q-difference $q \approx \epsilon / \hbar v_F$ leads to a phase shift π at a distance $L_\epsilon = \sqrt{\hbar D / \epsilon}$ from the N-S interface.

Thouless energy: When the normal metal has a finite thickness L , one can introduce a characteristic energy beyond which electrons and holes loose their phase coherence. The energy at which $L_\epsilon = L$ is actually by definition the Thouless energy $E_c = \hbar D / L^2$ in the diffusive limit. Here D is the diffusion coefficient in the normal metal. For energies below E_c , the phases of electrons and holes are correlated in the whole sample length L . When the energy scale is fixed by a reservoir's temperature T , this condition defines the thermal diffusion length $L_T = \sqrt{\hbar D / 2\pi k_B T}$: correlations are suppress when $L > L_T$. This situation is similar to the case of universal conductance fluctuation [23].

Pair amplitude: The elementary reflexion process can be equivalently described as an exchange of electron pairs between N and S. An incident electron with wavenumber $k_F + q/2$ combines with an electron of wavenumber $k_F - q/2$ to form a pair in S leaving a retroreflected hole on the N side. This pair injection has a reverse process: A pair $(k_F + q/2, -k_F + q/2)$ penetrates from the superconducting side into the N-conductor. The electron-hole correlation in N is suitably described by a non-zero pair amplitude F [24]. At the N-S boundary, the pair amplitude is fixed by the above phase relation condition. At large distance, F decays with the energy dependent characteristic length given by L_ϵ , which is very long at low energy. It is worth noticing that there is a finite pair amplitude in the N metal, although the interaction constant is assumed to be zero. This is one of the remark-

able features of the proximity effect: long-range electron correlations exist in the N metal in the absence of interaction. The quasiclassical approach used in this paper relies upon the spatial and energy dependence of the pair amplitude function.

Charge transfer: The conservation of normal current at the N-S interface requires full self-consistent treatment of the gap in S. As the normal current decays over a length scale given by ξ_s , a supercurrent carried by the superconducting condensed state (which must have a phase gradient) increases over the same length scale.

Supercurrent : In S-N-S circuit, Andreev reflexion gives rise to the so-called Andreev bound states [25,26] which carry a current without voltage at equilibrium. This current which depends on the phase of the order parameters is at the origin of the Josephson coupling through a N conductor. It is of same nature as the persistent current [27] which takes place in mesoscopic rings.

Disorder : The role of disorder is crucial in the description of interference effects in the normal metal. In Ref [28], Van Wees et al. gave a very clear semiclassical description the constructive quantum interferences induced by multiple reflexion at the interface. This effect also discussed quantitatively in Ref [29] is the origin of zero bias conductance enhancement in high conductance N-I-S tunnel junctions [30,31].

CONDUCTANCE IN MESOSCOPIC N-S STRUCTURES

Unlike the Josephson effect or the magnetic susceptibility, the electrical conductance is a non-equilibrium effect which requires imbalance of electron distribution functions. The mesoscopic conductance is defined from the chemical potential of electron reservoirs.

The prototype of proximity circuit is a N wire in perfect electrical contact with both a massive N electrode and a massive S electrode (see inset of Fig 2). The N electrode is considered as a perfect "reservoir" characterised by an equilibrium electron distribution function with temperature T and chemical potentials $\mu_N = eV$. Strong electron interaction is assumed in order to ensure a "black-body" distribution. Also inelastic processes must be frequent enough to destroy phase coherence. The S electrode, $\mu_S = 0$, only provides a perfect boundary conditions given by the Andreev reflexion (perfect "Andreev mirror"). Because of the chemical potentials difference eV , electrons flow through the N-wire giving a net current $I(V)$.

In the simplest approximation, we assume no inelastic collision. The total current is the sum of currents carried independently by the different energy states:

$$I = \frac{1}{e} \int_{-\infty}^{\infty} g(\epsilon) \delta f(\epsilon) d\epsilon \quad (2)$$

with $\delta f(\epsilon) = \frac{1}{2}[f_e(\epsilon) - f_h(\epsilon)]$ being the charge imbalance induced by the voltage bias of the reservoir.

$g(\epsilon)$ is called the spectral conductance of the wire. In absence of superconductivity and quantum interferences effects, $g(\epsilon) = G_0$ is energy independent and reduces to the ohmic conductance of the wire. On the other hand, the integral over energy of $\delta f(\epsilon)$ is simply eV and Eq 2 reduces to the Ohm's law.

Differential conductance: The temperature and voltage in a finite bias measurement are properties of the electron reservoir. The peculiar effects of microscopic parameters such as geometry, tunnel transparency, gap, enter in the spectral conductance $g(\epsilon)$. Using Eq 2, the I-V differential conductance is readily derived from the spectral conductance and the chemical potential of the N reservoir. $G(T, V)$ measures the contribution of the energy window ($eV, eV + e\delta V$):

$$G(T, V) = \frac{dI}{dV} = \int_{-\infty}^{\infty} g(\epsilon) \partial_V \delta f(\epsilon, T, V) d\epsilon \quad (3)$$

At zero temperature, the derivative $\partial_V f$ becomes a delta function centered at the chemical potential of the reservoir. The zero-temperature differential conductance is a direct measurement of the spectral conductance $G(eV)$. At zero bias ($V = 0$) and non zero temperature, the conductance $G(T)$ is the result of the convolution of the spectral conductance by a thermal kernel $[4k_B T \cosh^2 \epsilon/2k_B T]^{-1}$. Here k_B is the Boltzmann constant.

spectral conductance from quasiclassical model: In general the calculation of $g(\epsilon)$ is delicate and requires specific models [32]. It is a characteristic quantity of the mesoscopic circuit. Here we will see that the strong energy dependence of $g(\epsilon)$ leads to spectacular temperature dependence of zero bias conductance as well as strong non-linearities in the finite bias conductance. The different modern approaches have in common the boundary condition at the N-S interface which is governed by the Andreev reflexion. The scattering matrix theory has been extensively used to compute $g(\epsilon)$ in various circuits. Although less "physically transparent", the quasiclassical Green function method (referred to as Usadel equation when considering the diffusive limit) has proved to be very useful and predictive [32,33,36]. In the non-interacting case this theory provides two sets of equations that we write here in the one-dimensional and zero magnetic field limit. In contrast to the Ginzburg-Landau equations which describe the tail of the order parameter near the superconducting phase transition, the Usadel equations deal with the energy-dependent pair amplitude and are valid at any temperatures down to $T=0$.

1. A first equation for the pair amplitude $F(\epsilon, x)$ describes electron-hole correlations induced by the Andreev reflexion. Using the complexe variable $\theta = \theta_1 + i\theta_2$ defined by $F = i \sin \theta$, the simplest formulation is [33]:

$$\partial_x^2 \theta + \left[\frac{2i\epsilon}{\hbar D} - \frac{\cos \theta}{L_\phi^2} \right] \sin \theta = 0 \quad (4)$$

with boundary conditions $\theta = 0$ at the N contact ($x = L$) and $\theta = \pi/2 + i \tanh^{-1}(\epsilon/\Delta)$ ($\rightarrow \pi/2$ at $\epsilon \ll \Delta$) at the S contact ($x = 0$). It is worth noticing that the energy gap only appears in this boundary condition: it is of no significance in the low energy case. As can be seen this equation is independent of the distribution functions. In the limit of small pair amplitude, it can be linearized ($\sin \theta \approx \theta$, $\cos \theta \approx 1$) giving a diffusion-like equation for $F(\epsilon, x)$ with a cut-off length given by the phase memory length L_ϕ . The characteristic diffusion length, given by $L_\epsilon = \sqrt{\frac{\hbar D}{\epsilon}}$ describes how the pair amplitude decays in the normal metal. Equilibrium properties such as density of states or Josephson current can be derived from the function $\theta(\epsilon)$ [33,35].

2. A second equation gives the local normal current:

$$I_N(\epsilon, x) = \frac{1}{e} \sigma_N \cosh^2 \theta_2(\epsilon, x) \nabla \delta f_e \quad (5)$$

This equation is nothing else than a (local) diffusion law for the excess charges. It involves the gradient of the charge imbalance, in contrast to Eq 2. The prefactor describes the renormalized diffusion coefficient which is a function of the pair amplitude $F(\epsilon, x)$ through the imaginary term θ_2 .

Let us emphasize that both equations are local equations: each segment dx of the wire can be viewed as having its "local conductivity" enhanced by the factor $\cosh^2 \theta_2 \geq 1$. As already stressed the origin of this enhancement is the (non-local) $e - h$ correlations which originate in the superconducting electrode. The spectral conductance of a circuit can be determined from a very simple rule: a) Solve Eq 4 at each point x of the circuit using the appropriate boundary conditions: this provides $\theta(\epsilon, x)$ and the local conductivity, b) use classical circuit equations to determine the total spectral conductance.

From simple algebra, it can be shown that for infinite L_ϕ , θ_2 is a simple non monotonic function of x/L_ϵ with a maximum at $x = \frac{\pi}{4} L_\epsilon$. It is zero at both S ($x = 0$) and N ($x = L$) contacts. The spectral conductance $g(\epsilon)$ is obtained

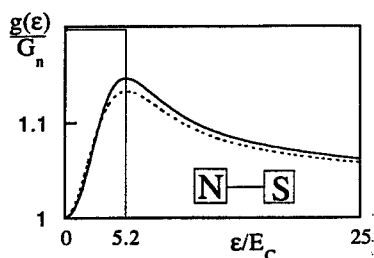


FIGURE 2. Spectral conductance of a N wire in contact with a S electrode, as calculated using Usadel equations with $\epsilon \ll \Delta$. Here $E_c \ll \Delta$. Dotted line: linear approximation. Inset: schematic of the circuit.

from integrating over spatial coordinate x . In Fig 2 we have plotted the spectral conductance as function of energy in units of the Thouless energy. Here L_ϕ is infinite. Also shown in Fig 2 is the solution of the linearized Eq 4. It differs by less than 5% from the exact solution, which means that in many cases, the main physical features can be obtained from linearized solutions. The conductance shows a maximum about 15% above the normal state conductance at $\epsilon \approx 5.2E_c$. The most remarkable feature is the suppression of proximity correction at zero energy: $g(\epsilon = 0) = g_N$. This statement which was first noticed by Lambert and Beenakker [37,38] means that the zero temperature conductance of a N-S device should be unchanged when S is replaced by N.

$G(T)$ has a peak at temperature $T \approx 5E_c/k_B$ and returns quadratically to G_N at vanishing temperature. The high temperature behaviour shows algebraic temperature dependence $G(T) \approx G_N \sqrt{E_c/k_B T} \approx G_N L_T/L$. This result is consistent with the intuitive view of the proximity effect where one just "remove" a length L_T from the normal conductor. The $T^{-1/2}$ law was first explained by Zhou and Spivak [33]. The suppression of proximity effect at zero temperature is far less intuitive. We will see that the experiments show this effect also called "re-entrance effect".

The above discussion can be readily extended to more complex circuits such as multiterminal devices. A matrix spectral conductance must be introduced. The angle $\theta(x, \epsilon)$ defined in Eq.4 is a very useful parameter for the proximity effect in N-S structures [39].

EXPERIMENTAL CONSIDERATIONS

Choice of the geometry: Various geometries have been used experimentally in order to identify the role played by the different elements of the circuit. Many crucial experiments have been published in the regime where the measured conductance is limited by that of the N-S tunnel junctions [30,31]. They have

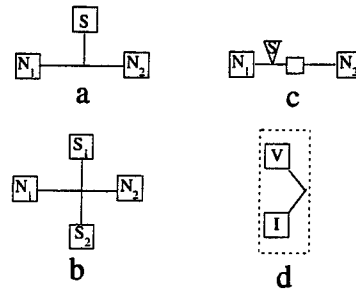


FIGURE 3. Example of measured circuits: a) T-shaped circuit, b) Phase-sensitive circuit: the conductance between N_1 and N_2 is measured *vs* the phase difference between S_1 and S_2 , c) Aharonov-Bohm loop circuit: here the proximity effect is induced by a single S contact. Phase sensitivity is measured by flux dependence of the conductance; d) Separate current (I) and voltage (V) contacts as modeled as a single reservoir.

revealed in particular that the tunnel conductance is strongly modified by the coherent electron scattering in the diffusive conductor.

We focus here on circuits without tunnel junctions and where the transport is dominated by the conductance of the metallic conductor. For example, in the T-shaped circuit shown in Fig.3a the conductance is measured between N_1 and N_2 , away from the N-S interface. We will discuss experimental results on this circuit.

-Phase-sensitive circuits: In order to test for sensitivity of the conductance to the superconducting phase, circuits such as that shown in Fig.3b have been studied both experimentally [40–42] and theoretically [37,36]. Here the 2-leads conductance in the $N_1 - n - N_2$ horizontal part of the circuit are measured *vs* the phase difference between S1 and S2. An alternative way of investigating phase-sensitivity uses an Aharonov-Bohm loop (circuit shown in Fig.3c). Here the phase is tuned by the magnetic flux in the loop.

-Non ideal reservoirs, 2-probes vs 4 probes: Since in proximity structures the spectral conductance is strongly energy-dependent, the transport properties are expected to be highly sensitive to the energy distribution of the electron sources, *i.e.* the reservoirs. As discussed above, the standard "mesoscopic" configuration for transport is a conductance measurement between two reservoirs. The practical realisation of ideal reservoirs is an easy task when the reservoir is weakly coupled to the circuit, for example with a low transparency tunnel junction, or when the circuit is a semiconductor with metallic contacts. For strong-coupling metallic circuits however (see picture in Fig.4) the reservoirs are made of broad two-dimensional electrodes. We will see that the experiment may show strong deviations with respect to ideal behaviour of the reservoirs: Firstly, Joule effect takes place in the leads and change the effective temperatures of "injected" electrons. Secondly, the inelastic processes are too slow in the metallic electrode to guarantee a "blackbody" distribution function. Both effects result in a broadening and shifting of the energy distribution function of injected electrons. In a geometry such as that shown in Fig.6 a four-probe experimental configuration is used. For analysis as a two probe systems, this configuration can be approximated by the circuit shown in Fig 3c: the pairs of leads (I^+, V^+) and (I^-, V^-) being modeled as independent reservoirs as shown in Fig 3d. This assumption is perfectly valid for zero bias experiments. It breaks down at very low temperature in finite bias experiments. In that regime subtle multiterminal effects [47] takes place.

Practical realizations: The main criteria for sample fabrication are the following (we restrict here to metallic proximity circuits):

- The circuit is "mesoscopic", or coherent: Accordingly, the length must be smaller than the phase memory length L_ϕ . L_ϕ is temperature dependent and saturates at very low temperatures [43] to a value ranging from about 100nm for very disordered metallic alloys to several micrometers for pure metals such

as Cu, Ag, The suppression of proximity corrections has been recently discussed for a semiconducting proximity circuit [44].

- The length must be of order of the thermal length L_T . This condition is identical to the condition that the thermal energy kT must be comparable to the Thouless energy E_c . With typical diffusion coefficient $D \approx 150\text{cm}^2/\text{s}$, L_T is of order of 130nm at 1K and $0.6\mu\text{m}$ at 40mK.
- A third constraint is the quality of the S-N interface. For optimum metallic contact, this means that residual oxides must be avoided between N and S. A practical characterization of barrier transparency is the equivalent length L_t of the barrier, *i.e.* the length of normal metal having the same conductance as the barrier. Good metallic contact means L_t much less than the sample length [33].

Two alternate methods are used for sample fabrication. In both case, the sub-micron size constraint imposes high resolution e-beam direct writing:

- The shadow evaporation technique [45] with bilayer or trilayer lift-off resist masks allows self- alignment of submicron wires. Using a two-axis rotating sample holder it is possible to deposit selectively and subsequently different materials in a ultra-high-vacuum environment [56]. This method uses one single lithographic process, does not require sophisticated nanofabrication e-beam machine and has shown particularly effective for single-electronic device fabrication. Unfortunately it is restricted to simple circuits. A possible disadvantage is the risk of contamination or material re-deposition between the stencil mask and the substrate [46].
- A more powerful technique uses sequential e-beam lithography steps with high-accuracy repositionning (better than 100nm). Since the sample has to be removed from the evaporation chamber between each step, it is necessary to perform in-situ cleaning of the metallic surface before deposition of the upper layer. The samples shown in Fig.4 and 6 were fabricated using 500 eV Ar^+ ions to remove a few atomic layers of copper before Al evaporation.

Measurements are performed in a μ -metal shielded dilution refrigerator. Particular care must be taken in filtering all electrical circuits against radiofrequency noise at the input of the cryostat. Simple L-R-C filters in hermetically sealed boxes are suitable. Most experiments on proximity effect have been performed on single mesoscopic circuits. This was considered essential in order to test sample dependent vs ensemble averaged contributions. In the investigation of ensemble average effects such as some manifestations of the electron-hole coherence, experiments on arrays could greatly enhance the signal to noise ratio.

ILLUSTRATIVE EXPERIMENTS

Here we present a selection of experimental results which illustrate some important aspects of proximity-enhanced conductance in mesoscopic structures.

-T-dependent excess conductance: The sample shown in Fig.4 were designed in order to reveal "re-entrance" effect, *i.e.* the suppression of proximity conductance at very low temperatures [47]. This T-shaped configuration allows measurements "without interface". The only physical interface is between the vertical Cu arm and the superconducting electrode. For the measured samples L_t is of order of one tenth of the sample length. This geometry also allows multi-terminal measurements. The Cu diffusion coefficient is $D = 30\text{cm}^2/\text{s}$ and the (elastic) electron mean free path is 6nm . The Thouless energy (referred to the length L) is $E_c \approx 12\mu\text{V}$ which corresponds to a "Thouless temperature" of 140 mK easily accessible in a dilution refrigerator. E_c is much smaller than the energy gap of the Al electrode ($\Delta = 190\mu\text{V}$).

-zero bias: Fig.4 shows the zero bias differential conductance measured between N_1 and N_2 as function of temperature. As the temperature decreases one first observes a jump in conductance near the critical temperature of aluminum ($T_c =$

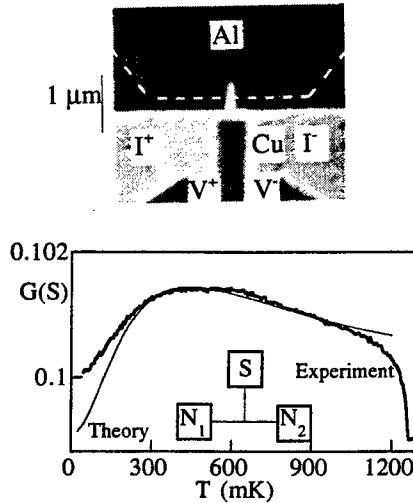


FIGURE 4. Top: Electron micrograph of the T-shape sample. The nominal length of the Cu wire between the two N-reservoirs is $L = 400\text{nm}$. The three arms of the T-shaped copper have same nominal length $L/2$. The cross-section is (width x thickness) $80 \times 50\text{nm}^2$. The normal resistance is $R_N = 10.1\Omega$ ($G_N = 0.099\text{S}$) at 1.5K . The interface resistance is about 1Ω . Bottom: Zero-bias conductance vs temperature. In comparison Usadel theory with finite temperature-independant gap. Above: micrograph of the sample in the two-probe geometry. The measurement current is 200nA .

1.25K). The conductance then increases to a maximum near 400mK and finally decreases at very low temperature. This non-monotonous behaviour is somehow paradoxical since this is precisely the temperature where the thermal length exceeds the sample length, or equivalently when the proximity region invades the whole sample.

This re-entrance effect is the consequence of the peak shape of the spectral conductance. The theoretical curve in Fig.4 has been obtained from Usadel equations with optimized parameters in order to fit simultaneously the conductance between N_1 and N_2 and the conductance between N_1 and S (not shown). The best fit parameter is $E_c = 15.5\mu V$. As can be seen both the peak position and the peak amplitude are well accounted for. This measurement is a clear illustration of the "thermal effect" discussed by Nazarov [39]. The large amplitude of this quantum contribution to conductance is quite remarkable: It exceeds the usual unit of quantum corrections (weak localization or conductance fluctuations), the conductance quantum e^2/h , by about 2 orders of magnitude. However the physics - quantum interference of electron trajectories - is the same. Since the N-S contact is separated from the measurement circuit, the behaviour near the superconducting transition is well identified: the conductance step at T_c is not due to a short-circuit by a pair current, rather it is due to the change in spectral conductance as the energy gap appears in the superconducting electrode. The theoretical curve does not describe the details of the transition region: the closure of the gap at T_c was not taken into account in the calculation. More important is the discrepancy between theory and experiment at very low temperature. The observed conductance does not return to the normal state conductance at $T \rightarrow 0$ in contrast to the prediction of the non interacting theory. A simple explanation in terms of incomplete thermalization of the electrons, *i.e.* temperature shift between the electrons and the thermometer, does not seem sufficient to explain the low temperature [47] behaviour. Whether or not it is related to electron-electron interactions [36] still remains to be elucidated.

-Non-linear conductance: Following Eq 3, the zero-temperature finite bias conductance is a direct measurement of the spectral conductance. Fig 5 shows the

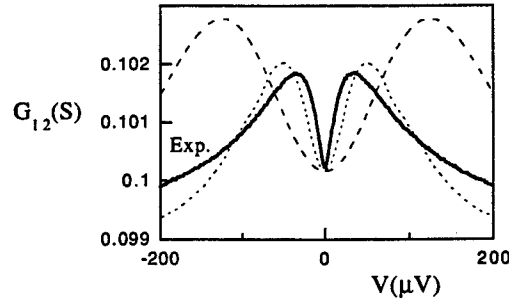


FIGURE 5. Same sample as in Fig.4: Finite bias conductance at 50 mK. Continuous line: experiment, dashed line: theory with ideal reservoirs, dotted line: theory with hot electron distribution in the N-reservoirs.

experimental differential conductance measured at $50mK$ as function of the bias voltage. As expected, a peak is observed at finite bias $V \approx 40\mu V$ which is of order of the Thouless energy. In fact the observed peak position is shifted as compared to the expected value. The dashed line in Fig 5 is the theoretical conductance as calculated assuming ideal reservoirs. It is believed that the discrepancy is due to the non-ideal electron distribution in the normal reservoirs. A hot electron distribution function with effective temperature $T_{eff} \propto V$ provides a much better agreement (Fig 5 dotted lines).

The high sensitivity of the conductance to the electron distribution functions gives rise to spectacular effects when electrons are injected from other terminals. For example the above measurements have been carried out with an additional bias current injected from the S electrode. P. Charlat [47] has completed a consistent analysis of the different combination of three terminal transport measurements: the whole data can be consistently understood by a model in which the T-shape sample is characterized by the spectral conductances g_1, g_2 and g_3 of the 3 branches. The temperature or bias dependence are derived from the reservoirs distribution functions. The data shown in Fig4 and Fig5 show how well the simple model accounts for the experiments.

Phase-sensitive conductance: We have seen that the theoretical models describes the temperature dependence of the excess conductance. Extensive studies of phase sensitive configurations has been carried out in the last years in order to demonstrate that this is an interference effect [40,41,50]. Presently there is a general agreement between the different phase sensitive experiments on both the amplitude and the main period (2π) of the magnetoconductance oscillations. Both h/e and $h/2e$ periods in magnetic flux have been observed. The possible occurrence of intrinsic $h/4e$ periodicity seems less clear: the experimental observation in Ref. [40] has been explained in terms of 2π -periodic proximity effect for the peculiar geometry of the circuit [48].

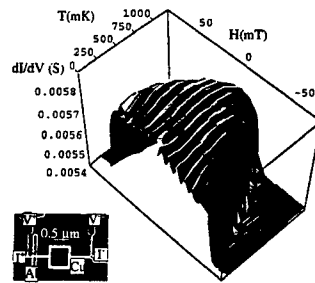


FIGURE 6. 3D view of the magnetoconductance as function of temperature. The increase of conductance takes place in the (H, T) domain where the Aluminum bar is superconducting. The critical field is close to $60mT$. Note the periodic oscillations with period $8.3mT$ which corresponds to a flux period $h/2e$ in the normal loop. Inset: micrograph of a $a = 0.5\mu m$ Cu Aharonov-Bohm square loop with a single superconducting contact. The Cu cross section is $25 \times 50nm$.

We present some experimental results on an Aharonov-Bohm geometry [49].

-Magnetococonductance: Fig6 insert shows a micrograph of a sample with a square loop of side $a = 0.5\mu\text{m}$ and cross section $25\times 50\text{nm}$. The superconducting contact is provided by an aluminum bar superposed onto the Cu wire. The magnetoconductance of this sample is shown in Fig 6 on a 3D plot *vs* temperature. The (H, T) region where the proximity effect enhances the conductance is bounded by the superconducting critical line (H, T) of the aluminum bar and forms a plateau in the figure. The zero temperature critical field of about 60mT is that expected for an evaporated Al strip of width $\approx 100\text{nm}$. From the geometry and the diffusion coefficient in this sample we estimate $E_c < 0.5\mu\text{V}$ which is about 30 times smaller than in the above T-shape sample and much less than $k_B T$. No conductance peak is observed.

The interesting feature is the presence of periodic oscillations up to the critical temperature. The period 8.3mT corresponds to a superconducting flux quantum $h/2e$ in the loop area $0.25\mu\text{m}^2$. These oscillations persist as far as the Al island is superconducting. They suddenly disappear when the magnetic field exceeds the critical field. Then only conductance fluctuations are observed. These fluctuations (not shown in Fig6) have a characteristic amplitude of order of the conductance quantum e^2/h and periodicity h/e . The presence of sample-dependent conductance fluctuations confirms that single electron trajectories are coherent over the perimeter of the loop [23].

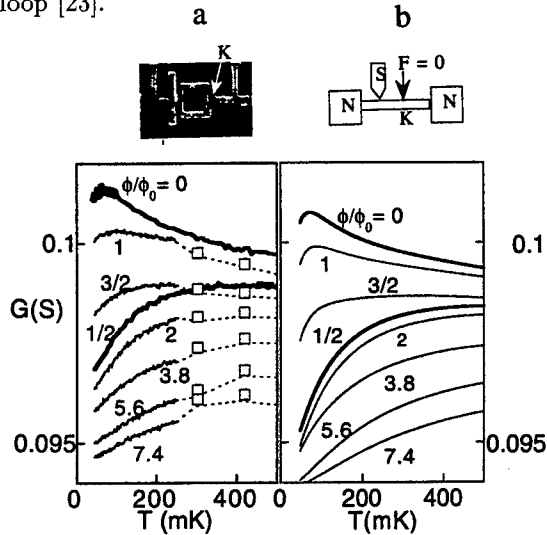


FIGURE 7. Left: Measured temperature dependence of the conductance at different values of the magnetic flux in units of the flux quantum: $\phi/\phi_0 = 0; 1/2; 3/2; 2; 3.8; 5.6; 7.4$. Right: Calculated conductance for the same flux values. The sample is modeled as shown in the inset. The arrow shows the location (K) where half flux quantum enforces a zero pair amplitude. The zero-magnetic phase breaking length is taken to be infinite.

Fig 7 shows detailed results on a sample with similar geometry but larger cross section Cu wires where the Thouless energy is larger [49]. Here $E_c \approx 1.1\mu V$. The temperature dependence of the conductance is shown for several values of the magnetic field in the loop. On this scale the conductance peak is hardly distinguishable around 60 mK (see upper trace). At half flux quantum the conductance maximum is shifted to 500mK. At one flux quantum, the conductance curve is close to the zero flux value. At higher magnetic flux, the conductance peak is displaced to higher temperatures and the periodic modulation is progressively suppressed. Hence, the magnetic field has two effects: (i) a periodic oscillation of the conductance and of the peak position; (ii) a monotonous shift of the peak to higher temperature.

These observations can be explained from a very simple application of the above Usadel equations. We first modelize the sample as shown in the inset of Fig7b. The most important contribution coming from the part on the right hand side of the loop (SKN). At zero magnetic flux the loop is ignored. At half flux quantum, destructive interference in the two arms of the loop suppresses the pair amplitude at point K.

An additional effect of the magnetic field is the renormalization of the phase breaking length due to the finite width of the Cu wire:

$$L_\phi^{-2}(H) = L_\phi^{-2}(0) + \frac{\pi^2}{3} \frac{H^2 w^2}{\phi_0^2} \quad (6)$$

When smaller than the sample length L , the phase memory length $L_\phi(H)$ plays the role of an effective length of the sample. As results, the maximum is shifted to higher temperatures as the magnetic field is increased. Fig 7 right shows the calculated conductance using this simple model. Indeed the main features of the experimental data are qualitatively reproduced. A detailed theoretical analysis of circuit with similar loop geometry has been worked out recently by Golubov et al [51].

- *Power law $1/T$ oscillation amplitude:* The difference between traces at zero and half flux quantum provides the amplitude of the magnetoconductance oscillations. A clear $1/T$ power law is found in various samples [50,49] (see Fig 8 below. Actually the relative amplitude is of order of E_c/kT at 1K. The observed $1/T$ behaviour is an important result which can be obtained from the Usadel Equations in the loop geometry. It illustrates the fact that in the high temperature regime ($kT \gg E_c$), the fraction E_c/kT of the electron distribution contributes to the interference effect. This ratio which also writes L_T^2/L^2 can be seen as the fraction of electron pairs that maintain phase coherence over the N-metal after diffusion from the S-electrode.

-**Pair current:** Josephson effect is irrelevant in a sample with a single superconducting electrode. To compare the contributions of supercurrent with the previously discussed conductance, we present some features of the data obtained on a sample with 2 superconducting electrodes [50].

Fig 8 inset shows the micrograph of a Cu loop with two symmetric superconducting Al bars. As previously described two pairs of normal I and V reservoirs are used to measure the conductance. The high temperature behaviour of the sample resistance is similar to that of the previous sample. A striking difference appears in the low temperature regime $kT < E_c$: the observed conductance suddenly increases as a Josephson current appears between the two superconducting electrodes. The corresponding critical current I_c is shown in Fig 8 as function of temperature. As expected, I_c is suppressed at high temperatures. The critical current data reveal specific features of the "long SNS junctions". Here long junctions refers to the condition $L \gg \xi_{sx}$ or equivalently $\Delta \gg E_c$. The $r_N I_c$ product is not limited by the superconducting energy gap but instead by the Thouless energy [50,56] which is much less than Δ . Here $r_N = 51\Omega$ and $r_N I_c \approx 7.5\mu V$. This behaviour, together with an unusual temperature dependence can be explained using the quasiclassical theory [57].

On the other hand, I_c is 100% modulated by the magnetic flux. This behaviour is reminiscent of a superconducting quantum interference device (SQUID) although the present mesoscopic geometry strongly differs from the classical design.

DISCUSSION AND CONCLUSION

In this lecture we have presented a few experiments which show how transport phenomena are modified in a diffusive metal by the proximity effect. In the theoretical description we have emphasized the role of quantum interferences in the "mesoscopic" normal metal. The role of the superconductor being simply that of a "mirror" which gives rise to very particular boundary conditions known as the Andreev reflexion. From the experimental point of view, it is crucial to have a well defined electron distribution, in particular in finite bias experiments. This is the role of electron reservoirs.

It appears that in conductance measurements, the "normal metal coherence

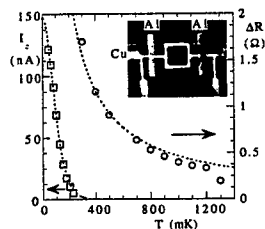


FIGURE 8. Coexistence of Josephson current and excess conductance. Left scale: temperature dependence of the critical current. The dashed line is a guide to the eyes. Right scale: Temperature dependence of the amplitude of the $h/2e$ magnetoresistance oscillations. The dashed line is a $1/T$ fit. Inset: micrograph of a sample of similar characteristics. The whole sample is copper, except the two superconducting Al islands

length L_T is not a cut-off length as it is the case in either in persistent current experiments [27] or in equilibrium Josephson pair current [11,25,26]. The excess conductance has a large amplitude that is of same order as the normal conductance itself. As a result, it hides the weaker contributions due to weak localization effects [58]. The so-called re-entrance effect, namely the suppression of the excess conductance at zero temperature is now well established experimentally (see Fig4). This effect is well accounted for by the different theoretical models. It still calls for a simple physical explanation. One could be tempted to invoke the suppression of superconductivity by the tight contact with the normal metal reservoirs. In fact tunneling experiments [59] as well as the theoretical models shows that the density of states is strongly affected at low energy. One may ask the question: does the loop shown in Fig 6 sustain a supercurrent? That experiment has not been done.

There is another situation where a re-entrance effect has been observed. The magnetic susceptibility of a normal metal cylinder with a superconducting core [65] shows a suppression of the Meissner effect at very low temperature. Experiments have been carried out at ultralow temperatures (microKelvin) on clean bulk NS cylinders. A typical sample is an Ag cylinder in good electrical contact with a superconducting Nb core. The external diameter is of order of 10 to 20 micrometers. The combination of large mean free path (ballistic regime) and very low temperatures results in huge thermal length L_T . These systems exhibit "mesoscopic" effect at unusually large length scales. This re-entrance effect appears under conditions similar to the that discussed here, namely when L_T exceeds the sample size. Let us note that the magnetization is an *equilibrium* property. It is likely of a different nature from that discussed here on a conductance experiment *i.e.* in a *non-equilibrium* situation. The observed features which are beyond the present understanding of proximity effect, calls for new theoretical developments and also for new experiments.

We have briefly discussed an experiment involving coexistence of a Josephson current with dissipative transport from normal reservoirs. This situation differs from the classical SNS junctions where N is a short bridge coupling two superconducting banks. The classical SNS junction is the basis of Josephson devices [11,52] and arrays of overdamped Josephson junctions [53,54]. Those devices are very useful since they are easier to control than tunnel devices. The Josephson coupling in a short SNS junction is usually modeled as a phase dependent inductance with shunt resistance given by the normal state resistance r_N . The mesoscopic point of view of SNS junctions is more subtle when dissipation effects and non-equilibrium situations are considered. We have seen that the Thouless energy E_c controls both the excess conductance and the Josephson current. It also controls the density of states in the normal metal: Recent tunneling experiments on a mesoscopic N-S wire demonstrated strong depression of the density of states in the N region [59]. In the structure studied in ref [59] the N metal is an "open" system where electrons (holes) are not confined. A true energy gap is not expected. In a "closed system", detailed calculations [60,61] predict the existence of a true minigap given by the Thouless energy and independent of the superconducting energy gap. This could be

surprising since E_c is typically a single particle property in the normal conductor. In fact "induced superconductivity" in a normal metal is a boundary effect. A non local interaction exists via the tail of electron wavefunctions in the superconductor. The Thouless energy precisely fixes the energy range where boundary effects are important.

The experimental study of pair current in SNS structures need clearly more attention. For example interesting predictions of negative pair current (π - junction) have been made by Volkov [62] for a SINIS junction when the states in N are driven out of equilibrium by a normal current. There is also a set of theoretical prediction in the case when N is a ballistic billard [64,63]. The subject of SNS calls for new experimental developments.

ACKNOWLEDGEMENTS

The experiments described in this lectures were performed in collaboration with Ph. Gandit. We thank D. Mailly for his contribution to this work. Enlightening discussions with A. Volkov, F. Zhou, B. Spivak, D. Estève, F. Wilhelm and A. Zaikin are gratefully acknowledged.

REFERENCES

1. See references in "Mesoscopic Superconductivity", ed. by F. Hekking, G. Schön, and D. Averin, *Physica B* **203**, (1994).
2. "Correlated Fermions and Transport in Mesoscopic Systems", ed. by G. Montambaux, T. Martin and J. Tran Thanh Van, Editions Frontieres, 1996.
3. C.W.J. Beenakker in "Mesoscopic Quantum Physics". Les Houches 1995.
4. G. Deutscher and P.G. de Gennes, in *Superconductivity*, Vol.2, R.D.Parks, ed. Marcel Dekker, New York (1969), p1005
5. "Non equilibrium Superconductivity, Phonons and Kapitza Boundaries", ed. K.E. Gray, NATO ASI vol.65, Plenum Press 1981.
6. W. Meissner and R. Ochsenfeld, *Naturwiss.* **21**, 787 (1932).
7. J. Clarke, *J. Phys. Colloque* **29**, C2-3 (1968); *Proc. Roy. Soc.* **A308**, 447 (1969).
8. A.C. Mota, *J. Low Temp. Phys.* **6**, 465 (1989).
9. L.N. Cooper, *Phys. Rev. Lett.* **6**, 689 (1961).
10. N.R. Werthamer, *Phys. Rev.* **132**, 2440 (1963).
11. P.G. de Gennes, *Rev. Mod. Phys.* **36**, 225 (1964).
12. W.L. MacMillan, *Phys. Rev.* **175**, 559 (1968).
13. A. Gilabert, *Ann. de Phys.* **2**, 203 (1977).
14. Orsay Group on Superconductivity, *Quantum Fluids* (D.F. Brewer ed.), *Proc. of the Sussex University Symposium* (1966).

15. C.J. Adkins and B.W. Kington, *Phil. Mag.* **13**, 971 (1966).
16. P. Manuel and J.J.H. Veyssié, *Solid State Com.* **13**, 1819 (1973).
17. E. Krätzig, *Solid State Com.* **9**, 1205 (1971).
18. D. Ralph, C.T. Black and M. Tinkham, *Phys. Rev. Lett.* **74**, 3241 (1995).
19. A.F. Andreev, *Zh. Eksp. Teor. Fiz.* **46**, 1823 (1964) [*Sov. J.E.T.P.* **19**, 1228 (1964)].
20. N.N. Bogolyubov, *Usp. Fiz. Nauk* **67**, 549 (1959) [*Sov. Phys. Usp.* **2**, (1059)]; P.G. de Gennes, *Superconductivity of Metals and Alloys*, Benjamin (1967); *Proc. Royal Soc. A* **308**, 447 (1969).
21. G.E. Blonder, M. Tinkham and T.M. Klapwijk, *Phys. Rev.* **B25**, 4515 (1982).
22. J.W. Wilkins, in *Tunneling Phenomena in Solids*, p333, ed. E. Burstein and S. Lundqvist, Plenum Press (1969).
23. S. Washburn and R.A. Webb, *Rep. Prog. Phys.* **55**, 1311 (1992).
24. See references in E.L. Wolf, *Principle of Electron Tunneling Spectroscopy*, Oxford University Press, (1985).
25. I.O. Kulik, *Soviet Phys. J.E.T.P.* **30**, 944 (1970).
26. L.G. Aslamasov, A.I. Larkin and Yu.N. Ovchinnikov, *Zh. Eksp. Teor. Fiz.* **55**, 323 (1968) [*Sov. Phys. JETP* **28** 171 (1969)].
27. E.K. Riedel and F. von Oppen, *Phys. Rev.* **B47**, 15449 (1993); Experimental references: L.P. Levy, G. Dolan, J. Dunsmuir and H. Bouchiat, *Phys. Rev. Lett.* **64**, 2074 (1990); V. Chandrasekhar, R.A. Webb, M.J. Brady, M.B. Ketchen, W.J. Gallagher and A. Kleinsasser, *Phys. Rev. Lett.* **67**, 3578 (1993); D. Mailly, C. Chapelier and A. Benoit, *Phys. Rev. Lett.* **70**, 2020 (1993).
28. B.J. van Wees, P. de Vries, P. Magnee and T.M. Klapwijk, *Phys. Rev. Lett.* **69**, 510 (1992).
29. F.W.J. Hekking and Y. Nazarov, *Phys. Rev. Lett.* **71**, 1625 (1993); *Phys. Rev.* **B71**, 6847 (1994).
30. A. Kastalsky, A.W. Kleinsasser, L.H. Greene, F.P. Milliken, and J.P. Harbison, *Phys. Rev. Lett.* **67**, 3026 (1991).
31. H. Pothier, S. Guéron, D. Estève and M.H. Devoret *Phys. Rev. Lett.* **73**, 2488 (1994).
32. For a review of theoretical methods, see C. Lambert, R. Raimondi and A. Volkov, this volume.
33. F. Zhou, B. Spivak, and A. Zyuzin, *Phys. Rev. B* **52**, 4467 (1995).
34. J.M. Rowell and W.L. McMillan, *Phys. Rev. Letters* **16**, 453 (1966).
35. D. Estève, in *Mesoscopic Electron Transport*, Eds. L.P. Kouwenhoven, G. Schön and L.L. Son, Kluwer Academic Publishers, Dordrecht, The Netherlands (1996).
36. Y. Nazarov and T.H. Stoof, *Phys. Rev. Letters* **76**, 823 (1996); *Phys. Rev.* **B53**, 14496 (1996).
37. V.C. Hui and C.J. Lambert, *J. Phys. Cond. Mat.* **5**, L651 (1993).
38. A. Volkov, N. Allsopp and C. Lambert, *J. Phys. Cond. Mat.* **8**, L45 (1996).
39. Nazarov developed a very general circuit theory which includes diffusive conductors, tunnel junctions and superconducting contacts with different phases. Y. Nazarov, *Phys. Rev. Lett.* **73**, 1420 (1994).
40. V.T. Petrashov, V.N. Antonov, P. Delsing and T. Cleason, *Phys. Rev. Letters* **70**, 347 (1993); *J.E.T.P. Lett.* **60**, 606 (1994); and *Phys. Rev. Letters* **74**, 5268 (1995).
41. P.G. de Vegvar and L. Glazmann, *Phys. Rev. Letters* **71**, 2351 (1993).

42. S. G. den Hartog, C. M. A. Kapteyn, B. J. van Wees, and T. M. Klapwijk, *Phys. Rev. Lett.* **76**, 4592 (1996); see also A. Dimoulas, J.P. Heida, B.J. van Wees and T.M. Klapwijk, *Phys. Rev. Lett.* **74**, 602 (1995)
43. P. Mohanty, E.M.Q. Jariwala and R.A. Webb *Phys. Rev. Lett.* **78**, 3366 (1997).
44. J. Kutchinsky, R. Taboryski, T. Clausen, C.B. Sørensen, A. Kristensen, P.E. Lindelof, J. Bindeslev Hansen, C. Shelde Jacobsen and J.L. Skov, *Phys. Rev. Lett.* **78**, 931 (1997).
45. G.J. Dolan and J.H. Dunsmuir, *Physica B* **152**, 7 (1988).
46. M. Giroud, unpublished.
47. P. Charlat, PhD thesis (1997), University J. Fourier, unpublished.
48. A.V. Zaitsev in Ref [1].
49. P. Charlat, H. Courtois, Ph. Gandit, D. Mailly, A. Volkov, and B. Pannetier, *Phys. Rev. Letters* **77**, 4950 (1996); and *Czech. J. of Phys* **46**, S6 (1996).
50. H. Courtois, Ph. Gandit, D. Mailly and B. Pannetier, *Phys. Rev. Letters* **76**, 130 (1996).
51. A.A. Golubov, F.K. Wilhelm and A.D. Zaikin, *Phys. Rev.* **B55**, 1123 (1997)
52. K.K. Likharev, *Rev. Mod. Phys.* **51**, 101 (1979); see also K.K. Likharev, *Dynamics of Josephson Junctions and Circuits*, Gordon and Breach, New York (1986).
53. M.G. Forrester, Hu Jong Lee, M. Tinkham and C.J. Lobb, *Phys. Rev.* **B37**, 5966 (1988).
54. A.L. Eichenberger, J. Affolter, M. Willemin, M. Mombelli, H. Beck and P. Martinoli, *Phys. Rev. Letters* **77**, 3905 (1996) and references there-in.
55. B.J. van Wees, K.M.H. Lensen and C.J.P.M. Harmans *Phys. Rev.* **B44** 470 (1991); see also B.J. van Wees and H. Takayanagi, in *Mesoscopic Electron Transport*, Eds. L.P. Kouwenhoven, G. Schön and L.L. Son, Kluwer Academic Publishers, Dordrecht, The Netherlands (1996).
56. H. Courtois, Ph. Gandit and B. Pannetier, *Phys. Rev.* **B52**, 1162 (1995); *Phys. Rev.* **B51**, 9360 (1995).
57. F.K. Wilhelm, A.D. Zaikin and G. Schön, *J. Low Temp. Phys.* **106**, 305 (1997).
58. B.Z. Spivak and D.E. Khmel'nitskii, *J.E.T.P. Lett.* **35**, 413 (1982).
59. S. Guéron, H. Pothier, N. O. Birge, D. Estève, M. Dévoret, *Phys. Rev. Letters* **77**, 3025 (1996).
60. A.A. Golubov, M.Y. Kupriyanov, *Pisma. Zh. Eksp. Teor. Fiz.* **61**, (1995), 830 [*J.E.T.P. Lett.* **61**, 851 (1995).]
61. F. Zhou, P. Charlat, B. Spivak and B. Pannetier, preprint *cond-mat/9707056*, submitted *J. Low Temp. Phys.* (1997).
62. A.F. Volkov, *J.E.T.P. Lett.* **61**, 5565 (1995).
63. A. Altland and M. Zirnbauer, *Phys. Rev. Letters* **76**, 3420 (1996).
64. K.M. Frahm, P.W. Brouwer, J.A. Melsen and C.W. Beenakker, *Phys. Rev. Letters* **76**, 2981 (1996).
65. P. Visani, A.C. Mota, A. Pollini and K. Aupke, *Physica B* **197**, 95 (1994); see also *Phys. Rev. Letters* **65**, 1514 (1990).

AUTHOR INDEX

B

Baert, M., 171
Bergsten, T., 313
Bruyndonex, V., 171
Bruynseraede, Y., 171

C

Charlat, P., 396
Chen, C. D., 313
Christiansen, P. L., 3
Ciria, J. C., 70
Claeson, T., 313
Costabile, G., 56
Courtois, H., 396

D

Darula, M., 144
Delsing, P., 313
Doderer, Th., 104

F

Fazio, R., 273
Filatrella, G., 56

G

Giovannella, C., 70

H

Hadley, P., 256
Haviland, D. B., 313

J

José, J. V., 217, 295

L

Lambert, C. J., 377

M

Minnhagen, P., 200
Moshchalkov, V. V., 171
Mygind, J., 126

P

Pannetier, B., 396
Pavlovskii, V. V., 343
Pedersen, N. F., 3
Puig, T., 171

R

Raimondi, R., 359
Rosseel, E., 171

S

Schön, G., 273
Strunk, C., 171

U

Ustinov, A., 31

V

Van Bael, M. J., 171
van der Zant, H. S. J., 237
Van Look, L., 171
Volkov, A. F., 343

Subject Index

Andreev		
	interferometer	351, 378
	reflection	398
	scattering	378
Bardeen-Stephens	dissipation	94, 348
Bloch	wave function	248
Bloch	oscillation	250
BKT	theory	378
BKT	transition	65, 208, 217, 220, 297, 313
Bogoliubov - de Gennes	equation	391, 399
Bose-Hubbard	model	276
Bose-Matsubara	frequency	299
boundary conditions		
	superconductor-vacuum	131
	quasiclassical Green function	347, 354
chaos		25
charge soliton		314
coarse-graining	approach	278
coherent length		175, 219, 344
conductance		
	differential	401
	excess	378, 406
	non linear	407
	matrix	384
	re-entrance	377, 412
	spectral	401
	subgap	349
	suppression	377
	two probe formula	386
conductivity oscillations		344
Coulomb		
	blockade	276, 321, 256
	interaction	276
	gas	203, 299
critical temperature		132, 208, 219, 273, 304
critical exponents		212, 220, 328
cryoelectronic devices		
	analog amplifiers	24
	analog-to-digital converter	129
	bit-error-rate	132
	digital-to-analog converter	129
	microwave oscillators (radiation sources)	24, 50, 112, 152

microwave detectors	37, 127
RSFQ	
(Rapid Single Flux Quantum)	
logic	126
time and clocking	140
SET	
transistor	257
logic	267
SIS mixers	146, 158
time-to-digital converter	129
transmission line	137
voltage standards	149
devil's staircase	98
differential equation resolution	84
diffusion coefficient	379, 399
dirty limit	368
dissipative Josephson effect	351
Drude formula	361
duality transformation	279
electron-hole phase coherence	399
fast Fourier Transform	88
Fiske steps	39, 59, 136
flux flow steps	37, 59, 136
Frenkel-Kontorova model	81
full matrix approximation	64, 74
gaussian elimination technique	391
Ginzburg-Landau equation	174
Ginzburg-Landau free energy	275
Green function	
arrays	225, 296
equation of motion	362
quasiclassical function	347, 359, 392
high T _c Josephson junctions	48, 144
Josephson inductance	133
Josephson junction arrays	
Biot-Savart equation	76
charging energy	237, 273, 296, 315
complex conductivity	210, 284
correlation length	328
degrees of freedom	86
effective penetration depth	74
elementary cell (SQUID)	61
Euler-Lagrange equation	75
extremely anisotropic (1D)	71
fabrication	105, 316
flux noise	226
frustration	
charge	274
magnetic	62, 73, 179, 213, 219,
	243, 274, 329
granular	76

Hall	
resistance	324
effect	333
quantum effect	260
Hamiltonian	219, 274, 296
helicity modulus	225, 303
imaging	104, 181
I - V characteristic	95, 107, 212, 244, 321
junction coupling energy	72, 237, 273, 295, 315
Kirchhoff law	76, 224
ladder	80
Lagrangian	72
locking	96, 113, 154
mesh current	74
microwave injection	112
microwave emission	116
partition function	278, 297
phase diagram	300
penetration depth	74, 203, 240
quantum phase model	275
quantum Hall phase	274
renormalization group	295
row-switching	96
self inductance	63, 77, 224, 240
(screening current)	
full matrix	64, 74, 91
Nakajima Sawada app.	
(mean field app.)	63
nearest neigh. app.	64
size effect	94
Shapiro steps	97, 113
spin waves excitation	239
supersolid phase	274
XY model	64, 73, 205, 217, 274
XXZ hamiltonian	279, 299
Josephson penetration depth	257
Keldysh technique	362
Landau levels	176
Landauer formula	382
locking	7, 96, 113, 154
LTSEM	38, 94, 108
matrix multiplication	87
mesoscopic	
regime	176
resistance measurement	179
structures	177, 256, 343, 405
Aharonov-Bohm geometry	404
electron reservoir	396
transport properties	343, 359, 377
magnetoconductance	410
S-N structure	343, 359, 377, 396

Montecarlo		
	simulations	220
	quantum	284, 306
Nakajima-Sawada approximation (mean field approximation)		63
nanofabrication		172, 316, 397
offset charge		264
parametric Amplification		28
proximity effect		343, 378, 396
quasi-ballistic transport		380
RSJ and CRSJ model		3, 62, 71, 147, 206, 224, 286
Runge-Kutta method		85
scattering		
	coefficient	365, 392
	matrix	365, 368
Schroedinger equation		174
Shapiro steps		97, 113, 345
single Josephson junction		
	annular	13, 33
	autonomous case	4
	I-V characteristic	12, 145, 354
	long	8, 57
	plasma frequency	6, 58
	single electron tunneling	256
	shapiro steps	147
	with external circuits	7
sine-Gordon		
	equation	9, 33, 58, 78
	discrete version	57, 78
soliton		8, 34
soliton stability		14
superconducting-insulator transition		248, 274, 307, 325
superconducting-normal structure		343
stacked Josephson Junction		43
Stewart-Mc Cumber parameter		5, 72, 106, 205, 224, 239 319
Swihart velocity		36
TDGL model		75, 206, 225
Thouless energy		399
Villain transformation		275, 298
voltage state logic		130
vortex		
	as a 'particle'	81, 237
	alternate vortex motion	94, 111
	-antivortex annihilation	11
	ballistic motion	96, 246
	bunching	42
	Cherenkov radiation	48
	depinning current	83

dispersion relation	60, 41, 244
energy	202
energy barrier	82, 103
energy dissipation	94
Gibbs energy	81
imaging	38, 109
mass	83, 95, 240
plasma waves interaction	241, 244
propagation	135
quantum dynamics	248
quantum tunneling	249
spontaneous creation	202
unbinding	208
velocity	10, 35, 93, 336
viscosity coefficient	83, 93, 241
zero bias anomaly	377
zero field step	8, 35, 58, 136
zero padding technique	87